XIV Advanced Research Workshop on High Energy Spin Physics

(DSPIN-11)

Proceedings

Joint Institute for Nuclear Research

XIV Advanced Research Workshop on High Energy Spin Physics

(DSPIN-11)

Dubna, September 20–24, 2011

Proceedings

Edited by *A.V. Efremov* and *S.V. Goloskokov*

Dubna 2012

УДК [539.12.01 + 539.12 ... 14 + 539.12 ... 162.8](063)
ББК [22.382.1 + 22.382.2 + 22.382.3]я431
А20

Sponsored by:
Joint Institute for Nuclear research,
International Committee for Spin Physics Symposia,
Russian Foundation for Basic Research.
DYNASTY Foundation,
European Physical Society

The contributions are reproduced from the originals presented by the Organizing Committee.

А20

Advanced Research Workshop on High Energy Spin Physics (13; 2011; Dubna).
Proc. of XIV Advanced Research Workshop on High Energy Spin Physics (DSPIN-11)(Dubna, September 20–24, 2011). — Dubna, JINR. — 412p.
ISBN 978-5-9530-0315-5

The collection includes contributions presented at the XIII Advanced Research Workshop on High Energy Spin Physics (DSPIN-09), (Dubna, September 20–24, 2011), on different theoretical, experimental and technical aspects of this branch of physics.

Рабочее совещание по физике спина при высоких энергиях (13; 2011; Дубна).
Тр. XIV Рабочего совещания по физике спина при высоких энергиях (DSPIN-11)(Дубна, 20–24 сентября 2011 г.) — Дубна: ОИЯИ, 2012. — 412 с.
ISBN 978-5-9530-0315-5

В сборник включены доклады представленные на XIV рабочее совещание по физике спина при высоких энергиях (Дубна, 20–24 сентября 2011 г.), по теоретическим, экспериментальным и техническим аспектам этой области физики.

УДК [539.12.01 + 539.12 ... 14 + 539.12 ... 162.8](063)
ББК [22.382.1 + 22.382.2 + 22.382.3] я 431

ISBN 978-5-9530-0315-5

Contents

Theory of spin physics

Experimental results

Technics and new developments

Related problems

WELCOME ADDRESS
by JINR Vice-Director R. Lednicky

Dear Colleagues,
Ladies and Gentlemen, on behalf of the Directorate of Joint Institute for Nuclear Research it is a pleasure to welcome you at the 14-th International Workshop on High Energy Spin Physics. The first Workshop of this series was held in Dubna already 30 years ago. It was chaired by Lev Lapidus, who, starting in the middle of fifties, contributed significantly to the development of High Energy Spin Physics for about three decades. Besides his own research, he stimulated a very fruitful and extensive participation of physicists from Eastern countries in a number of international projects devoted to this field of physics. Later on, these spin Workshops became regular due to the initiative of Anatoly Efremov, their chairman for many years.

I think there is no need to stress here the importance of the spin and polarization phenomena for deeper understanding of particle physics. The JINR laboratories are largely involved in this important field of physics including both theoretical and experimental studies. The latter have been carried out with unique polarized beams at JINR Nuclotron as well as in the outside experiments within collaborations HERMES, COMPASS and STAR. These studies will be continued also within the project NICA (Nuclotron based ion collider facility) which is presently realized in JINR.

After its completion in 2017, it will provide, besides the heavy ion beams, also polarized proton and deuteron beams in the energy range up to center-of-mass energy of about 27 GeV for proton collisions. Though the main physics goal of the NICA project is a study of the QCD matter at a highest net baryon density with a dedicated multipurpose detector MPD, we plan a construction of the second detector SPD, dedicated for Spin Physics studies. The following measurements are foreseen: Drell-Yan and J/ψ production processes with longitudinally and transversally polarized proton and deuteron beams for the extraction of unknown or poorly known parton distribution functions; spin effects in baryon, meson and photon production; spin effects in various exclusive reactions and diffractive processes; spin-dependent cross sections, helicity amplitudes and double spin asymmetries (Krisch effect) in elastic reactions; spectroscopy of quarkonia; polarimetry.

We are certainly very much interested in the assistance of the international spin community in preparation of the competitive program of polarization studies on this new facility. A worldwide cooperation is anticipated at all stages of the project - from the elaboration of the scientific program up to its realization.

Besides JINR, this Workshop is supported by the International Committee for Spin Physics as a joint Dubna-Prague-Warsaw Workshop by the Russian Foundation for Basic Research by the European Physical Society and by the DYNASTY foundation. I would like to thank the Workshop organizers for their uneasy work. I hope that you will benefit from the traditional friendly and fruitful atmosphere of this meeting. I wish you a productive work, interesting and stimulating discussions and, of course, a pleasant stay here in Dubna.

Using the occasion I would like to congratulate from the name of JINR Directorate Anatoly Radyushkin, one of the pioneers in proving the factorization in QCD and the Generalized Parton Distributions, with his 60-th anniversary. A special session is planned to be devoted to this event.

Thank you for the attention.

THEORY OF SPIN PHYSICS

Work Hard, Anatoly!

15 YEARS WITH GPDs

A.V. Radyushkin [1† 2,3]

(1) *BLTP, JINR, Dubna, Russia*
(2) *Old Dominion University, Norfolk, Virginia, USA*
(3) *Jefferson Lab, Newport News, Virginia, USA*
† *E-mail: radyush@theor.jinr.ru*

Abstract

An introductory review of Generalized Parton Distributions (GPDs) is given.

1 Introduction: What are GPDs?

The fundamental physics to be accessed via the generalized parton distributions (GPDs) [1–4] is the structure of hadrons. The situation in hadron physics may be illustrated in the following way:
i) All the relevant particles are already established, i.e., no "higgses" to find.
ii) The QCD Lagrangian is known.
iii) However, we still need to understand how QCD works, i.e., to understand hadronic structure in terms of quark and gluon fields.

Projecting quark and gluon fields $q(z_1)$, $q(z_2)$, ... onto hadronic states $|p,s\rangle$ gives matrix elements:

$$\langle\, 0\,|\,\bar q_\alpha(z_1)\, q_\beta(z_2)\,|\,M(p),s\,\rangle \quad , \quad \langle\, 0\,|\,q_\alpha(z_1)\; q_\beta(z_2)\, q_\gamma(z_3)|\,B(p),s\,\rangle \tag{1}$$

that can be interpreted as hadronic wave functions. In particular, in the light-cone (LC) formalism [5], a hadron is described by its Fock components in the infinite-momentum frame. For the nucleon, one can schematically write:

$$|P\,\rangle = |q(x_1P,k_{1\perp})q(x_2P,k_{2\perp})q(x_3P,k_{3\perp})\rangle + |qqqG\rangle + |qqq\bar qq\rangle + \dots\,, \tag{2}$$

where x_i are momentum fractions satisfying $\sum_i x_i = 1$; $k_{i\perp}$ are transverse momenta, $\sum_i k_{i\perp} = 0$. In principle, solving the bound-state equation $H|P\,\rangle = E|P\,\rangle$ one should get the wave function $|P\,\rangle$ that contains complete information about the hadron structure. In practice, however, the equation (involving an infinite number of Fock components) has not been solved yet in the realistic 4-dimensional case. Moreover, the LC wave functions are not directly accessible experimentally.

The way out in this situation is the description of hadron structure in terms of phenomenological functions. Among the "old" functions used for a long time we can list form factors, usual parton densities, and distribution amplitudes. The "new" functions, generalized parton distributions (for reviews, see [6–9]), are hybrids of form factors, parton densities and distribution amplitudes. Furthermore, the "old" functions are limiting cases of the "new" ones.

2 Form factors

The form factors are defined through matrix elements of electromagnetic (EM) and weak currents between hadronic states. In particular, the nucleon electromagnetic form factors are given by

$$\langle\, p',\, s' \,|\, J^\mu(0) \,|\, p,\, s \,\rangle = \bar{u}(p',s') \left[\gamma^\mu F_1(t) + \frac{r^\nu \sigma^{\mu\nu}}{2m_N} F_2(t)\right] u(p,s)\ ,$$

where $r = p - p'$ is the momentum transfer and $t = r^2$. The electromagnetic current is given by the sum of its flavor components:

$$J^\mu(z) = \sum_f e_f \bar{\psi}_f(z) \gamma^\mu \psi_f(z)\,.$$

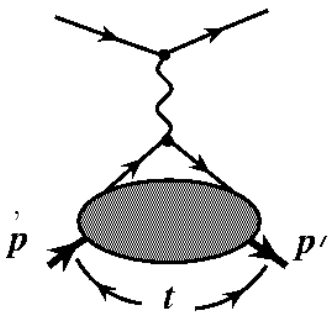

Figure 1: Elastic eN scattering in the one-photon exchange approximation.

The nucleon helicity non-flip form factor $F_1(t)$ can also be written as a sum $\sum_f e_f F_{1f}(t)$. A similar decomposition holds for the helicity flip form factor $F_2(t) = \sum_f e_f F_{2f}(t)$. At $t = 0$, these functions have well known limiting values. In particular, $F_1(t=0) = e_N = \sum_f N_f e_f$ gives total electric charge of the nucleon (N_f is the number of valence quarks of flavor f) and $F_2(t=0) = \kappa_N$ gives its anomalous magnetic moment. The form factors are measurable through elastic eN scattering.

3 Usual parton densities

The parton densities are defined through forward matrix elements of quark/gluon fields separated by light-like distances. In particular, in the unpolarized case we have

$$\langle\, p \,|\, \bar{\psi}_a(-z/2)\gamma^\mu \psi_a(z/2) \,|\, p \,\rangle\big|_{z^2=0} = 2p^\mu \int_0^1 \left[e^{-ix(pz)} f_a(x) - e^{ix(pz)} f_{\bar{a}}(x)\right] dx\ . \qquad (3)$$

In the local limit $z = 0$, the operators in this definition coincide with the operators contributing into the non-flip form factor F_1. Since $t = 0$ for the forward matrix element, we obtain the sum rule for the numbers of valence quarks:

$$\int_0^1 \left[f_a(x) - f_{\bar{a}}(x)\right] dx = N_a\,. \qquad (4)$$

The definition of parton densities has the form of the plane wave decomposition. This observation allows one to give the momentum space interpretation: $f_{a(\bar{a})}(x)$ is the probability to find $a\,(\bar{a})$-quark with momentum xp inside a nucleon with momentum p. The classic process to access the usual parton densities is deep inelastic scattering (DIS) $\gamma^* N \to X$.

Using the optical theorem, the $\gamma^* N \to X$ cross section is given by the imaginary part of the forward virtual Compton scattering amplitude. The momentum transfer q is spacelike $q^2 \equiv -Q^2$, and when it is sufficiently large, perturbative QCD factorization works. At the leading order, one deals with the so-called handbag diagram, see figure 2.

Through simple algebra, $\frac{1}{\pi}\mathrm{Im}\ 1/(q+xp)^2 \approx \delta(x - x_B)/2(pq)$, one finds that DIS measures parton densities at the point $x = x_B$, where the parton momentum fraction equals the Bjorken variable $x_B = Q^2/2(pq)$. Comparing parton densities to form factors, we note that the latter have a point vertex instead of a light-like separation and $p \neq p'$.

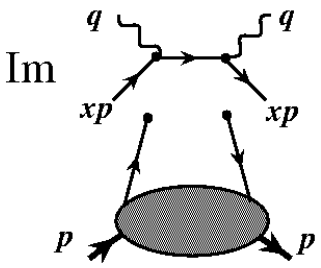

Figure 2: Lowest order pQCD factorization for DIS.

4 Nonforward parton densities

"Hybridization" of different parton distributions is the key idea of the GPD approach. As the first step, we can combine form factors with parton densities [10] and write the flavor components $F_{1a}(t)$ of form factors as integrals over the momentum fraction variable x:

$$F_{1a}(t) = \int_0^1 \left[\mathcal{F}_a(x,t) - \mathcal{F}_{\bar{a}}(x,t)\right] dx \ . \tag{5}$$

In the forward limit $t = 0$, the new objects—nonforward parton densities $\mathcal{F}_{a(\bar{a})}(x,t)$ (NPDs)—coincide with the usual ("forward") densities:

$$\mathcal{F}_{a(\bar{a})}(x, t=0) = f_{a(\bar{a})}(x)\,. \tag{6}$$

NPDs can be also treated as Fourier transforms of the impact parameter $b_\perp$ distributions $f(x, b_\perp)$ describing the variation of parton densities in the transverse plane [11, 12].

A nontrivial question is the interplay between x and t dependencies of $\mathcal{F}_{a(\bar{a})}(x,t)$. The simplest factorized ansatz $\mathcal{F}_a(x,t) = f_a(x)F_1(t)$ satisfies both the forward constraint, $\mathcal{F}_a(x, t=0) = f_a(x)$, and also the local constraint (5). The reality may be more complicated: light-cone wave functions with Gaussian $k_\perp$ dependence

$$\Psi(x_i, k_{i\perp}) \sim \exp\left[-\frac{1}{\lambda^2}\sum_i k_{i\perp}^2/x_i\right] \tag{7}$$

suggest that

$$\mathcal{F}^a(x,t) = f_a(x) e^{\bar{x}t/2x\lambda^2}\,, \tag{8}$$

where $\bar{x} \equiv 1 - x$. Taking $f_a(x)$ from existing parametrizations and adjusting λ^2 to provide the standard value of the quark intrinsic transverse momentum $\langle k_\perp^2 \rangle \approx (300\,\mathrm{MeV})^2$ gives a rather reasonable description of the proton form factor $F_1(t)$ in a wide range of momentum transfers $-t \sim 1 - 10$ GeV^2 [10]. To comply with the Regge behavior, one may wish to change $e^{\bar{x}t/2x\lambda^2} \to x^{-\alpha' t}$, where α' is the Regge trajectory slope. The modified Regge ansatz,

$$\mathcal{F}^a(x,t) = f_a(x) x^{-\alpha'(1-x)t}\,, \tag{9}$$

allows one to easily fit electromagnetic form factors for the proton and neutron [13]. A similar model was proposed in Ref. [14].

The same nonforward parton densities appear in the handbag diagrams for the wide-angle real Compton scattering, see figure 3.

The handbag contribution is approximately given by the product of a new form factor, $R_V^a(t)$, and the cross section of the Compton scattering off an elementary fermion (given by Klein–Nishina expression):

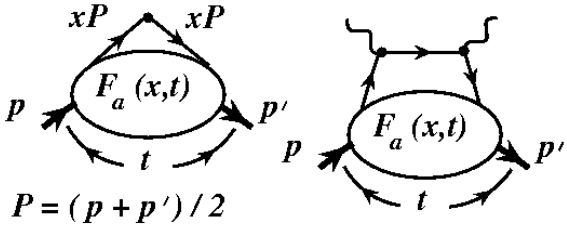

Figure 3: Compton scattering amplitude in terms of nonforward parton densities.

$$\frac{d\sigma}{dt} = \left[\sum_a e_a^2 R_V^a(t)\right]^2 \left.\frac{d\sigma}{dt}\right|_{KN} \quad \text{with} \quad R_V^a(t) = \int_0^1 \frac{\mathcal{F}^a(x,t)}{x}\, dx \ . \tag{10}$$

The predictions based on handbag dominance and NPDs [10, 15] are in much better agreement with the existing data [16] than the predictions based on two-gluon hard exchange mechanism of asymptotic perturbative QCD: the predicted cross section is too small in the latter case. The absolute normalization for predictions is settled by the form of the nonperturbative functions (NPDs in the handbag approach and nucleon distribution amplitudes in the pQCD approach) which were fixed by fitting the F_1 form factor data. Still, when there is an uncertain overall factor, it is risky to make strong statements. Remarkably, the perturbative QCD hard scattering mechanism and soft handbag mechanism give drastically different predictions for the polarization asymmetry A_{LL} [15]. Experiment E-99-114 performed at Jefferson Lab [16] strongly favors handbag mechanism that predicts the value close to the asymmetry for the scattering on a single quark.

5 Distribution amplitudes

Another example of nonperturbative functions describing the hadron structure are the distribution amplitudes (DAs). They can be interpreted as light cone wave functions integrated over transverse momentum, or as $\langle 0|\ldots|p\rangle$ matrix elements of light cone operators. In the case of the pion, we have

$$\langle\, 0\,|\,\bar\psi_d(-z/2)\gamma_5\gamma^\mu\psi_u(z/2)\,|\,\pi^+(p)\,\rangle\big|_{z^2=0} = ip^\mu f_\pi \int_{-1}^{1} e^{-i\alpha(pz)/2}\varphi_\pi(\alpha)\, d\alpha\,, \tag{11}$$

with $x_1 = (1+\alpha)/2,\ x_2 = (1-\alpha)/2$ being the fractions of the pion momentum carried by the quarks. The distribution amplitudes describe the hadrons in situations when the pQCD hard scattering approach is applicable to exclusive processes. The classic example is the $\gamma^*\gamma \to \pi^0$ transition; its amplitude is proportional to the $1/(1-\alpha^2)$ moment of $\varphi_\pi(\alpha)$, see figure 4. The predictions for the $\gamma^*\gamma \to \pi^0$ form factor based on two competing models for the pion DA, the asymptotic $\varphi_\pi^{as}(\alpha) = \frac{3}{4}(1-\alpha^2)$ and Chernyak-Zhitnitsky DA $\varphi_\pi^{CZ}(\alpha) = \frac{15}{4}\alpha^2(1-\alpha^2)$ differ by factor of 5/3, which allows for an experimental discrimination between them. A comparison with CLEO and CELLO data for $Q^2F_{\gamma^*\gamma\pi^0}(Q^2)$ favors $\varphi^{as}(\alpha)$. However, recent BaBar data [17] show increase of the combination $Q^2F(Q^2)$ in the region $Q^2 > 10$ GeV^2, which may be explained by assuming a flat distribution amplitude [18, 19].

It is also worth noting that perturbative QCD works here from rather small values of momentum transfer $Q^2 \sim 2\,\mathrm{GeV}^2$. Another classic application of pQCD to exclusive processes is the pion electromagnetic form factor, see figure 4. With the asymptotic pion DA $\varphi_\pi^{as}(\alpha)$, the hard pQCD contribution to $F_\pi(Q^2)$ is $(2\alpha_s/\pi)(0.7\,\mathrm{GeV}^2)/Q^2$, which is less than 1/3 of the experimental value. So, in this case we deal with the dominance of the competing soft mechanism which is described by nonforward parton densities, exactly in the same way as the proton form factor $F_1^p(t)$ discussed in the previous section.

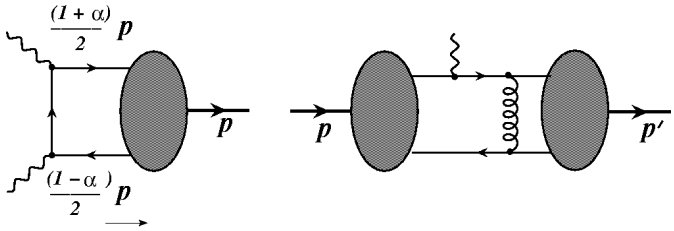

Figure 4: Lowest-order pQCD factorization for $\gamma^*\gamma \to \pi^0$ transition amplitude and for the pion electromagnetic form factor.

6 Hard electroproduction processes

Another attempt to use perturbative QCD to extract new information about hadronic structure is the study of deep exclusive photon [2] or meson [3, 4] electroproduction reactions. In the hard kinematics when both Q^2 and $s \equiv (p+q)^2$ are large while the momentum transfer $t \equiv (p-p')^2$ is small, one can use pQCD factorization which represents the amplitudes as a convolution of a perturbatively calculable short-distance amplitude and nonperturbative parton functions describing the hadron structure. The hard pQCD subprocesses in these two cases have different structure, see figure 5. Since the photon is a pointlike particle, the deeply virtual Compton scattering (DVCS) amplitude has the structure similar to that of the $\gamma^*\gamma\pi^0$ form factor: the pQCD hard term is of zero order in α_s (the handbag mechanism), and there is no competing soft contribution. Thus, we can expect that pQCD works from $Q^2 \sim 2\,\mathrm{GeV}^2$. On the other hand, the deeply virtual meson production process is similar to the pion EM form factor: the hard term has a $O(\alpha_s/\pi) \sim 0.1$ suppression factor. As a result, the dominance of the hard pQCD term may be postponed to $Q^2 \sim 5 - 10\,\mathrm{GeV}^2$.

One should also have in mind that the competing soft mechanism can mimic the same power-law Q^2-behavior (just like in case of pion and nucleon EM form factors). Hence, a mere observation of a "right" power-law behavior of the cross section may be insufficient to claim that pQCD is already working. One should look at other characteristics of the reaction, especially its spin properties, to make strong statements about the reaction mechanism.

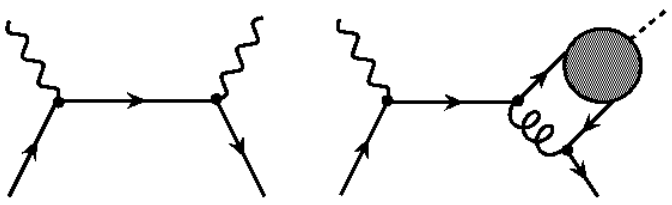

Figure 5: Lowest-order factorization for deeply virtual photon and meson production.

7 Deeply virtual Compton scattering and generalized parton distributions

It is convenient to visualize DVCS in the $\gamma^* N$ center-of-mass frame, with the initial hadron and the virtual photon moving in opposite directions along the z-axis. Since the momentum transfer t is small, the hadron and the real photon in the final state also move close to the z-axis. This means that the virtual photon momentum $q = q' - x_B p$ has the component $-x_B p$ canceled by the momentum transfer r. In other words, the momentum transfer r has the longitudinal component $r^+ = x_B p^+$, where $x_B = Q^2/2(pq)$ is the DIS Bjorken variable. One can say that DVCS has a skewed kinematics in which the final hadron has the "plus" momentum $(1-\zeta)p^+$ that is smaller than that of the initial hadron. In the particular case of DVCS, we have $\zeta = x_B$.

The parton picture for DVCS has some similarity to that of DIS, with the main difference that the plus-momenta of the incoming and outgoing quarks in DVCS are not equal; they are Xp^+ and $(X-\zeta)p^+$, see figure 5. Another difference is that the invariant momentum transfer t in DVCS is nonzero: the matrix element of partonic fields is essentially nonforward.

Thus, the nonforward parton distributions (NFPDs) $\mathcal{F}_\zeta(X,t)$ describing the hadronic structure in DVCS depend on X (the fraction of p^+ carried by the outgoing quark), ζ (the skewedness parameter characterizing the difference between initial and final hadron momenta), and t (the invariant momentum transfer). In the forward $r = 0$ limit, we have a reduction formula

$$\mathcal{F}^a_{\zeta=0}(X, t=0) = f_a(X) \tag{12}$$

relating NFPDs with the usual parton densities. The nontriviality of this relation is that $\mathcal{F}_\zeta(X,t)$ appear in the amplitude of the exclusive DVCS process, while the usual parton densities are measured from the cross section of the inclusive DIS reaction.

Another limit for NFPDs is zero skewedness $\zeta = 0$, where they correspond to nonforward parton densities: $\mathcal{F}^a_{\zeta=0}(X,t) = \mathcal{F}^a(X,t)$. The local limit relates NFPDs to form factors:

$$\int_0^1 \mathcal{F}^a_\zeta(X,t)\,\frac{dX}{1-\zeta/2} = F_1^a(t)\,. \tag{13}$$

The description in terms of NFPDs has the advantage of using the variables most close to those of the usual parton densities. However, the initial and final hadron momenta are not treated symmetrically in this scheme. Ji [2] proposed to use symmetric variables in which the plus-momenta of the hadrons are $(1+\xi)P^+$ and $(1-\xi)P^+$, and those of the active partons are $(x+\xi)P^+$ and $(x-\xi)P^+$, P being the average momentum $P = (p+p')/2$, see figure 6. In the simplified case of scalar fields, the GPD parametrization of the nonforward matrix element is

$$\langle P + r/2|\psi(-z/2)\psi(z/2)|P - r/2\rangle = \int_{-1}^1 e^{-ix(Pz)} H(x,\xi)\,dx + \mathcal{O}(z^2)\,. \tag{14}$$

To take into account the spin properties of hadrons and quarks, one needs four off-forward parton distributions $H, E, \tilde{H}, \widetilde{E}$, each of which is a function of x, ξ, and t. The skewness parameter $\xi \equiv r^+/2P^+$ can be expressed in terms of the Bjorken variable, $\xi = x_B/(2-x_B)$, but it does not coincide with it.

Depending on the value of x, each GPD has 3 distinct regions. When $\xi < x < 1$, GPDs are analogous to usual quark distributions; when $-1 < x < -\xi$, they are similar to antiquark distributions. In the region $-\xi < x < \xi$, the "returning" quark has a negative momentum and should be treated as an outgoing antiquark with momentum $(\xi - x)P$. The total $q\bar{q}$ pair momentum $r = 2\xi P$ is shared by the quarks in fractions $r(1 + x/\xi)/2$ and $r(1 - x/\xi)/2$. Hence, a GPD in the region $-\xi < x < \xi$ is similar to a distribution amplitude $\Phi(\alpha)$ with $\alpha = x/\xi$.

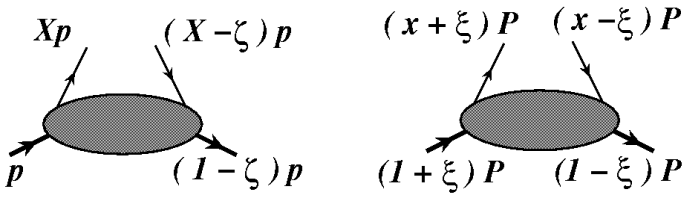

Figure 6: Comparison of NFPDs and OFPDs. .

In the local limit, GPDs reduce to elastic form factors:

$$\sum_a e_a \int_{-1}^{1} H^a(x,\xi;t)\,dx = F_1(t) \quad , \quad \sum_a e_a \int_{-1}^{1} E^a(x,\xi;t)\,dx = F_2(t)\,. \tag{15}$$

The E function, like $F_2(t)$, comes with the r_μ factor. Hence, it is invisible in DIS described by the forward $r = 0$ Compton amplitude. However, the $t = 0, \xi = 0$ limit of E exists:

$$E^{a,\bar{a}}(x, \xi = 0; t = 0) \equiv \kappa^{a,\bar{a}}(x)\,. \tag{16}$$

In particular, its integral gives the proton anomalous magnetic moment κ_p,

$$\sum_a e_a \int_{-0}^{1} (\kappa^a(x) - \kappa^{\bar{a}}(x))\,dx = \kappa_p\,, \tag{17}$$

while its first moment enters Ji's sum rule for the total quark contribution J_q to the proton spin:

$$J_q = \frac{1}{2}\sum_a \int_{-0}^{1} x\,[f^a(x) + f^{\bar{a}}(x) + \kappa^a(x) + \kappa^{\bar{a}}(x)]\,dx\ . \tag{18}$$

Note that only valence quarks contribute to κ_p, while J_q involves also sea quarks. Furthermore, the values of $\kappa_{p,n}$ (unlike $e_{p,n} \equiv F_1^{p,n}(0)$) strongly depend on dynamics, e.g., $\kappa_N \sim 1/m_q$ in constituent quark models.

8 Double distributions

To model GPDs, two approaches are used: a direct calculation in specific dynamical models: bag model, chiral soliton model, light-cone formalism, etc., and a phenomenological construction based on the relation of GPDs to usual parton densities $f_a(x), \Delta f_a(x)$ and form factors $F_1(t), F_2(t), G_A(t), G_P(t)$. The key question in the second approach is the interplay between x, ξ and t dependencies of GPDs. There are not so many cases in which the pattern of the interplay is evident. One example is the function $\widetilde{E}(x,\xi,t)$ which is

related to the $G_P(t)$ form factor and is dominated for small t by the pion pole term $1/(t-m_\pi^2)$. It is also proportional to the pion distribution amplitude $\varphi(\alpha) \approx \frac{3}{4} f_\pi (1-\alpha^2)$ taken at $\alpha = x/\xi$. The construction of self-consistent models for other GPDs is performed using the ansatz based on the formalism of double distributions (DD) [20].

The main idea behind the double distributions is a "superposition" of P^+ and r^+ momentum fluxes, i.e., the representation of the parton momentum $k^+ = \beta P^+ + (1+\alpha) r^+/2$ as the sum of a component βP^+ due to the average hadron momentum P (flowing in the s-channel) and a component $(1+\alpha) r^+/2$ due to the t-channel momentum r, see figure 7. In the simplified case of scalar fields, the DD parametrization reads

$$\langle P - r/2 | \psi(-z/2) \psi(z/2) | P + r/2 \rangle = \int_\Omega F(\beta,\alpha)\, e^{-i\beta(Pz) - i\alpha(rz)/2}\, d\beta\, d\alpha + \mathcal{O}(z^2)\ . \quad (19)$$

Thus, the double distribution $f(\beta,\alpha)$ (we consider here for simplicity the $t=0$ limit) looks like a usual parton density with respect to β and like a distribution amplitude with respect to α. The connection between the DD variables β, α and the GPD variables x, ξ is obtained from $r^+ = 2\xi P^+$, which results in the basic relation $x = \beta + \xi\alpha$. The formal connection between DDs and GPDs is

$$H(x,\xi) = \int_\Omega F(\beta,\alpha)\, \delta(x - \beta - \xi\alpha)\, d\beta\, d\alpha\ . \quad (20)$$

The forward limit $\xi = 0$, $t = 0$ corresponds to $x = \beta$, and gives the relation between DDs and the usual parton densities:

$$\int_{-1+|\beta|}^{1-|\beta|} F_a(\beta,\alpha;t=0)\, d\alpha = f_a(\beta)\ . \quad (21)$$

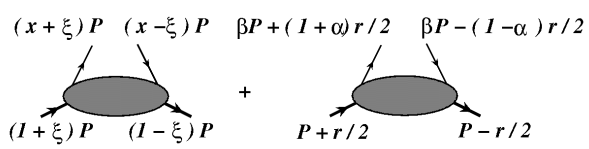

Figure 7: Comparison of GPD and DD descriptions.

The DDs live on the rhombus $|\alpha| + |\beta| \le 1$ [denoted by Ω in (19) and (20)] and are symmetric functions of the "DA" variable α: $f_a(\beta,\alpha;t) = f_a(\beta,-\alpha;t)$ ("Munich" symmetry [21]). These restrictions suggest a factorized representation for a DD in the form of a product of a usual parton density in the β-direction and a distribution amplitude in the α-direction:

$$F(\beta,\alpha) = f(\beta)\, h(\beta,\alpha)\ ,\ h_N(\beta,\alpha) \sim \frac{[(1-|\beta|)^2 - \alpha^2]^N}{(1-|\beta|)^{2N+1}}\ ,\ \int_{-1+|\beta|}^{1-|\beta|} h(\beta,\alpha)\, d\alpha = 1\,. \quad (22)$$

To obtain usual parton densities from DDs, one should integrate (scan) them over the vertical lines $\beta = x = \text{const}$. To obtain the GPD $H(x,\xi)$ with nonzero ξ from DDs $f(\beta,\alpha)$, one should integrate (scan) DDs along the parallel lines $\alpha = (x-\beta)/\xi$ with a ξ-dependent slope. One can call this process the DD-tomography. The basic feature of GPDs $H(x,\xi)$ resulting from DDs is that for $\xi = 0$ they reduce to usual parton densities, and for $\xi = 1$ they have a shape like a meson distribution amplitude. A more complete truth is that such a DD modeling misses terms invisible in the forward limit: meson-exchange contributions and so-called D-term, which can be interpreted as σ-exchange. The inclusion of the D-term induces nontrivial behavior in the central $|x| < \xi$ region (for details, see [22]).

9 GPDs and the structure of hadrons

Hadronic structure is a complicated subject, and it requires a study from many sides and in many different types of experiments. The description of specific aspects of hadronic structure is provided by several different functions: form factors, usual parton densities, distribution amplitudes. Generalized parton distributions provide a unified description: all these functions can be treated as particular or limiting cases of GPDs $H(x,\xi,t)$.

Usual parton densities $f(x)$ correspond to the case $\xi = 0, t = 0$. They describe a hadron in terms of probabilities $\sim |\Psi|^2$. However, QCD is a quantum theory: GPDs with $\xi \neq 0$ describe correlations $\sim \Psi_1^* \Psi_2$. Taking only the point $t = 0$ corresponds to integration over impact parameters $b_\perp$ — information about the transverse structure is lost.

Form factors $F(t)$ contain information about the distribution of partons in the transverse plane, but $F(t)$ involve integration over momentum fraction x — information about longitudinal structure is lost.

A simple "hybridization" of usual densities and form factors in terms of NPDs $\mathcal{F}(x,t)$ (GPDs with $\xi = 0$) shows that the behavior of $F(t)$ is governed both by transverse and longitudinal distributions. GPDs provide adequate description of nonperturbative soft mechanism. They also allow to study transition from sort to hard mechanism.

Distribution amplitudes $\varphi(x)$ provide quantum-level information about the longitudinal structure of hadrons. In principle, they are accessible in exclusive processes at large momentum transfer, when hard scattering mechanism dominates. GPDs have DA-type structure in the central region $|x| < \xi$.

Generalized parton distributions $H(x,\xi,t)$ provide a 3-dimensional picture of hadrons. GPDs also provide some novel possibilities, such as "magnetic distributions" related to the spin-flip GPD $E(x,\xi,t)$. In particular, the structure of nonforward density $E(x,\xi=0,t)$ determines the t-dependence of $F_2(t)$. Recent JLab data give $F_2(t)/F_1(t) \sim 1/\sqrt{-t}$ rather than $1/t$ expected in hard pQCD and many models — a puzzle waiting to be resolved. The forward reductions $\kappa^a(x)$ of $E(x,\xi,t)$ look as fundamental as $f^a(x)$ and $\Delta f^a(x)$: Ji's sum rule involves $\kappa^a(x)$ on equal footing with $f(x)$. Magnetic properties of hadrons are strongly sensitive to dynamics providing a testing ground for models. The GPDs for $N \to N + \text{soft } \pi$ processes can be used for testing the soft pion theorems and physics of chiral symmetry breaking.

An interesting problem is the separation and flavor decomposition of GPDs. The DVCS amplitude involves all four types of GPDs, $H, E, \widetilde{H}, \widetilde{E}$, so we need to study other processes involving different combinations of GPDs. An important observation is that, in hard electroproduction of mesons, the spin nature of produced meson dictates the type of GPDs involved, e.g., for pion electroproduction, only $\widetilde{H}, \widetilde{E}$ appear, with $\widetilde{E}$ dominated by the pion pole at small t. This gives an access to (generalization of) polarized parton densities without polarizing the target.

In summary, the structure of hadrons is the fundamental physics to be accessed via GPDs. GPDs describe hadronic structure on the quark-gluon level and provide a three-dimensional picture ("tomography") of the hadronic structure. GPDs adequately reflect the quantum-field nature of QCD (correlations, interference). They also provide new insights into spin structure of hadrons (spin-flip distributions, orbital angular momentum). GPDs are sensitive to chiral symmetry breaking effects, a fundamental property of QCD. Furthermore, GPDs unify existing ways of describing hadronic structure. The

GPD formalism provides nontrivial relations between different exclusive reactions and also between exclusive and inclusive processes.

References

[1] D. Muller, D. Robaschik, B. Geyer, F. M. Dittes and J. Horejsi, Fortsch. Phys. **42**, 101 (1994).

[2] X. D. Ji, Phys. Rev. Lett. **78**, 610 (1997), X. D. Ji, Phys. Rev. D **55**, 7114 (1997).

[3] A. V. Radyushkin, Phys. Lett. B **380**, 417 (1996), Phys. Lett. B **385**, 333 (1996), Phys. Rev. D **56**, 5524 (1997).

[4] J. C. Collins, L. Frankfurt and M. Strikman, Phys. Rev. D **56**, 2982 (1997).

[5] S. J. Brodsky and G. P. Lepage, in: A. H. Mueller (Ed.), Perturbative Quantum Chromodynamics, World Scientific, 1989.

[6] K. Goeke, M. V. Polyakov and M. Vanderhaeghen, Prog. Part. Nucl. Phys. **47**, 401 (2001).

[7] M. Diehl, Phys. Rept. **388**, 41 (2003).

[8] A. V. Belitsky and A. V. Radyushkin, Phys. Rept. **418**, 1 (2005).

[9] S. Boffi and B. Pasquini, Riv. Nuovo Cim. **30**, 387 (2007).

[10] A. V. Radyushkin, Phys. Rev. D **58**, 114008 (1998).

[11] M. Burkardt, Phys. Rev. D **62**, 071503 (2000) [Erratum-ibid. D **66**, 119903 (2002)]

[12] M. Burkardt, Int. J. Mod. Phys. A **18**, 173 (2003).

[13] M. Guidal, M. V. Polyakov, A. V. Radyushkin and M. Vanderhaeghen, Phys. Rev. D **72**, 054013 (2005)

[14] M. Diehl, T. Feldmann, R. Jakob and P. Kroll, Eur. Phys. J. C **39**, 1 (2005)

[15] M. Diehl, T. Feldmann, R. Jakob and P. Kroll, Eur. Phys. J. C **8**, 409 (1999).

[16] D. J. Hamilton *et al.* [Jefferson Lab Hall A Collaboration], Phys. Rev. Lett. **94**, 242001 (2005).

[17] B. Aubert *et al.* [The BABAR Collaboration], Phys. Rev. D **80** (2009) 052002 [arXiv:0905.4778 [hep-ex]].

[18] A. V. Radyushkin, Phys. Rev. D **80** (2009) 094009

[19] M. V. Polyakov, JETP Lett. **90** (2009) 228

[20] A. V. Radyushkin, Phys. Rev. D **59**, 014030 (1999).

[21] L. Mankiewicz, G. Piller and T. Weigl, Eur. Phys. J. C **5**, 119 (1998).

[22] M. V. Polyakov and C. Weiss, Phys. Rev. D **60** (1999) 114017

AN EXPLANATION OF THE NEW POLARIZATION DATA IN THE FRAMEWORK OF EFFECTIVE COLOR FIELD MODEL

V.V. Abramov [1]

(1) *Institute for High Energy Physics, Protvino, Russia*
† *E-mail: Victor.Abramov@ihep.ru*

Abstract

New data on the polarization and the SSA are discussed in the framework of the Effective Color Field (ECF) model. The origin of large spin effects is connected with the microscopic Stern-Gerlach mechanism and the spin precession of the quarks in the effective color field of the QCD strings. Along with data on inclusive processes for the first time in a global analysis are also included the exclusive reactions. From the analysis of the polarization data are obtained estimates of the size of ECF, the dynamical quark masses and their anomalous chromomagnetic moments.

In this report we discuss the semi-classical mechanism of single-spin phenomena in inclusive reactions $A^{\uparrow} + B \to C + X$ and $A + B \to C^{\uparrow} + X$. The explanation of new and some old but not yet interpret data is possible within a model of effective color field (ECF) [1, 2]. It is assumed in the ECF model that the color string field that is created after an initial color exchange, has a circular chromomagnetic and a linear chromoelectric components. Microscopic Stern-Gerlach like mechanism in a inhomogeneous ECF and the spin precession of the quark is a source of polarization phenomena. Circular chromomagnetic field has a focusing or defocusing effect on the probe quarks and this results in the first case in the resonance like energy dependence of the polarization observables. Contribution to the color field of $q\bar{q}$ pairs produced at high energies is a linear function of the hadron multiplicity in the event. Global analysis of worldwide single-spin data is done, which includes 86 inclusive and exclusive reactions with more than 5500 data points.

There are a longitudinal chromoelectric field $\mathbf{E^a}$ and a circular chromomagnetic field $\mathbf{B^a}$ of the ECF, which are shown schematically in Fig. 1a [3, 1].

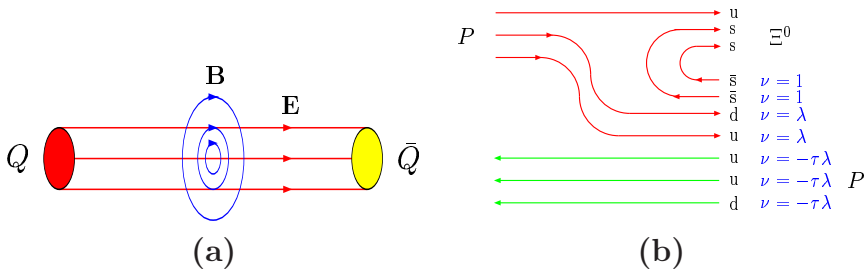

Figure 1: **(a)** Schematic picture of the string between a quark and an antiquark. **(b)** Quark flow diagram for the reaction $p + p \to \Xi^{0\uparrow} + X$. The weight ν of the spectator quark contribution to the ECF is indicated. Net contribution of the spectator quarks to the ECF is $\nu_A = (2 + 2\lambda - 3\tau\lambda)$.

The quark Q of the observed hadron C, which receives p_T kick of the Stern-Gerlach force and is spinning in the ECF is called a "probe" and it "measures" integrals of the

fields $\mathbf{B^a}$ and $\mathbf{E^a}$. The spectators are all the quarks, which are not constituents of the observed hadron C. For example, in the case $p+p \to \Xi^{0\uparrow} + X$ reaction (see Fig. 1b) the probe s quark from the Ξ^0 "measures" the field, created by forward moving spectator quarks with weight $\nu_A = \lambda$, by antiquarks with weight $\nu_A = 1$, and by backward moving target quarks with weight $\nu_B = -\tau\lambda$, respectively, where $\tau = 0.0534 \pm 0.0009$. The value of the color factor $\lambda = -0.1332 \pm 0.0006$, obtained in a global analysis of 86 reactions, is close to the expected $\lambda_0 = -|\Psi_{qq'}(0)|^2/|\Psi_{q\bar{q}'}(0)|^2 \approx 1 - e^{1/8} \approx -0.13315$, that is a strong argument in favor of the ECF model [1, 2].

The quark spin precession is described by the Bargman-Michel-Telegdi eqs. (1)-(2) [4]:

$$d\xi/dt = a[\xi \mathbf{B^a}] + d[\xi[\mathbf{E^a v}]], \tag{1}$$

$$a = g_S(g^a_Q - 2 + 2M_Q/E_Q)/2M_Q\,, \quad d = g_S[g^a_Q - 2E_Q/(E_Q + M_Q)]/2M_Q\,. \tag{2}$$

The precession frequency depends on the color charge g_S, quark mass M_Q and its energy E_Q, as well as color g^a_Q-factor. Variable $\Delta\mu^a_Q = (g^a_Q - 2)/2$ is called a color anomalous magnetic moment and it has a negative value in the instanton model [5, 6].

The equations describing the hadron SSA or hyperon polarization can be written as [1]

$$A_N = C(\sqrt{s})F(p_T, A)[G(\phi_A) - \sigma G(\phi_B)]; \tag{3}$$

$$G(\phi) = (1 - \cos\phi)/\phi + \epsilon \cdot \phi\,, \quad C(\sqrt{s}) = v_0/[(1 - E_R/\sqrt{s})^2 + \delta^2_R]^{1/2}\,; \tag{4}$$

$$F(p_T, A) = (1 - \exp[-(p_T/p^0_T)^3])(1 - \alpha \ln A)\,, \quad \phi_{A(B)} = \omega^0_{A(B)} y_{A(B)}\,; \tag{5}$$

$$v_0 = \frac{-Dg^a_Q \xi^0_y}{2\rho(g^a_Q - 2)}\,, \quad \omega^0_{A(B)} = \frac{g_s \alpha_s \nu_{A(B)} S_0 (g^a_Q - 2)}{M_Q v \rho^2}\,; \tag{6}$$

where $\xi^0_y = \pm\Theta(x_F - x_0)$ is polarization of the valence $u(d)$ quark in the proton, $\rho = 0.94 \pm 0.02$ fm is an effective transverse radius of ECF. The $G(\phi_{A(B)})$ takes into account the oscillating Stern-Gerlach force acting on the probe quark in the fragmentation region of the hadron $A(B)$. The $C(\sqrt{s})$ describes the effect of probe quark focusing in the ECF. The $F(p_T, A)$ is a color form-factor. The variable $y_{A(B)}$ takes into account the motion of quarks inside proton and the spin precession in ECF:

$$y_A = x_A - (E_0/\sqrt{s} + f_0)(1 + \cos\theta_{cm}) + a_0(1 - \cos\theta_{cm}), \tag{7}$$

$$y_B = x_B - (E_0/\sqrt{s} + f_0)(1 - \cos\theta_{cm}) + a_0(1 + \cos\theta_{cm}), \tag{8}$$

where $x_{A(B)} = (x_R \pm x_F)/2$ and θ_{cm} is the angle of registration of hadron in c.m., a_0, f_0 and E_0 are the phenomenological parameters [1, 2]. The $S_0 = 1.489 \pm 0.062$ fm is the length of ECF, and $\epsilon = -0.00461 \pm 0.00006$. There are 8 local parameters for each reaction: α, σ, E_0, E_R, f_0, a_0, x_0, p^0_T, some of which can be expressed as functions of global parameters. There are 43 global parameters for 86 reactions (S_0, ϵ, λ, τ, $\Delta\mu^a_Q$, ...).

Most of the data on $\bar{\Lambda}$ polarization in pp or pA collisions were obtained at high energy, $\sqrt{s} > 27$ GeV and have the polarization P_N, compatible with zero (diamonds in Fig. 2a). The only non-zero data are measured at $\sqrt{s} = 7.31$ GeV (solid points in Fig. 2a) [7]. In the ECF model the large P_N is due to the effect of quark focusing (eq. (4)) with the parameter $E_R = 7.2 \pm 1.1$ GeV. The $\bar{\Lambda}$ spin is carried by a single polarized $\bar{s}$, which makes the resonance parameter $\delta_R = 0.064$ smaller and focusing effect stronger, with almost zero polarization at high energies. In the case of other antibaryon production

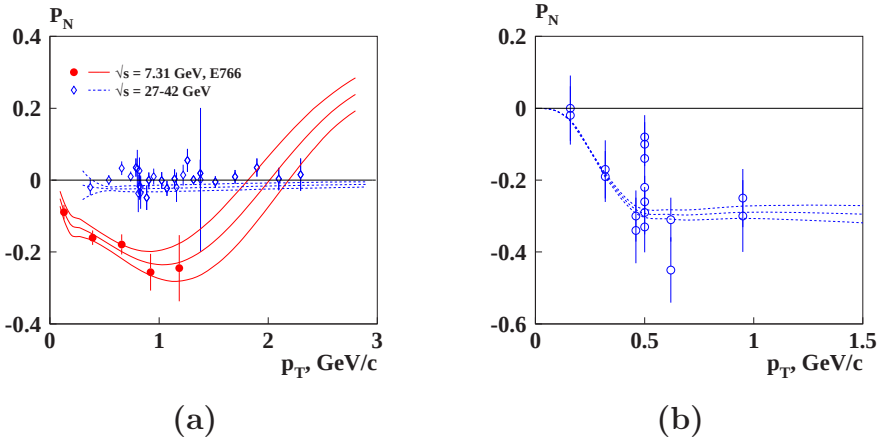

Figure 2: **(a)** The dependence of the $P_N(p_T)$ for $p + p(A) \to \bar{\Lambda}^{\uparrow} + X$ reaction. **(b)** The dependence of the $P_N(p_T)$ for $\nu_\mu + A \to \Lambda^{\uparrow} + X$ reaction at $\sqrt{s} = 6.82$ GeV. Predictions are made for $x_F = -0.23$ **(a)** and $x_F = -0.27$ (target fragmentation region) **(b)**, respectively.

we have three probe quarks of different flavors Q, which makes the resonance parameter $\delta_R \sim \delta(M_Q/\Delta\mu^a_Q) \approx 0.3$ larger and leads to a nonzero P_N at high energies.

The polarization of Λ in ν_μA collisions is measured in the NOMAD experiment [8] and is shown in Fig. 2b. We assume that W^+, emitted by ν_μ, interacts with the d quark and produces the u quark, which is moving forward, in the ν_μ direction. The ECF is created by this u beam from ν_μ, and by the two quarks from the target remnant, which are moving in the opposite direction in c.m. The model predictions are shown by the dashed line. The polarization of Λ is equal to the s quark polarization.

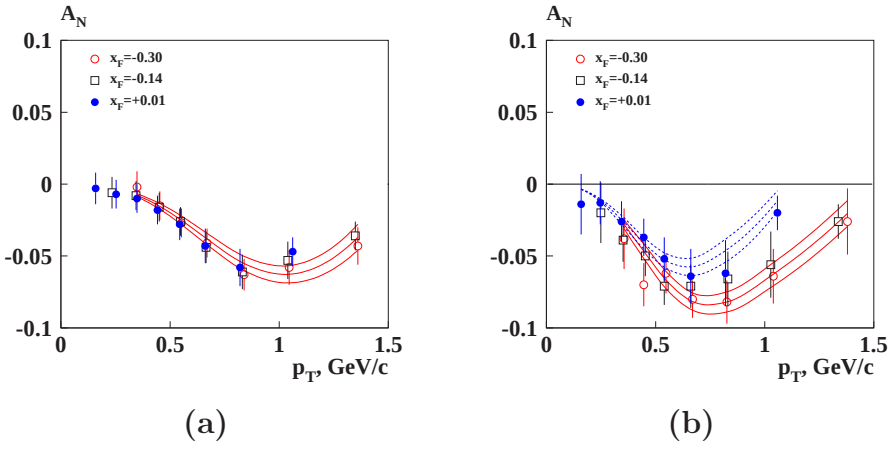

Figure 3: **(a)** The dependence of the $A_N(p_T)$ for $e^+p^{\uparrow} \to \pi^+ + X$ reaction. **(b)** The dependence of the $A_N(p_T)$ for $e^+p^{\uparrow} \to K^+ + X$ reaction. Predictions are made for $x_F = -0.30$ (solid curve) and $x_F = +0.01$ (dashed curve), respectively.

The π^+ (Fig. 3a) and K^+ (Fig. 3b) production SSA in e^+p collisions are measured in the HERMES experiment at $\sqrt{s} = 7.26$ GeV [9]. We assume that virtual photon produces $q\bar{q}$ pair (vector meson dominance), which interacts with the target quarks and produces a π^+ or a K^+. The probe quark for both reactions is the polarized u. The signs of A_N and x_F are changed to the opposite, as an assumption that the proton is the projectile.

The π^+ data do not show a significant x_F dependence, while for the K^+ the magnitude of A_N increases in the target fragmentation region. Not monotonic behavior of the $A_N(p_T)$ occurs because of the dependence of scaling variables y_A and y_B, eqs. (7) and (8), on the production polar angle θ_{cm}. This leads to the dependence on p_T of the quark spin precession angles ϕ_A, ϕ_B, and as a consequence, the dependence of the $A_N(p_T)$.

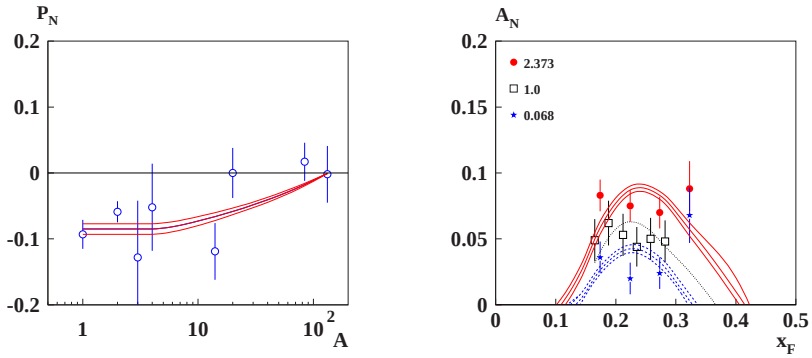

(a) (b)

Figure 4: **(a)** The A-dependence of the P_N for the Λ-hyperon polarization in e^+A collisions at $\sqrt{s} = 7.26$ GeV. **(b)** The $A_N(x_F)$ for inclusive production of π^+ in $p^\uparrow p$ collisions at $\sqrt{s} = 200$ GeV. The data are measured for three samples with the ratio R_m of charged multiplicity to the mean value, 2.373, 1.0 and 0.068, respectively. Predictions are made for $R_m = 2.373$ (solid curve), $R_m = 1$ (dotted curve), and $R_m = 0.068$ (dashed curve), respectively.

The A-dependence of Λ polarization P_N in e^+A collisions is measured in the HERMES experiment [10]. The effective number of quarks, creating ECF is specified by $\nu_A = 1 + \lambda(3A_{eff} - 2) - \tau(\lambda + 1)$, where $A_{eff} \approx 0.6A^{1/3}$ is the effective number of nucleons contributing to the ECF [1, 2]. The first term in the expression for ν_A is due to the contribution of one spectator $\bar{s}$, the second term is associated with the contribution of the nuclear target quarks, which cancels the first term. The ECF and $P_N \sim \nu_A$, which is close to zero for large $A \approx 120$. Solid curve in Fig. 4a is the model prediction.

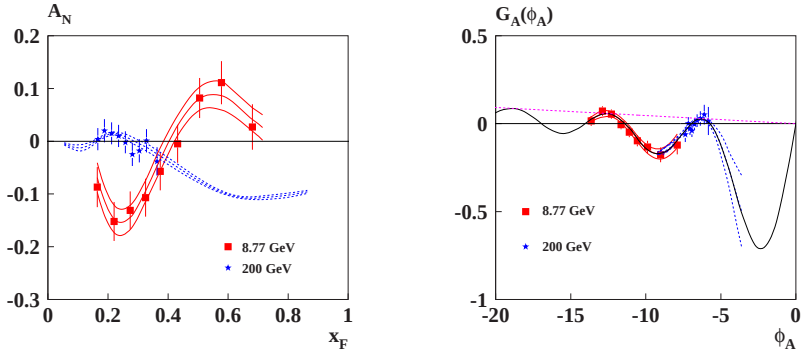

(a) (b)

Figure 5: **(a)** The A_N in the reaction $p^\uparrow p(A) \to p + X$ at $\sqrt{s} = 8.77$ GeV and $\sqrt{s} = 200$ GeV as a funcion of x_F. **(b)** The G_A as function of he quark spin persession angle ϕ_A.

The A_N of $\pi^\pm$ in $p^\uparrow p$ collisions is measured in the BRAHMS experiment [11]. The data are presented in Fig. 4b for three values of charged hadron multiplicity in the central

region, normalized to the average (R_m). The greatest R_m corresponds to a larger value of ECF due to the correlation of the number of strings and the multiplicity. The contribution of $q\bar{q}$ pairs in the ECF, f_N, has a factor $1 + a_m(R_m - 1)$, where $a_m = 0.025 \pm 0.004$ is a global parameter, which takes into account the correlation of R_m and A_N.

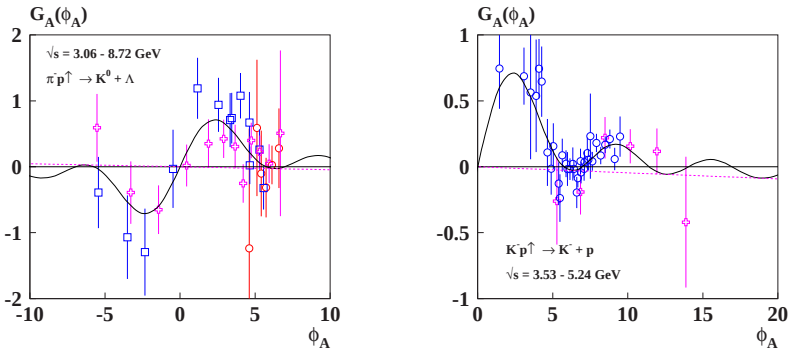

(a) **(b)**

Figure 6: The $G_A(\phi_A)$ in the reaction $\pi^- p^\uparrow \to K^0 + \Lambda$ **(a)** and $K^- p^\uparrow \to K^- + p$ **(b)**.

The proton A_N in $p^\uparrow p$(A) collisions is measured in the FODS-2 experiment at $\sqrt{s} = 8.77$ GeV [12] and in the BRAHMS experiment at $\sqrt{s} = 200$ GeV [13]. Oscillations of $A_N(x_F)$, displayed on Fig. 5a, are due to the quark spin precession and the microscopic Stern-Gerlach forces in the ECF. In Fig. 5b are shown the same data (A_N), but in a transformed way: $G_A(\phi_A) = A_N/C(\sqrt{s})/F(p_T, A) + \sigma G_B(\phi_B)$, using eq. (3).

The data for the exclusive reactions are shown in Fig. 6 and 7, depending on the quark spin precession angle ϕ_A. The data in Fig. 6 and 7 show an oscillating behavior with a decreasing magnitude, as expected for the $G_A(\phi_A)$ in (4).

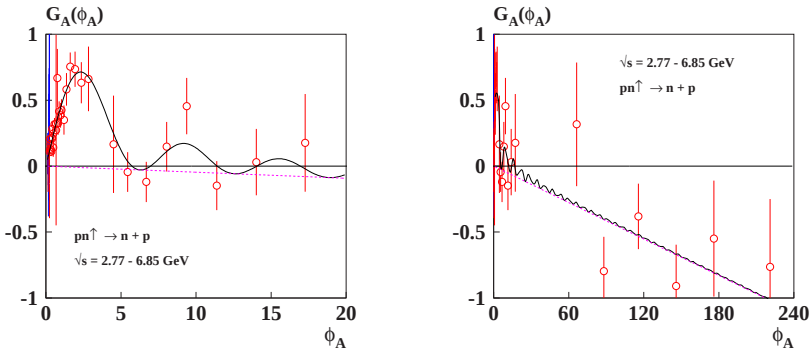

(a) **(b)**

Figure 7: The $G_A(\phi_A)$ in the reaction $pn^\uparrow \to n + p$ for $\phi_A < 20$ **(a)** and for $\phi_A < 240$ **(b)**.

Results of global analysis of 86 different reactions for the quark masses and their anomalous chromomagnetic moments are presented in Table 1.

Conclusion: A semi-classical mechanism is proposed to explain the existing polarization data. Dozens of reactions (86), the exclusive and inclusive, were analyzed in the framework of the Effective color field model, including those that are not normally considered or have recently been measured. The measured data could be used in global analysis

Table 1: Global analysis results. Used current quark masses m_q; additional dynamical quark mass, $\Delta M_Q(0)$; constituent masses $M_Q(0) = m_q + \Delta M_Q(0)$; and anomalous chromomagnetic moments of constituent quarks, $\Delta\mu_Q^a(0)$ at zero virtuality, $q = 0$.

Flavor	$m_{\rm q}$, GeV/c^2	$\Delta M_Q(0)$, GeV/c^2	$M_Q(0)$, GeV/c^2	$\Delta\mu_Q^a(0)$
u	0.0025	0.2350 ± 0.0009	0.2375	-0.524 ± 0.004
d	0.0050	0.2955 ± 0.0024	0.3005	-0.438 ± 0.005
s	0.1010	0.4215 ± 0.0048	0.5225	-0.510 ± 0.005
c	1.270	0.145 ± 0.062	1.415	-0.658 ± 0.025
b	4.357	0.056 ± 0.340	4.413	-0.621 ± 0.037

in order to estimate parameters that describe phenomena such as spontaneous chiral symmetry breaking, the origin of hadron and quark masses, confinement, color interaction of quarks and their transition into hadrons.

I would like to thank the DSPIN-11 Organizing Committee for their support and hospitality, H. Arthru, A.V. Efremov, N. Kochelev and K. Rith for fruitful discussions and valuable comments, A.N. Vasiliev for supporting this work, which was partially supported by RFBR grant 09-02-00198.

References

[1] V.V. Abramov, Yad. Fiz. **72** (2009) 1933 [Phys. At. Nucl. **72** (2009) 1872].

[2] V.V. Abramov, 2011 J. Phys.: Conf. Ser. **295** 012086.

[3] A.B. Migdal and S.B. Khokhlachev, JETP Lett. **41** (1985) 194.

[4] V. Bargmann, L. Michel and V. Telegdy, Phys. Rev. Lett. **2** (1959) 435.

[5] N.I. Kochelev, Phys. Lett. **B426** (1998) 149.

[6] D. Diakonov, Prog. Part. Nucl. Phys. **51** (2003) 173.

[7] J. Felix (E766 Collab.) *Inclusive $\bar{\Lambda}$ polarization in pp collisions at 27 GeV*, Proc. of the Adriatico Research Conference Trends in Collider Spin Physics, Trieste, 5-8 December, (1995) 125.

[8] D.V. Naumov, Acta Phys. Polon. **B33** (2002) 3791.

[9] K. Rith, 2011 J. Phys.: Conf. Ser. **295** 012056.

[10] K. Rith, Proc. of XVIII International Workshop on Deep-Inelastic Scattering and Related Subjects, Convitto della Calza, Firenze, 19th - 23rd April 2010, DIS 2010. PoS DIS2010: 131, 2010.

[11] J.H. Lee, F. Videbaek, DIS 2009 (2009), arXiv:0908.4551 [hep-ex].

[12] V.V. Abramov et al. Phys. Atom. Nucl. **70** (2007) 1515.

[13] J.H. Lee and F. Videbaek (BRAHMS Collab.), AIP Conf. Proc. **915** (2007) 533.

VALENCE AND SEA CONTRIBUTIONS TO THE PROTON SPIN FROM THE QCD ANALYSIS OF SIDIS DATA

O.Yu. Shevchenko [1]†, R.R. Akhunzyanov [1] and V.Yu. Lavrentyev [2]

(1) *Laboratory of Nuclear Problem, JINR*
(2) *Laboratory of Information Technology, JINR*
† *E-mail: shev@cern.ch, axruslan@mail.ru, basil77@jinr.ru*

Abstract

The first moments of the polarized valence parton distribution functions (PDFs) truncated to the wide Bjorken x region $0.004 < x < 0.7$ are extructed in NLO QCD from both COMPASS and HERMES data are directly (without any fitting procedure) extracted in NLO QCD from the combined SIDIS data of COMPASS and HERMES. Applying the proposed original procedure to these results we estimate the contributions of sea u and d quarks to the proton spin, which occur just zero within the errors.

The first moments of polarized parton distribution functions (PDFs), which directly compose the nucleon spin together with the orbital parton momenta, are of crucial importance for solution of the proton spin puzzle, attracting great both theoretical and experimental efforts during many years. The procedure of direct extraction in NLO QCD of n-th moments of the valence PDFs from the measured difference asymmetries is described in Refs. [1–3] in detail. The key equations allowing to find from the data on the difference asymmetries $A_{p,d}^{\pi^+-\pi^-}$ the n-th moments $\Delta_n' q \equiv \int_a^b dx\, x^{n-1} q(x)$ of valence PDFs truncated to the accessible for measurement x region (a, b) look as

$$\Delta_n' u_V \simeq \frac{1}{5}\frac{\mathcal{A}_p^{(n)} + \mathcal{A}_d^{(n)}}{L_{(n)1} - L_{(n)2}}; \quad \Delta_n' d_V \simeq \frac{1}{5}\frac{4\mathcal{A}_d^{(n)} - \mathcal{A}_p^{(n)}}{L_{(n)1} - L_{(n)2}}, \tag{1}$$

where all notations are almost the same as in Ref. [2] (see (9)-(16)) in [2]). The only difference is that we rewrite equation for the quantities $\mathcal{A}_{p,d}^{(n)}$ entering (1) in more convenient form[1] (compare with (16) in [2]):

$$\mathcal{A}_p^{(n)} = \sum_{i=1}^{N_{bins}} \frac{A_p^{\pi^+-\pi^-}(\langle x_i\rangle)}{1+R}\Big|_Z \int_{x_{i-1}}^{x_i} dx x^{n-1}(4u_V - d_V)(x) \int_Z^1 dz_h [1 + \otimes \frac{\alpha_s}{2\pi} C_{qq}^2 \otimes](D_1 - D_2), \tag{2}$$

and analogously for $\mathcal{A}_d^{(n)}$ with the replacements $(1+R)^{-1} \to (1+R)^{-1}(1-1.5\,\omega_D)^{-1}$ and $(4u_V - d_V) \to (u_V + d_V)$.

Both COMPASS [4, 5] and HERMES [6] collaborations published the data only on asymmetries $A_{p,d}^{\pi^\pm}$, while the published data on the pion difference asymmetries $A_{p,d}^{\pi^+-\pi^-}$ is

[1] This form allows to explicitelly account for the corrections due to the factor $R = \sigma_L/\sigma_T$ and the deutron D-state contribution $\omega_D = 0.05 \pm 0.01$ (see, for example, discussion around (10) in [10] and references therein).

still absent. That is why the special procedure was applied in [2] to construct asymmetries $A_{p,d}^{\pi^+-\pi^-}$ from the HERMES data on pion production, and we repeat here this procedure for the COMPASS case. Namely, in each i-th bin the pion difference asymmetries can be rewritten as

$$A^{\pi^+-\pi^-}(x_i) = \frac{R_i^{+/-}}{R_i^{+/-}-1} A^{\pi^+}(x_i) - \frac{1}{R_i^{+/-}-1} A^{\pi^-}(x_i), \tag{3}$$

where the quantity $R_i^{+/-}$ is just the ratio of unpolarized cross-sections for π^+ and π^- production: $R_i^{+/-} = \sigma^{\pi^+}_{\rm unpol}(x_i)/\sigma^{\pi^-}_{\rm unpol}(x_i) = N_i^{\pi^+}/N_i^{\pi^-}$. As it was argued in Ref. [2] this relative quantity is very well reproduced by the the LEPTO generator of unpolarized events [7], which gives a good description of the fragmentation processes. So, we again use here the LEPTO generator to this end.

Let us now discuss the question of Q^2 dependence of asymmetries and its influence on the final results. The point is that both DIS and SIDIS asymmetries very weekly depend on Q^2 (see, for instance, Fig. 5 in Ref. [8]), so that the approximation $A(x_i, Q_i^2) \simeq A(x_i, Q_0^2)$ is commonly used (see, for example, Refs. [9, 6, 5]) for analysis of the DIS and SIDIS asymmetries. Nevertheless, for more comprehensive analysis, it is useful to account for the corrections caused by the weak Q^2 dependence of the difference asymmetries, i.e., to estimate the shifts $\delta_i A_{p,d}^{\pi^+-\pi^-} = A_{p,d}^{\pi^+-\pi^-}(x_i, Q_0^2) - A_{p,d}^{\pi^+-\pi^-}(x_i, Q_i^2)$ in the difference asymmetries and their influence on the moments of the valence PDFs. To this end we operate just as in Ref. [2] and use two new parameterizations [11, 10] on polarized PDFs (elaborated with application of both DIS and SIDIS data). Of importance is the optimal choice of the common for evolved asymmetries scale Q_0^2, allowing as much as possible to reduce shifts in the results due to evolution. Our experience shows that for combined analysis of COMPASS and HERMES data (see below) the optimal choice is close to $Q_0^2 = 10\,\mathrm{GeV}^2$.

We perform the combined analysis of COMPASS [5, 4] and HERMES [6] data on pion production with both proton and deuteron targets. COMPASS collaboration published their data in the Bjorken x range $0.004 < x < 0.7$ and $0.004 < x < 0.3$ for proton and deuteron targets, respectively, while the HERMES data $A_{p,d}^{\pi^\pm}$ were presented in the range $0.023 < x < 0.6$ for both targets. Inclusion of HERMES data into the analysis is especially important because COMPASS data in the region $0.3 < x < 0.7$ for deuteron target is still absent. Besides, application of the combined data allows us to increase the available statistics, and therefore to decrease the errors.

The statistical addition of asymmetries $A_{p,d}^{\pi^\pm}$ and their errors is performed in accordance with the standard formulas

$$A_N^h|_{averaged} == \frac{A_N^h|_{exp1}/(\delta A_N^h|_{exp1})^2 + A_N^h|_{exp2}/(\delta A_N^h|_{exp2})^2}{1/(\delta A_N^h|_{exp1})^2 + 1/(\delta A_N^h|_{exp2})^2}, \tag{4}$$

$$(\delta A_N^h|_{averaged})^2 == \frac{1}{1/(\delta A_N^h|_{exp1})^2 + 1/(\delta A_N^h|_{exp2})^2}. \tag{5}$$

However this is the case only for the last three bins of COMPASS and HERMES experiments we deal with (after proper extrapolation[2] of HERMES data in the last bin from 0.6 to 0.7 upper x value). Besides, notice that for two last bins the COMPASS published

[2]Our experience show that a such extrapolation leads to negligible change in the final result, irrespective of the choice of the extrapolation procedure.

Table 1: Four first moments of polarized valence PDFs truncated to the region $0.004 < x < 0.7$ are presented at $Q^2 = 10\,GeV^2$. The moments are obtained as a result of NLO QCD analysis of the combined data on $A_{p,d}^{\pi^+-\pi^-}$, constructed with (3) from the COMPASS data on $A_{p,d}^{\pi^\pm}$ in the region $0.004 < x < 0.7$ and HERMES data on $A_{p,d}^{\pi^\pm}$ in the region $0.2 < x < 0.6$ (last three bins of HERMES). Capital letters A and B correspond to the application of AKK08 and DSS parameterizations for FFs, respectively. Rome numbers I and II correspond to the moments uncorrected and corrected due to evolution, respectively. Besides, the relative corrections $\delta_r(\Delta'_n q_V) \equiv \delta(\Delta'_n q_V)/\Delta'_n q_V$ for moments caused by evolution are presented here.

$\Delta'_n u_V$						
n	$\mathrm{A_I}$	$\mathrm{A_{II}}$	$\delta_r(\Delta'_n u_V)$	$\mathrm{B_I}$	$\mathrm{B_{II}}$	$\delta_r(\Delta'_n u_V)$
1	0.731 ± 0.087	0.695 ± 0.087	-3.8%	0.693 ± 0.084	0.713 ± 0.084	2.8%
2	0.166 ± 0.024	0.167 ± 0.024	0.8%	0.155 ± 0.024	0.158 ± 0.024	1.6%
3	0.055 ± 0.010	0.055 ± 0.010	1.3%	0.052 ± 0.010	0.052 ± 0.010	1.8%
4	0.022 ± 0.005	0.022 ± 0.005	1.5%	0.021 ± 0.005	0.021 ± 0.005	2.0%
$\Delta'_n d_V$						
n	$\mathrm{A_I}$	$\mathrm{A_{II}}$	$\delta_r(\Delta'_n d_V)$	$\mathrm{B_I}$	$\mathrm{B_{II}}$	$\delta_r(\Delta'_n d_V)$
1	-0.519 ± 0.162	-0.524 ± 0.162	0.9%	-0.473 ± 0.157	-0.481 ± 0.157	1.7%
2	-0.100 ± 0.054	-0.102 ± 0.054	1.8%	-0.090 ± 0.051	-0.092 ± 0.051	2.7%
3	-0.029 ± 0.023	-0.030 ± 0.023	2.5%	-0.026 ± 0.022	-0.027 ± 0.022	3.7%
4	-0.011 ± 0.011	-0.011 ± 0.011	3.1%	-0.010 ± 0.010	-0.010 ± 0.010	4.4%

SIDIS data for deuteron target is still absent. That is why it is of especial importance to include in the analysis of COMPASS data the HERMES data in the region $0.2 < x < 0.6$ (last three bins of HERMES). The respective results are presented in the Table 1.

In the Table 1 we present the results obtained both with and without corrections due to weak Q^2-dependence of asymmetries. One can see that the difference is not too significant (the relative corrections $\delta(\Delta'_n q_V)/\Delta'_n q_V$ take the small values).

Thus, we estimated in NLO QCD the contributions of valence quarks (first moments of polarized valence PDFs) to the nucleon spin. Let us now to find the respective contributions of light sea quarks.

Within this procedure one first of all uses some NLO QCD parameterization on the polarized PDFs to estimate the quantities $\Delta'_1 q + \Delta'_1 \bar{q}$ $(q = u, d)$. Since the sums $\Delta q(x) + \Delta\bar{q}(x)$ $(q = u, d)$ are well fitted by the reach purely inclusive DIS data (these quantities are considered as relatively well known and practically are the same for the different modern parameterizations) it is not especially important which parameterization one applies for this purpose (here we use the most popular and widely cited DSSV [11] parameterization). Then, having in his disposal both $(\Delta'_1 q + \Delta'_1 \bar{q})|_{\text{parameterization}}$ $(q = u, d)$ and (see Table 2) $(\Delta'_1 q_V$ $(q = u, d)$ quantities one easily gets the truncated first moments of sea u and d quarks, applying the obvious relation $\Delta'_1 \bar{q} = \frac{1}{2}\left((\Delta'_1 q + \Delta'_1 \bar{q})|_{\text{parameterization}} - \Delta'_1 q_V\right)$. The received in such a way first moments $\Delta'_1 \bar{u}$, $\Delta'_1 \bar{d}$, as well as their differences and sums are presented in the Table 2. Looking at this table one can draw the conclusion that irrespective of the procedure used in the SIDIS data analysis the first moments of sea PDFs are consistent with zero within the errors.

Conclusion. The pion difference asymmetries are constructed by combining the SIDIS data of COMPASS and HERMES on pion production. The new direct (free of any fitting procedures) method of QCD analysis is applied to these asymmetries. As a result, the valence contributions to the nucleon spin (first moments of polarized valence PDFs) are found in NLO QCD. Using these results on valence PDFs the contributions of light sea

Table 2: First moments of polarized sea PDFs truncated to the region $0.004 < x < 0.7$ are presented at $Q^2 = 10\,GeV^2$, as well as their sums and differences. DSSV parameterization is used to estimate $(\Delta'_1 q + \Delta'_1 \bar{q})|_{\text{parameterization}}$, while the first moments of valence PDFs are taken from the Table 1 (only HERMES data from three last bins are applied). Capital letters A and B correspond to the application of AKK08 and DSS parameterizations for FFs, respectively. Rome numbers I and II correspond to the moments uncorrected and corrected due to evolution, respectively.

	A_I	A_{II}	B_I	B_{II}
$\Delta'_1\bar{u}$	0.018 ± 0.044	0.036 ± 0.044	0.037 ± 0.042	0.027 ± 0.042
$\Delta'_1\bar{d}$	0.065 ± 0.081	0.067 ± 0.081	0.042 ± 0.079	0.046 ± 0.079
$\Delta'_1\bar{u} + \Delta_1\bar{d}$	0.082 ± 0.092	0.102 ± 0.092	0.078 ± 0.089	0.072 ± 0.089
$\Delta'_1\bar{u} - \Delta_1\bar{d}$	-0.047 ± 0.092	-0.032 ± 0.092	-0.005 ± 0.089	-0.019 ± 0.089

quarks to the nucleon spin are estimated. They occur surprisingly small: compatible with zeros within the errors.

The authors are grateful to N. Akopov, A. Efremov, O. Ivanov, A. Korzenev, A. Kotikov, V. Krivokhizhin,A. Maggiora, A. Nagaytsev, A. Olshevsky, G. Piragino, G. Pontecorvo, I. Savin, A. Sidorov, O. Teryaev, R. Windmolders and E. Zemlyanichkina for fruitful discussions.

References

[1] A. N. Sissakian, O. Y. Shevchenko and O. N. Ivanov, Phys. Rev. D **70** (2004) 074032
[2] A. N. Sissakian, O. Y. Shevchenko and O. N. Ivanov, Phys. Rev. D **73** (2006) 094026
[3] A. N. Sissakian, O. Y. Shevchenko and O. N. Ivanov, Phys. Part. Nucl. **39** (2008) 674.
[4] M. Alekseev *et al.* [COMPASS Collaboration], Phys. Lett. B **680** (2009) 217
[5] M. Alekseev *et al.* [COMPASS Collaboration], Phys. Lett. B **693** (2010) 227
[6] HERMES collaboration (A. Airapetyan et al.), Phys. Rev. **D71** (2005) 012003
[7] G. Ingelman, A. Edin and J. Rathsman, Comput. Phys. Commun. **101** (1997) 108
[8] COMPASS Collaboration (E.S. Ageev et al.), Phys. Lett. B**612** (2005) 154
[9] SMC collaboration (B. Adeva et al.), Phys. Lett. B **369** (1996) 93
[10] A. Sissakian, O. Shevchenko and O. Ivanov, Eur. Phys. J. C **65** (2010) 413
[11] D. de Florian, R. Sassot, M. Stratmann and W. Vogelsang, Phys. Rev. D **80** (2009) 034030
[12] COMPASS collaboration (G. Baum et al.), "COMPASS: A proposal for a common muon and proton apparatus for structure and spectroscopy", CERN-SPSLC-96-14 (1996).
[13] A. N. Sissakian, O. Y. Shevchenko and O. N. Ivanov, JETP Lett. **82** (2005) 53
[14] D. Adams *et al.* [Spin Muon Collaboration (SMC)], Phys. Rev. D **56** (1997) 5330
[15] A. N. Sissakian, O. Y. Shevchenko and O. N. Ivanov, Phys. Rev. D **68** (2003) 031502
[16] M. Alekseev *et al.* [COMPASS Collaboration], Phys. Lett. **B660** (2008) 458-465.
[17] S. Albino, B. A. Kniehl and G. Kramer, Nucl. Phys. B **803** (2008) 42
[18] K. Abe *et al.* [E143 Collaboration], Phys. Lett. B **452** (1999) 194
[19] D. de Florian, M. Stratmann and W. Vogelsang, Phys. Rev. D **57** (1998) 5811

DISTINGUISHING INDIRECT SIGNATURES OF NEW PHYSICS AT THE POLARIZED ILC: Z' VERSUS ANOMALOUS GAUGE COUPLINGS IN $e^+e^- \to W^+W^-$

V.V. Andreev [1,*], A.A. Pankov [2,†]

(1) *F. Skoryna Gomel State University, Gomel, Belarus*
(2) *Abdus Salam ICTP Affiliated Centre at Gomel State Technical University, Gomel, Belarus*
∗ *E-mail: quarks@gsu.by,*
† *E-mail: pankov@ictp.it*

Abstract

We discuss the foreseeable sensitivity to Z's of $W^{\pm}$-pair production cross sections at e^+e^- International linear collider (ILC), especially as regards the potential of distinguishing observable effects of the Z' from analogous ones due to competitor models with anomalous trilinear gauge couplings that can lead to the same or similar new physics experimental signatures at the ILC.

1 Introduction

The $W^{\pm}$ boson pair production process

$$e^+ + e^- \to W^+ + W^- \tag{1}$$

is one of the crucial process to study the electroweak gauge symmetry in e^+e^- annihilation. It is well known that properties of the weak gauge bosons are closely related to electroweak symmetry breaking and the structure of the gauge sector in general, detailed examination of W boson physics will throw light on what lies beyond the Standard Model (SM).

Electroweak theories beyond the SM based on spontaneously broken extended gauge symmetries naturally envisage the existence of new heavy neutral gauge bosons Z'. The variety of the proposed Z' models is somewhat broad, and for definiteness in the sequel we shall focus on the so-called $Z'_{\rm SSM}$, Z'_{E_6}, $Z'_{\rm LR}$ and $Z'_{\rm ALR}$ models. Particular attention has recently been devoted to the phenomenological properties and the search reaches on such scenarios, and in some sense we may consider these Z' models as representative of this New Physics (NP) sector [1].

NP may appear either directly, as in the case of new particle production, *e.g.*, Z', or indirectly through deviations of the observables from the predictions of the SM. In the case of direct production of Z', *e.g.*, at the LHC, its discovery and identification would be relatively straightforward once spin, masses and various couplings were determined through precision measurements [2]. In the case of indirect discovery the effects may be subtle and many different NP scenarios may lead to the same or similar experimental signatures. It is clear that determination of the origin of the NP in these cases will prove more difficult and new tools must be available to deal with this potentiality. In this note we propose such a technique that makes use of the specific modifications in angular

distributions of process (1) induced by $Z - Z'$ mixing and Z' exchange from those caused by anomalous trilinear gauge couplings (AGC).

Here we study the effects of extra gauge Z' bosons on the $W^{\pm}$ pair production (1) at the next generation e^+e^- International Linear Collider (ILC), with center of mass energy $\sqrt{s} = 0.5$ TeV and time-integrated luminosity $\mathcal{L}_{\rm int} = 0.5$ ab^{-1} [3,4], where the really high precision measurements that will be possible there.

2 Parameterizations of Z'-boson and AGC effects

2.1 Z' boson

The starting point of our analysis will be the expression of the invariant amplitude for the process (1). In Born approximation, this can be written as a sum of a t-channel and of an s-channel components. In SM case, the latter will be schematically written as follows:

$$\mathcal{M}_s^{(\lambda)} = \left(-\frac{1}{s} + \frac{\cot\theta_W (v - 2\lambda a)}{s - M_Z^2} \right) \times \mathcal{G}^{(\lambda)}(s, \theta), \tag{2}$$

where s and θ are the total c.m. squared energy and W^- production angle; electron vector and axial-vector couplings in SM, omitting the fermionic subscripts, are defined as $v = (T_{3,e} - 2Q_e\, s_W^2)/2 s_W c_W$ and $a = T_{3,e}/2 s_W c_W$, respectively, with $T_{3,e} = -1/2$; λ denotes the electron helicity ($\lambda = \pm 1/2$ for right/left-handed electrons); M_Z is the mass of Z-boson; finally, $\mathcal{G}^{(\lambda)}(s, \theta)$ is a kinematical coefficient, depending also on the final W's helicities. For simplicity we omit its explicit form.

The expression of the amplitude with extra Z' will be written as [5]:

$$\mathcal{M}_s^{(\lambda)} = \left(-\frac{1}{s} + \frac{g_{WWZ_1}(v_1 - 2\lambda a_1)}{s - M_1^2} + \frac{g_{WWZ_2}(v_2 - 2\lambda a_2)}{s - M_2^2} \right) \times \mathcal{G}^{(\lambda)}(s, \theta), \tag{3}$$

where $a_{1,2}$ and $v_{1,2}$ are correspondingly axial and vector couplings of Z_1 and Z_2 bosons to electrons, M_1 and M_2 are masses of Z_1 and Z_2 bosons respectively, g_{WWZ_1} and g_{WWZ_2} are corresponding trilinear gauge couplings.

It turns out that it is convenient to rewrite Eq. (3) in the following form:

$$\mathcal{M}_s^{(\lambda)} = \left(-\frac{g_{WW\gamma}}{s} + \frac{g_{WWZ}(v - 2\lambda a)}{s - M_Z^2} \right) \times \mathcal{G}^{(\lambda)}(s, \theta), \tag{4}$$

where the 'effective' gauge boson couplings $g_{WW\gamma}$ and g_{WWZ} are defined as:

$$g_{WW\gamma} = 1 + \delta_\gamma = 1 + \Delta_\gamma(Z_1) + \Delta_\gamma(Z_2), \tag{5}$$

$$g_{WWZ} = \cot\theta_W + \delta_Z = \cot\theta_W + \Delta_Z(Z_1) + \Delta_Z(Z_2), \tag{6}$$

Explicit expressions for $\Delta_\gamma(Z_1)$, $\Delta_\gamma(Z_2)$, $\Delta_Z(Z_1)$ and $\Delta_Z(Z_2)$ can be found in [5].

2.2 AGC

It has already been pointed out in previous subsection that a model with one extra Z' would produce virtual manifestations in the final W^+W^- channel at the ILC that in principle could mimic those of a model (of completely different origin) with AGC.

Using the notations of, e.g., Ref. [6], the relevant trilinear WWV interaction which conserves $U(1)_{e.m.}$, C and P, can be written as ($e = \sqrt{4\pi\alpha_{em}}$):

$$\begin{aligned}
\mathcal{L}_{eff} &= -ie(1+\delta_\gamma)\left[A_\mu\left(W^{-\mu\nu}W^+_\nu - W^{+\mu\nu}W^-_\nu\right) + F_{\mu\nu}W^{+\mu}W^{-\nu}\right] \\
&- ie\,(\cot\theta_W + \delta_Z)\,\left[Z_\mu\left(W^{-\mu\nu}W^+_\nu - W^{+\mu\nu}W^-_\nu\right) + Z_{\mu\nu}W^{+\mu}W^{-\nu}\right] \\
&- ie\,x_\gamma\,F_{\mu\nu}W^{+\mu}W^{-\nu} - ie\,x_Z\,Z_{\mu\nu}W^{+\mu}W^{-\nu} \\
&+ ie\,\frac{y_\gamma}{M_W^2}\,F^{\nu\lambda}W^-_{\lambda\mu}W^{+\mu}_{\ \ \nu} + ie\,\frac{y_Z}{M_W^2}\,Z^{\nu\lambda}W^-_{\lambda\mu}W^{+\mu}_{\ \ \nu}\,,
\end{aligned} \tag{7}$$

where $W^\pm_{\mu\nu} = \partial_\mu W^\pm_\nu - \partial_\nu W^\pm_\mu$ and $Z_{\mu\nu} = \partial_\mu Z_\nu - \partial_\nu Z_\mu$. In the SM at the tree-level, the anomalous couplings in (7) vanish: $\delta_\gamma = \delta_Z = x_\gamma = x_Z = y_\gamma = y_Z = 0$.

The general expression for the cross section of process (1) with longitudinally polarized electron and positron beams can be expressed as

$$\frac{d\sigma}{d\cos\theta} = \frac{1}{4}\left[(1+P_L)\left(1-\bar{P}_L\right)\frac{d\sigma^+(\lambda,\lambda')}{d\cos\theta} + (1-P_L)\left(1+\bar{P}_L\right)\frac{d\sigma^-(\lambda,\lambda')}{d\cos\theta}\right], \tag{8}$$

where P_L and $\bar{P}_L$ are the actual degrees of electron and positron longitudinal polarization, respectively, and $\sigma^\pm$ are the cross sections for right-handed and left-handed electrons.

3 Discovery and identification of Z'

The sensitivity of the polarized differential cross sections to δ_γ and δ_Z is assessed numerically by dividing the angular range $|\cos\theta| \leq 0.98$ into 10 equal bins, and defining a χ^2 function in terms of the expected number of events $N(i)$ in each bin:

$$\chi^2 = \sum_{\{P_L,\bar{P}_L\}}\sum_{i}^{bins}\left[\frac{N_{SM}(i) - N_{NP}(i)}{\delta N_{SM}(i)}\right]^2, \tag{9}$$

where $N(i) = \mathcal{L}_{int}\,\sigma_i\,\varepsilon_W$ with $\mathcal{L}_{int}$ the time-integrated luminosity, and ($z = \cos\theta$):

$$\sigma_i = \sigma(z_i, z_{i+1}) = \int_{z_i}^{z_{i+1}}\left(\frac{d\sigma}{dz}\right)dz, \tag{10}$$

Here ε_W is the efficiency for W^+W^- reconstruction, $\delta N_{SM}(i)$ is the uncertainty on the number of events, which combines both statistical and systematic errors.

As a criterion to derive the constraints on the coupling constants in the case where no deviations from the SM were observed, we impose that $\chi^2 \leq \chi^2_{CL}$, where χ^2_{CL} is a number that specifies the chosen confidence level.

In order to identify Z', i.e. to discriminate it from AGC effects, we can define χ^2 function analogous to Eq. (9) as

$$\chi^2 = \sum_{\{P_L,\bar{P}_L\}}\sum_{i}^{bins}\left[\frac{N_{Z'}(i) - N_{AGC}(i)}{\delta N_{Z'}(i)}\right]^2, \tag{11}$$

and apply the criterion $\chi^2 \leq \chi^2_{min} + \chi^2_{CL}$, which allows to identify Z'. Obviously it can be done in a model independent way on the basis of δ_γ, δ_Z parameters of Z'-boson.

To perform model dependent analysis (for different E_6 or LR models) one should switch from δ_γ and δ_Z parameters to such physical parameters as mass M_2 and $Z - Z'$-mixing angle ϕ and obtain discovery and identification (ID) reaches for a set of extended gauge models. Some results are shown in Fig. 1. Additional results are presented in Tab. 1.

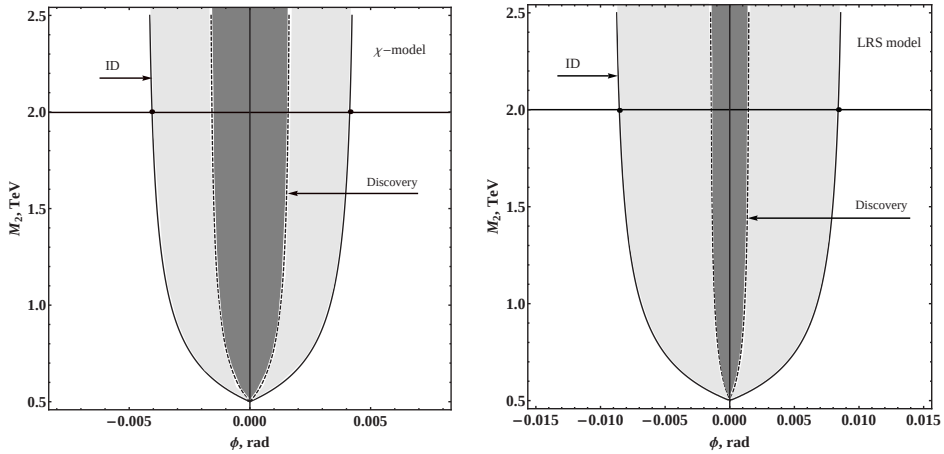

(a) **(b)**

Figure 1: **(a)** Discovery (dashed line) and identification (solid line) reach for χ-model (E_6) on (ϕ, M_2) plane obtained from polarized initial e^+ and e^- beams with ($P_L = \pm 0.8,\ \bar{P}_L = \mp 0.5$). **(b)** Same as in **(a)**, but for left-right symmetric (LRS) model.

Table 1: Discovery and ID reach on $Z - Z'$ mixing angle ϕ for Z' models with $M_2 = 2$ TeV for polarized initial ($P_L = \pm 0.8,\ \bar{P}_L = \mp 0.5$) states.

Z' model	χ	ψ	η	I	LRS	SSM
$\phi^{DIS}, 10^{-3}$	± 1.6	± 2.2	± 1.7	± 1.9	± 1.6	± 1.3
$\phi^{ID}, 10^{-3}$	± 3.8	± 42.6	± 17.6	± 4.4	± 8.0	–

Acknowledgements
This research has been partially supported by the Abdus Salam ICTP under the TRIL and STEP Programmes.

References

[1] A. Leike, Phys. Rept. **317**, 143 (1999) [arXiv:hep-ph/9805494].

[2] P. Osland, A. A. Pankov, A. V. Tsytrinov and N. Paver, Phys. Rev. D **79**, 115021 (2009) [arXiv:hep-ph/0904.4857].

[3] J. Brau *et al.* [ILC Collaboration], "ILC Reference Design Report Volume 1 - Executive Summary," arXiv:0712.1950 [physics.acc-ph].

[4] G. Aarons *et al.* [ILC Collaboration], "International Linear Collider Reference Design Report Volume 2: PHYSICS AT THE ILC," [arXiv:hep-ph/0709.1893].

[5] A. A. Pankov, N. Paver and C. Verzegnassi, Int. J. Mod. Phys. A **13** (1998) 1629 [arXiv:hep-ph/9701359].

[6] G. Gounaris, *et al.*, Proceedings of the Workshop e^+e^- *Collisions at 500 GeV: the Physics Potential*, Ed. P.M. Zerwas (1992), DESY 92-123B, p.735.

ASYMMETRIES ASSOCIATED WITH HIGHER TWISTS: GAUGE INVARIANCE, GLUONIC POLES AND TWIST THREE

I. V. Anikin [1,2†], O. V. Teryaev [1]

(1) *Bogoliubov Laboratory of Theoretical Physics, JINR, 141980 Dubna, Russia*
(2) *Institute for Theoretical Physics, University of Regensburg, D-93040 Regensburg, Germany*
† *E-mail: anikin@theor.jinr.ru*

Abstract

We explore the electromagnetic gauge invariance of the hadron tensor of the Drell-Yan process with one transversely polarized hadron. Due to the special role of the contour gauge for gluon fields, the prescription for the gluonic pole in the twist 3 correlator can be related to the causality prescriptions for exclusive hard processes. Because of this, we find the extra contributions, which naively do not have an imaginary phase. The single spin asymmetry for the Drell-Yan process is accordingly enhanced by the factor of two.

Introduction. The problem of the electromagnetic gauge invariance in the deeply virtual Compton scattering (DVCS) and similar exclusive processes has intensively been discussed during last few years, see for example [1–6]. This development explored the similarity with the earlier studied inclusive spin-dependent processes [7], and the transverse component of momentum transfer in DVCS corresponds to the transverse spin in DIS. Here we combine the different approaches to apply them in the relevant case of the Drell-Yan (DY) process where one of hadrons is the transversally polarized nucleon. The source of the imaginary part, when one calculates the single spin asymmetry associated with the DY process, is the quark propagator in the diagrams with quark-gluon (twist three) correlators. This leads [8, 9] to the gluonic pole contribution to SSA. The reason is that these boundary conditions provide the purely real quark-gluon function $B^V(x_1, x_2)$ which parameterizes $\langle\bar{\psi}\gamma^+ A^T_\alpha\psi\rangle$ matrix element. By this fact the diagrams with two-particle correlators do not contribute to the imaginary part of the hadron tensor related to the SSA [10]. In our paper, we perform a thorough analysis of the transverse polarized DY hadron tensor in the light of the QED gauge invariance, the causality and gluonic pole contributions. We show that, in contrast to the naive assumption, our new-found additional contribution is directly related to the certain complex prescription in the gluonic pole $1/(x_1 - x_2)$ of the quark-gluon function $B^V(x_1, x_2)$ (cf. [11] and see e.g. [12] and Refs. therein). Finally, the account for this extra contributions corrects the SSA formula for the transverse polarized Drell-Yan process by the factor of 2. Note that our analysis is also important in view of the recent investigation of DY process within both the collinear and the transverse-momentum factorization schemes with hadrons replaced by on-shell parton states [13].

Causality and contour gauge for the gluonic pole. We study the single spin (left-right) asymmetry measured in the Drell-Yan process with the transversely polarized nucleon. Since we perform our calculations within a *collinear* factorization, it is convenient (see,e.g., [14]) to fix the dominant light-cone directions for the DY process

$p_1 \approx Qn^{*+}/(x_B\sqrt{2})$, $p_2 \approx Qn^-/(y_B\sqrt{2})$. Focusing on the Dirac vector projection, containing the gluonic pole, let us start with the standard hadron tensor generated by the diagram depicted on Fig. 1(a):

$$\mathcal{W}^{(1)}_{\mu\nu} = \int d^4k_1\, d^4k_2\, \delta^{(4)}(k_1+k_2-q) \int d^4\ell\, \Phi^{(A)\,[\gamma^+]}_{\alpha}\, \bar{\Phi}^{[\gamma^-]} \times$$
$$\mathrm{tr}\left[\gamma_\mu\gamma^-\gamma_\nu\gamma^+\gamma_\alpha \frac{\ell^+\gamma^- - k_2^-\gamma^+ - \ell_T\gamma_T}{-2\ell^+k_2^- - \ell_T^2 + i\epsilon}\right], \tag{1}$$

where $\Phi^{(A)\,[\gamma^+]}_{\alpha}$ and $\bar{\Phi}^{[\gamma^-]}$ defined as in [15]. Analyzing the γ-structure, *i.e* $\gamma^+\gamma^\alpha\gamma^\pm$ in the trace, we may conclude that (i) the $\ell^+\gamma^-$ term singles out $\gamma^+\gamma^\alpha\gamma^-$ with $\alpha = T$ which will lead to $\langle\bar{\psi}\,\gamma^+A^T_\alpha\psi\rangle$ giving the contribution to SSA; (ii) the $k_2^-\gamma^+$ term separates out $\gamma^+\gamma^\alpha\gamma^+$ with $\alpha = -$. Therefore, this term will give $\langle\bar{\psi}\,\gamma^+\,A^+\,\psi\rangle$ which will be exponentiated in the Wilson line $[-\infty^-,\,0^-]$; (iii) the $\ell_T\gamma_T$ term separates out $\gamma^+\gamma^\alpha\gamma_T$ with $\alpha = T$ and, then, will be exponentiated in the Wilson line $[-\infty^-, -\infty_T\,; -\infty^-, 0_T]$. Indeed, integrating over ℓ^+, the k_2^--term contribution reads

$$\mathcal{W}^{(1)\,[k_2^-]}_{\mu\nu} = \int d\mu(k_i;x_1,y)\mathrm{tr}\left[\gamma_\mu\gamma^-\gamma_\nu\gamma^+\right]\bar{\Phi}^{[\gamma^-]}(k_2) \times$$
$$\int d^4\eta_1 e^{-ik_1\cdot\eta_1}\langle\bar{\psi}(\eta_1)\gamma^+ig\int\limits_{-\infty}^{+\infty}dz^-\theta(-z^-)A^+(z^-)\psi(0)\rangle\,. \tag{2}$$

Including all gluon emissions from the antiquark going from the upper blob on Fig. 1(a), the k_2^--type terms result in the following matrix element:

$$\int d^4\eta_1\, e^{-ik_1\cdot\eta_1}\langle p_1, S^T|\bar{\psi}(\eta_1)\,\gamma^+[-\infty^-,\,0^-]\psi(0)|S^T,p_1\rangle. \tag{3}$$

If we include the mirror contributions, we will obtain $\langle p_1, S_T|\bar{\psi}(\eta_1)\gamma^+[\eta_1^-,-\infty^-]\psi(0)|S_T,p_1\rangle$ which will ultimately give us the Wilson line connecting the points 0 and η_1. This is exactly what happens in the spin-averaged DY process. However, for the SSA we are interested in, these two (direct and mirror) diagrams have to be considered individually. Their contributions to SSAs differ in sign and the dependence on the boundary point at $-\infty^-$ does *not* cancel. To eliminate the unphysical gluons from our consideration and use the factorization scheme [7], we may choose a *contour* gauge [16] which actually implies also the axial gauge $A^+ = 0$ used in [7]. Imposing this gauge one arrives [16] at the following representation of the gluon field in terms of the strength tensor:

$$A^\mu(z) = \int\limits_{-\infty}^{\infty} d\omega^-\theta(z^- - \omega^-)G^{+\mu}(\omega^-) + A^\mu(-\infty)\,. \tag{4}$$

Moreover, if we choose instead an alternative representation for the gluon in the form with $A^\mu(\infty)$, keeping the causal prescription $+i\epsilon$ in (1), the cost of this will be the breaking of the electromagnetic gauge invariance for the DY tensor. Consider now the term with $\ell^+\gamma^-$ in (1) which gives us finally the matrix element of the twist 3 operator with the transverse gluon field. The parametrization of the relevant matrix elements is

$$\langle p_1, S^T|\bar{\psi}(\lambda_1\tilde{n})\,\gamma_\beta\, gA^T_\alpha(\lambda_2\tilde{n})\,\psi(0)|S^T,p_1\rangle \overset{\mathcal{F}_2^{-1}}{=} i\varepsilon_{\beta\alpha S^T p_1}\,B^V(x_1,x_2)\,. \tag{5}$$

Using the representation (4), this function can be expressed as

$$B^V(x_1,x_2)=\frac{T(x_1,x_2)}{x_1-x_2+i\epsilon}+\delta(x_1-x_2)B^V_{A(-\infty)}(x_1)\,, \tag{6}$$

where the real regular function $T(x_1,x_2)$ ($T(x,x)\neq 0$) parametrizes the vector matrix element of the operator involving the tensor $G_{\mu\nu}$ (cf. [17]). Owing to the time-reversal invariance, the function $B^V_{A(-\infty)}(x_1)$ can be chosen as $B^V_{A(-\infty)}(x)=0$. If the only source of the imaginary part of the hadron tensor is the quark propagator, one may realize this property by assumption: $B^V(x_1,x_2)=T(x_1,x_2)\mathcal{P}/(x_1-x_2)$ corresponding to asymmetric boundary condition for gluons [9]: $B^V_{A(\infty)}(x)=-B^V_{A(-\infty)}(x)$. Here we suggest another way of reasoning. The causal prescription for the quark propagator, generating its imaginary part, simultaneously leads to the imaginary part of the gluonic pole. Note that the fixed complex prescription $+i\epsilon$ in the gluonic pole of $B^V(x_1,x_2)$ (see, (6)) is one of our main results and is very crucial for an extra contribution to hadron tensor we are now ready to explore.

Hadron tensor and gauge invariance. We now return to the hadron tensor and calculate the part involving $\ell^+\gamma^-$, obtaining the following expression for the standard hadron tensor (see, the diagram on Fig. 1(a)):

$$\overline{\mathcal{W}}^{(1)\,[\ell^+]}_{\mu\nu}=-\bar q(y_B)\Im m\int dx_2\,\mathrm{tr}\left[\gamma_\mu\gamma_\beta\gamma_\nu\hat p_2\gamma^T_\alpha\frac{(x_B-x_2)\hat p_1}{(x_B-x_2)ys+i\epsilon}\right]B^V(x_B,x_2)\,\varepsilon_{\beta\alpha S^T p_1}\,. \tag{7}$$

We are now in position to check the QED gauge invariance by contraction with the photon momentum q_μ. Calculating the trace, one gets if the gluonic pole is present. We now focus on the contribution from the diagram depicted on Fig. 1(b). The corresponding hadron tensor takes the form:

$$\mathcal{W}^{(2)}_{\mu\nu}=\int d^4k_1\,d^4k_2\,\delta^{(4)}(k_1+k_2-q)\mathrm{tr}\left[\gamma_\mu\mathcal{F}(k_1)\gamma_\nu\bar\Phi(k_2)\right], \tag{8}$$

where the function $\mathcal{F}(k_1)$ reads

$$\mathcal{F}(k_1)=S(k_1)\gamma_\alpha\int d^4\eta_1\,e^{-ik_1\cdot\eta_1}\langle p_1,S^T|\bar\psi(\eta_1)\,gA^T_\alpha(0)\,\psi(0)|S^T,p_1\rangle\,. \tag{9}$$

Performing the collinear factorization, we derive the expression for the factorized hadron tensor which corresponds to the diagram on Fig. 1(b):

$$\overline{\mathcal{W}}^{(2)}_{\mu\nu}=\bar q(y_B)\,\mathrm{tr}\left[\gamma_\mu\left(\int d^4k_1\,\delta(x_Bp_1^+-k_1^+)\mathcal{F}(k_1)\right)\gamma_\nu\hat p_2\right]. \tag{10}$$

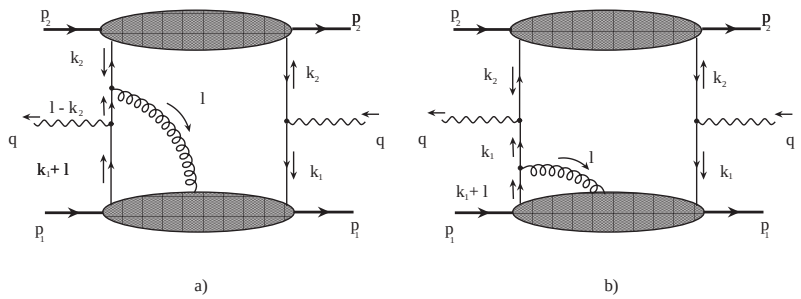

Figure 1: The Feynman diagrams which contribute to the polarized Drell-Yan hadron tensor.

After some algebra, the integral over k_1 in (10) can be rewritten as

$$\int d^4k_1\,\delta(x_1p_1^+ - k_1^+)\mathcal{F}^{[\gamma^+]}(k_1) = \frac{\hat{p}_2\gamma_\alpha^T\gamma_\beta}{2p_2^-p_1^+}\,\varepsilon_{\beta\alpha S^T p_1}\,\frac{1}{x_1+i\epsilon}\int\limits_{-1}^{1} dx_2\,B^V(x_1,x_2)\,, \tag{11}$$

where the parametrization (5) has been used. Taking into account (11) and calculating the Dirac trace, the contraction of the tensor $\overline{\mathcal{W}}_{\mu\nu}^{(2)}$ with the photon momentum q_μ gives us

$$q_\mu\,\overline{\mathcal{W}}_{\mu\nu}^{(2)} = \int dx_1\,dy\left[\delta(x_1-x_B)\delta(y-y_B)\right]\bar{q}(y)\;\varepsilon_{\nu p_2 S^T p_1}\int\limits_{-1}^{1} dx_2\,\Im m\,B^V(x_1,x_2)\,. \tag{12}$$

If the function $B^V(x_1,x_2)$ is the purely real one, this part of the hadron tensor does not contribute to the imaginary part. We now study the $\overline{\mathcal{W}}_{\mu\nu}^{(1)}$ and $\overline{\mathcal{W}}_{\mu\nu}^{(2)}$ contributions and its role for the QED gauge invariance. One can easily obtain:

$$q_\mu\,\overline{\mathcal{W}}_{\mu\nu}^{(1)} + q_\mu\,\overline{\mathcal{W}}_{\mu\nu}^{(2)} = \varepsilon_{\nu p_2 S^T p_1}\,\bar{q}(y_B)\,\Im m\int\limits_{-1}^{1} dx_2\,B^V(x_B,x_2)\left[\frac{x_B-x_2}{x_B-x_2+i\epsilon}-1\right]. \tag{13}$$

Assuming the gluonic pole in $B^V(x_1,x_2)$ exists, after inserting (6) into (13), one gets $q_\mu\,\overline{\mathcal{W}}_{\mu\nu}^{(1)} + q_\mu\,\overline{\mathcal{W}}_{\mu\nu}^{(2)} = 0$. This is nothing else than the QED gauge invariance for the imaginary part of the hadron tensor. We can see that the gauge invariance takes place only if the prescriptions in the gluonic pole and in the quark propagator of the hard part are coinciding. As we have shown, only the sum of two contributions represented by the diagrams on Fig. 1(a) and (b) can ensure the electromagnetic gauge invariance. We now inspect the influence of a "new" contribution 1(b) on the single spin asymmetry and obtain the QED gauge invariant expression for the hadron tensor. It reads

$$\overline{\mathcal{W}}_{\mu\nu}^{GI} = \overline{\mathcal{W}}_{\mu\nu}^{(1)} + \overline{\mathcal{W}}_{\mu\nu}^{(2)} = -\frac{2}{q^2}\,\varepsilon_{\nu S^T p_1 p_2}\left[x_B\,p_{1\,\mu} - y_B\,p_{2\,\mu}\right]\bar{q}(y_B)\,T(x_B,x_B)\,. \tag{14}$$

Within the lepton c.m. system, the SSA [8] related to the gauge invariant hadron tensor (14) reads

$$\mathcal{A}^{SSA} = 2\,\frac{\cos\phi\,\sin 2\theta\,T(x_B,x_B)}{M(1+\cos^2\theta)q(x_B)}, \tag{15}$$

where M is the dilepton mass. We want to emphasize that this differs by the factor of 2 in comparison with the case where only one diagram, presented on Fig. 1(a), has been included in the (gauge non-invariant) hadron tensor. Therefore, from the practical point of view, the neglecting of the diagram on Fig. 1(b) or, in other words, the use of the QED gauge non-invariant hadron tensor yields the error of the factor of two.

Conclusions and Discussions. Shortly summarizing, we want to notice that if we start to work within the axial (light-cone) gauge, without any referring to the contour gauge, we have to sort out all possible prescriptions in order to choose such ones which are in agreement with the gauge invariance [18]. Also, if we "blindly" work within the

axial (light-cone) gauge, in order to get the gauge invariance, we are forced to introduce a such specific subject as the so-called special propagator *a la* J.w.Qiu. [11, 13]. On the other hand, having considered the axial gauge as a particular case of the path-dependent contour gauge, we have no ambiguities with the prescriptions which automatically agree with the gauge invariance. The practical issue of that the gauge invariance has been restored is the new-found factor of 2 in the expression for SSA in the transverse polarized Drell-Yan process.

Thus, we showed that it is mandatory to include a contribution of the extra diagram which naively does not have an imaginary part. The account for this extra contribution leads to the amplification of SSA by the factor of 2. This additional contribution emanates from the complex gluonic pole prescription in the representation of the twist 3 correlator $B^V(x_1, x_2)$ which, in its turn, is directly related to the complex pole prescription in the quark propagator forming the hard part of the corresponding hadron tensor. The causal prescription in the quark propagator, involved in the hard part of the diagram on Fig.1(a), selects from the physical axial gauges the contour gauge. We argued that, in addition to the electromagnetic gauge invariance, the inclusion of new-found contributions corrects by the factor of 2 the expression for SSA in the transverse polarized Drell-Yan process. We proved that the complex prescription in the quark propagator forming the hard part of the hadron tensor, the starting point in the contour gauge, the fixed representation of $B^V(x_1, x_2)$ and the electromagnetic gauge invariance of the hadron tensor must be considered together as the deeply related items. In recent work [19], the factor 1/2 instead of 2 has been claimed. So, in addition to the sign puzzle, do we have a factor of 2 puzzle?!

Supported by grant RFBR 12-02-00613.

References

[1] P.A.M. Guichon, M. Vanderhaegen, 1998 *Prog. Part. Phys.* **41** 125 ; X. Ji, 1998 *J. Phys.* G **24** 1181.

[2] B. Pire, O.V. Teryaev, Proceeding of 13th International Symposium on High Energy Spin Physics, September 8-12, 1998, Protvino, Russia; arXiv:hep-ph/9904375.

[3] I. V. Anikin, B. Pire and O. V. Teryaev, 2000 *Phys. Rev.* D **62** 071501 [arXiv:hep-ph/0003203]; I. V. Anikin and O. V. Teryaev, Phys. Lett. B **509**, 95 (2001) [hep-ph/0102209].

[4] A. V. Belitsky, D. Mueller, L. Niedermeier and A. Schafer, 2001 *Nucl. Phys.* B **593** 289 [arXiv:hep-ph/0004059].

[5] M. Penttinen, M. V. Polyakov, A. G. Shuvaev and M. Strikman, 2000 *Phys. Lett.* B **491** 96 [arXiv:hep-ph/0006321].

[6] V. M. Braun and A. N. Manashov, Phys. Rev. Lett. **107**, 202001 (2011) [arXiv:1108.2394 [hep-ph]]; V. M. Braun and A. N. Manashov, arXiv:1111.6765 [hep-ph].

[7] A. V. Efremov and O. V. Teryaev, 1984 *Sov. J. Nucl. Phys.* **39** 962

[8] N. Hammon, O. Teryaev and A. Schafer, 1997 *Phys. Lett.* B **390** 409 [arXiv:hep-ph/9611359].

[9] D. Boer, P. J. Mulders and O. V. Teryaev, arXiv:hep-ph/9710525; 1998 *Phys. Rev.* D **57** 3057 [arXiv:hep-ph/9710223].

[10] O. V. Teryaev, 2000 *RIKEN Rev.* **28** 101

[11] D. Boer and J. w. Qiu, 2002 *Phys. Rev.* D **65** 034008 [arXiv:hep-ph/0108179].

[12] P. G. Ratcliffe and O. Teryaev, 2009 *Mod. Phys. Lett.* A **24** 2984 [arXiv:0910.5348 [hep-ph]].

[13] H. G. Cao, J. P. Ma and H. Z. Sang, 2010 *Commun. Theor. Phys.* **53** 313 [arXiv:0901.2966 [hep-ph]].

[14] I. V. Anikin and O. V. Teryaev, 2009 *Phys. Part. Nucl. Lett.* **6** 3 [arXiv:hep-ph/0608230];

[15] I. V. Anikin and O. V. Teryaev, 2010 *Phys. Lett.* B **690** 519 [arXiv:1003.1482 [hep-ph]].

[16] S. V. Ivanov, G. P. Korchemsky and A. V. Radyushkin, 1986 *Yad. Fiz.* **44** 230 [1986 *Sov. J. Nucl. Phys.* **44** 145]; S. V. Ivanov and G. P. Korchemsky, 1985 *Phys. Lett.* B **154** 197; S. V. Ivanov, 1990 *Fiz. Elem. Chast. Atom. Yadra* **21** 75.

[17] I. V. Anikin, D. Y. Ivanov, B. Pire, L. Szymanowski and S. Wallon, 2010 *Nucl. Phys.* B **828** 1 [arXiv:0909.4090 [hep-ph]].

[18] V. M. Braun, D. Y. Ivanov, A. Schafer and L. Szymanowski, Nucl. Phys. B **638**, 111 (2002) [arXiv:hep-ph/0204191].

[19] J. Zhou and A. Metz, arXiv:1011.5871 [hep-ph].

POLARIZED PARTON DISTRIBUTIONS IN SYMMETRY BREAKING SCENARIO

F. Arbabifar [1,2 †], Ali N. Khorramian [1,2] and S. Atashbar Tehrani [2]

(1) *Physics Department, Semnan University, Semnan, Iran*
(2) *School of Particles and Accelerators, Institute for Research in Fundamental Sciences (IPM), P.O.Box 19395-5531, Tehran, Iran*
† *E-mail: farbabifar@ipm.ir*

Abstract

The results of our new QCD analysis of helicity parton distributions of the nucleon up to NLO order will be presented. Doing a QCD fit on newest inclusive and semi-inclusive polarized deep inelastic scattering data, we are able to extract polarized structure function of nucleons by choosing new parton distributions at input scale Q_0^2. Particulary we have calculated parton distributions in SU(2) and SU(3) symmetry breaking scenario and the results are in good agreement with the experimental data and the most precise theoretical model obtained by DSSV09.

1 Introduction

One of the major goals of Quantum Chromo Dynamics (QCD) in recent years has been the detailed investigation of the spin structure of the nucleon and nuclei and determination of the partonic composition of their spin projection. Recently some theoretical and experimental studies on the spin structure of the nucleon has been discussed in great detail in several recent reviews mentioned in [1].

In our latest analysis we studied the impact of the recent very precise inclusive polarized DIS data on the determination of polarized parton distributions in symmetry scenario [1] and now we consider SU(2) and SU(3) symmetry breaking scenario and include semi inclusive polarized DIS (SIDIS) data for parton distributions from HERMES [2] and COMPASS [3]. These experiments give important information about the nucleon structure in quite different kinematic regions and also different data sets are complementary in the sense that they probe different aspects of the helicity dependent PDFs. Fully inclusive DIS data from the many different experiments are pivotal in precisely determining the sums of quark and anti-quark distributions and SIDIS data help to tell different quark flavors and quark and anti-quarks apart.

2 QCD Analysis & Parametrization

The idea behind a global analysis is to extract the universal PDFs entering factorized cross sections such as by optimizing the agreement between the measured polarized structure function from DIS, and polarized parton distributions from SIDIS experiments, relative

to the accuracy of the data, and corresponding theoretical calculations, through variation of the shapes of the polarized PDFs.

The twist-2 contributions to the spin-dependent structure function $g_1(x,Q^2)$ are given in terms of a Mellin convolution of the PDFs with the corresponding Wilson coefficient functions $\Delta C_{q,g}$ [4] by

$$\begin{aligned} g_1^p(N,Q^2) &= \frac{1}{2}\sum_{q=u,d,s} e_q^2 \Big\{ (1+\frac{\alpha_s}{2\pi}\Delta C_q^N) \times [\delta q(N,Q^2) + \delta\bar{q}(N,Q^2)] \\ &+ \frac{\alpha_s}{2\pi}\, 2\Delta C_g^N \delta g(N,Q^2) \Big\} \ . \end{aligned} \tag{1}$$

For our analysis we choose an initial scale for the evolution of $Q_0^2 = 4\ GeV^2$ and assume the helicity PDFs to have the following functional forms:

$$\begin{aligned} x\,\delta u_v &= \mathcal{N}_{u_v}\eta_{u_v} x^{a_{u_v}}(1-x)^{b_{u_v}}(1+d_{u_v}x), \\ x\,\delta d_v &= \mathcal{N}_{d_v}\eta_{d_v} x^{a_{d_v}}(1-x)^{b_{d_v}}(1+d_{d_v}x), \\ x\,(\delta\bar{d}-\delta\bar{u}) &= \mathcal{N}_{\bar{d}-\bar{u}}\eta_{\bar{d}-\bar{u}} x^{a_{\bar{d}-\bar{u}}}(1-x)^{b_{\bar{d}-\bar{u}}}(1+c_{\bar{d}-\bar{u}}\sqrt{x}), \\ x\,(\delta\bar{d}+\delta\bar{u}) &= \mathcal{N}_{\bar{d}+\bar{u}}\eta_{\bar{d}+\bar{u}} x^{a_{\bar{d}+\bar{u}}}(1-x)^{b_{\bar{d}+\bar{u}}}(1+c_{\bar{d}+\bar{u}}\sqrt{x}), \\ x\,\delta s = x\,\delta\bar{s} &= \mathcal{N}_q\eta_s x^{a_s}(1-x)^{b_s}(1+d_s x), \\ x\,\delta g &= \mathcal{N}_g\eta_g x^{a_g}(1-x)^{b_g}, \end{aligned} \tag{2}$$

where the normalization constants $\mathcal{N}_i$ are chosen such that η_i are the first moments of $\delta q_i(x,Q_0^2)$, $\eta_i = \int_0^1 dx \delta q_i(x,Q_0^2)$ [5]. Since the SIDIS data are not yet sufficient to distinguish s from $\bar{s}$, we assume $\delta s(x,Q^2) = \delta\bar{s}(x,Q^2)$ throughout, on the other hand the currently available data do not fully constrain the entire x dependence of δq imposed in Eq. (2), and we are forced to make some restrictions on the parameter space, so we tie the small x behavior, represented by the a_g in Eq. (2) of gluon to that of sea distribution by imposing $a_g = a_s + 1$ where we get $c = 1$ which is reasonable as gluon likely dominate in this region. The parameter $b_{\bar{d}-\bar{u}}$, $b_{\bar{d}+\bar{u}}$ and $b_{s=\bar{s}}$ always came out close to each other, so we set them equal.

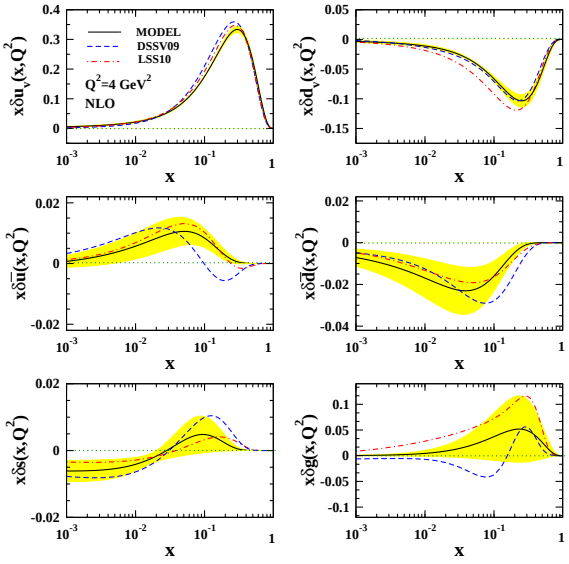

Figure 1: The quark densities in the NLO approximation as a function of x comparing with DSSV09 [7] model.

The parameters η_{u_v} and η_{d_v} are the first moments of the δu_v and δd_v polarized valence quark densities; these quantities can be related to F and D as measured in neutron and hyperon β–decays [6] under the assumption of $SU(2)$ and $SU(3)$ flavor symmetries; $\bar{u} = \bar{d} = \bar{s} = s$:

$$a_3 = \Delta\Sigma_u + \Delta\Sigma_d = \eta_{u_v} - \eta_{d_v} = F + D \ , \tag{3}$$

$$a_8 = \Delta\Sigma_u + \Delta\Sigma_d - 2\Delta\Sigma_s = \eta_{u_v} + \eta_{d_v} = 3F - D \ . \tag{4}$$

We make use of these constraints in our present analysis; however, as we are not interested in forcing flavor symmetry, we leave aside that strong assumption and relax the symmetry relations introducing two parameters, $\varepsilon_{SU(2)}$ and $\varepsilon_{SU(3)}$ respectively. These parameters account quantitatively for eventual departures from flavor symmetry considerations, including also some uncertainties on the low-x behavior, and higher order corrections. Specifically, we set [7]

$$\begin{aligned} \Delta\Sigma_u + \Delta\Sigma_d &= (F+D)\left[1+\varepsilon_{su(2)}\right], \\ \Delta\Sigma_u + \Delta\Sigma_d - 2\Delta\Sigma_s &= (3F-D)\left[1+\varepsilon_{su(3)}\right]. \end{aligned} \tag{5}$$

$\varepsilon_{SU(2,3)}$ parameterize the departures from exact $SU(2)$ and $SU(3)$ symmetries and are included in the QCD fit procedure. We note that the relative deviations of $F+D$ and $3F-D$ may not fully reflect the actual breaking of the $SU(2)$ and, in particular, $SU(3)$ symmetries, for which larger breaking effects have been discussed in the literature mentioned in [5]. This issue may need to be revisited in the future but for now we note that as a result of this the PDFs in our fits will naturally have a tendency to have relatively small $\varepsilon_{SU(2,3)}$ at the input scale.

The input distributions are evolved to the scale Q^2 and an inverse Mellin-transform to x-space is then performed [5], the resulting $\delta q(x)$ for the respective distribution depends on the parameters of the polarized parton distributions chosen at the input scale Q_0^2 and $\alpha_s(Q_0^2)$ which are determined by a fit to the experimental data.

Our analysis is performed using the QCD-PEGASUS program [8]. We work at NLO in the QCD evolution using $N_f = 3$ in the fixed-flavor number scheme with massless partonic flavors. For the proton, neutron and deuteron DIS data we use the same as [1] and for the polarized parton distributions SIDIS data we use HERMES [2] and COMPASS [3]. After the preliminary minimization, we then set the parameters d_{u_v}, d_{d_v}, b_g to their obtained value and fix them in the second minimization as these are relatively flat directions in χ-space, on the other hand according to Eq. (5) we extract η_{u_v} and η_{d_v} from the value of $\varepsilon_{su(2)}$ and $\varepsilon_{su(3)}$ indirectly, so we exclude them in the fit procedure. Finally we minimize the χ^2 with the 15 unknown parameters plus $\varepsilon_{su(2,3)}$ and an undetermined $\alpha_s(Q_0^2)$, the values of these parameters are summarized in Table 1. We find $\chi^2/\text{d.o.f.} = 392.25/473 = 0.829$ which yields an acceptable fit to the experimental data.

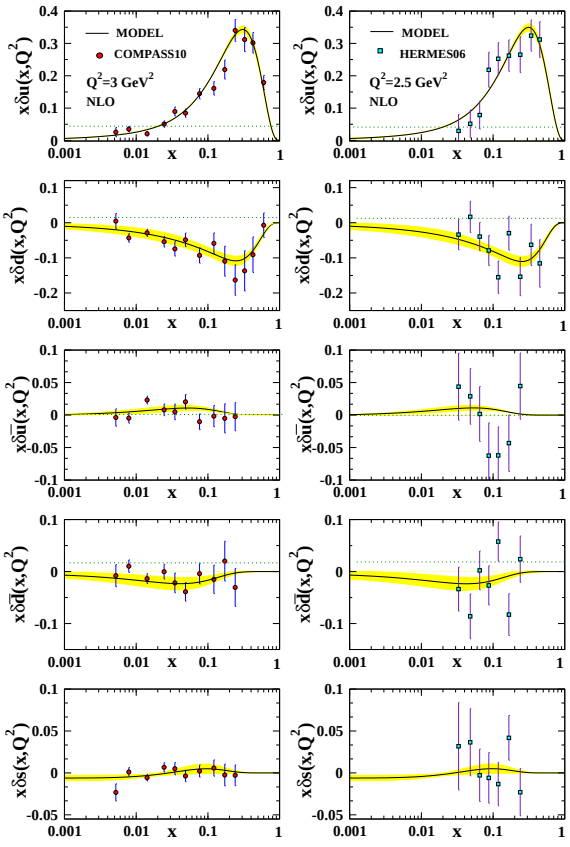

Figure 2: The quark helicity distributions evaluated at $Q^2 = 2.5,\ 3\ GeV^2$ comparing to the COMPASS10 [3] and HERMES06 [2] data.

3 Results

Figure 1 shows the extracted NLO polarized PDFs as compared with parametrizations from DSSV09 [7]. Examining the $x\delta u_v$ and $x\delta d_v$ distributions we see that both of the fits are in agreement. For the $x\delta s$, $x\delta\bar{u}$, $x\delta\bar{d}$ and $x\delta s$ distributions, the curves are also comparable while the DSSV analysis employs results from semi-inclusive DIS A_{LL} data including fragmentation functions which can impose individual constraints on individual quark flavor distributions in the nucleon [7]. Finally, for the gluon distribution, the DSSV results have a sign change in the region of $x \sim 0.1$ while the other fits, like our model, are positive. Using RHIC pp data by DSSV give a first direct constraint on gluon polarization as their mentioned in the literature, which is not included in our analysis. Figure 2 displays results for the polarized PDFs evaluated to $Q^2 = 2.5, 3$ comparing with COMPASS [3] and HERMES [2] data, the data are generally well described within errors.

$\varepsilon_{su(2)} = 0.0444 \pm 0.0439$			$\varepsilon_{su(3)} = -0.0122 \pm 0.0535$		
δu_v	η	0.707	$\delta\bar{u} + \delta d$	η	-0.0363 ± 0.065
	a	0.428 ± 0.043		a	0.032 ± 0.015
	b	3.221 ± 0.093		b	$b_{\delta\bar{d}-\delta\bar{u}}$
	d	51.076(fixed)		c	19.402 ± 20.560
δd_v	η	-0.244	δs	η	0.118 ± 0.037
	a	0.419 ± 0.117		a	0.057 ± 0.029
	b	3.901 ± 0.424		b	$b_{\delta\bar{d}-\delta\bar{u}}$
	d	34.341 (fixed)		d	-35.512 ± 15.38
$\delta\bar{d} - \delta\bar{u}$	η	-0.215 ± 0.056	δg	η	0.117 ± 0.149
	a	0.493 ± 0.060		a	$a_{\delta s} + 1$
	b	14.003 ± 3.551		b	3.425 (fixed)
	c	1.690 ± 2.003			
$\alpha_s(Q_0^2) = 0.340 \pm 0.021$			$\chi^2/NDF = 392.254/473 = 0.829$		

Table 1: Final parameter values and their statistical errors at the input scale $Q_0^2 = 4.0\ GeV^2$.

References

[1] A. Khorramian *et al.* Phys. Rev. D **83**, (2011) 054017.

[2] [HERMES Collaboration], Phys. Rev. D **71**, (2006) 012003.

[3] [COMPASS collaboration], Phys. Lett. B **693**, (2010) 227.

[4] B. Lampe and E. Reya, Phys. Rept. **332**, (2000) 1 [arXiv:hep-ph/9810270].

[5] J. Blumlein, H. Bottcher, Nucl. Phys. **B841**, (2010) 205-230 [arXiv:1005.3113 [hep-ph]].

[6] C. Amsler *et al.* (Particle Data Group), Phys. Lett. B **667**, (2008) 1.

[7] D. de Florian *et al.* Phys. Rev. **D80**, (2009) 034030 [arXiv:0904.3821 [hep-ph]].

[8] A. Vogt, Comput. Phys. Commun. **170**, (2005) 65 [arXiv:hep-ph/0408244].

STRING FRAGMENTATION MODEL WITH SPINNING QUARKS

X. Artru [1†] and Z. Belghobsi [2]

(1) *Université de Lyon, CNRS/IN2P3 and Université Lyon 1, IPNL, France*
(2) *Laboratoire de Physique Théorique, Université de Jijel, Algeria*
† *x.artru@ipnl.in2p3.fr*

Abstract

The quark spin degree of freedom is introduced in the string fragmentation model, using Pauli spinors and matrices. The hadron mass-shell constraints, which were omitted in a preliminary model, are now satisfied. The algorithm for a recursive Monte-Carlo generation of a polarized quark jet is described.

1 Introduction

Quark spin plays a dynamical role in jet formation, as confirmed by the Collins effect. The Collins asymmetry can be used as a *quark polarimeter* for transversity. Similarly, *jet handedness* provides a polarimeter for quark helicity. To optimize these polarimeters, a theoretical model is needed as a guide. Since helicity and transversity are non-commuting observables, a model describing both effects must start with *quantum amplitudes* rather than probabilities. In this direction a toy model was proposed in [1]. This model, which uses Pauli spinors, not only reproduces the transverse spin effects of the classical string + $^3P_0$ mechanism [2,3], but yields jet handedness in addition. However, it does not take into account the hadron mass-shell constraints. This approximation allows a full decoupling of longitudinal and transverse momenta and makes analytical calculations possible, but is too crude for realistic Monte-Carlo simulations of jets.

In this paper we propose a model with mass-shell constraints. It combines the spin factors of the toy model and the kinematical dependance of the string fragmentation model [2]. In Section 2 we review the two main models of quark jets without spin : the *ordinary recursive model* and the *string fragmentation model*. In Section 3 we review the toy model of [1]. In Section 4 we write the quantum amplitudes underlying the string fragmentation model and include spin matrix factors in them. In Section 5 we give the Monte-Carlo algorithm for a recursive processing of the model.

2 Spinless fragmentation models

Fig.1a depicts an event of e^+e^- annihilation or $W^\pm$ decay into quark q_A + antiquark $\bar{q}_B$, followed by the hadronisation process

$$q_A + \bar{q}_B \to h_1 + h_2 ... + h_N \,. \tag{1}$$

Hadrons at the right and left sides form the *quark* and *antiquark* jets. Here we will restrict ourselves to processes without hard gluon and without initial or final baryon.

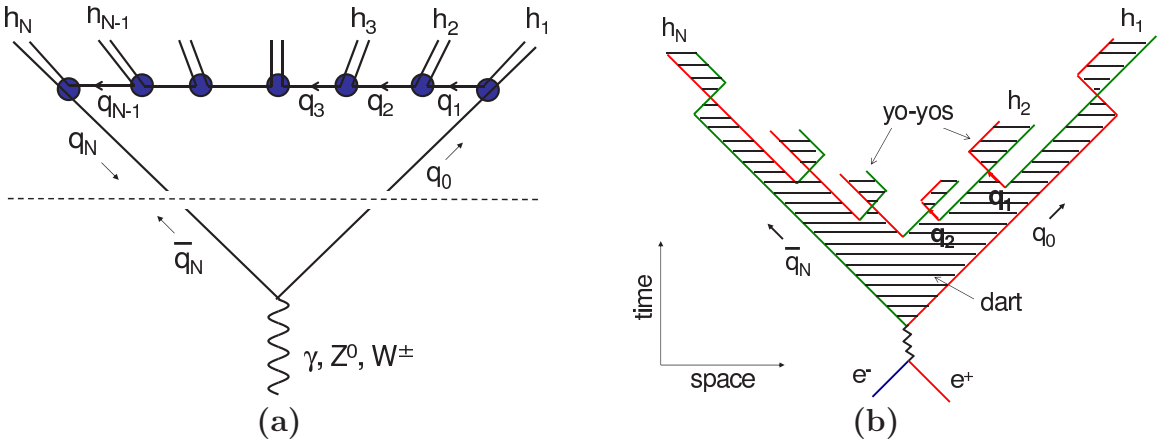

Figure 1: **(a)** e^+e^- annihilation or $W^\pm$ decay in quark-antiquark → hadrons. **(b)** String fragmentation.

The simple recursive model. The most simple model of quark jets for Monte-Carlo simulations is the *recursive model* [4, 5]. Looking from right to left at the upper part of Fig.1a, the process (1) can be decomposed in

$$\begin{aligned} q_0 &\to h_1 + q_1 \ , \\ q_1 &\to h_2 + q_2 \ , \\ \cdots\cdots \quad q_{N-1} &\to h_N + q_B \ . \end{aligned} \tag{2}$$

$q_0 \equiv q_A$ and $q_B \equiv q_N$ is the charge conjugate of $\bar{q}_B$ propagating "backward in time" with 4-momentum $q_B \equiv -\bar{q}_B$. The 4-momentum conservation $q_{n-1} = p_n + q_n$ holds at each step. p_n is the 4-momentum of *n^{th}-rank hadron*. q_n stands either for the species (u, d or s) of the $n^{\rm th}$-rank quark or for its 4-momentum. In the simplest receipe, the sharing between p_n and q_n is made according to the *splitting probability distribution*,

$$d\zeta_n \, d^2\mathbf{q}_{n\rm T} \, f(\zeta_n, q_{n\rm T}) \ , \tag{3}$$

where $\mathbf{q}_{\rm T} = (q^x, q^y)$, $\zeta_n = q_n^+/q_{n-1}^+$ and $q^\pm \equiv q^0 \pm q^z$. The $+z$ and $-z$ directions are along $\mathbf{q}_{\rm A}$ and $\bar{\mathbf{q}}_{\rm B}$.

Including the quark *flavor* degree of freedom is relatively easy. The $q \to h + q'$ splitting function depends on the flavors and writes $f_{q',h,q}(\zeta, q'_{\rm T})$.

Notations. The symbol $\{q_n\}$, with curly brackets, represents the momentum *and* the flavor of the $n^{\rm th}$ quark altogether. See, *e.g.* Eq.(5). A four-momentum q is separated in transverse part $\mathbf{q}_{\rm T} = (q^x, q^y)$ and time-longitudinal part $q_{\rm L} = (q^0, q^z)$. The virtual mass square is $q^2 = {q_{\rm L}}^2 - {\mathbf{q}_{\rm T}}^2 = q^+q^- - {\mathbf{q}_{\rm T}}^2$.

The polarization vector of a quark is decomposed as $\mathbf{S} = (S_{\rm L}, \mathbf{S}_{\rm T})$ where $S_{\rm L}/2 = \langle \text{helicity} \rangle$, $\mathbf{S}_{\rm T} = \langle \text{transversity} \rangle$. The density matrix is $\rho = (1 + \mathbf{S}.\vec{\sigma})/2$.

The string fragmentation model [2, 6]. One may consider Fig.1a as a diagram of the dual resonance model. Hadronization is the cascade decay of a massive string (the *dart*) stretching between q_A and $\bar{q}_B$. The space-time picture is shown in Fig.1b. At the $n^{\rm th}$ string breaking point (starting from the right) a $q_n\bar{q}_n$ pair is created. $\bar{q}_n$ moves to

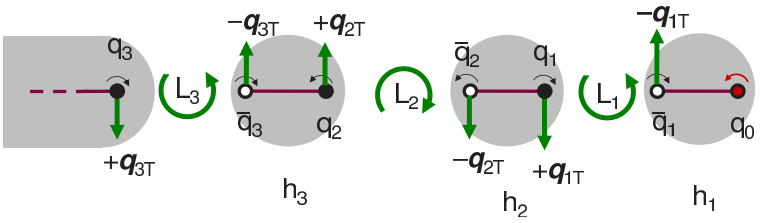

Figure 2: The string + $^3P_0$ mechanism for Collins effect.

the right, meets q_{n-1} which is moving to the left and both form the hadron h_n. If the null-plane coordinate $X^- = t - z$ is used as time variable, the hadrons are emitted in the ordering of (2) and the string model can be treated as a recursive one, with the *symmetric Lund splitting function* [2],

$$f_{q',h,q}(\zeta, \mathbf{q}'_{\mathrm{T}}, \mathbf{q}_{\mathrm{T}}) \propto Z^{a\{q\}}\ (1/Z-1)^{a\{q'\}}\ \exp\left(-b\,\frac{m_h^2 + \mathbf{p}_{\mathrm{T}}{}^2}{Z}\right). \tag{4}$$

$Z = 1-\zeta$ and $a\{q\} \equiv a_q(\mathbf{q}_{\mathrm{T}}^2)$, which generally depends on the quark flavor q and transverse momentum $\mathbf{q}_{\mathrm{T}}$. Eq.(4) is used in the Monte-Carlo simulation code PYTHIA.

The string fragmentation model is invariant under
– (a) rotations about the z-axis,
– (b) Lorentz transformations along the z-axis
– (c) mirror reflection about any plane containing the z-axis (equivalent to parity),
– (d) *quark chain reversal* or "left-right symmetry", *i.e.,* interchanging q_A and $\bar{q}_B$.
It is not covariant *locally* (*i.e.,* step-by-step), but *globally* for the whole process of Fig.1.

3 Review of the toy model of Ref. [1]

The classical *string* + $^3P_0$ mechanism [2, 3]. We consider the simplest case where all the emitted partices are pseudoscalar mesons. Then $(q_n\bar{q}_{n-1})$ in h_n is a spin singlet. At a string breaking the $q_n\bar{q}_n$ pair is assumed to be created in the $^3P_0$ state with zero total momentum (corresponding to the vacuum quantum numbers). Fig.2 depicts the recursive decay of the dart when q_0 has a transverse, anti-clockwise polarization. $(q_0\bar{q}_1)$ is a spin-singlet, therefore $\bar{q}_1$ spins clockwise. $(q_1\bar{q}_1)$ is a spin-triplet, therefore q_1 also spins clockwise. Due to the $^3P_0$ configuration, the relative $q_1 - \bar{q}_1$ orbital momentum $\mathbf{L}_1$ is opposite to the spins, therefore anti-clockwise. It makes $\bar{q}_1$ move upward and q_1 move downward in the figure. The upward momentum of q_1 is taken by hadron h_1, resulting in a Collins effect, with $\mathbf{p}_{1\mathrm{T}}$ on the side of $\mathbf{S}_{0\mathrm{T}} \times \hat{\mathbf{z}}$.

Iterating this reasoning, q_2 and $\bar{q}_2$ are spinning anti-clokwise, $\mathbf{L}_2$ is clokwise, etc. One obtains Collins effects of alternate sides for h_2, h_3, etc. Of course, successive spins are not so rigidly coupled and the Collins effect decays along the quark chain. Nevertheless the model predicts a Collins effect for h_2 opposite to that of h_1 and reinforced by the fact that q_1 and $\bar{q}_2$ move on the same side. This is in agreement with experiment.

The string + $^3P_0$ mechanism also explains the polarization of inclusive hyperons [2].

The covariant quark-multiperipheral amplitude. The upper half of Fig.1a looks like a multiperipheral diagram [7], but with quark exchanges instead of meson exchanges. We treat q_A and $\bar{q}_B$ as on mass-shell quarks and assume that the probability of the

whole process of Fig.1a factorizes in the probabilities of the upper and lower parts. The amplitude of (1) writes

$$\mathcal{M}\{q_A\bar{q}_B \to h_1 h_2 ... h_N\} = \\ \Gamma\{q_B, h_N, q_{N-1}\}\,\Delta\{q_{N-1}\}\cdots\Delta\{q_2\}\,\Gamma\{q_2, h_2, q_1\}\,\Delta\{q_1\}\,\Gamma\{q_1, h_1, q_A\}\,. \tag{5}$$

$\Delta\{q\} = D_q(q^2)\,(\mu_q + \gamma.q)$ is the quark propagator. μ_q is the quark mass. $D_q(q^2)$ is a fast decreasing function of $|q^2|$. $\Gamma\{q', h, q\} \equiv \Gamma_{q',h,q}(q', q)$ is the $q \to h + q'$ vertex function, which is a 4×4 matrix in the space of Dirac spinors. For the emission of a pseudoscalar meson, $\Gamma\{q', h, q\} = \gamma_5\, G_{q',h,q}(q'^2, q^2)$. The model is covariant *locally*, *i.e.,* at each vertex and propagator.

Another important approximation is to neglect interferences between several diagrams giving the same final state. Then the total hadronisation cross section writes

$$\mathcal{R}\{\bar{q}_B, q_A\} = \sum_N \sum_{h_1,...h_N} \int \frac{\mathrm{d}^3\mathbf{p}_1 \cdots \mathrm{d}^3\mathbf{p}_N}{p_1^0 \cdots p_N^0}\; \delta^4(p_1 + p_2 ... + p_N - q_A - \bar{q}_B\} \\ |\bar{v}(\bar{q}_B, \mathbf{S}_\mathrm{B})\,\mathcal{M}\{q_A\bar{q}_B \to h_1 h_2 ... h_N\}\,u(q_A, \mathbf{S}_\mathrm{A})|^2\;. \tag{6}$$

The second summation bears on the hadron species. $u(q_A, \mathbf{S}_\mathrm{A})$ and $v(\bar{q}_B, \mathbf{S}_\mathrm{B})$ are the Dirac spinors of q_A and $\bar{q}_B$.

Reduction to Pauli spinors. We now describe the spin degree of freedom in the most economical way, with Pauli instead of Dirac spinors. We give up local covariance, but maintain the invariances (a), (b), (c) and (d) listed in the introduction about the string model. For this we replace [1]

- $u(q_0, \mathbf{S}_0)$ by the Pauli spinor $\chi(\mathbf{S}_0)$
- $\bar{v}(q_{\bar{q}_B}, \mathbf{S}_{\bar{q}_B})$ by $-\chi^\dagger(-\mathbf{S}_{\bar{q}_B})\,\sigma_z$
- γ_5 by σ_z
- $\mu_q + \gamma.q$ by $\mu_q + \sigma_z\,\sigma.\mathbf{q}_\mathrm{T}$.

Thus, the propagators has the non-covariant form

$$\Delta\{q\} = D_q({q_\mathrm{L}}^2, {\mathbf{q}_\mathrm{T}}^2)\;(\mu_q + \sigma_z\,\sigma.\mathbf{q}_\mathrm{T})\;. \tag{7}$$

The toy model [1]. We consider only pseudo-scalar mesons, with the momentum-independent emission vertex σ_z, and take a factorized, flavor-independent quark propagator

$$\Delta\{q\} = D_L({q_\mathrm{L}}^2)\,\exp(-B{\mathbf{q}_\mathrm{T}}^2/2)\;(\mu + \sigma_z\,\sigma.\mathbf{q}_\mathrm{T})\,. \tag{8}$$

Furthermore we ignore the mass-shell constraint $m_n^2 = p_n^+ p_n^- - p_{n,\mathrm{T}}^2$. This crude approximation achieves the full decoupling of the longitudinal momenta from the transverse ones and from the quark spin. The joint $\mathbf{p}_T$ -distibutions of the n first mesons have simple expressions, for instance

$$I(\mathbf{p}_{1\mathrm{T}}, \mathbf{p}_{2\mathrm{T}}, \mathbf{p}_{3\mathrm{T}}) \propto \exp(-B\mathbf{q}_{\mathrm{T}1}^2 - B\mathbf{q}_{\mathrm{T}2}^2 - B\mathbf{q}_{\mathrm{T}3}^2)\;\mathrm{Tr}\left\{\mathbf{M}_3\,\mathbf{M}_2\,\mathbf{M}_1\,\rho_0\,\mathbf{M}_1^\dagger\,\mathbf{M}_2^\dagger\,\mathbf{M}_3^\dagger\right\}, \tag{9}$$

where $\rho_0 = (1 + \mathbf{S}_0.\sigma)/2$ is the spin density matrix of q_0 and $\mathbf{M}_n = (\mu + \sigma_z\sigma.\mathbf{q}_{\mathrm{T}n})\,\sigma_z$. For complex μ one obtains a Collins effect for each meson, the analyzing power of which depends only on the meson rank. See Ref. [1] for more properties of the model.

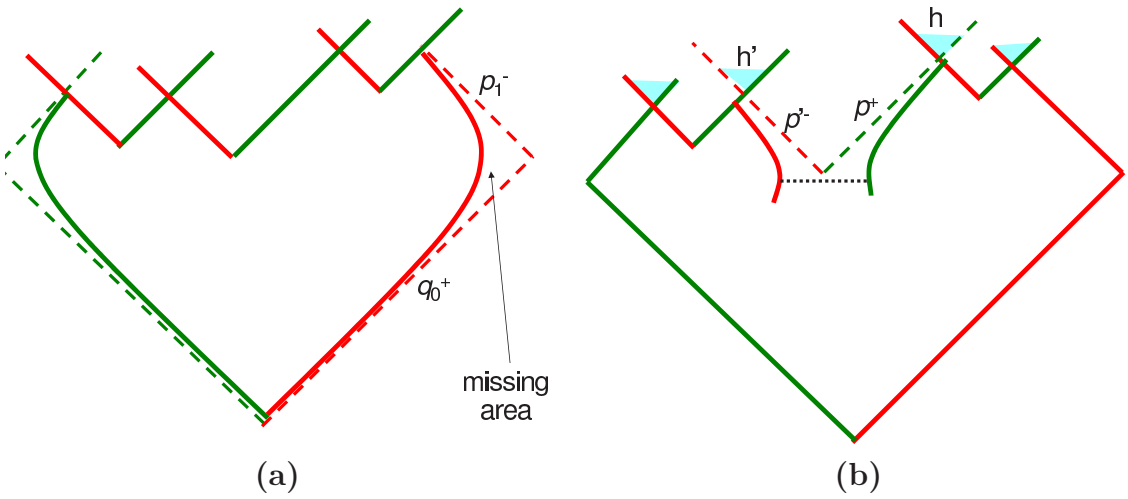

Figure 3: **(a)** Trajectories of massive q_A and $\bar{q}_B$. **(b)** Tunneling trajectories of q_n and $\bar{q}_n$.

4 The semi-quantized string model

Let us first consider spinless quarks and mesons. Following the sum-over-histories approach of Feynman, to the classical string history of Fig.1b we associate the amplitude

$$\begin{array}{c} \mathcal{M}(q_A\bar{q}_B \to h_1 h_2 ... h_N) = \exp[\,(-i\kappa_C + 2i\kappa)\,\mathcal{A}\,] \\ (q_A^+ p_1^-)^{\alpha\{q_A\}}\ (-p_1^+ p_2^- - i0)^{\alpha\{q_1\}}\ \cdots\ (-p_{N-1}^+ p_N^- - i0)^{\alpha\{q_{N-1}\}}\ (p_N^+ \bar{q}_B^{\,-})^{\alpha\{q_B\}} \\ g\{q_B, h_N, q_{N-1}\} \cdots g\{q_2, h_2, q_1\}\, g\{q_1, h_1, q_0\}\,. \end{array} \tag{10}$$

• $\mathcal{A}$ is the space-time area swept by the dart. $\kappa_C = \kappa - i\mathcal{P}/2$ is the *complex* string tension of the dart [8], accounting for its unstability (in analogy with the complex mass $m - i\Gamma/2$ of an unstable particle). We will use $b \equiv \mathcal{P}/(2\kappa^2)$.

The exponent of the first line contains the pure *string action* of the dart (proportional to $-\kappa_C$) and "missing propagation phases" (proportional to 2κ) of the final hadrons, taking into account their different emission points [9].

• The first and last power-law factors of the 2nd line takes into account the *quark actions* of q_A and $\bar{q}_B$, which in the case of non-zero mass follow the pieces of hyperbolas in Fig.3a. We have

$$\alpha\{q_A\} = (b - i/\kappa)\,\mu_A^2\,/2 \quad \text{(idem for } \bar{q}_B\text{)}. \tag{11}$$

These factors also take into account the "missing string area" between the hyperbolas and the brokenline trajectories that would be followed by massless quarks.

• The intermediate power-law factors of the 2nd line take into account the actions of the quarks and antiquarks created in pairs at string ruptures (Fig.3b). They simulate a multi-Regge behavior at large rapidity gaps, $\alpha\{q\}$ being the quark Regge trajectory. One may take the analytic continuation of (11), replacing q_A^+ by $-p_n^+$, p_1^- by p_{n+1}^- :

$$\alpha\{q_n\} = (\mu_n^2 + \mathbf{q}_{n\mathrm{T}}^2)\,(b - i/\kappa)/2\,. \tag{12}$$

For real μ_n the modulus square of the n^{th} factor is

$$(p_n^+ p_{n+1}^-)^{b(\mu_n^2 + \mathbf{q}_{n\mathrm{T}}^2)}\,\exp[-\pi(\mu_n^2 + \mathbf{q}_{n\mathrm{T}}^2)/\kappa]\,, \tag{13}$$

which exhibits the characteristic exponential factor of Schwinger tunneling [2]. This tunneling is represented by a dotted line in Fig.3b. There is however a limitation to Eq.(12). The tunneling length is $2E_{q\mathrm{T}}/\kappa = 2(\mu^2 + \mathbf{q}_\mathrm{T}^2)^{1/2}/\kappa$. It must be smaller than the string length, which is of the order of $\mathcal{P}^{-1/2}$. In fact the production of large E_T quarks should not be described by the string model, but by perturbative QCD. Besides, at large rapidity gap (large $p_n^+ p_{n+1}^-$), the first factor of (13) would too much favor heavy quarks.

A possible sensible choice is to use Eq.(12) with $b = 0$.

- The last line contains vertex functions

$$g\{q', h, q\} \equiv g_{q',h,q}(\mathbf{q}_\mathrm{T}'^2, \mathbf{q}_\mathrm{T}'.\mathbf{q}_\mathrm{T}, \mathbf{q}_\mathrm{T}^2) \tag{14}$$

which depend on flavours and *transverse* momenta, but not on longitudinal ones. Quark chain reversal imposes g to be symmetric under the interchange $\{q; \mathbf{q}_T\} \leftrightarrow \{q'; \mathbf{q}'_T\}$.

Taking the modulus square of (10) for the fully differential cross section of (1) is equivalent to the symmetric Lund model.

Inclusion of quark spin. Spin is simply included by inserting the 2×2 matrices of the toy model. Fig.4. indicates where such matrices operate. Restricting ourselves to pseudoscalar meson production, we have to multiply the expression (10) by the chain of 2×2 matrices

$$\begin{aligned}&\sigma_z\,(\mu_{N-1} + \sigma_z\sigma.\mathbf{q}_{\mathrm{T}N-1})\,\sigma_z\cdots\\ &\quad(\mu_2 + \sigma_z\sigma.\mathbf{q}_{\mathrm{T}2})\,\sigma_z\,(\mu_1 + \sigma_z\sigma.\mathbf{q}_{\mathrm{T}1})\,\sigma_z\,.\end{aligned} \tag{15}$$

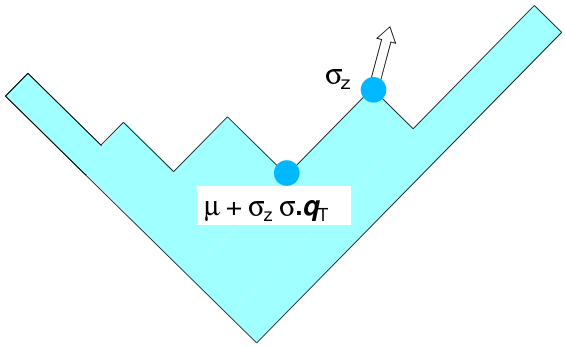

Figure 4: Spin matrices to be inserted in the string amplitude.

To sum up, the fully differential cross section of (1) with polarized q_A and $\bar{q}_B$ is given by

$$\begin{aligned}\mathcal{R}\{\bar{q}_B, q_A\} = \sum_N \sum_{h_1,\ldots h_N} \int \mathrm{d}^4q_1 \cdots \mathrm{d}^4q_{N-1}\; 2\delta(p_1^2 - m_1^2)\cdots 2\delta(p_N^2 - m_N^2)\\ \left|\chi^\dagger(-\mathbf{S}_\mathrm{B})\,\sigma_z\,\mathcal{M}\,\chi(\mathbf{S}_\mathrm{A})\right|^2,\end{aligned} \tag{16}$$

$\mathcal{M}$ being given by (10) times (15). Unlike the toy model, the present string fragmentation model takes into account the mass-shell conditions properly.

5 Recursive Monte-Carlo Algorithm

- The string amplitude (10) times (15) can be put in a multiperipheral form. The *splitting amplitude*, defined as the product of the n^{th} vertex and the n^{th} propagator, is given by

$$\begin{aligned}T_n \equiv T\{q_n, h_n, q_{n-1}\} \equiv \Delta\{q_n\}\,\Gamma\{q_n, h_n, q_{n-1}\} =\\ \exp\left(\frac{i-b}{2}\,q_{n-1}^+ p_n^-\right)(q_{n-1}^+ p_n^-)^{\alpha\{q_{n-1}\}}\left(\frac{-p_n^+ - i0}{q_n^+}\right)^{\alpha\{q_n\}} g\{q', h, q\}\,(\mu_n + \sigma_z\sigma.\mathbf{q}_{n\mathrm{T}})\,\sigma_z\,.\end{aligned} \tag{17}$$

Introducing the sub-amplitude $\mathcal{M}_{N-n}$ for $q_n + \bar{q}_B \to h_{n+1} + \cdots h_N$, we have

$$\mathcal{M} \equiv \mathcal{M}_N = \mathcal{M}_{N-n}\,T_n \cdots T_2\,T_1\;. \tag{18}$$

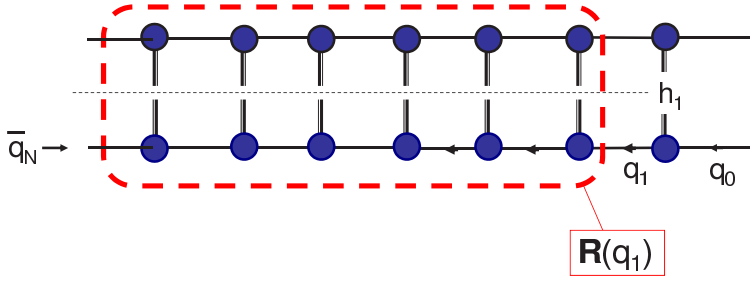

Figure 5: Unitarity diagram for $\mathcal{R}$.

- Using (18), the n-particle inclusive cross section with polarized quarks writes

$$\frac{d\sigma(q_A+\bar{q}_B\to h_1,\cdots h_n+X)}{d^3\mathbf{p}_1/p_1^0\cdots d^3\mathbf{p}_n/p_n^0}=\mathrm{Tr}\{\,\rho_0\;T_1^\dagger\,T_2^\dagger\cdots T_n^\dagger\;\mathcal{R}\{q_n\}\;T_n\cdots T_2\,T_1\}\,, \tag{19}$$

where ρ_0 is the spin density matrix of q_A and

$$\mathcal{R}\{q_n\}=\sum_{N>n}\int\frac{\mathrm{d}^3\mathbf{p}_{n+1}\cdots\mathrm{d}^3\mathbf{p}_N}{p_{n+1}^0\cdots p_N^0}\;\mathcal{M}_{N-n}^\dagger\,\sigma_z\,\frac{1-\sigma.\mathbf{S}(\bar{q}_B)}{2}\,\sigma_z\;\mathcal{M}_{N-n} \tag{20}$$

is the *cross section matrix* [10] of the reaction $q_n+\bar{q}_B\to$ hadrons. It operates in the spin space of q_n. It also depends on the antiquark polarization $\mathbf{S}(\bar{q}_B)$, but at large $(q_n+\bar{q}_B)^2$ this dependence is negligible and we may take $\mathbf{S}(\bar{q}_B)=0$. Fig.5 represents the unitarity diagram giving $\mathcal{R}\{q_A\}$. Encircled in dashed line is the unitarity diagram for $\mathcal{R}\{q_1\}$. The general cross section matrix $\mathcal{R}\{q\}$ satisfies the integral *recursion relation*

$$\mathcal{R}\{q\}=\sum_h\int\frac{\mathrm{d}^3\mathbf{p}}{p^0}\,T^\dagger\{q',h,q\}\,\mathcal{R}\{q'\}\,T\{q',h,q\}\,. \tag{21}$$

- We assume the following Regge behavior at large $(q+\bar{q}_B)^2$:

$$\mathcal{R}\{q\}\sim|(\bar{q}_B)^-q^+|^{\alpha_{\mathrm{out}}}\;\left[\beta_q(\mathbf{q}_{\mathrm{T}}^2)+\gamma_q(\mathbf{q}_{\mathrm{T}}^2)\,\sigma_z\sigma.\mathbf{q}_{\mathrm{T}}\right]. \tag{22}$$

α_{out} is the *output Regge intercept*. $a_{\{q\}}$ of Eq.(4) and $\alpha_{\{q\}}$ of Eq.(10) are linked by [8]

$$a_{\{q\}}=\alpha_{\mathrm{out}}-2\alpha_{\{q\}}\,. \tag{23}$$

A preliminary numerical task consists in calculating α_{out} and the *Regge residue functions* $\beta_q(\mathbf{q}_{\mathrm{T}}^2)$ and $\gamma_q(\mathbf{q}_{\mathrm{T}}^2)$, solving the integral equation(21).

- Suppose that we know the flavor and momentum of quark $\{q_{n-1}\}\equiv\{q\}$ and its polarization $\mathbf{S}_{n-1}\equiv\mathbf{S}$. From Eqs.(21) and (22), one can write

$$\sigma\{q+\bar{q}_B\}=\mathrm{Tr}\,\{\rho\;\mathcal{R}\{q\}\}=|(\bar{q}_B)^-|^{\alpha_{\mathrm{out}}}\sum_h\int\frac{\mathrm{d}^3\mathbf{p}}{p^0}$$
$$(q'^+)^{\alpha_{\mathrm{out}}}\;\mathrm{Tr}\left\{\;T\{q',h,q\}\;\rho\;T^\dagger\{q',h,q\}\;[\beta_{q'}(\mathbf{q'_{\mathrm{T}}}^2)+\gamma_{q'}(\mathbf{q'_{\mathrm{T}}}^2)\,\sigma_z\sigma.\mathbf{q}'_{\mathrm{T}}]\;\right\} \tag{24}$$

with $p+q'=q$ and $\rho=(1+\sigma.\mathbf{S})/2$. The second line is proportional to the probability that quark $\{q\}\equiv\{q_{n-1}\}$ emits a hadron $\{h_n\}$ of species h and 4-momentum p. In the Monte-Carlo method, one generates h and p at random according to this probability. $\{q'\}\equiv\{q_n\}$ is related to $\{h\}$ by the conservation of charge, strangeness and 4-momentum.

• Once the flavors and momenta of $\{p\} \equiv \{p_n\}$ and $\{q'\} \equiv \{q_n\}$ are known, the q' polarization is given by

$$\frac{1+\sigma.\mathbf{S}'}{2} \equiv \rho' = \frac{T\{q',h,q\}\ \rho\ T^\dagger\{q',h,q\}}{\mathrm{Tr}\,(\ T\{q',h,q\}\ \rho\ T^\dagger\{q',h,q\}\ )}\ . \tag{25}$$

Thus one has $\{q_n\}$ and $\mathbf{S}_n$. Iterating the last two steps, one generates the jet of a polarized quark.

6 Conclusion

We have given the principle of a recursive quark fragmentation model which includes the spin degree of freedom. Since spin has essentially quantum properties, we started from *amplitudes* rather *probabilities*. For that we took the amplitudes which underly the symmetric Lund fragmentation model.

When an imaginary part is given to the quark mass μ, the model produces the spin asymmetries of Collins and jet handedness, like in the toy model of [1] but with hadron mass shell contraints duly taken into account. For the moment we have no theoretical justification for taking a complex μ, but it provides a quantum realization of the string $+\ ^3P_0$ mechanism, which up to now is in qualitative agreement with experiment.

References

[1] X. Artru, *Proceedings of the Dubna spin meeting 2009* ; arXiv:1001.1061.

[2] B. Andersson, G. Gustafson, G. Ingelman and T. Sjöstrand, Phys. Rep. **97** (1983) 31.

[3] X. Artru, J. Czyżewski and H. Yabuki, Zeit. Phys. **C73** (1997) 527.

[4] A. Krzywicki and B. Petersson, Phys. Rev. D **6** (1972) 924.

[5] J. Finkelstein and R. D. Peccei, Phys. Rev. D **6** (1972) 2606.

[6] X. Artru and G. Mennessier, Nucl. Phys. **B70** (1974) 93.

[7] D. Amati, A. Stanghellini and S. Fubini, Nuov. Cim. **26** (1962) 896.

[8] X. Artru, Z. Phys. C - Particles and Fields **26** (1984) 23.

[9] X. Artru and M.G. Bowler, Z. Phys. C - Particles and Fields **37**, 293 (1988).

[10] X. Artru, M. Elchikh, J-M. Richard, J. Soffer and O.V. Teryaev, Phys. Reports **470** (2009).

SPIN MICROSCOPY WITH ENHANCED WILSON LINES IN THE TMD PARTON DENSITIES

I.O. Cherednikov [1,2,†], A.I. Karanikas [3] and N.G. Stefanis [4]

(1) *Departement Fysica, Universiteit Antwerpen, B-2020 Antwerpen, Belgium*
(2) *BLTP, JINR, RU-141980 Dubna, Russia*
(3) *Department of Physics, Nuclear and Particle Physics Section, Panepistimiopolis, GR-15771 Athens, Greece*
(4) *Institut für Theoretische Physik II, Ruhr-Universität Bochum, D-44780 Bochum, Germany*
† *E-mail: igor.cherednikov@ua.ac.be*

Abstract

We discuss the possibility of non-minimal gauge invariance of transverse-momentum-dependent parton densities (TMDs) that allows direct access to the spin degrees of freedom of fermion fields entering the operator definition of (quark) TMDs. This is achieved via enhanced Wilson lines that are supplied with the spin-dependent Pauli term $\sim F^{\mu\nu}[\gamma_\mu, \gamma_\nu]$, thus providing an appropriate tool for the "microscopic" investigation of the spin and color structure of TMDs. We show that this generalization leaves the leading-twist TMD properties unchanged but modifies those of twist three by contributing to their anomalous dimensions. We also comment on Collins' recent criticism of our approach.

Precise knowledge of the geometrical structure, as well as of the spin and color properties, of the Wilson lines (gauge links) in the operator formulation of TMDs is an essential ingredient of the QCD factorization approach to semi-inclusive hadronic processes [1, 2]. The path-$[\mathcal{C}]$-dependent non-Abelian gauge links $[y; x|\mathcal{C}] \equiv \mathcal{P} \exp\left[-ig \int_{x[\mathcal{C}]}^{y} dz^\mu A_\mu^a(z) t^a\right]$, which ensure the gauge invariance of nonlocal operator products and correlators, are intimately related to important issues of TMDs, like the ultraviolet (UV) and rapidity evolution equations, the generation of $T-$odd effects, the proof or violation of factorization, etc. [2, 3]. Different operator definitions of the TMDs can comprise bunches of longitudinal and transverse gauge links possessing a quite involved space-time structure, with non-trivial properties in color space as well (see, e.g., [3–8] and further discussions and references cited therein). Moreover, the location of the gauge integration contours in the $(z^+, z^-, \boldsymbol{z}_\perp)$-plane (in contrast to collinear PDFs, where they belong to a single lightlike ray and are, therefore, one-dimensional) necessitates the inclusion of (possible) contributions of *non-minimal* spin-dependent terms, expressed in terms of enhanced Wilson lines (more below). The path-dependence, being in some sense "hidden" in the case of collinear PDFs [7], becomes a key issue in TMDs. In particular, explicit spin-dependent terms in the gauge links can create significant effects in lattice simulations [2, 9], depending on the geometry of the integration paths, and may also affect the TMD-factorization properties [3].

To this end, we introduced in [10] an enhanced gauge link, denoted by [[...]], which contains the Pauli term proportional to the gluon strength tensor $\sim F^a_{\mu\nu} J_{\mu\nu} = (1/4) F^a_{\mu\nu}[\gamma_\mu, \gamma_\nu]$.

This is the simplest example to realize a direct product of two orthogonal "spaces": The first "space" is the color one, with the *minimal* Wilson lines in the fundamental or adjoint representation of $SU(3)_c$. In the second "space", the spin correlations are generated by the Pauli terms [10]. The spin-dependent terms yield next-to-leading-order twist effects with respect to the spin-"blind" ones, as it follows from usual power-counting.

We discuss below, the main results of our study of the renormalization-group properties of the TMD distribution functions with enhanced gauge-link insertions [10], focusing on the UV properties of the "quark-in-a-quark" TMD. According to our generalized concept of gauge invariance, the *unsubtracted* distribution function of a quark with momentum k and flavor a in a quark with momentum p reads

$$\mathcal{F}_a^{\Gamma}(x,\boldsymbol{k}_\perp) = \frac{1}{2}\mathrm{Tr}\int dk^- \int \frac{d^4\xi}{(2\pi)^4}\,\mathrm{e}^{-ik\cdot\xi}\langle p,s\;|\bar\psi_a(\xi)[[\xi^-,\boldsymbol{\xi}_\perp;\infty^-,\boldsymbol{\xi}_\perp]]^\dagger$$
$$\times[[\infty^-,\boldsymbol{\xi}_\perp;\infty^-,\boldsymbol{\infty}_\perp]]^\dagger\Gamma\;[[\infty^-,\boldsymbol{\infty}_\perp;\infty^-,\boldsymbol{0}_\perp]][[\infty^-,\boldsymbol{0}_\perp;0^-,\boldsymbol{0}_\perp]]\psi_a(0)|p,s\rangle\;, \quad (1)$$

where Γ stands for the Dirac structure constructed from one or several γ-matrices. The matrix elements interpolate between the one-fermion states with momentum p and spin s: $|p,s\rangle$. In the tree-approximation one has

$$\mathcal{F}^{\Gamma(0)}(x,\boldsymbol{k}_\perp) = \frac{1}{2}\mathrm{Tr}\left[(\hat p+m)\,(1+\gamma_5\hat s)\;\;\Gamma\right]\;\delta(p^+-xp^+)\delta^{(2)}(\boldsymbol{k}_\perp)\;. \quad (2)$$

For the unpolarized TMD PDF with $\Gamma=\gamma^+$, one obtains the (twist-two) result

$$\mathcal{F}^{\gamma^+(0)}(x,\boldsymbol{k}_\perp)=\frac{1}{2}\mathrm{Tr}\left[(\hat p+m)\,(1+\gamma_5\hat s)\,\gamma^+\right]\delta(p^+-xp^+)\delta^{(2)}(\boldsymbol{k}_\perp)=\delta(1-x)\delta^{(2)}(\boldsymbol{k}_\perp)\;. \quad (3)$$

The helicity and the transversity distributions read, respectively,

$$\mathcal{F}^{\gamma^+\gamma_5(0)}(x,\boldsymbol{k}_\perp)=\delta(1-x)\delta^{(2)}(\boldsymbol{k}_\perp)\cdot\lambda\;,\;\;\mathcal{F}^{i\sigma^{i+}\gamma_5(0)}(x,\boldsymbol{k}_\perp)=\delta(1-x)\delta^{(2)}(\boldsymbol{k}_\perp)\cdot\boldsymbol{s}^{\boldsymbol{i}}_\perp\;, \quad (4)$$

where λ is the helicity and $\boldsymbol{s}^{\boldsymbol{i}}_\perp$ is the transverse spin of parton i. Note that the above normalization conditions can only be obtained within the quantization procedure in the lightcone gauge, where the (minimal) longitudinal Wilson lines vanish and the equal-time canonical commutation relations for the quark creation and annihilation operators $\{a^\dagger(k,\lambda),a(k,\lambda)\}$ are consistent with the *parton-number interpretation* of the TMD in the tree-approximation (see [11] for more): $\mathcal{F}^{(0)}(x,\boldsymbol{k}_\perp)\sim\langle p|a^\dagger(k^+,\boldsymbol{k}_\perp;\lambda)\;a(k^+,\boldsymbol{k}_\perp;\lambda)|p\rangle$. In line with the above explanations, we define a generic enhanced gauge link evaluated along some fixed but else arbitrary direction w from zero to infinity according to

$$[[\infty;0]]=\mathcal{P}\exp\left[-ig\int_0^\infty d\sigma\;w_\mu\;A_a^\mu(w\sigma)t^a-ig\int_0^\infty d\sigma\;J_{\mu\nu}F_a^{\mu\nu}(w\sigma)t^a\right]\;, \quad (5)$$

where the four-vector w may be longitudinal (lightlike) $w_L=n^-$, or transverse $w_T=(0^+,0^-,\boldsymbol{l}_\perp)$. The enhanced Wilson lines (5) significantly enlarge the gauge-invariant formalism of quark and gluon operators entering the TMD correlators.

To investigate the structure of the UV singularities in the leading α_s-order, we evaluate all graphs contributing to this order given in [10], where one can also find the technical details and the appropriate Feynman rules. Note that there are two different perturbative expansions in the generalized TMD given by (1): one stems from the Heisenberg quark

field operators, i.e., $\psi_a(\xi) = \mathrm{e}^{-ig\left[\int d\eta\ \bar{\psi}\hat{\mathcal{A}}\psi\right]}\ \psi_a^{\mathrm{free}}(\xi)$, $\int dx\ \bar{\psi}\hat{\mathcal{A}}\psi\ \equiv \int d^4x\ \bar{\psi}(x)\gamma_\mu\psi(x)\mathcal{A}^\mu(x)$. The other originates from the evaluation of the product of the enhanced gauge links up to $\mathcal{O}(g^2)$. Applying the lightcone gauge $A^+ = 0$) one has

$$[[\infty^-, \boldsymbol{\infty}_\perp; \infty^-, \mathbf{0}_\perp]] \cdot [[\infty^-, \mathbf{0}_\perp; 0^-, \mathbf{0}_\perp]] = 1 - ig\,(\mathcal{U}_1 + \mathcal{U}_2 + \mathcal{U}_3) - g^2\,(\mathcal{U}_4 + \mathcal{U}_5 + \ldots \mathcal{U}_{10})\ , \tag{6}$$

where the individual contributions $\mathcal{U}_i$ have to be contracted with themselves as well as with corresponding terms in the Heisenberg field operators.

The singularity structure of the twist-two TMD with the Dirac structures $\Gamma_{\mathrm{tw-2}} = \{\gamma^+, \gamma^+\gamma^5, i\sigma^{i+}\gamma^5\}$, cancel by the Hermitean conjugated (mirror) diagrams, in contrast to the twist-three TMDs (e.g., $\Gamma_{\mathrm{tw-3}} = \gamma^i$) which receive non-trivial UV divergent contributions from the Pauli term, like

$$\Gamma_{\mathrm{tw-3}}\langle \mathbf{A}^\perp F^-\rangle + \langle \mathbf{A}^\perp F^-\rangle\Gamma_{\mathrm{tw-3}} = -C_{\mathrm{F}}\ \frac{1}{4\pi}[\gamma^+, \gamma^-]\ \Gamma(\varepsilon)\ \left(4\pi\frac{\mu^2}{\lambda^2}\right)^{\varepsilon}\ . \tag{7}$$

Here, $\langle \mathbf{A}^\perp F^-\rangle$ denotes the result stemming from the cross-talk between the minimal transverse gauge link and the enhanced longitudinal gauge link containing a Pauli term. In order to render the TMD singularity-free, one has to handle the overlapping UV and rapidity divergences induced by the gluon propagator in the lightcone gauge. To this end, we refurbished in [7] the untruncated definition in Eq. (1) by a soft renormalization factor along a particular gauge contour going off the lightcone. This soft factor takes care of the overlapping UV and infrared (rapidity) divergences which cannot be regularized dimensionally, as in the case of purely longitudinal gauge links—see [12] and references cited therein.

Recently, Collins [4] questioned the validity of this definition and proposed another one. He argues that the gluon propagator in the lightcone gauge subject to the Mandelstam-Leibbrandt (ML) boundary prescription, $D^{\mu\nu}_{\mathrm{ML}}$, is not transverse, i.e., $n_\mu D^{\mu\nu}_{\mathrm{ML}} \neq 0$. The propagator displayed by Collins as Eq. (15) in [4] is *not* the ML one but the result of using the Principal-Value prescription. This propagator, as well as the Retarded and the Advanced one, are indeed not transverse. In contrast, the *correct* ML propagator (see last entry in [7]) *is* transverse and the soft factor reduces to unity. The second argument by Collins is that the graphs shown in Eq. (16) in [4] give uncanceled rapidity divergences. If the displayed graphs are to be evaluated in the lightcone gauge, as used in our works in [7] and in [10], then they both vanish. In a general covariant gauge, these graphs contribute singularities that are indispensable in order to cancel those singular terms, induced by the gluon propagator, which contain the gauge parameter. There are no surviving singularities.

In conclusion, we discussed a new operator formulation of gauge-invariant TMDs which provides direct access to the spin degrees of freedom of the partonic fields by means of the Pauli term in the gauge links, hence allowing a microscopic analysis of the spin-color structure of TMDs relevant for phenomenology.

Acknowledgements The first author (I.O.C.) thanks the Organizers for the warm hospitality and exciting atmosphere during the conference.

References

[1] D. E. Soper, Phys. Rev. Lett. **43** (1979) 1847; J. C. Collins and D. E. Soper, Nucl. Phys. **B193** (1981) 381; Erratum ibid. **B213** (1983) 545; Nucl. Phys. **B194** (1982) 445.

[2] D. Boer et al., arXiv:1108.1713 [nucl-th]; U. D'Alesio and F. Murgia, Prog. Part. Nucl. Phys. **61** (2008) 394; A. V. Belitsky and A. V. Radyushkin, Phys. Rept. **418** (2005) 1.

[3] T. C. Rogers and P. J. Mulders, Phys. Rev. **D81** (2010) 094006; C. J. Bomhof and P. J. Mulders, Nucl. Phys. **B795** (2008) 409; C. J. Bomhof, P. J. Mulders and F. Pijlman, Eur. Phys. J. **C47** (2006) 147; A. Bacchetta, C. J. Bomhof, P. J. Mulders and F. Pijlman, Phys. Rev. **D72** (2005) 034030.

[4] J. C. Collins, Int. J. Mod. Phys. Conf. Ser. **4** (2011) 85. *Foundations of perturbative QCD*, (Cambridge University Press, Cambridge, 2011).

[5] S. M. Aybat and T. C. Rogers, Phys. Rev. **D83** (2011) 114042; S. M. Aybat, J. C. Collins, J.-W. Qiu and T. C. Rogers, arXiv:1110.6428 [hep-ph]; B. U. Musch, Ph. Hägler, M. Engelhardt, J. W. Negele and A. Schäfer, arXiv:1111.4249 [hep-lat].

[6] X.-d. Ji and F. Yuan, Phys. Lett. **B543** (2002) 66; A. V. Belitsky, X. Ji and F. Yuan, Nucl. Phys. **B656** (2003) 165; D. Boer, P. J. Mulders and F. Pijlman, Nucl. Phys. **B667** (2003) 201

[7] I. O. Cherednikov and N. G. Stefanis, Phys. Rev. **D77** (2008) 094001; Nucl. Phys. **B802** (2008) 146; Phys. Rev. **D80** (2009) 054008; N. G. Stefanis and I. O. Cherednikov, Mod. Phys. Lett. **A24** (2009) 2913.

[8] I. V. Anikin and O. V. Teryaev Phys. Lett. **B690** (2010) 519; J. Phys. Conf. Ser. **295** (2011) 012057.

[9] B. U. Musch, Ph. Hägler, J. W. Negele and A. Schäfer, AIP Conf. Proc. **1350** (2011) 321; Phys. Rev. **D83** (2011) 094507.

[10] I. O. Cherednikov, A. I. Karanikas and N. G. Stefanis, Nucl. Phys. **B840** (2010) 379; N. G. Stefanis, I. O. Cherednikov and A. I. Karanikas, PoS **LC2010** (2010) 053.

[11] I. O. Cherednikov, arXiv:1112.0696 [hep-ph]; I. O. Cherednikov and N. G. Stefanis, Int. J. Mod. Phys. Conf. Ser. **4** (2011) 135.

[12] N. G. Stefanis, Nuovo Cim. A **83**, 205 (1984).

TESTS FOR THE ASSUMPTIONS OF THE FRAGMENTATION FUNCTIONS [1]

E. Christova[1†] and E. Leader [2††],

(1) *Institute for Nuclear Research and Nuclear Energy, Bulgarian Academy of Sciences, Sofia, Bulgaria*
(2) *Imperial College, London University, London, UK*
E-mail: †*echristo@inrne.bas.bg*; ††*e.leader@imperial.ac.uk*;

Abstract

We summarize the assumptions made by the different groups in extracting the fragmentation functions. We define tests for the commonly used assumptions: $D_d^{K^+} = D_d^{K^-}$, $D_u^{\pi^+-\pi^-} = -D_d^{\pi^+-\pi^-}$ and the SU(2)-relations between $D_q^{K^++K^-}$ and $D_q^{K_s^0}$.

1 Introduction

At present, the main source of information about the fragmentation functions (FFs) are the semi-inclusive processes for hadron production h in e^+e^--annihilation:

$$e^+e^- \to h + X, \quad d\sigma^h \simeq \sum e_q^2 (D_q^h + D_{\bar{q}}^h), \quad h = \pi^\pm, K^\pm, p/\bar{p} ... \tag{1}$$

They determine directly the FFs $(D_q^h + D_{\bar{q}}^h)$, but cannot in principle distinguish the quark D_q^h and anti-quark $D_{\bar{q}}^h$ FFs. That's why in all analysis of e^+e^--annihilation data, information about D_q^h and $D_{\bar{q}}^h$ separately is based on the different assumptions made by the different groups, especially on the FFs for the light quarks. Bellow we summarize some of them.

- The assumptions used by the different groups for the kaon FFs:

I) The BKK group [1] introduces 2 independent FFs: all favoured FFs are equal and all unfavoured FFs are equal:

$$\begin{aligned} D_u^{K^+} &= D_{\bar{s}}^{K^+} \Leftarrow fav. \\ D_{\bar{u}}^{K^+} &= D_s^{K^+} = D_d^{K^+} = D_{\bar{d}}^{K^+} \Leftarrow unfav. \end{aligned} \tag{2}$$

II) The more recent analysis of HKNS [3] and DSS [4] take into account that the strange quark is heavier $m_s >> m_{u,d}$ and introduce 3 FFs: the favoured FFs are not equal, but all unfavoured FFs are equal:

$$\begin{aligned} D_u^{K^+}, \quad D_{\bar{s}}^{K^+} &\Leftarrow fav. \\ D_{\bar{u}}^{K^+} &= D_s^{K^+} = D_d^{K^+} = D_{\bar{d}}^{K^+} \Leftarrow unfav. \end{aligned} \tag{3}$$

[1]The paper is supported by 288/2008 Grant of Bulgarian National Science Foundation and a priority Grant between Bulgaria and JINR.

III) The most economic analysis is done by Kretzer [4], who uses only one FFs, assuming certain hierarchy of the FFs: favoured and unfavoured FFs are power suppressed:

$$\begin{aligned} D_{\bar{s}}^{K^+},\ D_u^{K^+} &= (1-z)\, D_{\bar{s}}^{K^+} \quad \Leftarrow \quad fav. \\ D_d^{K^+} &= D_{\bar{d}}^{K^+} = (1-z)^2 D_{\bar{s}}^{K^+} \quad \Leftarrow \quad unfav. \end{aligned} \tag{4}$$

IV) The most general analysis is performed by AKK [5], that uses 5 independent FFs: favoured and unfavoured FFs are not equal and the only assumption is on $D_{d,\bar{d}}^{K^+}$:

$$\begin{aligned} &D_u^{K^+}, \quad D_{\bar{s}}^{K^+} \ \Leftarrow fav. \\ &D_{\bar{u}}^{K^+}, \quad D_s^{K^+}, \quad D_d^{K^+} = D_{\bar{d}}^{K^+} \ \Leftarrow unfav. \end{aligned} \tag{5}$$

In general, the assumptions used by all groups are different, but common for them are the following two assumptions:

$$1) \quad D_d^{K^+} = D_{\bar{d}}^{K^+} \tag{6}$$

for the charged kaons, and

$$2) \quad D_d^{K^0+\bar{K}^0} = D_u^{K^++K^-}, \quad D_u^{K^0+\bar{K}^0} = D_d^{K^++K^-}, \quad D_s^{K^0+\bar{K}^0} = D_s^{K^++K^-} \tag{7}$$

that relate the neutral and charged kaon FFs. The last one follows from SU(2) invariance.

- The assumptions used by the different groups for the pion FFs are:

I) The HKNS group uses 2 FFs: one for the favoured and one for the unfavoured FFs:

$$\begin{aligned} D_u^{\pi^+} &= D_{\bar{d}}^{\pi^+} : \quad SU(2) \ \Leftarrow fav. \\ D_d^{\pi^+} &= D_{\bar{u}}^{\pi^+} = D_s^{\pi^+} = D_{\bar{s}}^{\pi^+} \ \Leftarrow unfav. \end{aligned} \tag{8}$$

II) The AKK group uses 3 FFs: one for the favoured and two for the unfavoured FFs:

$$\begin{aligned} D_u^{\pi^+} &= D_{\bar{d}}^{\pi^+} : \quad SU(2) \ \Leftarrow fav. \\ D_d^{\pi^+} &= D_{\bar{u}}^{\pi^+}\ D_s^{\pi^+} = D_{\bar{s}}^{\pi^+} \ \Leftarrow unfav. \end{aligned} \tag{9}$$

III) The DSS group fits the data with 3 independent FFs and 2 more fitted parameters $\mathcal{N}$ and $\mathcal{N}'$: the favoured and unfavoured FFs are proportional:

$$D_u^{\pi^+} = \mathcal{N} D_{\bar{d}}^{\pi^+} : \quad \mathcal{N} = 1.10 \ \Leftarrow fav. \tag{10}$$

$$D_{\bar{u}}^{\pi^+} = D_d^{\pi^+},\ D_s^{\pi^+} = \mathcal{N}' D_{\bar{u}}^{\pi^+} : \mathcal{N}' = 0.82 \quad \Leftarrow unfav. \tag{11}$$

IV) Kretzer uses one FF: the favoured are equal, the unfavoured are power suppressed:

$$\begin{aligned} D_u^{\pi^+} &= D_{\bar{d}}^{\pi^+} : \ SU(2) \ \Leftarrow fav. \\ D_s^{\pi^+} &= D_{\bar{s}}^{\pi^+} = D_d^{\pi^+} = (1-z)\, D_u^{\pi^+} \ \Leftarrow unfav. \end{aligned} \tag{12}$$

Common in all analysis are the following two assumptions:

$$1) \quad D_u^{\pi^+-\pi^-} = -D_d^{\pi^+-\pi^-} \tag{13}$$

and

$$2) \quad D_q^{\pi^0} = (D_q^{\pi^+} + D_q^{\pi^-})/2. \tag{14}$$

It is only the DSS analysis that introduces the parameters $\mathcal{N}$, eq. (10) to test eq.(13).

The data expected from COMPASS and HERMES on hadron production in semi-inclusive deep inelastic scattering (SIDIS):

$$l + N \to l + h + X, \quad d\sigma_N^h \simeq \sum e_q^2 \left(q\, D_q^h + \bar{q}\, D_{\bar{q}}^h\right), \quad h = \pi, K, p... \tag{15}$$

will allow to disentangle D_q^h and $D_{\bar{q}}^h$. However, this suggests implicitly a good knowledge for both the valence and the sea quarks parton distribution functions (PDFs). Even small uncertainties in the small sea quark PDFs would result in considerable errors in the FFs.

Here we show how relations (6), (7) and (13), used in all analysis, can be tested in SIDIS. The advantage of the proposed tests, as compared to global analysis of process (15), is that in the proposed tests only the best known valence quark PDFs enter. In addition, as we dial with non-singlets (NS) only, the gluon PDFs and FFs, that introduce most of the uncertainties in global analysis, do not enter. This would allow easier to evolve data at different Q^2. We show also that relation (7) can be tested using solely the most accurate e^+e^- annihilation kaon data.

The presented relations are based only on C-invariance, without any assumptions on the PDFs and the FFs and thus hold in any QCD order. The results are based only on the relations $D_g^{h^+-h^-} = 0$ and $D_q^{h^+-h^-} = -D_{\bar{q}}^{h^+-h^-}$ that follow from C-invariance:

We present our results in NLO in QCD, in more details they are given in [6].

2 Test of $D_d^{K^+} = D_d^{K^-}$

Assuming only $D_d^{K^+} = D_d^{K^-}$, we obtain that the difference cross sections of K^+ and K^- production in SIDIS on proton or deutron targets are expressed in terms of $D_u^{K^+-K^-}$:

$$d\sigma_p^{K^+-K^-} = \frac{4}{9} u_V \otimes (1 + \frac{\alpha_s}{2\pi} C_{qq}) \otimes D_u^{K^+-K^-} \tag{16}$$

$$d\sigma_d^{K^+-K^-} = \frac{4}{9} [u_V + d_V] \otimes (1 + \frac{\alpha_s}{2\pi} C_{qq}) \otimes D_u^{K^+-K^-}, \tag{17}$$

where C_{qq} are the known Wilson coefficients. As (6) is the only assumption used, eqs. (16) and (17) present tests for $D_d^{K^+} = D_d^{K^-}$.

3 Test of $D_u^{\pi^+-\pi^-} = -D_d^{\pi^+-\pi^-}$

If the usually made assumption (13) holds (motivated by SU(2) symmetry of the pion wave function), then the difference cross sections of π^+ and π^- on proton or deuteron targets in SIDIS are determined by the combination $D_u^{\pi^+-\pi^-}$:

$$d\sigma_p^{\pi^+-\pi^-} = \frac{1}{9} [4u_V - d_V] \otimes (1 + \frac{\alpha_s}{2\pi} C_{qq}) \otimes D_u^{\pi^+-\pi^-} \tag{18}$$

$$d\sigma_d^{\pi^+-\pi^-} = \frac{1}{3} [u_V + d_V] \otimes (1 + \frac{\alpha_s}{2\pi} C_{qq}) \otimes D_u^{\pi^+-\pi^-}. \tag{19}$$

As (13) is the only assumption, eqs. (18) and (19) test $D_u^{\pi^+-\pi^-} = -D_d^{\pi^+-\pi^-}$. It is only the DSS analysis that introduces a parameters $\mathcal{N}$, eq. (10), to test this assumption, but in addition to the assumptions in eq. (11). Their analysis indicates $\sim 10\%$ deviation.

Note that both in $d\sigma_N^{K^+-K^-}$ and $d\sigma_N^{\pi^+-\pi^-}$ only the best determined valence u_V and d_V PDFs enter and their are no gluon quantities g and D_g^h – eqs. (16) - (19) are non-singlets.

The difference cross sections of $K^\pm$ or $\pi^\pm$ production in pp collisions are also expressed in terms of the same quantities $D_u^{K^+-K^-}$ or $D_u^{\pi^+-\pi^-}$, respectively [6].

4 Test of SU(2) invariance for the kaons

If in addition to charged $K^\pm$, also neutral kaons $K_s^0 = (K^0 + \bar{K}^0)/\sqrt{2}$ are measured, due to SU(2) invariance (7), no new FFs are introduced. Then we show that the combinations

$$\sigma^{K^+ + K^- - 2K_s^0} \equiv \sigma^{K^+} + \sigma^{K^-} - 2\sigma^{K_s^0} \tag{20}$$

in the three types of semi-inclusive processes, $K = K^\pm$, K_s^0:

$$e^+ + e^- \to K + X, \tag{21}$$

$$e + N \to e + K + X, \qquad N = p,\, d \tag{22}$$

are expressed in terms of the single NS combination $D_{u-d}^{K^+ + K^-} \equiv (D_u - D_d)^{K^+ + K^-}$:

$$d\sigma_{e^+e^-}^{K^+ + K^- - 2K_s^0}(z, Q^2) = 6\,\sigma_0\,(\hat{e}_u^2 - \hat{e}_d^2)(1 + \frac{\alpha_s}{2\pi}\,C_q \otimes)\, D_{u-d}^{K^+ + K^-}(z, Q^2) \tag{23}$$

$$d\sigma_p^{K^+ + K^- - 2K_s^0}(x, z, Q^2) = \frac{1}{9}[(4\tilde{u} - \tilde{d}) \otimes (1 + \frac{\alpha_s}{2\pi} C_{qq}) + \frac{\alpha_s}{2\pi} g \otimes C_{gq}] \otimes\, D_{u-d}^{K^+ + K^-} \tag{24}$$

$$d\sigma_d^{K^+ + K^- - 2K_s^0}(x, z, Q^2) = \frac{1}{3}[(\tilde{u} + \tilde{d}) \otimes (1 + \frac{\alpha_s}{2\pi} C_{qq}) + 2\frac{\alpha_s}{2\pi}\, g \otimes C_{gq}] \otimes\, D_{u-d}^{K^+ + K^-} \tag{25}$$

$$\tilde{q} \equiv q + \bar{q}$$

As these relations rely only on (7) and do not involve *any* assumptions about PDFs or FFs, they test SU(2) invariance for kaons.

References

[1] J. Binnewies, B.A.Kniehl, G. Kramer, Z.Phys. bf C65 (1995) 471

[2] M. Hirai, S. Kumano, T. H. Nagai and K. Sudoh, Phys. Rev.**D 75** (2007) 094009.

[3] D. de Florian, R. Sassot and M.Stratmann, Phys.Rev. **D75**(2007) 114010; **D76** (2007) 074033.

[4] S. Kretzer, Phys. Rev. **D62** (2000) 054001

[5] S. Albino, B. A. Kniehl and G. Kramer, Nucl. Phys. **B 803** (2008) 42.

[6] E. Christova and E. Leader, Eur. Phys. J. **C51** 825 (2007), Phys.Rev. **D79** (2009) 014019.

STRANGENESS FORM FACTORS OF THE NUCLEON

Harleen Dahiya[1†] and Neetika Sharma[1]

(1) *Department of physics, Dr. B.R. Ambedkar National Institute Of Technology, Jalandhar-144011, India*
† *E-mail: dahiyah@nitj.ac.in*

Abstract

The measurements from the DIS experiments providing information on the electric and magnetic form factors of the nucleon have revealed a significant amount of strangeness in the nucleon. This has been further reinforced by the experiments performed in the recent past. In view of the very exciting recent developments in the field, we propose to apply the techniques of chiral constituent quark model to develop the structure of baryons using the electric and magnetic form factors.

In the context of deep inelastic scattering (DIS), the strange spin polarization of the nucleon looks to be well established through the measurements of polarized structure functions of the nucleon [1]. The recent measurements by several groups SAMPLE at MIT-Bates [2], G0 at JLab [3], A4 at MAMI [4] and by HAPPEX at JLab [5] regarding the contribution of strangeness to the electromagnetic form factors of the nucleon have triggered a great deal of interest in finding the strangeness magnetic moment of the proton $(\mu(p)^s)$.

The perturbative generation of "quark sea" from the quark-pair production by gluons is symmetric w.r.t. $\bar{u}$ and $\bar{d}$ [6] which is in contradiction with the observed value of $\bar{u} - \bar{d}$ asymmetry [7]. Therefore, one has to consider the "quark sea" produced by the non-perturbative mechanism. One such model which can yield an adequate description of the "quark sea" generation through the chiral fluctuations is the chiral constituent quark model (χCQM) [8] which is not only successful in giving a satisfactory explanation of "proton spin crisis" but is also able to account for the baryon magnetic moments and hyperon $\beta-$decay parameters [9]. It, therefore, becomes desirable to examine the strangeness contribution to the nucleon in the $\chi\text{CQM}_{\text{config}}$ thereby giving vital clues to the non-perturbative effects of QCD. In particular, we would like to calculate the strange spin polarization Δs, strangeness contribution to the weak axial vector couplings Δ_3, Δ_8 and Δ_0, strangeness contribution to the magnetic moments $\mu(p)^s$ and $\mu(n)^s$. For the sake of completeness, we would also like to calculate the strangeness contribution to the magnetic moments of decuplet baryons $\mu(\Delta^{++})^s$, $\mu(\Delta^{+})^s$, $\mu(\Delta^{o})^s$ and $\mu(\Delta^{-})^s$ which have not been observed experimentally.

The basic process in the χCQM formalism is the emission of a Goldstone boson (GB) by a constituent quark which further splits into a $q\bar{q}$ pair, for example, $q_{\pm} \rightarrow \text{GB}^0 + q'_{\mp} \rightarrow (q\bar{q}') + q'_{\mp}$, where $q\bar{q}' + q'$ constitute the "quark sea" [6] and the $\pm$ signs refer to the quark helicities. The effective Lagrangian describing interaction between quarks and a nonet of GBs, consisting of octet and a singlet, can be expressed as $\mathcal{L} = g_8 \bar{\mathbf{q}} \left(\Phi + \zeta \frac{\eta'}{\sqrt{3}} I \right) \mathbf{q} = g_8 \bar{\mathbf{q}} \left(\Phi' \right) \mathbf{q}$, where $\zeta = g_1/g_8$, g_1 and g_8 are the coupling constants for the singlet and octet

GBs, respectively, I is the 3×3 identity matrix. The GB field which includes the octet and the singlet GBs is written as

$$\Phi' = \begin{pmatrix} \frac{\pi^0}{\sqrt{2}} + \beta\frac{\eta}{\sqrt{6}} + \zeta\frac{\eta'}{\sqrt{3}} & \pi^+ & \alpha K^+ \\ \pi^- & -\frac{\pi^0}{\sqrt{2}} + \beta\frac{\eta}{\sqrt{6}} + \zeta\frac{\eta'}{\sqrt{3}} & \alpha K^0 \\ \alpha K^- & \alpha\bar{K}^0 & -\beta\frac{2\eta}{\sqrt{6}} + \zeta\frac{\eta'}{\sqrt{3}} \end{pmatrix} \text{ and } \quad q = \begin{pmatrix} u \\ d \\ s \end{pmatrix} . \quad (1)$$

The spin structure of a nucleon is defined as $\hat{B} \equiv \langle B|N|B\rangle$, where $|B\rangle$ is the nucleon wavefunction defined and N is the number operator giving the number of $q_\pm$ quarks. The spin polarization functions $\Delta q = q_+ - q_-$ are related to the non-singlet combinations of the quark spin polarizations (Δ_3 and Δ_8) as well as the flavor singlet combination (Δ_0)

$$\Delta_3 = \Delta u - \Delta d\,, \qquad \Delta_8 = \Delta u + \Delta d - 2\Delta s\,,$$

$$\Delta_0 = \frac{1}{2}\Delta\Sigma = \frac{1}{2}(\Delta u + \Delta d + \Delta s)\,. \quad (2)$$

The magnetic moment of a given baryon in the χCQM can be expressed as $\mu(B)_{\rm total} = \mu(B)_{\rm val} + \mu(B)_{\rm sea}$, where $\mu(B)_{\rm val}$ represents the contribution of the valence quarks and $\mu(B)_{\rm sea}$ corresponding to the quark sea. Further, $\mu(B)_{\rm sea}$ can be written as $\mu(B)_{\rm sea} = \mu(B)_{\rm spin} + \mu(B)_{\rm orbit}$, where the first term is the magnetic moment contribution of the q' coming from the spin polarization and the second term is due to the rotational motion of the two bodies, q' and GB and referred to as the orbital angular momentum by Cheng and Li [6].

The strangeness contribution to the magnetic moment of the proton $\mu(p)^s$ receives contributions only from the quark sea and is expressed as $\mu(p)^s = \mu(p)^s_{\rm spin} + \mu(p)^s_{\rm orbit}$ where $\mu(p)^s_{\rm spin} = \sum_{q=u,d,s} \Delta q(p)^s_{\rm sea}\mu_q$ and $\mu(p)^s_{\rm orbit} = \frac{4}{3}[\mu(u_+ \to s_-)] - \frac{1}{3}[\mu(d_+ \to s_-)]$. Here, $\mu_q = \frac{e_q}{2M_q}$ $(q = u, d, s)$ is the quark magnetic moment, e_q and M_q are the electric charge and the mass respectively for the quark q and $\mu(q_+ \to s_-) = \frac{e_s}{2M_q}\langle l_q\rangle + \frac{e_q - e_s}{2M_{GB}}\langle l_{GB}\rangle$. The quantities (l_q, l_{GB}) and (M_q, M_{GB}) are the orbital angular momenta and masses of quark and GB, respectively. The strangeness contribution to the magnetic moments of the neutron $n(ddu)$ as well as the decuplet baryons $\Delta^{++}(uuu)$, $\Delta^+(uud)$, $\Delta^o(udd)$ and $\Delta^-(ddd)$ can be calculated similarly.

The $\chi{\rm CQM}_{\rm config}$ parameters a, $a\alpha^2$, $a\beta^2$, $a\zeta^2$ representing respectively the probabilities of fluctuations to pions, K, η, η' have been fitted using Δu, Δ_3, $\bar{u} - \bar{d}$ and $\bar{u}/\bar{d}$ as inputs. A fine grained analysis leads to $a = 0.13$, $\zeta = -0.10$, $\alpha = \beta = 0.45$ as the best fit values. In Table 1, we have presented the results of our calculations pertaining to the strangeness dependent parameters in $\chi{\rm CQM}_{\rm config}$. For comparison sake, we have also given the corresponding quantities in constituent quark model (CQM) [10]. We find that we are able to achieve a fairly good fit in the case of spin polarization functions. In particular, the agreement in terms of the magnitude as well as the sign in the case of Δs is in good agreement with the latest data [1]. The agreement in the case of Δ_8 and Δ_0, which receives contribution from Δs also, not only justify the success of $\chi{\rm CQM}_{\rm config}$ but also strengthen our conclusion regarding Δs.

In the table, we have also presented the spin and orbital contributions pertaining to the strangeness magnetic moment of the nucleon and Δ baryons. The present result for the strangeness contribution to the magnetic moment of proton looks to be in agreement

Parameter	Data	CQM	χCQM$_{\rm config}$
$\bar{s}$	–	0	0.10
$\bar{u}-\bar{d}$	-0.118 ± 0.015 [7]	0	-0.118
$\bar{u}/\bar{d}$	0.67 ± 0.06 [7]	0	0.66
Δu	0.85 ± 0.05 [1]	1.333	0.867
Δd	-0.41 ± 0.05 [1]	-0.333	-0.392
Δs	-0.10 ± 0.04 [1]	0	-0.08
	-0.07 ± 0.03 [1]		
Δ_3	1.267 ± 0.0035 [14]	1.666	1.267
Δ_8	0.58 ± 0.025 [14]	1	0.59
Δ_0	0.19 ± 0.025 [14]	0.50	0.19
$\mu(p)^s_{\rm spin}$, $\mu(p)^s_{\rm orbit}$	$0.12 \pm 0.55 \pm 0.07$ [11]	0, 0	-0.09, 0.06
	$0.37 \pm 0.26 \pm 0.20$ [2]		
$\mu(n)^s_{\rm spin}$, $\mu(n)^s_{\rm orbit}$	–	0, 0	0.06, -0.09
$\mu(\Delta^{++})^s_{\rm spin}$, $\mu(\Delta^{++})^s_{\rm orbit}$	–	0, 0	-0.29, 0.18
$\mu(\Delta^{+})^s_{\rm spin}$, $\mu(\Delta^{+})^s_{\rm orbit}$	–	0, 0	-0.14, 0.11
$\mu(\Delta^{o})^s_{\rm spin}$, $\mu(\Delta^{o})^s_{\rm orbit}$	–	0, 0	-0.04, -0.03
$\mu(\Delta^{-})^s_{\rm spin}$, $\mu(\Delta^{-})^s_{\rm orbit}$	–	0, 0	-0.09, 0.15

Table 1: The calculated values of the strangeness dependent flavor and spin polarization functions as well as the magnetic moment of nucleon and Δ decuplet baryons in the CQM and χCQM$_{\rm config}$.

with the most recent results available for $\mu(p)^s$ [2, 11–13]. The spin and orbital angular momentum of the "quark sea" contributions are fairly significant and they cancel in the right direction to give the right magnitude to $\mu(p)^s$, For example, the spin contribution in this case is $-0.09\mu_N$ and the contribution coming from the orbital angular momentum is $0.06\mu_N$. These contributions cancel to give a small value for $\mu(p)^s$ $-0.03\mu_N$ which is consistent with the other observed results. Interestingly, in the case of $\mu(n)^s$, the magnetic moment is dominated by the orbital part as was observed in the case of the total magnetic moments [9] however, the total strangeness magnetic moment is same as that of the proton. The results of $\mu(\Delta^{++})^s$, $\mu(\Delta^{+})^s$, $\mu(\Delta^{o})^s$, $\mu(\Delta^{-})^s$ have also been presented and here also we find that there is a substantial contribution from spin and orbital angular momentum.

In conclusion, χCQM$_{\rm config}$ is able to give a quantitative description of the important parameters such as Δs, the weak axial vector couplings Δ_8 and Δ_0, strangeness contribution to the magnetic moment $\mu(p)^s$. In the case of $\mu(p)^s$, our result is consistent with the latest experimental measurements as well as with the other calculations. The constituent quarks and the weakly interacting Goldstone bosons constitute the appropriate degrees of freedom in the nonperturbative regime of QCD and the quark sea generation through the chiral fluctuation is the key in understanding the strangeness content of the nucleon.

Acknowledgments. The authors would like to thank the organizers of DSPIN2011 and DAE-BRNS, Government of India, for financial support.

References

[1] EMC Collaboration, J. Ashman *et al.*, Phys. Lett. **B 206**, 364 (1988); Nucl. Phys. **B 328**, 1 (1989); P. Adams *et al.*, Phys. Rev. **D 56**, 5330 (1997); SMC Collaboration, B. Adeva *et al.*, Phys. Rev. **D 58**, 112001 (1998); HERMES Collaboration, A. Airapetian *et al.*, Phys. Rev. **D 71**, 012003 (2005).

[2] SAMPLE Collaboration, D.T. Spayde *et al.*, Phys. Lett. **B 583**, 79 (2004).

[3] G0 Collaboration, D. Armstrong *et al.*, Phys. Rev. Lett. **95**, 092001 (2005).

[4] A4 Collaboration, F.E. Maas *et al.*, Phys. Rev. Lett. **94**, 152001 (2005).

[5] HAPPEX Collaboration, K.A. Aniol *et al.*, Phys. Rev. Lett. **98**, 032301 (2007); *ibid.* Eur. Phys. J. **A 31**, 597 (2007).

[6] T.P. Cheng and Ling Fong Li, Phys. Rev. **D 57**, 344 (1998); *ibid.* Phys. Rev. Lett. **80**, 2789 (1998); X. Song, Phys. Rev. **D 57**, 4114 (1998).

[7] E866/NuSea Collaboration, J.C. Peng *et al.*, Phys. Rev. **D 58**, 092004 (1998); R. S. Towell *et al.*, *ibid.* **64**, 052002 (2001).

[8] S. Weinberg, Physica **A 96**, 327 (1979); A. Manohar and H. Georgi, Nucl. Phys. **B 234**, 189 (1984); E.J. Eichten, I. Hinchliffe and C. Quigg, Phys. Rev. **D 45**, 2269 (1992).

[9] H. Dahiya and M. Gupta, Phys. Rev. **D 64**, 014013 (2001); *ibid.* **D 67**, 074001 (2003); *ibid.* **D 66**, 051501(R) (2002), *ibid.* **67**, 114015 (2003); *ibid.* Eur. Phys. J. **C 52**, 571 (2007); N. Sharma, H. Dahiya, P.K. Chatley, and M. Gupta, Phys. Rev. D **81** , 073001 (2010); N. Sharma and H. Dahiya, Phys. Rev. D **81**, 114003 (2010); H. Dahiya and N. Sharma, Mod. Phys. Lett. A **26**, 279 (2011).

[10] A.L. Yaouanc, L. Oliver, O. Pene, and J.C. Raynal, Phys. Rev. D **15**, 844 (1977); M. Gupta and A.N. Mitra, Phys. Rev. D **18**, 1585 (1978); N. Isgur and G. Karl, Phys. Rev. D **21**, 3175 (1980); N. Isgur, G. Karl, and D.W.L. Sprung, Phys. Rev. D **23**, 163 (1981); P. Geiger and N. Isgur, Phys. Rev. D **55**, 299 (1997).

[11] R.D. Young *et al.*, Phys. Rev. Lett. **97**, 102002 (2006).

[12] D.B. Leinweber, S. Boinepalli, I.C. Cloet, A.W. Thomas, A.G. Williams, R.D. Young, J.B. Zhang, J.M. Zanotti, J.B. Zhang, Eur. Phys. J. **A24S2**, 79 (2005); *ibid.* Phys. Rev. Lett. **94**, 212001 (2005).

[13] S.J. Dong, K.F. Liu, A.G. Williams, Phys. Rev. **D 58**, 074504 (1998); N. Mathur, Shao-Jing Dong, Nucl. Phys. Proc. Suppl. **94**, 311 (2001); R. Lewis, W. Wilcox, R. M. Woloshyn, Phys. Rev. **D 67**, 013003 (2003).

[14] K. Nakamura *et al.* (Particle Data Group), J. Phys. G **37**, 075021 (2010).

NEW LOOK AT THE QCD FACTORIZATION

B.I. Ermolaev [1,†] and S.I. Troyan [2]

(1) *Ioffe Physico-Technical Institute, 194021 St.Petersburg, Russia*
(2) *St.Petersburg Institute of Nuclear Physics, 188300 Gatchina, Russia*
† *E-mail: Boris.Ermolaev@cern.ch*

Abstract

We show that both the k_T- and collinear factorization for DIS structure functions can be obtained by consecutive reductions of the Compton scattering amplitude. Each of these reductions is an approximation valid under certain assumptions. In particular, the transitions to the k_T- factorization is possible when the virtualities of the partons connecting the perturbative and non-perturbative blobs are space-like. If the parton distribution in the k_T- factorization has a sharp maximum in $k_\perp$, this factorization can be reduced to the collinear factorization.

1 Introduction

The QCD factorization is the fundamental concept to provide theoretical grounds for applying the Perturbative QCD to description of hadronic reactions. According to the factorization, any scattering amplitude A in QCD can be represented as a convolution of a perturbative (E) and non-perturbative (T) contributions:

$$A = E \otimes T \tag{1}$$

There are two kinds of the factorization in the literature: Collinear factorization [1] and the k_T- factorization [2] where the DIS structure functions $f(x,Q^2)$ are respectively represented as follows:

$$f(x,Q^2) = \int_x^1 \frac{d\beta}{\beta} f^{(pert)}(x/\beta, Q^2/\mu^2)\phi(\beta,\mu^2) \tag{2}$$

and

$$f(x,Q^2) = \int_x^1 \frac{d\beta}{\beta} \int \frac{dk_\perp^2}{k_\perp^2} f^{(pert)}(x/\beta, Q^2/k_\perp^2)\Phi(\beta,k_\perp^2) \tag{3}$$

where $f^{(pert)}$ stand for the perturbative components of the structure functions; ϕ and Φ are the parton distributions and μ is the factorization scale. In what follows we obtain Eqs. (2,3), simplifying the factorized expression for the amplitude $A_{\mu\nu}$ of the Compton scattering off a hadron target. By doing so, we summarize and generalize the results obtained in [3]. Using appropriate projection operators P_r the Compton amplitude $A_{\mu\nu}$ can be expanded into a set of invariant amplitudes A_r. According to the Optical Theorem, every structure function f_r can be expressed through A_r:

$$f_r = \frac{1}{\pi}\Im A_r\,. \tag{4}$$

Among amplitudes A_r there is the amplitude A_S related to the structure function F_1 singlet. We will address this amplitude as the singlet and will address as non-singlets to all other invariant amplitudes and use for them the generic notation A_{NS}. We also will use the generic notation A for both the singlet and non-singlet amplitudes when it is relevant.

2 Basic Factorization for the Compton amplitude

Let us expand the invariant amplitude A into a set of convolutions depicted in Fig. 1 where the t- channel states involve arbitrary number of partons. Throughout the paper

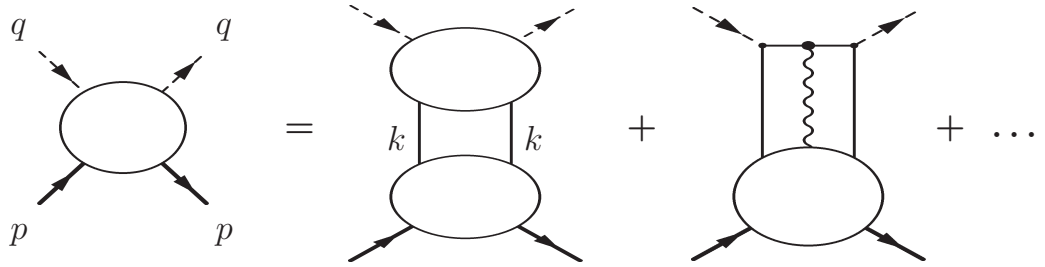

Figure 1: Representation of $A_{\mu\nu}$ through the convolution of two blobs.

we will consider only the first graph in Fig. 1 where the blobs are connected by the two-parton state, with the partons being quarks. Consideration of the two-gluon state yields the same results as shown in [3]. All blobs in Fig. 1 can contain both perturbative and non-perturbative contribution, so this kind of factorization does not correspond to the conventional scenario of the QCD factorization. We will address it as the primary convolution. Introducing the Sudakov parametrization of the moment r:

$$k = -\alpha(q + xp) + \beta p + k_\perp, \tag{5}$$

we can write the primary convolution as follows, using the :

$$A(q^2, w) = \int_{-\infty}^{\infty} \frac{d\beta}{\beta} \int_0^{\infty} dk_\perp^2 \int_{-\infty}^{\infty} d\alpha\, \widetilde{A}(w\beta, q^2, k^2) \frac{B}{(k^2)^2} T(w\alpha, k^2)\,, \tag{6}$$

where $\widetilde{A}$ and T denote the upper and lower blobs respectively; $w = 2pq$, $k^2 = -w\alpha\beta - k_\perp^2$ and factor B, with $B = w(\alpha^2 + \beta^2) + k_\perp^2$, appears because of simplification of the spin structure of the intermediate quarks. We have skipped in Eq. (6) dependence on unessential arguments like masses, spin, etc. The integrand in Eq. (6) becomes singular at $k^2 \to 0$. This infrared ($\equiv$ IR) divergence must be regulated. The IR-sensitive perturbative contents for the singlet and non-singlet amplitudes are different. A_{NS} contain the IR-sensitive perturbative logarithms whereas A_S includes both logarithms and the power-factor:

$$A_{NS} = A_{NS}\left(\ln(w\beta), \ln(Q^2/k^2)\right)\,, \qquad A_S = \left(w\beta/k^2\right) M_S\left(\ln(w\beta), \ln(Q^2/k^2)\right)\,. \tag{7}$$

Therefore in order to keep the integral Eq. (6) IR stable , amplitudes T must obey the following restrictions at small k^2:

$$T_{NS} \sim \left(k^2\right)^{\gamma}\,, \qquad T_S \sim \left(k^2\right)^{1+\gamma}\,, \tag{8}$$

with $\gamma > 0$. Similarly, in order to get the ultraviolet stability of A the blob T at large α should decrease with growth of $|\alpha|$:

$$T_{NS} \sim |\alpha|^{-1-h}\,, \qquad T_S \sim |\alpha|^{-h}\,. \tag{9}$$

Eq. (6) in the Born approximation is depicted in Fig. 2. Radiative corrections are absent

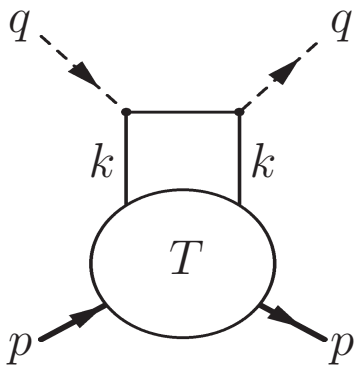

Figure 2: Born approximation for the amplitude of the forward Compton scattering.

there, so blob T is totally non-perturbative. Inserting the radiative corrections into the Born approximation is depicted in Fig. 3. We stress that we neglect graphs with extra

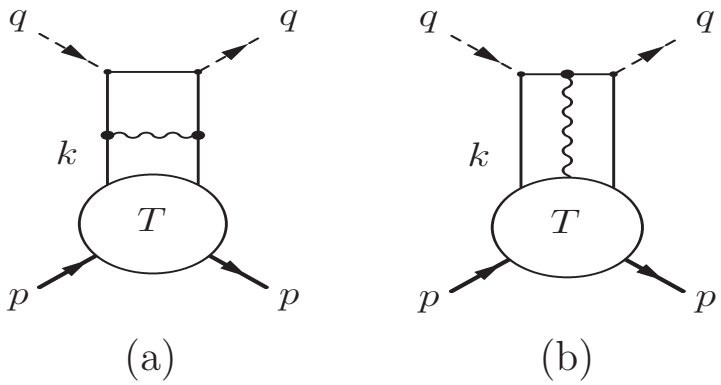

Figure 3: Radiative corrections to the Born amplitude.

propagators touching the lower blob (e.q. graph (b)) because they lead to the convolution with three or mote intermediate partons depicted in Fig. 1 and we do not consider such multiparton states in this paper. In order to back up this course of actions we would like to notice that all evolution equations available operate with the two-parton initial states only. So, we account for the graphs which do not touch it (e.q. graph (a)). Obviously all such graphs can be included into the upper blob, leaving the lower blob non-perturbative. As a result, we convert the convolution in Eq. (6) into the similarly looking convolution

$$A(q^2, w) = \int_{-\infty}^{\infty} \frac{d\beta}{\beta} \int_0^{\infty} dk_\perp^2 \int_{-\infty}^{\infty} d\alpha\, A^{(pert)}(w\beta, q^2, k^2) \frac{B}{(k^2)^2} T(w\alpha, k^2)\,, \tag{10}$$

where the upper blob $A^{(pert)}$ is perturbative and the lower blob T is non-perturbative. The integral in (10) is free of IR singularities at small k^2. Therefore, Eq. (10) corresponds to

the concept of QCD factorization, though this factorization differs from the Collinear and k_T- factorizations. By this reasons we will address it as the basic factorization. Applying Optical Theorem, we convert (10) into the basic factorization for the structure functions:

$$f(x,Q^2) = \int_{-\infty}^{\infty} \frac{d\beta}{\beta} \int_0^{\infty} dk_\perp^2 \int_{-\infty}^{\infty} d\alpha \, f^{(pert)}(x/\beta, Q^2/k^2) \frac{B}{(k^2)^2} \Psi(w\alpha, k^2) \tag{11}$$

where Ψ stands for the totally unintegrated parton distributions.

3 Reducing Basic factorization to k_T- and collinear factorizations

In order to proceed from Eq. (11) to (3), we need to integrate out the α- dependence without touching the perturbative . Obviously, it cannot be done straightforwardly because $f^{(pert)}$ depends on α trough k^2. However, imposing the restriction

$$w\alpha\beta \ll k_\perp^2 \,, \tag{12}$$

we can neglect this dependence in and integrate Ψ over α. As a result we arrive at (3) with

$$\Phi(\beta, k_\perp) = \int_{k_\perp^2/w}^{k_\perp^2/w\beta} d\alpha \, T(\alpha, k^2) \,. \tag{13}$$

In order to keep (3) IR stable at $k_\perp \to 0$, the parton distributions Φ should decrease with $k_\perp$:

$$\Phi_{NS} \sim \left(k_\perp^2\right)^\gamma \,, \qquad \Phi_S \sim \left(k_\perp^2\right)^{1+\gamma} \,. \tag{14}$$

Transition from the k_T- expression (3) to the collinear factorization (2) is also impossible in the straightforward way. Let us suppose that the $k_\perp$-dependence of $\Phi_{S,NS}$ in (3) has a peaked form with one or several sharp maximums at $k_\perp^2 = \mu_0^2, \mu_1^2, ...$ as shown in Fig. 4. We address such scales as intrinsic scales. We do not assume any special form for the curve

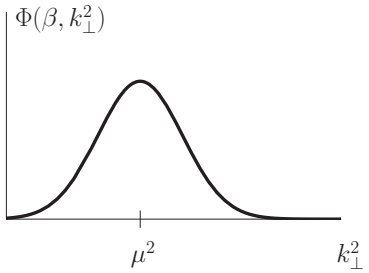

Figure 4: The peaked form of $\Phi(\beta, k_\perp^2)$ with one maximum.

in Fig. 3 save that it obeys the restriction (14). It allows us to approximately integrate over $k_\perp$ in (3), dealing with Φ only and arriving at

$$f(x,Q^2) = \int_x^1 \frac{d\beta}{\beta} f^{(pert)}(x/\beta, Q^2/\mu_0^2) \varphi(\beta, \mu_0^2) \tag{15}$$

where the parton distributions φ are expressed through the distributions Φ which have been used in the k_T- factorization:

$$\varphi(\beta,\mu_0^2)=\int_0^w \frac{dk_\perp^2}{k_\perp^2}\,\Phi(\beta,k_\perp^2)\,. \tag{16}$$

4 Comparison of conventional collinear factorization and Eq. (16).

The parton distribution ϕ in the conventional approach to the collinear factorization and distribution φ are widely different. The distribution ϕ includes both perturbative and non-perturbative contributions whereas φ is purely non-perturbative. The factorization scale μ used in the conventional approach is arbitrary while μ_0 corresponds to the maximum in Fig. 4. However, it is easy to relate them, using any kind of the perturbative evolution to evolve φ from scale μ_0 to μ. Naturally, the value of μ can be chosen anywhere between μ_0^2 and Q^2. At the same time the perturbative part, $f^{(pert)}(x/\beta,Q^2/\mu_0^2)$, should be evolved from μ_0 to μ. As a result, we arrive at the conventional formula (2) where the convolution is independent of μ. In other words, changing the factorization scale from the intrinsic scale μ_0 to an arbitrary scale μ leads to the re-distribution of the radiative corrections between the upper and lower blobs of the collinear convolution. We do not specify which kind of the perturbative evolution should be used because our approach is insensitive to details of this evolution. In particular, he DGLAP equations can be used for such evolution.

5 Restrictions on the DGLAP fits for the parton distributions

Combining Eqs. (9, 13. 16) leads to the following dependence of the parton distributions Φ and φ at small β:

$$\Phi_{NS}\sim\beta^h,\quad \Phi_S\sim\beta^{-1+h}\,,\qquad \varphi_{NS}\sim\beta^h\,,\qquad \varphi_S\sim\beta^{-1+h}\,. \tag{17}$$

As shown in Eq. (18), the standard DGLAP -fits for the DIS structure functions in the collinear factorization include a normalization N, the singular factors x^{-a}, with $a>0$, and the regular terms:

$$\delta q,\delta g = Nx^{-a}(1-x)^b(1+cx^d)\,, \tag{18}$$

where the parameters $N,a,b,c,d>0$. Such expressions do not look as the ones obtained with the perturbative methods, so we identify them with non-perturbative distributions φ. Eq. (17) excludes the use of the singular factors in the expressions for the non-singlet structure functions F_2, F_1^{NS}, g_1, etc and also suppress the singular factors with $a>1$ in the expressions for the singlet F_1. However, the parton distributions used for F_1 and F_2 are identical, therefore the suppression of the singular factors with $a>0$ can be applied to all structure functions, including the singlet F_1. The singular factors x^{-a} in the DGLAP fits for initial parton densities should be removed from the fits because they contradict to the integrability of the basic convolutions of the Compton amplitudes.

6 Conclusion

Both the k_T- and collinear factorizations are obtained by consecutive reductions of the Compton scattering amplitude represented as the convolution of two blobs connected by two parton lines. We neglect all convolutions with number of the intermediate states greater than two. It has no impact on our further analysis because every convolution should be finite independently of the multiplicity of intermediate states. Exploiting the IR stability of the convolution we convert it into the basic QCD convolution and to the K_T - factorization. This transition is performed with purely mathematical means. In contrast, the transition from the K_T-to the collinear factorization is based on the physical assumption: we assume that the $k_\perp$-dependence of the parton distribution has one or several sharp maximums which become the intrinsic factorization scales. The sharper the maximums are, the more accurate this reduction is. In order to keep the lower blob unperturbative, the value of the intrinsic scale(s) should be close to Λ_{QCD}. Our assumption of the peaked $k_\perp$- distributions can be checked by analysis of experimental data in the framework of the k_T-factorization. Transition to the conventional parton distributions ϕ defined at other factorization scales μ located in the domain of the perturbative QCD (conventionally $\mu \sim$ several GeV), can be done with the use of the evolution equations. On the other hand, this perturbative scale can be regarded as the one achieved with the perturbative evolution starting from a lower scale which can be associated with our intrinsic scale μ_0. Therefore, the conventional approach involves the intrinsic scale, though implicitly, while our approach sets this scale explicitly.

Acknowledgement. We are grateful to Organizing Committee of the workshop DSPIN-2001 for support. The work is partly supported by Grant RAS 9C237, Russian State Grant for Scientific School RSGSS-65751.2010.2 and EU Marie-Curie Research Training Network under contract MRTN-CT-2006-035505 (HEPTOOLS).

References

[1] D. Amati, R. Petronzio and G. Veneziano, Nucl. Phys, **B140** (1978) 54;
A.V. Efremov, A.V. Radyushkin, Teor. Mat. Fiz, **42** (1980) 147;
A.V. Efremov,A.V. Radyushkin, Theor. Math. Phys, **44** (1980) 573;
A.V. Efremov,A.V. Radyushkin, Teor.Mat.Fiz, **44** (1980) 17;
A.V. Efremov, A.V. Radyushkin, Phys.Lett, **B63** (1976) 449;
A.V. Efremov, A.V. Radyushkin, Lett.Nuovo Cim, **19** (1977) 83;
S. Libby, G. Sterman, Phys, Rev, **D18** (1978) 3252;
S.J. Brodsky, G.P. Lepage, Phys. Lett, **B87** (1979) 359;
S.J. Brodsky, G.P. Lepage, Phys. Rev, **D22** (1980) 2157;
J.C. Collins, D.E. Soper. Nucl. Phys, **B193** (1981) 381;
J.C. Collins, D.E. Soper. Nucl. Phys, **B194** (1982) 445;
J.C. Collins, D.E. Soper, G. Sterman, Nucl. Phys, **B250** (1985) 199;
A.V. Efremov and I.F. Ginzburg. Fortsch.Phys.**22** (1974) 575;
A.V. Efremov and A.V. Radyushkin. Report JINR **E2**-80-521;
Mod.Phys.Lett. **A24** (2009) 2803.

[2] S. Catani, M. Ciafaloni, F. Hautmann, Phys. Lett, **B242** (1990) 97;
S. Catani, M. Ciafaloni, F. Hautmann, Nucl.Phys. **B366** (1991) 135.

[3] B.I. Ermolaev, M. Greco, S.I. Troyan, arXiv:1005.2829

HARD MESON ELECTROPRODUCTION AND TWIST-3 EFFECTS.

S. V. Goloskokov

Bogoliubov Laboratory of Theoretical Physics, Joint Institute for Nuclear Research, Dubna 141980, Moscow region, Russia
E-mail: goloskkv@theor.jinr.ru

Abstract

We analyze light meson electroproduction within the handbag model. We study cross sections and spin asymmetries for various mesons. The essential role of the transversity $\tilde{H}_T$ and $\tilde{E}_T$ GPDs in electroproduction of pseudoscalar mesons is found. Our results are in good agrement with experiment.

In this report, investigation of the pseudoscalar meson leptoproduction is based on the handbag approach where the leading twist amplitude at high Q^2 factorizes into hard meson electroproduction off partons and the Generalized Parton Distributions (GPDs) [1].

The amplitude of the meson electroproduction off the proton reads as a convolution of the partonic subprocess amplitude $\mathcal{H}$ and GPDs H

$$\mathcal{M}^a_{\mu'\pm,\mu+} = \sum_a [\langle H^a\rangle + ...]; \;\; \langle H^a\rangle \propto \sum_\lambda \int_{xi}^1 d\overline{x} \mathcal{H}^a_{\mu'\lambda,\mu\lambda}(Q^2,\overline{x},\xi)\; H^a(\overline{x},\xi,t), \qquad (1)$$

where a denotes the gluon and quark contribution with the corresponding flavors; μ (μ') is the helicity of the photon (meson), and $\overline{x}$ is the momentum fraction of the parton with helicity λ. The skewness ξ is related to Bjorken-x by $\xi \simeq x/2$.

The subprocess amplitudes $\mathcal{H}^V$ are calculated within the modified perturbative approach (MPA) [2] where the quark transverse momenta $\mathbf{k}_\perp$ are taken into account together with the gluonic radiation, condensed as a Sudakov factor. The amplitude $\mathcal{H}^V$ contains a convolution of a perturbatively calculated hard part where we keep in the propagators the $\mathbf{k}^2_\perp$ terms and the $\mathbf{k}_\perp$- dependent wave function [3].

To estimate GPDs, we use the double distribution (DD) representation [4]

$$H_i(\overline{x},\xi,t) = \int_{-1}^1 d\beta \int_{-1+|\beta|}^{1-|\beta|} d\alpha \delta(\beta+\xi\,\alpha-\overline{x})\, f_i(\beta,\alpha,t). \qquad (2)$$

The GPDs are related with PDFs through the double distribution function

$$f_i(\beta,\alpha,t) = h_i(\beta,t)\,\frac{3}{4}\,\frac{[(1-|\beta|)^2-\alpha^2]}{(1-|\beta|)^3}\,. \qquad (3)$$

The functions h_i are expressed in terms of PDFs and parameterized as

$$h(\beta,t) = N\, e^{b_0 t}\beta^{-\alpha(t)}\,(1-\beta)^n. \qquad (4)$$

Here the t- dependence is considered in a Regge form and $\alpha(t)$ is the corresponding Regge trajectory. The parameters in (4) are obtained from the known information about

PDFs [5] e.g, or from the nucleon form factor analysis [6]. The model results on the cross sections and spin density matrix elements (SDME) for vector meson production obtained in [7–10] are in good agreement with experimental data in a wide energy range.

The hard exclusive pseudoscalar meson leptoproduction in the leading twist is sensitive to the polarized GPDs $\tilde{H}$ whose parameterization can be found in [9] and $\tilde{E}$. The pseudoscalar meson production amplitude with longitudinally polarized photons $\mathcal{M}^P_{0\nu',0\nu}$ dominates at large Q^2. The amplitudes with transversally polarized photons are suppressed as $1/Q$. The pseudoscalar meson production amplitude can be written as [11]:

$$\mathcal{M}^P_{0+,0+} \propto [\langle \tilde{H}^P \rangle - \frac{2\xi m Q^2}{1-\xi^2}\frac{\rho_P}{t-m_P^2}];\ \mathcal{M}^P_{0-,0+} \propto \frac{\sqrt{-t'}}{2m}\,[\xi\langle \widetilde{E}^P \rangle + 2mQ^2\frac{\rho_P}{t-m_P^2}]. \qquad (5)$$

The first terms in (5) represent the handbag contribution to the pseudoscalar (P) meson production amplitude (1) calculated within the MPA with the corresponding transition GPDs. For the π^+ production we have the $p \to n$ transition GPD where the combination $\tilde{F}^{(3)} = \tilde{F}^{(u)} - \tilde{F}^{(d)}$ contributes. The second terms in (5) appear for charged meson production and are connected with the P meson pole. In calculations we use the fully experimentally measured electromagnetic form factor of P meson.

In addition to the pion pole and the handbag contribution, which in the leading twist is determined by the $\widetilde{H}$ and $\widetilde{E}$ GPDs, a twist-3 contribution to the amplitudes $\mathcal{M}_{0-,++}$ and $\mathcal{M}_{0+,++}$ is required to describe the polarized data at low Q^2. To estimate this effect, we use a mechanism that consists of the transversity GPD H_T, $\bar{E}_T$ in conjugation with the twist-3 pion wave function. For the $\mathcal{M}_{0-,\mu+}$ amplitude we have [11]

$$\mathcal{M}^{P,twist-3}_{0-,\mu+} \propto \int_{-1}^{1} d\overline{x}\mathcal{H}_{0-,\mu+}(\overline{x},...)\,[H_T^P + ...O(\xi^2\,E_T^P)]. \qquad (6)$$

The H_T GPD is connected with transversity PDFs as

$$H^a_T(x,0,0) = \delta^a(x); \quad \delta^a(x) = C\,N^a_T\,x^{1/2}\,(1-x)\,[q_a(x) + \Delta q_a(x)]. \qquad (7)$$

Here we parameterize the PDF δ using the model [12]. The DD form (2,3) is used to calculate GPD H_T. It is important that the H^u_T and H^d_T GPDs are different in sign.

The twist-3 contribution to the amplitude $\mathcal{M}_{0+,\mu+}$ has a form [13] similar to (6)

$$\mathcal{M}^{P,twist-3}_{0+,\mu+} \propto \frac{\sqrt{-t'}}{4m}\int_{-1}^{1} d\overline{x}\mathcal{H}_{0-,\mu+}(\overline{x},...)\,\bar{E}_T^P. \qquad (8)$$

The information on $\bar{E}_T$ was obtained only in the lattice QCD [14]. The lower moments of $\bar{E}^u_T$ and $\bar{E}^d_T$ were found to be quite large, have the same sign and a similar size. This means that we have an essential compensation of the $\bar{E}_T$ contribution in the π^+ amplitude: $\bar{E}^{(3)}_T = \bar{E}^u_T - \bar{E}^d_T$. H_T does not compensate in this process. For the π^0 production we have the opposite case. We find here a large contribution from $\bar{E}^{\pi^0}_T = 2/3\bar{E}^u_T + 1/3\bar{E}^d_T$, H_T effects are not so essential here. The parameters for individual PDFs were taken from the lattice results, and DD model was used to estimate E_T.

In Fig. 1a, we show the full unseparated cross section of the π^+ production which describes fine the HERMES data [15]. The longitudinal cross section determined by leading-twist dominates at small momentum transfer $-t < 0.2\text{GeV}^2$. At larger $-t$ we

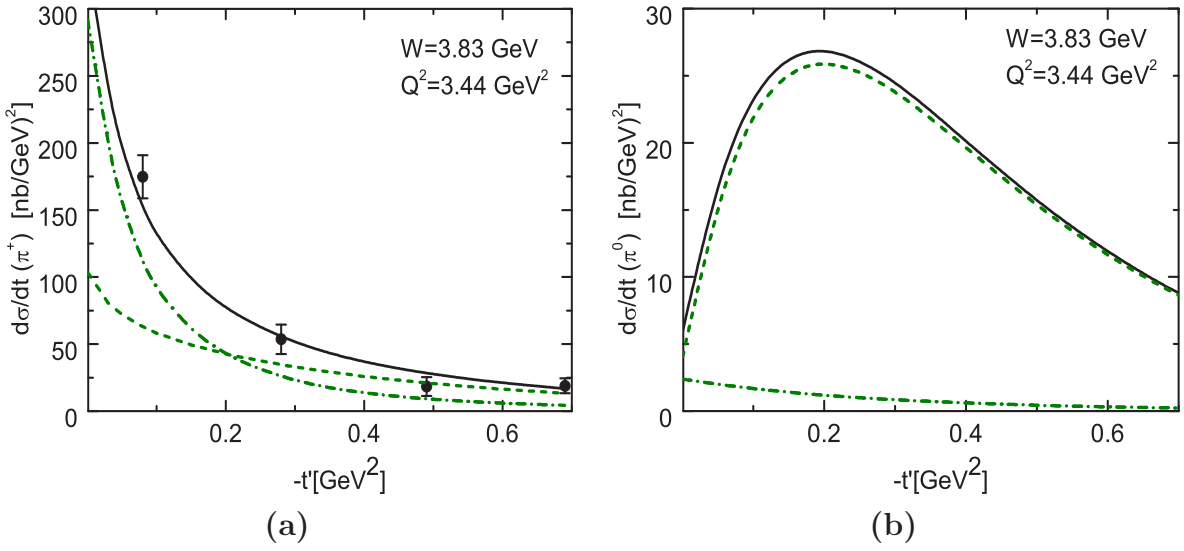

Figure 1: **(a)**The cross section of the π^+ production together with HERMES data. **(b)** π^0 production at HERMES. For both: full line- unseparated cross section, dashed-dotted- σ_L, dotted line- σ_T.

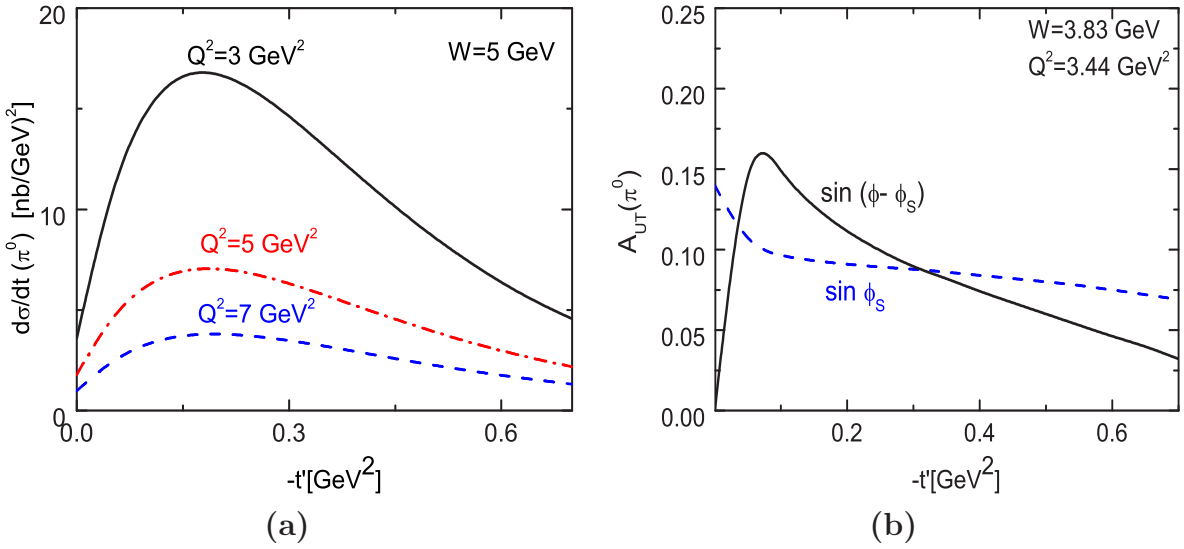

Figure 2: **(a)** Q^2 dependence of π^0 production cross section at HERMES. **(b)** Predictions for the moments of A_{UT} asymmetry of π^0 production at HERMES.

find a not small contribution from the transverse cross section. Effects of E_T is negligible here.

For the π^0 production we show above that the transversity effect should be essential. They lead to a large transverse cross section σ_T. The longitudinal cross section, which is under control of the leading twist contribution and expected to play an important role, is much smaller with respect to the transverse σ_T cross section. The predominated role of transversally polarized photons is mainly generated by the E_T GPDs contribution.

This surprising result for the cross section of the π^0 production at HERMES energies [13] is presented in Fig. 1b. It was found that the transversity GPDs leads to a large

σ_T for all reactions of pseudoscalar meson production with the exception of π^+ and η' channels [13]. These twist-3 effects have $1/Q$ suppression with respect to the leading twist contribution. The Q^2 dependence of the transverse cross section in Fig. 2.a shows a rapid decrease of σ_T at HERMES energies. It is important that the $\mathcal{M}^{P,twist-3}_{0+,\mu+}$ amplitude (7) which is under control of E_T GPDs has a zero for $-t' = 0$. This provides a minimum of the cross section at zero momentum transfer, Figs. 1b, 2a.

In Fig. 2b, our predictions for the $\sin(\phi - \phi_s)$ and $\sin(\phi)$ moments of A_{UT} asymmetry for the transversally polarized target are presented. Predicted asymmetries are quite large and can be measured experimentally.

If Fig. 3a we show the ratio of the η/π^0 cross section at CLAS energies for two parameterizations of H_T GPDs. Different combinations of the quark contributions to these processes leas to the essential role of H_T effects at $-t < 0.2\text{GeV}^2$ in this ratio. At larger momentum transfer the E_T contributions predominate. That leads to the rapid t-dependence of the η/π^0 cross section ratio. The preliminary CLAS data [16] confirm the large E_T effects in π^0 production found in the model.

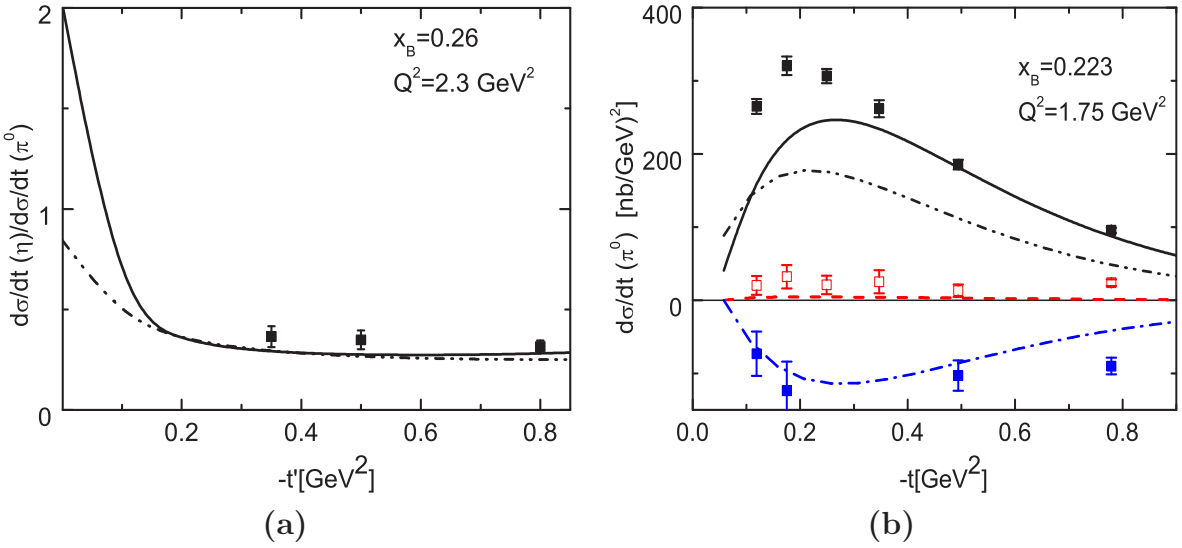

Figure 3: **(a)** The ratio of the η/π^0 cross section at CLAS together with preliminary CLAS data. **(b)** The π^0 cross section at CLAS together with preliminary CLAS data. Full line- unseparated cross section, dashes- σ_{LT}, dashed dotted- σ_{TT}. Dashed-dot-dotted line– the alternative parameterizations of H_T

In Fig 3b, we show our prediction for π^0 production at the CLAS energy range together with preliminary experimental data. The data are not far from our predictions at the CLAS energy [16] and definitely show the dip at low momentum transfer which is less with respect to the standard H_T parameterization (full line). The alternative H_T parameterization [13] shows a smaller dip at $t' = 0$ and a smaller cross section at large t' as well. The main prediction of the model- large σ_T cross section can be checked if the data on the separated σ_L and σ_T cross section will be available.

In a similar way we can estimate E_T effects in the vector meson leptoproduction. Some details can be found in [11]. The $M_{0+,++}$ amplitude and correspondingly the transversity twist-3 effects are essential in the r^1_{00} and r^5_{00} SDME. Our results are shown in Fig. 4. They are consistent in signs and values with HERMES data [17] without any free parameters.

However, such estimations now can be made only for the quark contribution and cannot be used for the low x_B range.

In this report, the hard pseudoscalar meson electroproduction is calculated within the MPA which takes into account the quark transverse degrees of freedom and the Sudakov suppressions. At the leading-twist accuracy this class of reactions is sensitive to the GPDs $\widetilde{H}$ and $\widetilde{E}$. However, rather strong contributions from the amplitudes $M_{0-,++}$ and $M_{0+,++}$ are required to describe experimental data. These amplitudes are generated by the transversity GPDs H_T and $\bar{E}_T$ accompanied by the twist-3 pseudoscalar meson wave functions. Our parameterizations of GPDs are consistent with the lattice QCD results and other information like nucleon form factors. The model predicts the large η/π^0 cross section ratio ~ 1 at small momentum transfer and its small value $\sim .3$ at $-t' > 0.2\text{GeV}^2$. The small value of the ratio is compatible with the CLAS data. At the same time, JLAB data on unseparated cross section have definite dip at $t' \sim 0$. These model results are determined by the twist-3 transversity E_T effects compatible with the data.

Our calculations of the twist-3 transversity effects in SDME of ρ^0 production are not far from the HERMES data. Since our parameterization of $\bar{E}_T$ fully depends on the lattice QCD estimations, our results for the cross sections of electroproduction of pseudoscalar mesons are real predictions. All these observations can indicate the large transversity effects in the mentioned reactions. To check them, additional investigation is needed. For example, the analysis of separated σ_L and σ_T cross section in π^0 production is important to get the definite conclusion about $\bar{E}_T$ GPDs.

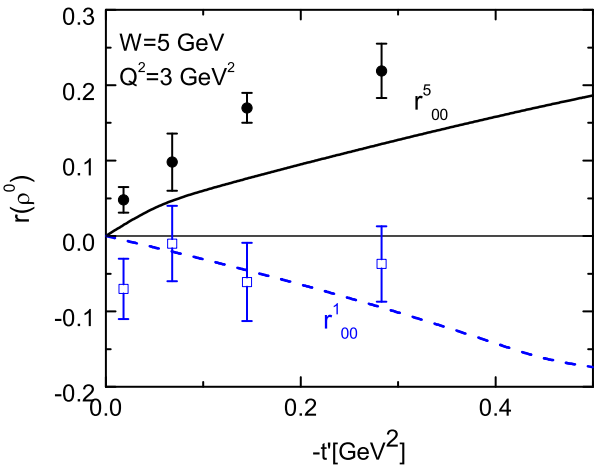

Figure 4: Twist-3 effects in spin density matrix elements of ρ^0 production at HERMES.

We describe fine the well-known data on the cross section and spin observables for various meson productions [7–10]. We give predictions for cross sections and spin asymmetries for all pseudoscalar meson channels [11, 13] at low skewness and small momentum transfer. Our predictions can be examined in future experiments and shed light on the role of transversity effects in these reactions.

Thus, we can conclude that information about twist-3 transversity effects can be obtained from pseudoscalar meson electroproduction for example at JLAB energies.

This work is supported in part by the Russian Foundation for Basic Research, Grants 09-02-01149, 12-02-00613 and by the Heisenberg-Landau program.

References

[1] X. Ji, Phys. Rev. **D55**, (1997) 7114;
A.V. Radyushkin, Phys. Lett. **B380**, (1996) 417;
J.C. Collins, et al., Phys. Rev. **D56**, (1997) 2982.

[2] J. Botts and G. Sterman, Nucl. Phys. **B325**, (1989) 62.
[3] J. Bolz, J.G. Körner and P. Kroll, Z. Phys. **A350**, (1994) 145.
[4] I.V. Musatov and A.V. Radyushkin, Phys. Rev. **D61**, (2000) 074027.
[5] J. Pumplin, et al., JHEP **0207**, (2002) 012.
[6] M. Diehl, T. Feldmann, R. Jakob and P. Kroll, Eur0. Phys. J. **C39**, (2005) 1.
[7] S.V. Goloskokov, P. Kroll, Euro. Phys. J. **C42**, (2005) 281.
[8] S.V. Goloskokov, P. Kroll, Euro. Phys. J. **C50**, (2007) 829.
[9] S.V. Goloskokov, P. Kroll, Euro. Phys. J. **C53**, (2008) 367.
[10] S.V.Goloskokov, P.Kroll, Euro. Phys. J. **C59**, (2009) 809.
[11] S.V.Goloskokov, P.Kroll, Euro. Phys. J. **C65**, (2010) 137.
[12] M. Anselmino, M. Boglione, U. D'Alesio, A. Kotzinian, F. Murgia, A. Prokudin and S. Melis, Nucl. Phys. Proc. Suppl. **191**, (2009) 98.
[13] S.V.Goloskokov, P.Kroll, Euro. Phys. J. **A47**, 112 (2011).
[14] M. Gockeler *et al.* [QCDSF/UKQCD Collaborations], Phys. Rev. Lett. **98**, (2007) 222001.
[15] A. Airapetian et al. [HERMES collaboration], Phys. Lett. **B659**, (2008) 486.
[16] V. Kubarovsky. [CLAS Collab.], this proceedings.
[17] A. Airapetian *et al* [HERMES collaboration], Eur. Phys. J. C **62**, (2009) 658.

HIGH-ENERGY PHYSICS WITH PARTICLES CARRYING NON-ZERO ORBITAL ANGULAR MOMENTUM

I. P. Ivanov[1, 2, †]

(1) *IFPA, Université de Liège, Liège, Belgium*
(2) *Sobolev Institute of Mathematics, Koptyug av. 4, 630090, Novosibirsk, Russia*
† *E-mail: Igor.Ivanov@ulg.ac.be*

Abstract

Thanks to progress in optics in the past two decades, it is possible to create photons carrying well-defined non-zero orbital angular momentum (OAM). Boosting these photons into high-energy range preserving their OAM seems feasible. Intermediate energy electrons with OAM have also been produced recently. One can, therefore, view OAM as a new degree of freedom in high-energy collisions and ask what novel insights into particles' structure and interactions it can bring. Here we discuss generic features of scattering processes involving particles with OAM in the initial or final state.

1 Introduction

Laser beams carrying non-zero orbital angular momentum (OAM) are well-known and routinely used in optics, [1]. The lightfield in such beams is described via non-plane wave solutions of the Maxwell equations, for example by Bessel or Laguerre-Gaussian beams. Each photon in this lightfield, which we call a *twisted photon*, carries a well-defined energy and longitudinal momentum directed along axis z as well as a definite OAM projection onto this axis quantized in units of $\hbar$. The wavefronts of such a lightfield are not planes but helices.

So far, experiments with twisted light were confined mostly to the optical energy range. However it was recently noted that one can use Compton backscattering of twisted optical photons off an ultra-relativistic electron beam to generate high-energy photons carrying non-zero OAM [2]. Technology necessary for such convertion already exists. In addition, successful creation of twisted electrons has also been reported recently, [3]. Such electrons carried the energy as high as 300 keV and the orbital quantum number up to $m \sim 100$. Finally, it was recently noted that OAM is naturally transmitted from one to another particles in a generic elastic scattering, [4]. Future progress in this field will lead to creation of even more energetic twisted electrons and other particles, which can then be used in scattering experiments. Thus, OAM can be viewed as a new degree of freedom which one can exploit in preparing initial states of a high-energy process. It is therefore timely to ask how such a collision can be described and what new insights into the properties of particles and their interactions it can bring.

In this contribution we consider generic features of scattering processes involving twisted particles More details about the results presented here can be found in [5].

2 Describing twisted states

Here we briefly summarize the formalism of Bessel-beam twisted states introduced in [2] starting with the scalar field.

We first fix the z axis and solve the free wave equation in cylindric coordinates r, φ_r, z. A solution $|\kappa, m\rangle$ with definite frequency ω, longitudinal momentum k_z, modulus of the transverse momentum $|\mathbf{k}| = \kappa$ and a definite z-projection of the orbital angular momentum m has the form

$$|\kappa, m\rangle = e^{-i\omega t + ik_z z} \cdot \psi_{\kappa m}(\mathbf{r}) \,, \quad \psi_{\kappa m}(\mathbf{r}) = \frac{e^{im\varphi_r}}{\sqrt{2\pi}} \sqrt{\kappa} J_m(\kappa r) \,, \tag{1}$$

where $J_m(x)$ is the Bessel function. A twisted state can be represented as a superposition of plane waves:

$$|\kappa, m\rangle = e^{-i\omega t + ik_z z} \int \frac{d^2\mathbf{k}}{(2\pi)^2} a_{\kappa m}(\mathbf{k}) e^{i\mathbf{kr}} \,, \quad a_{\kappa m}(\mathbf{k}) = (-i)^m e^{im\varphi_k} \sqrt{2\pi} \, \frac{\delta(|\mathbf{k}| - \kappa)}{\sqrt{\kappa}} \,. \tag{2}$$

More details about properties of twisted states, their normalization and phase space density can be found in [2, 5].

Description of photons carrying non-zero OAM is subtler than for scalar particles due to their polarization degree of freedom. A plane wave photon with helicity $\lambda = \pm 1$ is described, in addition to the fixed four-momentum k^μ, by an appropriately defined polarization vector $e^\mu_\lambda(k)$, with the properties $e_{\lambda\mu} k^\mu = 0$ and $e^*_{\lambda\mu} e^\mu_{\lambda'} = -\delta_{\lambda\lambda'}$. In the plane wave case, the polarization vector appears as an overall factor in front of the space-time wave function: the components of the polarization vector, which can be selected to be only transverse, remain constant across the transverse plane orthogonal to the Poynting vector. The same is valid for the Stokes parameters for a general elliptic polarization state.

In the twisted case both the polarization vector of a pure helicity state and the Stokes parameters of an elliptically polarized state acquire non-trivial spatial dependence. Even worse, the polarization vectors taken at different points cannot lie in the same plane because the directions of the Poynting vector calculated at distinct spatial points are different. One can represent a pure helicity twisted photon state in the coordinate space similarly to (2):

$$A^\mu_{\lambda\,\kappa m}(x) = \sqrt{4\pi} \int \frac{d^2\mathbf{k}}{(2\pi)^2} \, e^\mu_\lambda(k) \, a_{\kappa m}(\mathbf{k}) e^{-ik_\mu r^\mu} \,, \tag{3}$$

Even with the four-potential (3) depending non-trivially on the coordinates, the gauge invariance in its usual definition as an invariance under $A_\mu(x) \to A_\mu(x) + \partial_\mu f(x)$ still holds. Note however that the definition (3) should be accompanied with a prescription of how vectors $e^\mu_\lambda(k)$ for different k are related to each other. Recall that for the plane waves with $\vec{k} = (0, 0, k)$, the polarization vector is defined up to an overall phase: $\vec{e}_\lambda = -(\lambda, i, 0) \cdot e^{i\alpha}/\sqrt{2}$, but the (arbitrary) α disappears in the matrix elements squared. This phase shift is equivalent to the shift of the zero moment of time.

This can be repeated for each plane wave inside a twisted state. If the three-momentum $\vec{k} = \omega(\sin\theta\cos\phi, \sin\theta\sin\phi, \cos\theta)$, we can introduce, following [6], the unit vectors $\vec{e}_\theta$, $\vec{e}_\phi$ and construct circular polarizations as $\vec{e}_\lambda(\vec{k}) = -(\lambda\vec{e}_\theta + i\vec{e}_\phi) \cdot e^{i\alpha(\phi)}/\sqrt{2}$, where $\alpha(\phi)$ is,

in principle, an arbitrary periodic function, which, however, does not affect the physical observables. We choose $\alpha(\phi) = \lambda\phi$ which yields the correct paraxial limit.

At this point it is necessary to address the issue of spin-OAM separation, which (in the non-abelian case of QCD) is a hot topic in the high-energy physics community, especially in the context of the spin proton puzzle [7]. Here we talk about photons with a definite value of OAM and a definite helicity λ. However this is not the spin/OAM separation that one usually has in mind due to two reasons: (1) this is a separation of spin and OAM degrees of freedom not at the level of operators, but at the level of their average values over certain states, and (2) the average vales of only z components of these operators are involved. At this level, the possibility to separate these two degrees of freedom is not unexpected, see e.g. a detailed discussion in [8]. Let us also mention that for the paraxial twisted light beams the separation of OAM and helicity is also easily derived, see [9]. For non-paraxial beams this issue is more tricky; in this case the evolution of OAM and helicity in the course of beam propagation can be cast into the form of an effective spin-orbital interaction, [6].

3 Scattering of twisted states

Let us now consider a generic collision of a twisted particle with a plane wave: $|\kappa, m\rangle + |PW(\mathbf{p})\rangle \to X$. The final system X is assumed to be describable by plane waves. The passage from the plane wave to the twisted state is given by (2) and is applied at the level of scattering matrix:

$$S_{tw} = \int \frac{d^2\mathbf{k}}{(2\pi)^2} a_{\kappa m}(\mathbf{k}) S_{PW}(\mathbf{k}, \mathbf{p})\,. \tag{4}$$

Its square is

$$\begin{aligned} |S_{tw}|^2 &= \int \frac{d^2\mathbf{k}}{(2\pi)^2}\frac{d^2\mathbf{k}'}{(2\pi)^2} a_{\kappa m}(\mathbf{k}) a^*_{\kappa m}(\mathbf{k}') S_{PW}(\mathbf{k}, \mathbf{p}) S^*_{PW}(\mathbf{k}', \mathbf{p}) \\ &= \int \frac{d^2\mathbf{k}}{(2\pi)^4} a_{\kappa m}(\mathbf{k}) a^*_{\kappa m}(\mathbf{k}) \delta^{(2)}(\mathbf{k} + \mathbf{p} - \mathbf{p}_X) |\mathcal{M}(\mathbf{k}, \mathbf{p})|^2\,. \end{aligned}$$

Here $\mathbf{p}_X$ is the transverse momentum of the final system X. The last line here contains the expression that enters the plane wave cross section of the same process. Skipping details which can be found in [5], we give the final result which links the single-twisted cross section to the plane wave cross section:

$$d\sigma_{tw} = \int \frac{d\phi_k}{2\pi}\, d\sigma_{PW}(\mathbf{k}) \cdot \frac{j_{PW}(\mathbf{k})}{j_{tw}}\,. \tag{5}$$

Here j_{PW} and j_{tw} are the plane-wave and the twisted flux functions. Discussions on subtle aspects of the definitions of the (averaged) cross section and the flux functions for the twisted scattering can be found in [2, 5]. Here we just note that the ratio of the fluxes in (5) is very close to unity for κ values achievable with today's technology.

The expession (5) is remarkable in several aspects. First, it is an unusual quantity in the sense that it involves averaging over the initial particle's azimuthal angle at fixed final momenta. Second, the single-twisted cross section is m-independent, which proves that twisted particles scatter as easily as plane waves. Third, the cross section (5) stays finite in

the small κ limit. Fourth, $d\sigma_{tw}$ is represented as an incoherent sum of $d\sigma_{PW}(\mathbf{k})$ for different angles ϕ_k, although the initial twisted state itself is a coherent superposition. The initial coherence is lost not during the interaction itself, but as a result of the usual condition that final states with distinct momenta do not interfere in the incoherent detectors we have.

Consider now the same process but assume that the twisted particle is in a superposition of states with different m, for example, $a|\kappa, m\rangle + a'|\kappa, m'\rangle$, with $|a|^2 + |a'|^2 = 1$. The calculation can be repeated yielding $d\sigma = d\sigma_{tw} + 2|aa'|d\sigma_{tw}^{\Delta m}$, where $d\sigma_{tw}$ is given by (5) and the new term is

$$d\sigma_{tw}^{\Delta m} = \int \frac{d\phi_k}{2\pi} \cos(\Delta m\, \phi_k + \alpha)\, d\sigma_{PW}(\mathbf{k}) \cdot \frac{j_{PW}(\mathbf{k})}{j_{tw}}\,, \tag{6}$$

with $\Delta m = m - m'$ and α being the relative phase between a and a'.

Looking at (5) and (6) can observes that with a well controlled m distribution of the initial twisted state one can perform the Fourier-analyzer of the plane wave cross section with respect to the initial azimuthal angle ϕ_k. This tool can be complementary to the usual partial wave analysis.

Let us now consider a collision of two twisted particles: $|\kappa, m\rangle + |\eta, n\rangle \to X$. Now, the scattering matrix squared is proportional to

$$\int \frac{d^2\mathbf{k}\, d^2\mathbf{p}\, d^2\mathbf{k}'\, d^2\mathbf{p}'}{(2\pi)^8} a_{\kappa m}(\mathbf{k}) a_{\eta n}(\mathbf{p}) a^*_{\kappa m}(\mathbf{k}') a^*_{\eta n}(\mathbf{p}')$$
$$\times\, \delta^{(2)}(\mathbf{k} + \mathbf{p} - \mathbf{p}_X)\delta^{(2)}(\mathbf{k}' + \mathbf{p}' - \mathbf{p}_X)\mathcal{M}(\mathbf{k}, \mathbf{p})\mathcal{M}^*(\mathbf{k}', \mathbf{p}')\,.$$

Trying to satisfy all the kinematical restrictions which enter this expression at fixed final transverse momentum $\mathbf{p}_X$, we end up with exactly two kinematical configurations, which are at work both for $\mathcal{M}(\mathbf{k}, \mathbf{p})$ and the conjugate of $\mathcal{M}(\mathbf{k}', \mathbf{p}')$:

$$\begin{aligned} \text{direct:} \quad & \mathbf{k}' = \mathbf{k}\,,\ \mathbf{p}' = \mathbf{p}\,, \\ \text{reflected:} \quad & \mathbf{k}' = \mathbf{k}^* \equiv -\mathbf{k} + 2(\mathbf{k}\mathbf{n}_X)\mathbf{n}_X\,,\ \mathbf{p}' = \mathbf{p}^* \equiv -\mathbf{p} + 2(\mathbf{p}\mathbf{n}_X)\mathbf{n}_X\,, \end{aligned} \tag{7}$$

with $\mathbf{n}_X \equiv \mathbf{p}_X/|\mathbf{p}_X|$. Since these two possibilities interfere, the double-twisted cross section will depend not only on $|\mathcal{M}(\mathbf{k}, \mathbf{p})|^2$ but also on $\mathcal{M}(\mathbf{k}, \mathbf{p})\mathcal{M}^*(\mathbf{k}^*, \mathbf{p}^*)$, the *autocorrelation function* of the amplitude. Note that such a quantity is inaccessible with plane wave scattering.

Again, skipping the details which can be found in [5] we show the result for the cross section:

$$d\sigma_{2tw} = \frac{1}{8\pi \sin(\delta_k + \delta_p)} \int d\phi_k d\phi_p \frac{j_{PW}(\mathbf{k}, \mathbf{p})}{j_{2tw}} \left[d\sigma_{PW}(\mathbf{k}, \mathbf{p}) + d\sigma'_{PW}(\mathbf{k}, \mathbf{p})\right]\,, \tag{8}$$

where $d\sigma_{PW}(\mathbf{k}, \mathbf{p})$ is the usual plane wave cross section, while

$$\begin{aligned} d\sigma'_{PW}(\mathbf{k}, \mathbf{p}) \;&=\; \frac{(2\pi)^4 \delta(E_i - E_f)\delta(p_{zi} - p_{zf})\delta^{(2)}(\mathbf{k} + \mathbf{p} - \mathbf{p}_X)}{4E_p \omega j_{PW}} \\ &\times\; \mathrm{Re}\left[e^{2im(\phi_k - \phi_X) + 2in(\phi_p - \phi_X)} \mathcal{M}(\mathbf{k}, \mathbf{p})\mathcal{M}^*(\mathbf{k}^*, \mathbf{p}^*)\right] d\Gamma_X\,. \end{aligned} \tag{9}$$

and

$$\delta_k = \arccos\left(\frac{\mathbf{p}_X^2 + \kappa^2 - \eta^2}{2|\mathbf{p}_X|\kappa}\right)\,, \quad \delta_p = \arccos\left(\frac{\mathbf{p}_X^2 - \kappa^2 + \eta^2}{2|\mathbf{p}_X|\eta}\right)\,.$$

Note that, in contrast to the single-twisted case, the double-twisted cross section is m, n-dependent and, similarly to the single-twisted case, stays finite at small κ, η.

4 Detecting final OAM

Twisted particles can have even stronger impact on particle physics, if the OAM of a final high-energy particle can be measured. Although OAM of low-energy photons and electrons can be measured, these techniques become impractical above MeV energy range. Here we propose an indirect method of observing the OAM of an energetic charged particle: via detection of the OAM of the photons emitted in bremsstrahlung.

Consider the standard process $ep \to ep\gamma$ where the initial and final electron (proton) momenta are denoted by $k_1(p_1)$ and $k_2(p_2)$, respectively, while the emitted photon momentum is k_3. The scattering matrix element of the process can be written as

$$S_{PW} = i(2\pi)^4 \delta^{(4)}(k_1 + p_1 - k_2 - k_3 - p_2) \cdot \mathcal{M}\,, \quad (10)$$

and In the soft photon limit, $\omega \ll E_e$, the amplitude $\mathcal{M}$ splits into the elastic scattering amplitude and an extra factor due to bremsstrahlung:

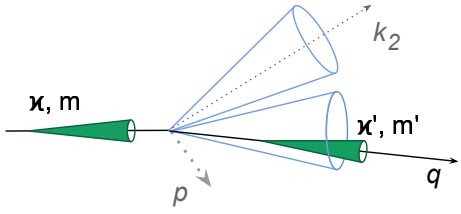

Figure 1: Kinematical conventions for bremsstrahlung of a twisted electron.

$$\mathcal{M} \approx e\mathcal{M}_{el} \cdot \left(\frac{(ek_1)}{(k_3k_1)} - \frac{(ek_2)}{(k_3k_2)} \right) . \quad (11)$$

If now the initial electron and the final photon are described by twisted states $|\kappa, m\rangle$ and $|\kappa', m'\rangle$, see Fig. 1. Then in the paraxial approximation, the scattering matrix element is proportional to

$$S_{tw} \propto \frac{\cos(m\varphi^* - m'\varphi'^*)}{\sqrt{\kappa'^2 - \kappa^2 \cos^2\beta}}\, \delta\left[\kappa'^2 + (k'_{z'} - q)^2 - \kappa^2\right] \quad (12)$$

where

$$\cos\varphi^* = \frac{\sin\xi}{\sin\beta}\,, \quad \cos\varphi'^* = \frac{\tan\xi}{\tan\beta}\,, \quad \text{with } \cos\xi \equiv \frac{\kappa'}{\kappa}\,.$$

For pure Bessel states $\kappa' < \kappa$, but m' can be arbitrarily large. As it was found in [10], this is an artefact of taking infinite pure Bessel states. If transverse wave packets are used for the initial state, $|i\rangle_e = \int d\kappa\, f(\kappa)|\kappa, m\rangle$ and $|i\rangle_p = \int d^2\mathbf{p}\, g(\mathbf{p})|PW(\mathbf{p})\rangle$, with weight functions: $f(\kappa)$ peaked at κ_0 with width σ_e, $g(\mathbf{p})$ peaked at zero with width σ_p, then S_{tw} is suppressed for large $|m - m'|$:

$$|m - m'| \lesssim \frac{\kappa_0}{\sigma_p}\,. \quad (13)$$

The m'-distribution is peaked at $m' = m$; therefore, measuring m', we can deduce m. Numerical results confirm this analytic estimate. Due to the sensitivity to the σ_p of the initial beam, this scattering represents a novel beam-size effect, which can be used, for example, to coherently monitor the transverse state of a beam.

5 Conclusions

Orbital angular momentum (OAM) is a new degree of freedom, which can be used in high-energy physics to gain more insight into properties of particles and their interactions.

Electron and photon beams carrying OAM (twisted electrons and photons) have already been realized experimentally, and suggestions exist how to obtain high-energy twisted protons and other particles.

Scattering experiments with particles carrying OAM in the initial state can probe subtler features than the usual plane wave scattering, such as the autocorrelation function of the amplitude. If the OAM of a final twisted particle can be detected (for example, of the final twisted electrons in a twisted version of DIS), even greater insight can be gained with these novel beams.

Acknowledgements

This work was supported by the Belgian Fund F.R.S.-FNRS via the contract of Chargé de recherches, and in part by grants of the Russian Foundation for Basic Research 09-02-00263-a and 11-02-00242-a as well as NSh-3810.2010.2.

References

[1] S. Franke-Arnold, L. Allen, M. Padgett, Laser and Photonics Reviews **2** (2008) 299; A. M. Yao and M. J. Padgett, Advances in Optics and Photonics, **3** (2011) 161.

[2] U. D. Jentschura and V. G. Serbo, Phys. Rev. Lett. **106** (2011) 013001; Eur. Phys. J. **C71** (2011) 1571.

[3] M. Uchida and A. Tonomura, Nature **464** (2010) 737; J. Verbeeck, H. Tian, P. Schlattschneider, Nature **467** (2010) 301; B. J. McMorran et al, Science **331** (2011) 192.

[4] I. P. Ivanov, arXiv:1110:5760 [quant-ph].

[5] I. P. Ivanov, Phys. Rev. **D83** (2011) 093001.

[6] K. Y. Bliokh et al, Phys. Rev. **A82** (2010) 063825.

[7] S. D. Bass, Rev. Mod. Phys. **77** (2005) 1257; F. Myhrer, A. W. Thomas, J. Phys. **G37** (2010) 023101.

[8] E. Leader, Phys. Rev. **D83** (2011) 096012.

[9] L. Allen, M. J. Padgett, M. Babiker, Prog. Opt. **39** (1999) 291.

[10] I. P. Ivanov and V. G. Serbo, Phys. Rev. A **84**, 033804 (2011).

BJORKEN SUM RULES AT FOUR LOOPS

V.L. Khandramai [1 †], R.S. Pasechnik [2], D.V. Shirkov [3], O.V. Teryaev [3], O.P. Solovtsova [1,3]

(1) *ICAS, Gomel State Technical University, 246746 Gomel, Belarus*
(2) *Uppsala University, SE-75121 Uppsala, Sweden*
(3) *Bogoliubov Lab, JINR, 141980 Dubna, Moscow Region, Russia*
† *E-mail: v.khandramai@gmail.com*

Abstract

We study the polarized Bjorken sum rule at low momentum transfers using precise Jefferson Lab (JLab) data with the four-loop expression for the coefficient function $C_{\rm Bj}(\alpha_{\rm s})$ in the framework of the common QCD perturbation theory (PT) and the singularity-free analytic perturbation theory (APT). Our analysis of the PT series for $C_{\rm Bj}$ gives a hint to its asymptotic nature manifesting itself in the region $Q < 1$ GeV. Besides, the related values of the higher twists (HT) coefficients turn out to be highly unstable with respect to the PT order. On the contrary, the APT approach allows us to describe accurately the whole bulk of the JLab data down to $Q \sim 300$ MeV and gives a possibility for reliable extraction of stable values for the HT coefficients providing accuracy of theoretical predictions higher then accuracy of current data.

Recently we have investigated [1] the interplay between higher orders of the PT expansion up to $\alpha_{\rm s}^3$-order and higher-twist contributions using the high-precision JLab data on the lowest moments of the spin-dependent proton and neutron structure functions $\Gamma_1^{p,n}(Q^2)$ and $\Gamma_1^{p-n}(Q^2)$ in the range $0.05 < Q^2 < 3\,{\rm GeV}^2$ [2, 3]. We have demonstrated that in the singularity-free APT the convergence of both the higher orders and HT series is much better and the satisfactory description of the data down to $Q_{min} \sim \Lambda_{\rm QCD} \simeq 350$ MeV can be achieved.

In this report we continue the line of previous investigations and using the fresh four-loop expression for the coefficient function $C_{\rm Bj}(\alpha_{\rm s})$ [4], we explore our analysis of the Bjorken sum rule (BSR) up to $\alpha_{\rm s}^4$-order. In the following we use the total expression for the BSR, $\Gamma_1^{p-n}(Q^2)$, which is a sum of two series in powers of the QCD running coupling $\alpha_{\rm s}$ and in powers of $1/Q^2$:

$$\Gamma_1^{p-n}(Q^2) = \frac{g_A}{6}\left[1 - \Delta_{\rm Bj}(Q^2)\right] + \sum_{i=2}^{\infty} \frac{\mu_{2i}}{Q^{2i-2}}\,, \tag{1}$$

where the standard PT series for $\Delta_{\rm Bj}(Q^2)$ up to the known the four-loop (N^{3}LO) level in the massless case with the number of active quarks $n_f = 3$ can be written as

$$\Delta_{\rm Bj} = 0.3183\,\alpha_{\rm s} \,+\, 0.3631\,\alpha_{\rm s}^2 + \,0.6520\,\alpha_{\rm s}^3 + \,1.804\,\alpha_{\rm s}^4 = \sum_{i\le 4} \delta_i(\alpha_{\rm s})\,. \tag{2}$$

As is know the moments of the structure functions are analytic functions in the complex Q^2-plane with a cut along the negative part of the real axis (see Ref. [5] for details). The

perturbative representation (2) violates these analytic properties due to the unphysical singularities of $\alpha_s(Q^2)$ in the physical region $Q^2 > 0$. To resolve the issue, we apply the APT method [6], which allows one to combine the RG invariance with correct analytical properties of the QCD coupling and observables. At small enough $Q \leq 1 - 2$ GeV the properties of the APT expansion become considerably different from the PT one. At large momentum transfers, all the APT functions $\mathcal{A}_k(Q^2)$ become proportional to the k-th power of the usual perturbative coupling $[\alpha_s(Q^2)]^k$ and the APT expansion for $\Delta_{\rm Bj}(Q^2)$ reduces to the power series (2).

In Fig. 1, we illustrate the behavior of the perturbative part of the BSR in different orders (NLO, N^{2}LO, N^{3}LO) in both the PT and APT approaches. As a normalization point, we take the most accurate α_s-value $\alpha_s(M_Z) = 0.1184 \pm 0.0007$ [7]. For completeness, we also give the combined SLAC and JLab data on $\Gamma_1^{p-n}(Q^2)$ used in our analysis. The SLAC points [8] are denoted by squares, the JLab CLAS Hall A 2002 – by downward pointing triangles, the JLab CLAS Hall B 2003 – by diamonds [3], and the most recent JLab data [2] – by circles. The horizontal dotted line shows the limiting value $\Gamma_1^{p-n}(\infty) = g_A/6$, where the nucleon axial charge $g_A = 1.267 \pm 0.004$ [7].

One sees from Fig. 1 that the APT curves in all three orders practically (at about 1 % accuracy) coincide with each other, so we represent the APT result by a single heavy broken curve. At the same time, the deviation of APT curve from the data clearly shows for necessity of the HT contribution which is also quite stable [1]. The PT four-loop curve describes the data quite well at $Q^2 \geq 0.7$ GeV^2. But, at $Q^2 \leq 0.7$ GeV^2 the four-loop curve describes the data equally bad as the three- and two-loop ones. This is a signal that one has to account for HT contributions, which strongly depend on the PT order used for its extraction [1]. This changes in the APT case where the higher-loop stability is achieved due to the absence of unphysical singularities. To test that, we present in Fig. 2 the relative contributions $N_i(Q^2) = \delta_i(Q^2)/\Delta_{\rm Bj}(Q^2)$ of separate terms in the four-loop expansion in both the PT and APT approaches (see Eq. (2)).

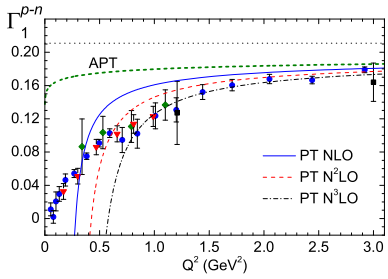

Figure 1: Perturbative part of the BSR as a function of Q^2 in different orders in both the APT and standard PT approaches against the combined set of the Jefferson Lab and SLAC data.

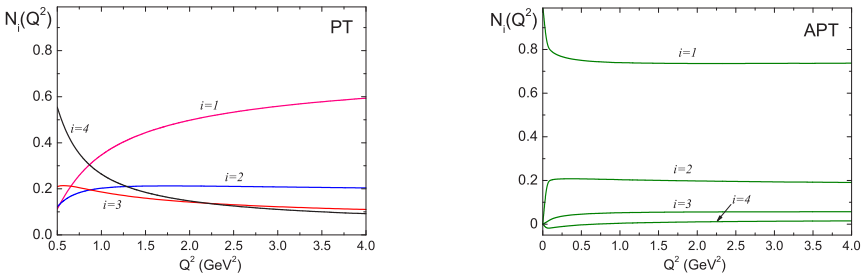

(a) **(b)**

Figure 2: The Q^2-dependence of the relative contributions at the four-loop level in the PT **(a)** and APT **(b)** approach.

Figures 2a and 2b demonstrate the essential difference between the PT and APT cases, namely, the APT expansion converges much better than the PT one. In the APT case, the higher order contributions are stable at all Q^2 values, with the one-loop contribution giving about 70 %, two-loop – 20 %, three-loop – not exceeds 5%, and four-loop – up to 1 %. The four-loop APT term can be important, only if the theoretical accuracy to better than 1 % will be actual.

Using expression (1) fitted to the above mentioned data [2, 3] we can extract the coefficients μ_{2i} of the HT OPE corrections. In Figs. 3a and 3b we present the results of 1- and 3-parametric fits in various orders of PT and APT. The corresponding fit results for HT terms, extracted in different orders of PT and APT, are given in Table 1 (all numerical results are normalized to the corresponding powers of the nucleon mass M). From these

Table 1: Results of HT extraction from the JLab data on the BSR in various orders of PT and all orders of APT with left border Q^2_{min} [GeV^2] of fitting domain.

Method	Q^2_{min}	μ_4/M^2	μ_6/M^4	μ_8/M^6	$\chi^2_{d.f.}$
The best μ_4-fit results					
PT NLO	0.5	−0.028(3)	–	–	0.80
PT N^{2}LO	0.66	−0.014(5)	–	–	0.59
PT N^{3}LO	0.71	0.006(7)	–	–	0.51
APT	0.47	−0.050(2)	–	–	0.82
The best $\mu_{4,6,8}$-fit results					
PT NLO	0.27	−0.026(9)	−0.01(1)	0.008(4)	0.69
PT N^{2}LO	0.34	0.01(2)	−0.06(4)	0.04(2)	0.67
PT N^{3}LO	0.47	0.05(3)	−0.17(9)	0.12(6)	0.46
APT	0.08	−0.061(2)	0.009(1)	−0.0004(1)	0.91

figures and Table follows that APT allows one to move further down to $Q^2 \sim 0.1$ GeV^2 in description of the data [1]. At the same time, in the framework of the standard PT the lower border shifts up to higher Q^2 scales with increasing of the PT expansion order. This is due to the more strong resulting singularities in the higher powers of usual strong coupling. The magnitude of HT ($\mathcal{O}(1/Q^2)$) decreases with an order of PT and becomes compatible to zero at the four-loop level, but the APT application leads to higher loops stability of the HT extraction.

We investigate additionally the sensitivity of the extracted values of the HT term μ_4 to the Λ in various orders of PT. In Fig. 4 we show values of the coefficient μ_4 extracted from

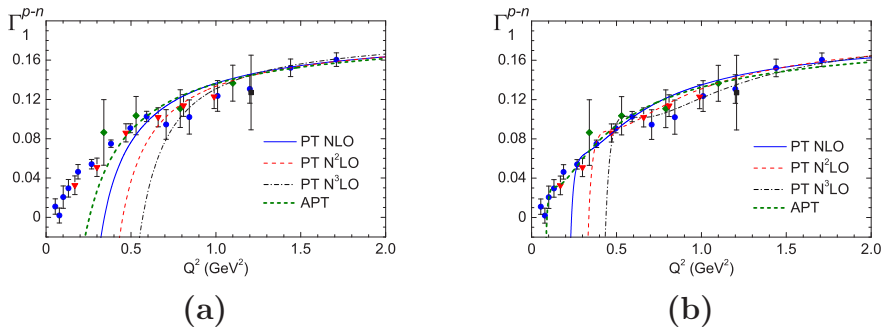

Figure 3: The one-parametric μ_4-fits **(a)** and three-parametric $\mu_{4,6,8}$-fits **(b)** of the BSR JLab data in various orders of the PT and the all-order APT expansions.

the JLab data using two-, three- and four-loop PT at $Q^2_{min} = 0.66$ GeV^2 vs the Λ variation.

In the APT, the sensitivity of μ_4 to the Λ is weak, and it does not depend on the order of the loop expansion. Correspondingly, the values of the HT coefficients turn out to be considerably more precise than those extracted in the PT approach (see also Table 1). The PT does not lead to a stable results. The extracted coefficient μ_4 changes quite strongly between different orders of the PT expansion and it happens in both in absolute value and sign. On the other hand, these data tell us that the absolute value of μ_4 decreases with the order of PT and just at four-loop order becomes compatible to zero. This may be considered as a manifestation of duality between higher orders of PT and HT (see Ref. [9]). Moreover, when PT series reveals the asymptotic behavior (and becomes closer to data), the HT (which may be considered as a contribution completing the PT series) can be reduced to zero.

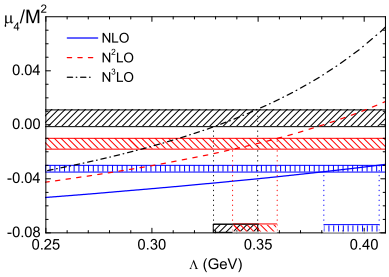

Figure 4: Value of the HT coefficient μ_4 extracted from the JLab data using the PT at different orders at $Q^2_{min} = 0.66$ GeV^2 with error bands. Vertical lines denote the corresponding uncertainty ranges in the Λ value.

Thus, the remarkable properties of the APT approach allows us to describe accurately the whole bulk of the JLab data down to $Q \sim 300$ MeV and gives a possibility for reliable extraction of stable values for the HT coefficients providing accuracy of theoretical predictions higher then accuracy of current data.

This work was partly supported by the Russian presidential grant Scient. School–3810.2010.2, the RFBR grants 09-02-00732, 09-02-01149, 11-01-00182, the BelRFFR-JINR grant F10D-001, and by the Carl Trygger Foundation.

References

[1] R.S. Pasechnik, D.V. Shirkov, O.V. Teryaev, O.P. Solovtsova, V.L. Khandramai, Phys. Rev. **D81** (2010) 016010.

[2] Y. Prok *et al.*, Phys. Lett. **B672** (2009) 12.

[3] R. Fatemi *et al.*, Phys. Rev. Lett. **91** (2003) 222002; M. Amarian *et al.*, Phys. Rev. Lett. **92** (2004) 022301; A. Deur *et al.*, Phys. Rev. Lett. **93** (2004) 212001.

[4] P.A. Baikov, K.G. Chetyrkin, J.H. Kühn, Phys. Rev. Lett. **104** (2010) 132004.

[5] I.L. Solovtsov, Part. Nucl. Lett. **4** [**101**] (2000) 10.

[6] D.V. Shirkov, I.L. Solovtsov, Theor. Math. Phys. **150** (2007) 132.

[7] K. Nakamura *et al.* (Particle Data Group), J. Phys. **G37** (2010) 075021.

[8] K. Abe *et al.*, Phys. Rev. Lett. **79** (1997) 26; P.L. Anthony *et al.*, Phys. Lett. **B493** (2000) 19.

[9] S. Narison, V.I. Zakharov, Phys. Lett. **B679** (2009) 355.

TOP QUARK POLARIZATION AT A POLARIZED LINEAR e^+e^-–COLLIDER

S. Groote [1,2] and J.G. Körner [1 †]

(1) *Institut für Physik, Johannes-Gutenberg-Universität, Mainz, Germany*
(2) *Füüsika Instituut, Tartu Ülikool, Tartu, Estonia*
† *E-mail: koerner@thep.physik.uni-mainz.de*

Abstract

We discuss the polarization of top quarks produced at a polarized linear e^+e^-–collider. Close-to-maximal values of the top quark polarization can be achieved with longitudinal beam polarizations ($h_- \sim -0.80$, $h_+ \sim +0.625$) or ($h_- \sim +0.80$, $h_+ \sim -0.625$) at intermediate beam energies. The option ($h_- \sim -0.80$, $h_+ \sim +0.625$) has to be preferred since this choice is quite stable against variations of the beam polarization. All our quantitative results have been obtained at NLO QCD.

1 Introductory remarks

It is well–known that the top quark keeps its polarization acquired in production when it decays since $\tau_{\rm hadronization} \gg \tau_{\rm decay}$. One can test the Standard Model (SM) and/or non-SM couplings through polarization measurements involving top quark decay (mostly $t \to b + W^+$). New observables involving top quark polarization can be defined such as $< \vec{P} \cdot \vec{p} >$ (see e.g. [1–6]). It is clear that the analyzing power of such observables is largest for large values of the polarization of the top quark $|\vec{P}|$. This calls for large polarization values. It is, nevertheless, desirable to have a control sample with small polarization of the top quark.

In this talk we report on the results of investigations in [7] whose aim was to find maximal and minimal values of top quark polarization at a linear e^+e^-–collider by tuning the longitudinal beam polarization [7]. At the same time one wants to keep the top quark pair production cross–section large. It is a lucky coincidence that all these goals can be realized at the same time.

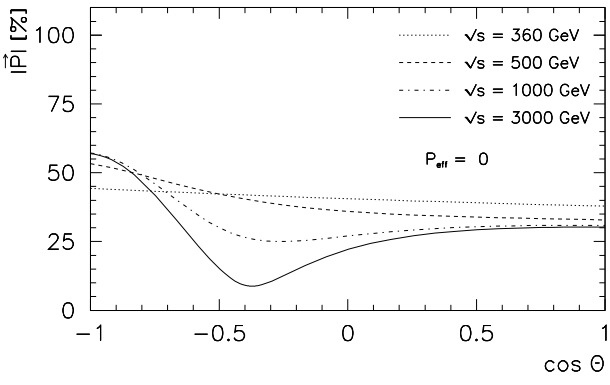

Figure 1: Total NLO top quark polarization for zero beam polarization

Let us remind the reader that the top quark is polarized even for zero beam polarization through vector-axial vector interference effects $\sim v_e a_e$, $v_e a_f$, $v_f a_e$, $v_f a_f$, where

$$v_e, a_e \quad : \quad \text{electron current coupling} \tag{1}$$

$$v_f, a_f \quad : \quad \text{top quark current coupling} \tag{2}$$

In Fig. 1 we plot the $\cos\theta$ dependence of the zero beam polarization top quark polarization for different characteristic energies at $\sqrt{s} = 360$ GeV (close to threshold), $\sqrt{s} = 500$ GeV (ILC phase 1), $\sqrt{s} = 1000$ GeV (ILC phase 2) and $\sqrt{s} = 3000$ GeV (CLIC). We mention that the planning of the ILC has reached a stage where the Technical Design Report (TDR) will be submitted in 2012.

2 Top quark polarization at threshold and in the high energy limit

The polarization of the top quark depends on the c.m. energy $\sqrt{s}$, the scattering angle $\cos\theta$, the electroweak coupling coefficients g_{ij} and the effective beam polarization $P_{\rm eff}$, i.e. one has

$$\vec{P} = \vec{P}\,(\sqrt{s}, \cos\theta, g_{ij}, P_{\rm eff})\,, \tag{3}$$

where the effective beam polarization appearing in (3) is given by

$$P_{\rm eff} = \frac{h_- - h_+}{1 - h_- h_+}\,. \tag{4}$$

and where h_- and h_+ are the longitudinal polarization of the electron and positron beams ($-1 < h_\pm < 1$), respectively.

For general energies the functional dependence Eq.(3) is not simple. Even if the electroweak couplings g_{ij} are fixed one remains with a three–dimensional parameter space $(\sqrt{s}, \cos\theta, P_{\rm eff})$. However, the polarization formula considerable simplifies at nominal threshold $\sqrt{s} = 2m$ and in the high energy limit $\sqrt{s} \to \infty$.

At threshold and at the Born term level one has

$$\vec{P}_{\rm thresh} = \frac{P_{\rm eff} - A_{LR}}{1 - P_{\rm eff} A_{LR}}\ \hat{n}_{e^-}\,, \tag{5}$$

where A_{LR} is the left-right beam polarization asymmetry $(\sigma_{LR} - \sigma_{RL})/(\sigma_{LR} + \sigma_{RL})$ at threshold and $\hat{n}_{e^-}$ is a unit vector pointing into the direction of the electron momentum. We use a notation where $\sigma(LR/RL) = \sigma(h_- = \mp 1; h_+ = \pm 1)$. In terms of the electroweak coupling parameters g_{ij}, the nominal polarization asymmetry at threshold $\sqrt{s} = 2m_t$ is given by $A_{LR} = -(g_{41} + g_{42})/(g_{11} + g_{12}) = 0.409$. Eq.(5) shows that, at threshold and at the Born term level, the polarization $\vec{P}$ is parallel to the beam axis irrespective of the scattering angle and has maximal values $|\vec{P}| = 1$ for $P_{\rm eff} = \pm 1$. Zero polarization is achieved for $P_{\rm eff} = A_{LR} = 0.409$.

In the high energy limit the polarization of the top quark is purely longitudinal, i.e. the polarization points into the direction of the top quark. At the Born term level one finds $\vec{P}(\cos\theta) = P^{(\ell)}(\cos\theta) \cdot \hat{p}_t$ with

$$P^{(\ell)}(\cos\theta) \;=\; \frac{(g_{14} + g_{41} + P_{\rm eff}(g_{11} + g_{44}))(1 + \cos\theta)^2 + (g_{14} - g_{41} - P_{\rm eff}(g_{11} - g_{44}))(1 - \cos\theta)^2}{(g_{11} + g_{44} + P_{\rm eff}(g_{14} + g_{41}))(1 + \cos\theta)^2 + (g_{11} - g_{44} - P_{\rm eff}(g_{14} - g_{41}))(1 - \cos\theta)^2} \tag{6}$$

In the same limit, the electroweak coupling coefficients appearing in (6) take the numerical values $g_{11} = 0.601$, $g_{14} = -0.131$, $g_{41} = -0.201$ and $g_{44} = 0.483$.

It is quite evident that the two limiting cases have quite a different characteristics and different functional behaviour. The question is whether the two limiting cases can be taken as guiding principles for intermediate energies and for which. The answer is yes and no, or sometimes.

Take, for example, the differential $\cos\theta$ rate which is flat at threshold and shows a strong forward peak in the high energy limit with very little dependence on $P_{\rm eff}$. This can be seen by substituting the numerical high energy values of the gauge couplings g_{ij} in the denominator of Eq.(6). One finds

$$\frac{d\Gamma}{d\cos\theta}(s\to\infty) \;\propto\; (1.084-0.332P_{\rm eff})(1+\cos\theta)^2+(0.118-0.007P_{\rm eff})(1-\cos\theta)^2\,. \quad (7)$$

More detailed calculations show that the strong forward dominance of the rate sets in rather fast above threshold [7]. This is quite welcome since the forward region is favoured from the polarization point of view.

As another example take the vanishing of the polarization which, at threshold, occurs at $P_{\rm eff}=0.409$. In the high energy limit, and in the forward region where the numerator part of (6) proportional to $(1+\cos\theta)^2$ dominates, one finds a polarization zero at $P_{\rm eff}=(g_{14}+g_{41})/(g_{11}+g_{44})=0.306$. The two values of $P_{\rm eff}$ do not differ much from another.

3 Effective beam polarization

Let us briefly recall how the effective beam polarization $P_{\rm eff}$ defined in Eq.(4) enters the description of polarized beam effects. Consider the rates σ_{LR} and σ_{RL} for 100% longitudinally polarized beams. The rate $\sigma(beampol)$ for partially polarized beams is then given by (see. e.g. [8])

$$\begin{aligned}\sigma(beampol) &= \frac{1-h_-}{2}\frac{1+h_+}{2}\sigma_{LR}+\frac{1+h_-}{2}\frac{1-h_+}{2}\sigma_{RL}\\ &= \tfrac{1}{4}(1-h_-h_+)\Big(\sigma_{LR}+\sigma_{RL}+P_{\rm eff}(-\sigma_{LR}+\sigma_{RL})\Big). \end{aligned}\quad (8)$$

The rate $\sigma(beampol)$ carries an overall helicity alignment factor $(1-h_-h_+)$ which drops out when one calculates the normalized polarization components of the top quark as in Eqs.(5) and (6). This explains why the polarization depends only on $P_{\rm eff}$ and not separately on h_- and h_+. Note also that there is another smaller rate enhancement factor in (8) for negative values of $P_{\rm eff}$ due to the fact that generally $\sigma_{LR}>\sigma_{RL}$.

Next consider contour plots $P_{\rm eff}=$ const in the (h_-,h_+)–plane as shown in Fig.2. If one wants large production rates one has to keep to Quadrants II and IV in Fig.2 because of the helicity alignment factor $(1-h_-h_+)$ in Eq.(8). Fig.2 shows that near maximal values of $P_{\rm eff}$ can be achieved with non-

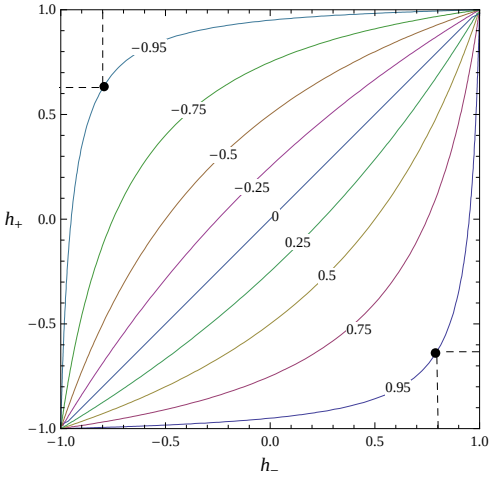

Figure 2: Contour plot in (h_+,h_-)–plane

maximal values of (h_-, h_+). The two examples shown in Fig.2 refer to

$$\begin{aligned} (h_- = -0.80,\, h_+ = +0.625) \qquad & \text{leads to} \quad P_{\text{eff}} = -0.95 \\ (h_- = +0.80,\, h_+ = -0.625) \qquad & \text{leads to} \quad P_{\text{eff}} = +0.95 \end{aligned} \tag{9}$$

These two options are at the technical limits what can be can achieved [9]. In the next section we shall see that the choice $P_{\text{eff}} \sim -0.95$ is to be preferred since the polarization is more stable against small variations of P_{eff}. Furthermore, a negative value of P_{eff} gives yet another enhancement of the rate [7] as also indicated in the denominator of Eq.(5) and in the rate formula (7).

4 Stability of polarization against variations of P_{eff}

Extrapolations of $|\vec{P}|$ away from $P_{\text{eff}} = \pm 1$ are more stable for $P_{\text{eff}} = -1$ than for $P_{\text{eff}} = +1$. Take, for example, the magnitude of the top quark polarization at threshold Eq. (5) and differentiate it w.r.t. P_{eff} at $P_{\text{eff}} = \pm 1$. One finds

$$\frac{d|\vec{P}_{\text{thresh}}|}{dP_{\text{eff}}} = \pm \frac{1 \pm A_{LR}}{1 \mp A_{LR}}. \tag{10}$$

For $P_{\text{eff}} = -1$ one has a slope of $-(1 - A_{LR})/(1 + A_{LR}) = -0.42$ while one has a much larger positive slope of $(1 + A_{LR})/(1 - A_{LR}) = +2.38$ for $P_{\text{eff}} = +1$. This feature persists at higher energies [7].

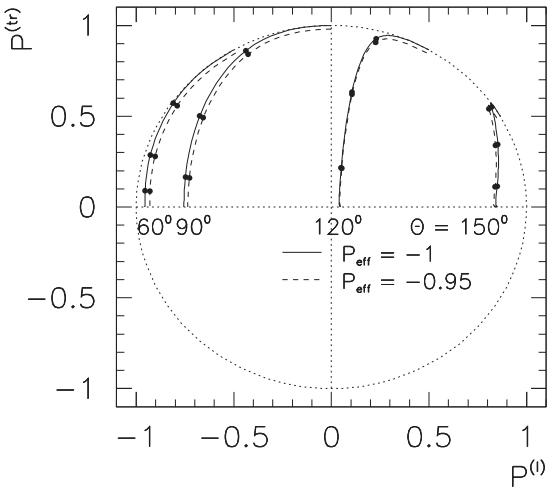

Figure 3: Parametric plot of the orientation and the length of the polarization vector in dependence on the c.m. energy $\sqrt{s}$ for values $\theta = 60°$, $90°$, $120°$, and $150°$ for $P_{\text{eff}} = -1$ (solid lines) and $P_{\text{eff}} = -0.95$ (dashed lines). The three tics on the trajectories stand for $\sqrt{s} = 500\,GeV$, $1000\,GeV$, and $3000\,GeV$.

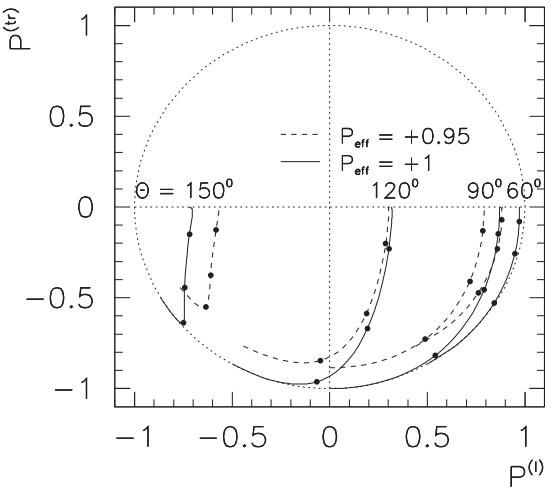

Figure 4: Same as Fig.3 but for $P_{\text{eff}} = +1$ (solid lines) and $P_{\text{eff}} = +0.95$ (dashed lines).

5 Longitudinal and transverse polarization $P^{(\ell)}$ vs. $P^{(tr)}$ for general energies

In Figs. 3 and 4 we plot the longitudinal component $P^{(\ell)}$ and the transverse component $P^{(tr)}$ of the top quark polarization for different scattering angles θ and energies $\sqrt{s}$ starting from threshold up to the high energy limit. $P^{(tr)}$ is the transverse polarization component perpendicular to the momentum of the top quark in the scattering plane. Fig. 3 is drawn for $P_{\rm eff} = (-1, -0.95)$ and Fig. 4 for $P_{\rm eff} = (+1, +0.95)$. The apex of the polarization vector $\vec{P}$ follows a trajectory that starts at $\vec{P} = P_{\rm thresh}(-\cos\theta, \sin\theta)$ and $\vec{P} = P_{\rm thresh}(\cos\theta, -\sin\theta)$ for negative and positive values of $P_{\rm eff}$, respectively, and ends on the line $P^{(tr)} = 0$. The two 60° trajectories for 60° show that large values of the size of the polarization $|\vec{P}|$ close to the maximal value of 1 can be achieved in the forward region for both $P_{\rm eff} \sim \mp 1$ and at all energies. However, the two figures also show that the option $P_{\rm eff} \sim -1$ has to be preferred since the $P_{\rm eff} = -1$ polarization is more stable against variations of $P_{\rm eff}$ whereas the polarization in Fig. 4 has changed considerably when going from $P_{\rm eff} = 1$ to $P_{\rm eff} = 0.95$.

The plots Figs. 3 and 4 are drawn for NLO QCD. At NLO there is also a normal component $P^{(n)}$ generated by the one–loop contribution which, however, is quite small (of $O(3\%)$).

6 Summary

The aim of the investigation in [7] was to maximize and to minimize the polarization vector of the top quark $\vec{P} = \vec{P}\,(P_{\rm eff}, \sqrt{s}, \cos\theta)$ by tuning the beam polarization. Let us summarize our findings.

A. Maximal polarization.

Large values of $\vec{P}$ can be realized for $P_{\rm eff} \sim \pm 1$ at all intermediate energies. This is particularly true in the forward region where the rate is highest. Negative large values for $P_{\rm eff}$ with aligned beam helicities ($h_- h_+$ neg.) are preferred for two reasons. First there is a further gain in rate apart from the helicity alignment factor $(1 - h_- h_+)$ due to the fact that generally $\sigma_{LR} > \sigma_{RL}$ as explained after (8) . Second, the polarization is more stable against variations of $P_{\rm eff}$.

B. Minimal polarization.

Close to zero values of the polarization vector $\vec{P}$ can be achieved for $P_{\rm eff} \sim 0.4$. Again the forward region is favoured. In order to maximize the rate for the small polarization choice take quadrant IV in the (h_-, h_+)–plane.

Acknowledgements: J.G.K. would like to thank X. Artru and E. Christova for discussions and G. Moortgat-Pick for encouragement. We thank B. Melic and S. Prelovsek for their participation in this project. The work of S. G. is supported by the Estonian target financed project No. 0180056s09, by the Estonian Science Foundation under grant No. 8769 and by the Deutsche Forschungsgemeinschaft (DFG) under grant 436 EST 17/1/06.

References

[1] E. Christova and D. Draganov, Phys. Lett. B **434** (1998) 373

[2] M. Fischer, S. Groote, J. G. Körner, M. C. Mauser and B. Lampe, Phys. Lett. B **451** (1999) 406

[3] M. Fischer, S. Groote, J. G. Körner and M. C. Mauser, Phys. Rev. D **65** (2002) 054036

[4] S. Groote, W. S. Huo, A. Kadeer and J. G. Körner, Phys. Rev. D **76** (2007) 014012

[5] J. A. Aguilar-Saavedra and J. Bernabeu, Nucl. Phys. B **840** (2010) 349

[6] J. Drobnak, S. Fajfer and J. F. Kamenik, Phys. Rev. D **82** (2010) 114008

[7] S. Groote, J. G. Körner, B. Melic and S. Prelovsek, Phys. Rev. D **83** (2011) 054018

[8] X. Artru, M. Elchikh, J. -M. Richard, J. Soffer and O. V. Teryaev, Phys. Rept. **470** (2009) 1

[9] G. Alexander, J. Barley, Y. Batygin, S. Berridge, V. Bharadwaj, G. Bower, W. Bugg and F. J. Decker *et al.*, Nucl. Instrum. Meth. A **610** (2009) 451

SPIN PHOTONICS IN THE CLASSICAL AND QUANTUM ELECTRODYNAMICS

V.A. Bordovitsyn†, O.A. Konstantinova††

National Research Tomsk State University, Tomsk, Russia
† *E-mail: vabord@sibmail.com*
†† *E-mail: olgakonst87@mail.ru*

Abstract

Considering the spin properties of elementary particles and the spin precession in an external electromagnetic field we are going to give a systematic exposition of a classical approach to describing the precession of the spin relativistic particles for the different initial conditions and its correspondence with the quantum mechanical calculations.

Introduction

For a long time a misconception that the classical theory of spin does not possible (see p. 277 in [1]) was existed among many of physicists. Such conclusion was done because the quantum theory often leads to various paradoxes that go far beyond the classical theory. Only with the advent of the equation Bargmann-Michel-Telegdi (BMT) [2], it was possible to take into account opened by those time the anomalous magnetic moment, which made it possible to give the accurate semiclassical representation of the spin precession in external fields.

According to the classical theory the spin precession is a rotation of the proper magnetic moment vector of a particle around a certain direction (e.g. the direction of the magnetic field). In terms of the quantum theory this process does not exist, and only spin-flip transitions along two preferred directions are possible. But we can show here that in the semiclassical approximation $\hbar \to 0$ the classical and quantum theories of precession give the totally identity results. This statement is the subject of our investigation.

1 Description of spin precession in the classical and quantum theory

A consistent description of the quantum method of the study of neutron radiation in an external magnetic field can be found in the pioneering work [3] (see also work [4]).

In the classical theory the spin precession of the neutron with magnetic moment $\mu_N = -|\mu| = -1,93\mu_{nucl.} < 0$ in a uniform magnetic field $\boldsymbol{H} = (0, 0, H)$ is described by solution of Bargmann-Michel-Telegdi (BMT) equation [5]

$$\Pi^{\mu\nu} = \Pi_1^{\mu\nu} - \frac{1}{\Omega} q^{[\mu\alpha}\Pi_{\alpha 1}^{\nu]} \sin\Omega\tau - (2\Pi_1^{\mu\nu} + \frac{1}{\Omega^2} q^{[\mu\alpha} q_{\alpha\beta}\Pi_1^{\beta\nu]})(1 - \cos\Omega\tau).$$

Here $\Pi^{\mu\nu}$ is a dimensionless spin tensor with the invariant

$$\frac{1}{2}\Pi_{\mu\nu}\Pi^{\mu\nu} = \frac{1}{2}\Pi_{\mu\nu 1}\Pi_1^{\mu\nu} = 1.$$

Index "1" corresponds to the initial conditions, the square brackets denote an antisymmetrization $a^{[\mu}b^{\nu]} = a^\mu b^\nu - a^\nu b^\mu$, Ω is a neutron spin precession frequency in the units of the proper time τ:

$$\Omega = \frac{2|\mu|H}{\hbar}\sqrt{1-\beta^2 cos^2\alpha} = \omega\gamma, \tag{1}$$

when it moves in accordance with $\boldsymbol{\beta} = \beta(sin\alpha, 0, cos\alpha)$, the tensor $q^{\mu\nu}$ is space-like part of the tensor $h^{\mu\nu} = -2(|\mu|/\hbar)H^{\mu\nu}$.

Description of the spin precession in quantum theory is given by a non-stationary wave function of Dirac-Pauli equation [3], [6]

$$\psi(\boldsymbol{r},t) = A\psi_1(\boldsymbol{r})exp(-i\frac{m_0c^2}{\hbar}\gamma_1 t) + B\psi_{-1}(\boldsymbol{r})exp(-i\frac{m_0c^2}{\hbar}\gamma_{-1}t). \tag{2}$$

Here $\gamma_{\pm 1}$ is a dimensionless gamma-factor with respect to the spin direction, $p^\mu = -i\hbar\partial^\mu$ is an operator of the four-dimensional impulse,$\gamma^\mu = i\rho_3(1, \hat{\boldsymbol{\alpha}})$, $\sigma^{\mu\nu} = (-i\hat{\boldsymbol{\alpha}}, \hat{\boldsymbol{\sigma}})$ - Dirac's matrixes, numeric coefficients A and B ($A^+A + B^+B = 1$) are determined by the initial condition

$$(\hat{\boldsymbol{\Pi}}\boldsymbol{n})\psi(\boldsymbol{r},0) = \lambda\psi(\boldsymbol{r},0). \tag{3}$$

which are given by the projection of the spin operator

$$\hat{\boldsymbol{\Pi}} = m_0c^2\hat{\boldsymbol{\sigma}} + c\rho_2[\hat{\boldsymbol{\sigma}}\hat{\boldsymbol{p}}], \tag{4}$$

on the arbitrary direction $\boldsymbol{n} = (\sin\theta\cos\varphi, \sin\theta\sin\varphi, \cos\theta)$.

2 Analysis of the initial conditions

To take into account the initial conditions required to impose additional conditions on the time-dependent wave function (2). In the calculation of the probability densities of the spin operator we use the definition

$$\langle\hat{Q}(t)\rangle = A^+A\langle\psi_1|\hat{Q}|\psi_1\rangle + A^+B\langle\psi_1|\hat{Q}|\psi_{-1}\rangle\exp\left(i\frac{m_0c}{\hbar}(\gamma_1-\gamma_{-1})t\right) +$$

$$+AB^+\langle\psi_{-1}|\hat{Q}|\psi_1\rangle\exp\left(i\frac{m_0c}{\hbar}(\gamma_{-1}-\gamma_1)t\right) + B^+B\langle\psi_{-1}|\hat{Q}|\psi_{-1}\rangle,$$

or in the easiest form

$$\langle\hat{Q}(t)\rangle = A^+A\langle 1|\hat{Q}|1\rangle + A^+B\langle 1|\hat{Q}|-1\rangle\exp(i\omega t) +$$

$$+AB^+\langle -1|\hat{Q}|1\rangle\exp(-i\omega t) + B^+B\langle -1|\hat{Q}|-1\rangle. \tag{5}$$

Now, let as perform a comprehensive analysis of the initial conditions (3).

1. *Initial spin is directed along the x-axis.* For this special case $\Pi_{1x} = (\Pi_1, 0, 0)$, $\varphi = 0$, $\theta = \pi/2$. The coefficients of normalization and the eigenvalue of the spin operator are the following

$$A = -\frac{1}{\sqrt{2}}\sqrt{1 - \frac{\zeta\gamma\beta^2 \sin\alpha\cos\alpha}{\sqrt{1+\gamma^2\beta^4\sin^2\alpha\cos^2\alpha}}}, \quad B = \frac{1}{\sqrt{2}}\sqrt{1 + \frac{\zeta\gamma\beta^2 \sin\alpha\cos\alpha}{\sqrt{1+\gamma^2\beta^4\sin^2\alpha\cos^2\alpha}}},$$

$$\lambda = \zeta\sqrt{1+\gamma^2\beta^2\cos^2\alpha}.$$

Using the matrix elements from (5) one can obtain the average value of the spin operator

$$\langle\hat{\Pi}_x(t)\rangle = \zeta\frac{\gamma^2\beta^2\cos^2\alpha + \cos\omega t}{\sqrt{(1-\beta^2\cos^2\alpha)(1+\gamma^2\beta^4\sin^2\alpha\cos^2\alpha)}},$$

$$\langle\hat{\Pi}_y(t)\rangle = \zeta\frac{\gamma\sin\omega t}{\sqrt{1+\gamma^2\beta^4\sin^2\alpha\cos^2\alpha}}, \quad \langle\hat{\Pi}_z(t)\rangle = -\zeta\frac{\gamma^2\beta^2\sin\alpha\cos\alpha}{\sqrt{1+\gamma^2\beta^2\cos^2\alpha}}.$$

2. *Initial spin is directed along the y-axis.* Calculating the corresponding values with respect to $\Pi_{1y} = (0, \Pi_1, 0)$, $\varphi = \pi/2$, $\theta = \pi/2$ it is easy to show that

$$A = \frac{i}{\sqrt{2}}, \quad B = \frac{\zeta}{\sqrt{2}}, \quad \lambda = \gamma\zeta,$$

$$\langle\hat{\Pi}_x(t)\rangle = -\zeta\frac{\sin\omega t}{\sqrt{1-\beta^2\cos^2\alpha}}, \quad \langle\hat{\Pi}_y(t)\rangle = \zeta\gamma\cos\omega t, \quad \langle\hat{\Pi}_z(t)\rangle = 0.$$

3. *Spin is directed along the z-axis.* Finally, applying the same procedure to $\Pi_{1z} = (0, 0, \Pi_1)$ and $\theta = 0$ we have two expressions for λ

$$\lambda_1 = \frac{\cos^2\alpha + \gamma^2\sin^2\alpha}{\gamma\sqrt{1-\gamma^2\beta^2\cos^\alpha}}, \quad A \neq 0, \quad B = 0,$$

$$\lambda_2 = -\frac{\cos^2\alpha + \gamma^2\sin^2\alpha}{\gamma\sqrt{1-\gamma^2\beta^2\cos^\alpha}}, \quad A = 0, \quad B \neq 0,$$

$$\langle\hat{\Pi}_x(t)\rangle = -\zeta\frac{\gamma\beta^2\sin\alpha\cos\alpha}{\sqrt{1-\beta^2\cos^2\alpha}}, \quad \langle\hat{\Pi}_y(t)\rangle = 0, \quad \langle\hat{\Pi}_z(t)\rangle = \zeta\gamma\sqrt{1-\beta^2\cos^2\alpha}.$$

It can be shown, that in the second case (spin is directed along the y-axis) all the formulas for $\langle\hat{\Pi}(t)\rangle$ have a total correspondence between the classical and quantum theories. Thus, there is am agreement with the BMT equation's solution, and the frequency of the spin precession corresponds to the quantum spin-flip transition $\zeta \to -\zeta$. It equals to

$$\omega = \frac{m_0c^2}{\hbar}(\gamma_\zeta - \gamma_{-\zeta}) = \zeta^2\frac{2|\mu|H}{\hbar}\sqrt{1-\beta^2\cos^2\alpha},$$

and (1) is also the same.

Conclusion

Thus, we propose here two methods to verify the fact that in our consideration of the results of classical and quantum theories are the same:

1. Direct checking: we can show that, in general, an arbitrary choice of initial conditions, taking into account the quantum structure of the expressions $\langle\hat{\mathbf{\Pi}}\rangle_t$ of the classical equations of spin precession is unchanged. So, it all comes down to the following replacing $\mathbf{\Pi} \to \langle\hat{\mathbf{\Pi}}\rangle_t$

2. Inverse checking by the substitution in solutions of BMT-equation: the substitution of the initial values $\langle\hat{\mathbf{\Pi}}_1\rangle$ of the quantum expressions in the classical solutions $\langle\hat{\mathbf{\Pi}}\rangle_t$ can yield the exactly same expression as in the quantum theory.

In this paper, we give an overview of the current state of theoretical research problem of spin precession of relativistic particles. We also completely examined the role of initial conditions for the spin orientation in the classical and quantum theories, and the total agreement with the correspondence principal of the classical and quantum spin precession was found.

Acknowledgments

The work was partially supported by the Federal Targeted Program "Scientific and scientific - pedagogical personnel of innovative Russia", contract No 02.740.11.0238; No P789.

References

[1] A. A. Sokolov, Yu. M. Loskutov, I. M. Ternov, Quantum mechanics, (Holt, Reinhart, and Winston, New York) 1966.

[2] V. Bargmann, L. Michel, V. L. Telegdi, Phys. Rev. Lett. **2** (1959) 435.

[3] I. M. Ternov, V. G. Bagrov, A. M. Khapaev, JETF **21** (1965) 613.

[4] V. L. Lyuboshits, Yad.Fiz. **4** (1966) 2693.

[5] V. A. Bordovitsyn, in Synchrotron Radiation Theory and it's Development. In Memory of Ternov, ed. by V. A. Bordovitsyn, (World Scientific, Singapore) 1999.

[6] V. A. Bordovitsyn, O. A. Konstantinova, Rus. Phys. J. **53** (2010) 1210.

ON THE SPIN CORRELATIONS OF MUONS AND TAU LEPTONS GENERATED IN THE ANNIHILATION PROCESSES $e^+e^- \to \mu^+\mu^-$, $e^+e^- \to \tau^+\tau^-$

V.L. Lyuboshitz and V.V. Lyuboshitz †

Joint Institute for Nuclear Research,
141980 Dubna, Moscow Region, Russia
† *E-mail: Valery.Lyuboshitz@jinr.ru*

Abstract

Using the technique of helicity amplitudes, the electromagnetic process $e^+e^- \to \mu^+\mu^-$ is theoretically investigated in the one-photon approximation. The structure of the triplet states of the final $(\mu^+\mu^-)$ system is analyzed. It is shown that in the case of unpolarized electron and positron the final muons are also unpolarized, but their spins are strongly correlated. Explicit expressions for the components of the correlation tensor of the final $(\mu^+\mu^-)$ system are derived. The formula for the angular correlation at the decays of final muons μ^+ and μ^-, produced in the process $e^+e^- \to \mu^+\mu^-$, is obtained. It is demonstrated that spin correlations of muons in the process of electron-positron pair annihilation have the purely quantum character, since one of the incoherence inequalities for the correlation tensor components is always violated.

1. In the first non-vanishing approximation over the electromagnetic constant $e^2/\hbar c$, the process of conversion of the electron-positron pair into the muon pair is described by the well-known one-photon Feynman diagram.

Due to the electromagnetic current conservation, the virtual photon with a time-like momentum transfers the angular momentum $J = 1$ and negative parity. Taking into account that the internal parities of muons μ^+ and μ^- are opposite, the $(\mu^+\mu^-)$ pair is generated in the triplet states (the total spin $S = 1$) with the total angular momentum $J = 1$ and with the orbital angular momenta $L = 0$ and $L = 2$, being the superpositions of the states $^3S_1$ and $^3D_1$ with the negative space parity.

The respective helicity amplitudes have the following structure:

$$f_{\Lambda'\Lambda}(\theta, \phi) = R_{\Lambda'\Lambda}(E)\ d^{(1)}_{\Lambda'\Lambda}(\theta)\ \exp(i\Lambda\phi), \tag{1}$$

where θ and ϕ are the polar and azimuthal angles of the flight direction of the positively charged muon (μ^+) in the center-of-mass (c.m.) frame of the considered reaction with respect to the initial positron momentum;
$d^{(1)}_{\Lambda'\Lambda}(\theta)$ are the Wigner functions (elements of the finite rotation matrix) for the angular momentum $J = 1$;
Λ is the difference of helicities of the positron and electron, coinciding with the projection of total spin and with the projection of total angular momentum of the (e^+e^-) pair onto the direction of positron momentum in the c.m. frame (the projection of orbital angular momentum onto the momentum direction equals zero);
Λ' is the difference of helicities of the muons μ^+ and μ^-, coinciding with the projection

of total angular momentum of the $(\mu^+\mu^-)$ pair onto the direction of momentum of the positively charged muon μ^+ in the c.m. frame (see, for example, [1,2]).

Due to the factorizability of the Born amplitude, we can write:

$$R_{\Lambda'\Lambda}(E) = r^{(\mu)}_{\Lambda'}(E)\, r^{(e)}_{\Lambda}(E). \tag{2}$$

Here Λ' and Λ take the values $+1, 0, -1$; in doing so, the parameters $r^{(\mu)}_{\Lambda'}$, $r^{(e)}_{\Lambda}$ depend upon the initial energy E of the positron (electron) in the c.m. frame of the pair e^+e^-, but do not depend upon the angles θ and ϕ.

On account of the space parity conservation in the electromagnetic interactions, we have:

$$r^{(\mu)}_{+1} = r^{(\mu)}_{-1} = r^{(\mu)}_{1}, \quad r^{(e)}_{+1} = r^{(e)}_{-1} = r^{(e)}_{1}. \tag{3}$$

In accordance with the structure of electromagnetic current for the pairs e^+e^- and $\mu^+\mu^-$ in the c.m. frame [1], the following relations are valid:

$$r^{(\mu)}_{0} = \frac{m_\mu}{E} r^{(\mu)}_{1} = \sqrt{1-\beta^2_\mu}\; r^{(\mu)}_{1}, \quad r^{(e)}_{0} = \frac{m_e}{E} r^{(e)}_{1}, \tag{4}$$

where m_μ and m_e are the masses of the muon and electron, respectively, β_μ is the muon velocity in the c.m. frame. Since for the process $e^+e^- \to \mu^+\mu^-$ the inequality $E \geq m_\mu \gg m_e$ is always satisfied, the contribution of electron-positron states with antiparallel spins (equal helicities) can be neglected. In doing so, $R_{\Lambda 0}(E) \approx 0$.

The calculation of the one-photon diagram gives:

$$r^{(\mu)}_{1}(E) = r^{(e)}_{1}(E) = \frac{|e|}{\sqrt{2E}}, \tag{5}$$

where e is the electron charge. If the relativistic invariant

$$s = (p_{e^+} + p_{e^-})^2 = (p_{\mu^+} + p_{\mu^-})^2 = 4E^2$$

is introduced, the expression for the cross section of the process $e^+e^- \to \mu^+\mu^-$ takes the following form [1]:

$$\sigma = \frac{4\pi}{3}\frac{e^2}{s}\left(1 + \frac{2m^2_\mu}{s}\right)\sqrt{1 - \frac{4m^2_\mu}{s}}. \tag{6}$$

Taking into account the explicit formulas for d-functions corresponding to the angular momentum $J = 1$ [1,2], we find the angular distribution of muon emission, normalized by unity, in the c.m. frame :

$$dW_{\mu^+\mu^-} = \frac{3}{16\pi}\frac{1 + \cos^2\theta + (m^2_\mu/E^2)\sin^2\theta}{1 + (m^2_\mu/2E^2)} d\,\Omega = \frac{3}{8\pi}\frac{2 - \beta^2_\mu \sin^2\theta}{3 - \beta^2_\mu} d\,\Omega, \tag{7}$$

where $d\,\Omega$ is the element of solid angle.

2. Taking into account the relations (1) -(4) for the helicity amplitudes, it is clear that if the positron and electron are totally polarized along the positron momentum in the c.m. frame, then the $(\mu^+\mu^-)$ system is produced in the triplet state of the following form:

$$|\Psi\rangle^{(+1)} = \frac{\sqrt{2}}{\sqrt{2 - \beta^2_\mu \sin^2\theta}}\left(\frac{1+\cos\theta}{2}|+1\rangle - \sqrt{1-\beta^2_\mu}\,\frac{\sin\theta}{\sqrt{2}}|\,0\,\rangle + \frac{1-\cos\theta}{2}|-1\rangle\right). \tag{8}$$

Here $\beta_\mu = \sqrt{1-(m_\mu^2/E^2)}$ is the velocity of each of the muons, as before;

$$|+1\rangle = |+1/2\rangle^{(\mu^+)} \otimes |+1/2\rangle^{(\mu^-)}, \quad |-1\rangle = |-1/2\rangle^{(\mu^+)} \otimes |-1/2\rangle^{(\mu^-)},$$

$$|0\rangle = \frac{1}{\sqrt{2}}\Big(|+1/2\rangle^{(\mu^+)} \otimes |-1/2\rangle^{(\mu^-)} + |-1/2\rangle^{(\mu^+)} \otimes |+1/2\rangle^{(\mu^-)}\Big)$$

are the states with the projection of total spin of the $(\mu^+\mu^-)$ pair onto the direction of momentum of the muon μ^+ in the c.m. frame of the reaction $e^+e^- \to \mu^+\mu^-$, equaling $+1$, -1 and 0, respectively.

Let us note that the real values of the coefficients of superposition of the triplet states $|+1\rangle$, $|0\rangle$ and $|-1\rangle$ in the state $|\Psi\rangle^{(+1)}$ (8) correspond to the choice of the quantization axes z' and z along the positron momentum and μ^+ momentum, respectively, in the c.m. frame of the reaction $e^+e^- \to \mu^+\mu^-$, and the axis y - along the normal to the plane of this reaction.

If the positron and electron are totally polarized in the direction being antiparallel to the positron momentum, then the $(\mu^+\mu^-)$ pair is generated in the following triplet state:

$$|\Psi\rangle^{(-1)} = \frac{\sqrt{2}}{\sqrt{2-\beta_\mu^2\sin^2\theta}}\left(\frac{1-\cos\theta}{2}|+1\rangle + \sqrt{1-\beta_\mu^2}\,\frac{\sin\theta}{\sqrt{2}}|0\rangle + \frac{1+\cos\theta}{2}|-1\rangle\right). \quad (9)$$

3. If the positron and electron are not polarized, then, since $r^{(e)} \approx 0$, the final state of the $(\mu^+\mu^-)$ pair represents a noncoherent mixture of spin states $|\Psi\rangle^{(+1)}$ and $|\Psi\rangle^{-1}$, each of them being realized with the relative probability of 1/2. Taking into account Eqs. (8) and (9), we can find the elements of the spin density matrix of the $(\mu^+\mu^-)$ system in the representation of triplet states $|+1\rangle$, $|0\rangle$ and $|-1\rangle$ [3].

The spin states of two particles with spin 1/2 are characterized by the polarization vectors $\boldsymbol{\zeta}_1 = \langle\hat{\boldsymbol{\sigma}}^{(1)}\rangle$, $\boldsymbol{\zeta}_2 = \langle\hat{\boldsymbol{\sigma}}^{(2)}\rangle$ and the components of the correlation tensor $T_{ik} = \langle\hat{\sigma}_i^{(1)} \otimes \hat{\sigma}_k^{(2)}\rangle$. Here $\hat{\boldsymbol{\sigma}} = \{\hat{\sigma}_x, \hat{\sigma}_y, \hat{\sigma}_z\}$ is the vector Pauli operator, $\hat{\sigma}_i$, $\hat{\sigma}_k$ are the Pauli matrices, $i,k \to \{1,2,3\} \to \{x,y,z\}$; the axis z is directed along the momentum of the positively charged muon μ^+ in the c.m. frame of the considered reaction, and the axis y is directed along the normal to the reaction plane; the symbol $\langle ...\rangle$ denotes the averaging over the quantum ensemble. If both the particles are not polarized and the correlations are absent, then $T_{ik} = 0$. For two independent particles with the polarization vectors $\boldsymbol{\zeta}_1$ and $\boldsymbol{\zeta}_2$ the correlation tensor is factorized : $T_{ik} = \zeta_i\,\zeta_k$.

It is easy to see that, at the annihilation $e^+e^- \to \mu^+\mu^-$ of the unpolarized positron and electron, the produced muons μ^+ and μ^- are unpolarized ($\boldsymbol{\zeta}_{\mu^+} = \boldsymbol{\zeta}_{\mu^-} = 0$), but their spins are correlated: the correlation tensor components have the following form (see also [5]):

$$T_{xx}^{(\mu^+\mu^-)} = \frac{(2-\beta_\mu^2)\sin^2\theta}{2-\beta_\mu^2\sin^2\theta}, \quad T_{yy}^{(\mu^+\mu^-)} = -\frac{\beta_\mu^2\sin^2\theta}{2-\beta_\mu^2\sin^2\theta}, \quad T_{zz}^{(\mu^+\mu^-)} = \frac{2\cos^2\theta+\beta_\mu^2\sin^2\theta}{2-\beta_\mu^2\sin^2\theta},$$

$$T_{xz}^{(\mu^+\mu^-)} = -\frac{(1-\beta_\mu^2)^{1/2}\sin 2\theta}{2-\beta_\mu^2\sin^2\theta}, \quad T_{xy}^{(\mu^+\mu^-)} = T_{yz}^{(\mu^+\mu^-)} = 0. \quad (10)$$

The "trace" of the correlation tensor of the $(\mu^+\mu^-)$ pair is:

$$T^{(\mu^+\mu^-)} = \langle \hat{\boldsymbol{\sigma}}_{\mu^+} \otimes \hat{\boldsymbol{\sigma}}_{\mu^-} \rangle = T_{xx}^{(\mu^+\mu^-)} + T_{yy}^{(\mu^+\mu^-)} + T_{zz}^{(\mu^+\mu^-)} = 1, \tag{11}$$

just as it should hold for any triplet state [1)].

4. The "trace" of the correlation tensor T determines the angular correlation between flight directions for the products of decay of two unstable particles with spin 1/2 in the case when space parity is not conserved [4-8].

Actually, the angular distribution at the decay of any polarized unstable particle with spin 1/2 under space parity nonconservation, normalized by unity, has the form (see, for example, [9]):

$$d\,W = \frac{1}{4\pi}(1 + \alpha\,\boldsymbol{\zeta}\,\mathbf{n})d\,\Omega_{\mathbf{n}},$$

where $\boldsymbol{\zeta}$ is the polarization vector of the unstable particle, α is the angular asymmetry coefficient, $\mathbf{n}$ is the unit vector along the momentum of the particle, formed in the decay, in the rest frame of the decaying unstable particle.

Then the double distribution for the flight directions of the decay products of two unstable particles under space parity nonconservation, normalized by unity, is as follows [4,5]:

$$d^2W = \frac{1}{16\pi^2}\,(1 + \alpha_1\,\boldsymbol{\zeta_1}\,\mathbf{n_1} + \alpha_2\,\boldsymbol{\zeta_2}\,\mathbf{n_2} + \alpha_1\alpha_2 \sum_{i=1}^{3}\sum_{k=1}^{3} T_{ik}\,n_{1,i}\,n_{2,k})d\,\Omega_{\mathbf{n}_1}\,d\,\Omega_{\mathbf{n}_2}. \tag{12}$$

Here $\boldsymbol{\zeta_1}$ and $\boldsymbol{\zeta_2}$ are the polarization vectors of the first and second unstable particle, α_1 and α_2 are the coefficients of angular asymmetry for the decays of the first and second particle; $\mathbf{n}_1$ and $\mathbf{n}_2$ are unit vectors defined in the rest frames of the first and second unstable particle, respectively, and specified with respect to a unified system of spatial coordinate axes [7, 8]; just as before, $i, k \to \{1, 2, 3\} \to \{x, y, z\}$.

Using the method of moments, the components of the polarization vectors and correlation tensor can be found as a result of averaging the corresponding combinations of trigonometric functions of angles over the double distribution of decay directions [4,5].

The integration of the double distribution of flight directions over all angles, except the angle δ between the vectors $\mathbf{n}_1$ and $\mathbf{n}_2$, leads to the following formula for the angular correlation [4,5]:

$$dW = \frac{1}{2}\left(1 + \frac{\alpha_1\alpha_2 T}{3}\cos\delta\right) d(-\cos\delta); \quad \cos\delta = \mathbf{n}_1\mathbf{n}_2. \tag{13}$$

Let us apply Eq. (13) to the decays of the muons μ^+ and μ^- produced in the process of electron-positron pair annihilation $e^+e^- \to \mu^+\mu^-$. According to Eq. (11), in this case the "trace" of the correlation tensor of the muon pair is equal to unity ($T = 1$). It is known that the asymmetry coefficient in the angular distribution of electrons at the decay of the polarized negatively charged muon $\mu^- \to e^-\nu_\mu\bar{\nu}_e$, integrated over the electron energy spectrum, equals $-1/3$ ($\alpha_1 = -1/3$) [9]. Due to the CP invariance, the asymmetry

[1)] For the singlet state $T = -3$; in the general case, $T = \rho_t - 3\rho_s$, where ρ_t and ρ_s are the fractions of the triplet and singlet state, respectively [4-6].

coefficient in the angular distribution of positrons at the decay of the polarized positively charged muon $\mu^+ \to e^+\bar{\nu}_\mu\nu_e$, integrated over the positron energy spectrum, amounts to $+1/3$ ($\alpha_2 = +1/3$). As a result, we obtain the following formula for the angular correlation at the decays $\mu^- \to e^-\nu_\mu\bar{\nu}_e$ and $\mu^+ \to e^+\bar{\nu}_\mu\nu_e$:

$$dW^{(\mu^+\mu^-)} = \frac{1}{2}\left(1 - \frac{1}{27}\cos\delta\right) d(-\cos\delta). \tag{14}$$

5. Previously it was shown in the papers [4,5] that in the case of incoherent mixtures of factorizable states of two particles with spin 1/2 the modulus of the sum of any two (and three) diagonal components of the correlation tensor cannot exceed unity, i.e. the following inequalities are satisfied:

$$|T_{xx} + T_{yy}| \leq 1, \quad |T_{xx} + T_{zz}| \leq 1, \quad |T_{yy} + T_{zz}| \leq 1, \quad |T| = |T_{xx} + T_{yy} + T_{zz}| \leq 1.$$

However, for nonfactorizable (entangled) states some of these inequalities may be violated.

In the process of annihilation of the unpolarized positron and electron $e^+e^- \to \mu^+\mu^-$, the muon pair is produced in the nonfactorizable two-particle quantum states $|\Psi\rangle^{(+1)}$ and $|\Psi\rangle^{(-1)}$ (see Eqs. (8) and (9)). In so doing, one of the incoherence inequalities is violated: indeed, using Eqs. (10), we obtain at the angle $\theta \neq 0$:

$$T_{xx}^{(\mu^+\mu^-)} + T_{zz}^{(\mu^+\mu^-)} = 1 - T_{yy}^{(\mu^+\mu^-)} = \frac{2}{2 - \beta_\mu^2 \sin^2\theta} > 1. \tag{15}$$

Our consideration relates, of course, also to the process $e^+e^- \to \tau^+\tau^-$, with the replacements $m_\mu \to m_\tau$, $\beta_\mu \to \beta_\tau$.

6. At very high energies the annihilation processes $e^+e^- \to \mu^+\mu^-$, $e^+e^- \to \tau^+\tau^-$ are conditioned not only by the electromagnetic interaction through the virtual photon, but also by the weak interaction of neutral currents through the Z^0 boson [9].

The interference of amplitudes of the purely electromagnetic and weak interaction leads to the charge asymmetry in lepton emission and to the effects of space parity violation. In the framework of the standard model of electroweak interaction, at the electron-positron pair annihilation the pairs $\mu^+\mu^-$, $\tau^+\tau^-$ are produced in the states $^3S_1$, $^3D_1$ with the negative space parity and, due to the weak interaction, also in the state $^3P_1$ with the positive space parity. In doing so, the total angular momentum is $J = 1$ and CP parity of the pairs is positive.

If the weak interaction contribution is neglected, then the lepton pairs, generated at the annihilation of the unpolarized positron and electron, are correlated but unpolarized. Analysis shows that, due to the weak interaction through the exchange by the virtual Z^0 boson with the nonconservation of space parity, the final leptons acquire the longitudinal polarization. Since the lepton pairs are produced in the triplet states, the polarization vectors of the positively and negatively charged leptons are the same, and their average helicities $\lambda_+ = -\lambda_-$ have different signs in consequence of the opposite directions of momenta in the c.m. frame [3].

The structure of the correlation tensor of the final leptons is, on the whole, similar to that for the case of purely electromagnetic annihilation at very high energies ($\beta_\mu \to 1$,

$\beta_\tau \to 1$). In doing so, the nonzero components of the correlation tensor are: $T_{zz} = 1$, $T_{xx} = -T_{yy}$, as before. Again one of the incoherence inequalities for the correlation tensor components is violated: $T_{xx} + T_{zz} > 1$ (see [3]).

Thus, the consequences of the quantum-mechanical coherence for two-particle quantum systems with nonfactorizable internal states manifest themselves distinctly in spin correlations of lepton pairs produced in the annihilation processes $e^+e^- \to \mu^+\mu^-$, $e^+e^- \to \tau^+\tau^-$, and they can be verified experimentally.

References

[1] V.B. Berestetsky, E.M. Lifshitz and L.P. Pitaevsky, *Kvantovaya Elektrodynamika (Quantum Electrodynamics)* (Moscow, Nauka, 1989), pp. 68, 69, 81.

[2] A.M. Baldin, V.I. Gol'dansky, V.M. Maksimenko and I.L. Rosental', *Kinematika Yadernykh Reakcij (Kinematics of Nuclear Reactions)* (Moscow, Atomizdat, 1968), part II, p. 11.

[3] V.L. Lyuboshitz and V.V. Lyuboshitz, Yad. Fiz. **72** (2009) 340 [Phys. At. Nucl. **72** (2009) 311].

[4] V.L. Lyuboshitz, Proc. XXXIV Winter School of PNPI "Physics of Atomic Nuclei and Elementary Particles" (St. Petersburg, 2000), p.402.

[5] R. Lednicky and V.L. Lyuboshitz, Phys. Lett. **B 508** (2001) 146.

[6] G. Alexander and H.J. Lipkin, Phys. Lett. **B 352** (1995) 162.

[7] R. Lednicky, V.V. Lyuboshitz and V.L. Lyuboshitz, Yad. Fiz. **66** (2003) 1007 [Phys. At. Nucl. **66** (2003) 975].

[8] R. Lednicky, V.L. Lyuboshitz and V.V. Lyuboshitz, Czech. J. Phys. (Suppl. B) **54** (2004) B43.

[9] L.B. Okun, *Leptony i kwarki (Leptons and Quarks)* (Moscow, Nauka, 1990), pp. 3, 8, 22.

HELICITY AND INVARIANT AMPLITUDES FOR EXCLUSIVE VECTOR-MESON ELECTROPRODUCTION

S.I. Manayenkov

B.P. Konstantinov Petersburg Nuclear Physics Institute
† *E-mail: sman@pnpi.spb.ru*

Abstract

Relations between invariant and helicity amplitudes for exclusive vector-meson electroproduction on spinless nuclei and nucleons are established. It is shown that the proposed choice of the kinematic tensors guarantees the absence of singularities of the invariant amplitudes in the kinematic region of the vector-meson production. The obtained relations between invariant and helicity amplitudes are compared with those presented by Fraas and Schildknecht for scalar targets. The asymptotic behaviour at small photon virtuality, transverse momentum transferred to the nucleon, and the vector meson mass is considered. Certain ratios of the invariant amplitudes of the ρ^0-meson production are obtained from the HERMES data.

1. Introduction. Recent interest to the exclusive vector-meson production in deep-inelastic scattering (DIS) of leptons on nucleons and nuclei is caused by a possibility to extract the Generalized Parton Distributions (GPDs) [1–3] which give a wealth of information on the nucleon structure (see, for instance, review [4]). But the factorization theorem [5] is proven not for all amplitudes of the process under discussion. Hence we have to extract all the amplitudes directly from the experimental data to obtain GPDs from those for which the factorization theorem is proven. The direct extraction of the amplitude ratios from the data on the vector-meson electroproduction in DIS was first performed by the H1 and HERMES collaborations [6, 7]. The extraction of the amplitudes permits to distinguish between the production of final particles through intermediate vector-mesons (resonance process) from the direct electroproduction of final particles (background process). This is hardly possible in the usually used extraction method of the spin-density matrix elements proposed in the pioneer work [8].

2. Vector-Meson Production on Spinless Nucleus. In the one-photon-exchange approximation, all the observables in electroproduction can be expressed through the helicity amplitudes $\mathrm{F}_{\lambda_\mathrm{V}\lambda_2\lambda_\gamma\lambda_1}$ of the process

$$\gamma^*(\lambda_\gamma) + T(\lambda_1) \to V(\lambda_V) + T'(\lambda_2) \tag{1}$$

where the helicities of the virtual photon (γ^*), vector meson (V), initial (T) and final (T') target nucleus are given in parentheses in (1). If the nucleus spin is zero the helicity indexes λ_1 and λ_2 will be canceled in the amplitudes. For production on the nucleon, we shall replace $T \to N$, $T' \to N'$ in all formulas.

The helicity amplitudes $\mathrm{T}_{\lambda_\mathrm{V}\lambda_\gamma}$ for the production on targets with zero spin can be expressed through five invariant amplitudes F_n, $n = 1, .., 5$ by the formulas [9]

$$\mathrm{T}_{\lambda_\mathrm{V}\lambda_\gamma} = \varepsilon^{*\mu}(\lambda_\mathrm{V})\mathcal{T}_{\mu\tau}\mathrm{e}^{\tau}(\lambda_\gamma), \tag{2}$$

$$\mathcal{T}_{\mu\tau} = -F_1(h_3)_\mu(g_0)_\tau - \frac{F_2}{\sqrt{2}}(h_3)_\mu(g_1)_\tau + \frac{F_3}{\sqrt{2}}(g_1)_\mu(g_0)_\tau - F_4 S_{\mu\tau} + F_5 A_{\mu\tau} \tag{3}$$

where $e^{\tau}(\lambda_\gamma)$ denotes the virtual-photon polarization vector while $\varepsilon^{*\mu}(\lambda_V)$ is the complex-conjugate polarization vector of the vector meson; λ_γ and λ_V equal to ± 1 correspond to the transverse polarization while λ_γ and λ_V equal to zero describe the longitudinal polarization. The symmetric $S_{\mu\tau}$ and anti-symmetric $A_{\mu\tau}$ kinematic tensors in (3) are

$$S_{\mu\tau} = (g_1)_\mu(g_1)_\tau + (g_2)_\mu(g_2)_\tau = (g_0)_\mu(g_0)_\tau - (g_3)_\mu(g_3)_\tau - g_{\mu\tau}, \tag{4}$$

$$A_{\mu\tau} = -(g_1)_\mu(g_1)_\tau + (g_2)_\mu(g_2)_\tau. \tag{5}$$

The unit four-vectors in $(3) - (5)$ are expressed through the four-momenta of the photon q, vector meson v, initial p_1 and final p_2 nucleus, $p = (p_1 + p_2)/2$ and pseudo-vector $d_\mu = \epsilon_{\mu\nu\theta\kappa}q^\nu v^\theta p^\kappa$ where $\epsilon_{\mu\nu\theta\kappa}$ is the totally anti-symmetric tensor by Levi-Civita ($\epsilon^{0123} = 1$)

$$h_3 = \frac{qm_v^2 - v(qv)}{zm_v}, \;\; g_0 = \frac{Q^2 v + (qv)q}{Qz}, \; g_2 = \frac{d}{v_t M_T\sqrt{\nu^2 + Q^2}}, \; g_3 = \frac{q}{Q}, \tag{6}$$

$$g_1 = \frac{[\nu M_T - (m_v^2 + Q^2 - t)/4][v(m_v^2 + Q^2 - t)/2 - q(m_v^2 + Q^2 + t)/2] - pz^2}{M_T z v_t\sqrt{\nu^2 + Q^2}}, \tag{7}$$

where M_T (m_v) is the target nucleus (vector-meson) mass, $\nu = (qp_1)/M_T$, $Q^2 = -q^2$, $W^2 = 2M_T\nu + M_T^2 - Q^2$, $t = (p_1 - p_2)^2$, $z^2 = (qv)^2 + Q^2 m_v^2$, v_t is the transverse part of the vector-meson three-momentum in the $\gamma^* T$ center-of-mass (CM) system.

Let us define a Lorentz system of frame called below the Collinear System (CS) where the three-momenta of the virtual photon and vector meson are collinear and their energies are equal to each other. We have from $(2) - (7)$ in the CS system [9]

$$\mathrm{T}_{00} = \mathrm{F}_1, \; \mathrm{T}_{11} = \mathrm{F}_4, \; \mathrm{T}_{01} = \mathrm{F}_2, \; \mathrm{T}_{10} = \mathrm{F}_3, \; \mathrm{T}_{1-1} = \mathrm{F}_5. \tag{8}$$

Since the transverse $d\sigma_T/dt \propto |\mathrm{T}_{11}|^2 + |\mathrm{T}_{01}|^2 + |\mathrm{T}_{1-1}|^2$ and longitudinal $d\sigma_L/dt \propto |\mathrm{T}_{00}|^2 + 2|\mathrm{T}_{10}|^2$ cross sections cannot be infinite formulas (8) show that all the invariant amplitudes are finite in the kinematic region of reaction (1). The invariant amplitudes $F_1^{(FS)}, ..., F_5^{(FS)}$ introduced by Fraas and Schildknecht (FS) in Ref. [10] can be expressed in terms of $F_1, ..., F_5$ defined by equations $(2) - (7)$. As shown in [9] the coefficients of these relations contain the scalar product (qv) in the denominator which is zero at $Q^2 = m_v^2 - t$. We conclude that the FS invariant amplitudes contain non-physical poles in the kinematic region of reaction (1). Therefore they are inconvenient for fitting the experimental data.

If the tensor $\mathcal{T}_{\mu\nu}$ is non-singular and single-valued, then the helicity amplitudes are non-singular and single-valued functions of the kinematic variables. But at $Q \to 0$ the components of the four-vector g_0 become infinite according to (6). To avoid singularities at $Q \to 0$ in expression (3), the amplitudes F_1 and F_3 which are multiplied by g_0 should go to zero at least as Q. Remembering (8) we see that $\mathrm{T}_{00} \to 0$, $\mathrm{T}_{10} \to 0$ at $Q \to 0$. These relations are very natural since the virtual photon at $Q \to 0$ becomes real which

has no longitudinal polarization ($\lambda_\gamma \neq 0$). Using representation (4) of $S_{\mu\tau}$ in terms of g_1 and g_2 we see that $S_{\mu\tau}$ is regular at $Q \to 0$. Hence F_4 may go to a non-zero constant when $Q \to 0$. The same is true for the amplitudes F_2 and F_5. Since the components of the four-vectors g_1 and g_2 are proportional to $1/v_t$ at $v_t \to 0$ we conclude in the analogous way that $\mathrm{T}_{01} \propto \mathrm{v_t}$, $\mathrm{T}_{10} \propto \mathrm{v_t}$, $\mathrm{T}_{1-1} \propto \mathrm{v_T^2}$ while T_{00} and $\mathrm{T}_{11} \propto (\mathrm{v_t})^0$. Indeed, using representation (4) for $S_{\mu\tau}$ in terms of g_0 and g_3 we see that $S_{\mu\tau}$ has no singularity at $v_t \to 0$. Hence F_4 has not to go to zero at $v_t \to 0$. The product $h_3 g_0$ is also finite at $v_t \to 0$ which permits F_1 to be non-zero at $v_t \to 0$. The above discussed behaviour at $v_t \to 0$ means the existence of the hierarchy of amplitudes at small v_t: $\mathrm{T}_{00} \sim \mathrm{T}_{11} \gg \mathrm{T}_{01} \sim \mathrm{T}_{10} \gg \mathrm{T}_{1-1}$ which was confirmed experimentally in Ref. [7] at the CM energy $W \approx 5$ GeV and $v_t^2 \leq 0.4$ GeV^2. Since h_3 behaves as $1/m_v$ at $m_v \to 0$ according to (6) the amplitude F_1 multiplied by h_3 in (3) has to be proportional to m_v at small m_v.

3. Vector-Meson Production on Nucleon. The relation between invariant and helicity amplitudes is described by the formula

$$\mathrm{F}_{\lambda_\mathrm{V}\lambda_2\lambda_\gamma\lambda_1} = \varepsilon^{*\mu}(\lambda_\mathrm{V})\bar{\mathrm{u}}_2(\mathrm{p}_2,\lambda_2)\hat{\mathcal{T}}_{\mu\tau}\mathrm{u}_1(\mathrm{p}_1,\lambda_1)\mathrm{e}^\tau(\lambda_\gamma) \tag{9}$$

where the Dirac bispinor $u_1(p_1,\lambda_1)$ and the Dirac-conjugate bispinor $\bar{u}_2(p_2,\lambda_2)$ describe the initial and final nucleon, respectively. Any amplitude $\mathrm{F}_{\lambda_\mathrm{V}\lambda_2\lambda_\gamma\lambda_1}$ can be decomposed into the sum of the Natural Parity Exchange (NPE) amplitude $\mathrm{T}_{\lambda_\mathrm{V}\lambda_2\lambda_\gamma\lambda_1}$ and the Unnatural Parity Exchange (UPE) amplitude $\mathrm{U}_{\lambda_\mathrm{V}\lambda_2\lambda_\gamma\lambda_1}$ [8]. The tensor $\hat{\mathcal{T}}_{\mu\tau}$ can also be represented with the sum of the NPE ($\hat{\mathcal{N}}_{\mu\tau}$) and UPE ($\hat{\mathcal{U}}_{\mu\tau}$) parts [9]

$$\mathrm{F}_{\lambda_\mathrm{V}\lambda_2\lambda_\gamma\lambda_1} = \mathrm{T}_{\lambda_\mathrm{V}\lambda_2\lambda_\gamma\lambda_1} + \mathrm{U}_{\lambda_\mathrm{V}\lambda_2\lambda_\gamma\lambda_1}, \;\; \hat{\mathcal{T}}_{\mu\tau} = \hat{\mathcal{N}}_{\mu\tau} + \hat{\mathcal{U}}_{\mu\tau}. \tag{10}$$

The NPE and UPE tensors can also be decomposed into the sum of two terms [9]

$$\hat{\mathcal{N}}_{\mu\tau} = \mathcal{N}^{(1)}_{\mu\tau} I + \mathcal{N}^{(2)}_{\mu\tau}\gamma_5\hat{g}_2, \;\; \hat{\mathcal{U}}_{\mu\tau} = \mathcal{U}^{(1)}_{\mu\tau}\gamma_5 + \mathcal{U}^{(2)}_{\mu\tau}\hat{g}_2 \tag{11}$$

where γ_τ, $\tau = 0,\ 1,\ 2,\ 3$ and γ_5 are the Dirac matrices and $\hat{g}_2 \equiv (g_2)^\tau\gamma_\tau$ where the unit four-vector g_2 is defined in (6). The representation of $\mathcal{N}^{(j)}_{\mu\tau}$ for $j = 1$ or 2 with using the tensors $S_{\mu\tau}$ and $A_{\mu\tau}$ and the unit vectors defined by (4)-(7) generalizes equation (3)

$$\mathcal{N}^{(j)}_{\mu\tau} = -F^{(j)}_1(h_3)_\mu(g_0)_\tau - \frac{F^{(j)}_2}{\sqrt{2}}(h_3)_\mu(g_1)_\tau + \frac{F^{(j)}_3}{\sqrt{2}}(g_1)_\mu(g_0)_\tau - F^{(j)}_4 S_{\mu\tau} + F^{(j)}_5 A_{\mu\tau} \tag{12}$$

and contains five invariant amplitudes $F^{(j)}_n$, $n = 1,\ ...,\ 5$ for any j. Therefore the total number of the NPE invariant amplitudes and hence the linearly independent NPE helicity amplitudes is ten. The representation of $\mathcal{U}^{(j)}_{\mu\tau}$ for $j = 1,\ 2$ looks like

$$\mathcal{U}^{(j)}_{\mu\tau} = G^{(j)}_1(h_3)_\mu(g_2)_\tau + G^{(j)}_2\frac{(g_1)_\mu(g_2)_\tau + (g_2)_\mu(g_1)_\tau}{2} + G^{(j)}_3(g_2)_\mu(g_0)_\tau + G^{(j)}_4\frac{\epsilon_{\mu\tau\alpha\beta}q^\alpha v^\beta}{z\sqrt{2}}. \tag{13}$$

As obvious from (13) the total number of the UPE invariant amplitudes (linearly independent UPE helicity amplitudes) is equal to eight.

The asymptotic behaviour of $F_n^{(1)}$ at small Q, v_t, and m_v is the same as for the spinless targets. Since $\mathcal{N}_{\mu\tau}^{(2)}$ is multiplied by $\hat{g}_2$ having the singularity $1/v_t$ the invariant amplitudes $F_n^{(2)}$ have additional factor v_t compared to $F_n^{(1)}$. The asymptotic behaviour at small Q and m_v of $F_n^{(2)}$ is the same as for $F_n^{(1)}$. In the same way as for the spinless case, it can be established that $G_3^{(j)} \propto Q$ for $Q \to 0$ for $j = 1,\ 2$ while $G_n^{(j)}$ for $n \neq 3$ can be non-zero at $Q = 0$. The small-m_v behaviour of $G_1^{(j)} \propto m_v$ at $j = 1,\ 2$ follows from the singularity of $h_3 \propto 1/m_v$ while all other $G_n^{(j)}$ at $n \neq 1$ can be non-zero at $m_v = 0$. The components of the vectors g_1 and g_2 behave as $1/v_t$ at $v_t \to 0$. Therefore $G_4^{(1)} \propto (v_t)^0$, $G_1^{(1)} \propto v_t$, $G_3^{(1)} \propto v_t$, and $G_2^{(1)} \propto (v_t)^2$. Since $\mathcal{U}_{\mu\tau}^{(2)}$ is multiplied by $\hat{g}_2$ which has the singularity $1/v_t$ at $v_t \to 0$ the amplitude $G_n^{(2)}$ has the addition factor v_t compared to $G_n^{(1)}$ for any n.

The ratios of the helicity amplitudes $\mathrm{T}_{\lambda_\mathrm{V}\lambda_\gamma} \equiv \mathrm{T}_{\lambda_\mathrm{V}\frac{1}{2}\lambda_\gamma\frac{1}{2}}$ in the CM system were extracted in Ref. [7] from the HERMES data on the ρ^0-meson production in DIS of electrons/positrons off unpolarized protons at 3.0 GeV $< W <$ 6.3 GeV and 0.5 GeV^2 $< Q^2 <$ 7.0 GeV^2. The amplitudes with the nucleon helicity flip $\mathrm{T}_{\lambda_\mathrm{V}-\frac{1}{2}\lambda_\gamma\frac{1}{2}}$ were neglected. The certain ratios versus Q^2 and $-t' = v_t^2$ are shown in Fig. 1 by the full circles. The calculated helicity amplitude ratios in the CS are shown in Fig. 1 by the full squares. They are named "invariant amplitudes" since the invariant amplitudes coincide with the CS helicity amplitudes in agreement with relations (8). As seen $\mathrm{Re}\{\mathrm{T}_{11}/\mathrm{T}_{00}\}$ in the CS and CM system are close to each other. The ratio $\mathrm{Re}\{\mathrm{T}_{01}/\mathrm{T}_{00}\}$ shows definitely that the helicity-flip amplitude T_{01} is non-zero in the CM system. This corresponds to the s-channel helicity violation actively discussed in literature (see, for instance, review [11]). In contrast, $\mathrm{Re}\{\mathrm{T}_{01}/\mathrm{T}_{00}\}$ in the CS is compatible with zero. This shows probably that the helicity violation in the CS is far less than in the CM system.

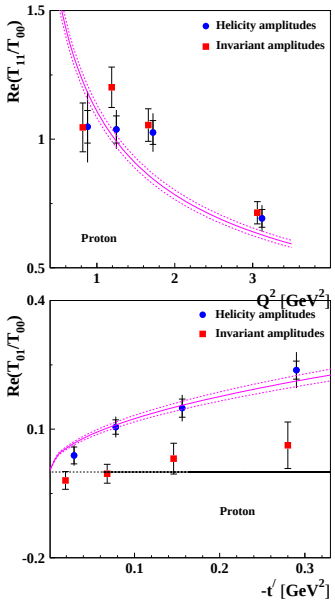

Figure 1: Kinematic dependence of amplitude ratios $\mathrm{Re}(\mathrm{T}_{11}/\mathrm{T}_{00})$ and $\mathrm{Re}(\mathrm{T}_{01}/\mathrm{T}_{00})$. The full circles are taken from Ref. [7] while the full squares show the result of the present work. Inner error bars show the statistical uncertainty while the outer ones (for the circles only) indicate statistical and systematic uncertainties added in quadrature. The solid curves show the fit result of Ref. [7] while the dotted lines show the total uncertainty of the fitting curves.

References

[1] D. Müller et al., Fortschr. Phys. **42** (1994) 101.
[2] A.V. Radyushkin, Phys. Lett. **B380** (1996) 417.
[3] X. Ji, Phys. Rev. Lett. **78** (1997) 610.
[4] M. Diehl, Phys. Rep. **388** (2003) 41
[5] J.C. Collins, L. Frankfurt, M. Strikman Phys. Rev. **D56** (1997) 2982.
[6] F.D. Aaron et al., J. High Energy Phys. **1005** (2010) 32.
[7] A. Airapetian et al., Eur. Phys. J. **C71** (2011) 1609.
[8] K. Schilling, G. Wolf, Nucl. Phys. **B61** (1973) 381.
[9] S.I. Manayenkov, Preprint PNPI 2856, Gatchina, 2010.
[10] H. Fraas and D. Schildknecht, Nucl. Phys. **B14** (1969) 542.
[11] I.P. Ivanov, N.N. Nikolaev, A.A. Savin, Phys. Part. Nucl. **37** (2006) 1.

ANOMALY AND TRANSITION FORM FACTORS

Ya.N. Klopot [1 †], A.G. Oganesian [1,2] and O.V. Teryaev [1]

(1) *Joint Institute for Nuclear Research, Dubna*
(2) *Institute of Theoretical and Experimental Physics, Moscow*
† *E-mail: klopot@theor.jinr.ru*

Abstract

The anomaly sum rule (ASR) for meson transition form factors based on the dispersive representation of axial anomaly and quark-hadron duality in octet channel is obtained and analyzed. It is valid at all virtual photon momenta and allows one to express the transition form factors entirely in terms of meson decay constants. This relation is in a good agreement with experimental data.

Axial anomaly is known to be a fundamental notion of nonperturbative QCD and hadronic physics. The dispersive form of axial anomaly can be considered for the case of virtual photons [1], which we will interesting in. By use of dispesion representation an exact anomaly sum rule (ASR) can be obtained, which does not have both perturbative corrections (due to Adler-Bardeen theorem) as well as nonperturbative QCD corrections (due to 't Hooft consistency principle). Recently, this sum rule was applied to the analysis of pion transition form factors [2] which attracted much attention because of unexpected and provocative data of BABAR collaboration.

Recently, the BABAR collaboration extended the analysis and presented the data for η and η' meson transition form factors [3]. In this work we analyze the η and η' transition form factors by means of generalized ASR which account meson mixing.

Let us briefly remind the dispersive representation for axial anomaly and derive anomaly sum rule for the octet channel of axial current. We start from the VVA triangle graph correlator

$$T_{\alpha\mu\nu}(k,q) = \int d^4x d^4y e^{(ikx+iqy)} \langle 0|T\{J_{\alpha 5}(0) J_\mu(x) J_\nu(y)\}|0\rangle \tag{1}$$

where $J_\mu = (e_u \bar{u}\gamma_\mu u + e_d \bar{d}\gamma_\mu d + e_s \bar{s}\gamma_\mu s)$; k, q are momenta of photons and the octet component of axial current: $J^{(8)}_{\alpha 5} = \frac{1}{\sqrt{6}}(\bar{u}\gamma_\alpha\gamma_5 u + \bar{d}\gamma_\alpha\gamma_5 d - 2\bar{s}\gamma_\alpha\gamma_5 s)$.

Following [1]we write the tensor decomposition of correlator (1) in a form:

$$\begin{aligned} T_{\alpha\mu\nu} = F_1\, \varepsilon_{\alpha\mu\nu\rho}k^\rho + F_2\, \varepsilon_{\alpha\mu\nu\rho}q^\rho + \;& F_3\, k_\nu \varepsilon_{\alpha\mu\rho\sigma}k^\rho q^\sigma + F_4\, q_\nu \varepsilon_{\alpha\mu\rho\sigma}k^\rho q^\sigma \\ + \;& F_5\, k_\mu \varepsilon_{\alpha\nu\rho\sigma}k^\rho q^\sigma + F_6\, q_\mu \varepsilon_{\alpha\nu\rho\sigma}k^\rho q^\sigma, \end{aligned} \tag{2}$$

where the coefficients $F_j = F_j(k^2, q^2, p^2; m^2)$, $p = k+q$, $j = 1, \ldots, 6$ are the corresponding Lorentz invariant amplitudes constrained by current conservation and Bose symmetry.

In this paper we are interested in the case of one real ($k^2 = 0$) and one virtual photon ($Q^2 = -q^2 > 0$). Then for the invariant amplitude $F_3 - F_6$ the anomaly sum rule (ASR) takes the form [1]:

$$\int_{4m^2}^{\infty} A_{3a}(t; q^2, m^2) dt = \frac{1}{2\pi} N_c C^{(a)}\ , \tag{3}$$

where $N_c = 3$ is a number of colors and $A_{3a} = \frac{1}{2} Im(F_3 - F_6), C^{(3)} = \frac{1}{\sqrt{2}}(e_u^2 - e_d^2), C^{(8)} = \frac{1}{\sqrt{6}}(e_u^2 + e_d^2 - 2e_s^2), C^{(0)} = \frac{1}{\sqrt{3}}(e_u^2 + e_d^2 + e_s^2)$.

As I have told before, ASR (3) is an exact relation, i.e. it does not have any7 corrections to the integral. Another important property of this relation is that it holds for an arbitrary quark mass m and for any q^2.

Saturating the l.h.s. of the 3-point correlation function (1) with the resonances and singling out their contributions to ASR (3) we get the sum of resonances with appropriate quantum numbers:

$$f_\eta^8 F_\eta + f_{\eta'}^8 F_{\eta'} + (other\ resonances) = \int_{4m^2}^{\infty} A_{3a}(t; q^2, m^2) dt = \frac{1}{2\pi} N_c C^{(8)}. \tag{4}$$

Here the coupling constants f_M^a are defined as: $\langle 0|J_{\alpha 5}^{(a)}(0)|M(p)\rangle = ip_\alpha f_M^a$, and the form factors $F_{M\gamma}$ of the transition $\gamma\gamma^* \to M$ are defined by the matrix elements:

$$\int d^4x e^{ikx} \langle M(p)|T\{J_\mu(x) J_\nu(0)\}|0\rangle = \epsilon_{\mu\nu\rho\sigma} k^\rho q^\sigma F_{M\gamma} \ . \tag{5}$$

The relation (4) is exact and expresses the global duality between hadrons and quarks. The contributions of higher resonances can be accounted in usual way as continuum contribution, i.e. the integral of spectral density starting from some parameter, called continuum threshold s_0. As we will see, in the case of anomaly it is fixed by anomaly itself, so in our case we really do not need the local quark-hadron duality hypothesis, it enough the global one.

One should note that the particles with nonzero two-photon decays cannot be included in the continuum as it vanishes at $Q^2 = 0$, so they should be taken into account explicitly in the ASR. For heavy mesons the corresponding coupling constants should be suppressed [4] at least as $(m_\eta/m_{res})^2$ which follows from the conservation of axial current $J_{\mu 5}^{(8)}$ in the chiral limit (if only strong interaction is taken into account). That is why we restrict ourselves only to η and η' mesons. The ASR for the octet channel finally reads:

$$\pi f_\eta^8 F_{\eta\gamma}(Q^2) + \pi f_{\eta'}^8 F_{\eta'\gamma}(Q^2) = \frac{1}{2\pi\sqrt{6}} \frac{s_0}{Q^2 + s_0}. \tag{6}$$

Let us stress that this relation is correct for all Q^2 due to the absence of the corrections to the $Im(F_3 - F_6)$ [5] which allows to utilize the above expression for different Q^2.

By the way, for real photons ($Q^2 = 0$) the above expression coincides with the expression in [4], which was obtained from dispersive approach to axial anomaly in somewhat different way by use of PCAC relation:

The equation (6) allows us to fix the continuum threshold s_0 by considering the limit $Q^2 \to \infty$ where the QCD factorization [6,7] is applicable (contrary to ASR the exploration of this limit in generic QCD sum rules is obscured by possible corrections). The form factors at large Q^2 [8, 9] are:

$$Q^2 F_{\eta\gamma}^{as} = 2(C^{(8)} f_\eta^8 + C^{(0)} f_\eta^0) \int_0^1 \frac{\phi^{as}(x)}{x} dx \tag{7}$$

and the same for η'. We take into account that in the limit $Q^2 \to \infty$ the light cone distribution amplitudes of both η, η' mesons are described by their asymptotical form [6,7]: $\phi^{as}(x) = 6x(1-x)$.

Then the ASR for the octet channel at large Q^2 leads to:

$$s_0 = 4\pi^2((f_\eta^8)^2 + (f_{\eta'}^8)^2 + 2\sqrt{2}[f_\eta^8 f_\eta^0 + f_{\eta'}^8 f_{\eta'}^0]). \tag{8}$$

Substituting (8) into (6) we express ASR in terms of meson decay constants f_M^a only, which is our main result:

$$f_\eta^8 F_{\eta\gamma}(Q^2) + f_{\eta'}^8 F_{\eta'\gamma}(Q^2) = \frac{\sqrt{\frac{2}{3}}}{4\pi^2 + Q^2/((f_\eta^8)^2 + (f_{\eta'}^8)^2 + 2\sqrt{2}[f_\eta^8 f_\eta^0 + f_{\eta'}^8 f_{\eta'}^0])}. \tag{9}$$

Let us now pass to applications of (9). As an example, let us analyze the ASR (9) for usual mixing scheme with one angle, where matrix of decay constants is:

$$\mathbf{F} \equiv \begin{pmatrix} f_\eta^8 & f_{\eta'}^8 \\ f_\eta^0 & f_{\eta'}^0 \end{pmatrix} = \begin{pmatrix} f_8 \cos\theta & f_8 \sin\theta \\ -f_0 \sin\theta & f_0 \cos\theta \end{pmatrix}. \tag{10}$$

This mixing scheme was analyzed in many papers (see e.g. [10] and references therein), giving the values of mixing angle in the range $\theta = -12^o \div -22^o$.

In this case the ASR acquires a simple form:

$$Q^2(F_{\eta\gamma}(Q^2)\cos\theta + F_{\eta'\gamma}(Q^2)\sin\theta) = \sqrt{\frac{2}{3}}\frac{Q^2}{4\pi^2 f_8 + Q^2/f_8}, \tag{11}$$

where constant f_8 is defined by the anomaly sum rule at $Q^2 = 0$ ([4]):

$$f_8 = \frac{\alpha}{4\sqrt{6}\pi^{3/2}}\left(\sqrt{\frac{\Gamma_{\eta\to 2\gamma}}{m_\eta^3}}\cos\theta + \sqrt{\frac{\Gamma_{\eta'\to 2\gamma}}{m_{\eta'}^3}}\sin\theta\right)^{-1}. \tag{12}$$

Thus, (11) and (12) determine the mixing angle in terms of physical quantities (decay widths and transition form factors).

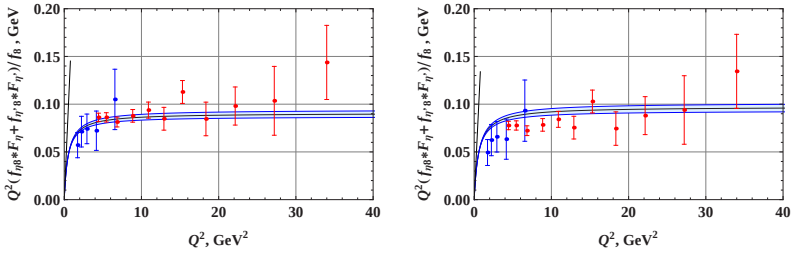

(a) **(b)**

Figure 1: **(a)** ASR for one-angle mixing scheme $\theta = -14^o$. **(b)** ASR for one-angle mixing scheme $\theta = -16^o$.

The corresponding relation is plotted for different mixing angles in Fig.1. The dots with error bars correspond to the l.h.s. of Eq. (11), where the form factors of η, η' mesons are taken from experimental data of CLEO [11] and BABAR [3] collaborations.

We thank B. L. Ioffe, P. Kroll, S. V. Mikhailov, T. N. Pham, A. V. Radyushkin for useful discussions and elucidating comments. This work was supported in part by RFBR (Grants 09-02-00732, 09-02-01149, 11-02-01538,11-02-01454) and by fund from CRDF Project RUP2-2961-MO-09.

References

[1] J. Horejsi, O. Teryaev, Z. Phys. **C65**, (1995) 691-696.

[2] Y. N. Klopot, A. G. Oganesian, O. V. Teryaev, Phys. Lett. **B695**, (2011) 130-135.

[3] P. del Amo Sanchez *et al.* [BABAR Collaboration], arXiv:1101.1142 [hep-ex]. V. P. Druzhinin, PoS (ICHEP 2010) **144**

[4] Y. N. Klopot, A. G. Oganesian, O. V. Teryaev, [arXiv:0911.0180 [hep-ph]].

[5] F. Jegerlehner, O. V. Tarasov, Phys. Lett. **B639** (2006) 299-306.

[6] A. V. Efremov, A. V. Radyushkin, Phys. Lett. **B94** (1980) 245-250.

[7] G. P. Lepage, S. J. Brodsky, Phys. Lett. **B87** (1979) 359-365.

[8] V. V. Anisovich, D. I. Melikhov, V. A. Nikonov, Phys. Rev. **D55** (1997) 2918-2930.

[9] T. Feldmann, P. Kroll, Eur. Phys. J. **C5** (1998) 327-335.

[10] P. Ball, J. M. Frere, M. Tytgat, Phys. Lett. **B365** (1996) 367-376.

[11] J. Gronberg *et al.* [CLEO Collaboration], Phys. Rev. **D57** (1998) 33-54.

CONSISTENT GAUGE INVARIANT NUCLEON SPIN DECOMPOSITION

D.G. Pak [1 †] and P.M. Zhang [1,2]

(1) *Institute of Modern Physics, Chinese Academy of Sciences, Lanzhou 730000, China*
(2) *Research Center for Hadron and CSR Physics, Lanzhou University, Lanzhou 730000, China*
† *E-mail: dmipak@gmail.com*

Abstract

We consider a non-uniqueness problem of gauge invariant nucleon spin decomposition. A gauge invariant decomposition with a generalized Coulomb constraint for the physical gluon has been constructed. The decomposition scheme is consistent with the concept of helicity in non-Abelian gauge theory. We provide an explicit representation for the gauge invariant Abelian projection which implies further separation of gluon into binding and valence parts.

It has been a long standing problem of gauge invariant definition of gluon spin and orbital angular momentum [1, 2]. Recently a gauge invariant decomposition of the total nucleon angular momentum into quark and gluon constituents has been proposed [3], and subsequently other possible gauge invariant decompositions for nucleon spin have been suggested [4, 5]. Despite on this progress there are still principal controversies on fundamental conceptual level in determining a consistent notion for spin and orbital angular momentum [6]. In the present article we revise the problem of nucleon spin decomposition and existence of a consistent gauge invariant concept of spin in the non-Abelian gauge theory.

Let us start with the well known canonical decomposition of total angular momentum in quantum chromodynamics (QCD)

$$J^{can}_{\mu\nu} = \int d^3x \big\{ \bar{\psi}\gamma^0 \frac{\Sigma_{\mu\nu}}{2}\psi - i\bar{\psi}\gamma^0 x_{[\mu}\partial_{\nu]}\psi - \vec{A}_{[\mu}\cdot\vec{F}_{\nu]0} - \vec{F}_{0\alpha}\cdot x_{[\mu}\partial_{\nu]}\vec{A}_{\alpha}\big\}, \qquad (1)$$

where we use vector notations for vectors in color space. All terms in this decomposition, except the first one, are gauge non-invariant. In the series of papers [3] Chen et al have proposed gauge invariant decomposition of the total angular momentum in quantum electrodynamics (QED) and QCD. The basic idea in Chen et al approach is to separate pure gauge and physical degrees of freedom of the gauge potential in a gauge covariant way

$$\vec{A}_{\mu} = \vec{A}^{pure}_{\mu} + \vec{A}^{phys}_{\mu}. \qquad (2)$$

Adding an appropriate surface term one can obtain the following expression for the total angular momentum tensor

$$\begin{aligned} J^{can}_{\mu\nu} &= \int d^3x \Big\{ \bar{\psi}\gamma^0 \frac{\Sigma_{\mu\nu}}{2}\psi - i\bar{\psi}\gamma^0 x_{[\mu}\mathcal{D}_{\nu]}\psi - \\ &\vec{F}_{0[\mu}\cdot\vec{A}^{phys}_{\nu]} - \vec{F}_{0\alpha}\cdot x_{[\mu}(\mathcal{D}_{\nu]}\vec{A}^{phys}_{\alpha} - \vec{\mathcal{F}}_{\nu]\alpha}(A^{pure}))\Big\}, \end{aligned} \qquad (3)$$

where $\mathcal{D}_\mu$ contains a pure gauge field $\vec{A}^{pure}_\mu$ only. The given expression for the angular momentum is valid for any split of the gauge potential before imposing any constraint on physical and pure gauge fields. In the case of QCD a consistent gauge invariant decomposition for the nucleon angular momentum has been proposed by requiring two conditions on pure gauge $\vec{A}^{pure}$ and physical $\vec{A}^{phys}$ components of the gauge field [3]

$$\vec{\mathcal{F}}_{\mu\nu}(A^{pure}) = 0, \qquad\qquad \mathcal{D}_i \vec{A}^{phys}_i = 0, \tag{4}$$

where Latin letters are used for space indices, $i, k, ... = (1, 2, 3)$. Solving these conditions leads to the gauge invariant decomposition in the form corresponding to the vector part of (3) [3]. In the gauge $\vec{A}^{pure} = 0$ the decomposition reduces to the canonical one in the Coulomb gauge. One should notice, that this decomposition is not Lorentz invariant, so that the notion of gluon spin is frame dependent. The gauge invariant and Lorentz invariant nucleon spin decomposition has been suggested in [5]. However, in that decomposition the solving a constraint for the physical gauge potential on mass-shell encounters a serious problem.

To choose a proper physical nucleon spin decomposition we require consistence condition with the helicity notion, which will guarantee the Lorentz invariance. We will construct explicitly such a spin decomposition using gauge invariant variables in non-Abelian theory [7]. The main idea in constructing gauge invariant variables is to find a pure gauge $SU(2)$ matrix field in terms of the initial gauge potential $\vec{A}$. Using the equation of motion for the temporal component A^a_0 one can write down the equation for the matrix function $\mathbf{v} \in SU(2)$

$$\partial_0 \mathbf{v}(A) = \mathbf{v}(A)\Big(\frac{1}{D^2(A)} D_j(A)\partial_0 \hat{A}_j - \hat{j}_0\Big), \tag{5}$$

where $\hat{A}_i \equiv A^a_i \tau^a/2$. Due to the equation of motion for A^a_0 it follows that $\mathbf{v}$ transforms covariantly, $\mathbf{v}(A^g) = \mathbf{v} g^{-1}$. The solution to equation (5) can be obtained in the form of time ordered exponent [7]

$$\mathbf{v}(A) = T \exp\Big\{ \int^t dt \frac{1}{D^2(A)} D_j(A)\partial_0 \hat{A}_j - \hat{j}_0\Big\}. \tag{6}$$

This allows to define the gauge invariant variables [7]

$$\hat{A}^I_i(A) = \mathbf{v}(A)(\partial_i + \hat{A}_i)\mathbf{v}^{-1}(A), \qquad \psi^I(A, \psi) = \mathbf{v}(A)\psi. \tag{7}$$

One can check that $\hat{A}^I_i$ satisfies a constraint which represents a generalized covariant Coulomb gauge condition

$$D_i(A^I)\partial_0 \hat{A}^I_i - \hat{j}_0 = 0. \tag{8}$$

One should stress, that we do not impose this condition, it follows from the definition of $\hat{A}^I_i$ and $\mathbf{v}(\mathbf{A})$. Finally, from Eqn. (7) one finds the following split for the gauge potential

$$\hat{A}_i = \hat{v}^{-1}(A)\partial_i \hat{v}(A) + \hat{v}^{-1}(A)\hat{A}^I_i(A)\hat{v}(A) \equiv \hat{A}^{pure}_i + \hat{A}^{phys}_i, \tag{9}$$

where we can identify the first and second terms as the pure gauge and physical components needed to make the desired gauge invariant decomposition. The pure gauge temporal component is defined by $\mathbf{v}^{-1}(A)\partial_0 \mathbf{v}(A)$. The presented construction of the pure gauge

and physical fields in terms of the unconstrained gauge potential provides an explicit realization of the gauge invariant nucleon spin decomposition (3) with $\vec{\mathcal{F}}_{\nu\alpha}(A^{pure})=0$. The decomposition reduces to the canonical one in the gauge $\vec{A}^{pure}=0$, i.e., in the generalized covariant Coulomb gauge (8).

Let us check consistence of our construction with the concept of helicity. This will provide frame independent relationship between our gauge invariant definition of gluon spin density and gluon helicity Δg measured in experiment. The helicity states are described by representations of the little group $E(2)$ [8,9] which is a subgroup of the Lorentz group. Transformations of the little group leave the four-momentum of gluon invariant. If gluon momentum is directed along the z axis, $p_\mu=(\omega,0,0,\omega)$, the generators of the little group $E(2)$ are given by rotation generator J_3 and combinations of Lorentz boost and rotation

$$N_1=K_1-J_2, \qquad N_2=K_2+J_1. \tag{10}$$

The gauge potential represents helicity eigenstates of the operator J_3 if the following helicity conditions are satisfied $\vec{A}_0^{phys}=0, \vec{A}_3^{phys}=0$ [9]. To provide both helicity conditions in a consistent manner with equations of motion has been an unresolved problem in the case of non-Abelian gauge theory. In our approach, since one has the first condition $\vec{A}_0^{phys}=0$ on mass-shell by construction, the second helicity condition $\vec{A}_3^{phys}=0$ can be realized by choosing a gauge of either Coulomb or axial or light-cone type. This is our main result which allows to select a physical gauge covariant operator $\vec{A}^{phys}(A)$ and corresponding spin density consistently with the helicity notion.

Another application of our gauge invariant spin decomposition is the possibility to provide an explicit representation for the gauge invariant Cho-Duan Abelian projection [10,11] which may play an important role in definition of spin decomposition with dynamic quark momentum [5]

$$\begin{aligned}
&\vec{A}_\mu=A_\mu\hat{n}+\vec{C}_\mu+\vec{X}_\mu\equiv\hat{A}_\mu+\vec{X}_\mu,\\
&\vec{C}_\mu=-\frac{1}{g}\hat{n}\times\partial_\mu\hat{n}, \qquad \vec{X}_\mu\cdot\hat{n}=0,
\end{aligned} \tag{11}$$

where A_μ is a binding gluon, $\vec{X}_\mu$ is the valence potential and $\hat{n}$ is a unit color triplet. The restricted potential $\hat{A}_\mu$ transforms as $SU(2)$ gauge connection, whereas the valence gluon $\vec{X}_\mu$ transforms as a covariant vector. Let us define the vector $\hat{n}$ by the relation $\mathbf{v}(A)=\exp[i\omega\hat{n}^i\vec{\tau}^i]$. The pure gauge field $\vec{A}_\mu^{pure}$ can be constructed in terms of $\hat{n}$ as follows [12]

$$\vec{A}_\mu^{pure}=-\tilde{C}_\mu\hat{n}+\vec{C}_\mu, \tag{12}$$

where $\tilde{C}_\mu$ is a dual magnetic potential. With this we decompose the gauge potential into pure gauge and physical parts

$$\vec{A}_\mu=-\tilde{C}_\mu\hat{n}+\vec{C}_\mu+\vec{A}_\mu^{phys}, \qquad \vec{A}_\mu^{phys}\equiv\vec{A}_\mu-\vec{A}_\mu^{pure}=A_\mu\hat{n}+\vec{X}_\mu. \tag{13}$$

Using decompositions (11) one can derive the expression for the gluon total angular momentum (3) which is simplified crucially on mass-shell due to the property $\vec{A}_0^{phys}=0$, i.e., $A_0=\vec{X}_0=0$,

$$J_{\mu\nu}^{gluon}=\int d^3x\Big\{-F_{0[\mu}A_{\nu]}-\partial_0\vec{X}_{[\mu}\cdot\vec{X}_{\nu]}+F_{0\alpha}x_{[\mu}\partial_{\nu]}A_\alpha+\partial_0\vec{X}_\alpha\cdot x_{[\mu}\partial_{\nu]}\vec{X}_\alpha\Big\}, \tag{14}$$

where $F_{\mu\nu} = \partial_\mu A_\nu - \partial_\nu A_\mu$. The given decomposition implies further separation of spin densities of binding and valence gluons. This allows to define a new spin decomposition with dynamic quark momentum containing only binding gluon. By splitting the gauge potential $\vec{A}_\mu = \hat{A}_\mu + \vec{X}_\mu$ and adding an appropriate surface term to the canonical expression (1) one results in a gauge invariant decomposition given by Eqn. (3) with replacement ($\vec{A}^{pure}_\mu \leftrightarrow \hat{A}_\mu$, $\vec{A}^{phys}_\mu \leftrightarrow \vec{X}_\mu$). A new feature of this decomposition is that it does not contain the spin density for the binding gluon. Since the binding gluon supposed to have a dominant gluon contribution to nucleon spin [5], this supports the experimental data on a small value for the gluon helicity, $\Delta g \approx 0$.

In conclusion, one has a unique Lorentz invariant nucleon spin decomposition [5], however, it is not defined on mass-shell and its physical meaning remains unclear. Other known decompositions [3, 4] are not Lorentz invariant and lead to frame dependent definitions for gluon spin. The only gauge invariant and frame independent notion of spin in the gauge theory is the helicity. In the present work we have proposed a spin decomposition which is consistent with helicity concept and leads to correct expression for the gluon helicity Δg.

We acknowledge the Organizing Committee for invitation to participate in the Workshop DSPIN-2011. We thank N.I. Kochelev, A.E. Dorokhov, I.V. Anikin, O.V. Teryaev, A.V. Efremov for numerous discussions and hospitality. We thank Y.M. Cho, F. Wang and W.M. Sun for critical comments and useful discussions. The work was supported by NSFC Grants (Nos. 11035006 and 11175215), and the CAS Visiting Professorship (No. 2011T1J31).

References

[1] R. L. Jaffe and A. Manohar, Nucl. Phys. B337, 509 (1990).

[2] X. Ji, Phys. Rev. Lett. 78, 610 (1997).

[3] X. S. Chen, X. F. Lu, W. M. Sun, F. Wang, and T. Goldman, Phys. Rev. Lett. **100**, 232002 (2008); Phys. Rev. Lett. **103**, 062001 (2009).

[4] M. Wakamatsu, Phys. Rev. **D81**, 114010 (2010); Phys.Rev.D83:014012 (2011).

[5] Y. M. Cho, M. L. Ge, and P. M. Zhang, arXiv:1010.1080 [nucl-th]; Y. M. Cho, M. L. Ge, D. G. Pak, and P. M. Zhang, arXiv:1102.1130 [nucl-th].

[6] X. Ji, Phys. Rev. Lett. **104**, 039101 (2010); E. Leader, Phys.Rev.D83:096012,2011.

[7] V. N. Pervushin, Nuovo Cim. **8**, 1 (1985); Phys. Rev. **D23**, 2415 (1981).

[8] E.P. Wigner, Ann. Math. **149**, 40 (1939); S. Weinberg, Phys. Rev. D134, B882 (1964).

[9] D. Han, Y.S. Kim and D. Son, Phys. Rev. D31, 328 (1985).

[10] Y. M. Cho, Phys. Rev. **D21**, 1080 (1980); Phys. Rev. Lett. **46**, 302 (1981).

[11] Y. S. Duan and Mo-Lin Ge, Sci. Sinica **11**, 1072 (1979).

[12] Y. M. Cho, Phys. Lett. **B644**, 208 (2007).

INVESTIGATING ORBITAL ANGULAR MOMENTUM WITH MEASUREMENTS OF ΔG/G

Gordon P. Ramsey [1†], Y. Binder [2] and D. Sivers [3]

(1) *Loyola University Chicago and Argonne National Laboratory*
(2) *Quantum Code and Loyola University Chicago*
(3) *Portland Physics Institute and University of Michigan*
† *E-mail: gpr@hep.anl.gov*

Abstract

Measurements involving the gluon spin density, $\Delta G(x,t)$, can play an important role in the understanding of proton structure. The shape of the gluon asymmetry, $A(x,t) \equiv \Delta G(x,t)/G(x,t)$, contains significant dynamical information about non-perturbative spin-orbit effects. This asymmetry can be written in a form that we can use to calculate it within a given factorization prescription from evolution and known parton distributions. This is a complementary approach to using data directly to determine ΔG. Combining this with the $J_z = \frac{1}{2}$ sum rule provides a way to determine the amount of orbital angular momentum generated by mechanisms associated with confinement and chiral dynamics. The results are consistent with alternate non- perturbative approaches for determination of L_z in the proton.

Several experimental programs [1] have devised strategies aimed at providing a significant measure $\Delta G(x,t)$ in the proton, where $t \equiv \log[\alpha_s(Q_0^2)]/\log[\alpha_s(Q^2)]$ is the evolution variable. The interest in these measurements is often framed using the $J_z = \frac{1}{2}$ sum rule,

$$J_z = \frac{1}{2} \equiv \frac{1}{2} < \Delta\Sigma(t) > + < \Delta G(t) > + L_z(t), \tag{1}$$

where $< \Delta\Sigma(t) >$ and $< \Delta G(t) >$ are the projections of the spin carried by all quarks and the gluons on the helicity (or z)-axis, respectively. Also $L_z(t)$ is the net z-component of the orbital angular momentum of the constituents.

Recent DIS experiments [2] have significantly lowered the measurement errors of the quark spin contribution ($\Delta\Sigma$) to equation (1). The COMPASS collaboration analysis quotes a result

$$< \Delta\Sigma >= 0.30 \pm 0.01(\text{stat}) \pm 0.02(\text{evol}), \qquad \text{all data} \tag{2}$$

while the HERMES collaboration analysis quotes a result

$$< \Delta\Sigma >= 0.330 \pm 0.025(\text{exp}) \pm 0.011(\text{th}) \pm 0.028(\text{evol}), \qquad \text{all data.} \tag{3}$$

These values can be used with the $J_z = \frac{1}{2}$ sum rule to evaluate the impact of existing and potential gluon asymmetry measurements.

Recent experimental results sensitive to $\Delta G(x,t)$ and the gluon asymmetry, $A(x,t) \equiv \Delta G(x,t)/G(x,t)$ have provided important new information. So far, the analysis of these experiments is limited in sensitivity and range of $< x >$,so the results have not determined

the shape nor overall magnitude of $\Delta G(x,t_0)$. Understanding the shape of $\Delta G(x,t)$ for the whole range $x \in (0,1)$ is important in understanding the structure of the nucleons. Experimental evidence on $\Delta G(x,t_0)$ for a limited range of x and t_0 must be combined with an extrapolation in order to specify the nature of $< \Delta G(t) >$ and $L_z(t)$ at large t. The specific approach in this paper helps to illuminate these possibilities and to fix onto crucial experimental results.

We write the polarized gluon asymmetry using the decomposition

$$A(x,t) \equiv \Delta G(x,t)/G(x,t) = A_0^\epsilon(x) + \epsilon(x,t), \tag{4}$$

where $A_0^\epsilon(x)$ is dependent only upon x, calculable in PQCD by the using definition

$$A_0^\epsilon(x) \equiv \Big[(\frac{\partial \Delta G(x,t)}{\partial t})/(\frac{\partial G(x,t)}{\partial t})\Big]. \tag{5}$$

The numerator and denominator on the right side of equation (5) are calculable from the DGLAP equations and each depends strictly upon x via the respective convolutions. The small correction, $\epsilon(x,t)$ describes shape-dependent differences in the evolutions of $G(x,t)$ and $\Delta G(x,t)$ at leading order (LO) in QCD perturbation theory.

The expression (4) for $A(x,t)$ at some initial $t = t_0$ leads to an equivalent decomposition for $\Delta G(x,t)$ in the form

$$\Delta G(x,t_0) = A_0^\epsilon(x) \cdot G(x,t_0) + \Delta g_\epsilon(x) \tag{6}$$

where the "polarized gluon excess", $\Delta g_\epsilon(x)$, is given by

$$\Delta g_\epsilon(x) = \epsilon(x,t) \cdot G(x,t) \tag{7}$$

and is $t-$independent. This provides a boundary condition for the partial differential equation (5) that defines $A_0^\epsilon(x)$ and can be used to characterize possible different shapes for $A(x,t)$ in equation (4). This boundary condition for the partial differential equation (5) occurs at an unphysical region in that the decomposition in (6) cannot be valid when $G(x,t_0) = 0$. In practice, this means that there are nontrivial constraints on the magnitude of $\Delta g_\epsilon(x)$.

The solution of equations based on equations (4) and (5) was proposed by Ramsey and Sivers [3]. The calculation of the asymmetry provided a method to determine ΔG without theoretical biases on its shape. This was followed by analysis of the relation between the Δg_ϵ parameterizations and the corresponding range of possible L_z [3]. Since new data for the asymmetry have been made available, this method has allowed us to refine the range of possible $< \Delta G >$ and L_z consistent with this data [4]. The culmination of this work is presented here.

The perturbative component of the polarized gluon asymmetry $A_0^\epsilon(x)$ can be calculated from a parameterization of the correction $\Delta g_\epsilon(x)$ by inserting equation (6) into the expression (5) for $A_0^\epsilon(x)$. Then equation (5) can then be solved using $\partial \Delta G/\partial t$ and $\partial G/\partial t$ given by DGLAP evolution. In kinematic regions where the DGLAP evolution equations are valid, equation (5) allows one to generate $A_0^\epsilon(x)$ by

$$A_0^\epsilon(x) = \left[\frac{\Delta P_{gq} \otimes \Delta q + \Delta P_{gg} \otimes (\Delta G)}{P_{gq} \otimes q + P_{gg} \otimes G}\right]. \tag{8}$$

Then equations (5) and (6) can be used to generate the corresponding asymmetry using the equation

$$A_0^\epsilon(x) = \left[\frac{\Delta P_{Gq} \otimes \Delta q + \Delta P_{GG} \otimes [A_0^\epsilon \cdot G + \Delta g_\epsilon]}{P_{Gq} \otimes q + P_{GG} \otimes G}\right]. \tag{9}$$

Since the $A_0^\epsilon(x)$ term occurs on both sides of the equation, we parametrize $A_0^\epsilon(x)$ and $\Delta g_\epsilon(x)$ subject to theoretical constraints and determine the coefficients of the parameterizations that satisfy equation (9). For each parameterization of $\Delta g_\epsilon(x)$, the resulting asymmetry $A(x,t)$ and corresponding ΔG from equation (6) can then be checked for positivity with the corresponding unpolarized gluon at LO. The various parametrizations of $\Delta g_\epsilon(x)$ were chosen to have integrals over all x between -0.5 and 0.5. One parametrization was selected to change sign, consistent with instanton models. This possibility has not been ruled out by data [1]. The process to determine the NLO corrections to the asymmetry is similar to that of LO with the appropriate corrections to the splitting functions and evolution parameters. Since most data are analyzed at LO, our analysis is done here at LO as well.

The calculation of $A_0^\epsilon(x)$ in equation (9) has been done using the CTEQ5 and MRST [6] unpolarized parton distributions for comparison and the polarized quark distributions from reference [6]. All are evaluated at $Q_0^2 = 1$ GeV ^{2} for the LO distributions. The polarized distributions given by GGR [6] in terms of the unpolarized ones. To establish an initial reference point for the solution of equation (9), practical constraints for the asymmetry at LO should include:

- strong positivity: $|A(x,t_0)| \leq 1$ for all $0 \leq x \leq 1$, and
- endpoint values: $A(0,t_0) = 0$ and $A(1,t_0) = 1$.

Simple positivity for the gluon asymmetry at LO requires $|A(x,t)| \leq 1$. The strong positivity constraint enforces the restriction that $\Delta g_\epsilon(x)$ is small. We start with an $A_0^\epsilon(x)$ parameterization in the form

$$A_0^\epsilon(x) \equiv Ax^\alpha - (B-1)x^\beta + (B-A)x^{\beta+1}, \tag{10}$$

which automatically satisfies the endpoint constraints provided the exponents α and β are positive. This parameterization includes substantial flexibility in adjusting shapes while keeping the number of free parameters to a minimum.

Using the current data for $\Delta\Sigma$ as input, we combine equations (1), (2) and (3) to write

$$L_z(t) + < \Delta G(t) > \approx \frac{1}{2}(1 - < \Delta\Sigma >) \approx 0.34 \pm 0.02 \tag{11}$$

in a chiral factorization prescription. The quoted error is entirely due to the data uncertainties in equations (2) and (3). Our approach to the study of $\Delta G(x,t)$ is largely complementary to the usual global analysis determination discussed, for example, by Hirai and Kumano and others [5] where the main input for $\Delta G(x,t)$ involves measurement of the scaling violations for $\Delta q(x,t)$. Since it is highly unlikely that future experiments sensitive to $\Delta G(x,t)$ will determine this distribution with an accuracy similar to that found in the determination of Δq or to that of $G(x,t)$ and $q(x,t)$, our method takes into account the similarities between the evolution of $\Delta G(x,t)$ and $G(x,t)$ to provide the

necessary extrapolations to all x. Using knowledge of $\Delta q(x,t)$, $q(x,t)$ and $G(x,t)$ data sensitive to values of $\Delta G(x,t)$ in limited regions of x and t can then be used efficiently to obtain valid estimates for $L_z(t)$.

For those parameterizations of $\Delta g_\epsilon(x)$ for which a stable solution to Eq. (9) exists at $t = 0$, we can insert the decomposition of Eq. (6) into Eq. (11) to write

$$L_z(0) = 0.34 \pm 0.04 - < A_0^\epsilon(x) \cdot G(x,0) > - < \Delta g_\epsilon(x) > \tag{12}$$

and evolve the equivalent possible forms of $\Delta G(x,0)$ to compare with experimental extractions of $\Delta G(x,t)$ found through processes such as prompt photon and photon + jet measurements. The terms in Eq. (12) use the experimental averages for $< \Delta\Sigma >$ from COMPASS and HERMES, and the CTEQ or MRST parameterizations for $G(x,t_0)$. The error quoted here is due to the uncertainties in the data, as previously mentioned and the small theoretical uncertainties associated with the unpolarized distributions.

Table 1: Best Fit Gluon Asymmetries at $Q_0^2 = 1$ GeV^2

Δg_ϵ	$< \Delta g_\epsilon >$	A_0^ϵ	$< \Delta G >$
0	0	$3x^{1.5} - 3x^{2.2} + x^{3.2}$	0.28
$-90x^2(1-x)^7$	-0.25	$3.5x^{1.3} - 4.5x^{2.2} + 2x^{3.2}$	0.25
$9x(1-x)^7$	0.125	$3.75x^{1.4} - 3x^{1.6} + 0.25x^{2.6}$	0.40
$-9x(1-x)^7$	-0.125	$3.25x^{1.4} - 3.75x^{2.2} + 1.5x^{3.2}$	0.25
$-4.5x(1-x)^7$	-0.0625	$2.25x^{1.1} - 2.25x^{1.9} + x^{2.9}$	0.43

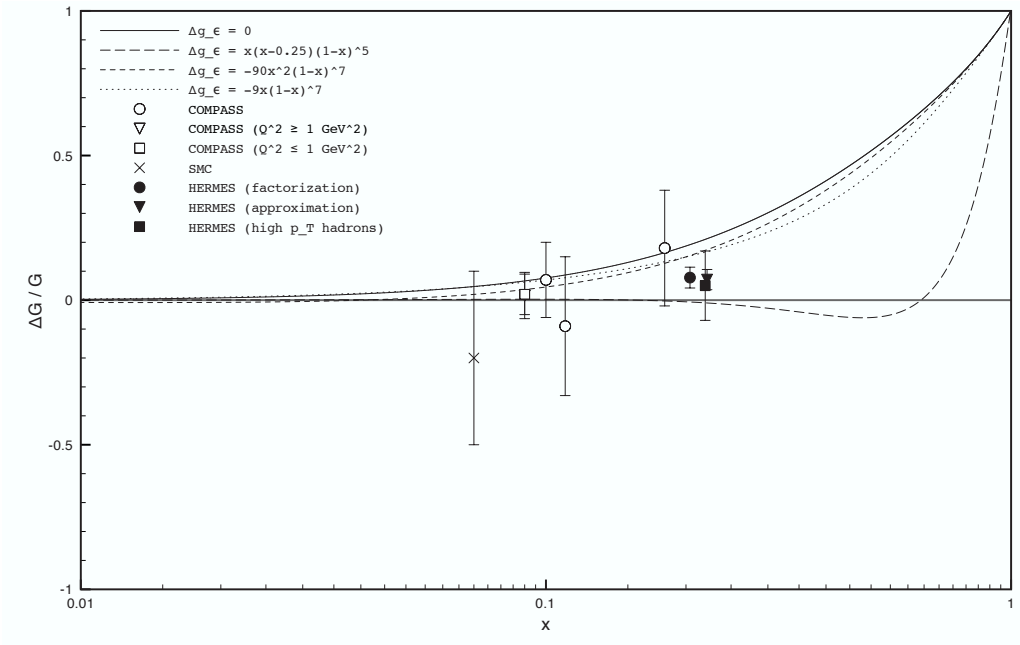

Figure 1: Best fit model asymmetries compared with data.

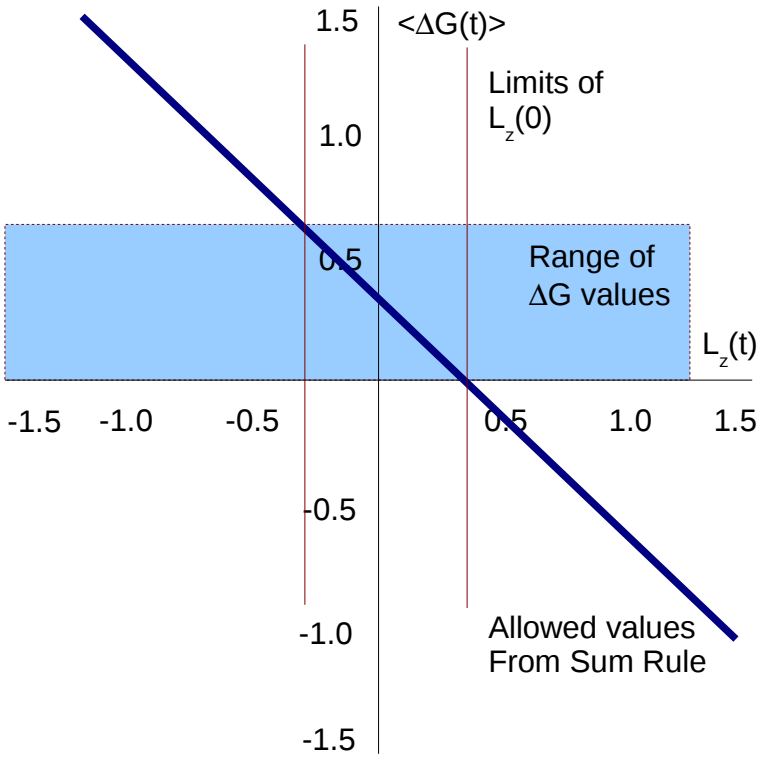

Figure 2: Allowed L_z values versus ΔG.

From these results, a strictly theoretical approach to finding feasible values to L_z yields a range allowed by the "practical" constraints of

$$\begin{aligned} -0.13 \quad &\leq < \Delta G > \leq 0.63 \quad \text{and} \\ -0.29 \quad &\leq L_z(0) \leq 0.47, \end{aligned} \tag{13}$$

where the theoretical and experimental uncertainties have been included in the quoted inequality values. The range is not sensitive to the unpolarized input distributions and the corresponding theoretical uncertainties have been included in this range. The ranges of $< \Delta G >$ and $< L_z >$ appear to be numerically limited by the constraints on $< \Delta g_\epsilon >$, which is limited in absolute value to 0.25 by the constraints. From a theoretical point of view, this results in relatively small values of ΔG and L_z, but the range is still considerable. Using the parameterizations that best agree with data (Table 1) narrows the ranges of ΔG and L_z:

$$0.21 \quad \leq < \Delta G > \leq 0.47 \quad \text{and} \tag{14}$$

$$-0.13 \quad \leq \; L_z(0) \; \leq 0.13, \tag{15}$$

where, again, the uncertainties are included in the extreme values. A sample of parametrizations and data are shown in Figure 1. These results are consistent with data and the MIT Bag model, discussed by Chen and Ji. [7] The corresponding range of L_z for these ΔG values are shown in Figure 2. Using present data, the range of ΔG and L_z have been narrowed, but clearly, accurate data over a wider kinematic range can more significantly constrain both the gluon polarization and the orbital angular momentum of the constituents. The results for the scenarios we have shown are not significantly different from each other.

Our results indicate that the integrated $< \Delta G >$ is likely positive and small at $Q_0^2 \approx 1$ GeV^2. This is consistent with data [1], chiral quark models and the MIT bag model [7]. Although most of our parameterizations of the asymmetry are positive definite, the one in the second line of Table 2 changes sign and is consistent with data. This possibility has been discussed by others and is not ruled out by present data [1, 7]. Many of our parameterizations give a gluon polarization consistent with zero, in agreement with much of the data from RHIC. [1] Clearly there is still work to be done. However, we have provided a mechanism for calculating the gluon asymmetry that allows extraction of information on both ΔG and L_z.

The author would like to thank Krzysztof Kurek for discussions regarding the asymmetry data.

References

[1] A. Airpetian, *et al.,*, Phys. Rev. Lett., **84** (2000) 2584. (HERMES Collaboration); B. Adeva, *et al.,*, (Spin Muon Collaboration), Phys. Rev., **D70** (2004) 012002; B I Abelev, *et al.,*, Phys. Rev. Lett., **97** (2006) 252001 and R Fatemi, arXiv:0710.3207 [hep-ex] (STAR Collaboration); A. Adare, *et al.,*, Phys. Rev., **D76** (2007) 051106 and S. S. Adler, *et al.,*, Phys. Rev., **D73** (2006) 091102 (PHENIX Collaboration); M. Alekseev, *et al.,*, Phys. Lett., **B676** (2009) 31 (COMPASS Collaboration).

[2] A. Airpetian, *et al.,*, Phys. Rev., **D75** (2007) 012007 (HERMES Collaboration); F. Bradamante, Prog. Part. Nucl. Phys., **61** (2008) 229; M. Alekseev, *et al.,*, Phys. Lett., **B660** (2008) 458 (COMPASS Collaboration)

[3] G. P. Ramsey, Y. Binder and D. Sivers, Proceedings of DSPIN-07, Dubna, Russia, Eds., A. V. Efremov and S. V. Goloskokov, c2008, World Scientific, p. 138.

[4] G. P. Ramsey, p. 353, AIP Conference Proceedings **1149**, SPIN-2008, University of Virginia, Charlottesville.

[5] M. Hirai and S. Kumano, Nucl. Phys., **B813** (2009) 106 and M. Burkardt, C. A. Miller and W-D Nowak, arXiv:0812.2208v3 [hep-ph].

[6] CTEQ Collaboration, H. L. Lai *et al.,* Eur. Phys. J., **C12** (2000) 375; D. Stump, *et. al.,* Phys. Rev., **D65** (2002) 014012; MRST Collaboration, A. D. Martin *et al.,* Eur. Phys. J., **C4** (1998) 463 and L. E. Gordon, M. Goshtasbpour and G. P. Ramsey, Phys. Rev., **D58** (1998) 094017.

[7] M. Wakamatsu, Phys. Lett., **B646** (2007) 24 and P. Chen and X. Ji, Phys. Lett., **B660** (2008) 193 and references therein.

EFFECTIVE THREE-PHOTON VERTEX IN A DENSE FERMIONIC MEDIUM

V. V. Skalozub [1†], E.V. Reznikov [2]

(1) *Dnipropetrovsk National University, Dnipropetrovsk, Ukraine*
† *E-mail: reznikovevgenii@mail.ru*

Abstract

The tensor of an effective three-photon vertex has been calculated in the one-loop approximation for a medium with non-zero chemical potential. The tensor properties at various photon wavelengths and frequencies have been analyzed. The case of photon scattering by a magnetic field has been studied in detail. Possible applications of the results obtained have been discussed.

The physical vacuum is the subject of quantum nature, and a variety of phenomena due to the nature was the theoretically calculated and experimentally measured more than fifty years ago. Is, for example, the Casimir effect [1] or scattering of light by light. However, in contrast to the processes in dense media, for these phenomena c-parity remains, and even the presence of a small number of particles does not cause qualitative changes in the photons interaction. In contrast, Furry theorem is violated in dense media [2], and photon vertices with the odd number of external photon lines can exist, and a three-photon vertex is have greatest value of all other new unlocked vertexes. This object also was investigated in the works [3, 4]. In the work [3] processes in a two-dimensional space are considered (so the elements of the tensor can be calculated in exact form, even for the most general case), in the work [4] we have three-dimensional space, but in both cases used the static approximation. Obtained results very interesting, but they describe the phenomena, localized in the media. These processes have a significant influence on the evolution of large objects, consisting of dense matter, like neutron stars and, possibly, white dwarfs, but at the same time, in terms, available to us, experimentally observing of static effects are extremely difficult. One of the important results of works [3, 4] is the proof that the using of Feynman parametrization violate the transversality three-photon vertex, hence to calculate their tensors such parametrization is not applicable. In this work we used the approximation low-frequency photons, which is sufficient to describe most of the new phenomena in a medium, since to high-energy photons medium are asymptotically transparent.

1 Three-photon Vertex in the Static-field Case

In this section, we aim at calculating the nonzero components of the three-photon vertex tensor in a medium; they exist in the one-loop approximation for the state of rest at zero temperature. In a $(3+1)$-dimensional space, this case was examined in more details in work [4]. In case of static fields, the form of the vertex function becomes considerably simpler, with only the following tensor components remaining nonzero:

$$\Pi_{444} = \frac{ie^3}{2\pi^3}(4\sum_{i=1}^{3} J_2(k^{(i)}) + \sum_{n=1,n\neq l}^{3}\sum_{l=1}^{3} J_1(k^{(l)},k^{(n)})((k^{(l)})^2 + (k^{(n)})^2 + (k^{(l)},k^{(n)}) - 4m^2) - 4J_3(k^{(l)},k^{(n)})), \tag{1}$$

$$\Pi_{ij4} = \frac{ie^3}{2\pi^3}\left(\sum_{n=1,n\neq l}^{3}\sum_{l=1}^{3} J_1(k^{(l)},k^{(n)})(k_j^{(1)}k_i^{(3)} - (k^{(1)}k^{(3)})\delta_i j) - 4J_3(k^{(2)})(\delta_{ij} + (k_j^{(1)}k_i^{(3)})\frac{(k^{(1)}k^{(3)}) - (k^{(1)})^2 - (k^{(3)})^2}{(k^{(1)}k^{(3)})^2})\right). \tag{2}$$

Here, J_1, J_2, and J_3 are the functions of the external momenta $k^{(1)}$, $k^{(2)}$, and $k^{(3)}$, the chemical potential μ, and the mass m. The analytical integration for the functions J_1, J_2,

and J_3 to a final result can be fulfilled only in the case where all the momenta are collinear. Otherwise, asymptotic approximations can be derived for J_1 and J_3. The symmetric components Π_{i4j} and Π_{4ij} are obtained by making the corresponding substitutions $k^{(1)} \to k^{(2)}$, $k^{(2)} \to k^{(3)}$, and $k^{(3)} \to k^{(1)}$ for the former, and $k^{(1)} \to k^{(3)}$, $k^{(3)} \to k^{(2)}$, and $k^{(2)} \to k^{(1)}$ for the latter.

For large momenta, $\left(\frac{k^{(1)}}{a}, \frac{k^{(2)}}{a}\right) \gg 1$, and in the symmetric limit, formulas (1) and (2) give the following result for tensor components:

$$\Pi_{444} = O(\frac{k^{(1)}}{a}), \Pi_{ij4} = O(\frac{k^{(1)}}{a}). \tag{3}$$

It testifies that, in the high-momentum and, accordingly, short-distance approximation, the medium becomes asymptotically transparent, and its influence on the field properties is insignificant. This takes place, because the vertex function is proportional to the chemical potential, the latter being a small parameter in the case of high momenta. However, for linear scales $r \geq (\mu^2 - m^2)^{-\frac{1}{2}}$, the substitution of $\Pi_{\mu\nu\gamma}$ by its asymptotic value does not violate the adequacy of description for the properties of an electromagnetic field with an arbitrary strength distribution. Under such conditions, the quantity $\sqrt{\mu^2 - m^2}/k$ is a large parameter, and there is no necessity to use the "adiabatic expansion".

2 Three-photon Vertex in the Case of Low-frequency Photons

In the case of low-frequency photons and, hence, low k_4-values, the determination of multipliers H_n demands that the linear approximation be used and the obtained expressions be expanded into power series of k_4. After carrying out the corresponding calculations, those multipliers can be expressed as follows:

$$\begin{aligned}
H_1 &\approx \frac{n_e(\varepsilon_0) - n_p(\varepsilon_0)}{2i\varepsilon_0[2\mathbf{pk}^{(1)} + (\mathbf{k}^{(1)})^2][-2\mathbf{pk}^{(2)} + (\mathbf{k}^{(2)})^2]}; \\
H_2 &\approx (n_e(\varepsilon_1) - n_p(\varepsilon_1))(2i\varepsilon_1[2\mathbf{pk}^{(1)} - (\mathbf{k}^{(1)})^2][-2\mathbf{p}(\mathbf{k}^{(2)} + \mathbf{k}^{(1)}) + (\mathbf{k}^{(2)})^2 - (\mathbf{k}^{(1)})^2])^{-1}; \\
H_3 &\approx (n_e(\varepsilon_2) - n_p(\varepsilon_2))(2i\varepsilon_2[2\mathbf{pk}^{(2)} - (\mathbf{k}^{(2)})^2](-2\mathbf{p}(\mathbf{k}^{(2)} + \mathbf{k}^{(1)}) + (\mathbf{k}^{(1)})^2 - (\mathbf{k}^{(2)})^2))^{-1},
\end{aligned} \tag{4}$$

where $n_e(\varepsilon_n)$ and $n_p(\varepsilon_n)$ are the electron and positron, respectively, density functions, which look like $n_e(\varepsilon_n) = [1 + \exp(\beta(\varepsilon_n - \mu)]^{-1}$, $n_p(\varepsilon_n) = [1 + \exp(\beta(\varepsilon_n + \mu)]^{-1}$.

The H_n-multipliers generate three groups of terms for each vertex function component, each of the latter including k_4 raised to a certain power ranging from 0 to 4, and terms with k_4 raised to a power larger than one can be neglected. At the same time, the terms without k_4 comprise a static part of the components, which was calculated in work [4]. Then, all we need is to calculate those terms, which depend linearly on k_4:

$$\begin{aligned}
F_{444} &\approx F_{444}^{stat} + Re\{H_1[\mathbf{pk}^{(2)}k_4^{(1)} + (\mathbf{pk}^{(1)} - \varepsilon_0^2)k_4^{(2)}] + H_2[(\varepsilon_0^2 + \mathbf{pk}^{(1)} + \varepsilon_1^2)k_4^{(2)} + \\
&+ (2\varepsilon_0^2 + \mathbf{pk}^{(2)} - \mathbf{k}^{(1)}\mathbf{k}^{(2)} + 2\varepsilon_1^2)k_4^{(1)}] - H_3[(\varepsilon_0^2 - \mathbf{pk}^{(2)} + \varepsilon_2^2)k_4^{(1)} + (2\varepsilon_0^2 - \mathbf{pk}^{(1)} - \mathbf{k}^{(1)}\mathbf{k}^{(2)} + 2\varepsilon_2^2)k_4^{(2)}]\}.
\end{aligned} \tag{5}$$

The function F is coupled with Π by the relation $\Pi_{\mu\nu\gamma} = \frac{ie^3}{(2\pi)^3\beta}\int d^3pF_{\mu\nu\gamma}$. While calculating F_{ij4}, we should take into consideration that $i \neq 4$ and $j \neq 4$, so that $\delta_{i4} = \delta_{j4} = 0$.

Moreover, we use the approximation, for which $k_4^{(a)}k_4^{(b)} = 0$. Therefore, we find

$$\begin{aligned} F_{ij4} &\approx F_{ij4}^{stat} + Re\{\varepsilon_0\delta_{ij}(H_2\varepsilon_1 k_4^{(1)} + H_3\varepsilon_2 k_4^{(2)}) + H_1[(\mathbf{pk}^{(2)}\delta_{ij} + 2p_ip_j - p_ik_j^{(2)} - p_jk_i^{(2)})k_4^{(1)} + \\ &+ (\mathbf{pk}^{(1)}\delta_{ij} + 2p_ip_j - p_ik_j^{(1)} - p_jk_i^{(1)})k_4^{(2)}] + H_2[((\mathbf{p}(2\mathbf{k}^{(1)} + \mathbf{k}^{(2)}) + (k^{(1)}))^2\delta_{ij} + 2p_ip_j + p_ik_j^{(2)} + \\ &+ p_jk_i^{(2)})k_4^{(1)} - ((\mathbf{p}\ \mathbf{k}^{(1)} + (\mathbf{k}^{(1)})^2\delta_{ij} + 2p_ip_j + p_ik_j^{(1)} + p_jk_i^{(1)})k_4^{(2)}] - H_3[((\mathbf{p}(2\mathbf{k}^{(2)} + \mathbf{k}^{(1)}) - \\ &- (\mathbf{k}^{(2)}))^2\delta_{ij} - 2p_ip_j + p_ik_j^{(1)} + p_jk_i^{(1)})k_4^{(2)} + ((-\mathbf{p}\ \mathbf{k}^{(2)} + (\mathbf{k}^{(2)})^2\delta_{ij} + 2p_ip_j - p_ik_j^{(2)} - p_jk_i^{(2)})k_4^{(1)}]\}. \end{aligned} \quad (6)$$

In a similar way, we make transformations for other tensor elements. Taking into account that $F_{i44}^{\rm stat} = F_{ijl}^{\rm stat} = 0$ in the static case, we obtain

$$\begin{aligned} F_{ijl} \approx Im\Bigg[& H_1\varepsilon_0\Big\{\begin{matrix}\{(k_l^{(2)}\delta_{ij}+k_j^{(2)}\delta_{il}- \\ -k_i^{(2)}\delta_{jl}-2p_j\delta_{il})\end{matrix}\Big\}k_4^{(1)} + \\ & + \Big\{\begin{matrix}(k_l^{(1)}\delta_{ij}-k_j^{(1)}\delta_{il}+ \\ +k_i^{(1)}\delta_{jl}+2p_i\delta_{jl})\end{matrix}\Big\}k_4^{(2)}\Big\} + H_2\varepsilon_1\Big\{\begin{matrix}\{(k_i^{(2)}\delta_{jl}-k_l^{(2)}\delta_{ij}-k_j^{(2)}\delta_{il}+(k_i^{(1)}+2p_i)\times \\ \times\delta_{jl}+(k_l^{(1)}+2p_l)\delta_{ij}-(k_j^{(1)}+2p_j)\delta_{il})\end{matrix}\Big\}\times \\ & \times k_4^{(1)} + \Big\{\begin{matrix}(k_l^{(1)}\delta_{ij}-k_j^{(1)}\delta_{il}+ \\ +k_i^{(1)}\delta_{jl}+2p_i\delta_{jl})\end{matrix}\Big\}k_4^{(2)}\Big\} + \\ & H_3\varepsilon_2\Big\{\begin{matrix}\{(k_j^{(1)}\delta_{il}-k_l^{(1)}\delta_{ij}-k_i^{(1)}\delta_{jl}+(k_j^{(1)}-2p_j)\times \\ \times\delta_{il}+(k_l^{(1)}-2p_l)\delta_{ij}-(k_i^{(1)}-2p_i)\delta_{jl})\end{matrix}\Big\}\times \\ & \times k_4^{(2)} + \Big\{\begin{matrix}(k_l^{(2)}\delta_{ij}+k_j^{(2)}\delta_{il}- \\ k_i^{(2)}\delta_{jl}-2p_i\delta_{jl})\end{matrix}\Big\}k_4^{(1)}\Big\}\Bigg], \end{aligned} \quad (7)$$

$$\begin{aligned} F_{i44} &\approx Im[H_2\varepsilon_1[((k_i^{(1)} + 2p_i) - k_i^{(2)})k_4^{(1)} + (k_i^{(1)} + 2p_i)k_4^{(2)}] + H_3\varepsilon_2[((k_i^{(2)} - 2p_i) - k_i^{(1)})k_4^{(2)} + (k_i^{(2)} - 2p_i)k_4^{(1)}] \\ &- \varepsilon_0(H_2 + H_3)[(k_i^{(2)} - 2p_i)k_4^{(1)} + (k_i^{(1)} + 2p_i)k_4^{(2)}]]. \end{aligned} \quad (8)$$

The expressions derived for all tensor elements in the long-wave approximation compose a system that describes such photon–photon processes as the photon decay into two photons, the decay of an electric field into free photons, the generation of a magnetic field in the presence of the electric one, and the interaction between a free photon and a magnetic field. The expressions found for the tensor components testify that the processes of creation of real photons take place only in alternating fields, because the corresponding tensor components include only dynamic parts. Unlike the static case, dynamic processes can be observed "from outside" the medium. Therefore, they are suitable for studying the microscopic volumes in a dense medium.

On the basis of the results obtained, let us consider a case of the interaction between photons and a classical magnetic field in the presence of fermionic plasma. In this case, we have a state of the external field without energy transfer and with a definite fixed spatial momentum, which can be designated as $(k_l^{(1)} + k_l^{(2)})$, where $l \in 1, 3$. Then, the element of the scattering cross-section looks like

$$S = F_{ijl}k_i^{(1)}k_j^{(2)}(k_l^{(1)} + k_l^{(2)}) + F_{44l}k_4^{(1)}k_4^{(2)}(k_l^{(1)} + k_l^{(2)}) + F_{i4l}k_i^{(1)}k_4^{(2)}(k_l^{(1)} + k_l^{(2)}) + F_{4jl}k_4^{(1)}k_j^{(2)}(k_l^{(1)} + k_l^{(2)}). \quad (9)$$

According to the assumption that k_4 is small, the term $F_{44l}k_4^{(1)}k_4^{(2)}(k_l^{(1)} + k_l^{(2)})$ approximately equals zero, whereas the components with k_4 in the terms $F_{i4l}k_i^{(1)}k_4^{(2)}(k_l^{(1)} + k_l^{(2)})$ and $F_{4jl}k_4^{(1)}k_j^{(2)}(k_l^{(1)} + k_l^{(2)})$ – all of them are dynamic contributions – are also reduced. However, since they are written down as $(k_l^{(1)} + k_l^{(2)})$, the equality $k_4^{(1)} = -k_4^{(2)}$ must be satisfied, and we have a process of elastic photon scattering by a magnetic field. Then, the nonzero tensor elements look like $F_{i4l} = F_{i4l}^{\rm stat}$, $\quad F_{4jl} = F_{4jl}^{\rm stat}$,

$$\begin{aligned} & F_{ijl} \approx Imk_4^{(1)}\{H_1\varepsilon_0((k_l^{(2)} - k_l^{(1)})\delta_{ij} + (k_j^{(2)} + k_j^{(1)})\delta_{il} - (k_i^{(2)} + k_i^{(1)})\delta_{jl} - 2p_i\delta_{jl} - 2p_j\delta_{il}) + \\ + \quad & H_2\varepsilon_1[k_i^{(2)}\delta_{jl} - k_l^{(2)}\delta_{ij} - k_j^{(2)}\delta_{il} + p_l\delta_{ij} - p_j\delta_{il}] + H_3\varepsilon_2[k_j^{(1)}\delta_{il} - k_l^{(1)}\delta_{ij} - k_i^{(1)}\delta_{jl} - p_l\delta_{ij} + p_i\delta_{jl}]\}. \end{aligned} \quad (10)$$

One can see that all dynamics of the process is contained in the element F_{ijl}, whereas the other nonzero tensor components describe only the statics. In addition, since we consider

the process of free photon scattering by a magnetic field, the dispersion relations must be satisfied. Therefore, $\mathbf{k}^{(1)} = \mathbf{k}^{(2)} = k$, because $|k_4^{(1)}| = |k_4^{(2)}|$. We can take advantage of this property by multiplying the tensor by the corresponding vectors k. Then, we immediately obtain an expression for the scattering cross-section; it contains only scalar products $(\mathbf{k}^{(1)}, \mathbf{k}^{(2)})$ that can be equalized to each other. The final expression for the effective scattering cross-section has the form

$$\begin{aligned} k_i^{(1)} k_j^{(2)} F_{ijl}(k_l^{(2)} + k_l^{(1)}) &\approx -Imk_4^{(1)}(\mathbf{k})^2\{2(1+\cos\gamma)(\cos\alpha+\cos\beta)\frac{n_e(\varepsilon_0)-n_p(\varepsilon_0)}{2i[2\mathbf{p}\cos\alpha+\mathbf{k}][-2\mathbf{p}\cos\beta+\mathbf{k}]}\mathbf{p} + \\ &+ (\mathbf{k}(1+\cos\gamma) + \frac{\mathbf{p}(\cos\alpha+\cos\beta)}{[-2\mathbf{p}(\cos\beta+\cos\alpha)]}(\frac{n_e(\varepsilon_1)-n_p(\varepsilon_1)}{2i[2\mathbf{p}\cos\alpha-\mathbf{k}]} + \frac{n_e(\varepsilon_2)-n_p(\varepsilon_2)}{2i[2\mathbf{p}\cos\beta-\mathbf{k}]})\}, \end{aligned} \quad (11)$$

where γ is the angle between the vectors $k^{(1)}$ and $k^{(2)}$, and α and β are the angles between the vector p and the corresponding k. As follows from the general form of expression (11), the cross-section of photon scattering by a magnetic field is proportional to the squared absolute value of the photon wave vector. The behavior of this dependence can be used, while studying this scattering process experimentally. Notice that, for instance, in the case of an external magnetic field without a medium, the scattering cross-section is proportional to k^4 [7, 8].

3 Discussion of Results

Thus, we have obtained the explicit expressions for the components of the three-photon vertex tensor in two approximations, the static-field and low-frequency ones, and a special case of the interaction between free photons and a magnetic field is analyzed. The static-case approximation demonstrates the essence of why the nonlinear behaviour of fields emerges in a dense medium. At the same time, it forms a necessary basis for the description of various processes considered above. The low-frequency approximation describes a large number of nonlinear photon–photon interactions and allows dynamic processes to be studied. We consider the photon scattering by a magnetic field as the most interesting case. Therefore, it was examined in more details. As a result, we derived an exact expression for the scattering cross-section. The obtained dependence for the cross-section is a quadratic function of the absolute value of photon momentum. It can be used to experimentally check the presence (formation) of a dense medium.

The phenomena arising in media with broken C-parity are of great interest, first of all, because they are an experimental confirmation of theoretical principles used in quantum electrodynamics. However, physical phenomena of such an origin can also find practical applications even today, mainly, as a detector of the presence of dense fermionic substances and a tool of their research. Using the asymptotic relations that describe processes in the medium, the internal characteristics of such media—first of all, the chemical potential—can be measured.

The low-frequency approximation used in this work reveals new opportunities for taking the influence of a medium on the interaction between fields into consideration. This case can be reduced to a number of probable processes. In our opinion, the process of free photon scattering by a magnetic field is the most interesting. The scattering parameters depend only on the field characteristics and the chemical potential μ of a medium. Theoretically, this process allows one to measure μ by detecting scattered photons. The phenomenon of such a type can find application in the NICA and FAIR projects (where collisions between heavy nuclei are studied) both as a tool for the reliable detection of the very fact of the generation of a dense fermionic matter and to study the properties of this matter.

References

[1] M. Bordag, G.L. Klimchitskaya, U. Mohideen, and V.M. Mostepanenko, *Advances in the Casimir Effect* (Oxford Univ. Press, Oxford, 2009).

[2] W. Furry, Phys. Rev. **51**, 125 (1937).

[3] V.V. Skalozub and A.Yu. Tishchenko, Zh. Eksp. Teor. Fiz. **104**, 3921 (1993).

[4] A.I. Pas'ko and V.V. Skalozub, Ukr. Fiz. Zh. **41**, 1013 (1996).

[5] V. De la Insera V, E. Ferrer, and A.E. Shabad, Trudy Fiz. Inst. Akad. Nauk SSSR **169**, 183 (1986).

[6] V.O. Papanyan and V.I. Ritus, Zh. Eksp. Teor. Fiz. **65**, 1756 (1973).

[7] S.L. Adler, J.N. Bahcall, C.G. Callan, and M.N. Rosenbluth, Phys. Rev. Lett. **25**, 1061 (1970).

[8] A.V. Kuznetsov and N.V. Mikheev, *Electroweak Processes in an External Active Medium* (Yaroslavl State Univ., Yaroslavl, 2010) (in Russian).

THE SLOPE OF THE HADRON SPIN-FLIP AMPLITUDE AND THE DETERMINATION OF $\rho(s,t)$

O.V. Selyugin[1], J.-R. Cudell[2], E. Predazzi[3]

[1] *BLTPh, Joint Institute for Nuclear Research, Dubna, Russia*
[2] *IFPA, AGO Dept., Université de Liège, Liège, Belgium*
[3] *Dipartamento di Fisica Teorica, Università di Torino, Italy*

Abstract

We re-examine the extraction of $\rho(s,t)$, the ratio of the real part to the imaginary part of the scattering amplitude, and of the spin-flip amplitude, from the existing experimental data in the Coulomb-hadron interference region. We show that it is not possible to find reasonable assumptions about the structure of the scattering amplitude of proton-proton and proton-antiproton elastic scattering at high energy that would lead, in proton-antiproton scattering for $3.8 < p_L < 6.0$ GeV/c, to an agreement between data and an analysis based on dispersion relations.

1 Introduction

The calculation via dispersion relations of the ratio of the real part to the imaginary part of the forward spin-non-flip amplitude, $\rho(s,t)$, does not agree with the data until one gets to high energies, and it misses all the interesting intermediate-energy structures.

On the theory side, the situation is very complex and uncertain. Analyticity showed that one could not do without a real part, while polarization data proved that it was not possible to ignore spin complications, as the real part of the spin-non-flip amplitude has a zero, around which the contribution of the spin-flip amplitude, which decreases quite slowly with energy, cannot be ignored.

On the experimental side, the situation is not entirely clear cut either [1], and one of the difficulties is due to the lack of experimental data at high energies and small momentum transfer.

In this talk, we consider in great detail the situation concerning $\rho(s,t)$. The model we propose takes into account all known features of the near-forward proton-proton and proton-antiproton data, *i.e.* different slopes for the spin-non-flip and the spin-flip amplitudes, the value of total cross sections and of $\rho(s,t)$, the relative phase of the Coulomb and hadron amplitudes and the form factors of the nucleons.

[1] selugin@theor.jinr.ru
[2] jr.cudell@ulg.ac.be
[3] predazzi@to.infn.it

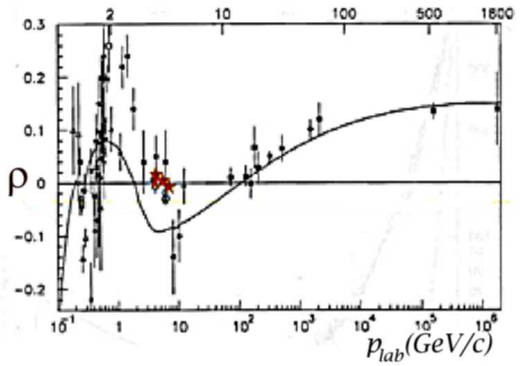

Figure 1: $\rho(s,0)$ - the ratio of the real part to the imaginary part of the elastic scattering amplitude for proton-antiproton scattering at low energies. The curve shows the dispersion relation description for $p\bar{p}$ scattering [8], and the stars are the result of our analysis.

2 Impact of the Coulomb-hadron phase

Let us first compare different approximations for the Coulomb-hadron interference used in fits to the experimental $p\bar{p}$-scattering data [2]. First, we use the simple West-Yennie form of the relative phase [3]. This leads to values for $\rho(s,0)$ shown in the second column of Table 1. The results show the distribution of the values of $\rho(s)$ extracted from the experiments. In two cases, they lie slightly above ρ_{exp} (at $p_L = 4.066,\ 5.603,\ 5.94$ GeV/c); in three cases they lie considerably higher than ρ_{exp} (at $p_L = 5.72,\ 6.23$ GeV/c) and in one case they lie below (at $p_L = 3.7$ GeV/c).

If we take the slightly more complicated phase proposed by Cahn [4], the results are almost the same (see the third column of Table 1). Finally, if we use the expression derived by one of us [5, 6], taking into account the two-photon amplitude and using a dipole form factor, the fit gives different values for $\rho(s)$ (see the last column of Table 1): the results lie above ρ_{exp} for all the considered energies, so that the difference with the predictions of the dispersion analysis gets worse, as shown in Fig. 1.

3 Impact of the spin-flip amplitude

In most analyses, one assumes that the imaginary and real parts of the spin-non-flip amplitude have an exponential behaviour with the same t slope, and that the imaginary and real parts of the spin-flip amplitudes, without the kinematic factor $\sqrt{|t|}$, are proportional to the corresponding spin-non-flip parts of the amplitude, with a proportionality constant independent of s. In [7] it was shown that if the slope of the spin-flip amplitude is bigger than that for spin non-flip, $B_{sf} = 2B_{nf}$, the contribution of the spin-flip amplitude can be felt in the differential cross sections of elastic hadron scattering at small $|t|$. As it is not possible to calculate the hadronic amplitudes from first principles, we have to resort to some assumptions about their s and t dependencies [9, 10].

Here, we use this simple model for the spin-flip amplitude and study its impact on the determination of $\rho(s,t)$. We take the spin-non-flip and spin-flip amplitudes in the

Table 1: The dependence of $\rho(s,0)$ on the model used for the Coulomb-hadron phase in proton-antiproton scattering. N is the number of data points.

$p_L(GeV/c)$	N	$\rho_{exper.}$ [2]	ρ (phase [3])	ρ (phase [4])	ρ (phase [5,6])
3.702	34	$+0.018 \pm 0.03$	$+0.0077 \pm 0.02$	$+0.0078 \pm 0.08$	$+0.028 \pm 0.08$
4.066	34	-0.015 ± 0.03	$+0.0377 \pm 0.02$	$+0.0378 \pm 0.08$	$+0.0324 \pm 0.08$
5.603	215	-0.047 ± 0.03	$+0.035 \pm 0.02$	$+0.036 \pm 0.08$	-0.0017 ± 0.08
5.724	115	-0.051 ± 0.03	$+0.0139 \pm 0.02$	$+0.014 \pm 0.08$	-0.0088 ± 0.08
5.941	140	-0.063 ± 0.03	-0.0003 ± 0.02	-0.004 ± 0.08	-0.0055 ± 0.08
6.234	34	-0.06 ± 0.03	$+0.0162 \pm 0.02$	$+0.0162 \pm 0.08$	-0.0216 ± 0.08

simplest exponential form

$$F^h_{nf} = h_{nf}\ [i + \rho(s,0)]\ e^{B_{nf}t/2}; \quad (1)$$

$$F^h_{sf} = \sqrt{-t}/m_p\ h_{sf}\ [i + \rho(s,0)]\ e^{B^{sf}t/2}, \quad (2)$$

with $B_{sf} = 2B_{nf}$. The differential cross section in this case will be

$$\frac{d\sigma}{dt} = 2\pi\ [|F_{nf}|^2 + 2|F_{sf}|^2], \quad (3)$$

where the amplitudes F_{nf} and F_{sf} will include the corresponding electromagnetic parts and the Coulomb-hadron phase factors as mentioned previously.

The results of our new fits of the proton-antiproton experimental data for p_L in [3.7, 6.2] GeV/c are presented in Table 2. The changes of χ^2 after the inclusion of the spin-flip amplitude are measured by the coefficient

$$R_\chi = \frac{\chi^2_{without\ sf.} - \chi^2_{with\ sf.}}{\chi^2_{without\ sf.}}. \quad (4)$$

We again obtain values of ρ close to zero and prevalently positive. Once again, as seen from Fig. 1, the results do not agree with the prediction by the dispersion analysis [8].

4 Conclusion

The present analysis, which includes the contributions of Coulomb interference and spin effects, shows a contradiction between the extracted value of $\rho(s,0)$ and the predictions from the analysis based on dispersion relations.

If such a situation is confirmed by future new data from the LHC experiments, it could reveal new effects such as , for example, a fundamental length of the order of 1 TeV.

It is likely, however, that the theoretical analysis can be further developed, to include additional corrections connected with possible oscillations in the scattering amplitude and

Table 2: Spin dependence of proton-antiproton elastic scattering

$p_{L(GeV/c)}$	N	$\rho_{exp.}$	R_χ	ρ_{model}	h_{sf}, GeV
3.702	34	$+0.018 \pm 0.03$	8%	$+0.057 \pm 0.02$	49.8 ± 1.4
4.066	34	-0.015 ± 0.03	25%	$+0.052 \pm 0.009$	48.9 ± 0.7
5.603	215	-0.047 ± 0.03	3.5%	$+0.014 \pm 0.005$	$35.6 \pm 4.$
5.724	115	-0.051 ± 0.03	6.5%	$+0.023 \pm 0.004$	38.2 ± 4.5
5.941	140	-0.063 ± 0.03	4.5%	$+0.007 \pm 0.003$	43.2 ± 0.4

with the t-dependence of the spin-flip scattering amplitude. We hope that the forward experiments at NICA will also give valuable information for the improvement of our theoretical understanding of this question.

References

[1] R. Fiore, L. L. Jenkovszky, R. Orava, E. Predazzi, A. Prokudin and O. Selyugin, Int. J. Mod. Phys. A **24** (2009) 2551 [arXiv:0810.2902 [hep-ph]].

[2] S. Trokenheim, Precision measurements of anti-proton - proton elastic scattering at small momentum transfers, Fermilab-Thesis-1995-40 (1995); Durham HepData Project, M.R. Whalley, http://durpdg.dur.ac.uk/hepdata/reac.html;

[3] G. B. West and D. R. Yennie, Phys. Rev. **172** (1968) 1413.

[4] R. Cahn, Z. Phys. C **15** (1982) 253.

[5] S. V. Goloskokov, S. P. Kuleshov and O. V. Selyugin, Mod. Phys. Lett. A **9**, 1207 (1994) [arXiv:hep-ph/9312244].

[6] O. V. Selyugin, Phys. Rev. D **60** (1999) 074028.

[7] O.V. Selyugin, O. V. Selyugin, Mod. Phys. Lett. A **14** (1999) 223.

[8] P. Kroll and W. Schweiger, Nucl. Phys. A **503** (1989) 865.

[9] E. Predazzi and O. V. Selyugin, Eur. Phys. J. A **13** (2002) 471 [arXiv:hep-ph/0111367].

[10] J. R. Cudell, E. Predazzi and O. V. Selyugin, Eur. Phys. J. A **21** (2004) 479 (2004) [arXiv:hep-ph/0401040].

CROSS SECTION AND SINGLE TRANSVERSE TARGET SPIN ASYMMETRY FOR BACKWARD PION ELECTROPRODUCTION

B. Pire[1], K. Semenov-Tian-Shansky[1,2†] and L. Szymanowski[3]

(1) *CPhT, École Polytechnique, CNRS, 91128, Palaiseau, France*
(2) *IFPA, AGO Dept., Université de Liège, 4000 Liège, Belgium*
(3) *National Center for Nuclear Research (NCBJ), Warsaw, Poland*
† *E-mail: Kirill.Semenov@cpht.polytechnique.fr*

Abstract

Nucleon to meson transition distribution amplitudes (TDAs), non-diagonal matrix elements of nonlocal three quark operators between a nucleon and a meson states, arise within the collinear factorized description of hard exclusive electroproduction of mesons off nucleons in the backward direction. Below we address the problem of modelling pion to nucleon TDAs. We suggest a factorized Ansatz for quadruple distributions with input from the soft pion theorem for πN TDAs. In order to satisfy the polynomiality property in its full form the spectral representation is complemented with a D-term like contribution from the nucleon exchange in the u-channel of the reaction. We present our estimates for the backward pion electroproduction unpolarized cross section and its transverse target single spin asymmetry within our composite model for πN TDAs.

The possibility to provide a description for hard exclusive electroproduction of mesons (specifically here pions) off nucleons

$$e(k_1) + N(p_1) \to \big(\gamma^*(q) + N(p_1)\big) + e(k_2) \to e(k_2) + \pi(p_\pi) + N'(p_2). \tag{1}$$

in terms of the fundamental degrees of freedom of QCD resides on the collinear factorization theorem [1] valid in the so-called generalized Bjorken limit: large $Q^2 = -q^2$ and $s = (p+q)^2$; fixed $x_{\rm Bj} = \frac{Q^2}{2(p\cdot q)}$ and the skewness ξ, defined with respect to the t-channel momentum transfer: $\xi = -\frac{(p_2-p_1)\cdot n}{(p_1+p_2)\cdot n}$ (n is the conventional light cone vector occurring in the Sudakov decomposition of the relevant momenta) and small t-channel momentum transfer squared $t \equiv (p_2-p_1)^2$. This factorization theorem allows to present the scattering amplitude as a convolution of the hard part (coefficient function - CF) with non-perturbative soft parts (generalized parton distributions - GPDs and distribution amplitudes - DAs) describing hadronic contents.

According to the conjecture made in [2], a similar collinear factorization theorem for the reaction (1) should be valid in the *complementary* kinematical regime: large Q^2 and s; fixed $x_{\rm Bj}$ and the skewness variable, which is now defined with respect to the u-channel momentum transfer $\Delta \equiv p_\pi - p_1$: $\xi = -\frac{(\Delta\cdot n)}{(p_1+p_\pi)\cdot n}$ and small u-channel momentum transfer squared $u \equiv (p_\pi - p_1)^2$ (rather than small t). Under these assumptions, referred to as the backward kinematics regime, the amplitude of the reaction (1) factorizes as it is presented on Fig.1 (see Ref. [5] for the detailed framework).

This requires the introduction of supplementary non-perturbative objects in addition to GPDs – nucleon to pion transition distribution amplitudes (πN TDAs) defined through the Fourier transform of the πN matrix element of the three-local quark operator on the light cone [3], [4]:

$$\hat{O}^{\alpha\beta\gamma}_{\rho\tau\chi}(\lambda_1 n,\, \lambda_2 n,\, \lambda_3 n) = \Psi^{\alpha}_{\rho}(\lambda_1 n)\Psi^{\beta}_{\tau}(\lambda_2 n)\Psi^{\gamma}_{\chi}(\lambda_3 n). \quad (2)$$

Here α, β, γ stand for quark flavor indices and ρ, τ, χ denote the Dirac spinor indices; antisymmetrization in color is implied; gauge links are omitted in the light-like gauge $A \cdot n = 0$.

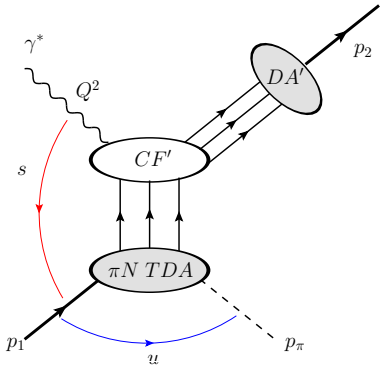

Figure 1: Factorization for hard production of pions off nucleons in the backward kinematics.

The physical picture encoded in baryon to meson TDAs is conceptually close to that contained in baryon GPDs [6]. By Fourier transforming baryon to meson TDAs to the impact parameter space ($\Delta_T \to b_T$) a comprehensible three dimensional physical picture may be obtained. Baryon to meson TDAs encode complementary information on the hadron structure in the transverse plane. In particular, they allow to probe the localization of baryonic charge in the transverse plane and perform the femto-photography of hadrons [7] from a new perspective. There are also hints [8] that πN TDAs may be used as a tool to perform spatial imaging of the structure of nucleon's meson cloud. This point, which still awaits a detailed exploration, opens a fascinating window for the investigation of the various facets of the nucleon's interior. πN TDAs were recently estimated within the light cone quark model [9].

Below we briefly discuss how πN TDAs meet the fundamental requirements following from the symmetries of QCD, summarizing the main results of Refs. [10], [11].

- For given flavor contents spin decomposition of the leading twist-3 πN TDA involve eight invariant functions $V^{\pi N}_{1,2}$, $A^{\pi N}_{1,2}$, $T^{\pi N}_{1,2,3,4}$ each depending on the longitudinal momentum fractions x_i ($\sum_{i=1}^{3} x_i = 2\xi$), skewness parameter ξ and the u-channel momentum transfer squared $\Delta^2 \equiv (p_\pi - p_1)^2$ as well as on the factorization scale μ^2.

- Not all πN TDAs are independent. Taking the account of the isotopic and permutation symmetries (see [11]), one may check that in order to provide description of all isotopic channels of the reaction (1) it suffices to introduce eight independent πN TDAs: four in both the isospin-$\frac{1}{2}$ and the isospin-$\frac{3}{2}$ channels.

- The evolution properties of πN TDAs are described by the appropriate generalization [12] of the Efremov-Radyushkin-Brodsky-Lepage/ Dokshitzer-Gribov-Lipatov-Altarelli-Parisi (ERBL/DGLAP) evolution equations.

- The support of πN TDAs in the longitudinal momentum fractions x_i is given by the intersection of three stripes $-1 + \xi \leq x_i \leq 1 + \xi$ ($\sum_{i=1}^{3} x_i = 2\xi$) [10]. One can distinguish the ERBL-like domain, in which all x_i are positive and two type of DGLAP-like domains, in which one or two x_i turn negative.

- The polynomiality property for the Mellin moments of πN TDAs in the longitudinal momentum fractions x_i is the direct consequence of the underlying Lorentz symmetry. Similarly to the GPD case, the $(n_1,\, n_2,\, n_3)$-th ($n_1 + n_2 + n_3 \equiv N$) Mellin

moments of nucleon to meson TDAs in x_1, x_2, x_3 are polynomials of power N or $N+1$ in the skewness variable ξ.

- Crossing transformation relates πN TDAs to πN generalized distribution amplitudes (GDAs), defined by the matrix element of the same operator (2) between the πN state and the vacuum. The soft pion theorem [13] for πN GDAs [14] also constrains πN TDAs near the soft pion threshold $\xi = 1$, $\Delta^2 = M^2$, where M is the nucleon mass.

The most direct way to ensure both the polynomiality and the support properties for πN TDAs is to employ the spectral representation in terms of quadruple distributions [10]. Our strategy of modeling πN TDAs [15] is completely analogous to that employed for modeling nucleon GPDs with the help of Radyushkin's double distribution Ansatz [16]. The main difficulty is that, contrary to GPDs, baryon to meson TDAs lack a comprehensible forward limit ($\xi = 0$). In order to propose a model for quadruple distributions it is illuminating to consider the alternative limit $\xi = 1$, in which πN TDAs are constrained by the chiral dynamics through the soft pion theorem [13] for πN GDAs. In this limit πN TDAs are expressed through the nucleon DAs $\{V^p,\, A^p,\, T^p\}$ [17]. For example, πN TDAs $V_1^{\pi^0 p}$, $A_1^{\pi^0 p}$, $T_1^{\pi^0 p}$ reduce to the following combination of the nucleon DAs

$$\begin{aligned}
&\big\{V_1^{\pi^0 p},\, A_1^{\pi^0 p}\big\}(x_1, x_2, x_3, \xi = 1) = -\frac{1}{4} \times \frac{1}{2}\big\{V^p,\, A^p\big\}\left(\frac{x_1}{2}, \frac{x_2}{2}, \frac{x_3}{2}\right);\\
&T_1^{\pi^0 p}(x_1, x_2, x_3, \xi = 1) = \frac{1}{4} \times \frac{3}{2} T^p\left(\frac{x_1}{2}, \frac{x_2}{2}, \frac{x_3}{2}\right),
\end{aligned} \tag{3}$$

and $\big\{V_2^{\pi^0 p},\, A_2^{\pi^0 p},\, T_2^{\pi^0 p}\big\}(x_1, x_2, x_3, \xi = 1) = -\frac{1}{2}\big\{V_1^{\pi^0 p},\, A_1^{\pi^0 p},\, T_1^{\pi^0 p}\big\}(x_1, x_2, x_3, \xi = 1)$.

With appropriate change of spectral parameters the spectral representation for πN TDAs of Ref. [10] can be rewritten as:

$$\begin{aligned}
H(w_i,\, v_i,\, \xi) = &\int_{-1}^{1} d\kappa_i \int_{-\frac{1-\kappa_i}{2}}^{\frac{1-\kappa_i}{2}} d\theta_i \int_{-1}^{1} d\mu_i \int_{-\frac{1-\mu_i}{2}}^{\frac{1-\mu_i}{2}} d\lambda_i\, \delta\big(w_i - \frac{\kappa_i - \mu_i}{2}(1-\xi) - \kappa_i \xi\big)\\
&\times \delta\big(v_i - \frac{\theta_i - \lambda_i}{2}(1-\xi) - \theta_i \xi\big)\, F(\kappa_i,\, \theta_i, \mu_i,\, \lambda_i).
\end{aligned} \tag{4}$$

The index $i = 1, 2, 3$ here refers to one of three possible choices of independent variables (quark-diquark coordinates): $w_i = x_i - \xi$, $v_i = \frac{1}{2}\sum_{k,l=1}^{3} \varepsilon_{ikl} x_k$. We suggest to use the following factorized Ansatz for the quadruple distribution F in (4):

$$F(\kappa_i,\, \theta_i,\, \mu_i,\, \lambda_i) = 4V(\kappa_i,\, \theta_i)\, h(\mu_i,\, \lambda_i), \tag{5}$$

where $V(\kappa_i,\, \theta_i)$ is the combination of nucleon DAs to which πN TDA in question reduces in the limit $\xi = 1$ (*c.f.* Eq. (3)), rewritten in terms of independent variables: $\kappa_i = 2y_i - 1$; $\theta_i = \sum_{k,l=1}^{3} \varepsilon_{ikl} y_k$.

The profile function $h(\mu_i,\, \lambda_i)$ is normalized as $\int_{-1}^{1} d\mu_i \int_{-\frac{1-\mu_i}{2}}^{\frac{1-\mu_i}{2}} d\lambda_i\, h(\mu_i,\, \lambda_i) = 1$. The support of the profile function h is also that of a baryon DA. The simplest assumption for the profile is to take it to be determined by the asymptotic form of baryon DA ($120 y_1 y_2 y_3$ with $\sum_{i=1}^{3} y_i = 1$) rewritten in terms of variables $\mu_i = 2y_i - 1$, $\lambda_i = \sum_{k,l=1}^{3} \varepsilon_{ikl} y_k$:

$$h(\mu_i,\, \lambda_i) = \frac{15}{16}\,(1+\mu_i)((1-\mu_i)^2 - 4\lambda_i^2). \tag{6}$$

Similarly to the GPD case [18], in order to satisfy the polynomiality condition in its complete form the spectral representation for πN TDAs $\{V_{1,2},\, A_{1,2},\, T_{1,2}\}^{\pi N}$ should be complemented by a D-term like contribution. The simplest possible model for such a D-term is the contribution of the u-channel nucleon exchange into πN TDAs computed in [11]. In this way we come to a two component model for πN TDAs involving the spectral representation part, based on the factorized Ansatz (5) with the profile (6) and with input from the soft pion theorem, and the D-term, originating from the nucleon exchange in the u-channel. It provides a model for πN TDAs in the complete domain of their definition.

Within the factorized approach the leading order (both in α_s and $1/Q$) amplitude of backward hard pion production $\mathcal{M}^{\lambda}_{s_1 s_2}$ reads [5]:

$$\mathcal{M}^{\lambda}_{s_1 s_2} = \mathcal{C}\frac{1}{Q^4}\Big[\mathcal{S}^{\lambda}_{s_1 s_2}\mathcal{I}(\xi,\Delta^2) + \mathcal{S}'^{\lambda}_{s_1 s_2}\mathcal{I}'(\xi,\Delta^2)\Big]. \tag{7}$$

The spin structures $\mathcal{S}$ and $\mathcal{S}'$ are defined as $\mathcal{S}^{\lambda}_{s_1 s_2} \equiv \bar{U}(p_2,s_2)\hat{\mathcal{E}}(\lambda)\gamma^5 U(p_1,s_1)\,;\ \mathcal{S}'^{\lambda}_{s_1 s_2} \equiv \frac{1}{M}\bar{U}(p_2,s_2)\hat{\mathcal{E}}(\lambda)\hat{\Delta}_T\gamma^5 U(p_1,s_1)$, where $\mathcal{E}$ denotes the polarization vector of the virtual photon and U is the usual nucleon Dirac spinor. $\mathcal{C}$ is the normalization constant $\mathcal{C} \equiv -i\frac{(4\pi\alpha_s)^2\sqrt{4\pi\alpha_{em}}f_N^2}{54 f_\pi}$, where $\alpha_{em}(\alpha_s)$ stands for the electromagnetic (strong) coupling, $f_\pi = 93$MeV is the pion decay constant and f_N is the normalization constant of the nucleon DA [17].

The coefficients $\mathcal{I}$, $\mathcal{I}'$ result from the calculation of 21 diagrams contributing to the hard scattering amplitude [5]:

$$\big\{\mathcal{I},\,\mathcal{I}'\big\}(\xi,\Delta^2) \equiv \int d^3x\,\delta\Big(\sum_i x_i - 2\xi\Big)\int d^3y\,\delta\Big(\sum_i y_i - 1\Big)\left(2\sum_{\alpha=1}^{7}\big\{T_\alpha,\,T'_\alpha\big\} + \sum_{\alpha=8}^{14}\big\{T_\alpha,\,T'_\alpha\big\}\right),$$

where the convolution integrals in x_i and y_i stand over the supports of πN TDAs and nucleon DAs respectively. The explicit expressions for the coefficients T_α and T'_α for $\gamma^\star p \to \pi^0 p$ channel are presented in the Table I of Ref. [5]. The result for $\gamma^\star p \to \pi^+ n$ channel can be read off the same Table with the obvious changes: $Q^u \rightleftarrows Q^d$; $\{V_{1,2}, A_{1,2}, T_{1,2,3,4}\}^{p\pi^0} \to \{V_{1,2}, A_{1,2}, T_{1,2,3,4}\}^{p\pi^+}$; $\{V,\,A,\,T\}^p \to \{V,\,A,\,T\}^n$. In [15] we develop a reliable method for the calculation of the corresponding convolution integrals.

Within the suggested factorization mechanism for backward pion electroproduction only the transverse cross section $\frac{d^2\sigma_T}{d\Omega_\pi}$ receives a contribution at the leading twist level. We establish the following formula for the unpolarized transverse cross section through the coefficients $\mathcal{I}$, $\mathcal{I}'$ introduced in (7):

$$\frac{d^2\sigma_T}{d\Omega_\pi} = |\mathcal{C}|^2\frac{1}{Q^6}\frac{\Lambda(s,m^2,M^2)}{128\pi^2 s(s-M^2)}\frac{1+\xi}{\xi}\big(|\mathcal{I}|^2 - \frac{\Delta_T^2}{M^2}|\mathcal{I}'|^2\big), \tag{8}$$

where $\Lambda(x,y,z) = \sqrt{x^2+y^2+z^2-2xy-2xz-2yz}$ is the usual Mandelstam function. Within our two component model for πN TDAs $\mathcal{I}$ receives contributions both from the spectral representation component and nucleon pole exchange contribution. $\mathcal{I}'$ is determined solely by the nucleon pole contribution. On Fig. 2 we present our estimates for the unpolarized cross section $\frac{d^2\sigma_T}{d\Omega_\pi}$ of backward production of π^+ and π^0 off protons for $Q^2 = 10\text{GeV}^2$ and $u = -0.5\text{GeV}^2$ in nb/sr. CZ solution [17] for the nucleon DAs is used

as phenomenological input for our model. The magnitude of the cross sections is large enough for a detailed investigation to be carried at high luminosity experiments such as J-lab@12GeV and EIC. The scaling law for the unpolarized cross section (8) is $1/Q^8$.

Asymmetries, being ratios of the cross sections, are less sensitive to perturbative corrections. Therefore, they are usually considered as more reliable observables to test the factorized description of hard reactions. For the backward pion electroproduction the evident candidate is the single transverse target spin asymmetry (STSA) [19] defined as:

$$\mathcal{A} = \frac{1}{|\vec{s}_1|}\frac{\left(\int_0^{\pi} d\tilde{\varphi}|\mathcal{M}_T^{s_1}|^2 - \int_{\pi}^{2\pi} d\tilde{\varphi}|\mathcal{M}_T^{s_1}|^2\right)}{\left(\int_0^{2\pi} d\tilde{\varphi}|\mathcal{M}_T^{s_1}|^2\right)} = -\frac{4}{\pi}\frac{\frac{|\Delta_T|}{M}\,\mathrm{Im}(\mathcal{I}'(\mathcal{I})^*)}{|\mathcal{I}|^2 - \frac{\Delta_T^2}{M^2}|\mathcal{I}'|^2}. \qquad (9)$$

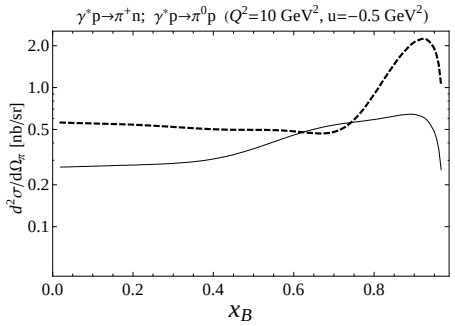

Figure 2: Unpolarized cross section for backward π^+ (solid) and π^0 (dashed) production off proton.

Here $\tilde{\varphi} \equiv \varphi - \varphi_s$, where φ is the angle between leptonic and hadronic planes and φ_s is the angle between the leptonic plane and the transverse spin of the target. Our two component model for πN TDAs provides a non-vanishing numerator in the last equality of (9) thanks to the interfering contributions of the spectral part into $\mathrm{Im}\mathcal{I}(\xi)$ and of the nucleon pole part into $\mathrm{Re}\mathcal{I}'(\xi)$.

On Fig. 3 we show the result of our calculation of the STSA for backward π^+ and π^0 electroproduction off protons for $Q^2 = 10\,\mathrm{GeV}^2$ and $u = -0.5\,\mathrm{GeV}^2$. STSA turns out to be sizable in the valence region and its measurement should be considered as a crucial test of the applicability of our collinear factorized scheme for backward pion electroproduction.

Our estimates of backward pion electroproduction cross section and single transverse spin asymmetry make us hope for bright experimental prospects for measuring baryon to meson TDAs with high luminosity electron beams such as J-lab@ 12 GeV and EIC. Experimental data from J-lab@ 6 GeV on backward π^+, π^0, η and ω meson production are currently being analyzed [20]. We eagerly await for the experimental evidences for validity of the factorized picture of backward electroproduction reactions suggested in our approach.

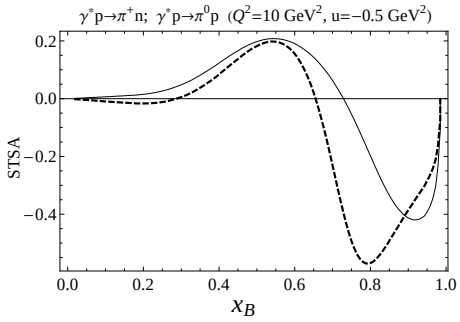

Figure 3: Single transverse spin asymmetry for backward π^+ (solid) and π^0 (dashed) production off proton.

This work is supported in part by the Polish NCN grant DEC-2011/01/B/ST2/03915 and by the French-Polish Collaboration Agreement Polonium.

References

[1] J. C. Collins, L. Frankfurt and M. Strikman, Phys. Rev. D **56** (1997) 2982.

[2] L. L. Frankfurt, P. V. Pobylitsa, M. V. Polyakov and M. Strikman, Phys. Rev. D **60** (1999) 014010; L. Frankfurt, M. V. Polyakov, M. Strikman, D. Zhalov and M. Zhalov, arXiv:hep-ph/0211263.

[3] A. V. Efremov and A. V. Radyushkin, Theor. Math. Phys. **42** (1980) 97 [Teor. Mat. Fiz. **42** (1980) 147].

[4] G. P. Lepage and S. J. Brodsky, Phys. Rev. D **22** (1980) 2157.

[5] J. P. Lansberg, B. Pire and L. Szymanowski, Phys. Rev. D **75** (2007) 074004 [Erratum-ibid. D **77** (2008) 019902].

[6] M. Burkardt, Phys. Rev. D **62** (2000) 071503.

[7] J. P. Ralston and B. Pire, Phys. Rev. D **66** (2002) 111501.

[8] M. Strikman and C. Weiss, Phys. Rev. D **80** (2009) 114029.

[9] M. Pincetti, B. Pasquini and S. Boffi, arXiv:0807.4861 [hep-ph]; B. Pasquini, M. Pincetti and S. Boffi, Phys. Rev. D **80** (2009) 014017.

[10] B. Pire, K. Semenov-Tian-Shansky and L. Szymanowski, Phys. Rev. D **82** (2010) 094030.

[11] B. Pire, K. Semenov-Tian-Shansky, L. Szymanowski, Phys. Rev. D **84** (2011) 074014.

[12] B. Pire and L. Szymanowski, Phys. Lett. B **622** (2005) 83.

[13] P. V. Pobylitsa, M. V. Polyakov and M. Strikman, Phys. Rev. Lett. **87** (2001) 022001.

[14] V. M. Braun, D. Y. Ivanov, A. Lenz and A. Peters, Phys. Rev. D **75** (2007) 014021.

[15] J. P. Lansberg, B. Pire, K. Semenov-Tian-Shansky and L. Szymanowski, *in preparation.*

[16] I. V. Musatov and A. V. Radyushkin, Phys. Rev. D **61** (2000) 074027.

[17] V.L. Chernyak and I.R. Zhitnitsky, Nucl. Phys. **B 246** (1984) 52.

[18] M. V. Polyakov and C. Weiss, Phys. Rev. D **60** (1999) 114017.

[19] J. P. Lansberg, B. Pire, L. Szymanowski, J. Phys. Conf. Ser. **295** (2011) 012090.

[20] K. Park, V. Kubarovsky, P. Stoler, *private communication.*

MAGNETIC MOMENT OF N^* RESONANCES IN CHIRAL CONSTITUENT QUARK MODEL

Neetika Sharma and Harleen Dahiya

Department of Physics, Dr. B.R. Ambedkar National Institute of Technology, Jalandhar, 144011, India

Abstract

The chiral quark model gives a reasonably good description of many low-energy observables by incorporating the effective degrees carried by the constituent quarks and Goldstone bosons. We calculate the magnetic moments of negative-parity low-lying nucleon resonances in the chiral constituent quark model and discuss the effect of Goldstone boson degrees of freedom. The results obtained are compared with the calculations of the other phenomenological models.

The study of magnetic moments of the nucleon and its resonances is one of the interesting topics in hadron physics as it provides valuable insight into the nonperturbative aspects of QCD. One of the important lowest lying nucleon resonance with $J^P = \frac{1}{2}^-$ is the $S_{11}(1535)$. In particular, the large mass splitting between the nucleon ground state $N(939)$ and its negative parity partner $N^*(1535)$ is connected to the spontaneous breaking of the chiral symmetry [1]. For the $S_{11}(1535)$ resonance, it is believed that its magnetic moment can be extracted through the process of $\gamma p \to \gamma\eta p$ [2]. Since this resonance strongly couples to the ηN channel, the η meson in the final state can be regarded as a probe of the $S_{11}(1535)$ resonance in intermediate state.

In the low energy regime, chiral constituent quark model with spin-spin generated configuration mixing (χCQM) [3] successfully explains the "Proton spin crisis" and other related properties [4–8]. The χCQM is further extended to calculate the octet and decuplet baryon magnetic moments incorporating the sea quark polarizations and their orbital angular momentum through a generalization of the Cheng-Li mechanism [9, 10]. In this work, we intend to extend the applicability of the model to study the magnetic moments of the negative-parity low-lying nucleon resonances with orbital angular moment being 1.

In the nonrelativistic SU(6) constituent quark model, the lowest-lying negative-parity nucleon resonances are $|N^2P_{1/2}\rangle$ and $|N^4P_{1/2}\rangle$, where the usual spectroscopic notations $^2P_{1/2}$ and $^4P_{1/2}$ are used to indicate their total quark spin $S = 1/2,\ 3/2$ ($2S+1 = 2,\ 4$), orbital angular momentum $L = 1$ (P-wave), and total angular momentum $J = 1/2$ [11]. The wavefunctions of the $|N^2P_{1/2}\rangle$ and $|N^4P_{1/2}\rangle$ states are explicitly given as

$$|N^2P_{1/2}\rangle = \frac{1}{\sqrt{2}}\sum_{m_l m_s}\langle\, 1\,\frac{1}{2}\; m_l\, m_s \,|\, \frac{1}{2}\,\frac{1}{2}\,\rangle \left\{\psi^{\rho}_{1m_l}\Big[\frac{1}{\sqrt{2}}\big(\chi^{\lambda}_{m_s}\,\phi^{\rho} + \chi^{\rho}_{m_s}\,\phi^{\lambda}\big)\Big] + \psi^{\lambda}_{1m_l}\Big[\frac{1}{\sqrt{2}}\big(\chi^{\rho}_{m_s}\,\phi^{\rho} - \chi^{\lambda}_{m_s}\,\phi^{\lambda}\big)\Big]\right\}, \tag{1}$$

$$|N^4P_{1/2}\rangle = \frac{1}{\sqrt{2}}\sum_{m_l m_s}\langle\, 1\,\frac{3}{2}\; m_l\; m_s \,|\, \frac{1}{2}\,\frac{1}{2}\,\rangle \Big[\,\psi^{\rho}_{1m_l}\,\chi^{s}_{m_s}\,\phi^{\rho} + \,\psi^{\lambda}_{1m_l}\,\chi^{s}_{m_s}\,\phi^{\lambda}\,\Big], \tag{2}$$

where ψ, χ, and ϕ denote the spatial, spin, and flavor wavefunctions [12].

The spin angular momentum $S = 1/2$ couples with the orbital angular momentum $L = 1$ to give the total angular momentum $J = 1/2$ and $J = 3/2$. The physical eigenstates are linear combinations of these two states. The physical states for the four L=1 negative-parity resonances are:

$$|S_{11}(1535)\rangle = \cos\theta|N^2P_{1/2}\rangle - \sin\theta|N^4P_{1/2}\rangle\,, |S_{11}(1650)\rangle = \sin\theta|N^2P_{1/2}\rangle + \cos\theta|N^4P_{1/2}\rangle\,. \tag{3}$$

The magnetic moments of the $S_{11}(1535)$ and $S_{11}(1650)$ resonances, in terms of the $|N^2P_{1/2}\rangle$ and $|N^4P_{1/2}\rangle$ states are expressed as

$$\mu(S_{11}(1535)) = \mu(N^2P_{1/2})\cos^2\theta + \mu(N^4P_{1/2})\sin^2\theta - 2\,\langle\, N^2P_{1/2}\,|\,\mu_z\,|\,N^4P_{1/2}\,\rangle\sin\theta\cos\theta\,,$$

$$\mu(S_{11}(1650)) = \mu(N^2P_{1/2})\sin^2\theta + \mu(N^4P_{1/2})\cos^2\theta + 2\,\langle\, N^2P_{1/2}\,|\,\mu_z\,|\,N^4P_{1/2}\,\rangle\sin\theta\cos\theta\,.$$

The magnetic moments of the qqq baryons has contributions coming from both quark spin and orbital angular momentum, i.e. $\boldsymbol{\mu} = \boldsymbol{\mu^S} + \boldsymbol{\mu^L}$ with

$$\boldsymbol{\mu^S} = \sum_i \boldsymbol{\mu_i^s} = \sum_i \frac{Q_i}{2m_i}\,\boldsymbol{s}_i = \Delta u\mu_u + \Delta d\mu_d + \Delta s\mu_s\,, \tag{4}$$

$$\boldsymbol{\mu^L} = \sum_i \boldsymbol{\mu_i^l} = \sum_i \frac{Q_i}{2m_i}\,\boldsymbol{l}_i = \Delta u^{(1)}\mu_u + \Delta d^{(1)}\mu_d + \Delta s^{(1)}\mu_s\,, \tag{5}$$

where the index i sums over three quarks. The spin polarizations $\Delta q = q^\uparrow - q^\downarrow$ ($q^\uparrow$ or $q^\downarrow$ being the number of quarks with spin up or spin down) and $\Delta q^{(1)} = q^{(1)} - q^{(-1)}$ [6] ($q^{(1)}$ or $q^{(-1)}$ being the number of quarks with the projection of the orbital angular momentum to be $m_L = -1$). Here, $\mu_q = \frac{e_q}{2M_q}$ ($q = u, d, s, c$) is the quark magnetic moment, e_q and M_q are the electric charge and mass for the q quark, respectively.

The magnetic moment of the $S_{11}(1535)$ and $S_{11}(1650)$ states in the constituent quark model are expressed as

$$\begin{aligned}
\mu(S_{11}^+(1535)) &= \left(-\frac{2}{9}\mu_u^S - \frac{1}{9}\mu_d^S + \frac{4}{9}\mu_u^L + \frac{2}{9}\mu_d^L\right)\cos^2\theta + \left(\frac{10}{9}\mu_u^S + \frac{5}{9}\mu_d^S\right. \\
&\quad \left. -\frac{1}{9}\mu_u^L - \frac{2}{9}\mu_d^L\right)\sin^2\theta - 2\sin\theta\cos\theta\left(\frac{4}{9}\mu_u^S - \frac{4}{9}\mu_d^S\right)\,, \qquad (6)\\
\mu(S_{11}^0(1535)) &= \left(-\frac{1}{9}\mu_u^S - \frac{2}{9}\mu_d^S + \frac{2}{9}\mu_u^L + \frac{4}{9}\mu_d^L\right)\cos^2\theta + \left(\frac{5}{9}\mu_u^S + \frac{10}{9}\mu_d^S\right. \\
&\quad \left. -\frac{2}{9}\mu_u^L - \frac{1}{9}\mu_d^L\right)\sin^2\theta - 2\sin\theta\cos\theta\left(-\frac{4}{9}\mu_u^S + \frac{4}{9}\mu_d^S\right)\,, \qquad (7)\\
\mu(S_{11}^+(1650)) &= \left(-\frac{2}{9}\mu_u^S - \frac{1}{9}\mu_d^S + \frac{4}{9}\mu_u^L + \frac{2}{9}\mu_d^L\right)\sin^2\theta + \left(\frac{10}{9}\mu_u^S + \frac{5}{9}\mu_d^S\right. \\
&\quad \left. -\frac{1}{9}\mu_u^L - \frac{2}{9}\mu_d^L\right)\cos^2\theta + 2\sin\theta\cos\theta\left(\frac{4}{9}\mu_u^S - \frac{4}{9}\mu_d^S\right)\,, \qquad (8)\\
\mu(S_{11}^0(1650)) &= \left(-\frac{1}{9}\mu_u^S - \frac{2}{9}\mu_d^S + \frac{2}{9}\mu_u^L + \frac{4}{9}\mu_d^L\right)\sin^2\theta + \left(\frac{5}{9}\mu_u^S + \frac{10}{9}\mu_d^S\right. \\
&\quad \left. -\frac{2}{9}\mu_u^L - \frac{1}{9}\mu_d^L\right)\cos^2\theta + 2\sin\theta\cos\theta\left(-\frac{4}{9}\mu_u^S + \frac{4}{9}\mu_d^S\right)\,. \qquad (9)
\end{aligned}$$

The key to understand the magnetic moment of the baryons, in the χCQM formalism [4], is the fluctuation process $q^{\pm} \rightarrow \mathrm{GB} + q^{'\mp} \rightarrow (q\bar{q}^{'}) + q^{'\mp}$, where GB represents the Goldstone boson and $q\bar{q}^{'} + q^{'}$ constitute the "quark sea" [6, 5]. The effective Lagrangian describing the interaction between quarks and a nonet of GBs, can be expressed as $\mathcal{L} = g_8 \bar{\mathbf{q}} \left(\Phi + \zeta \frac{\eta'}{\sqrt{3}} I \right) \mathbf{q} = g_8 \bar{\mathbf{q}} \left(\Phi' \right) \mathbf{q}$, where $\zeta = g_1/g_8$, g_1 and g_8 are the coupling constants for the singlet and octet GBs, respectively, I is the 3×3 identity matrix. The GB field can be expressed as

$$\Phi' = \begin{pmatrix} \frac{\pi^0}{\sqrt{2}} + \beta\frac{\eta}{\sqrt{6}} + \zeta\frac{\eta^{'}}{\sqrt{3}} & \pi^+ & \alpha K^+ \\ \pi^- & -\frac{\pi^0}{\sqrt{2}} + \beta\frac{\eta}{\sqrt{6}} + \zeta\frac{\eta^{'}}{\sqrt{3}} & \alpha K^0 \\ \alpha K^- & \alpha \bar{K}^0 & -\beta\frac{2\eta}{\sqrt{6}} + \zeta\frac{\eta^{'}}{\sqrt{3}} \end{pmatrix} \text{ and } \quad q = \begin{pmatrix} u \\ d \\ s \end{pmatrix} . \quad (10)$$

The parameter $a(= |g_8|^2)$ denotes the probability of chiral fluctuation $u(d) \rightarrow d(u) + \pi^{+(-)}$, whereas $\alpha^2 a$, $\beta^2 a$ and $\zeta^2 a$ respectively denote the probabilities of fluctuations $u(d) \rightarrow s + K^{-(0)}$, $u(d,s) \rightarrow u(d,s) + \eta$, and $u(d,s) \rightarrow u(d,s) + \eta^{'}$.

The sea and orbital quark spin polarizations corresponding to each baryon can be calculated by substituting for each valence quark

$$q^{\uparrow} \rightarrow P_q q^{\uparrow} + |\psi(q^{\uparrow})|^2 , \quad (11)$$

$$q^{(1)} \rightarrow T_q q^{(1)} + |\psi(q^{(1)})|^2 , \quad (12)$$

where P_q and T_q are the probability of no emission of GBs from quark $q^{\uparrow}$ and $q^{(1)}$, respectively, and $|\psi(q^{\uparrow})|^2$ and $|\psi(q^{(1)})|^2$ are the probability of transforming a $q^{\uparrow}$ and $q^{(1)}$ quark [6]. For the orbital angular momentum contributions readers are requested to refer to the Ref. [10].

We can calculate the magnetic moment of the N^* resonances in the same framework. In this work, we have calculated the magnetic moment of the states $S_{11}^+(1535)$, $S_{11}^0(1535)$, $S_{11}^+(1650)$, and $S_{11}^0(1650)$ states. The calculation of magnetic moments in χCQM involve the symmetry breaking parameters a, $a\alpha^2$, $a\beta^2$, $a\zeta^2$, representing, respectively, the probabilities of fluctuations of a constituent quark into pions, K, η, $\eta^{'}$. The best fit to the set of parameters obtained by carrying out a fine grained analysis of the spin and flavor distribution functions of proton [6, 7] leading to $a = 0.12$, $\alpha = \beta = 0.45$, $\zeta = -0.15$.

Using the value $\theta = -31.7^{\circ}$ in Eqs. (6)-(9), we obtain

$$\begin{aligned} \mu_{S_{11}^+(1535)} &= 1.89\ \mu_N \quad \text{and} \quad \mu_{S_{11}^0(1535)} = -1.28\ \mu_N , \\ \mu_{S_{11}^+(1650)} &= 0.11\ \mu_N \quad \text{and} \quad \mu_{S_{11}^0(1650)} = 0.95\ \mu_N , \end{aligned}$$

Using the Eqs. (11)-(12) and the set of χCQM parameters discussed above, we obtain

$$\begin{aligned} \mu_{S_{11}^+(1535)} &= 2.09\ \mu_N \quad \text{and} \quad \mu_{S_{11}^0(1535)} = -1.57\ \mu_N , \\ \mu_{S_{11}^+(1650)} &= -0.29\ \mu_N \quad \text{and} \quad \mu_{S_{11}^0(1650)} = 0.98\ \mu_N . \end{aligned}$$

Acknowledgments

The authors would like to thank DAE-BRNS (Ref No: 2010/37P/48/BRNS/1445) and the organizers of DSPIN-2011 for the financial support.

References

[1] N. Isgur and G. Karl, Phys. Lett. **B**72 (1977) 109; Phys. Lett. **B**74 (1978) 353; Phys. Rev. **D**18 (1978) 4187; Phys. Rev. **D**19 (1979) 2653.

[2] W.T. Chiang, S.N. Yang, M. Vanderhaeghen, and D. Drechsel, Nucl. Phys. **A**723 (2003) 205.

[3] S. Weinberg, Physica **A**96 (1979) 327; A. Manohar and H. Georgi, Nucl. Phys. **B**234 (1984) 189.

[4] T.P. Cheng and L.F. Li, Phys. Rev. Lett. **7**4 (1995) 2872; Phys. Rev. **D**57 (1998) 344.

[5] J. Linde, T. Ohlsson, and H. Snellman, Phys. Rev. **D**57 (1998) 452; **D**57 (1998) 5916.

[6] H. Dahiya and M. Gupta, Phys. Rev. **D**64 (2001) 014013; Int. Jol. Mod. Phys. **A**19 (2004) 5027.

[7] N. Sharma and H. Dahiya, Phys. Rev. **D**81 (2010) 114003; H. Dahiya and N. Sharma, Mod. Phys. Lett. **A**26 (2011) 279.

[8] N. Sharma, H. Dahiya, P.K. Chatley, and M. Gupta, Phys. Rev. **D**79 (2009) 077503; N. Sharma, H. Dahiya, and P.K. Chatley, Eur. Phys. J. **A**44 (2010) 125.

[9] T.P. Cheng and L.F. Li, Phys. Rev. Lett. **8**0 (1998) 2789.

[10] H. Dahiya and M. Gupta, Phys. Rev. **D**66 (2002) 051501(R); Phys. Rev. **D**67 114015 (2003); N. Sharma, H. Dahiya, P.K. Chatley, and M. Gupta, Phys. Rev. **D**81 (2010) 073001.

[11] N. Kaiser, P.B. Siegel, and W. Weise, Phys. Lett. **B**362 (1995) 23.

[12] N. Isgur and G. Karl, Phys. Lett. **B**72 (1977) 109.

THE STRANGE QUARK POLARIZATION PUZZLE

E. Leader [1], A.V. Sidorov [2,†] and D.B. Stamenov [3]

(1) *Imperial College London, Prince Consort Road, London SW7 2BW, England*
(2) *Theoretical Laboratory, Joint Institute for Nuclear Research, Dubna, Russia*
(3) *Institute for Nuclear Research and Nuclear Energy, Bulgarian Academy of Sciences, Sofia, Bulgaria*
† *E-mail: sidorov@theor.jinr.ru*

Abstract

The strange quark polarization puzzle, i.e. the contradiction between the negative polarized strange quark density obtained from analysis of inclusive DIS data and the positive values obtained from combined analysis of inclusive and semi-inclusive SIDIS data using de Florian et. al. (DSS) fragmentation functions, is discussed. To this end the results of a new combined NLO QCD analysis of the polarized inclusive and semi-inclusive DIS data, using the Hirai et. al. (HKNS) fragmentation functions, are presented. It is demonstrated that the polarized strange quark density is very sensitive to the kaon fragmentation functions, and if the set of HKNS fragmentation functions is used, the polarized strange quark density from the *combined* analysis turns out to be *negative* and well consistent with values obtained from the pure DIS analysis.

In the absence of neutrino reactions on a polarized target, the inclusive polarized deep inelastic lepton-hadron reactions determine only the sum of quark and antiquark polarized parton density functions (PDFs), $\Delta q(x) + \Delta\bar{q}(x)$, and provide no information at all about the individual polarized antiquark densities. All analysis of the polarized *inclusive* DIS data have produced results for the polarized strange quark density function, $\Delta s(x)+\Delta\bar{s}(x)$, which are significantly *negative* for all values of x[1] (for more recent analysis see [1, 2]). One way to determine polarized quark and sea-quark densities separately is to use the data on polarized *semi-inclusive* reactions (SIDIS) like $l + p \to l + h + X$, where h is a detected hadron. In the past few years more data on polarized SIDIS processes have become available and have led to assertions that $\Delta s(x) + \Delta\bar{s}(x)$ is *positive* for most of the range of measured x. This contradiction between the behaviour of the polarized strange quark densities extracted from the analysis of pure inclusive and the combined inclusive and semi-inclusive deep inelastic scattering data, respectively, is known as the strange quark polarization puzzle. In this talk we discuss the role of the fragmentation functions (FFs) in determining of the sea-quark densities, and in particular, a possible resolution of the puzzle.

The key to resolving the puzzle lies, we believe, in the properties of FFs needed in the theoretical expressions for the measured SIDIS cross-sections and asymmetries, which involve convolutions of either unpolarized or polarized PDFs with the FFs. There are

[1]Note that in all the QCD analysis of the pure inclusive DIS data an input parameterization for $\Delta s(x) + \Delta\bar{s}(x)$ which does not allow its changing sign behaviour was used. We have recently shown that a more general input parameterization of $\Delta s(x) + \Delta\bar{s}(x)$ does not change the result.

three modern versions of the FFs in the literature, Hirai et al. (HKNS) [3], de Florian et al. (DSS) [4] and Albino et. al. (AKK) [5], sometimes differing significantly from each other. They are based mainly on semi-inclusive e^+e^- annihilation data (HKNS), e^+e^- annihilation and RHIC data on reactions like $pp \to \pi\,\mathrm{or}\,K + X$ (AKK), and a global analysis (DSS) of the data on semi-inclusive e^+e^- annihilation, the proton-proton collisions at RHIC and unpolarized SIDIS processes.

The early claim by the HERMES Collaboration [6] that the polarized SIDIS data implied marginally positive $\Delta s(x) + \Delta\bar{s}(x)$ in the measured x range [0.023-0.3] was based on a LO QCD analysis of the data. In 2008, de Florian, Sassot, Stratmann and Vogelsang (DSSV) carried out a combined NLO QCD analysis [7] of polarized DIS, SIDIS and RHIC data using the DSS fragmentation functions and effectively confirmed the LO result. More precisely, using the assumption $\Delta s(x) = \Delta\bar{s}(x)$ they obtained a sign-changing solution for $\Delta s(x) + \Delta\bar{s}(x)$, negative for $x < 0.03$ and positive in the region $x > 0.03$. Later we repeated this analysis [8], using polarized DIS and SIDIS data and found substantial agreement with DSSV. We confirmed the sign-changing behavior of $\Delta\bar{s}(x)$, though our $\Delta\bar{s}(x)$ is less negative at $x < 0.03$ and less positive for large x and compatible with zero within the errors. Note that the polarized pp data from RHIC are not important for the determination of the polarized quark and antiquark densities; they constrain mainly the gluon polarization.

In order to understand better the issue of the strange quark polarization puzzle we first carried out a combined NLO QCD analysis [9] of the polarized world DIS data and *just the pion* SIDIS data [10], using the DSS FFs. Note that in this case only the sum $x(\Delta s+\Delta\bar{s})(x, Q^2)$ can be determined from the data because of the reasonable assumption $D_s^\pi = D_{\bar{s}}^\pi$ used for all the sets of the fragmentation functions. The result for $x(\Delta s+\Delta\bar{s})/2$ is illustrated in Fig. 1 (dashed curve) and compared to those obtained from the LSS'06 DIS analysis [2] (dotted curve) and the combined LSS'10 fit to the DIS and SIDIS data [8] (solid curve). As seen from Fig. 1, in the presence of only the A_{1N}^π data, $x(\Delta s(x) + \Delta\bar{s}(x))/2$ (dashed curve) is still *negative* in the measured x range as in the analysis of the purely inclusive data.

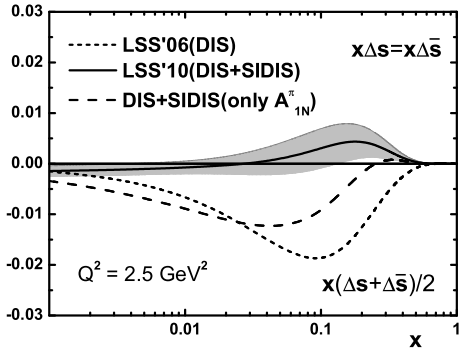

Figure 1: Comparison between polarized strange quark densities obtained from different kinds of NLO QCD analysis (see the text).

This definitely seemed to point towards the kaon FFs as the source of the conflict. Note also that it had already been pointed out by COMPASS Collaboration (2nd and 3rd references in [10]) that in the LO QCD approximation the value of the first moment of $\Delta s(x)$ in the measured range of x is very sensitive to the assumed value of the ratio of the $\bar{s}$-quark to u-quark fragmentation functions into positive kaons. Therefore, we carried out a new combined NLO QCD analysis [11] of the world polarized DIS [12] and *all* the SIDIS data [10, 13] using the HKNS set of FFs [3], which differ significantly from the DSS ones in the kaon sector, especially for the transition $\bar{s} \to K^+$, as shown in Fig 2. In Fig. 2 two error bands for the HKNS FFs are presented. The narrow one corresponds to $\Delta\chi^2 = 1$ while the wide corridor corresponds to $\Delta\chi^2 = 19.2$. The latter value corresponds

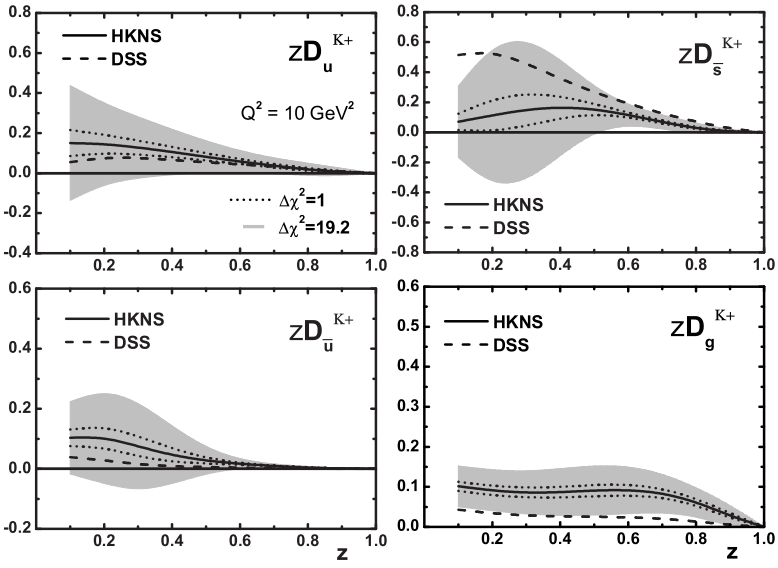

Figure 2: Comparison between NLO HKNS and DSS kaon FFs at $Q^2 = 10\ GeV^2$.

to 17 parameters fit in the MINUIT-procedure when only the statistical errors are taken into account. However, the authors of [3] apply this procedure for the statistical and systematic errors added in quadrature which definitely overestimates the uncertainties.

The significant difference in the kaon sector between the DSS FFs and the other sets of FFs, including HKNS, is due to the unpublished HERMES'05 data on the hadron multiplicities used only in the DSS analysis. It turns out, however, that the DSS predictions are NOT in agreement with the new preliminary HERMES [14] and the COMPASS data [15] on the multiplicities. So, there is no reason to favor the DSS FFs until the final HERMES and COMPASS data on the hadron multiplicities are presented.

The method used in this analysis is the same as in our previous one [8] of the same set of data when the DSS FFs were used. Note that the present SIDIS data are not precise enough to determine separately $\Delta s(x)$ and $\Delta\bar{s}(x)$. So, as in our previous analysis the assumption $\Delta s(x) = \Delta\bar{s}(x)$ was used. A good description of the SIDIS data (χ^2_{NrP}=0.92) is achieved using the HKNS FFs (NrP is the number of corresponding experimental points). The quality of the fit to the data is demonstrated in Fig. 3 (solid curves) for some of the SIDIS asymmetries obtained by the HERMES and COMPASS Collaborations. The new curves are compared to our previous theoretical curves (dashed ones) obtained from the best fit to the data using the DSS FFs (χ^2_{NrP}=0.87). As seen from Fig. 3 the results from both the fits are very close to each other and for some of the asymmetries the curves are almost identical.

Let us discuss the impact of the HKNS fragmentation functions on the polarized sea-quark densities. It is known that the present SIDIS data do not influence the gluon polarization. It is mainly determined from inclusive DIS and semi-inclusive pp RHIC data. The new values of the sea quark and gluon polarized densities (solid curves) are presented in Fig. 4 together with their error bands and compared to those obtained

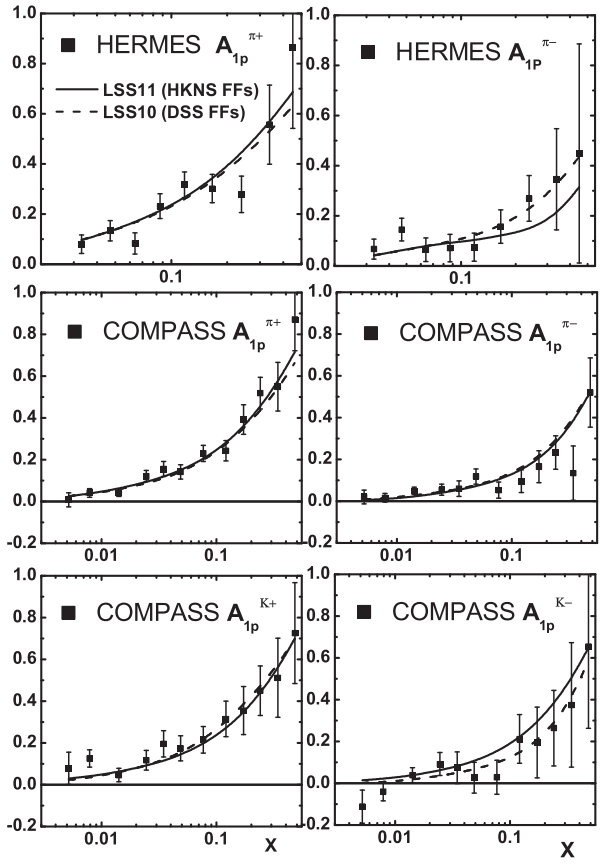

Figure 3: Comparison of our NLO LSS'11 (solid curves) and LSS'10 (dash curves) results for the SIDIS asymmetries with the data at measured x and Q^2.

using the DSS FFs (LSS'10). As seen from Fig. 4 the changes in the polarized sea quark densities are as follows: negligible for $x\Delta\bar{d}(x)$, visible for $x\Delta\bar{u}(x)$ at $x > 0.03$ and dramatic for $x\Delta\bar{s}(x)$, although the central values of the first moments of $\Delta\bar{s}$(DSS) and $\Delta\bar{s}$(HKNS) are very close to each other (-0.052 ± 0.016 and -0.048 ± 0.012 at $Q^2 = 1\ GeV^2$ for DSS and HKNS FFs, respectively) and coincide within the errors. In Fig. 4 our LSS'06 result [2] for $x(\Delta s(x) + \Delta\bar{s}(x))/2$ (dot curve) obtained from the NLO QCD analysis of the world inclusive DIS data is presented too. We find now that if the HKNS FFs are used, $\Delta\bar{s}(x)$ is *negative* and well consistent with $(\Delta s(x) + \Delta\bar{s}(x))/2$ obtained from the pure DIS analyses [1, 2].

In conclusion, we have found that in the presence of semi-inclusive DIS data the strange quark density is very sensitive to the choice of the FFs. We have also demonstrated that the strange quark polarization puzzle can be resolved by using the HKNS set of fragmentation functions rather than the DSS ones. Finally, we like to stress we do not claim to have presented a unique resolution to the strange polarization puzzle. The final HERMES and COMPASS data on multiplicities will be crucial for a more reliable determination of FFs and a possible resolution of the strange quark polarization puzzle.

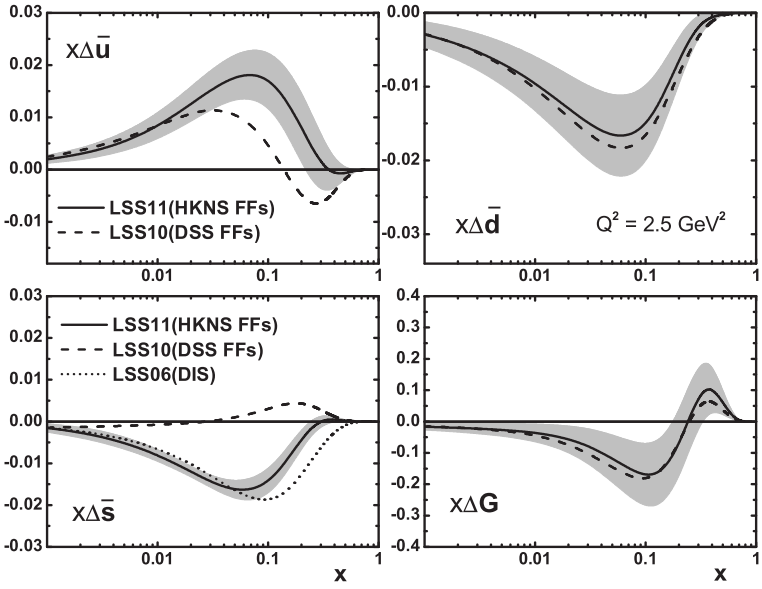

Figure 4: Comparison between NLO LSS'11(HKNS FFs) and LSS'10(DSS FFs) sea quarks and gluon polarized PDFs at $Q^2 = 2.5\ GeV^2$. The dot curve corresponds to $x(\Delta s(x) + \Delta\bar{s}(x))/2$ obtained from the pure DIS analysis [2].

Acknowledgments: This research was supported by the JINR-Bulgaria Collaborative Grant, by the RFBR Grants (No 09-02-01149, 11-01-00182 and 12-02-00613) and by the Bulgarian National Science Fund under Contract 02-288/2008.

References

[1] M. Hirai, S. Kumano, N. Saito (Asymmetry Analysis Collaboration), *Phys. Rev.* **D74** (2006) 014015; V.Y. Alexakhin *et al.* (COMPASS Collaboration), *Phys. Lett.* **B647** (2007) 8; J. Blumlein, H. Böttcher, *Nucl. Phys.* **B841** (2010) 205.

[2] E. Leader, A.V. Sidorov, D.B. Stamenov, *Phys. Rev.* **D75** (2007) 074027.

[3] M. Hirai, S. Kumano, T.-H. Nagai, K. Sudoh, *Phys. Rev.* **D75** (2007) 094009.

[4] D. de Florian, R. Sassot, M. Stratmann, *Phys. Rev.* **D75** (2007) 114010; *Phys. Rev.* **D76** 074033 (2007).

[5] S. Albino, B. A. Kniehl, G. Kramer, *Nucl. Phys.* **B803** (2008) 42.

[6] U. Stosslein, *Acta Phys. Polonica* **B33** (2002) 2813; A. Airapetian et al. (HERMES Collaboration), *Phys. Rev. Lett.* **92** (2004) 012005.

[7] D. de Florian, R. Sassot, M. Stratmann, W. Vogelsang, *Phys. Rev.* **D80** (2009) 034030.

[8] E. Leader, A.V. Sidorov, D.B. Stamenov, *Phys. Rev.* **D82** (2010) 114018.

[9] E. Leader, A.V. Sidorov, D.B. Stamenov, arXiv:1012.5033 [hep-ph].

[10] A. Airapetian *et al.* (HERMES Collaboration), *Phys. Rev.* **D71** (2005) 012003; M.G. Alekseev *et al.* (COMPASS Collaboration), *Phys. Lett.* **B680** (2009) 217; **B693** (2010) 227.

[11] E. Leader, A.V. Sidorov, D.B. Stamenov, *Phys. Rev.* **D84** (2010) 014002.

[12] J. Ashman *et al.* (EMC Collaboration), Phys. Lett. **B206** (1988) 364; Nucl. Phys. **B328** (1989) 1; P.L. Anthony *et al.* (SLAC E142 Collaboration), Phys. Rev. **D54** (1996) 6620; K. Abe *et al.* (SLAC E143 Collaboration), Phys. Rev. **D58** (1998) 112003; K. Abe *et al.* (SLAC/E154 Collaboration), Phys. Rev. Lett. **79** (1997) 26; P.L. Anthony *et al.* (SLAC E155 Collaboration), Phys. Lett. **B493** (2000) 19; Phys. Lett. **B463** (1999) 339; A. Airapetian *et al.* (HERMES Collaboration), Phys. Rev. **D71** (2005) 012003; X. Zheng *et al.* (JLab/Hall A Collaboration), Phys. Rev. Lett. **92** (2004) 012004; Phys. Rev. **C70** (2004) 065207; K.V. Dharmwardane *et al.* (CLAS Collaboration), Phys. Lett. **B641** (2006) 11; B. Adeva *et al.* (SMC Collaboration), Phys. Rev. **D58** (1998) 112001; V.Yu. Alexakhin *et al.* (COMPASS Collaboration), Phys. Lett. **B647** (2007) 8; M.G. Alekseev *et al.* (COMPASS Collaboration), Phys. Lett. **B690** (2010) 466.

[13] B. Adeva *et al.* (SMC Collaboration), *Phys. Lett.* **B420** (1998) 180; M.G. Alekseev *et al.* (COMPASS Collaboration), *Phys. Lett.* **B660** (2008) 458.

[14] S.J. Joosten (on behalf of the HERMES collaboration), a talk at the 19th DIS'2011 International Workshop, 11-15 April, 2011, Newport News, VA, USA.

[15] Y. Bedfer (on behalf of the COMPASS collaboration), a talk at this Workshop.

STATISTICAL PARTON DISTRIBUTIONS, TMD, POSITIVITY AND ALL THAT

Jacques Soffer

Department of Physics, Temple University Philadelphia, Pennsylvania 19122-6082, USA
E-mail: jacques.soffer@gmail.com

Abstract

We briefly recall the main physical features of the parton distributions in the quantum statistical picture of the nucleon. Some predictions from a next-to-leading order QCD analysis are successfully compared to recent unpolarized and polarized experimental results. We will discuss the extension to the transverse momentum dependence of the parton distributions and its relevance for semiinclusive deep inelastic scattering. Finally, we will present some new positivity constraints for spin observables and their implications for parton distributions.

1 A short review on the statistical approach

Let us first recall some of the basic ingredients for building up the parton distribution functions (PDF) in the statistical approach, as oppose to the standard polynomial type parametrizations, based on Regge theory at low x and counting rules at large x. The fermion distributions are expressed by the sum of two terms [1], the first one, a quasi Fermi-Dirac function, for a given helicity and flavor, and the second one, a flavor and helicity independent diffractive contribution equal for light quarks. So we have, at the input energy scale $Q_0^2 = 4\text{GeV}^2$,

$$xq^h(x,Q_0^2) = \frac{AX_{0q}^h x^b}{\exp[(x-X_{0q}^h)/\bar{x}]+1} + \frac{\tilde{A}x^{\tilde{b}}}{\exp(x/\bar{x})+1}\ , \tag{1}$$

$$x\bar{q}^h(x,Q_0^2) = \frac{\bar{A}(X_{0q}^{-h})^{-1}x^{2b}}{\exp[(x+X_{0q}^{-h})/\bar{x}]+1} + \frac{\tilde{A}x^{\tilde{b}}}{\exp(x/\bar{x})+1}\ . \tag{2}$$

Notice the change of sign of the potentials and helicity for the antiquarks. The parameter $\bar{x}$ plays the role of a *universal temperature* and $X_{0q}^{\pm}$ are the two *thermodynamical potentials* of the quark q, with helicity $h = \pm$. It is important to remark that the diffractive contribution occurs only in the unpolarized distributions $q(x) = q_+(x) + q_-(x)$ and it is absent in the valence $q_v(x) = q(x) - \bar{q}(x)$ and in the helicity distributions $\Delta q(x) = q_+(x) - q_-(x)$ (similarly for antiquarks). The *eight* free parameters[1] in Eqs. (1,2) were determined at the input scale from the comparison with a selected set of very precise unpolarized and polarized Deep Inelastic Scattering (DIS) data [1]. They have the following values

$$\bar{x} = 0.09907,\ b = 0.40962,\ \tilde{b} = -0.25347,\ \tilde{A} = 0.08318, \tag{3}$$

$$X_{0u}^+ = 0.46128,\ X_{0u}^- = 0.29766,\ X_{0d}^- = 0.30174,\ X_{0d}^+ = 0.22775\ . \tag{4}$$

[1] $A = 1.74938$ and $\bar{A}\ = 1.90801$ are fixed by the following normalization conditions $u - \bar{u} = 2$, $d - \bar{d} = 1$.

For the gluons we consider the black-body inspired expression

$$xG(x,Q_0^2) = \frac{A_G x^{b_G}}{\exp(x/\bar{x}) - 1} \ , \tag{5}$$

a quasi Bose-Einstein function, with $b_G = 0.90$, the only free parameter[2], since $A_G = 20.53$ is determined by the momentum sum rule. We also assume that, at the input energy scale, the polarized gluon distribution vanishes, so $x\Delta G(x,Q_0^2) = 0$. For the strange quark distributions, the simple choice made in Ref. [1] was greatly improved in Ref. [2]. More recently, new tests against experimental (unpolarized and polarized) data turned out to be very satisfactory, in particular in hadronic collisions, as reported in Refs. [3, 4].

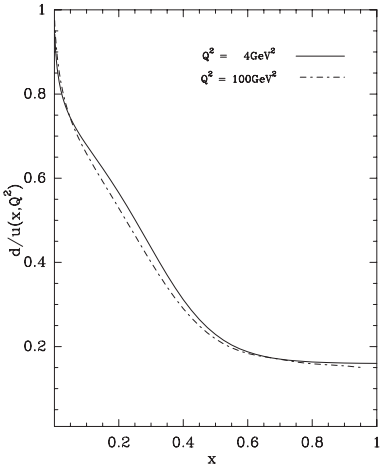

Figure 1: The ratio $d(x)/u(x)$ as function of x for $Q^2 = 4\text{GeV}^2$ (solid line) and $Q^2 = 100\text{GeV}^2$ (dashed-dotted line).

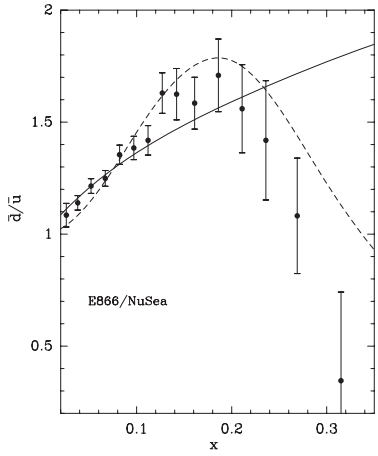

Figure 2: Comparison of the data on $\bar{d}/\bar{u}(x,Q^2)$ from E866/NuSea at $Q^2 = 54\text{GeV}^2$ [6], with the prediction of the statistical model (solid curve) and the set 1 of the parametrization proposed in Ref. [7] (dashed curve).

An interesting point concerns the behavior of the ratio $d(x)/u(x)$, which depends on the mathematical properties of the ratio of two Fermi-Dirac factors, outside the region dominated by the diffractive contribution. So for $x > 0.1$, this ratio is expected to decrease faster for $X_{0d}^+ - \bar{x} < x < X_{0u}^+ + \bar{x}$ and then above, for $x > 0.6$, it flattens out.

This change of slope is clearly visible in Fig. 1 , with a very little Q^2 dependence. Note that our prediction for the large x behavior, differs from most of the current literature, namely $d(x)/u(x) \to 0$ for $x \to 1$, but we find $d(x)/u(x) \to 0.16$ near the value 1/5, a prediction originally formulated in Ref. [5]. This is a very challenging question, since the very high-x region remains poorly known. To continue our tests of the unpolarized parton distributions, we must come back to the important question of the flavor asymmetry of the light antiquarks. Our determination of $\bar{u}(x,Q^2)$ and $\bar{d}(x,Q^2)$ is perfectly consistent with the violation of the Gottfried sum rule, for which we found the value $I_G = 0.2493$ for $Q^2 = 4\text{GeV}^2$. Nevertheless there remains an open problem with the x distribution of the ratio $\bar{d}(x)/\bar{u}(x)$ for $x \geq 0.2$. According to the Pauli principle, this ratio is expected to remain above 1 for any value of x. However, the E866/NuSea Collaboration [6] has

[2]In Ref. [1] we were assuming that, for very small x, $xG(x,Q_0^2)$ has the same behavior as $x\bar{q}(x,Q_0^2)$, so we took $b_G = 1 + \tilde{b}$. However this choice leads to a too much rapid rise of the gluon distribution, compared to its recent determination from HERA data, which requires $b_G = 0.90$.

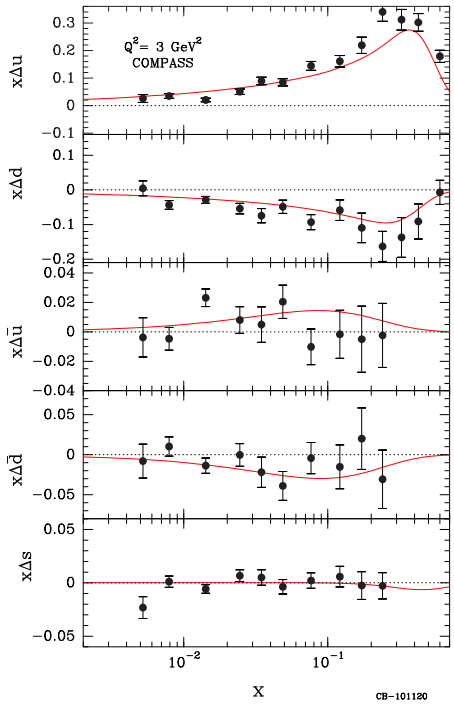

Figure 3: Quark and antiquark helicity distributions as a function of x for $Q^2 = 3\text{GeV}^2$. Data from COMPASS [16]. The curves are predictions from the statistical approach.

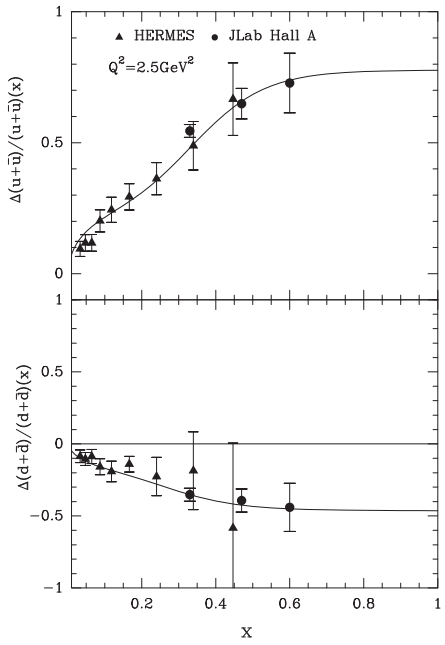

Figure 4: Ratios $(\Delta u + \Delta\bar{u})/(u + \bar{u})$ and $(\Delta d + \Delta\bar{d})/(d + \bar{d})$ as a function of x. Data from Hermes for $Q^2 = 2.5\text{GeV}^2$ [11] and a JLab Hall A experiment [12]. The curves are predictions from the statistical approach..

released the final results corresponding to the analysis of their full data set of Drell-Yan yields from an 800 GeV/c proton beam on hydrogen and deuterium targets and they obtain the ratio, for $Q^2 = 54\text{GeV}^2$, $\bar{d}(x)/\bar{u}(x)$ shown in Fig. 2. Although the errors are rather large in the high-x region, the statistical approach disagrees with the trend of the data. Clearly by increasing the number of free parameters, it is possible to build up a scenario which leads to the drop off of this ratio for $x \geq 0.2$. For example this was achieved in Ref. [7], as shown by the dashed curve in Fig. 2. There is no such freedom in the statistical approach, since quark and antiquark distributions are strongly related. On the experimental side, there are now new opportunities for extending the $\bar{d}(x)/\bar{u}(x)$ measurement to larger x up to $x = 0.7$, with the upcoming E906 experiment at the 120 GeV Main Injector at Fermilab [8] and a proposed experiment at the new 30-50 GeV proton accelerator at J-PARC [9].

Analogous considerations can be made for the corresponding helicity distributions, whose most recent determinations are shown in Fig. 3. By using a similar argument as above, the ratio $\Delta u(x)/u(x)$ is predicted to have a rather fast increase in the x range $(X^-_{0u} - \bar{x}, X^+_{0u} + \bar{x})$ and a smoother behaviour above, while $\Delta d(x)/d(x)$, which is negative, has a fast decrease in the x range $(X^+_{0d} - \bar{x}, X^-_{0d} + \bar{x})$ and a smooth one above. This is exactly the trends displayed in Fig. 4 and our predictions are in perfect agreement with the accurate high-x data. We note the behavior near $x = 1$, another typical property of the statistical approach, is also at variance with predictions of the current literature. The fact that $\Delta u(x)$ is more concentrated in the higher x region than $\Delta d(x)$, accounts for the change of sign of $g_1^n(x)$, which becomes positive for $x > 0.5$, as first observed at Jefferson Lab [12].

Concerning the light antiquark helicity distributions, the statistical approach imposes

a strong relationship to the corresponding quark helicity distributions. In particular, it predicts $\Delta\bar{u}(x) > 0$ and $\Delta\bar{d}(x) < 0$, with almost the same magnitude, in contrast with the simplifying assumption $\Delta\bar{u}(x) = \Delta\bar{d}(x)$, often adopted in the literature. According to the COMPASS experiment at CERN [13], $\Delta\bar{u}(x) + \Delta\bar{d}(x) \simeq 0$, in agreement with our prediction.

2 The TMD extension

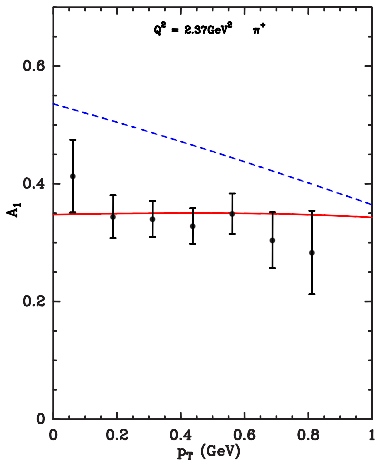

Figure 5: The double longitudinal-spin asymmetry A_1 for π^+ production on a proton target, versus the π^+ momentum p_T, compared to the JLab data Ref. [17]. The solid lines are the results from the TMD statistical distributions [15] and the dashed lines correspond to the relativistic covariant distributions [16].

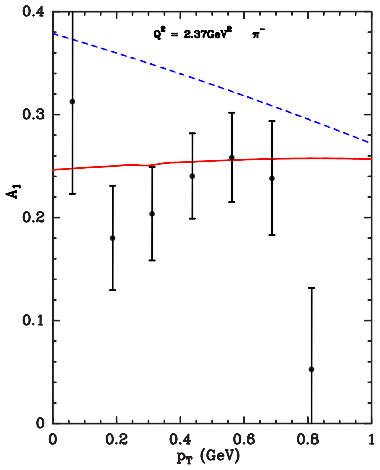

Figure 6: The double longitudinal-spin asymmetry A_1 for π^- production on a proton target, versus the π^- momentum p_T, compared to the JLab data Ref. [17]. The solid lines are the results from the TMD statistical distributions [15] and the dashed lines correspond to the relativistic covariant distributions [16].

We now turn to another important aspect of the statistical PDF and very briefly discuss a new version of the extension to the transverse momentum dependence (TMD). In Eqs. (1,2) the multiplicative factors X_{0q}^h and $(X_{0q}^{-h})^{-1}$ in the numerators of the non-diffractive parts of q's and $\bar{q}$'s distributions, imply a modification of the quantum statistical form, we were led to propose in order to agree with experimental data. The presence of these multiplicative factors was justified in our earlier attempt to generate the TMD [14], but it was not properly done and a considerable improvement was achieved recently [15]. We have introduced some thermodynamical potentials Y_{0q}^h, associated to the quark transverse momentum k_T, and related to X_{0q}^h by the simple relation $\ln(1 + \exp[Y_{0q}^h]) = kX_{0q}^h$. We were led to choose $k = 3.05$ and this method involves another parameter μ^2, which plays the role of the temperature for the transverse degrees of freedom and whose value was determined by the transverse energy sum rule. We have calculated the p_T dependence of semiinclusive DIS cross sections and double longitudinal spin asymmetries, taking into account the effects of the Melosh-Wigner rotation, for $\pi^\pm$ production by using this set of TMD statistical parton distributions and another set coming from the relativistic covariant approach [16]. Both sets do not satisfy the usual factorization assumption of the dependence in x and k_T and they lead to different results, which can be compared to recent experimental data from CLAS at JLab, as shown on Figs. 5-6.

3 Positivity bounds

Spin observables for any particle reaction, contain some unique information which allow a deeper understanding of the nature of the underlying dynamics and this is very useful to check the validity of theoretical assumptions. We emphasize the relevance of positivity in spin physics, which puts non-trivial model independent constraints on spin observables. If one, two or several observables are measured, the constraints can help to decide which new observable will provide the best improvement of knowledge. Different methods can be used to establish these constraints and they have been presented together with many interesting cases in a review article [18]. For lack of space, here we will only briefly discuss some new results obtained very recently [19, 20].

Let us consider the inclusive reaction of the type $A(\text{spin } 1/2) + B(\text{spin } 1/2) \to C + X$, where both initial spin 1/2 particles can be in any possible directions and no polarization is observed in the final state. The spin-dependent corresponding cross section $\sigma\left(P_a, P_b\right) = \text{Tr}\left(M\rho\right)$, can be defined through the 4×4 cross section matrix M and the spin density matrix ρ, where P_a, P_b are the spin unit vectors of A and B, $\rho = \rho_a \otimes \rho_b$ is the spin density matrix with $\rho_a = (I_2 + P_a \cdot \vec{\sigma}_a)/2$, and similar for ρ_b. Here I_2 is the 2×2 unit matrix, and $\sigma = (\sigma_x, \sigma_y, \sigma_z)$ stands for the 2×2 Pauli matrices. M can be parametrized in terms of 8 parity-conserving asymmetries and 8 parity-violating asymmetries. The crucial point is that M is a Hermitian and positive matrix and this allows to derive some positivity conditions. Since one of the necessary conditions for a Hermitian matrix to be positive definite is that all the diagonal matrix elements has to be positive $M_{ii} \geq 0$, we thus derive $1 \pm A_{NN} \geq |A_{aN} \pm A_{bN}|$, valid in full generality, for both parity-conserving and parity-violating processes, where A_N denotes the single transverse spin asymmetry and A_{NN} the double transverse spin asymmetry. In the case $p^\uparrow + p^\uparrow \to C + X$ where the initial particles are identical, we have $A_{aN}(y) = -A_{bN}(-y)$. Using this relation , one obtains, $1 \pm A_{NN}(y) \geq |A_N(y) \mp A_N(-y)|$. This is an interesting result which, can be used, in principle, with available data on A_N for $\pi^\pm$, $K^\pm$, π^0, η production, to put some non trivial constrain on $A_{NN}(y)$.

Let us now study the implications of the above relation for the parity-violating process $p^\uparrow + p^\uparrow \to W^\pm + X$. Since $A_{NN} \approx 0$, to a very good approximation, it reduces to $1/2 \geq |A_N(y = 0)|$, to be compared with the usual trivial bound $1 \geq |A_N(y = 0)|$.

The TMD quark distribution in a transversely polarized hadron can be expanded as $f_{q/h^\uparrow}(x, \mathbf{k}_\perp, \vec{S}) \equiv f_{q/h}(x, k_\perp) + \frac{1}{2}\Delta^N f_{q/h^\uparrow}(x, k_\perp)\, \vec{S} \cdot \left(\hat{p} \times \hat{\mathbf{k}}_\perp\right)$, where $\hat{p}$ and $\hat{\mathbf{k}}_\perp$ are the unit vectors of $\vec{p}$ and $\mathbf{k}_\perp$, respectively. $f_{q/h}(x, k_\perp)$ is the spin-averaged TMD distribution, and $\Delta^N f_{q/h^\uparrow}(x, k_\perp)$ is the Sivers function. There is a trivial positivity bound for the Sivers functions which reads $|\Delta^N f_{q/h^\uparrow}(x, k_\perp)| \leq 2 f_{q/h}(x, k_\perp)$. Since A_N is directly expressed in terms of $\Delta^N f_{q/h^\uparrow}(x, k_\perp)$, this trivial bound can be improved as shown in Ref. [20].

In the helicity basis it is easy to obtain the explicit form of M and now from $M_{ii} \geq 0$, we have $1 \pm A_{LL}(y) \geq |A_{aL}(y) \pm A_{bL}(y)|$, where A_L denotes the single helicity asymmetry and A_{LL} the double double asymmetry. It is important to note that for identical initial particles scattering, one has $A_{aL}(y) = A_{bL}(-y)$, so one gets $1 \pm A_{LL}(y) \geq |A_L(y) \pm A_L(-y)|$. These bounds should be tested in RHIC experiments for $W^\pm$ or Z^0 production in longitudinal pp collisions, $\vec{p}\vec{p} \to W^\pm/Z^0 + X$. In perturbative QCD formalism, at leading-order and restricting to only up and down quarks, one has simple expressions for the single and double helicity asymmetries, involving only quark helicity distributions.

The statistical PDF satisfy the positivity bound. Finally at $y = 0$, since $A_{LL}(0)$ is expected to be very small, the bound implies $A_L(0) \leq 1/2$, a remarquable simple result which must be satisfied by future experimental data.

Acknowledgments. I am grateful to the organizers of DSPIN2011 for their warm hospitality at JINR and for their invitation to present this talk. My special thanks go to Prof. A.V. Efremov for providing a full financial support and for making, once more, this meeting so successful.

References

[1] C. Bourrely, F. Buccella and J. Soffer, Euro. Phys. J. **C23**, (2002) 487.
For a practical use of these PDF, we refer the reader to the following web site:
www.cpt.univ-mrs.fr/∼bourrely/research/bbs-dir/bbs.html.

[2] C. Bourrely, F. Buccella and J. Soffer, Phys. Lett. **B648**, (2007) 39.

[3] C. Bourrely, F. Buccella and J. Soffer, Mod. Phys. Letters **A18**, (2003) 771 ; Euro. Phys. J. **C41**, (2005) 327.

[4] C. Bourrely, F. Buccella and J. Soffer, Euro. Phys. J. **C41**, (2005) 327.

[5] G.R. Farrar and D.R. Jackson, Phys. Rev. Lett. **35**, (1975) 1416.

[6] R.S. Towell *et al.*, [FNAL E866/Nusea Collaboration], Phys. Rev. **D64**, (2001) 052002.

[7] A. Daleo, C.A. García Canal, G.A. Navarro and R. Sassot, Int. J. Mod. Phys. **A17**, (2002) 269.

[8] D.F. Geesaman *et al.*, [E906 Collaboration], FNAL Proposal E906, April 1, 2001.

[9] J.C.. Peng *et al.*, hep-ph/0007341.

[10] M. Alekseev *et al.*, [COMPASS Collaboration], Phys. Lett. **B693**, (2010) 227.

[11] K. Ackerstaff *et al.*, [Hermes Collaboration], Phys. Lett. **B464**, (1999) 123.

[12] X. Zheng *et al.*, [Jefferson Lab Hall A Collaboration], Phys. Rev. **C70**, (2004) 065207.

[13] M. Alekseev *et al.*, [COMPASS Collaboration], Phys. Lett. **B660**, (2008) 458.

[14] C. Bourrely, F. Buccella and J. Soffer, Mod. Phys. Letters **A21**, (2006) 143.

[15] C. Bourrely, F. Buccella and J. Soffer, Phys. Rev. **D83**, (2011) 074008.

[16] P. Zavada, Eur. Phys. J. **C52**, 121 (2007) and references therein. A.V. Efremov, P. Schweitzer, O.V. Teryaev and P. Zavada, Proceedings of XIII Workshop on High Energy Spin Physics DSPIN-09, Dubna, Russia, Sept. 1-5, 2009. arXiv:0912.3380v3 [hep-ph] and references therein. See also arXiv:1008.3827v1 [hep-ph].

[17] H. Avakian *et al.*, [CLAS Collaboration], Phys. Rev. Lett. **105**, (2010) 262002.

[18] X. Artru, M. Elchikh, J.M. Richard, J. Soffer and O. Teryaev, Physics Reports **470**, (2009) 1.

[19] Zhong-Bo Kang and J. Soffer, Phys. Rev. **D83**, (2011) 114020.

[20] Zhong-Bo Kang and J. Soffer, Phys. Lett **B695**, (2011) 275.

APPLICATIONS OF THE TRUNCATED MELLIN MOMENTS OF THE PARTON DISTRIBUTIONS IN ANALYSIS OF THE SPIN STRUCTURE FUNCTIONS

D. Strózik-Kotlorz [1†] and A. Kotlorz [2]

(1) *Division of Physics, Opole University of Technology*
(2) *Division of Mathematics and Applied Informatics, Opole University of Technology*
† *E-mail: d.strozik-kotlorz@po.opole.pl*

Abstract

We review our previous studies of the truncated Mellin moments of the parton distributions. We apply the truncated moments formalism to QCD analysis of the spin structure functions of the nucleon, g_1 and g_2. We present the generalization of the Wandzura-Wilczek relation in terms of the truncated moments and new sum rules. We show the evolution equation for the twist-2 part of g_2. We present also useful relations between the truncated and untruncated moments. Higher-twist corrections in the truncated moments approach are discussed.

Truncated Mellin moments (TMM) of the parton distributions were introduced and developed in the QCD analysis by S. Forte, J. Latorre, L. Magnea, A. Piccione and G. Ridolfi [1]- [4]. The authors obtained the non-diagonal evolution equations, where each n-th truncated moment couples to all higher ones. Then, the idea of TMM was successfully applied in the leading ln^2x approximation, where we found diagonal solutions [5]. Also A. Sissakian, O. Shevchenko and O. Ivanov used the TMM technique in their NLO analysis of SIDIS data, incorporating polynomial expansion [6]. Several years ago, we derived the DGLAP-type diagonal, exact evolution equations for the TMM in a case of a single truncation [7] and then also for double truncated moments [8], [9]. The latter were also found and discussed by A. Psaker, W. Melnitchouk, M. E. Christy and C. Keppel in a context of the quark-hadron duality [10].

The evolution equations for the truncated Mellin moments of the parton distributions can be an additional tool in the perturbative QCD analysis of the structure functions. In [11] we have utilized this approach to the determination of the parton distribution functions. Here, we present useful relations between the truncated and untruncated Mellin moments and also applications of the TMM approach in analysis of the polarized structure function g_2.

1 The evolution equations for the truncated Mellin moments of the parton densities

In the standard PQCD formalism, a central role play the parton densities, which depend on the kinematic variables Q^2 and x. Then the truncated or untruncated Mellin moments, which are e.g. contributions to the sum rules, can be obtained by integrating of the parton distribution $q(x, Q^2)$ over the Bjorken-x. Alternatively, one can study directly the Q^2

evolution of the moments. The TMM approach allows one to avoid the problem of the unphysical region $x \to 0$ with infinite energy s. Furthermore, this approach refers directly to the physical values - moments (rather than to the parton distributions), what enables one to use a wide range of deep-inelastic scattering data in terms of a smaller number of parameters. The evolution equations for the truncated moments are universal - they can be used in each order of the approximation (LO, NLO etc.) and for unpolarized, as well as polarized parton densities.

Double truncated moments

$$\bar{q}^{\,n}(x_{min}, x_{max}, Q^2) = \int\limits_{x_{min}}^{x_{max}} dx\, x^{n-1}\, q(x, Q^2) \tag{1}$$

satisfy the DGLAP-type evolution

$$\frac{d\bar{q}^{\,n}(x_{min}, x_{max}, Q^2)}{d\ln Q^2} = \frac{\alpha_s(Q^2)}{2\pi} \int\limits_{x_{min}}^{1} \frac{dz}{z}\, P'(n,z)\, \bar{q}^{\,n}\left(\frac{x_{min}}{z}, \frac{x_{max}}{z}, Q^2\right) \tag{2}$$

with splitting function P' given by

$$P'(n,z) = z^n\, P(z). \tag{3}$$

The above equations are a generalization of those for the single truncated ($x_{max} = 1$) and untruncated moments ($x_{min} = 0$, $x_{max} = 1$):

$$\frac{d\bar{q}^{\,n}(x_{min}, Q^2)}{d\ln Q^2} = \frac{\alpha_s(Q^2)}{2\pi} \int\limits_{x_{min}}^{1} \frac{dz}{z}\, P'(n,z)\, \bar{q}^{\,n}\left(\frac{x_{min}}{z}, Q^2\right), \tag{4}$$

$$\frac{d\bar{q}^{\,n}(Q^2)}{d\ln Q^2} = \frac{\alpha_s(Q^2)}{2\pi} \int\limits_{0}^{1} \frac{dz}{z}\, P'(n,z)\, \bar{q}^{\,n}(Q^2) = \frac{\alpha_s(Q^2)}{2\pi}\, \gamma_n\, \bar{q}^{\,n}(Q^2). \tag{5}$$

One can solve the evolution equations for truncated moments with use of standard methods of solving the DGLAP equations. Analysis performed in moment space implies dealing with 'Moment of Moment'

$$M^{s,n} = \int\limits_{0}^{1} dx\, x^{s-1} \int\limits_{x}^{1} dz\, z^{n-1} q(z). \tag{6}$$

We have found useful relations between truncated and untruncated moments, which allow to replace this unphysical value $M^{s,n}$:

$$M^{s,n} = \frac{1}{s}\, \bar{q}^{\,s+n}, \tag{7}$$

$$\bar{q}^{\,n}(x, Q^2) = \frac{1}{2\pi i} \int\limits_{c-i\infty}^{c+i\infty} ds\, \frac{x^{-s}}{s}\, \bar{q}^{\,s+n}(Q^2) \tag{8}$$

and

$$\bar{q}^{\,s}(Q^2) = (s-n)\int\limits_0^1 dx\, x^{s-n-1}\,\bar{q}^{\,n}(x,Q^2). \tag{9}$$

Particularly Eq. (8) seems to have a large practical meaning and could be applied when the untruncated moments are known e.g. from lattice calculations.

2 Applications to spin structure functions

The experimental value of the function g_2, measured in the small to intermediate Q^2 region, consists of two parts: the twist-2 (leading) and the higher twist term:

$$g_2(x,Q^2) = g_2^{LT}(x,Q^2) + g_2^{HT}(x,Q^2). \tag{10}$$

The leading-twist term g_2^{LT} can be determined from the other structure function - g_1 via the Wandzura-Wilczek (WW) relation [12]

$$g_2^{LT}(x,Q^2) = g_2^{WW}(x,Q^2) = -g_1(x,Q^2) + \int_x^1 \frac{dy}{y}\, g_1(y,Q^2). \tag{11}$$

Then, from the measurements of g_1 and g_2, using the WW approximation, one is able to extract the higher-twist term g_2^{HT}.

We found a generalization of the WW relation, which in terms of the truncated moments has a form

$$\bar{g}_2^{\,n}(x_0,Q^2) = \frac{1-n}{n}\,\bar{g}_1^{\,n}(x_0,Q^2) - \frac{x_0^n}{n}\,\bar{g}_1^{\,0}(x_0,Q^2), \tag{12}$$

where $\bar{g}_i^{\,n}(x_0,Q^2)$ is the single truncated moment of the structure function g_i:

$$\bar{g}_i^{\,n}(x_0,Q^2) = \int\limits_{x_0}^1 dx\, x^{n-1}\, g_i(x,Q^2). \tag{13}$$

Basing on the TMM approach, one can also find the partial twist-2 contribution to the BC sum rule

$$\int\limits_{x_1}^{x_2} dx\, g_2^{WW}(x,Q^2) = (x_2-x_1)\int\limits_{x_2}^1 \frac{dx}{x}\, g_1(x,Q^2) - x_1\int\limits_{x_1}^{x_2}\frac{dx}{x}\, g_1(x,Q^2), \tag{14}$$

which can be helpful in determination of the HT effects.

Since, according to Eq. (3), the $n=0$-th truncated moment of the parton distribution q evolves in the same way as q itself ($P'(0,z) = P(z)$), one can obtain from WW relation evolution equation for the leading twist of g_2:

$$\frac{dg_2^{WW}(x,Q^2)}{d\ln Q^2} = \frac{\alpha_s(Q^2)}{2\pi}\int\limits_x^1 \frac{dz}{z}\, P\left(\frac{x}{z}\right)\, g_2^{WW}(z,Q^2). \tag{15}$$

This, together with the evolution equation for the twist-3 component [13], offers unified description of g_2 behavior.

D. S.-K. thanks the organizers for the opportunity to participate in this interesting Workshop and for financial support.

References

[1] S. Forte, L. Magnea, Phys. Lett. **B448** (1999) 295, [hep-ph/9812479].

[2] S. Forte, L. Magnea, A. Piccione, G. Ridolfi, Nucl. Phys. **B594** (2001) 46, [hep-ph/0006273].

[3] A. Piccione, Phys. Lett. **B518** (2001) 207, [hep-ph/0107108].

[4] S. Forte, J. Latorre, L. Magnea Nucl. Phys. **B643** (2002) 477, [hep-ph/0205286].

[5] D. Kotlorz, A. Kotlorz, Acta Phys. Pol. **B35** (2004) 705, [hep-ph/0403061].

[6] A. N. Sissakian, O. Yu. Shevchenko, O. N. Ivanov, JETP Lett. **82** (2005) 53, [hep-ph/0505012], Phys. Rev. **D73** (2006) 094026, [hep-ph/0603236].

[7] D. Kotlorz, A. Kotlorz, Phys. Lett. **B644** (2007) 284, [hep-ph/0610282].

[8] D. Kotlorz, A. Kotlorz, Acta Phys. Pol. **B40** (2009) 1661, [arXiv:0906.0879].

[9] D. Kotlorz, A. Kotlorz, Acta Phys. Pol. **B42** (2011) 1231, [arXiv:1106.3753].

[10] A. Psaker, W. Melnitchouk, M. E. Christy, C. Keppel, Phys. Rev. **C78** (2008) 025206, [arXiv:0803.2055].

[11] D. Kotlorz, A. Kotlorz, Acta Phys. Pol. **B39** (2008) 1913, [arXiv:0810.0606].

[12] S. Wandzura, F. Wilczek, Phys. Lett. **B72** (1977) 195.

[13] V. M. Braun, G. P. Korchemsky and A. N. Manashov, Phys. Lett. **B476** (2000) 455, [hep-ph/0001130], Nucl. Phys. **B597** (2001) 370, [hep-ph/0010128], Nucl. Phys. **B603** (2001) 69, [hep-ph/0102313].

NLO CORRECTIONS TO TIMELIKE AND SPACELIKE DVCS

B. Pire [1], L. Szymanowski [2†] and J. Wagner [2]

(1) *CPhT, École Polytechnique, CNRS, 91128 Palaiseau, France*
(2) *National Center for Nuclear Research, Warsaw, Poland*
† *E-mail: Lech.Szymanowski@fuw.edu.pl*

Abstract

Generalized Parton Distributions (GPDs) offer a new way to access the quark and gluon nucleon structure. We advocate the need to supplement the experimental study of deeply virtual Compton scattering by its crossed version, timelike Compton scattering. We review recent progress in this domain, emphasizing the need to include NLO corrections to any phenomenological program to extract GPDs from experimental data.

The study of the internal structure of the nucleon has been the subject of many developments in the past decades and the concept of generalized parton distributions has allowed a breakthrough in the 3 dimensional description of the quark and gluon content of hadrons. Hard exclusive reactions have been demonstrated to allow to probe the quark and gluon content of protons and heavier nuclei.

In this short review, we concentrate on the complementarity of timelike and spacelike studies of hard exclusive processes, taking as an example the case of timelike Compton scattering (TCS) [1] where data at medium energy should be available at JLab@12 GeV and COMPASS, supplemented by higher energy data thanks both to the study of ultraperipheral collisions at RHIC and the LHC [2] and to a forthcoming electron-ion collider [3].

A considerable amount of theoretical and experimental work has been devoted to the study of deeply virtual Compton scattering (DVCS), i.e., $\gamma^* p \to \gamma p$, an exclusive reaction where generalized parton distributions (GPDs) factorize from perturbatively calculable coefficient functions, when the virtuality of the incoming photon is large enough. An extended research program for DVCS at JLab@12 GeV and Compass is now proposed to go beyond this first set of analysis. This will involve taking into account next to leading order in α_s and next to leading twist contributions. We advocate that it should be supplemented by the experimental study of its crossed version, TCS, or even double DVCS [4] where both photons are off-shell.

The physical process where to observe the inverse reaction, TCS [1],

$$\gamma(q) N(p) \to \gamma^*(q') N(p') \tag{1}$$

is the exclusive photoproduction of a heavy lepton pair, $\gamma N \to \mu^+ \mu^- N$ or $\gamma N \to e^+ e^- N$, at small $t = (p' - p)^2$ and large *timelike* final state lepton pair squared mass $q'^2 = Q'^2$; TCS shares many features with DVCS. The generalized Bjorken variable in that case is $\tau = Q'^2/s$ with $s = (p + q)^2$. One also defines $\Delta = p' - p$ ($t = \Delta^2$) and the skewness variables η and ξ , as

$$\xi = \frac{(q + q')^2}{2(p + p') \cdot (q + q')} \;\; ; \;\; \eta = -\frac{(q - q') \cdot (q + q')}{(p + p') \cdot (q + q')}.$$

For DVCS, $\eta = \xi$ while for TCS, $\eta = -\xi \approx \frac{Q'^2}{2s - Q'^2}$. At the Born order, both DVCS and TCS amplitudes are described by the handbag diagram of Fig. 1 and its crossed version. They both interfere with a Bethe-Heitler QED process where the hadron structure enters through the well known nucleon form factors $F_1(t)$ and $F_2(t)$. The interference signal is a precise way to get an access to the DVCS and TCS amplitudes.

The cross section for photoproduction in hadron collisions is given by:

$$\sigma_{pp} = 2 \int \frac{dn(k)}{dk} \sigma_{\gamma p}(k) dk \,, \tag{2}$$

where $\sigma_{\gamma p}(k)$ is the cross section for the $\gamma p \to p l^+ l^-$ process and k is the photon energy. $\frac{dn(k)}{dk}$ is an equivalent photon flux. The relationship between γp energy squared s and k is given by $s \approx 2\sqrt{s_{pp}} k$, where s_{pp} is the proton-proton energy squared. Figure 2 shows the interference contribution to the cross section in comparison to the Bethe Heitler and Compton processes, for various values of γN c.m. energy squared $s = 10^7\,\mathrm{GeV}^2$ and $10^5\,\mathrm{GeV}^2$. We restrict the phase space integral to $\theta = [\pi/4, 3\pi/4]$ in order to avoid the overdominance of the QED process at forward angles. We observe [2] that for large energies the Compton process dominates in these kinematics, whereas for $s = 10^5\,\mathrm{GeV}^2$ all contributions are comparable. This lowest order estimate shows that indeed TCS can be measured in ultraperipheral collisions at hadron colliders. For instance, we anticipate a rate of the order of 10^5 TCS events per year at LHC with its nominal luminosity. This is mainly due to the large sea quark GPDs at very small x. It also calls for NLO corrections where gluon GPDs start to contribute.

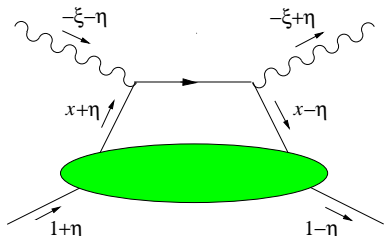

Figure 1: The handbag mechanism controls both DVCS (where $\xi = \eta$) and TCS (where $\xi = -\eta$).

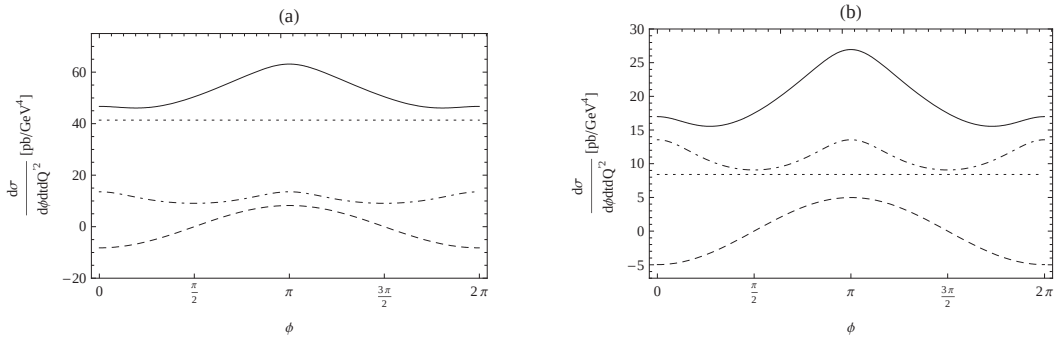

Figure 2: The differential cross sections (solid lines) for $t = -0.2\,\mathrm{GeV}^2$, $Q'^2 = 5\,\mathrm{GeV}^2$ and integrated over $\theta = [\pi/4, 3\pi/4]$, as a function of φ, for $s = 10^7\,\mathrm{GeV}^2$ (a), $s = 10^5\,\mathrm{GeV}^2$(b), with $\mu_F^2 = 5\,\mathrm{GeV}^2$. We also display the Compton (dotted), Bethe-Heitler (dash-dotted) and Interference (dashed) contributions.

Our calculations [5] of NLO corrections show important differences between the coefficient functions describing the TCS case and those describing DVCS. One defines the quark and gluon coefficient functions as

$$T^q = C_0^q + C_1^q + \frac{1}{2}\log(\frac{|Q^2|}{2\mu_F^2}) C_{coll}^q \quad ; \quad T^g = C_1^g + \frac{1}{2}\log(\frac{|Q^2|}{2\mu_F^2}) C_{coll}^g \,,$$

where C_0^q is the Born order coefficient function, C_{coll}^q and C_{coll}^g are directly related to the evolution equation kernels and μ_F is the factorization scale..

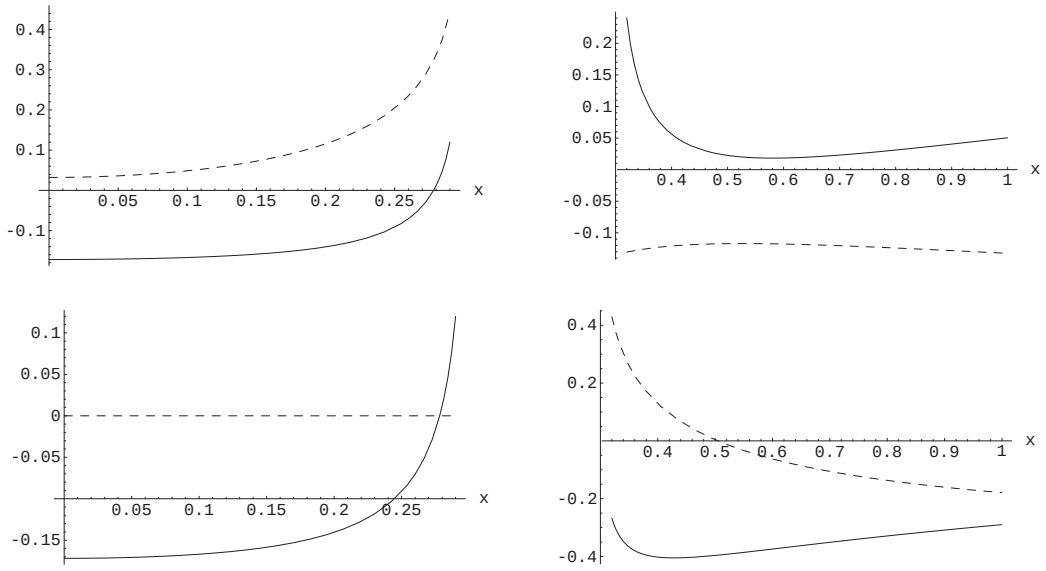

Figure 3: Real (solid line) and imaginary (dashed line) part of the ratio R^q of the NLO quark coefficient function to the Born term in TCS (up) and DVCS(down) as a function of x in the ERBL (left) and DGLAP (right) region for $\eta = 0.3$, for $\mu_F^2 = |Q^2|/2$.

On Fig. 3 we show the real and imaginary parts of the ratio $R^q = C_1^q/C_0^q$ in timelike and spacelike Compton Scattering. We fix $\alpha_s = 0.25$ and restrict the plots to the positive x region, as the coefficient functions are antisymmetric in that variable. We see that in the TCS case, the imaginary part of the amplitude is present in both the ERBL and DGLAP regions, contrarily to the DVCS case, where it exists only in the DGLAP region. The magnitudes of these NLO coefficient functions are not small and neither is the difference of the coefficient functions ${C^q_{1(TCS)}}^* - C^q_{1(DVCS)}$. The conclusion is that extracting the universal GPDs from both TCS and DVCS reactions requires much care.

An important part of NLO corrections to dVCS and TCS, especially at high energy, come from the gluon GPDs Let us summarize our findings on the gluon coefficient functions. The real parts of the gluon contribution are equal for DVCS and TCS in the ERBL region. The differences between TCS and DVCS emerges in the ERBL region through the imaginary part of the coefficient function which is non zero only for the TCS case and is of the order of the real part. In Fig. 4 we plot the ratio $\frac{C^g_{1(TCS)}}{C^g_{1(DVCS)}}$ of the NLO gluon correction to the hard scattering amplitude in TCS to the one in DVCS in the DGLAP region for $\eta = 0.05$.

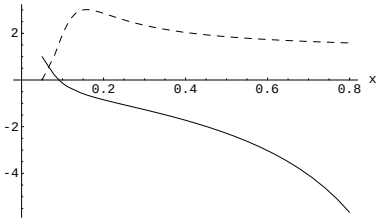

Figure 4: Ratio of the real (solid line) and imaginary (dashed line) part of the NLO gluon coefficient function in TCS to the same quantity in DVCS in the DGLAP region.

To quantify the effects of this NLO calculations, we need to parameterize the quark and gluon GPDs and convolute them with the coefficient functions to get the Compton form factors that enter observable quantities, defined as

$$\mathcal{H} = -\int_{-1}^{1} dx\,[\sum T^q(x,\xi,\eta)H^q(x,\xi,\eta) + T^g(x,\xi,\eta)H^g(x,\xi,\eta)],$$

for the case of the GPD H, and corresponding definitions for other GPDs. Using the G-K

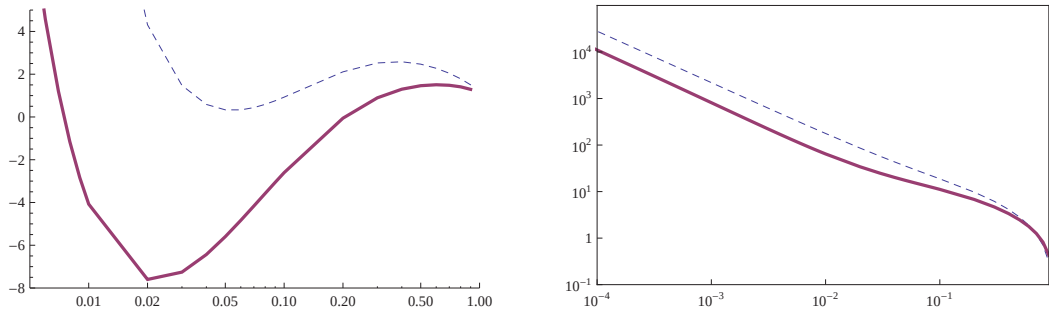

Figure 5: Real part (left) and imaginary part (right) of the DVCS Compton form factor $\mathcal{H}$ at LO (dashed) and NLO (solid) as a function of ξ for $\mu_F^2 = Q^2 = 4$ GeV^2.

model [6], we get, in the DVCS case, the results shown on Fig. 5 which may be compared to earlier calculations [7] . At small ξ, the imaginary part overdominates the real part, but the inclusion of NLO significantly diminishes its size. Note that the inclusion of NLO changes the sign of the real part in the valence region. We are now calculating the corresponding Compton form factors for the timelike case.

We acknowledge useful discussions with Franck Sabatié and Hervé Moutarde and the partial support by the Polish Grant NCN No DEC-2011/01/D/ST2 /02069 and by the French-Polish Collaboration Agreement Polonium.

References

[1] E. R. Berger, M. Diehl and B. Pire, Eur. Phys. J. C **23**, 675 (2002).

[2] B. Pire, L. Szymanowski and J. Wagner, Phys. Rev. D **79**, 014010 (2009); Nucl. Phys. Proc. Suppl. **179-180**, 232 (2008) and Acta Phys. Polon. Supp. **2**, 373 (2009).

[3] D. Boer *et al.*, arXiv:1108.1713 [nucl-th].

[4] M. Guidal and M. Vanderhaeghen, Phys. Rev. Lett. **90**, 012001 (2003); A. V. Belitsky and D. Mueller, Phys. Rev. Lett. **90**, 022001 (2003).

[5] B. Pire, L. Szymanowski, J. Wagner, Phys. Rev. **D83**, 034009 (2011).

[6] S. V. Goloskokov and P. Kroll, Eur. Phys. J. C **50**, 829 (2007).

[7] A. V. Belitsky, D. Mueller, L. Niedermeier and A. Schafer, Phys. Lett. B **474**, 163 (2000).

ANGULAR DISTRIBUTIONS OF DILEPTONS IN HADRONIC AND HEAVY ION COLLISIONS

O.V. Teryaev [1,†]

(1) *Bogoliubov Laboratory of Theoretical Physics, JINR, Dubna, Russia*
† *E-mail: teryaev@theor.jinr.ry*

Abstract

I discuss several consequences of the inequalities for the coefficients of decay angular distributions of the dileptons produced in hadronic and and nuclear collisions. They allow one to bound from below the twist-4 contributions to Drell-Yan process, to derive the new bound(s) relating the T-even and T-odd transverse momentum dependent distributions and provide the new measure of transverse momentum. One may also constrain the action of magnetic field generated in heavy-ion collisions to the angular distribution of soft dileptons.

Introduction. Positivity constraints play a prominent role [1] in high energy physics providing important model-independent inequalities for various non-perturbative inputs. Here we address the applications of such inequalities for angular distributions of dilepton pairs, in particular, in Drell-Yan process [2]. These angular asymmetries, from one side, may be relatively easy studied experimentally, and from the other side, are directly related to the virtual photon tensor polarization and serve as a probe for the production dynamics.

Angular ditributions, positivity and transverse momentum. The angular distribution of dileptons in *any* inclusive hadronic or nuclear process has the following form [4]

$$d\sigma \propto 1 + \lambda \cos^2\theta + \mu \sin 2\theta \cos\phi + \frac{\nu}{2} \sin^2\theta \cos 2\phi + \rho \sin 2\theta \sin\phi + \sigma \sin^2\theta \sin 2\phi \qquad (1)$$

where θ and ϕ are polar and azimuthal angles of one of leptons in their c.m. frame, while $\lambda,\ \mu,\ \nu,\ \rho,\ \sigma$ are angle independent coefficients encoding the information on tensor polarization of virtual photon. In unpolarized or longitudinally polarized Drell-Yan process $\rho = \sigma = 0$ if azimuthal angle is measures w.r.t. scattering plane.

The (symmetric) hadronic tensor in the rest frame can be expressed in terms of these coefficients (for negligibly small lepton mass) as follows

$$W_{ij} = \begin{pmatrix} W_{zz} & W_{zy} & W_{zx} \\ W_{yz} & W_{yy} & W_{yx} \\ W_{xz} & W_{xy} & W_{xx} \end{pmatrix} = N \begin{pmatrix} \frac{1-\lambda}{2} & \mu & \rho \\ \mu & \frac{1+\lambda-\nu}{2} & \sigma \\ \rho & \sigma & \frac{1+\lambda+\nu}{2} \end{pmatrix}, \qquad (2)$$

where N is the angles independent factor. The coordinate axes z, x, y may be chosen in such a way that the beams in the dilepton rest frame are in the plane (z, x), with respect to which the azimuthal angle is measured, while the polar one is measured, as usual, with respect to the axis z. At the same time, the direction of axes can be chosen in some

other way, say, using the direction of transverse polarization for x or y. Let us stress that there are no further restrictions for the orientation of axes. Not also that if the tensor component has at least one time index, it is zero

$$W_{\mu 0} = W_{0\mu} = 0$$

because of electromagnetic gauge invariance. The positivity constraints can be easily obtained [4] from the positivity of this matrix and read:

$$|\lambda| \leq 1,\ |\nu| \leq 1 + \lambda,\ \mu^2 \leq \frac{(1-\lambda)(1+\lambda-\nu)}{4} \tag{3}$$

$$\rho^2 \leq \frac{(1-\lambda)(1+\lambda+\nu)}{4},\ \sigma^2 \leq \frac{(1+\lambda)^2-\nu^2}{4}$$

$$\det(M_0) \geq 0 \tag{4}$$

The bounds (2) coincide with the obtained earlier by structure functions method [2].

The special role in the analysis of azimuthal asymmetries is played by Lam-Tung (LT) relation [2].

$$\lambda + 2\nu = 1 \tag{5}$$

It was shown [4] , that LT relations describes the azimuthal asymmetry belonging to the class of *kinematical* ones. Namely, the azimuthal asymmetry is absent at all in the natural reference frame, defined by the collision kinematics, and emerges solely as a kinematical effect when passing to the actual reference frame. To show that one should start with the following expression with respect to some (partonic) axis m

$$d\sigma \propto 1 + \lambda_0(\vec{n}\vec{m})^2 = 1 + \lambda_0 \cos^2\theta_{nm}^2 \tag{6}$$

where

$$\cos\theta_{nm} = \cos\theta\cos\theta_0 + \sin\theta\sin\theta_0\cos\phi.. \tag{7}$$

Note that θ_0 and θ are the angles formed by the axis m and lepton direction n with coordinate axis z, while ϕ is their relative azimuthal angle. As a result one gets the azimuthal dependence with respect to this coordinate axis, so that

$$\lambda = \lambda_0\frac{2-3\sin^2\theta_0}{2+\lambda_0\sin^2\theta_0},\ \ \nu = \lambda_0\frac{2sin^2\theta_0}{2+\lambda_0\sin^2\theta_0}. \tag{8}$$

One may exclude θ_0 and get

$$\lambda_0 = \frac{\lambda + \frac{3}{2}\nu}{1-\frac{1}{2}\nu}. \tag{9}$$

This relation [4] is reduced to the standard LT relation in the case of transverse virtual photon when $\lambda_0 = 1$. Note that if $\lambda_0 = 1$, kinematical equations for λ and ν coincide with the ones derived long ago in pQCD [5], provided the transverse momentum of the pair p_T satisfies the relation

$$\tan^2\theta_0 = \rho^2 \equiv \frac{p_T^2}{Q^2}. \tag{10}$$

At the same time, while no simple expressions for μ were found in [5], the kinematical relation (6) immediately leads to the obvious expression for μ which happens to saturate the positivity bound (2) with λ and ν from (8). Thus, μ provides the complementary probe of transverse momentum, linear in its value and therefore sensitive to its sign as well. The analysis of the data presented here [6] shows that this positivity bound is indeed often close to saturation.

One may also combine [4] the positivity bound for ν with the kinematic relation. As a result, the total positivity region being the triangle in λ, ν plane with the vertices $(1,2), (-1,0), (1,-2)$ is reduced to two triangles with the vertices $(1,0), (-1/3, 2/3), (0,0)$ and $(-1,0), (1,-2), (0,0))$ for positive and negative λ_0, respectively.

Bounding the TMDs. The simplest way to get the bounds for T-odd TMDs is to use their relations to particular twist-3 correlators (gluonic poles). In the case of the first moment of Sivers function the correspondent pole leads to the specific single spin asymmetry in Drell-Yan process [7]. One may rewrite the equation (21) from that Ref. in terms of $\lambda = 1$ and $\mu = 2T(x,x)/Qq(x)$ (recall that the azimuthal angle is measured with respect to the plane containing the transverse polarization). Considering the external ("lepton") currents coupled to each quark flavour separately one may derive the bound

$$1 - \lambda \geq \mu^2 = 4\frac{T^2(x,x)}{Q^2 q^2(x)}, \tag{11}$$

showing that the denominator of SSA must be corrected by the twist four term bounded from below, which represents the particular case of general situation(see [1]).

To get the bounds for TMDs themselves rather than for their moments one may consider the bound $\nu \leq 1 + \lambda$ for the particular case of $p\bar{p}$ DY process in the central region ($y = 0$). As a result, the contributions of two hadrons participating in DY process will be described by the same functions depending on the same longitudinal momentum fraction x. As to transverse momentum, one may use [4] the second theorem on averages allowing to substitute the ratio of integrals defining ν by the ratio of integrands, in which the functions from different hadrons should depend on the same transverse momentum for symmetry reason. Taking into account contributions of transversity $h_1(x, k_T)$, Boer-Mulders function $h_{1\perp}(x, k_T)$ and pretzelosity $h_{T1\perp}(x, k_T)$ to ν and choosing the signs of polarizations and transverse momentum to maximize ν one get:

$$f(x, k_T) \geq |h_1(x, k_T) - \frac{k_T^2}{2M^2} h_{T1\perp}(x, k_T)| + \frac{k_T}{M}|h_{1\perp}(x, k_T)|. \tag{12}$$

This bound differs [1] (and maybe stronger in some cases) from the one obtained by helicity or Cartesian amplitudes method (see eq. (4.87) in [1] and Ref. therein). One may consider as a some advantage of method proposed here that it relies on the expression used to calculate the observables (without addressing the issue whether it can be proved rigorously). It remains to be studied whether the bounds [1] can be obtained by, say, choice of reference frames. The possibility to obtain other bounds is also interesting.

[1] I am indebted to Jacques Soffer for illuminating discussions of these issues.

Dilepton angular distributions in heavy-ion collisions. The analog of hadronic tensor in heavy-ion collsions describes the dilepton production rate [8] and angular asymmetries [9]. Let us stress that the general bounds (2,4) are also valid for heavy-ion collisions.

Let us mention only one application of these bounds, corresponding to the action of strong magnetic field generated in heavy-ion collisions. The lattice calculation [10] of conductivity tensor which is the direct counterpart of hadronic tensor W results in the dominance of its zz component (z being the direction of magnetic field) for low mass dileptons. One can immediately see from (2) that this corresponds to longitudinal polarization $\lambda = -1$ with respect to this axis. Note that positivity bounds lead to nullification of all other components of W, if only diagonal are found to be equal to zero.

Discussion. We found that the positivity bounds provide the important constraints for angular distributions of dileptons. They may be used to get the valuable infirmation about partonic transverse momentum, higher twist and dynamics of heavy-ion collisions.

This work was supported in part by the RFBR (Grants No. 11-02-01538, No. 12-02-91526, No. 11-02-01454 and 12-02-00613)

References

[1] X. Artru, M. Elchikh, J. M. Richard, J. Soffer and O. V. Teryaev, Phys. Rept. **470**, 1 (2009) [arXiv:0802.0164 [hep-ph]].

[2] C. S. Lam and W. K. Tung, Phys. Rev. D **21**, 2712 (1980).

[3] O. Teryaev, Nucl. Phys. Proc. Suppl. **214** (2011) 118.

[4] O.V. Teryaev, *Kinematical azimuthal asymmetries and Lam-Tung relation*, Proceedings of X1 Advanced Research Workshop on High Ebergy Spin Physics, Dubna, 2005, pp. 171-175.

[5] J. C. Collins, Phys. Rev. Lett. **42**, 291 (1979).

[6] J-C.Peng, J. Roloff and O.V. Teryaev, These Proceedings

[7] I.V. Anikin and O.V. Teryaev, These Proceedings

[8] L. D. McLerran and T. Toimela, Phys. Rev. D **31** (1985) 545.

[9] E. L. Bratkovskaya, O. V. Teryaev and V. D. Toneev, Phys. Lett. B **348**, 283 (1995).

[10] P. V. Buividovich, M. N. Chernodub, D. E. Kharzeev, T. Kalaydzhyan, E. V. Luschevskaya and M. I. Polikarpov, Phys. Rev. Lett. **105** (2010) 132001 [arXiv:1003.2180 [hep-lat]].

POSITIVITY BOUNDS FOR ANGULAR DISTRIBUTIONS OF DILEPTONS IN HADRONIC COLLISIONS

J. C. Peng [1], J. Roloff [1] and O.V. Teryaev [2,†]

(1) *University of Illinois at Urbana-Champaign, Urbana, IL 61801*
(2) *Bogoliubov Laboratory of Theoretical Physics, JINR, Dubna, Russia*
† *E-mail: teryaev@theor.jinr.ry*

Abstract

We study an inequality for the coefficients of decay angular distributions of the Drell-Yan process. This relation is checked against existing $\pi^- + W$ and $p + p$ and $p + d$ Drell-Yan data. It is found that this inequality relation is satisfied by most of the data, although a significant violation is observed for a small fraction of the data.

Introduction. Positivity constraints play a prominent role [1] in high energy physics providing important model-independent inequalities for various non-perturbative inputs. Here we address the applications of such inequalities for angular distributions of Drell-Yan dilepton pairs [2]. These azimuthal asymmetries, from one side, may be relatively easy studied experimentally, and from the other side, are directly related to the virtual photon tensor polarization and serve as a probe for the production dynamics.

Here we test the particular inequality against the available data and find it quite close to saturation. The reason can be [3] that it emerges due to transverse momentum of quarks and provides therefore its complementary probe.

Angular ditributions and positivity. The angular distribution of dileptons in (unpolarized) Drell-Yan process has the following form

$$d\sigma \propto 1 + \lambda \cos^2\theta + \mu \sin 2\theta \cos\phi + \frac{\nu}{2} \sin^2\theta \cos 2\phi \tag{1}$$

where θ and ϕ are polar and azimuthal angles of one of leptons in their c.m. frame, while $\lambda,\ \mu,\ \nu$ are angle independent coefficients encoding the information on tensor polarization of virtual photon. The positivity of its density matrix leads to the bounds for the angular coefficients [4].

$$|\lambda| \leq 1,\ |\nu| \leq 1 + \lambda,\ \mu^2 \leq \frac{(1-\lambda)(1+\lambda-\nu)}{4} \tag{2}$$

These bounds (2) coincide with the obtained earlier by structure functions method [2]. We are going to test them paying the special role to the bound for μ.

Comparison with existing data. Measurements of the azimuthal angular distributions for Drell-Yan process have been reported by the NA10 [5] and E615 [6] Collaborations for the $\pi^- + W$ interaction and by the E866 Collaboration for the $p + d$ [7] and $p + p$ [8] reactions. The inequality $(1 - \lambda)(1 + \lambda - \nu)/4 > \mu^2$ is checked by evaluating the quantity

$$\delta = (1 - \lambda)(1 + \lambda - \nu)/4 - \mu^2,$$

which is positive if the inequality is satisfied. The uncertainty of this quantity is evaluated by assuming that the errors in λ, ν, and μ are uncorrelated.

Figure 1 shows the comparison of the inequality relation with the NA10 $\pi^- + W$ data [5]. The NA10 data consist of measurements performed at three beam energies with the highest statistics at 184 GeV/c. The data at 184 GeV/c clearly satisfy the inequality relation (being not too far from saturating it) with the values of δ all positive. The data at 140 and 286 GeV/c are also consistent with the inequality within the experimental uncertainties.

Figure 2 shows the Drell-Yan data from the Fermilab E615 on $\pi^- + W$ at 252 GeV/c [6]. The inequality relation was checked using the values of λ, μ, and ν evaluated in three different dimuon rest frames: the Collins-Soper (CS) frame [9], the Gottfried-Jackson (GJ) frame [10], and the u-channel (UC) frame. The values $(1-\lambda)(1+\lambda-\nu)/4-\mu^2$ tend to be slightly negative, indicating that the inequality relation is barely satisfied. It is not clear how the E615 data, taken at a slight higher energy than the NA10 data, appear to be significantly different from the NA10 data.

Figure 3 shows the comparison between the inequality relation and the recent data from Fermilab E866 [7,8]. With the exception of the data at the lowest p_T bin, the inequality relation is quite well satisfied by the proton-induced Drell-Yan data.

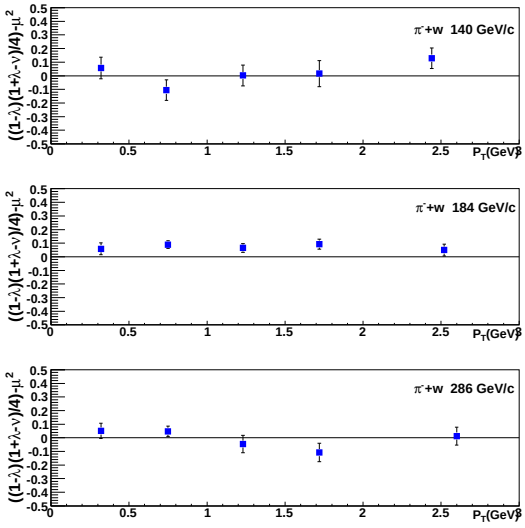

Figure 1: The quantity δ versus p_T for the NA10 $\pi^- + W$ data at three beam energies.

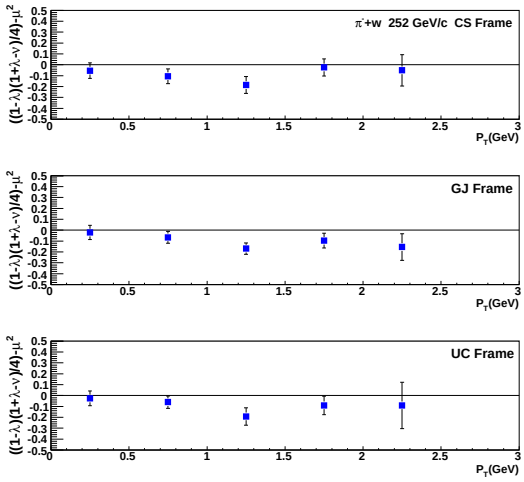

Figure 2: The quantity δ versus p_T for the E615 $\pi^- + W$ data at 252 GeV/c in the CS, GJ, and UC frames.

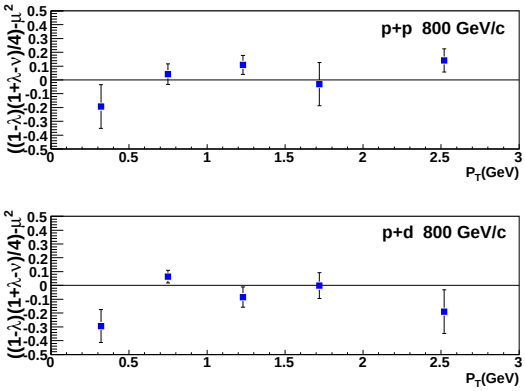

Figure 3: The quantity δ versus p_T for the E866 $p + p$ and $p + d$ data at 800 GeV/c.

Table 1: Mean values of the λ, μ, ν parameters and the quantity $\langle\delta\rangle \equiv (1-\langle\lambda\rangle)(1+\langle\lambda\rangle-\langle\nu\rangle)/4-\langle\mu\rangle^2$ for the $\pi^- + W$, $p+p$, and $p+d$ DY measurements.

	$\pi^- + W$ 140 GeV/c	$\pi^- + W$ 184 GeV/c	$\pi^- + W$ 286 GeV/c	$p+p$ 800 GeV/c	$p+d$ 800 GeV/c
$\langle\lambda\rangle$	1.01 ± 0.08	0.83 ± 0.04	0.99 ± 0.06	0.85 ± 0.10	0.83 ± 0.04
$\langle\mu\rangle$	0.002 ± 0.02	0.008 ± 0.01	-0.027 ± 0.01	0.026 ± 0.02	0.008 ± 0.01
$\langle\nu\rangle$	0.082 ± 0.016	0.091 ± 0.009	0.09 ± 0.012	0.04 ± 0.015	0.09 ± 0.009
$\langle\delta\rangle$	-0.0048 ± 0.04	0.074 ± 0.016	0.004 ± 0.028	0.067 ± 0.04	0.074 ± 0.016

Table I shows the comparison of the quantity $(1-\langle\lambda\rangle)(1+\langle\lambda\rangle-\langle\nu\rangle)/4-\langle\mu\rangle^2$ with the NA10 and E866 data, where $\langle\lambda\rangle$, $\langle\mu\rangle$, and $\langle\nu\rangle$ refer to the averaged values of the λ, μ, and ν, respectively. Table I shows that the inequality relation is well satisfied by the NA10 and E866 data. For the Fermilab E615 data, these averaged quantities were not available. Nevertheless, Fig. 2 suggests that the inequality would not be satisfied by the averaged values of λ, μ, and ν measured in E615.

Figure 4 shows the comparison of the inequality relation with the NA10 $\pi^- + W$ data [5] plotted as a function of ρ, where $\rho = p_T/Q$.

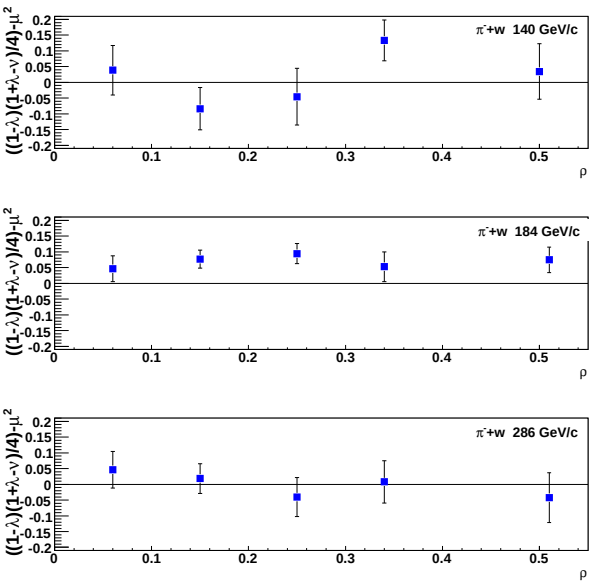

Figure 4: The quantity δ versus ρ for the NA10 $\pi^- + W$ data at three beam energies.

Discussion. We found that the positivity bound for μ is often close to saturation. The reason can be the kinematical nature of azimuthal asymmetries. The parameter μ is than a complementary probe of parton transverse momenta, both intrinsic and generated by gluon emission. At the same time, the violation of the bound may likely signal on the necessity to reconsider the interpretation and errors of the data. Only after such a reconsideration the more exotic sources of positivity violation like the contributions of coloured states [1, 11] may be discussed.

This work was supported in part by the RFBR (Grants No. 11-02-01538, 11-02-01454 and 12-02-00613).

References

[1] X. Artru, M. Elchikh, J. M. Richard, J. Soffer and O. V. Teryaev, Phys. Rept. **470**, 1 (2009) [arXiv:0802.0164 [hep-ph]].

[2] C. S. Lam and W. K. Tung, Phys. Rev. D **21**, 2712 (1980).

[3] O.V. Teryaev, *Kinematical azimuthal asymmetries and Lam-Tung relation*, Proceedings of X1 Advanced Research Workshop on High Ebergy Spin Physics, Dubna, 2005, pp. 171-175, and *Angular asymmetries in hadronic and heavy-ion collisions*, These Proceedings.

[4] O. Teryaev, Nucl. Phys. Proc. Suppl. **214** (2011) 118.

[5] S. Falciano *et al.*, Z. Phys. C **31**, 513 (1986); M. Guanziroli *et al.*, Z. Phys. C **37**, 545 (1988).

[6] J. S. Conway *et al.*, Phys. Rev. D **39**, 92 (1989).

[7] L. Y. Zhu *et al.*, Phys. Rev. Lett. **99**, 082301 (2007).

[8] L. Y. Zhu *et al.*, Phys. Rev. Lett. **102**, 182001 (2009).

[9] J. C. Collins and D. E. Soper, Phys. Rev. D **16**, 2219 (1977).

[10] K. Gottfried and J. D. Jackson, Nuovo Cimento **33**, 309 (1964).

[11] J. P. Ralston, arXiv:0810.0871 [hep-ph]; AIP Conf. Proc. **1149** (2009) 207.

DISTINGUISHING SPIN OF NEW HEAVY RESONANCES IN DIPHOTON AND DILEPTON CHANNELS AT THE CERN LHC

A.V. Tsytrinov [1†], A.A. Pankov [1] and V.A. Bednyakov [2]

(1) *Abdus Salam ICTP Affiliated Centre, Pavel Sukhoi State Technical University of Gomel, Gomel, 246746 Belarus.*
(2) *Laboratory of Nuclear Problems, Joint Institute for Nuclear Research, Dubna, Moscow region, 141980 Russia.*
† *E-mail: tsytrin@gstu.by*

Abstract

Many new physics models predict the existence of very heavy resonances with mass above 1 TeV that can possibly be observed at the CERN LHC. These resonances, predicted by different nonstandard models can generate peaks with the same mass and same number of events under the peak. In this case, spin determination of a peak becomes crucial in order to identify the relevant new physics model. Here we focus on using a center-edge asymmetry, applied to Drell-Yan dilepton and diphoton events at the LHC, for spin identification of spin-2 Randall-Sundrum graviton excitations against spin-1 heavy neutral gauge bosons Z' and spin-0 SUSY R-parity violating sneutrinos.

Numerous new physics (NP) scenarios (models with extra spatial dimensions, E_6 GUT and LR models of Z'-bosons, SUSY with R-parity violating), widely presented in the literature [1–3], predict narrow resonant peaks in dilepton and diphoton invariant mass distributions in proton-proton collisions at the CERN Large Hadron Collider (LHC). Once a heavy resonance is discovered in the processes:

$$p + p \to l^+ l^- + X \quad (l = e, \mu) \quad \text{and} \quad p + p \to \gamma\gamma + X, \tag{1}$$

its observables can be used in the attempt to identify the theoretical framework to which it belongs. The measurement of the total number of events, the angular distribution and the center-edge asymmetry A_{CE} of lepton/photon decay products at the resonance peak is a powerful tool [4–7] to disentangle the spin of the resonance in the processes (1). We will here discuss the identification of the spin-2 graviton excitation predicted by the Randall-Sundrum (RS) model with one warped extra dimension [1], against the spin-1 and the spin-0 hypotheses for a heavy neutral resonance discovered in dilepton and diphoton inclusive production (1) at the LHC. As an example of the spin-1 hypothesis we assume the Z's predicted by extended electroweak gauge symmetries [2], for the spin-0 – sneutrinos ($\tilde{\nu}$) envisaged by R-parity violating SUSY extensions of the SM [3]. Signature spaces of considered here models has a confusion regions of their respective parameters allowed by current experimental limits, in which s-channel exchanges of the above mentioned particles can in the process (1) produce narrow peaks in the dilepton and diphoton invariant mass with the same values of mass and event rates. Therefore, for the spin-2 hypothesis discrimination against the spin-1 and spin-0 we will use the difference in the characteristic angular distributions of the different scenarios.

The total cross section for a heavy resonance discovery in events (1) at an invariant dilepton or diphoton mass $M = M_R$ (with $R = G, Z', \tilde{\nu}$ denoting graviton, Z' and sneutrino, respectively) is:

$$\sigma(pp \to R) \cdot \mathrm{BR}(R \to l^+l^-, \text{ or } \gamma\gamma) = \int_{-z_{\mathrm{cut}}}^{z_{\mathrm{cut}}} \mathrm{dz} \int_{M_R-\Delta M/2}^{M_R+\Delta M/2} \mathrm{dM} \int_{y_{\min}}^{y_{\max}} \mathrm{dy} \frac{\mathrm{d}\sigma}{\mathrm{dM\,dy\,dz}}. \quad (2)$$

For determination of our basic observable – center edge asymmetry – we will use the differential angular distributions:

$$\frac{\mathrm{d}\sigma}{\mathrm{d}z} = \int_{M_R-\Delta M/2}^{M_R+\Delta M/2} \mathrm{d}M \int_{y_{\min}}^{y_{\max}} \frac{\mathrm{d}\sigma}{\mathrm{d}M\,\mathrm{d}y\,\mathrm{d}z}\,\mathrm{d}y. \quad (3)$$

The correspondence between spin and angular distributions is quite sharp: a spin-0 resonance determines a flat angular distribution, spin-1 corresponds to a parabolic shape, and spin-2 yields a quartic distribution. In Eqs. (2) and (3), $z = \cos\theta_{\mathrm{cm}}$ and y are the lepton-quark (or photon-quark) angle in the dilepton (or diphoton) center-of-mass and the dilepton rapidity, respectively, and cuts on phase space due to detector acceptance are indicated, ΔM is an invariant mass bin around M_R, reflecting the detector energy resolution [9]. To evaluate the number N_S of resonant signal events we assume LHC energy of 14 TeV, time-integrated luminosity of 100 fb^{-1} and reconstruction efficiencies of 90% for both electrons and muons and 80% for photons. Typical experimental cuts are: $p_\perp > 20$ GeV and pseudorapidity $|\eta| < 2.5$ for both leptons; $p_\perp > 40$ GeV and $|\eta| < 2.4$ for photons. To evaluate Eqs. (2) and (3) the parton subprocesses cross sections will be convoluted with the PDFs. NLO QCD effects can be accounted for by K-factor equal to 1.3 for all considered processes. More detailed study on NLO QCD in diphoton channel has been done recently in [8]. The completely symmetric pp initial state at the LHC lead to some unambiguity of the sign of z. One can avoid this difficulty by using as the basic observable for angular analysis the z-evenly integrated center-edge angular asymmetry [10, 4, 6, 7]:

$$A_{\mathrm{CE}} = \frac{\sigma_{\mathrm{CE}}}{\sigma} \quad \text{with} \quad \sigma_{\mathrm{CE}} \equiv \left[\int_{-z^*}^{z^*} - \left(\int_{-z_{\mathrm{cut}}}^{-z^*} + \int_{z^*}^{z_{\mathrm{cut}}}\right)\right] \frac{\mathrm{d}\sigma}{\mathrm{d}z}\,\mathrm{d}z. \quad (4)$$

In Eq. (4), $0 < z^* < z_{\mathrm{cut}}$ defines the separation between the "center" and the "edge" kinematical regions (here we use $z^* = 0.5$). Another advantage of using A_{CE} is that it much less sensitive to systematic uncertainties than the absolute angular distributions.

RS model with one compactified extra dimension in the simplest version [1], originally proposed as a rationale for the gauge hierarchy problem $M_{\mathrm{EW}} \ll M_{\mathrm{Pl}}$, consists of one warped extra spatial coordinate y with exponential warp factor $\exp(-k\pi|y|)$ (with $k > 0$ the 5D curvature assumed of order M_{Pl}), and two three-dimensional branes placed at a compactification distance R_c in y. The SM fields are localized to the so-called TeV brane, while gravity originates on the other, so-called Planck-brane, but is allowed to propagate everywhere in the full 5D space. These consist of a tower of spin-2 graviton excitations that can be exchanged in processes (1) at the LHC and show up as narrow peaks in M with a specific mass spectrum. The model can be conveniently parametrized in terms of M_G, the mass of the lowest graviton excitation, and of the universal dimensionless coupling $c = k/\bar{M}_{\mathrm{Pl}}$. Theoretically, $0.01 < c < 0.1$. Current 95% CL experimental limits [11] are in the range $M_G > 700$ GeV ($c \cong 0.01$) up to $M_G > 1.8$ TeV ($c \cong 0.1$).

The spin-1 hypothesis in process (1) can be realized by $q\bar{q}$ annihilation into lepton pairs through Z' intermediate state. Such bosons are generally predicted by electroweak models beyond the SM, based on extended gauge symmetries. Generally, Z' models depend on $M_{Z'}$ and on the left- and right-handed couplings to SM fermions. In the sequel, results will be given for a popular class of models for which the values of these couplings are fixed theoretically, so that only $M_{Z'}$ is a free parameter. These are the Z'_{χ}, Z'_{ψ}, Z'_{η}, $Z'_{\rm LR}$, $Z'_{\rm ALR}$ models, and the "sequential" $Z'_{\rm SSM}$ model with Z' couplings identical to the Z ones. Current experimental lower limits (95% CL) on $M_{Z'}$ depend on models, for Z'_{SSM} it is $M_{Z'} > 1.8$ TeV [11].

R-parity is defined as $R_p = (-1)^{(2S+3B+L)}$, and distinguishes particles from their superpartners. In scenarios where this symmetry can be violated, supersymmetric particles can be singly produced from ordinary matter. In the dilepton process (1) of interest here, a spin-0 sneutrino can be exchanged through the subprocess $\bar{d}d \to \tilde{\nu} \to l^+l^-$ and manifest itself as a peak at $M = M_{\tilde{\nu}}$ with a flat angular distribution. Besides $M_{\tilde{\nu}}$, the cross section is proportional to the R-parity violating product $X = (\lambda')^2 B_l$ where B_l is the sneutrino leptonic branching ratio and λ' the relevant sneutrino coupling to the $\bar{d}d$ quarks. Current limits on the relevant λ's are of the order of 10^{-2} [12], and the experimental 95% CL lower limits on $M_{\tilde{\nu}}$ range from 397 GeV (for $X = 10^{-4}$) to 866 GeV (for $X = 10^{-2}$) [13]. We take for X, presently not really constrained for sneutrino masses of order 1 TeV or higher, the interval $10^{-5} < X < 10^{-1}$.

The nonstandard models briefly described above can mimic each other as sources of an observed peak in M, for values of the parameters included in so-called "confusion regions", where they can give same numbers of signal events N_S. In such confusion regions, one can try to discriminate models from one another by means of the angular distributions of the events, directly reflecting the different spins of the exchanged particles. We start from the assumption that an observed peak at $M = M_R$ is the lightest spin-2 graviton ($M_R = M_G$). We define a "distance" among models accordingly:

$$\Delta A^{Z'}_{\rm CE} = A^{G}_{\rm CE} - A^{Z'}_{\rm CE} \qquad \text{and} \qquad \Delta A^{\tilde{\nu}}_{\rm CE} = A^{G}_{\rm CE} - A^{\tilde{\nu}}_{\rm CE}. \tag{5}$$

To assess the domain in the (M_G, c) plane where the competitor spin-1 and spin-0 models giving the same N_S under the peak can be excluded by the starting RS graviton hypothesis, a χ^2 criterion can be applied, which compares the deviations (5) with the statistical uncertainty $\delta A^{G}_{\rm CE}$ relevant to the RS model. We impose the two conditions

$$\chi^2 \equiv |\Delta A^{Z',\tilde{\nu}}_{\rm CE}/\delta A^{G}_{\rm CE}|^2 > \chi^2_{\rm CL}. \tag{6}$$

Eq. (6) contains the definition of χ^2, and the $\chi^2_{\rm CL}$ specifies a desired confidence level (3.84 for 95% CL). This condition determines the minimum number of events, $N_S^{\rm min}$, needed to exclude the spin-1 and spin-0 hypotheses (hence to establish the graviton spin-2), and this in turn will determine the RS graviton *identification* domain in the (M_G, c) plane which is shown in Fig. 1. One should note that for the diphoton channel, due to spin-1$\not\to \gamma\gamma$, the viable hypotheses reduce to spin-2 and spin-0 exchanges only. An analogous procedure can be applied to the identification of Z' and $\tilde{\nu}$ exchanges against the two competing ones as sources of a peak in process (1).

Figure 1 shows the expected 5σ discovery reaches on lowest lying graviton and its 95% CL identification range in the (M_G, c) plane from dilepton ($l = e, \mu$ combined) and diphoton events with time-integrated luminosity of 100 fb^{-1}.

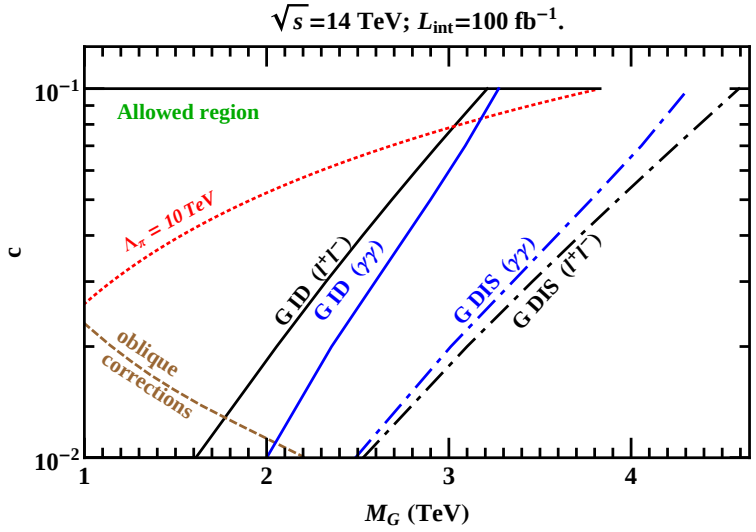

Figure 1: Discovery and identification reaches on RS graviton in the processes (1) at the LHC with $\sqrt{s} = 14$ TeV and $\mathcal{L}_{\rm int}$ =100 fb^{-1}.

Figure 1 also shows that, for the graviton coupling constants of 0.01 and 0.1, the graviton 5σ discovery reaches are, respectively, 2.4 (2.5) and 4.3 (4.6) TeV for diphotons (dileptons), while the graviton identification reaches are, respectively, 1.6 (2.0) and 3.2 (3.4) TeV at a 95% C.L. for dileptons (diphotons).

Acknowledgments

We would like to thank Prof. P. Osland and Prof. N. Paver for the enjoyable collaboration on the subject matter covered here. This research has been partially supported by the Abdus Salam ICTP under Associate and TRIL programmes and by the Belarusian Republican Foundation for Fundamental Research.

References

[1] L. Randall and R. Sundrum, Phys. Rev. Lett. **83** (1999) 3370 ; Phys. Rev. Lett. **83** (1999) 4690.

[2] P. Langacker, Rev. Mod. Phys. **81** (2008) 1199.

[3] J. Kalinowski *et al.,* Phys. Lett. B **406** (1997) 314; **414** (1997) 297; R. Barbier *et al.,* Phys. Rept. **420** (2005) 1.

[4] P. Osland *et al.,* Phys. Rev. D **82** (2010) 115017.

[5] V. A. Bednyakov *et al.,* Phys. Atom. Nucl. **73** (2010) 1266.

[6] P. Osland *et al.,* Phys. Rev. D **79** (2009) 115021.

[7] P. Osland *et al.,* Phys. Rev. D **78** (2008) 035008.

[8] M. C. Kumar *et al.,* arXiv:1108.3764 [hep-ph] (to appear in Phys. Rev. D 2011).

[9] ATLAS Collaboration, Reports No. CERN-LHCC-99-14, CERN-LHCC-99-15

[10] E. W. Dvergsnes *et al.,* Phys. Rev. D **69** (2004) 115001.

[11] ATLAS Collab., arXiv:1108.1582; CMS Collab., Report No. CMS PAS EXO-11-09.

[12] R. Barbier *et al.,* Phys. Rept. **420** (2005) 1; H. K. Dreiner *et al.,* Phys. Rev. D **82** (2010) 055027.

[13] Aaltonen A *et al.,* [CDF Collaboration] Phys. Rev. Lett. **102** (2009) 091805.

KINEMATICS OF DEEP INELASTIC SCATTERING IN LEADING ORDER OF COVARIANT APPROACH

P. Zavada

Institute of Physics of the AS CR, Na Slovance 2, CZ-182 21 Prague 8, Czech Republic
E-mail: zavada@fzu.cz

Abstract

We study the kinematics of deep inelastic scattering corresponding to the rotationally symmetric distribution of quark momenta in the nucleon rest frame. It is shown that rotational symmetry together with Lorentz invariance can in leading order impose constraints on the quark intrinsic momenta. Obtained constraints are discussed and compared with the available experimental data.

1. Introduction. The motion of quarks inside the nucleons plays an important role in some effects which are at present intensively investigated both experimentally and theoretically. Actual goal of this effort is to obtain a more consistent 3-D picture of the quark-gluon structure of nucleons. For example the quark transversal momentum creates the asymmetries in particle production in polarized (SIDIS) or in unpolarized (Cahn effect) experiments on deep inelastic scattering (DIS). Relevant tool for the study of these effects is the set of the transverse momentum dependent distributions (TMDs). Apparently, a better understanding of the quark intrinsic motion is also a necessary condition to clarify the role of quark orbital angular momenta in generating nucleon spin.

We have paid attention to these topics in our recent studies, see [1] and citations therein. In particular we have shown that the requirements of Lorentz invariance (LI) and the nucleon rotational symmetry in its rest frame (RS), if applied in the framework of the 3-D covariant quark-parton model (QPM), generate a set of relations between parton distribution functions. Recently we obtained within this approach relations between usual parton distribution functions and the TMDs. The Wanzura-Wilczek approximate relation (WW) and some other known relations between the g_1 and g_2 structure functions were similarly obtained in the same model before [2]. Let us remark that the WW relation has been obtained independently also in another approaches [7, 6] in which the LI represents a basic input.

The aim of the present report is to consistently apply the assumption LI&RS to the kinematics of DIS and to obtain the constraints on related kinematical variables. That is a complementary task to the study of above mentioned relations between distribution functions, which depend on these variables. So, the report can be considered as an addendum to our former papers related to the covariant QPM [1–3].

Since the present discussion is motivated and based on our earlier study of a covariant version of QPM, obtained results correspond only to the leading order of a more consistent QCD treatment. In this sense it would be interesting to compare our results with the leading order of a real QCD approach, like e.g. the recent study of perturbative QCD evolution of TMDs [4]. However such task would go beyond the scope of this short report. Anyway, in general a comparison between the experimental data and the leading order predictions can be important and instructive.

2. The Bjorken variable and light-cone coordinates. First, let us shortly remind the properties of the Bjorken variable

$$x_B = \frac{Q^2}{2Pq}, \tag{1}$$

which plays a crucial role in phenomenology of lepton – nucleon scattering. Regardless of mechanism of the process, this invariant parameter satisfies

$$0 \leq x_B \leq 1. \tag{2}$$

Now let us consider a QPM approach, where the process of lepton – nucleon scattering is initiated by the lepton interaction with a quark (see Fig. 1), which obeys

$$p' = p + q, \qquad p'^2 = p^2 + 2pq - Q^2; \qquad Q^2 = -q^2. \tag{3}$$

The second equality implies

$$Q^2 = 2pq - \delta m^2; \qquad \delta m^2 = p'^2 - p^2, \tag{4}$$

which with the use of relation (1) gives

$$\frac{pq}{Pq} = x_B \left(1 + \frac{\delta m^2}{Q^2}\right). \tag{5}$$

The basic input for the construction of QPM is the assumption

$$Q^2 \gg \delta m^2, \tag{6}$$

which allows us to identify

$$x_B = \frac{Q^2}{2Pq} = \frac{pq}{Pq} \tag{7}$$

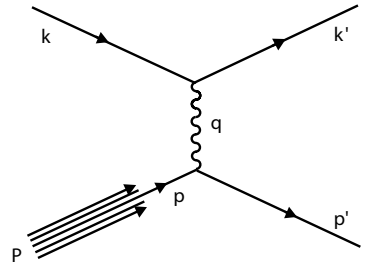

Figure 1: Diagram describing DIS as a one photon exchange between the charged lepton and quark. Lepton and quark momenta are denoted by k, p (k', p') in initial (final) state, P is initial nucleon momentum.

and to directly relate the quark momentum to the parameters of scattered lepton. Moreover, if one assumes

$$Q^2 \gg 4M^2 x_B^2, \tag{8}$$

where M is the nucleon mass, then one can identify

$$x_B = x \equiv \frac{p_0 - p_1}{P_0 - P_1} \tag{9}$$

in any reference frame in which the first axis orientation is defined by the vector $\mathbf{q}$. This relation can be proved as follows. Let us consider Eq. (7) in the same frame:

$$x_B = \frac{p_0 q^0 - p_1 |\mathbf{q}|}{P_0 q^0 - P_1 |\mathbf{q}|}. \tag{10}$$

In the nucleon rest frame we denote the vector components by subscript R and use the usual symbol $\nu = q^0_R$ so we have

$$|\mathbf{q}_R|^2 = \nu^2 + Q^2, \tag{11}$$

which with the use of Eq. (1) gives

$$\frac{|\mathbf{q}_R|^2}{\nu^2} = 1 + \frac{4M^2x_B^2}{Q^2}. \tag{12}$$

It means that for $Q^2 \gg 4M^2x_B^2$ we obtain

$$\frac{|\mathbf{q}_R|}{\nu} = 1 + O\left(\frac{4M^2x_B^2}{Q^2}\right). \tag{13}$$

(Since for $Q^2 \to \infty$ we have also $|\mathbf{q}_R|, \nu \to \infty$, so the ratio $|\mathbf{q}_R|/\nu \to 1$ does not contradict Eq. (11).) In a reference frame connected with the rest frame by the Lorentz boost in the direction opposite to $\mathbf{q}_R$ we have the corresponding ratio

$$\frac{q^1}{q^0} = \frac{|\mathbf{q}_R| + \beta\nu}{\nu + \beta\,|\mathbf{q}_R|}. \tag{14}$$

Now one can easily check that Eq. (7) with the use of this ratio and Eq. (13) imply

$$x_B = \frac{p_0q^0 - p_1q^1}{P_0q^0 - P_1q^1} = \frac{p_0 - p_1}{P_0 - P_1}\left(1 + O\left(\frac{4M^2x_B^2}{Q^2}\right)\right). \tag{15}$$

In this way we have proved that replacement of Bjorken variable by the invariant light-cone ratio in Eq. (9) is valid provided the inequality (8) is satisfied.

The relation (9) expressed in the nucleon rest frame reads

$$x = \frac{p_0 - p_1}{M}, \tag{16}$$

which after inserting into (2) gives

$$0 \le \frac{p_0 - p_1}{M} \le 1. \tag{17}$$

However the most important reason why we require large Q^2 is in physics. If we accept scenario when a probing photon interact with a quark, we need sufficiently large momentum transfer Q^2 at which the quarks can be considered as effectively free due to asymptotic freedom. At small Q^2 the picture of quarks (with their momenta and other quantum numbers) inside the nucleon disappear.

3. Rotational symmetry. The RS means that the probability distribution of the quark momenta $\mathbf{p} = (p_1, p_2, p_3)$ in the nucleon rest frame depends, apart from Q^2, on $|\mathbf{p}|$. It follows that also $-\mathbf{p}$ is allowed, so together with the inequality (17) we have

$$0 \le \frac{p_0 + p_1}{M} \le 1. \tag{18}$$

The combinations of (17),(18) imply

$$0 \le |p_1| \le p_0 \le M, \qquad |p_1| \le \frac{M}{2}. \tag{19}$$

And if we again refer to RS, then further inequalities are obtained:

$$0 \leq |\mathbf{p}| \leq p_0 \leq M, \quad |\mathbf{p}| \leq \frac{M}{2}, \quad 0 \leq p_T \leq p_0 \leq M \tag{20}$$

and

$$p_T \leq \frac{M}{2}, \tag{21}$$

where

$$|\mathbf{p}| = \sqrt{p_1^2 + p_2^2 + p_3^2}, \qquad p_T = \sqrt{p_2^2 + p_3^2}.$$

Obviously inequality (21) is satisfied also in any reference frame boosted in the directions $\pm\mathbf{q}$. Further, the above inequalities are apparently valid also for average values $\langle p_0 \rangle, \langle p_1 \rangle, \langle |\mathbf{p}| \rangle$ and $\langle p_T \rangle$. In addition, if one assumes that p_T- distribution is a decreasing function, then necessarily

$$\langle p_T \rangle \leq \frac{M}{4}. \tag{22}$$

The above relations are valid for sufficiently high Q^2 suggested by Eqs. (6) and (8). Let us note that the on-mass-shell assumption has not been applied for obtaining these relations.

These inequalities can be compared with relations obtained in [2], where the additional on-mass-shell condition $m^2 = p^2 = p_0^2 - \mathbf{p}^2$ had been applied. Corresponding relations are more strict:

$$\frac{m^2}{M^2} \leq x \leq 1, \quad p_0 \leq \frac{M^2 + m^2}{2M}, \quad |\mathbf{p}| \leq \frac{M^2 - m^2}{2M} \tag{23}$$

and

$$p_T^2 \leq M^2 \left(x - \frac{m^2}{M^2} \right) (1 - x). \tag{24}$$

However, it is clear that in general the on-mass-shell assumption is not realistic. In the next we will assume only the off-mass-shell approach.

4. Discussion. First let us summarize more accurately what we have done in the previous section. We assumed:

a) Lorentz invariance

It means that the theoretical description in terms of the standard kinematical variables (see Fig. 1)

$$q, \ x_B, \ x, \ p = (p_0, p_1, p_2, p_3), \ P = (P_0, P_1, P_2, P_3)$$

can be boosted also to the nucleon rest frame.

b) Inequality $0 \leq x \leq 1$

It means that the light-cone ratio x satisfies the same bound (2) as the Bjorken variable x_B.

c) Rotational symmetry

The kinematical region $\mathcal{R}^3$ of the quark intrinsic momenta $\mathbf{p} = (p_1, p_2, p_3)$ in the nucleon rest frame has rotational symmetry (i.e. $\mathbf{p} \in \mathcal{R}^3 \Rightarrow \mathbf{p}' = \mathbf{R}\mathbf{p} \in \mathcal{R}^3$, where $\mathbf{R}$ is any rotation in $\mathcal{R}^3$). For example, in terms of the covariant QPM it means that probabilistic distribution of the quark momenta is controlled by some function $G(pP/M, Q^2)$.

We proved these assumptions imply bounds (17)–(21). Now we will shortly comment on the obtained results:

i) The ratio x of light-cone variables (9) has a simple interpretation in a frame, where the proton momentum is large - x is the fraction of this momentum carried by the quark. However an interpretation of the same variable in the nucleon rest frame is more complicated. In this frame the quark transversal momentum cannot be neglected and x depends on the both, longitudinal and transversal quark momenta components. In the limit of massless quarks the connection between the variable x in (16) and the quark momenta components is given by the relations:

$$x = \frac{p_0 - p_1}{M}; \quad p_0 = \sqrt{p_1^2 + p_T^2}, \quad p_1 = -\frac{Mx}{2}\left(1 - \frac{p_T^2}{M^2x^2}\right), \quad p_0 = \frac{Mx}{2}\left(1 + \frac{p_T^2}{M^2x^2}\right).$$

These variables were used in our recent papers on TMDs [1, 2]. Simply the value of invariant variable x does not depend on the reference frame, but its interpretation e.g. in the rest frame differs from that in the infinite momentum frame.

ii) The relations (20), (21), which follow from RS, can be confronted with the experimental data on $\langle p_T \rangle$ or $\langle |\mathbf{p}| \rangle$. We have discussed the available data in the papers cited above and apparently relation (21) is compatible with the set of lower values $\langle p_T \rangle$ corresponding to the 'leptonic data'. On the other hand the second set giving substantially greater $\langle p_T \rangle$ and denoted as the 'hadronic data', seems to contradict this relation. Actually the conflict with the relation (21) would mean either the conflict with some of the assumptions *a)–c)* or simply it can be due to absence of the higher order QCD corrections. However, for possible comparison with the perturbative QCD approach [4] let us remark the following. This approach generate evolved TMDs using as input the existing phenomenological parametrizations extracted from the experimental data. For example, one of the inputs is the scale-independent Gaussian fit [5]

$$F_{f/P}(x, p_T) = f_{f/P}(x) \frac{\exp\left[-p_T^2 / \langle p_T^2 \rangle\right]}{\pi \langle p_T^2 \rangle}, \tag{25}$$

where $\langle p_T^2 \rangle = (0.38 \pm 0.06)\,\mathrm{GeV}^2$. Obviously our concept RS defined above is hardly compatible with this distribution. In fact in the rest frame this distribution gives much greater $\langle p_T^2 \rangle$ than the corresponding longitudinal term $\langle p_1^2 \rangle$. However RS requires $\langle p_T^2 \rangle = 2\langle p_1^2 \rangle$ only. Let us remark that this imbalance is of the same order as a difference between the two data sets mentioned above.

In the most recent paper [2] we explained why the RS, if applied on the level of QPM, follows from the covariant description. In fact it means the assumptions *a)–c)* are common for our QPM and for the approaches like [6, 7] where only Lorentz invariance is explicitly required. The predictions of all these models are compatible with the bound (21). This is just a consequence of the fact that general conditions *a)–c)* are satisfied in these approaches. Another theoretical reasons for RS have been suggested in [2]. Let us remark that the rotational-symmetry properties of the nucleon state in its rest frame play an important role also in the recent studies [9].

iii) The relation (24) is obtained for the quarks on-mass-shell. In a more general case, where only inequalities (20), (21) hold, this relation is replaced by

$$p_T^2 \leq M^2 \left(x - \frac{\mu^2}{M^2}\right)(1 - x); \qquad \mu^2 \equiv p_0^2 - \mathbf{p}^2, \tag{26}$$

where the term μ^2 is not a parameter corresponding to the fixed mass, but it is only a number varying in the limits defined by (20). The last relation implies for any μ^2:

$$p_T^2 \leq M^2 x\,(1-x)\,, \tag{27}$$

which is equivalent to the on-mass-shell relation (24) for $m = 0$. This general upper limit for p_T^2 depending on x is displayed in Fig. 2. Let us remark that results on $\langle p_T^2(x)\rangle$ obtained in [7, 6] are compatible also with the bound (27). An equivalent form of this inequality was probably for the first time presented in [10].

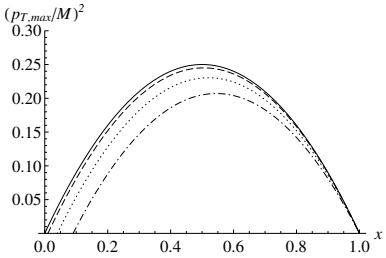

Figure 2: Upper limit of the quark transversal momentum as a function of x for $\mu = 0$ (solid line), 0.1 (dashed line), 0.2 (dotted line) and 0.3 (dash-dotted line).

To conclude, in the present report we studied the kinematic constraints due to the rotational symmetry of the quark momenta distribution inside the nucleon in the leading order approach. In particular, we have shown that the light-cone formalism combined with the assumption on the rotational symmetry in the nucleon rest frame imply $p_T \leq M/2$. Only part of existing experimental data on $\langle p_T\rangle$ satisfies this bound, but the another part does not. In general, the existing methods for reconstruction of $\langle p_T\rangle$ from the DIS data are rather model-dependent. These are the reasons why more studies are needed to clarify these inconsistencies, since the phenomenological distributions in the $x - p_T$ plane at present serve also as an input for a more fundamental calculation of the QCD evolution and other effects.

Acknowledgments. I am grateful to A.V. Efremov, P. Schweitzer and O.V. Teryaev for many useful discussions and valuable comments.

References

[1] A. V. Efremov, P. Schweitzer, O. V. Teryaev and P. Zavada, PoS **DIS2010**, 253 (2010) [arXiv:1008.3827 [hep-ph]]; Phys. Rev. D **80**, 014021 (2009); D **83**, 054025 (2011).

[2] P. Zavada, Phys. Rev. D **55**, 4290 (1997), D **65**, 054040 (2002); D **67**, 014019 (2003); D **83**, 014022 (2011) [arXiv:0908.2316 [hep-ph]]; Eur. Phys. J. C **52**, 121 (2007).

[3] A. V. Efremov, O. V. Teryaev and P. Zavada, Phys. Rev. D **70**, 054018 (2004).

[4] S. M. Aybat and T. C. Rogers, Phys. Rev. D **83**, 114042 (2011) [arXiv:1101.5057 [hep-ph]].

[5] P. Schweitzer, T. Teckentrup and A. Metz, Phys. Rev. D **81**, 094019 (2010).

[6] U. D'Alesio, E. Leader and F. Murgia, Phys. Rev. D **81**, 036010 (2010) [arXiv:0909.5650 [hep-ph]].

[7] J. D. Jackson, G. G. Ross and R. G. Roberts, Phys. Lett. B **226**, 159 (1989).

[8] R. K. Ellis, W. Furmanski and R. Petronzio, Nucl. Phys. B **212** (1983) 29; Nucl. Phys. B **207**, 1 (1982).

[9] C. Lorce' and B. Pasquini, arXiv:1111.6069 [hep-ph], arXiv:1109.5864 [hep-ph], arXiv:1107.3809 [hep-ph].

[10] J. Sheiman, Nucl. Phys. **B171**, 445 (1980).

EXPERIMENTAL RESULTS

1-HADRON TRANSVERSE TARGET SPIN ASYMMETRIES AT COMPASS

Christoph Adolph, on behalf of the COMPASS collaboration

Universität Erlangen-Nürnberg
E-mail: christoph.adolph@physik.uni-erlangen.de

Abstract

COMPASS is a fixed target experiment at CERN where the nucleon spin structure is investigated using a 160 GeV/c polarized μ^+ beam and polarized solid state targets. After taking data in the years 2002–2004 using a transversely polarized ^{6}LiD (deuteron) target, in 2007 and 2010 data were collected on a transversely polarized NH_3 (proton) target. The measurements of single spin asymmetries in semi-inclusive deep inelastic scattering (SIDIS) on a transversely polarized target are an important part of the COMPASS physics program. They allow to investigate the transversity distribution functions, *e.g.* coupled to the Collins fragmentation function, as well as transverse momentum dependent distribution functions, like the Sivers distribution function, by measuring azimuthal asymmetries in hadron production. In this contribution we present the results from the 2010 data for the Collins and Sivers asymmetries.

1 Introduction

The spin structure of the nucleon at twist-two level in the collinear case can be fully characterized by three independent parton distribution functions (PDF) for each quark flavour: the unpolarized distribution function $f_1(x)$, the helicity distribution function $g_1(x)$ and the transverse spin distribution function $h_1(x)$. The latter, also called transversity, is chiral odd and decouples from inclusive deep inelastic scattering (DIS). In combination with another chirally odd function like the Collins fragmentation function (FF) $H_1^h(z, p_T^2)$ [1] it is possible to measure transversity in semi inclusive DIS (SIDIS) in single hadron production. At the COMPASS experiment transversity can also be measured in Λ hyperon polarization and in two-hadron inclusive production [2], where it is coupled to the interference fragmentation function $H_1^{\sphericalangle}$.

When the intrinsic transverse momentum of the quarks $\vec{k_T}$ is taken into account, the nucleon structure at leading twist can be described by eight PDFs, which are all measured at COMPASS. This contribution will concentrate on the Collins function as well as on the Sivers function [3], which is correlated to the Sivers distribution function $f_{1T}^{\perp}(x, \vec{k_T})$.

COMPASS is a fixed target experiment at the CERN M2 beamline where the nucleon spin structure is investigated using a 160 GeV/c polarized μ^+ beam and polarized solid state targets. For measuring transverse spin effects a transversely polarized 6LiD (deuterium) target (years 2002–2004) [4] and a transversely polarized NH_3 (proton) target (years 2007 and 2010) [5] were used. The proton target consists of three target cells, where the outer ones are polarised oppositely to the inner one. The achieved polarisation is up to 95% with a dilution factor of 0.15.

2 The Collins asymmetry

The Collins mechanism leads to an azimuthal modulation in the distribution of the unpolarized hadrons produced in the fragmentation of a transversely polarized quark. The number of produced hadrons is then given by $N_h(\phi_C) = N_h^0[1 + f\ P_T\ D_{NN}\ A_{Coll}\ \sin(\phi_C)]$, where f is the target dilution factor, P_T is the target polarization and $D_{NN} = \frac{(1-y)}{(1-y+y^2/2)}$ is the spin transfer coeffizient from the initial to the struck quark. The Collins angle $\phi_C = \phi_h + \phi_s - \pi$ is the sum of the azimuthal angle of the produced hadron and the azimuthal angle of the nucleon spin with respect to the scattering plane. The Collins asymmetry A_{Coll} is given by

$$A_{Coll} = \frac{\sum_q e_q^2 \cdot h_1(x) \otimes H_1^h(z, p_T^2)}{\sum_q e_q^2 \cdot f_1(x) \otimes D_q^h(z, p_T^h)}$$

with the convolution of the transversity distribution $h_1(x)$ and the Collins fragmentation function $H_1^h(z, p_T^2))$ in the nominator. Here $z = E_h/(E_\mu - E_{\mu'})$ is the fraction of the virtual photon energy energy carried by the hadron and p_T^h is the transverse momentum of the hadron with respect to the photon direction.

To select events in the DIS region, kinematic cuts on the photon virtuality $Q^2 > 1\,(\mathrm{GeV}/c)^2$, on the fractional energy transfer of the muon $0.1 < y < 0.9$ and on the invariant hadronic mass $W > 5\,\mathrm{GeV}/c^2$ are applied. Furthermore $z > 0.2$ and $p_T^h > 0.1\,\mathrm{GeV}/c$ are required for the selection of the hadrons. In the following this selection will be referred to as the standard sample.

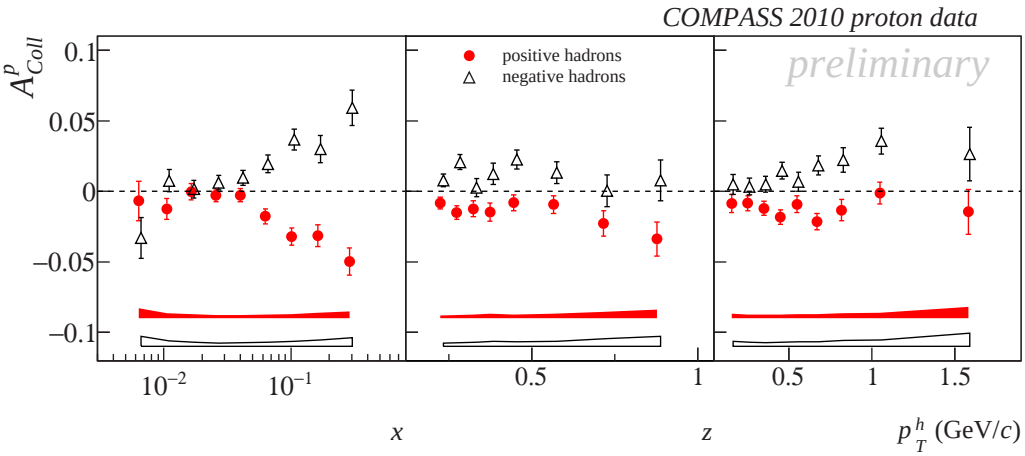

Figure 1: Collins asymmetries of 2010 proton data as a function of x, z and p_T^h for positive and negative hadrons. The bands correspond to the systematical error.

The preliminary results for the Collins asymmetry from the 2010 measurement on the proton target are shown in Fig. 1 as a function of x, z and p_T^h for positive and negative hadrons. For $x > 0.1$ the asymmetries are clearly different from zero and of opposite sign for positive and negative hadrons. At lower values of x the asymmetries are compatible with zero. In bins of z and p_T, the asymmetries show no clear trend but are different from zero in average. The 2010 results are in perfect agreement with the measurements on the Collins asymmetries of 2007, but with smaller error bars due to the higher statistics gained in 2010. The HERMES experiment [6] at DESY has also

measured the Collins asymmetries on a proton target using a polarized electron beam at a lower Q^2. In comparison the results from both experiments are in very good agreement. This indicates a weak Q^2 dependence of the Collins FF.

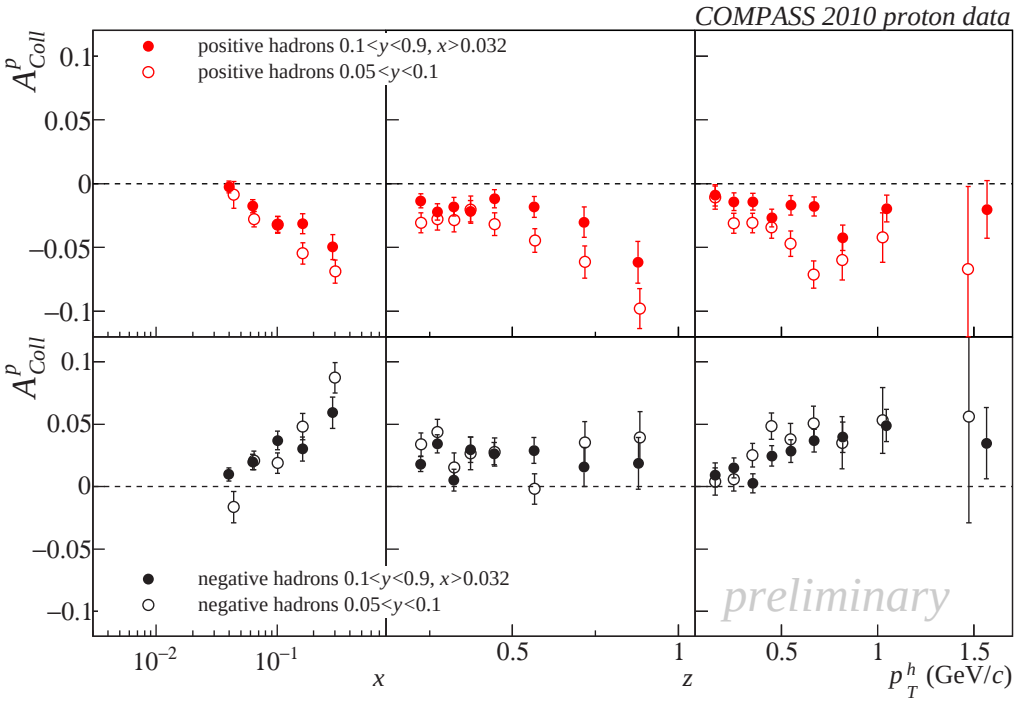

Figure 2: Collins asymmetries of 2010 proton data as a function of x, z and p_T^h for $0.1 < y < 0.9$ and $0.05 < y < 0.1$ with $x > 0.032$. Upper row shows positive hadrons, lower row negative hadrons.

With the higher statistics achieved during the 2010 measurment it is now possible to explore kinematical regions different from the standard sample described above. In one of the new analyses y was restricted to the region of $0.05 < y < 0.1$. The cut on W was dropped and the remaining cuts on z and p_T were kept the same as for the standard sample. Since there is no data for $x < 0.032$ at this low-y selection, for comparison an additional cut $x > 0.032$ was applied on the standard sample. Fig. 2 shows the results of the $0.05 < y < 0.1$ analysis in comparison with the standard sample. The upper row shows the asymmetries for positve hadrons and the lower row for negative hadrons. For positive hadrons the trend of the asymmetries stays the same but the absolute value increases in all bins of x, z and p_T. For negative hadrons no effect is visible. In a third analysis the sample corresponding to $0.1 < z < 0.2$ (low-z sample) was choosen while all other cuts were like the ones for the standard sample. The results are shown in Fig. 3 for the standard sample and the $0.1 < z < 0.2$ sample. The upper row shows the asymmetries for positve hadrons and the lower row for negative hadrons. In bins of x the low-z sample follows the standard sample but with slightly decreased values for large x values, both for positive and negative hadrons. In bins of p_T no difference can be seen.

3 The Sivers asymmtery

The Sivers function $f_{1T}^{\perp}(x, \vec{k_T})$ gives the correlation between the transverse spin of a nucleon and the intrinsic transverse momentum of unpolarized quarks. The number of

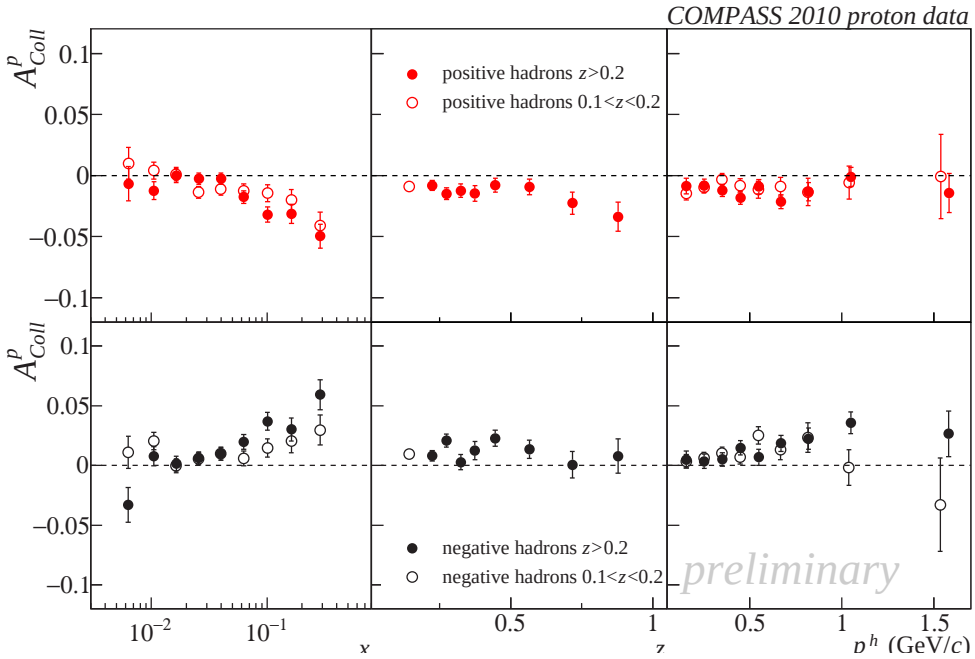

Figure 3: Collins asymmetries of 2010 proton data as a function of x, z and p_T^h for $z > 0.2$ and $0.1 < z < 0.2$. Upper row shows positive hadrons, lower row negative hadrons.

produced hadrons $N_h(\phi_S) = N_h^0[1 + f\ P_T\ A_S\ \sin(\phi_S)]$ depends on the Sivers angle $\phi_S = \phi_h - \phi_s$, the difference of the azimuthal angle of the produced hadron and the azimuthal angle of the nucleon spin in the gamma-nucleon system. The Sivers asymmetry A_S is given by the convolution of the Sivers function and the unpolarised fragmentation function:

$$A_S = \frac{\sum_q e_q^2 \cdot f_{1T}^{\perp}(x, \vec{k_T}) \otimes D_q^h(z, p_T^h)}{\sum_q e_q^2 \cdot f_1(x) \otimes D_q^h(z, p_T^h)}$$

The preliminary Sivers asymmetries of the 2010 measurement on the proton target at COMPASS are shown in Fig. 4 in bins of x, z and p_T. For positive hadrons the asymmetries show a positive signal in all three kinematic variables, even at small values of x, whereas for negative hadrons (triangles) the asymmetries are compatible with zero within the error bars. There is again a very good agreement with the published results from the 2007 data taken at COMPASS. Compared to the HERMES results [7] on the proton target the asymmetries measured at COMPASS show the same trend but are smaller in absolute value.

Fig. 5 shows the Sivers asymmetries for the low-y ($0.05 < y < 0.1$) selection in bins of x, z and p_T for positive hadrons in comparison to the standard sample ($0.1 < y < 0.9$). Here a clear increase of the Sivers asymmetries is visible for the low-y sample, which could be explained by the smaller values of Q^2 and W in this selection. A Q^2 dependance is expected and has been calculated [8], but no dependece on W is foreseen. The asymmetries for negative hadrons (not shown) are again compatible with zero. In Fig. 6 the measured Sivers asymmetries from the low-z sample and the standard sample are shown for positive hadrons. As it can be seen from the plot, the Sivers asymmetries become much smaller in size for low-z. The asymmetries for negative hadrons (not shown) stay compatible with zero also for the low-z sample.

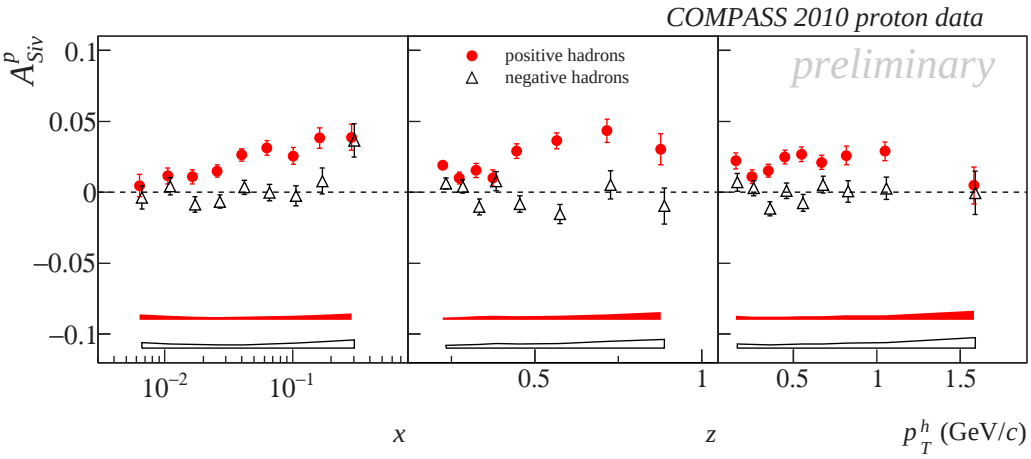

Figure 4: Sivers asymmetries of 2010 proton data as a function of x, z and p_T^h for positive and negative hadrons. The bands correspond to the systematical error.

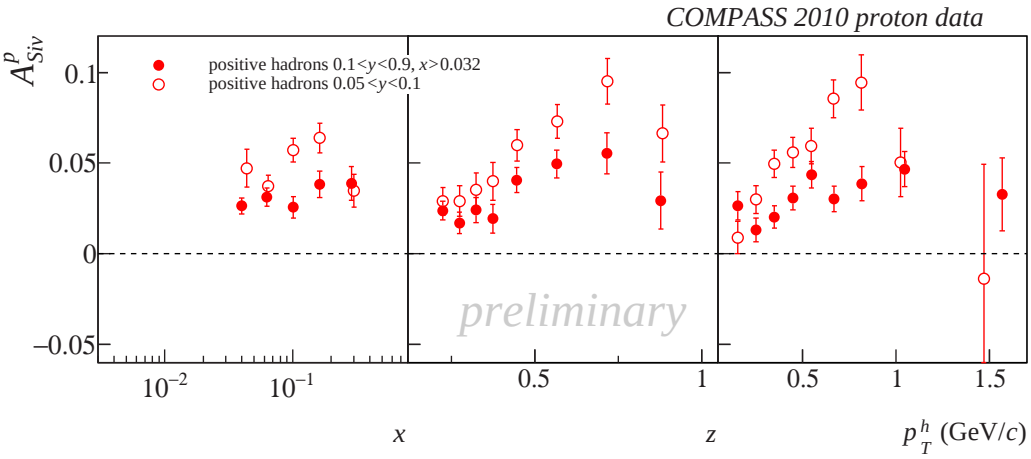

Figure 5: Sivers asymmetries of 2010 proton data as a function of x, z and p_T^h for $0.1 < y < 0.9$ and $0.05 < y < 0.1$ with $x > 0.032$, positve hadrons only.

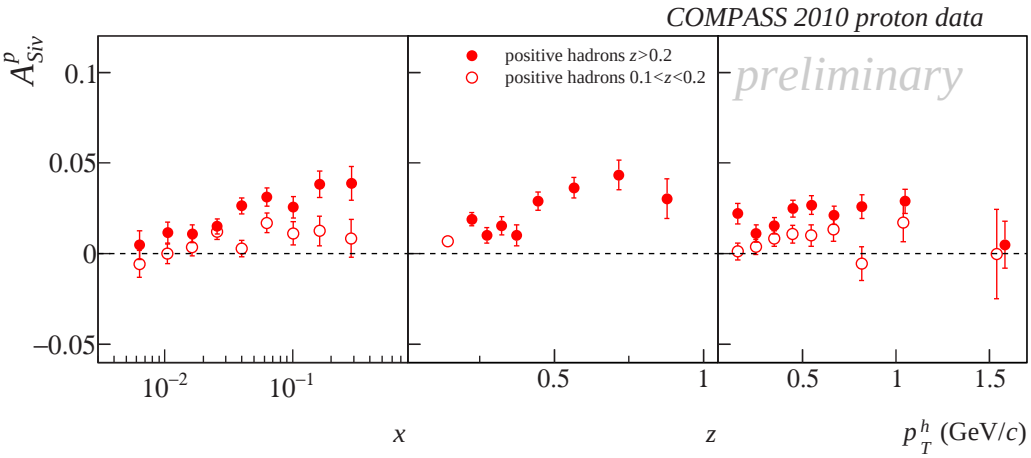

Figure 6: Sivers asymmetries of 2010 proton data as a function of x, z and p_T^h for $z > 0.2$ and $0.1 < z < 0.2$, positve hadrons only.

4 Conclusion

The present results from the 2010 measurement on the proton target at COMPASS show non-zero asymmetries for Collins and Sivers which are in very good agreement with the

published results from the 2007 run. In contrast in the measurement on a deuterium target 2002–2004 the asymmetries were compatible with zero [4]. Dedicating the whole data taking period 2010 to measure on a transversely polarized proton target led to a decrease of the statistical error by a factor of about 1.7 compared to the 2007 measurement. This also allows the investigation of different kinematical regions which show very interesting results, expecially for the Sivers asymmetries. Work is ongoing to extract the asymmetries for identified hadrons as well as the other six transverse spin dependent asymmetries which are present in the expression of the SIDIS cross-section.

References

[1] J. Collins, Fragmentation of Transversely Polarized Quarks Probed in Transverse Momentum Distributions, Nucl. Phys. **B396** (1993) 161.

[2] C. Elia, Two-hadron asymmetries, these Proceedings.

[3] D. Sivers, Single-spin production asymmetries from the hardscattering of pointlike constituents, Phys. Rev. **D41** (1) (1990) 83-90.

[4] V. Alexakhin et. al. [COMPASS Collaboration], First Measurement of the Transverse Spin Asymmetries of the Deuteron in Semi-inclusive Deep Inelastic Scattering, Phys. Rev. Lett. **94** (20) (2005);

[5] M.G. Alekseev et. al [COMPASS Collaboration], Measurement of the Collins and Sivers asymmetries on transversely polarised protons, Physics Letters **B692** (4) (2010) 240-246.

[6] A. Airapetian et al. [HERMES Colaboration], Effects of transversity in deep-inelastic scattering by polarized protons, Physics Letters **B693** (1) (2010) 11-16

[7] A. Airapetian et al. [HERMES Colaboration], Observation of the Naive-T-Odd Sivers Effect in Deep-Inelastic Scattering, Phys. Rev. Lett. **103** (15) (2009)

[8] S. Mert Aybat and Ted C. Rogers, Universality and Evolution of TMDs, arXiv:1110.6099v1 [hep-ph]

MEASUREMENTS OF DOUBLE SPIN TRANSVERSE ASYMMETRIES IN THE ELASTIC PROTON-PROTON SCATTERING IN THE CNI REGION AT STAR

Igor Alekseev [1 †] for the STAR collaboration

(1) *Institute for Theoretical and Experimental Physics, B. Cheremushkinskaya 25, 117218, Moscow, Russia*

† *E-mail: igor.alekseev@itep.ru*

Abstract

At high energies and small momentum transfer $(0.001 < -t < 0.1)$ $(\mathrm{GeV/c})^2$ proton-proton elastic scattering of transversely polarized protons is described by the interference of the Coulomb amplitude and pomeron exchange amplitude. These mechanisms can not induce double spin flip amplitudes and therefore can only produce small double spin asymmetries. A measurement of non-zero transverse double spin analyzing power (A_{NN}) would provide an evidence in favor of contribution of other Reggeons, including a hypothetical Odderon, to the scattering amplitude.

Preliminary results on the double spin asymmetries A_{NN} and A_{SS} from the analysis of 20 million of elastic events collected with transversely polarized p+p collisions at $\sqrt{s} = 200$ GeV in the STAR experiment at RHIC are discussed. The data covers $-t$ range $0.003 < -t < 0.035$ $(\mathrm{GeV/c})^2$.

This contribution is dedicated to the measurements of double spin asymmetries A_{NN} and A_{SS} at STAR using the same dataset as our measurements of the single spin asymmetry A_N [1]. The detector, experimental conditions and elastic event selection is the same as in our single spin asymmetry A_N measurement. Here we will concentrate only on the aspects specific to the double spin asymmetries.

Transverse double spin asymmetries A_{NN} and A_{SS} for the elastic scattering of the two identical spin 1/2 fermions can be described by the amplitudes as [2–4]:

$$A_{NN}\frac{d\sigma}{dt} = \frac{4\pi}{s^2}\{2|\phi_5|^2 + Re(\phi_1^*\phi_2 - \phi_3^*\phi_4)\} \quad (1)$$

$$A_{SS}\frac{d\sigma}{dt} = \frac{4\pi}{s^2}\{Re(\phi_1\phi_2^* + \phi_3\phi_4^*)\} \quad (2)$$

Each amplitude is a sum of hadron and Coulomb amplitudes $\phi_i = \phi_i^{em} + \phi_i^h$. The Coulomb amplitude is strictly calculable from QED, while the hadron amplitude is usually calculated using Regge theory. At ultra relativistic energies the main contribution to the hadron amplitude comes from pomeron or, in modern terms, multigluon exchange [5]. Particular interest to measurements of the transverse double spin asymmetries comes from their sensitivity to the hypotetical charge conjugation partner to the pomeron - odderon [6]. The effect is illustrated by the simple picture (fig. 1) in which A_{NN} is calculated for the pomeron and odderon contributions to the double spin flip amplitude $|\phi_2^{pom,odd}| = 0.05|\phi_1|$. In the later work by T.L. Trueman [7] it was shown, based on the analysis of single spin asymmetry experimental data in the CNI region, that pomeron contribution was small and sizable double spin asymmetries could be found only if the odderon coupling to double spin flip amplitudes was strong.

Precise measurements of A_{NN} were performed recently using RHIC polarized hydrogen jet target (HJET) at $\sqrt{s} = 6.8$ and 13.7 GeV [8]. The result was compatible with sero within errors. The only experiment in the collider energy range was performed by pp2pp collaboration at $\sqrt{s} = 200$ GeV [9], but it had a limited statistics. The results reported here are based on the preliminary analysis of of 20 millions events of proton-proton elastic scattering at $\sqrt{s} = 200$ GeV [1].

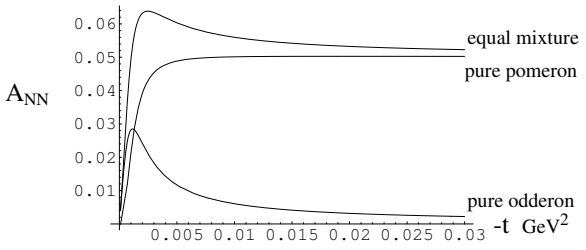

Figure 1: Illustration of odderon contribution to A_{NN} from [6].

The double spin raw asymmetry is given by the equation:

$$\epsilon_{NN}(\phi) = P_B P_Y (A_{NN}\cos^2(\phi) + A_{SS}\sin^2(\phi)) = \frac{(\frac{N^{++}}{L^{++}} + \frac{N^{--}}{L^{--}}) - (\frac{N^{+-}}{L^{+-}} + \frac{N^{-+}}{L^{-+}})}{(\frac{N^{++}}{L^{++}} + \frac{N^{--}}{L^{--}}) + (\frac{N^{+-}}{L^{+-}} + \frac{N^{-+}}{L^{-+}})}, \qquad (3)$$

where $N^{ij}(\phi)$ - number of events with bunch polarization pattern ij at the azimuthal angle ϕ. $P_{B/Y}$ are polarizations of blue and yellow beams, measured by HJET and pCarbon polarimeters [10]. The event weighted beam polarization for this measurement was $P_B P_Y = 0.372 \pm 0.023$. L^{ij} are relative luminosities for the corresponding polarization pattern. For the preliminary results we used relative luminosities obtained from counts of inelastic triggers produced by the vertex position detector (VPD) and beam-beam counters (BBC). Normalization coefficients are given in the Tab. 1.

Table 1: Normalization

	Counts	L^{++}	L^{+-}	L^{-+}	L^{--}	$\sigma_{stat}/L^{\pm\pm}$
VPD	38246243	0.24544	0.24676	0.24940	0.25839	0.00028
BBC	449686340	0.24512	0.24595	0.25028	0.25864	0.00008
average		0.24528	0.24636	0.24984	0.25852	

The systematic uncertainty in the normalization can be estimated by the average square of the difference between VPD and BBC normalizations which turned out to be 0.25%. The statistical uncertainty of both methods is much smaller. The averaged coefficients were used in the further analysis. A careful normalization analysis, including data from zero degree calorimeter (ZDC) and wall current monitors (WCM), is under way.

Another check of the normalization quality was performed by the extraction of the single spin asymmetry A_N using normalized counts and comparison of the result with the analysis preformed using square root formula [1]. The single spin raw asymmetry can be written as:

$$\epsilon_N(\phi) = \frac{(P_B + P_Y)A_N}{1 + \delta(\phi)}\cos(\phi) = \frac{\frac{N^{++}}{L^{++}} - \frac{N^{--}}{L^{--}}}{\frac{N^{++}}{L^{++}} + \frac{N^{--}}{L^{--}}} \qquad (4)$$

The plot for the -t range $0.005 < -t < 0.010$ $(\mathrm{GeV/c})^2$ is shown in fig. 2a. The value of $(P_B + P_Y)A_N = 0.03404 \pm 0.00095$ is well within statistical error from the result of the analysis used square root formula $(P_B + P_Y)A_N = 0.03435 \pm 0.00096$.

The preliminary result on the raw double spin asymmetry is shown in fig. 2b for the whole t-range. The t-dependence of A_{NN} and A_{SS} is shown in fig. 3. Though some effects of the order of 10^{-3} could be seen, they are small and comparable with the normalization uncertainty. A careful study of systematic effects produced by normalization should be done before making any conclusions.

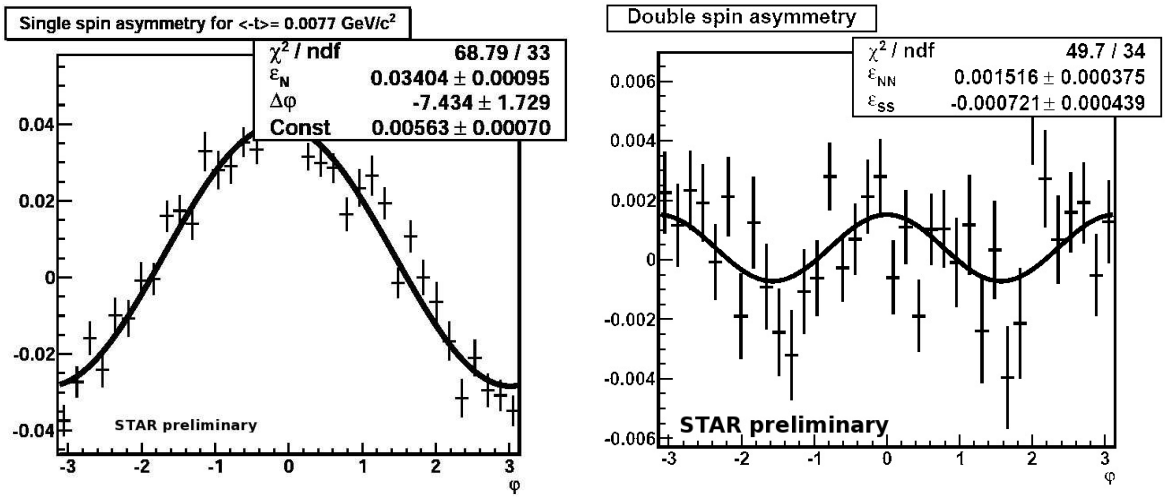

a) b)

Figure 2: The preliminary result on the raw single spin asymmetry $\epsilon_N(\phi)$ from the normalized counts for the -t range $0.005 < -t < 0.010$ (GeV/c)^2 (a) and the preliminary result on the raw double spin asymmetry $\epsilon_{NN}(\phi)$ for the whole t-range (b).

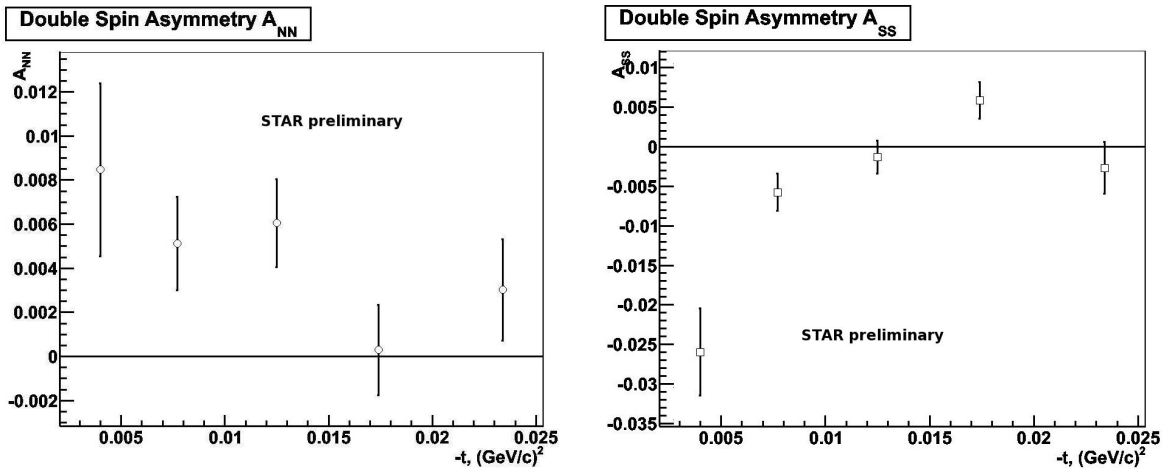

a) b)

Figure 3: The preliminary result on t-dependence of A_{NN} (a) and A_{SS} (b). Only statistical errors are shown.

Our preliminary results agree with the hypothesis that only Pomeron exchange, which contributes only to non-spin flip amplitudes ϕ_1 and ϕ_3, survives at high energies. Along with other cited measurements of the proton-proton elastic scattering with $\sqrt{s} > 10$ GeV we see no evidence of contribution of other amplitudes. Our future plans include measurement of A_{LL} in the same kinematics and getting data at $\sqrt{s} = 500$ GeV in order to

measure the cross section and the slope parameter of the elastic peak B.

We thank the RHIC Operations Group and RCF at BNL, the NERSC Center at LBNL and the Open Science Grid consortium for providing resources and support. This work was supported in part by the Offices of NP and HEP within the U.S. DOE Office of Science, the U.S. NSF, the Sloan Foundation, the DFG cluster of excellence 'Origin and Structure of the Universe' of Germany, CNRS/IN2P3, FAPESP CNPq of Brazil, Ministry of Ed. and Sci. of the Russian Federation, NNSFC, CAS, MoST, and MoE of China, GA and MSMT of the Czech Republic, FOM and NWO of the Netherlands, DAE, DST, and CSIR of India, Polish Ministry of Sci. and Higher Ed., Korea Research Foundation, Ministry of Sci., Ed. and Sports of the Rep. Of Croatia, and RosAtom of Russia.

References

[1] D. Svirida for the STAR collaboration, these Proceedings.
[2] N.H. Buttimore, E. Gotsman and E. Leader, Phys.Rev. **D18** (1978) 694
[3] T.L. Trueman, **arXiv**:hep-ph/9610316
[4] N.H. Buttimore et al., Phys. Rev. **D59** (1999) 114010
[5] S. Nussinov, Phys. Rev. Lett.**34** (1975) 1286; S. Nussinov, Phys. Rev. **D14** (1976) 246
[6] E. Leader and T.L. Trueman, Phys. Rev. **D61** (2000) 077504
[7] T.L. Trueman, **arXiv**:hep-ph/0604153
[8] I.G. Alekseev et al., Phys. Rev. **D79** (2009) 094014
[9] S. Bültmann et al., Phys. Lett. **B647** (2007) 98
[10] http://www4.rcf.bnl.gov/~cnipol/pubdocs/Run09Offline/

LONGITUDINAL SPIN PROGRAM AT RHIC: RESULTS AND PLANS

A. Bazilevsky[1†], for the RHIC Spin Collaboration

(1) *Brookhaven National laboratory*
† *E-mail: shura@bnl.gov*

Abstract

We present recent results from RHIC Spin measurements related to gluon and (anti-)quark polarizations in the proton. We discuss plans for future measurements along with machine and experimental upgrade programs to further improve constraints for polarized parton distribution functions.

1 Introduction

The spin structure of the proton has been measured since 1980s in polarized lepton-nucleon deep-inelastic scattering (DIS) experiments, which revealed that only 20–30% of the proton spin can be attributed to the spins of the quarks and anti-quarks [1] indicating that the proton spin must be largely carried by the spin of the gluons and/or orbital angular momentum of the quarks and gluons. Since then, the main goal of spin physics has been to elucidate the role of gluon spin (Δg) as well as flavor separated contribution of quark and anti-quark spin (Δq and $\Delta\bar{q}$) in the proton spin. Getting access to the orbital angular momentum remains a challenging task from both theoretical and experimental point of view, which will be a major part of the new 12 GeV program at Jefferson Lab and at future Electron-Ion Collider (EIC).

DIS experiments have been providing data to constrain Δg from the scaling violation in inclusive polarized scattering [2] and from semi-inclusive measurements of high transverse momentum (p_T) hadron pairs [3] and heavy flavor production [4] to utilize the photon-gluon process. The flavor separated contribution of quarks and anti-quarks to the proton spin is determined in semi-inclusive DIS using fragmentation processes, which correlate final state hadron with quark flavor.

Polarized proton-proton collisions at the Relativistic Heavy-Ion Collider (RHIC) provide complementary approach to study proton spin structure. Gluon-spin contribution is accessed through the hard scattering directly involving gluons. Flavor decomposition of quark and anti-quark polarization can elegantly be obtained from the measurements of W bosons, which couple left-handed quarks and right-handed anti-quarks: $u_L\bar{d}_R \to W^+$ and $d_L\bar{u}_R \to W^-$. This approach is free of uncertainties in fragmentation functions, if Ws are measured through their leptonic decays.

2 Spin Measurements at RHIC

The measured quantities in spin physics experiments at RHIC are spin asymmetries, which are defined as an asymmetry in production cross section between different beam spin

configurations. Experimentally they are measured as a difference in the production rates for different bunch pair spin configurations divided by the sum, and normalized by beam polarization for single spin measurements or by a product of two beam polarizations for double spin measurements. Production rate is defined from the measured yield normalized by the luminosity, for each colliding bunch pair spin configuration.

RHIC provides polarized proton collisions in wide center of mass energy range up to $\sqrt{s}$ =500 GeV. Since the first polarized proton run in 2002 RHIC experiments have collected data at $\sqrt{s}$ =62.4, 200 and 500 GeV with both longitudinally and transversely polarized proton beams. From year to year RHIC has been improving its performance in terms of both luminosity and polarization. The store average beam polarization of more than 60% (50%) has been achieved at $\sqrt{s}$ =200 GeV (500 GeV).

The stable direction of the proton spin in RHIC is vertical, but the regions around two RHIC experimental areas, PHENIX and STAR, include sets of magnets (spin rotators) to rotate the spin to the longitudinal direction at a collision point, and then back to vertical after the collision point. The RHIC polarimeters [5] measure the transverse beam polarization away from the experimental areas, independent of the operation of the spin rotators. Bunches with alternating spin direction collide every 106 ns, so that all four two-bunch spin configurations occur in sequences of four bunch crossings. This significantly reduces false asymmetries and systematic uncertainties in spin asymmetry measurements due to slow variations in luminosity and detector acceptances and efficiencies.

Two large experiments, PHENIX [6] and STAR [7] have been used to carry on longitudinal spin program at RHIC. PHENIX detector utilizes a variety of detector technologies. A pair of central arms, each with acceptance of $\pi/2$ in azimuth and $|\eta|$ <0.35 in pseudorapidity, have excellent energy and momentum resolution and particle identification capabilities and are used to measure electrons, hadrons and photons. A pair of forward spectrometers with full azimuthal acceptance and $1.2 < |\eta| < 2.4$ are used to measure muons. STAR detector was designed to do measurements over a large solid angle with full azimuthal acceptance, providing high precision tracking, momentum analysis and particle identification, which makes it particularly well suited for jet detection.

Each of RHIC experiments is equipped with local polarimeters [5] to control the residual transverse spin polarization when spin rotators are on, and by that to measure the degree of longitudinal beam polarization. The transverse spin component P_T/P in longitudinal spin runs usually was 5–15%, which translates to longitudinal spin component P_L/P of $\sim$ 99%.

3 Δg Measurements

Polarized proton-proton collisions at RHIC provide a laboratory to study the gluon-spin contribution to the proton spin structure, Δg, with strongly interacting probes via measurements of double helicity asymmetries (A_{LL}) [8]. Experimentally, for example for inclusive π^0 or jet production, it is determined from the measured yields as:

$$A_{LL} = \frac{1}{|P^B \cdot P^Y|} \cdot \frac{N_{++} - R \cdot N_{+-}}{N_{++} + R \cdot N_{+-}}; \quad R = \frac{L_{++}}{L_{+-}}, \tag{1}$$

where N is the number of π^0's or jets measured from the colliding bunches with the same $(++)$ and opposite $(+-)$ helicities, R is the relative luminosity between bunches with

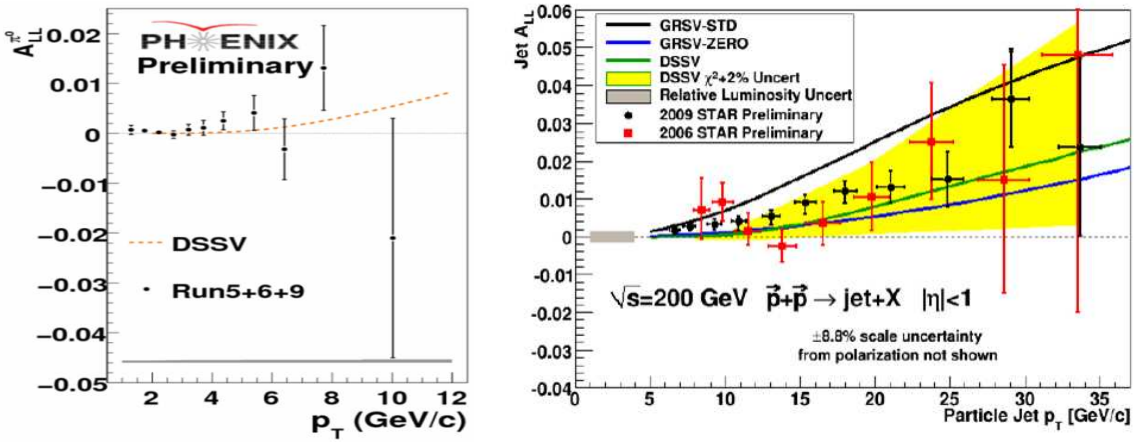

(a) (b)

Figure 1: **(a)** Double helicity asymmetry in inclusive π^0 production as a function of p_T from RHIC runs of 2005, 2006 and 2009, combined, measured by PHENIX; dashed line corresponds to DSSV global fit [10] **(b)** Double helicity asymmetry in inclusive jet production as a function of p_T from RHIC runs of 2006 and 2009, measured by STAR; theoretical curves are from GRSV parametrization of polarized PDFs [11] and from DSSV global fit [10].

the same and opposite helicities, and P^B and P^Y are the polarizations of the two RHIC beams.

Extraction of Δg is based on a next-to-leading order (NLO) perturbative Quantum Chromodynamics (pQCD) framework, which was proved to well describe RHIC unpolarized cross section data [9]. RHIC A_{LL} results at mid-rapidity in inclusive π^0 production (by PHENIX) and jet production (by STAR) have been used in NLO global fit (DSSV) of polarized parton densities and played the dominant role in determining the polarized gluon distribution in the proton [10]. In the accessed range of the gluon momentum fraction Δg was found to be consistent with zero.

Since then, both PHENIX and STAR have considerably decreased the uncertainties in their measurements (by a factor of ~ 1.5 in PHENIX and by a factor of 3–4 in STAR) by collecting more data in 2009 RHIC run and by improving systematic uncertainties. The results are shown in Fig. 1. Data points from both data sets tend to be above the curve corresponding to DSSV fit, which may indicate the non-zero Δg in the range of probed gluon momentum fraction $0.02 < x < 0.3$. Inclusion of these data to the global fit would help to derive a more precise quantitative statement on gluon spin contribution in the proton spin.

The main limitations of the presented results are the limited gluon x range they probe, and a poor sensitivity to the shape of Δg as a function of x, due to inclusive nature of the presented measurements and due to that several processes contribute to inclusive jet or hadron production at mid-rapidity (effectively gg and qg scattering). Both PHENIX and STAR plan to measure asymmetries at forward rapidities, which give sensitivity to lower x. Correlation measurements, di-jets or di-hadrons, will help to better constrain the partonic kinematics and hence determine the shape of Δg vs x. With planned RHIC upgrades to considerably improve luminosity, the direct photon measurements will become of great interest, because they provide a theoretically clean access to Δg through quark-gluon Compton scattering $qg \rightarrow q\gamma$, the dominant mechanism for direct photon production in

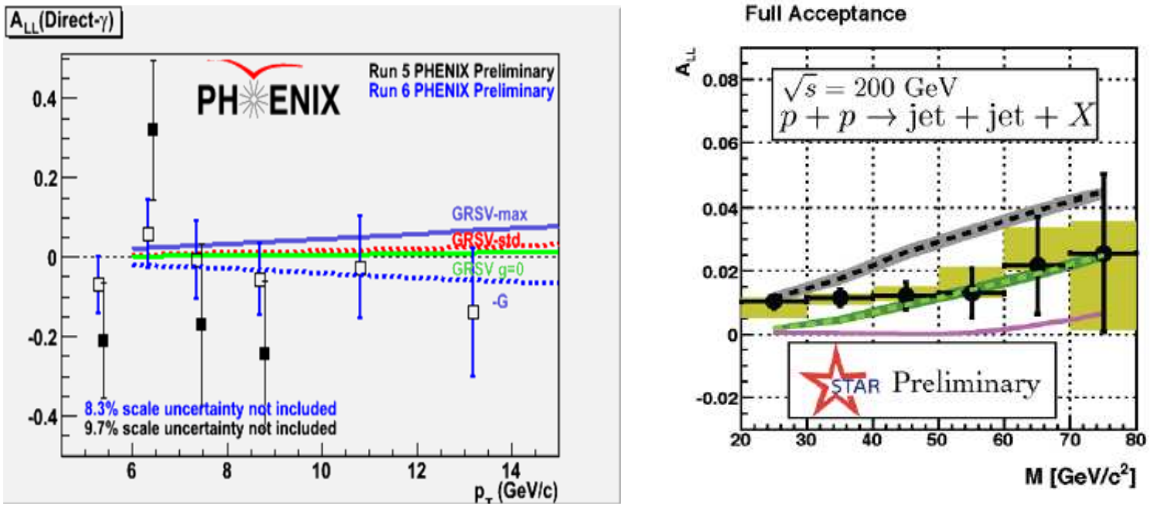

(a) (b)

Figure 2: **(a)** Double helicity asymmetry in direct photon production as a function of p_T from RHIC runs of 2005 and 2006, measured by PHENIX; theoretical curves are from GRSV parametrization of polarized PDFs [11]. **(b)** Double helicity asymmetry in di-jet production as a function of jet-pair invariant mass from RHIC run 2009, measured by STAR; theoretical curves (from lower to upper one) are from GS-C [12], DSSV [10] and GRSV-std [11].

high energy pp collisions. The preliminary results on these are already available from RHIC experiments, see Fig. 2.

Measuring different probes (e.g. η, charged hadrons, heavy flavor mesons) is important to study systematic uncertainties in Δg constraint. Some of them require larger luminosity to get good statistical sensitivity to gluon polarization. They will start contributing to Δg constraint with increasing integrated luminosity delivered to RHIC experiments.

4 Flavor Separated Helicity Distributions

Production of W bosons in pp collisions is uniquely suited for testing symmetry of the light anti-quark sea in both unpolarized and polarized collisions. W boson production selects the quark flavors through their charge and, due to the maximally parity-violating weak interaction, it also selects only one helicity of nearly massless quarks: left-handed helicity for quarks and right-handed helicity for anti-quarks. Hence the asymmetry of the W yield from flipping the helicity of a polarized proton is sensitive to the flavor dependence of light quark and anti-quark helicity distribution in the proton.

At leading order, the single helicity asymmetry in W^+ production is proportional to light quark and anti-quark helicity distribution in the proton:

$$A_L^{W^+} = -\frac{\Delta u(x_1)\Delta\bar{d}(x_2) - \Delta\bar{d}(x_1)\Delta u(x_2)}{u(x_1)\bar{d}(x_2) + \bar{d}(x_1)u(x_2)}, \tag{2}$$

and similarly for W^- by exchanging $u \to d$ and $\bar{d} \to \bar{u}$. These asymmetries are generally more sensitive to the quark polarizations for forward W rapidities with respect to the polarized proton, while the anti-quark polarizations are probed in the backward direction.

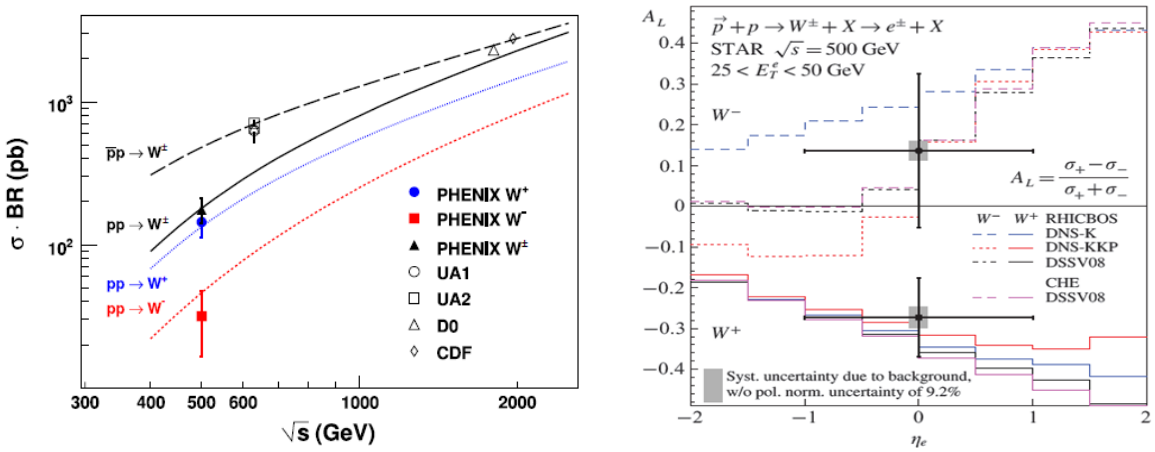

Figure 3: **(a)** Inclusive cross sections for W leptonic decay channel of PHENIX measurements along with $\bar{p}p$ measurements, in comparison to theory calculations ([14] and the references therein). **(b)** Longitudinal single-spin asymmetry for $W^{\pm}$ production as a function of the decay lepton pseudorapidity in comparison to theory predictions ([15] and the references therein).

Central rapidity W^+ (W^-) production asymmetry is basically a linear combination of $\Delta\bar{u}/\bar{u}$ and $\Delta d/d$ ($\Delta\bar{d}/\bar{d}$ and $\Delta u/u$).

Measurements of W bosons at RHIC are done by detecting their decay leptons, either electrons/positrons or muons (in PHENIX forward spectrometers). A theoretical framework has been developed to describe decay lepton production [13] to be compared with data to eventually get constraint on light quark and anti-quark helicity distribution in the proton. First RHIC results on cross section and helicity asymmetry in W production at mid-rapidity in polarized pp collisions at $\sqrt{s}$ =500 GeV have been already published by PHENIX [14] and STAR [15] collaborations, see Fig. 3. Results were found to be consistent with theoretical expectations. The first observation of non-zero parity-violating asymmetry in W production has been reported by both collaborations, which due to limited statistics didn't yet allow to distinguish between different scenarios of anti-quark polarization in the proton. In the next a few years, RHIC increased luminosity and higher proton beam polarizations along with PHENIX and STAR detector upgrades in progress will make it possible to significantly reduce the uncertainties in A_L measurements and to extend the measurements to forward rapidities, which will significantly improve our knowledge of flavor-separated quark and anti-quark helicity distributions.

PHENIX upgrade includes high momentum muon trigger in forward spectrometers. It consists of fast front end electronics (FEE) for the existing muon trackers and three planes of resistive plate counters (RPCs) in each arm. FEE electronics was installed and checked in 2009. One plane of RPCs in each arm was installed in 2010. This system has already been commissioned and used to collect high p_T muon data in RHIC run of 2011 and demonstrated good efficiency and expected rejection power. In 2012 after installation of another plane of RPCs we hope to further improve the performance of the new muon trigger system.

STAR plans to extend the measurements of electrons/positrons from W boson decays from central rapidity ($|\eta| < 1$) to forward rapidity region ($1 < \eta < 2$). A new tracking upgrade is needed to determine the charge of highly energetic electrons/positrons. The

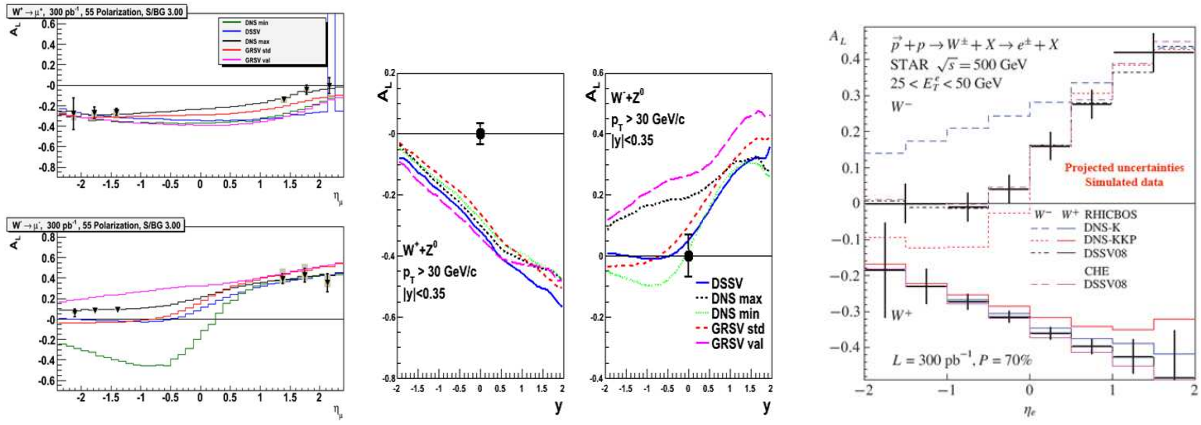

(a) (b) (c)

Figure 4: **(a)** Expected uncertainties of PHENIX A_L^W measurements in forward (muon) spectrometers for assumed integrated luminosity of 300 pb^{-1} and 55% polarization. **(b)** Expected uncertainties of PHENIX A_L^W measurements in central spectrometers for assumed integrated luminosity of 300 pb^{-1} and 55% polarization. **(c)** Expected uncertainties of STAR A_L^W measurements for assumed integrated luminosity of 300 pb^{-1} and 70% polarization.

forward GEM Tracker (FGT) will be installed and commissioned in the coming RHIC run of 2012.

Fig. 4 shows the projected uncertainties for the A_L^W measurements as a function of lepton rapidity along with different model expectations. These will allow to considerably constrain the $\Delta\bar{u}$ and $\Delta\bar{d}$ for momentum fraction $x > 0.1$ [13].

5 Summary and Longer Term Plans

RHIC as the only polarized proton collider in the world continues improving its performance gradually improving luminosity and beam polarizations. Two main goals of longitudinal spin measurements at RHIC are to constrain gluon and anti-quark polarizations inside the proton.

Double helicity asymmetry measurements in inclusive π^0 production by PHENIX and inclusive jet production by STAR have been playing the dominant role in constraining the Δg in the range of gluon momentum fraction $0.02 < x < 0.3$. The recent data from RHIC run of 2009 tend to indicate the non-zero gluon polarization in this x range. Inclusion of these data in the global NLO fit is important to make more quantitative statement. To extend the probed x range both experiments plan to perform A_{LL} measurements in forward region. Di-jet, di-hadron and direct photon-jet (at higher RHIC luminosities) channels will be used to get access to parton kinematics and hence to measure the shape of Δg versus x.

First W boson measurements at RHIC showed good consistency with theoretical expectations. Larger statistics from collisions with higher beam polarizations to be collected by PHENIX and STAR at both mid- and forward-rapidities in the next 2–3 years will considerably improve our knowledge on quark and anti-quark polarizations in the proton at $x > 0.1$.

RHIC upgrade plans include increasing the center of mass energy from $\sqrt{s}$ =500 GeV

to 650 GeV, and the possibility to accelerate polarized ^3He. The former is important for W measurements, for which the production cross section will increase twice; the latter is important for full flavor separation in polarized parton distribution functions.

References

[1] J. Ashman *et al.* (EMC), Phys. Lett. **B206** 364 (1988), Nucl. Phys. **B328**, 1 (1989); A. Airapetian *et al.* (HERMES), Phys. Rev. **D75**, 012007 (2007); V.Yu. Alexakhin *et al.* (COMPASS), Phys. Lett. **B647**, 8 (2007).

[2] B. Adeva *et al.*, Phys. Rev. D **58**, 112002 (1998); P.L. Antony *et al.*, Phys. Lett. B **493**, 19 (2000);

[3] B. Adeva *et al.*, Phys. Rev. D **70**, 012002 (2004); A. Airapetian *et al.*, Phys. Rev. Lett. **84**, 2584 (2000);

[4] C. Franco (COMPASS), these proceedings.

[5] A. Bazilevsky *et al.*, Proc. of XIII Advanced Research Workshop on High Energy Spin Physics (DSPIN-09), p389, and references therein.

[6] A. Adare *et al.*, Nucl. Instrum. Methods **A 499**, 469 (2003).

[7] A. Adare *et al.*, Nucl. Instrum. Methods **A 499**, 624 (2003).

[8] G. Bunce *et al.*, Ann. Rev. Nucl. Part. Sci. **50**, 525 (2000).

[9] S.S. Adler *et al.* (PHENIX), Phys. Rev. Lett. **91**, 241803 (2003); J. Adams *et al.* (STAR), Phys. Rev. Lett. **92**, 171801 (2004); B.I. Abelev *et al.* (STAR), Phys. Rev. Lett. **97**, 252001 (2006); S.S. Adler *et al.* (PHENIX), Phys. Rev. Lett. **98**, 012002 (2007); A. Adare *et al.* (PHENIX), Phys. Rev. D **76**, 051106 (2007).

[10] D. de. Florian, R. Sassot, M. Stratmann, and W. Vogelsang, Phys. Rev. Lett. **101**, 072001 (2008).

[11] B. Jäger, A. Schäfer, M. Stratmann, and W. Vogelsang, Phys. Rev. D **67**, 054005 (2003).

[12] T. Gehrmann and W.J. Stirling, Phys. Rev. D **53**, 6100 (1996).

[13] D. de Florian and W. Vogelsang, Phys. Rev. D **81**, 094020 (2010).

[14] A. Adare *et al.*, Phys. Rev. Lett. **106**, 062001 (2011).

[15] M.M. Aggarwal *et al.*, Phys. Rev. Lett. **106**, 062002 (2011).

SINGLE HADRON MULTIPLICITIES IN SIDIS AT COMPASS

Y. Bedfer [1]

(1) *CEA Saclay, IRFU/SPhN*
† *E-mail: Yann.Bedfer@cern.ch*

Abstract

Single hadron fragmentation functions, FFs, play an important role in several aspects of hadronic spin physics. In particular, they are crucial for the determination of flavour separated polarized parton distribution functions (polarized $PDFs$) from Semi-Inclusive DIS data.

The COMPASS collaboration at CERN is undertaking a programme of measurements of pion and kaon multiplicities in $SIDIS$ for the purpose of extracting these FFs. Preliminary results, derived from muon-nucleon scattering data collected on an LiD target, are presented.

The dependence of the multiplicities upon transverse momentum, p_T, is also investigated, having in view, this time, the dependence of the $PDFs$ and FFs upon the parton intrinsic motion. Preliminary findings, obtained for unidentified charged hadrons, are reported.

1 Introduction

FFs are universal non perturbative objects appearing in the observables of many hard reactions. In the presence of the hard scale, and within the collinear factorization framework, the cross-section can be written as a convolution of the hard partonic cross-section, $PDFs$ and FFs. In the frame of hadronic spin physics, the FFs are needed for *e.g.*, the analysis of the production of hadrons with high p_T, in high energy proton-proton collisions at RHIC or in photoproduction at COMPASS [1], and in $SIDIS$.

The latter plays an important role in the spin sector, because in inclusive polarized DIS, only electromagnetic currents can be used (neutrino scattering from polarized targets being impractical) and therefore quarks and anti-quarks enter symmetrically and cannot be disentangled. $SIDIS$ breaks this symmetry: at LO in pQCD, *e.g.*, the cross-section for the production of hadron h reads:

$$\sigma^h(x,z) \;=\; \sum e_q^2\, q(x)\, D_q^h(z)\;,$$

where the summation runs on all quark flavours, x and z are the momentum fractions of quark q and hadron h and D_q^h is the FF of q into h. It is therefore able to achieve a complete flavour separation of the polarized $PDFs$, in the fixed target realm.

Such an exercise was performed by HERMES [2]. It yielded the surprising result that the strange polarized PDF, Δs, is compatible with zero (in the measured x range) contrary to expectations based on QCD fits of inclusive data. COMPASS has confirmed this result [3], over an extended x range and with improved precision, *cf.* Fig. 1, which

makes it now challenging for global fits to reconcile inclusive and semi-inclusive data. COMPASS showed, though, that the magnitude of the discrepancy is very sensitive to the choice of FFs, in particular to the magnitude of the kaon fragmentation, $D_s^{K-} = D_{\bar{s}}^{K+}$ [3].

$SIDIS$ can also be analyzed, in the low p_T domain, in terms of unintegrated $PDFs$ and FFs where the transverse distributions are modeled by a Gaussian ansatz [5]. Such models can then be used to extract transverse momentum dependent distributions $TMDs$ [6].

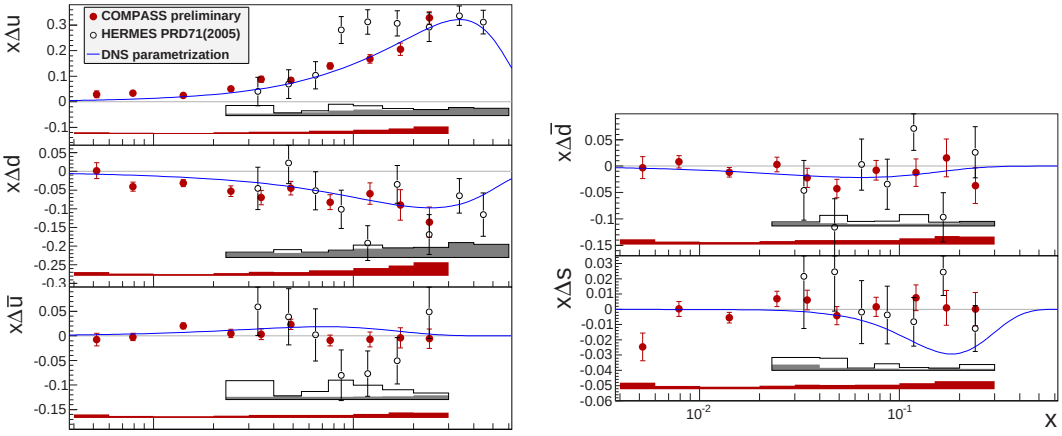

Figure 1: The quark $PDFs$ at $Q^2 = 3\,\mathrm{GeV}^2$ as a function of x. The values are derived from LO analyses of $SIDIS$ asymmetries. The curves are from the DNS fit [4], *i.e.* an NLO QCD fit of both DIS and $SIDIS$ data, using FFs from [7].

2 Multiplicity measurement

FF have been initially extracted from mostly high energy e^+e^- collider data [7] [8]. Such extractions suffer from two limitations. They can only separate quarks from anti-quarks based on model assumptions. Their evolution to the Q^2 accessible to fixed target $SIDIS$, $\sqrt{s} \simeq 17$ GeV in our case, relies heavily on the poorly constrained gluon distributions, D_g^h. More reliable and versatile FFs can be obtained form a global fit of data comprising, in addition to e^+e^-, pp and $SIDIS$ data, such as the DSS fit [9].

In $SIDIS$, one studies the fragmentation process by determining multiplicity distributions for the detected hadrons. At COMPASS, we identify the hadrons with a RICH detector which places strict constraints on the measured momenta. The range retained for the kaon momenta in the present analysis, is [10,50] GeV/c. In order for the acceptance of our spectrometer to remain sizable over the measured domain, we impose a cut on the mass of the hadronic system, $W > 7$ GeV. For the other kinematic variables, we follow a standard DIS selection scheme, *viz.*: $Q^2 > 1$ GeV^2, $0.1 < y < 0.9$. The measured multiplicities are shown on Fig. 2. They agree with DSS for the pions at low z, but significantly depart from it at high z and for the kaons.

Our intent is now to repeat the analysis on 2006 data, which were acquired with an experimental apparatus differing in several aspects from that of 2004 ones, in order to better understand our systematics.

The analysis of K_S^0 along similar lines is under way. An interesting application of this work is that, combined with the $K^\pm$, it gives access to the non-singlet combination $(D_u - D_d)^{K^+ + K^-}$ in a model independent way, following the approach described in [10].

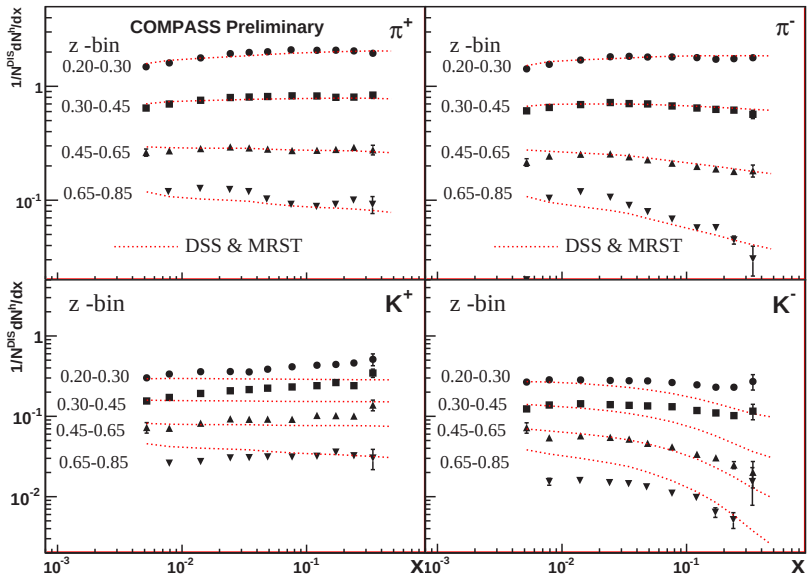

Figure 2: Multiplicities of pions and kaons at COMPASS as a function of x for various bins in z compared to a LO pQCD calculation based on MRST04 $PDFs$ and DSS FFs

.

The presently discussed data were acquired on our polarized deuterium target, which is a mixture of LiD and He, *i.e.* an isoscalar target for which nuclear medium effects are expected to be small. We plan to take $SIDIS$ data on a liquid H_2 target in 2012.

3 p_T dependent hadron multiplicities

We also analyze our LiD data as a function of the transverse momentum with respect to the virtual photon, p_T, following the model approach described in [5]. The multiplicities distributions along p_T lend themselves to a good Gaussian fit, provided the fitted domain is restricted to low p_T in order to avoid the region where pQCD effects become dominant. We perform such a fit for p_T <0.85 GeV/c, in z intervals, for a series of two-dimensional (x, Q^2) bins.

The z dependence of the resulting Gaussian widths, $\langle p_T^2 \rangle$, is of particular interest because of its relation to the intrinsic transverse momenta $k_\perp$ and $p_\perp$; $p_\perp$ representing the motion of the detected hadron with respect to the fragmenting parton and $k_\perp$, the motion of the parton inside the initial nucleon. The authors of [5] approximate this dependence by a simple $\langle p_\perp^2 \rangle + z^2 \langle k_\perp^2 \rangle$ expression. Such a linear relation fails to describe our data over the wide z range ($0.2< z <0.8$) they cover. Instead, inspired by a similar ansatz for the FFs in [7], we assume a z dependence for the fragmentation such that:

$$\langle p_T^2 \rangle \;=\; z^\alpha (1-z)^\beta \langle p_\perp^2 \rangle \;+\; z^2 \langle k_\perp^2 \rangle \qquad (1)$$

where α and β are constants which best-fit values are $\alpha = 0.5$, $\beta = 1.5$. It must be noted that this non-linear behavior is reproduced qualitatively by an update of the model of [5] published recently [11].

Using equation (1), the intrinsic average square momenta $\langle k_\perp^2 \rangle$ and $\langle p_\perp^2 \rangle$ are extracted for each of our (x, Q^2) bins. As an example, the extracted $\langle k_\perp^2 \rangle$ are plotted *vs.* Q^2 in

Fig. 3. They clearly exhibit a strong Q^2 dependence. When plotted *vs.* x instead (figure not shown), they display only a weak trend at low Q^2, which vanishes as Q^2 increases.

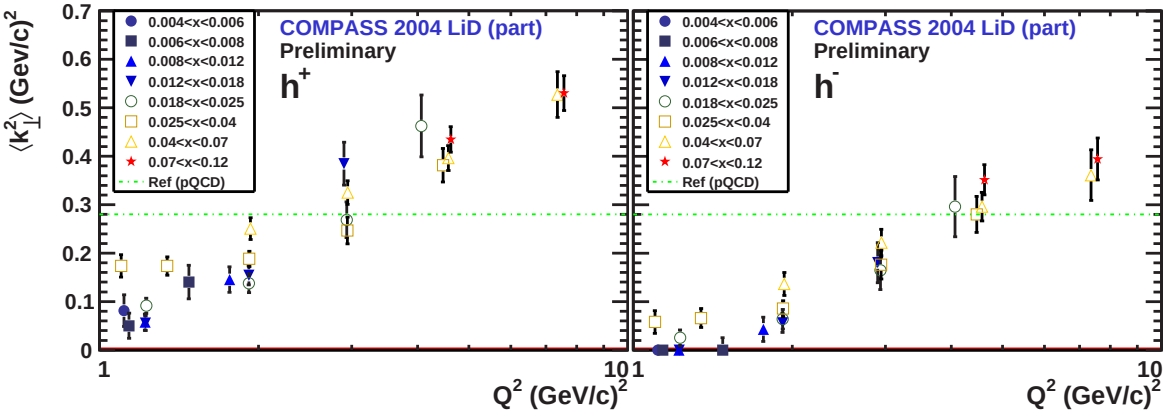

Figure 3: $\langle k_\perp^2 \rangle$ *vs.* Q^2 for positive and negative hadrons. Each data point corresponds to a two-dimensional (x, Q^2) bin. The dotted line is the result of a global fit to data from many experiments [5].

Also, $\langle k_\perp^2 \rangle$ is systematically higher for positive hadrons than for negative ones, suggesting a flavour dependence. We plan to further investigate this hypothesis by extending the present p_T analysis to identified hadrons. Kaon identification could provide access to characteristics of the strange quark $TMDs$.

References

[1] Astrid Morreale, contribution to these proceedings.

[2] A. Airapetian *et al.* [HERMES Collaboration], Phys. Rev. D **71** (2005) 012003.

[3] M. G. Alekseev *et al.* [COMPASS Collaboration], Phys. Lett. B **693** (2010) 227.

[4] D. de Florian, G. A. Navarro and R. Sassot, Phys. Rev. D **71** (2005) 094018 [hep-ph/0504155].

[5] M. Anselmino, M. Boglione, A. Prokudin and C. Turk, Eur. Phys. J. A **31** (2007) 373 [hep-ph/0606286].

[6] M. Anselmino, M. Boglione, U. D'Alesio, A. Kotzinian, F. Murgia and A. Prokudin, Phys. Rev. D **72** (2005) 094007 [Erratum-ibid. D **72** (2005) 099903] [hep-ph/0507181].

[7] S. Kretzer, Phys. Rev. D **62** (2000) 054001 [hep-ph/0003177].

[8] B. A. Kniehl, G. Kramer and B. Potter, Nucl. Phys. B **597** (2001) 337.

[9] D. de Florian, R. Sassot and M. Stratmann, Phys. Rev. D **75** (2007) 114010.

[10] S. Albino, E. Christova and E. Leader, arXiv:1102.2305 [hep-ph].

[11] M. Boglione, S. Melis and A. Prokudin, arXiv:1107.4436 [hep-ph].

OVERVIEW OF THE SPIN TRANSFER MEASUREMENTS IN THE PRODUCTIONS OF BARYONS AND HYPERONS

M.A. Chetvertkov[1†], V.A. Chetvertkova[2] and S.B. Nurushev[3]

(1) *Lomonosov Moscow State University, Moscow, Russia*
(2) *Skobeltsyn Institute of nuclear physics, Moscow State University, Moscow, Russia*
(3) *Institute of High Energy Physics, Protvino, Russia*
† *E-mail: chetvertkov@physics.msu.ru*

Abstract

The survey of the experimental measurements of different types of the spin transfer tensors is given. These tensors relate the polarization of the secondary baryons and hyperons to the polarization of the primary beam or target. They depend on the type of the primary and secondary particles, on the energy of the initial interacting particles, the energy and production angle of a secondary particle as well as on the orientations of the initial and final polarizations. In case of the elastic scattering of baryons there are five tensors: D, R, R', A and A', so called the Wolfenstein parameters (four of them are independent). According to Ann Arbor convention, for the case when beam is polarized, the target is not polarized and the scattered particle polarization is measured they correspond to the notations: $D = A_{n0;n0}$, $R = A_{s0;s'0}$, $A = A_{k0;s'0}$, $R' = A_{s0;k'0}$, $A' = A_{k0;k'0}$. For the case when the target is polarized and beam is not, the smaller letter notations for Wolfenstein's parameters were proposed in [3] (in this paper the asymmetry definition is different from Ann Arbor Convention: $A_{scattered,recoil;beam,target}$). So they are $d = A_{0n;0n}$, $r = A_{0s;0s'}$, $a = A_{0k;0s'}$,$r' = A_{0s;0k'}$, $a' = A_{0k;0k'}$. For inclusive production of spin 1/2 baryons and hyperons by the polarized beam or target the similar tensors are applicable.

The review covers the experimental data on the above listed spin tensors in elastic hadron-proton scattering in momentum range from approximately 1 GeV/c up to 45 GeV/c, in inclusive neutron production at momentum 1.1 GeV/c,in inclusive Λ production at $\sqrt{s} = 20$ GeV and 200 GeV. There is an indication that some of the spin transfer tensors decrease with energy (for example D), while other ones seem to be weakly depending on energy (for example R). The highest values close to one may have the parameter A which reaches almost 1 in elastic scattering of the polarized protons on the target with spin zero. At inclusive lepto-production of $\overline{\Lambda}$ the tensor A' reaches 0.3 at $p_T = 1.2$ Gev/c (COMPASS). There is the model prediction for this parameter at RHIC. It should be around 10%.

The data are scarce at high energies especially for stable baryons. No measurement was done for inclusive antiproton production. One needs to put more effort on such measurements.

Introduction. The polarization transfer tensors of the second rank or so called Wolfenstein parameters D, R, A, R' and A' were defined for the NN - elastic scattering [1]. They relate the polarization of the secondary baryons and hyperons to the polarization of the primary beam or target protons. Four of them are independent, since there is one relation between them $\frac{R'+A}{A'-R} = \tan\theta_1$, where θ_1 is the angle of the scattered particle

in lab. system. Measurements of these parameters are necessary for getting the unique phase shift solution, for direct reconstructions of scattering amplitudes; these parameters are sensitive to the spin structure functions and Regge poles. Besides, their asymptotics deserves a special study since they would serve as a source of polarized particles like neutrons, antiprotons, antineutrons, hyperons, etc. The goal of the present work is to survey the status of such measurements and to study the asymptotic behavior of these parameters.

Before proceeding further, the notations should be defined. The measured asymmetry is denoted as $A_{beam,target;scattered,recoil}$ [2]. The sub-indices present the status of the polarization direction of the corresponding particles. For the case when beam is polarized, the target is not polarized and the scattered particle polarization is measured, they correspond to the notations: $D = A_{n0;n0}$, $R = A_{s0;s'0}$, $A = A_{k0;s'0}$, $R' = A_{s0;k'0}$, $A' = A_{k0;k'0}$. Unit vectors are: k - along the particle momentum, n - normal to the production plane, $\overrightarrow{s} = \frac{[\overrightarrow{n}\times\overrightarrow{k}]}{|[\overrightarrow{n}\times\overrightarrow{k}]|}$; the prime in superscript - for scattered, double primes - for recoil and no prime - for initial particles. For the case when the target is polarized and beam is not, the small letter notations for Wolfenstein parameters were proposed [3]. There is again one relation between Wolfenstein parameters, namely, $\frac{a+r'}{r-a'} = \tan\theta_2$, where θ_2 is the angle of the recoil particle in lab. system. The superscript labels r and s are introduced when the parameters connect the polarized beam particle to the recoil and the polarized target particle to the scattered particle, respectively. In the following sections we survey the parameters measured in elastic pion-nucleon and elastic nucleon-nucleon scattering, in inclusive neutron production, and in inclusive Lambda production. We formulate the helicity conservation hypothesis for binary reactions. Some predictions of such hypothesis are tested using the experimental data. The importance of the further testing of this hypothesis, e.g. at RHIC, is emphasized.

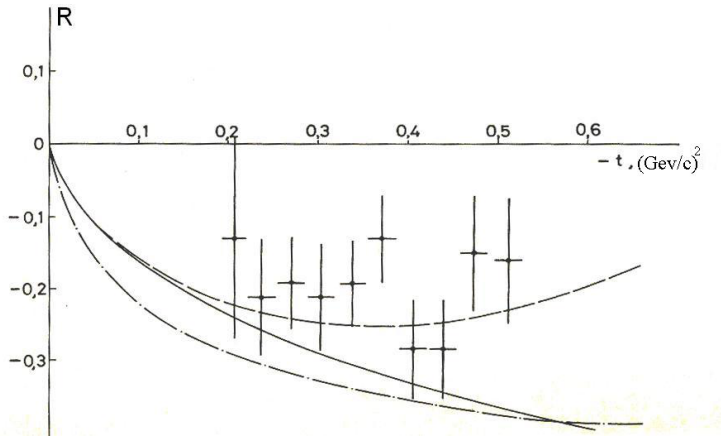

Figure 1: Results for R in elastic $\pi^- p$ - scattering at 40 GeV/c. The predictions of refs [5] and [6] are presented by the dashed and the dot-dashed lines respectively. The solid line represents the function $R = -\cos\Theta_p$, where θ_p is the recoiled proton angle.

Elastic pion-nucleon scattering. Pion-nucleon elastic scattering is described by 3 independent observables. There are the unique data on spin rotation parameter r for pion-nucleon elastic scattering at 6, 16, and 40 GeV/c. Fig. 1 presents data on r at 40 GeV/c [4] (this figure was obtained before the small-letter notation was introduced. Using the new notations, this would be $r(-t)$ dependence).

These data give some indications that the prediction $r = -\cos\theta_2$, following from the helicity conservation hypothesis (see below), from the model of rotating hadronic matter, and from Regge Pomeron pole, might be almost reached at $\sqrt{s} \sim 10$ GeV. It's important to check this statement more precisely including the measurements of the other spin transfer tensors too. For example, one expects $a = \sin\theta_2$ in asymptotics.

Elastic nucleon-nucleon scattering. Fig. 2 shows angular dependence (in c.m.s.) of D, R and A in pp-scattering around 1 GeV (kinetic energy).

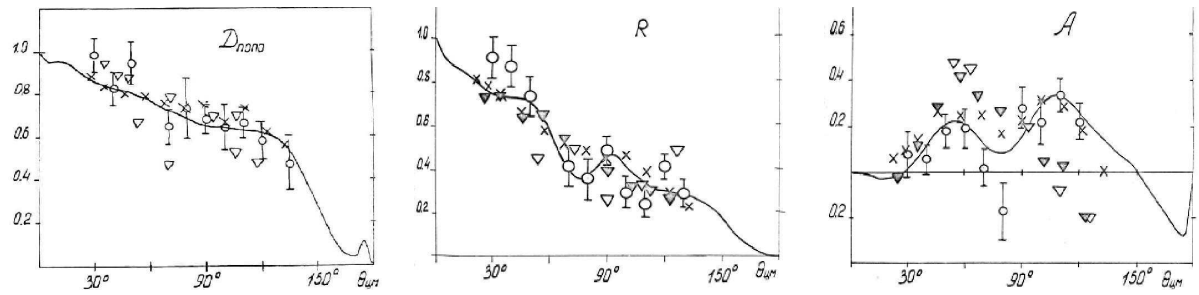

(a) **(b)** **(c)**

Figure 2: Angular dependence of parameters D **(a)**, R **(b)** and A**(c)** in pp-scattering around 1 GeV (kinetic energy). ∇ - 640 MeV (JINR), $\times$ - 800 MeV (LAMPF), $\circ$ - 1 GeV (SPNPI). Solid line is PSA results for pp - scattering [7].

Analyzing these figures one could make the following conclusions: D is close to 1 at small angles, it drastically changes around 90° and it is not in asymptotic regime ($D \neq 1$). R is large enough at small angles, it drastically changes around 90°, it is not in asymptotic regime ($R \neq -\cos\theta_1$). A is negligible at small angles, it might be oscillating around 90°, it is not in asymptotic regime ($A \neq \sin\theta_1$).

The experimental data on parameter R at momentum 45 GeV/c for elastic pp - scattering are shown in the Fig. 3 [8]. These data are consistent with asymptotic expectation $R = -\cos\theta_2$ following from several models like the rotating hadron matter, the helicity conservation model, the leading Pomeron exchange.

Therefore the elastic scattering data give some hints to the energy where the helicity conservation hypothesis becomes important: this is the energy $\sqrt{s} > 10$ GeV. Today this conclusion may be experimentally checked at the polarized RHIC.

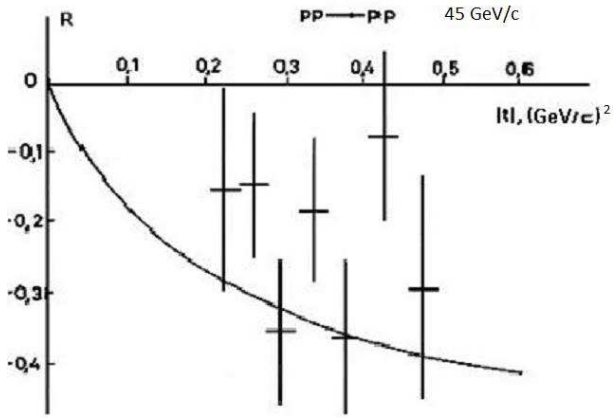

Figure 3: Spin rotation parameter R in elastic pp - scattering at momentum of 45 GeV/c vs. $-t$ in $(GeV/c)^2$. The solid line is the dependence $R = -\cos\theta_p$, where θ_p is the recoiled proton angle.

Inclusive neutron production. The reaction $C(p,n)X$ with longitudinally polarized proton beam of 590 MeV (beam polarization $P = 75\%$, $pc = 1.205$ GeV $\pm$ 0.1%, beam intensity 10 μA) was used for production of the longitudinally polarized neutron beam. It was found experimentally that the transfer of polarization from longitudinally polarized protons was the most effective method. Neutrons emitted at the angle of 0° with respect to the proton beam at the target were selected by a collimator and travelled into the experimental area. The absolute neutron beam intensity was about 10^8 n/s for neutron energies from 100 to 590 MeV [9]. Neutron polarization is presented as a function of the neutron kinetic energy in Fig. 4. As seen from this figure the polarization transfer tensor (analogous to A') is practically constant and is equal to 60% for $x_F > 0.7$. It's important to repeat such measurements at the polarized RHIC.

Inclusive lambda-production. Fig. 5 presents the depolarization D as a function of x_F at 200 GeV/c [10]. Data from BNL at 18.5 GeV/c and $p_T \sim 1$ GeV/c are presented as well [11]. The figure shows that D depends on p_T and x_F. $D = 0.37 \pm 0.11$ ($< x_F >= 0.79, < p_T >= 0.84$ GeV/c) at 200 GeV/c, while at 6 GeV/c (ZGS) $D = 0.27 \pm 0.29$ [12]).

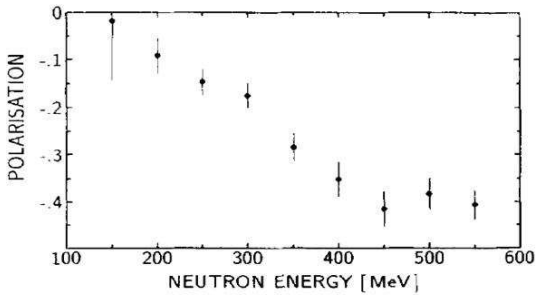

Figure 4: Inclusive neutron polarization as a function of the neutron kinetic energy.

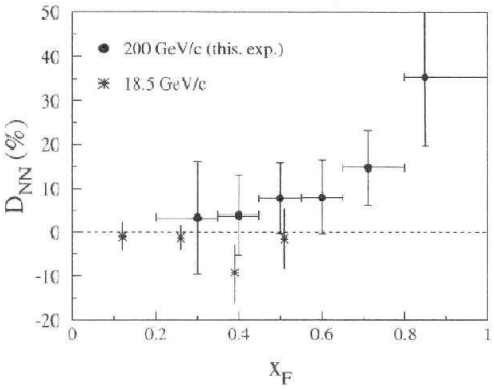

Figure 5: Depolarization D as a function of x_F at 200 GeV/c. $*$ - data from BNL at 18.5 GeV/c and $p_T \sim 1$ GeV/c.

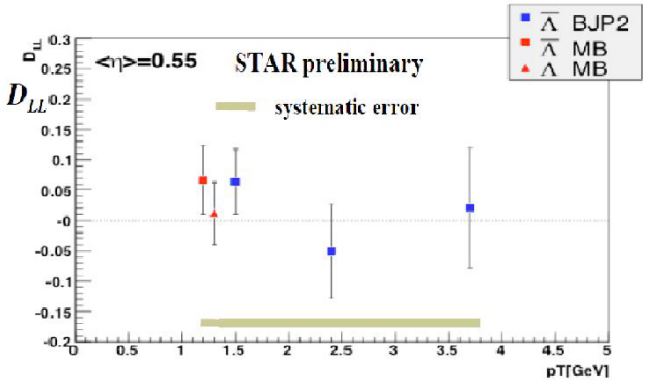

Figure 6: Comparison of Λ and $\overline{\Lambda}$ spin transfer D_{LL} in polarized proton-proton collisions at $\sqrt{s} = 200$ GeV for (a) positive and (b) negative pseudorapidity η versus p_T, respectively.

The sizable spin transfer effect has been inferred in Ω^- - production at Tevatron by high- energy neutral beam containing transversal polarized Λ° and Ξ° [13]. We are not aware of any theoretical explanation of these effects.

Fig. 6 [14] gives the comparison of Λ and $\overline{\Lambda}$ spin transfer D_{LL} in longitudinally polarized proton-proton collisions at $\sqrt{s} = 200$ GeV for (a) positive and (b) negative pseudorapidity η versus p_T. The vertical bars and bands indicate the sizes of the statistical and systematic uncertainties, respectively. The Λ data points have been shifted slightly in p_T for clarity. The dotted vertical lines indicate the p_T intervals in analysis of HT and JP data. The horizontal lines show model predictions. According to Fig. 6, the longitudinally polarized protons do not transfer their polarizations to the Λ and $\overline{\Lambda}$ at $\sqrt{s} = 200$ GeV at the central region. According to the theorem of Abarbanel-Gross [15] it should be expected that non-zero transfer of polarization occurs when the rapidity gap between the initial protons and final baryons (hyperons) is small. Therefore it is very important to measure such processes in the fragmentation region of initial polarized protons. STAR Collaboration is preparing such an experiment.

Helicity conservation hypothesis for NN-scattering. We assume that the helicity conserves at sufficiently high energies in s-channel. In this case the only two helicity non flip amplitudes M_1 and M_3 survive. If we take $M_1 = M_3$ therefore, using formulae from [3], we obtain the asymptotic behavior of Wolfenstein parameters when we study the spin transfer from the beam to the scattered nucleon (Table 1); from the target to

the recoil nucleon (Table 2).

Table 1. Spin transfer from the beam to the scattered nucleon				
D	R	A	R'	A'
1	$-\cos\theta_1$	$\sin\theta_1$	$\sin\theta_1$	$\cos\theta_1$
$\frac{R'+A}{A'-R} = \tan\theta_1$				

Table 2. Spin transfer from the target to the recoil nucleon				
d	r	a	r'	a'
1	$-\cos\theta_2$	$-\sin\theta_2$	$-\sin\theta_2$	$\cos\theta_2$
$\frac{a+r'}{r-a'} = \tan\theta_2$				

Wolfenstein parameters R and A' are significant at the angle θ_1 close to 0°, while A and R' are significant when θ_1 is close to 90°.

Again, if we take $M_1 = M_3$, the Wolfenstein parameters transferring the spin from the beam to the recoil nucleon and from the target to the scattered nucleon are zero. The predictions of the helicity conservation hypothesis for parameter $r = -\cos\theta_2$ are confirmed by the experimental results on elastic $\pi^- p$ - scattering at momentum of 40 GeV/c and elastic pp - scattering at momentum of 45 GeV/c. The other predictions of the helicity conservation hypothesis may be tested at existing experimental facilities. The main goal of this paper was to study the Wolfenstein parameters surviving at the asymptotics. For this the helicity conservation hypothesis, which predicts the values of Wolfenstein parameters in asymptotics, was proposed. The experimental confirmation of the hypothesis was found in reactions: $\pi^- p$ at 40 GeV and pp at 45 GeV, namely, $r = -\cos\theta_2$. However the data exist for parameter r only, the other parameters are not measured at these and higher energies. There is a tendency that in pp - elastic scattering D^r and $R^r \to 0$ at large angles (see Fig. 2) as it is predicted by helicity conservation hypothesis. Why D_{LL} is small in inclusive Λ production? Unfortunately, there is no model for inclusive reaction analogues to the helicity conservation model for elastic scattering. If elastic models were valid in this case, then D_{LL} could behave like $a' = \cos\theta_2$ and be zero at large angles. At STAR it was measured at 90°. To check the asymptotics, the measurements at small angles should be done.

Conclusions.

1) The Wolfenstein parameters D, R and A were studied in details experimentally at the kinetic energy region $100 - 3000$ MeV and were used in the phase shift analysis and in the direct reconstruction of the NN - elastic scattering amplitudes. The data on parameters R' and A' are scarce.

2) There are the unique data on parameter r: for pion-nucleon elastic scattering at 6, 16, and 40 GeV/c and on pp - elastic scattering at 45 GeV/c. They give some indications that the predictions $r = -\cos\theta_2$ following from the helicity conservation hypothesis might be almost reached at $\sqrt{s} \sim 10$ GeV. It's important to check this statement more precisely including the measurements of other spin transfer tensors too. The special attention should be devoted to the measurement of the depolarization parameter D, since it is expected to be equal to one.

3) E-704 experiment clearly showed that the depolarization parameter D survives for inclusively produced Λ up to momentum 200 GeV/c. We hope to see soon the similar data from STAR in the polarized proton beam fragmentation region.

4) The spin transfer observables are very important tool for understanding the spin structure of nucleons. The theoretical development of the formalism for inclusive reactions similar to one for the elastic scattering is needed. The concrete predictions for the spin transfer in reactions $pp \to hX$, where h - antiproton, nucleon, hyperons, are required.

5) Practical application: if the spin transfer parameter "survives" and becomes large (> 0.5) it could be a source of polarized particles. $p \uparrow A \to h \uparrow X$ ($h \uparrow = n \uparrow, p \uparrow, \Lambda \uparrow, n^- \uparrow, p^- \uparrow, \Lambda^- \uparrow, etc$).

6) For study the spin transfer tensors in production of the stable baryons at high energy one needs to develop the efficient polarimeters with high factor of merit.

Acknowledgements. We are thankful for stimulating discussions and help in preparation of this presentation to F. Lehar, M.B. Nurusheva, S.S. Nurushev, M.F. Runtso and M.G. Ryskin.

References

[1] L. Wolfenstein, Phys. Rev. 96 (1954) 654.

[2] The Ann Arbor Convention for Spin Parameters, in Higher Energy Polarized Proton Beams, AIP Conference Proceedings No. 42, edited by A.D. Krisch and A. J. Salthouse, 1977 (American Institute of Physics, New York, 1978).

[3] J. Bystricky and F. Lehar, Le Journal de Physique , tome 39, #1, Janvier 1978, 1-35.

[4] J. Pierrard et al., Measurement of spin rotation parameter in $\pi^- p$ and $K^- p$ elastic scattering at 40 GeV/c , Phys. Lett.57B, 393 (1975).

[5] V. Barger and R.J.N. Philips, Phys. Rev. 187, 2210 (1969).

[6] G. Girardi et al., Nuclear Physics B47, 445 (1972).

[7] V. Vovcenko et al., Yad. Fiz. 37, 158 (1983).

[8] J. Pierrard et al, Phys. Lett. B61, 107 (1976).

[9] J. Arnold et al., Nucl. Instr. Meth. A386, 211 (1997).

[10] A. Bravar et al., Phys. Rev. Lett., 78, 4003 (1997) .

[11] B.E. Bonner et al., Phys. Rev. D38, 729 (1988).

[12] E. Swallow, Polarization effects in inclusive Λ production: Prospects for polarized hyperon beams. Proc. of Symposium on high-energy physics with polarized beams. Argonne National Laboratory, February 8, 1974, p. X1-1.

[13] N.B. Wallace et al., Phys.Rev.Lett. 74, 3732 (1995).

[14] Qinghun Xu, Longitudinal spin transfer to and in polarized proton-proton collisions at 200 GeV. Proc. of the XIII Advanced Workshop on High Energy Spin Physics, September 1-5, 2009, Dubna, pp 313-318.

[15] H.D.I.Abarbanel and D.J. Gross, Phys. Rev. Lett. 26, 732 (1971), Phys. Rev. D 5, 699 (1972).

THE Q_{Weak} EXPERIMENT: A SEARCH FOR NEW PHYSICS AT THE TeV SCALE

W. Deconinck [1 †], for the Q_{Weak} Collaboration

(1) *College of William & Mary, Williamsburg, VA, USA*
† *E-mail: wdeconinck@wm.edu*

Abstract

The Q_{Weak} experiment, which started in May 2010 and will run until May 2012 in Hall C at Jefferson Lab, aims to determine the weak charge of the proton, $Q_W^p = 1 - 4\sin^2\theta_W$, to a precision of 4%, and the weak mixing angle $\sin^2\theta_W$ to a precision of 0.3%. With this precision the experiment will be sensitive to parity-violating new physics at the TeV scale. We access the weak charge by measuring the small parity-violating asymmetry in the elastic scattering of polarized electrons with positive and negative helicity on unpolarized protons in a liquid hydrogen target. Due to the interference of the photon and Z-boson exchange diagrams, this asymmetry is proportional to the weak charge of the proton. To achieve the high precision, we scatter the 150 to 180 μA polarized electron beam on a 35 cm long liquid hydrogen target with 2.5 kW of cryogenic cooling power. The signals of the scattered electrons in eight fused silica detectors are integrated in custom electronics modules. During the first running period, the Q_{Weak} experiment has collected 25% of the total expected data volume.

1 Introduction

The Standard Model of particle physics has been very successful in describing a wide range of phenomena in nuclear and particle physics. Proposed four decades ago, the Standard Model combines the strong interaction between quarks and gluons described by Quantum Chromodynamics, and the unified electroweak interaction between fermions by the exchange of photons and weak bosons. However, despite its successes there are compelling experimental and theoretical reasons to search for effects which would require an extension to the current Standard Model: there is no dark matter candidate, the expected mass of the Higgs boson is unnatural, etc.

In the Standard Model, quarks do not just possess an electric charge given by their coupling strength under the electromagnetic exchange of photons. They also possess weak charges under the exchange of the weak bosons. An overview of the electromagnetic and weak vector charges is giving in table 1. The weak charge for the proton is given by $Q_W^p = 1 - 4\sin^2\theta_W$, with θ_W the Weinberg angle describing the mixing of the electromagnetic and weak sectors. The value of $\sin^2\theta_W \approx 1/4$ results in a small value for the weak charge of the proton, $Q_W^p \approx 0.07$, which makes a measurement of the weak charge of the proton very sensitive to $\sin^2\theta_W$. Notice that in contrast to the small weak charge for the proton the weak charge of the neutron is larger, $Q_W^n = -1$.

Table 1: Electromagnetic and weak vector couplings of the light quarks and nucleons.

Particle	Electromagnetic charge	Weak vector charge
u	$+\frac{2}{3}$	$-2C_{1u} = 1 - \frac{8}{3}\sin^2\theta_W \approx \frac{1}{3}$
d	$-\frac{1}{3}$	$-2C_{1d} = -1 + \frac{4}{3}\sin^2\theta_W \approx -\frac{2}{3}$
$p(uud)$	$+1$	$Q_W^p = 1 - 4\sin^2\theta_W \approx 0.07$
$n(udd)$	0	$Q_W^n = -1$

The Q_{Weak} experiment will measure for the first time the weak charge of the proton Q_W^p. By measuring the weak charge of the proton Q_W^p and the electroweak mixing angle $\sin^2\theta_W$ to a high precision, we are sensitive the indirect effects from particles beyond the Standard Model that are out of reach of present accelerators. The prediction for the running of $\sin^2\theta_W$ with momentum transfer Q^2 is indicated by the solid line in figure 1. Significant deviations from the predicted values would indicate that extensions or modifications to the Standard Model are required [1, 2].

The sensitivity of the weak charge to new physics (leptoquarks, R-parity violating supersymmetry) can be estimated in a model-independent way [4]. Assuming an interaction with coupling constant g and mass scale Λ and effective charges $h_V^u = \cos\theta_h$ and $h_V^d = \sin\theta_h$, we can write the interaction Lagrangian for electron-quark scattering as $\mathcal{L} = \frac{g^2}{4\Lambda^2}\bar{e}\gamma_\mu\gamma_5 e\sum_q h_q^V \bar{q}\gamma^\mu q$. The sensitivity of the Q_{Weak} experiment as a function of the interaction mixing angle θ_h is shown as the short-dashed green line in figure 2. The Q_{Weak} experiment will increase the reach beyond the

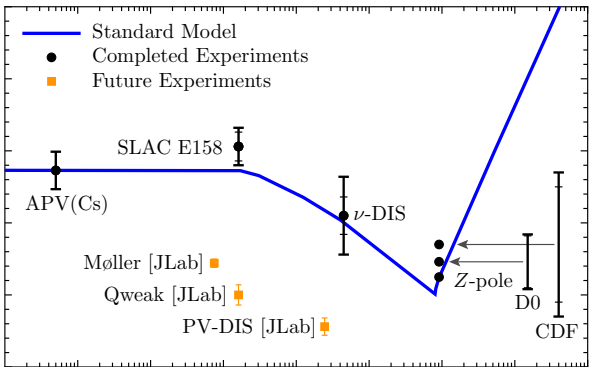

Figure 1: Running of the electroweak mixing angle $\sin^2\theta_W$ with momentum tranfer Q^2 as calculated in the Standard Model (blue line) [3]. The available experimental data points are shown in black. Projected data points for the Q_{Weak} and other experiments are shown in red.

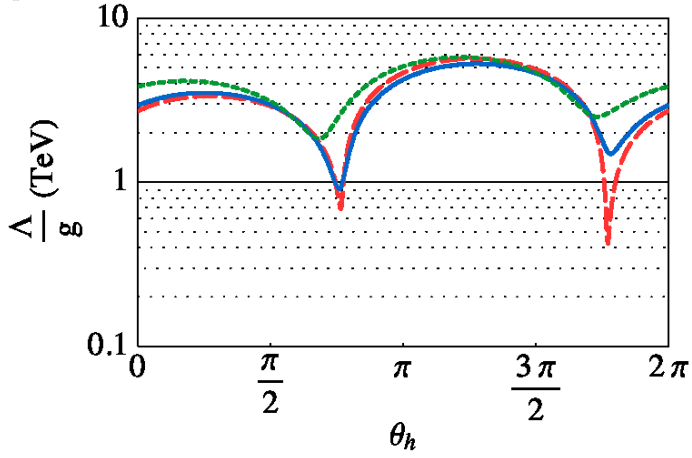

Figure 2: Model-independent analysis of the sensitivity to physics beyond Standard Model [4]. The long-dashed red curve indicates the limits without results from parity-violating electron scattering experiments. The solid blue curve includes results from parity-violating electron scattering experiments without the Q_{Weak} experiment. The short-dashed green curve shows the projected constraints including the Q_{Weak} experiment, assuming agreement with the Standard Model.

1 TeV scale at 95% confidence.

2 Parity-Violating Electron Scattering

The Q_{Weak} experiment uses the technique of parity-violating electron scattering to access the weak charge of the proton. A longitudinally polarized electron beam with quickly alternating helicity strikes a cryogenic liquid hydrogen target. Elastically scattered electrons are detected in quartz Čerenkov detectors, and custom-built data acquisition electronics measures the integrated photomultiplier current generated by the rapid succession of electron pulses.

A helicity asymmetry can be constructed from the integrated detector response in consecutive helicity intervals. Although the total scattering cross section from protons or electrons in hydrogen is dominated by the parity-conserving exchange of photons, independent of the incoming electron helicity, a small parity-violating asymmetry is introduced by the interference of the photon exchange and Z-boson exchange diagrams. Based on the propagators of the interactions the size of the parity-violating asymmetry can be easily estimated as

$$A_{PV} = \frac{\sigma_R - \sigma_L}{\sigma_R + \sigma_L} \propto \frac{Q^2}{M_Z^2}, \tag{1}$$

where Q^2 is the squared momentum transfer, and $M_Z = 91.2\,\text{GeV}$ is the mass of the Z-boson. At momentum transfers common at Jefferson Lab (Q^2 values up to a few GeV), the small asymmetry is usually expressed in parts per million (ppm) or parts per billion (ppb).

For elastic scattering the parity-violating asymmetry on the proton can more accurately be written as

$$A_{PV}(p) = \frac{-G_F Q^2}{4\pi\alpha\sqrt{2}} \left[\frac{\epsilon G_E^\gamma G_E^Z + \tau G_M^\gamma G_M^Z - (1 - 4\sin^2\theta_W)\epsilon' G_M^\gamma G_A^Z}{\epsilon (G_E^\gamma)^2 + \tau (G_M^\gamma)^2} \right], \tag{2}$$

with G_F the Fermi coupling constant, Q^2 the squared four-momentum transfer, and α the fine structure constant. The dimensionless kinematic factors $\tau = Q^2/4M^2$, $\epsilon = (1 + 2(1+\tau)\tan^2\theta/2)^{-1}$, and $\epsilon' = \sqrt{\tau(1+\tau)(1-\epsilon^2)}$ combine with the electric and magnetic form factors G_E^γ, G_E^Z, G_M^γ, G_M^Z under γ and Z exchange and the electron axial form factor G_A^e to complete the expression.

In the forward-angle limit $\theta \to 0$, where the momentum transfer Q^2 is small, the expression for the

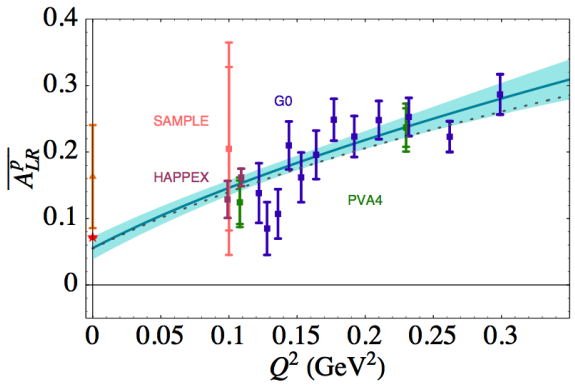

Figure 3: Normalized parity-violating asymmetry $\overline{A_{PV}^p} = Q_W^p + Q^2 \cdot B(Q^2)$ measured by other parity-violating experiments on a proton target and extrapolated to the forward-angle limit [4]. The extrapolation to $Q^2 = 0$ of the fit to the data represents the weak charge of the proton. The prediction of the Standard Model is shown with the red star.

Table 2: Summary of projected uncertainties on the asymmetry A_{PV} for the Q_{Weak} experiment.

Source of uncertainty	$\delta A_{PV}/A_{PV}$	$\delta Q_W^p/Q_W^p$
Statistical uncertainty	2.1%	3.2
Hadronic structure	N/A	1.5%
Beam polarization	1.0%	1.5%
Absolute value of Q^2	0.5%	1.0%
Inelastic *ep* scattering	0.5%	0.7%
First order beam properties	0.5%	0.7%
Systematic uncertainty	1.3%	2.5%
Total uncertainty	2.5%	4.1%

asymmetry simplifies to

$$A_{PV}(p) \xrightarrow{Q^2 \to 0} \frac{-G_F Q^2}{4\pi\alpha\sqrt{2}} \left[Q_W^p + Q^2 \cdot B(Q^2) \right]. \tag{3}$$

In this expression the function $B(Q^2)$ contains corrections due to the hadronic substructure of the proton. The normalized parity-violating asymmetry $\overline{A_{PV}^p} = Q_W^p + Q^2 \cdot B(Q^2)$ measured by other parity-violating experiments and extrapolated to the forward-angle limit is shown in figure 3. By extrapolating the expression for the asymmetry to $Q^2 = 0$, we obtain the weak charge of the proton.

3 Experimental Apparatus

The Q_{Weak} experiment is located in Hall C at the Thomas Jefferson National Accelerator Facility or Jefferson Lab. The experiment started in May 2010 and will collect data until May 2012, with a six month long break between May 2011 and November 2011 separating the experiment in two data taking phases. The experiments consists of three major components: the longitudinally polarized electron beam, the liquid hydrogen target, and the spectrometer and detector system. A summary of the projected systematic uncertainties in the experiment is presented in table 2.

Polarized Electron Beam Polarized electrons are generated in a strained GaAs superlattice photocathode. Left or right circularly polarized laser strikes the surface of the GaAs crystal and electrons of the corresponding helicity are photo-emitted and pre-accelerated in the injector. Beam currents after the injector of 180 μA and beam polarizations exceeding 85% are routinely achieved.

The circular polarization of the laser light is determined by the polarity of the high voltage on a Pockels cell. The polarity is changed at a rate of 960 Hz, corresponding to a settling time of 70 μ and an integration time of 971 μs. To reduce the sensitivity to low frequency noise components and drifts in the beam parameters we do not simply toggle the helicity states (*e.g.* $+-+-+-$) but we use a pseudo-random sequence of quartets of the form $+--+$ or $-++-$. Electronic cross-talk between the helicity signal and detector

signals is avoided by reporting the actual helicity state with a delay of eight quartets. To remove the effects of helicity correlated beam properties, the circular polarization of the laser is inverted every eight hours by inserting or removing a half-wave plate, and every week by performing a Wien rotation of the electron polarization in the injector.

The beam transport line from the polarized electron source and injector to the liquid hydrogen target in the experimental hall is instrumented with beam intensity and beam position monitors. The measurements of several beam position monitors are combined to determine the beam position and beam direction at the target itself. The beam position monitors in dispersive regions are used to measure the beam energy.

Liquid Hydrogen Target The target consists of a 35 cm long aluminum cell filled with liquid hydrogen (LH2). To maintain a temperature of 20 K while operating with electron beam currents up to 180 μA a cryogenic cooling system requires 2500 W of cooling power, provided by liquid helium coolant at 4 K and 15 K in a heat exchanger with three layers of coils. An important design criterion for the target was to minimize pressure and temperature fluctuations. This was achieved by extensive computational fluid dynamics simulations to determine the optimal shape of the target and the flow velocity transverse to the beam. During short intervals without beam a high-power heater in the LH2 loop compensates for the lost beam heating to stabilize the loop and to prevent the LH2 from freezing. Observed pressure variations are substantially slower than the helicity reversal rate.

Spectrometer and Detector System. The spectrometer and detector system are shown schematically in figure 4. Electrons scatter off the protons in the liquid hydrogen target, and the scattered electrons in the angular region of interest pass through the octagonally symmetric holes of the three collimators. The toroidal magnet coils bend the scattered electrons outwards, as indicated by the envelope in the top octant. Behind the 8 m tall shield wall all eight octants have quartz bar Čerenkov detectors with custom-built integrating data acquisition electronics.

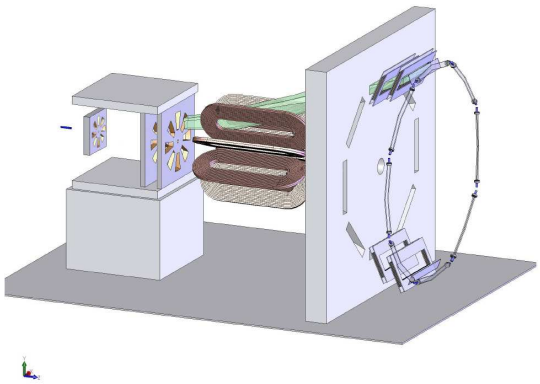

Figure 4: Schematic view of the Q_{Weak} experiment in Hall C at Jefferson Lab.

Two opposite octants are instrumented with tilted particle tracking detectors, horizontal drift chambers before and vertical drift chambers after the toroidal magnet. The horizontal and vertical drift chamber packages can be rotated independently for measurements of the momentum transfer Q^2 in each octant. For both types of drift chambers there is one pair of octants can be reached by both positive and negative rotations, providing us with redundancy that aids in determining systematic effects.

Polarimetry Two beam polarimetry techniques are used to reach the required 1% systematic uncertainty on the measurement of the electron beam polarization. In the existing Møller polarimeter the electron beam is scattered from the polarized outer-shell electrons in an iron foil that has been magnetized to saturation in a large external magnetic field. The Møller measurements are invasive to the Q_{Weak} experiment and have to be conducted at beam currents below $10\,\mu$A to avoid depolarization due to foil heating. There is therefore an uncertainty associated with extrapolating to the experimental conditions.

To measure the beam polarization non-invasively and continuously, a new Compton polarimeter was commissioned for the Q_{Weak} experiment. The polarized electron beam is collided nearly head-on with a high-intensity circularly polarized laser beam in a low-gain Fabry-Pérot cavity in the center of a magnetic chicane. The scattered photons (with energies up to 50 MeV) are detected in a $PbWO_4$ calorimeter. The scattered electrons are bent away from the primary beam by the dipole field of the chicane and their separation, measured in four diamond strip detector planes, is used to deduce their momentum. An asymmetry in the cross section for left and right circularly polarized laser light is proportional to the polarization of the electron beam.

Analysis The measured asymmetry A_{meas} of the signal yields Y in the quartz bars is related to the physical asymmetry A_{PV} by

$$A_{meas} = \frac{Y_+ - Y_-}{Y_+ + Y_-} = P_e(1-f)A_{PV} + fA_{bkg} + A_{false}, \tag{4}$$

where P_e is the electron polarization, f is the dilution factor determined by the fraction of background over signal plus background, A_{bkg} is the background asymmetry, and A_{false} is the false asymmetry due to helicity-correlated beam properties.

The integrated yields in the detectors depend on the beam intensity, beam energy, bean position, and beam direction. During data taking we measure the beam intensity and feed this information back to the high voltage of the Pockels cell in the polarized electron source to reduce the helicity-correlated beam intensity asymmetry.

Because these beam properties X_i are generally correlated with the helicity, they result in a false asymmetry. Using the measured helicity-correlated differences ΔX_i we can correct the measured asymmetry for this false asymmetry given knowledge of the correlation sensitivities α_i:

$$A_{false} = \sum_i \alpha_i \Delta X_i. \tag{5}$$

Using natural beam motion the helicity-correlated beam properties are correlated, and the sensitivities require a diagonalization of their correlation matrix. We also use an active beam modulation system that drives the beam energy and the horizontal and vertical beam position and direction separately, largely removing the internal correlations between the beam properties.

Backgrounds The two largest sources of background events are the aluminum walls of the target cell and inelastic scattering off the protons. Because the experiment integrates the detector response for all tracks, it is impossible to remove these background events individually and their collective effect has to be corrected for.

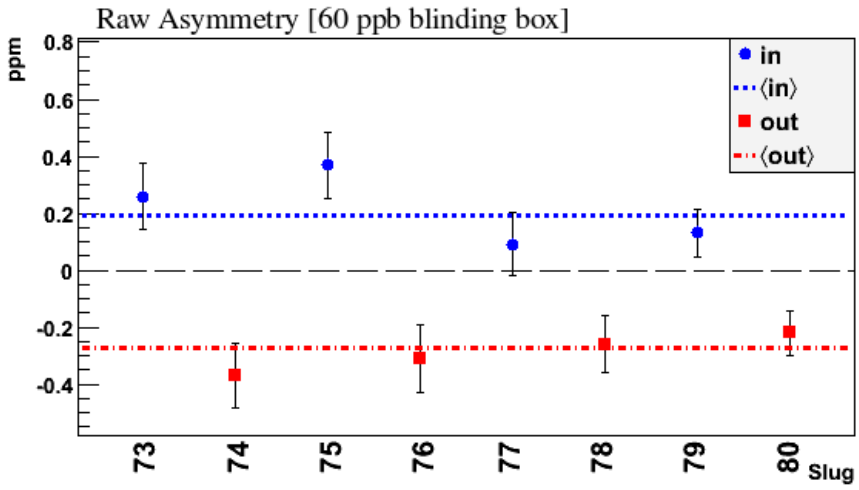

Figure 5: Uncorrected and blinded "raw" experimental asymmetries, averaged over all eight main detector octants, for a selection of "slugs" (periods of constant insertable half-wave plate settings). Each slug corresponds to approximately eight hours of data taking. Slugs with the insertable half-wave plate inserted are shown as blue disks, slugs with the insertable half-wave plate out are show as red squares. The corresponding blue and red lines show the average asymmetry for this subset of slugs. All asymmetries are blinded by an unknown additional asymmetry to avoid biases during the analysis.

Neutrons have a larger weak charge than protons ($Q_W^n = -1$ versus $Q_W^p \approx 0.07$). The parity-violating asymmetry for aluminum is therefore significantly larger than the asymmetry for liquid hydrogen. The approximately 100 μm thin target cell windows lead to a correction to the asymmetry of approximately 20%. To reduce the uncertainty present in this correction, a substantial amount of data has been collected on aluminum dummy targets to measure the parity-violating asymmetry in aluminum.

4 Preliminary Results

4.1 Integrating Mode Data

The width of the measured parity-violating asymmetry distribution at a beam current of 165 μA is 236 ppb. This value is in agreement with the expectation from counting statistics (215 ppm), when taking into account detector resolution, current normalization, and target density fluctuations.

The measured asymmetry is expected to change sign when the helicity is reversed at the polarized electron source by inserting a half-wave plate in the laser path. Each period during which this half-wave plate remains in the same state is called a "slug." In figure 5 the average asymmetry for a series of slugs is shown, and the expected sign change for alternating half-wave plate states is clearly visible. The asymmetries shown in figure 5 are uncorrected and blinded asymmetries, and therefore not amenable to interpretation in terms of Q_W^p.

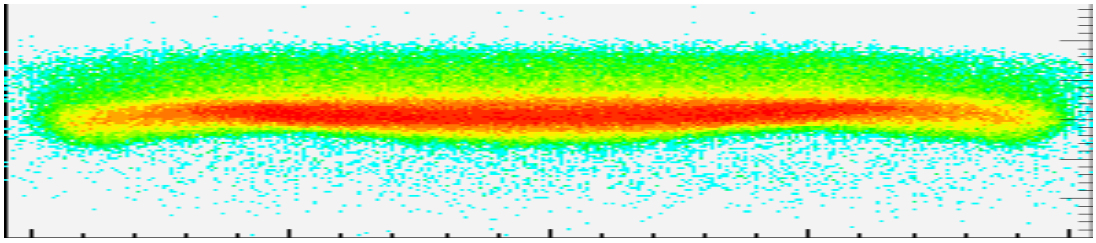

Figure 6: Projection of the electron tracks reconstructed in the vertical drift chambers to the main detector quartz bars. The figure corresponds to one 2 m × 18 cm large quartz bar.

4.2 Event Mode Data

During dedicated tracking runs at low currents from 50 nA to a few μA the tracking detectors were commissioned, and are being used to measure the distribution of the momentum transfer Q^2.

The horizontal drift chambers are functioning well, and the shape and mean value of the scattering angle distribution is in agreement with predictions from Monte Carlo simulations. The corresponding mean momentum transfer of tracks reaching the main detector is also consistent with simulations.

The performance of the vertical drift chamber has been excellent. As a qualitative demonstration of their performance, figure 6 shows the projection of the electron tracks reconstructed in the vertical drift chambers to the surface of the main detector quartz bars. The characteristic "mustache" shape of the event distribution is in agreement with the predictions from Monte Carlo simulations.

5 Conclusion

The Q_{Weak} experiment has successfully completed the first phase of data taking in May 2011, and accumulated approximately 25% of the total data volume necessary to achieve the 4% uncertainty on the weak charge of the proton. The second phase of the experiment will start in November 2011 and continue until May 2012.

Acknowledgements

The author would like to thank the organizers for the invitation to present these results at the workshop.

References

[1] J. Erler, M. J. Ramsey-Musolf, Phys. Rev. **D72** (2005) 073003; arXiv:hep-ph/0409169.

[2] M. J. Ramsey-Musolf, S. Su, Phys. Rept. **456**, 1–8 (2008); arXiv:hep-ph/0612057.

[3] W. Bentz, I. C. Cloet, J. T. Londergan, A. W. Thomas, Phys. Lett. **B693** (2010) 462–466.

[4] R. D. Young, R. D. Carlini, A. W. Thomas, J. Roche, Phys. Rept. **99**, 122003 (2007); arXiv:0704.2618 [hep-ex].

DRELL-YAN STUDIES AT FAIR

M. Destefanis [1 †]
on behalf of the PANDA Collaboration

(1) *Università degli Studi di Torino and INFN*
† *E-mail: marco.destefanis@to.infn.it*

Abstract

The nucleonic structure is far to be completely understood, in particular when considering those degrees of freedom related to the partons' transverse momentum, a main goal for several forthcoming studies in a wide range of experimental scenarios. The physics program of the future PANDA experiment includes the investigation of the non-perturbative region of the QCD by mean of antiproton beams, with a beam momentum up to 15 GeV/c. The current layout of the PANDA spectrometer includes detectors specifically devoted to the muon identification, allowing the background rejection that is needed to investigate the Drell-Yan (DY) production of muon pairs. Such reactions, in an experimental scenario characterized by a high luminosity as foreseen for PANDA at FAIR, represent an unique tool to access the spin depending properties of the nucleon, and in particular its transverse degrees of freedom, by means of experimental asymmetries leading to Transverse Momentum Dependent Parton Distribution Functions (TMD PDF's). In later stages of FAIR single- and double-spin asymmetries could be investigated making use of polarized protons and eventually of polarized antiprotons as well. The spin physics program that could be addressed in the different phases of FAIR will be discussed in details, with a particular focus on the PANDA experiment.

In the last decade, the difficult interpretation of several experimental polarized cross sections data suggests that other factors have to be taken into account when describing the nucleonic structure [1]. The latter being the final goal, a worldwide investigation performed in different experimental scenarios has focused on the role of the intrinsic transverse momentum of the partons ($\mathbf{k}_T$). A leading twist Transverse Momentum Dependent (TMD) description of the nucleon requires eight independent Parton Distribution Functions (PDF), functions of the longitudinal momentum fraction x and $\mathbf{k}_T$. Those functions have been and will be investigated with different beam-target configurations and in a wide energy range. In Semi-Inclusive Deep Inelastic Scattering (SIDIS) the TMD PDF's are convoluted with the Fragmentation Functions (FF), posing hence experimental and theoretical challenges to their extraction. On the contrary, in Drell-Yan (DY) processes the TMD PDF's could be directly accessed, since one can define experimental asymmetries depending on the TMD PDF's only.

The DY process is an electromagnetic interaction in which a quark and antiquark annihilation proceeds through a virtual photon into a final state containing a lepton pair: $h_1 h_2 \rightarrow \gamma^* \rightarrow l^+ l^- X$. In order to study the DY process, the Collins-Soper frame [2], the virtual photon rest frame, is used. In this frame, a hadron plane and a lepton plane are defined. If one defines the angle between the two planes as φ, then $\varphi_{S_{1,2}}$ is the angle between the nucleon spin ($S_{1,2}$) with respect to the lepton plane.

The differential cross sections of the completely unpolarised and single-polarised DY processes [3] show dependences on $h_1^\perp$, and on $h_1^\perp$, $f_{1T}^\perp$ and h_{1T}, respectively. $h_1^\perp$ is the so called Boer-Mulders (BM) function, which describes the distribution of transversely polarised quarks in an unpolarised hadron. The Sivers function $f_{1T}^\perp$ describes how the distribution of unpolarised quarks depends on the transverse polarisation of the parent hadron. The Transversity function h_{1T} describes the density of transversely polarised quarks into a transversely polarised hadron. As described in details in [4], these functions can be obtained from experimental asymmetries weighted by the following azimuthal angular terms: $\cos 2\varphi$, $\sin(\varphi - \varphi_{S_2})$ and $\sin(\varphi + \varphi_{S_2})$, respectively. In the double-polarized DY process, the differential cross section, after integrating upon $d\mathbf{q}_T$, shows a dependence on h_{1T} convoluted with itself. The corresponding experimental asymmetry is in this case weighted by the azimuthal term $\cos(2\varphi - \varphi_{S_1} - \varphi_{S_2})$.

The comparison of the Sivers distribution function obtained in SIDIS and DY processes could also provide an effective test of QCD Universality. The different role in the two processes of the Wilson-lines, which ensure the colour gauge invariance, is in fact expected to lead to opposite signs for the Sivers function ($f_{1T}^\perp$) when extracted from DY data or from SIDIS data: $f_{1T}^\perp|_{DY} = -f_{1T}^\perp|_{SIDIS}$ [5].

The center of mass energy (s) which should be available at FAIR should grant access to an unique kinematic region. At larger s (as for example the $\sqrt{s} = 200$ GeV of the RHIC scenario) one can access TMD PDF's mostly related to the sea quarks, and hence the above described asymmetries are expected to be remarkably small and experimentally hard to be determined. On the contrary, the FAIR scenario is characterized by a lower center of mass energy range and by the availability of antiproton beams: each valence quark can take part to the DY diagram and hence the contributions of the valence quarks to the TMD PDF's could be directly accessed free of any convolution with sea-quark PDF's. Two experiments focusing on the TMD challenge have been proposed for the different stages of the FAIR lifetime: the PANDA experiment [4, 6] will investigate an energy range up to $s \approx 30$ GeV^2, while the PAX experiment should focus on much larger energies, up to $s \approx 200$ GeV^2 [7].

The PANDA Collaboration is planning to investigate the unpolarized and, possibly, the single-polarized processes. The PAX experiment will focus first on the single-polarized processes and later, if antiprotons could be significantly polarized, on double-polarized processes, the real golden scenario.

The present FAIR facility layout foresees different storage rings: among the others the High Energy Storage Ring (HESR) is designed to host and accumulate the antiprotons. The PANDA spectrometer, optimized for a fixed-target HESR mode and shown in Fig. 1, is divided into two parts: the Target Spectrometer (TS) and the Forward Spectrometer (FS), both equipped with different detectors providing tracking of charged particles in magnetic fields, particle identification and calorimetry [4, 6]. The two further rings that have been proposed in a later FAIR stage, the Antiproton Polarizer Ring (APR) to polarize $\bar{p}$ and the Cooler Synchrotron Ring (CSR) to accelerate them inside the HESR, should allow the PAX Collaboration to investigate processes involving polarized antiprotons; which one can be the experimental technique most suitable to polarize antiprotons is currently the main focus of the investigation that the PAX people should soon start at CERN. The PAX spectrometer, shown in Fig. 2, is optimized to detect electromagnetic final states in an HESR asymmetric collider mode. Its detectors will provide particle tracking inside a

toroidal magnetic field, PID, triggering, and energy deposit measurements [7].

The variable τ, defined as the product between the momentum fractions (x_1 and x_2) of the two partons taking part to the annihilation vertex, is normally used to describe the kinematic range that can be accessed in the phase space by DY processes. Constant values of τ indicate a constant available center of mass energy transferred to the γ^*. The DY safe region ($4 \leq M_{\gamma^*} \leq 9$ GeV/c^2), so called because selecting those DY events produced in a kinematic region free from resonances, would correspond in the PANDA scenario to the top-right corner of Fig. 3, i.e. to τ values larger than 0.5. Since in such a case the kinematic region that could be access would be too small to infer the PDF's from the experimental data, PANDA will investigate also another region, $1.5 \leq M_{\gamma^*} \leq 2.5$ GeV/c^2 ($0.05 < \tau \leq 0.2$), not-resonant as well and characterized by a much larger (almost three order of magnitude) cross section [4].

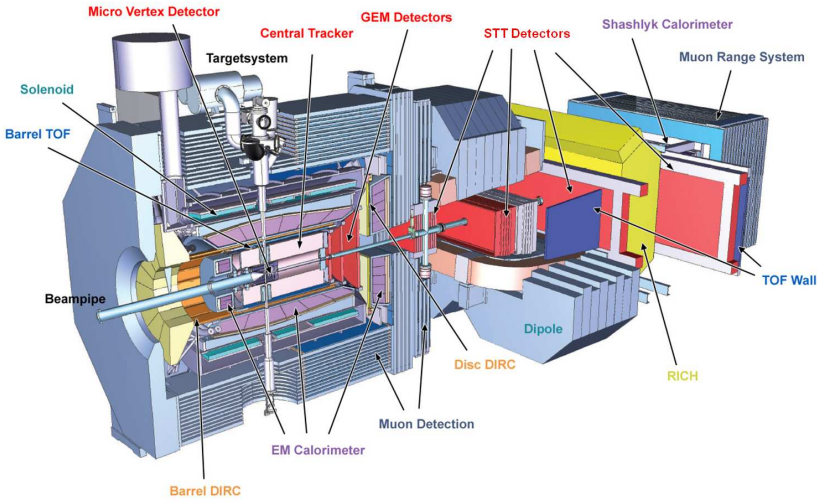

Figure 1: Setup of the PANDA detector (3D view).

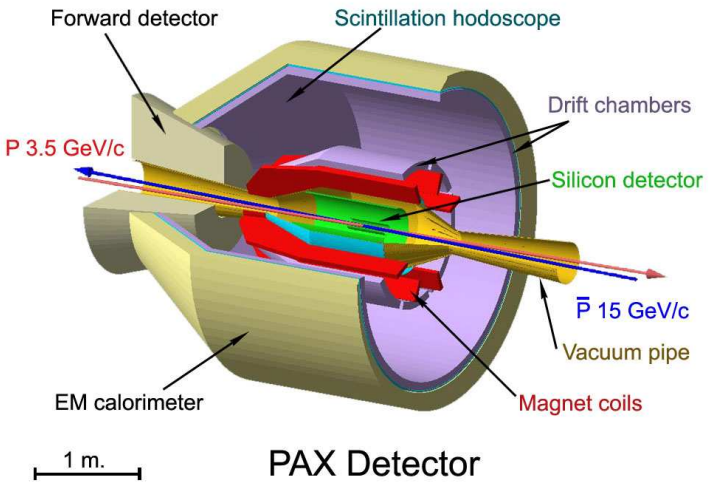

Figure 2: Setup of the PAX detector (3D view).

The investigation of electromagnetic processes is a relevant goal of the PANDA Collaboration physics program. The foreseen luminosity (up to $2{\cdot}10^{32}$ cm^{-2}s^{-1}) should give access to processes like the Drell-Yan production of muon pairs in annihilations as $\bar{p}p \rightarrow \gamma^* X \rightarrow \mu^+\mu^- X$. At the maximum foreseen beam energy ($s = 30$ GeV^2) the expected DY cross section is $\sigma \sim 1$ nb [4]. The background to the DY signal should be mostly composed of events of the type $\bar{p}p \rightarrow n(\pi^+\pi^-)X$, n being the number of pion pairs; their extimated cross section $\sigma \sim 20 \div 30$ mb [4] leads to a required background rejection factor $\sim 10^7$.

In order to obtain a better signal to background ratio, the PANDA Collaboration poses a particular attention to the muon detection. In fact, the design of the spectrometer [4,8] includes in both the TS and FS several planes of muon detector stations. The muon counters (MUO), located within the segmented iron yoke, will be composed of Iarocci tubes [9] (Mini Drift Tubes, or MDT), operating in proportional mode. In the MDT, the stainless steel cover is replaced by fiberglass strip boards (STRIP), which allow for the read out of the second coordinate by collecting the induced charge. A mixture of Ar+CO_2 is used to fill the MDT volumes. A full scale prototype ($3912 \times 2116 \times 32$ mm^3) of the muon counters has already been constructed and then transported to CERN for test purposes. To clearly understand the PANDA layout, also a "Range System" (RS) prototype has been prepared. The RS is a segmented iron block with the dimensions $1530 \times 1060 \times 1000$ mm^3 which reproduces the exact PANDA layout with the MUO planes in between the segmented iron volumes [8].

We simulated the production of DY muon pairs using the generator provided by A. Bianconi [10]: making use of the data available in the literature in can provide final states containing muon pairs produced in $\bar{p}$ and π^- interactions with unpolarized or polarized

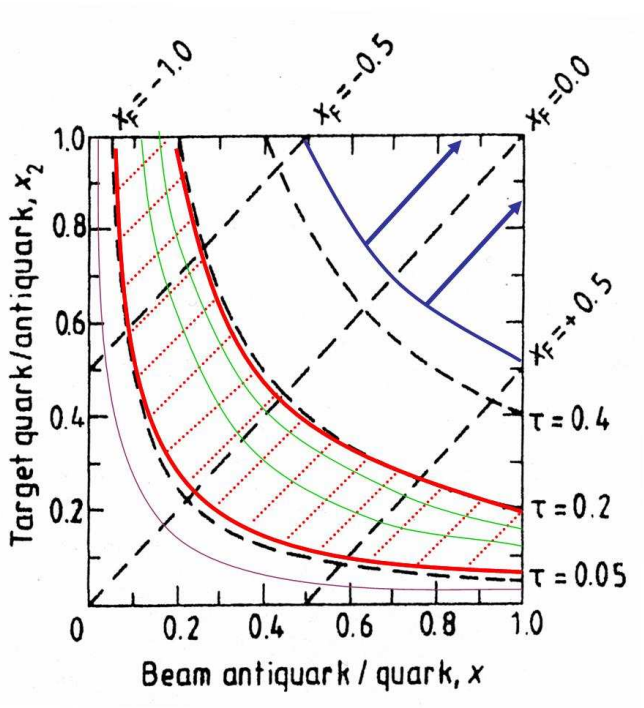

Figure 3: Phase space regions covered by the PANDA experiment: $\tau \geq 0.5$ corresponds to $4 \leq M_{\gamma^*} \leq 9$ GeV/c^2, and $0.05 < \tau \leq 0.2$ to $1.5 \leq M_{\gamma^*} \leq 2.5$ GeV/c^2.

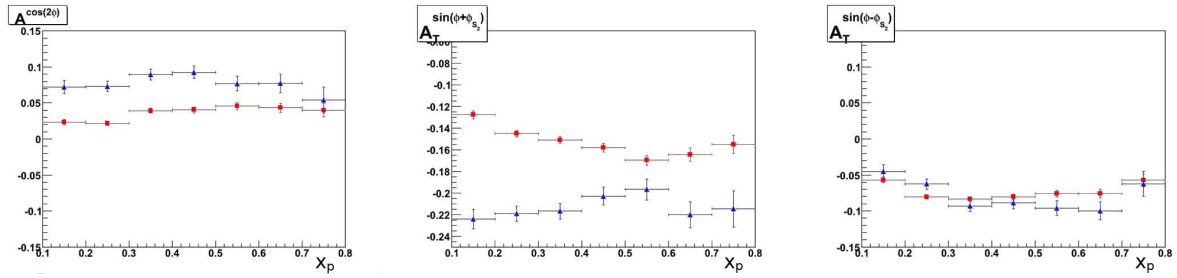

(a) **(b)** **(c)**

Figure 4: Simulated experimental asymmetries related respectively to the $\cos 2\varphi$ term **(a)**, the $\sin(\varphi + \varphi_{S_2})$ term **(b)**, and the $\sin(\varphi - \varphi_{S_2})$ term **(c)**, plotted as a function of x_p, longitudinal momentum fraction of the hadronic probe.

nuclear targets.

500000 DY events were simulated, and the above described asymmetries are shown in Fig. 4a, 4b, and 4c, as functions of the longitudinal momentum fraction of the hadronic probe (x_p) for the unpolarised and single-polarised cases. Different transverse momenta range of the muon pair (q_T) were selected: $1 \leq \ q_T \ \leq 2$ GeV/c (square dots), and $2 \leq \ q_T \ \leq 3$ GeV/c (triangular dots). Efficiencies and acceptance corrections are still under investigation. Those plots are not intended to reflect a detailed expectation of the asymmetry itself, because the parton dynamics is roughly extimated and questionable; the key point is the size of the error bars, that allows to probe the feasibility of such a measurement. In the unpolarised case, it should be possible to investigate the asymmetry dependency on the lepton pair transverse momentum. A complete scan on the full transverse momentum range should allow an investigation on a possible inversion of such dependence probing, thus, the balance between soft and hard processes for the DY production in the PANDA energy range. The single-polarised case is more complex, and the dependence of the considered TMD PDF's could be probably only partially determined. Further studies on the evaluation of the expected experimental errors from asymmetry measurements have been performed, and are reported in details in [11]. A rough estimation of the material budget, of the geometrical acceptance, and of the reconstruction efficiency leads to an overall factor $\varepsilon = 0.33$; assuming the design higher HESR luminosity mode, we expect 130 Kev/month. One year of data taking should hence be enough to reproduce the error bars quoted in the simulations.

Further efforts have been devoted to optimize the background substraction, the corresponding needed kinematic cuts and their effects [12]. In order to countercheck the achieved rejection factors, and to develope a complete kinematic event selection scheme, those investigations will be soon performed with a larger statistic (10^8 simulated events).

This work was supported in part by Università degli Studi di Torino, Regione Piemonte, and INFN Torino.

References

[1] C. Bourrely, and J. Soffer, Eur. Phys. J. **C36**, 371 (2004)

[2] J. C. Collins, and D. E. Soper, Phys. Rev. **D16**, 2219 (1977)

[3] R. D. Tangerman, and P. J. Mulders, Phys. Rev. **D51**, 3357 (1995)

[4] W. Erni, et al., *Physics Performance Report for: PANDA, Strong Interaction Studies with Antiproton*, (2009) arXiv:0903.3905

[5] J. C. Collins, Phys. Lett. **B 536**, 43-48 (2002)

[6] M. Kotulla et al., *PANDA Technical Progress Report, Strong Interaction Studies with Antiproton*, (2005)

[7] V. Barone et al., *Technical Proposal for PAX*, (2005)

[8] W. Erni et al., *Technical Design Report for the PANDA Muon System*, 2^{nd} Draft (May 2011)

[9] E.Iarocci, Nucl. Instr. and Meth. **217**, 30 (1983)

[10] A. Bianconi, Nucl. Inst. Meth. A593, 562-571 (2008)

[11] M. Destefanis et al., *Azimuthal asymmetries for Drell-Yan di-muon production in the PANDA scenario*, Proceedings of the XLVII International Winter Meeting on Nuclear Physics, 26-30 January 2009, Vol.99 Italian Physical Society, Bologna (2010)

[12] M. Destefanis, *Spin Physics at FAIR*, PoS (Bormio 2011) 012, (2011)

MEASUREMENT OF THE TWO-HADRON TRANSVERSE SPIN ASYMMETRIES AT COMPASS

Carmine Elia[1 †]
on behalf of the COMPASS collaboration

(1) *Trieste University and INFN*
† *E-mail: carmine.elia@ts.infn.it*

Abstract

The transversity distribution function can be studied in semi-inclusive deep inelastic scattering (SIDIS) off transversely polarized targets by measuring the azimuthal distributions of single hadrons or hadron-pairs in the final state. The measurement of the spin asymmetries in the azimuthal distribution of the hadron pairs and the measurement of the two-hadrons fragmentation functions, allow to access the transversity distribution function without involving the partonic transverse momenta. The COMPASS collaboration has measured these asymmetries using polarised deuteron (^6LiD) and proton (NH_3) targets and the results are reviewed in this talk. More space is given to the very new measurements from the 2010 proton data, which reduces the statistical error by a factor of 1.7 with respect to the previous measurement from the 2007 proton data.

1 Theoretical motivations

Three independent parton distribution function (PDF) are necessary to describe the nucleon structure at leading-twist in the collinear case [1]: the unpolarized PDF (f_1^q or q), the helicity PDF (g_1^q or Δq) and the transversity PDF (h_1^q or $\Delta_T q$) [2]. The f_1^q PDF gives the probability of finding a quark with a fraction x of the longitudinal momentum of parent nucleon; g_1^q is the difference of the quark density for quark spin antiparallel and parallel to the spin of the longitudinally polarized parent nucleon; h_1^q is the analogous distribution for transversely polarized quark in a transversely polarized nucleon. While the first and second PDFs are well known from DIS experiments, the third one is a new object, still poorly known. The transversity PDF is chiral-odd and it cannot be accessed in inclusive DIS because in this process the chirality is conserved. It can, however, be observed in SIDIS reactions where it can appear coupled with another chiral-odd function. In COMPASS three different channels are measured to access transversity: the one-hadron production in which h_1^q is coupled with the Collins fragmentation function [3], a Λ production in which h_1^q is coupled with the fragmentation function of a quark in a Λ [4] and the two-hadron production in which h_1^q is coupled with the "di-hadron" fragmentation function [5,6]. The di-hadron fragmentation function describes the correlation between the transverse polarization of the fragmenting quark and the azimuthal orientation of the plain containing the momenta of the detected hadron pair. The published and the new results for the Collins asymmetry can be found in [7,8]. Here only the two-hadron production $lN \to l'h_1h_2X$ will be discussed. In this reaction a lepton with 4-momentum

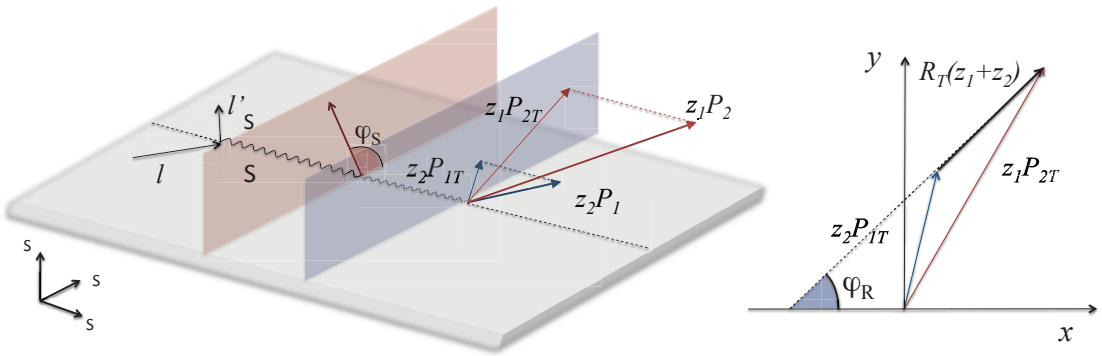

Figure 1: Left: definition of momenta and azimuthal angles in two hadrons production in SIDIS. Right: definition of the φ_R azimuthal angle

l exchanges a virtual photon with 4-momentum q with a quark and at least two final state hadrons with momenta P_1 and P_2 are detected. A graphical representation of the two-hadron production is given in Fig.1 where $\boldsymbol{P_{1T}}$ and $\boldsymbol{P_{2T}}$ are the transverse components of the momenta of the hadrons with respect to the direction $\hat{\boldsymbol{q}}$ of the virtual photon, $z_i = E_i/\nu$ is the fraction of the total energy carried by the hadron i, φ_S is the azimuthal angle of the spin of the nucleon. Introducing the vector $\boldsymbol{R_T} = (z_2\boldsymbol{P_{1T}} - z_1\boldsymbol{P_{2T}})/(z_1+z_2)$, φ_R is the azimuthal angle of $\boldsymbol{R_T}$ given by:

$$\varphi_R = \frac{(\boldsymbol{q}\times\boldsymbol{l})\cdot\boldsymbol{R_T}}{|(\boldsymbol{q}\times\boldsymbol{l})\cdot\boldsymbol{R_T}|}\arccos\left(\frac{(\boldsymbol{q}\times\boldsymbol{l})\cdot(\boldsymbol{q}\times\boldsymbol{R_T})}{|\boldsymbol{q}\times\boldsymbol{l}||\boldsymbol{q}\times\boldsymbol{R_T}|}\right) \tag{1}$$

The two-hadron cross-section at leading twist for a trasversely polarized target is given by [5]:

$$\begin{aligned}\frac{d^6\sigma}{d\xi dM_h^2 d\varphi_{RS} dz dx dy} = \frac{2\alpha^2}{4\pi s x y^2}\sum_q e_q^2\Big\{A(y) f_1^q(x) D_1^{q\to h^+h^-}(z,\xi,M_h^2)+ \\ B(y)|S_\perp|\frac{|R_T|}{M_h} h_1^q(x) H_1^{\sphericalangle q\to h^+h_1^-}(z,\xi,M_h^2)\sin(\varphi_{RS})\Big\}\end{aligned} \tag{2}$$

where $D_1^{q\to h^+h^-}$ is the unpolarized fragmentation function which gives the probability for an unpolarized quark to fragment into the unpolarized hadron pair and $H_1^{\sphericalangle q\to h^+h^-}$ is the di-hadron spin dependent fragmentation function which has been measured at Belle [9]. In Eq. 2 $\varphi_{RS} = \varphi_R + \varphi_S - \pi$ and $z = z_1 + z_2$. The variable ξ is defined as z_1/z and M_h is the invariant mass of the hadron pair. The quantities $A(y)$ and $B(y)$ are kinematical quantities depending on the relative energy lost by the incoming lepton y and their ratio $D_{NN} = B(y)/A(y) = (1-y)/(1-y+y^2/2)$ is the spin transfer coefficient from the initial to the struck quark.

If we introduce the quantity:

$$A_{2h} = \frac{\sum_q e_q^2 \frac{|R_T|}{M_h} h_1^q(x) H_1^{\sphericalangle q\to h^+h^-}(z,\xi,M_h^2)}{\sum_q e_q^2 f_1^q(x) D^{q\to h^+h^-}(z,\xi,M_h^2)} \tag{3}$$

the number of final state hadron pairs as a function of φ_{RS} is given by:

$$N_{2h}^{\pm}(\varphi_{RS}) \propto (1 \pm |S_\perp| D_{NN} A_{2h}\sin\varphi_{RS}) \tag{4}$$

where $\pm$ is the nucleon spin orientation and $S_T = fP_T$ with P_T nucleon polarization and f the fraction of polarized material in the target. From the measurement of the azimuthal distributions it is thus possible to extract the A_{2h} spin asymmetry and access the transversity distribution.

2 Data selection

Standard kinematical cuts have been applied to select DIS events: we ask for a squared four momentum transfer $Q^2 > 1$, the hadronic invariant mass $W > 5$ (GeV/c)^2 and $0.1 < y < 0.9$.

The selection of the hadrons to be used in the analysis has been done requiring $z_i > 0.1$ and $x_F > 0.1$. A cut on R_T has been applied to improve the resolution in the φ_R. Finally a cut on the missing energy $E_{miss} > 3$ GeV has been applied to exclude the exclusively produced ρ^0 in the 2010 data analyisys. The invariant mass spectrum after all cuts for all the combinations of oppositely charged hadrons originating from the primary vertex is shown in Fig. 2. It has been obtained from the 2010 data, assuming the charged particles to be pions.

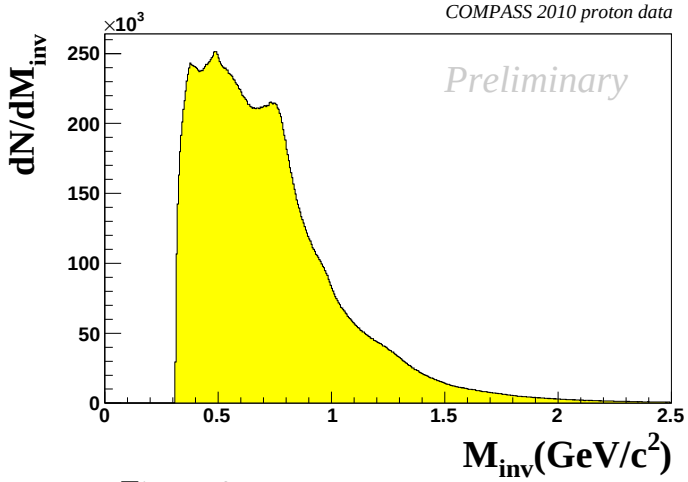

Figure 2: Invariant mass spectrum

3 Results

In 2002, 2003 and 2004 COMPASS has collected data with a transversely polarized deuteron target. Preliminary results have been shown at several conferences [10–14]. The asymmetries have been measured for all opposite charge hadron pairs, for identified charged hadrons, ordering the hadron by increasing z_i and P_{Ti}. As an example the results for all opposite charge hadron pairs as function of x, z and M_h are shown in Fig. 3. All the measured asymmetries turned out to be compatible with zero within few percent statistical errors. The small asymmetries on the deuteron can be explained as cancellation between the u and d quark contributions.

In 2007 COMPASS has collected the first data with the transversely polarized proton target. The preliminary results for the two hadron asymmetries extracted from these data are shown in Fig.4 [15]. As in the case of the Collins asymmetry a large range (from 0.004 to 0.7) in x is covered and the invariant mass region investigated in our measurement goes from 0.3 up to 1.7 (Gev/c^2)^2 A large asymmetry up to 5-10% in the valence x-region has been measured, as large as the Collins asymmetry [16]. The z dependence is smooth and the dependence on the invariant mass is not clear.

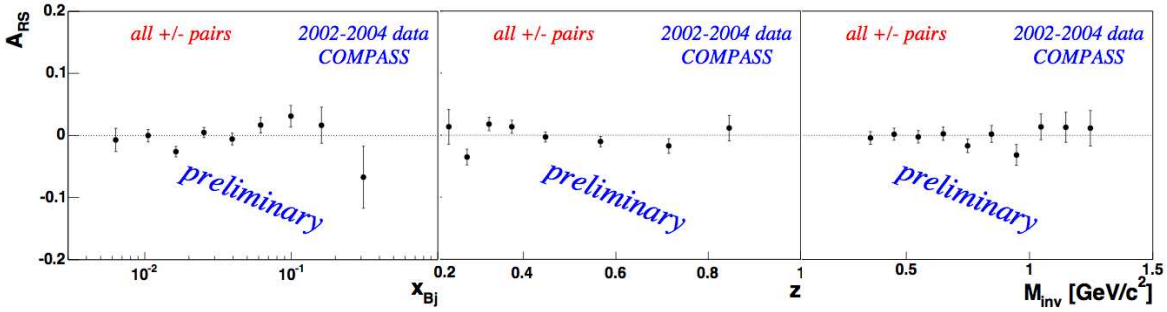

Figure 3: Two-hadron asymmetries from the 2002, 2003 and 2004 deuteron data for charged particles as a function of x,z and M_h. The error bars are the statistical errors and the band show the systematic errors

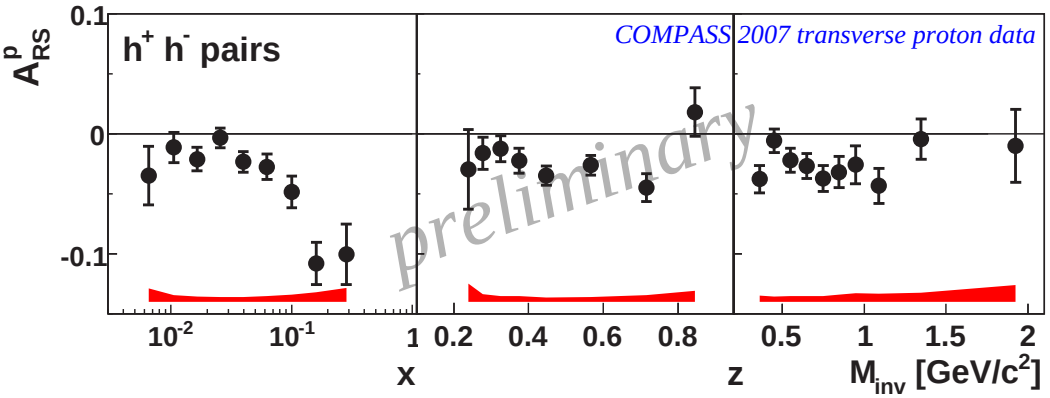

Figure 4: Two-hadron asymmetries from the 2007 proton data for charged particles as a function of x,z and M_h. The error bars are the statistical errors and the band show the systematic errors

The results are in good agreement with the HERMES results [17] in the overlapping x region (the kinematical range of the our measurement is considerably larger), once the HERMES data are rescaled by the D_{NN} factor.

New proton data have been collected in COMPASS in 2010 and preliminary results have been very recently produced [7, 18]. The two-hadrons asymmetries as a functions of x,z and M_h are shown in Fig. 5.

The results confirm the results obtained from the 2007 proton data with almost a factor two smaller statistical errors. With respect to the previous results there is a clearer and interesting dependence on the invariant mass which is even more clear when the $x > 0.032$ region is selected, as shown in Fig 6.

This dependence on the invariant mass is somehow at variance with the present predictions [19, 20], as can be seen in Fig. 7, where our new data are compared with the calculations of [19] rescaled by a factor of three [21]. While the x and z dependences agree with the data, the description of the asymmetries as function of the invariant mass is not satisfactory and there is room for improvements.

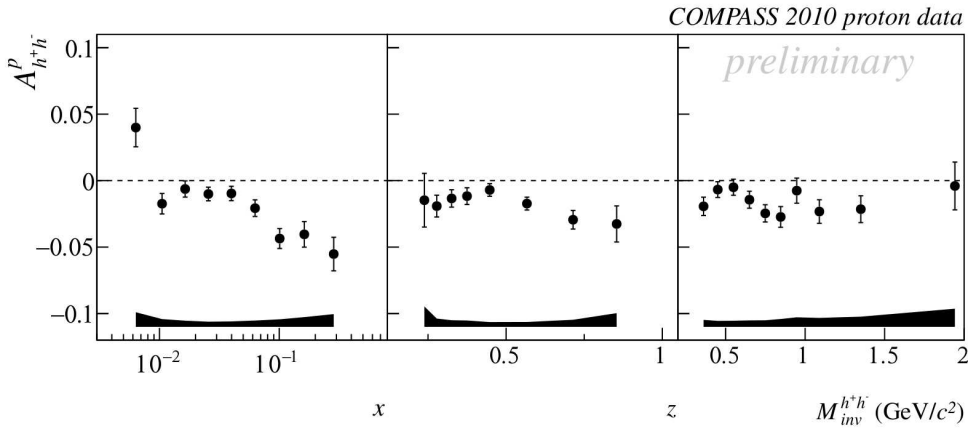

Figure 5: Two-hadron asymmetries from 2010 proton data for charged particles as a function of x,z and M_h. The error bars are the statistical errors and the band show the systematic errors

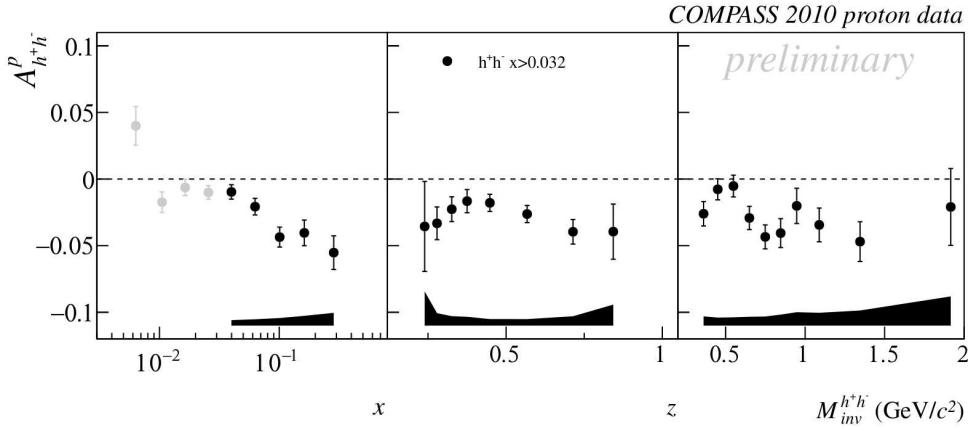

Figure 6: Two-hadron asymmetries from the 2010 proton data for charged particles and for $x > 0.032$ as a function of x,z and M_h. The error bars are the statistical errors and the band show the systematic errors

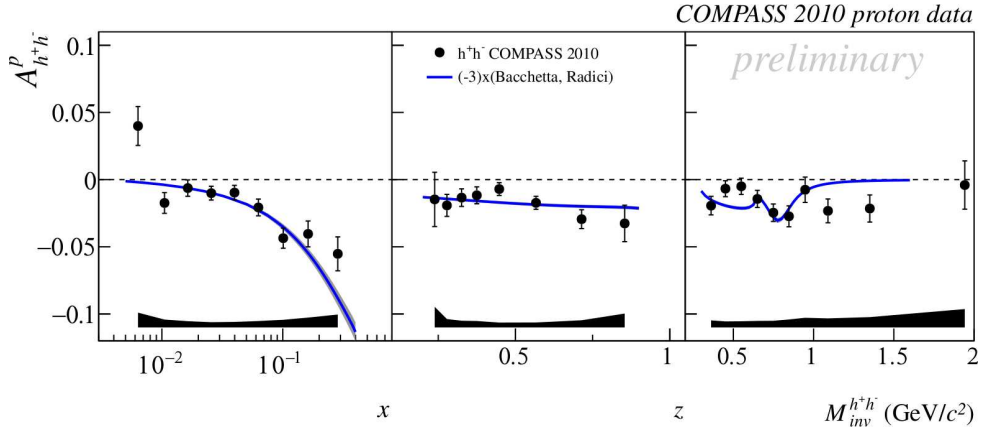

Figure 7: Two-hadron asymmetries from 2010 proton data for charged particles as a function of x,z and M_h compared with the theoretical predictions of [19]. The error bars are the statistical errors and the band show the systematic errors

4 Conclusions

The new measurement of the two-hadron asymmetry in SIDIS from the 2010 COMPASS proton data improves considerably the existing data set. The large signal measured in the valence region confirms that transversity can be accessed in this channel too.

These new data, together with the previous COMPASS and HERMES results and the recent measurement of the di-hadron fragmentation function performed at Belle [9] constitute a quite complete data set which which will allow for a significant increase of the knowledge of both the spin structure of the nucleon and the fragmentation mechanism.

References

[1] R.L. Jaffe and X. D. Ji, Phys. Rev. Lett **67** (1991) 552.

[2] J. P. Ralston and D. E. Soper, Nucl. Phys. **B152** (1979) 109.

[3] J. Collins, Nucl. Phys. **B396** (1993) 161.

[4] M. Anselmino, M. Boglione, U. DтАЩЦAlesio, E. Leader, and F. Murgia, Phys. Lett. **B509** (2001) 246.

[5] M. Radici, R. Jakob, A. Bianconi, Phys. Rev, **D65** (2002) 074031.

[6] X. Artru, hep-ph/0207309 (2002).

[7] F. Bradamante, Transversity 2011 Proceedings, arXiv:1111.0869 [hep-ex].

[8] C. Adolph, These proceedings.

[9] A. Vossen et al. (Belle Collaboration), Phys. Rev. Lett. **107** (2011) 072004.

[10] F. Bradamante, DUBNA-SPIN-05 Proceedings, arXiv:hep-ex/0602013.

[11] R. Joosten, DIS2005, AIP Conf. Proc. **7**92 (2005) 957 .

[12] A. Vossen, MORIOND QCD 2007 proceedings, arXiv:0705.2865 [hep-ex].

[13] F. Massmann, SPIN Praha-2007 Proceedings, Eur. Phys. J. ST **1**62 (2008) 85.

[14] R. Joosten, SPIN06 Proceedings, AIP Conf. Proc. **915** 646 (2007)

[15] H. Wollny, DIS2009, Conf. Proc. (2009)

[16] M.G. Alekseev et al., Phys. Lett. **B692** (2010) 240тАУ246

[17] A. Airapetian *et al.* (HERMES collaboration) , JHEP **0**806 (2008) 066

[18] C. Braun Transversity 2011 Proceeding in preparation.

[19] A.Bacchetta and M.Radici, Phys. Rev., **D74** (2006) 114007.

[20] B.-Q. Ma , V. Barone,J. S. Huang and Y. Huang, Phys. Rev. **D77** (2008) 014035.

[21] A.Bacchetta and M.Radici, private comunication.

TRANSVERSE SPIN PHYSICS IN PHENIX

K.O. Eyser[1†], for the PHENIX collaboration

(1) *University of California, Riverside, USA*
† *E-mail: keyser@bnl.gov*

Abstract

The PHENIX experiment has measured transverse single spin asymmetries at center-of-mass energies $\sqrt{s}$=62.4 GeV and 200 GeV. Observed asymmetries in forward direction are of significant size and consistent with previous measurements of different species and at lower energies. Mid-rapidity and backward asymmetries are consistent with zero. The statistical accuracy of the mid-rapidity result supersedes our previously published measurement by more than a factor of 20 which will lead to a significant improvement on the constraint of the gluon Sivers function.

1 Introduction & formalism

The nucleon structure can be described in the probabilistic terms of parton distribution functions. Here, the unpolarized $q_i(x, Q^2)$ and the longitudinally polarized helicity distributions $\Delta q_i(x, Q^2)$ for quark flavors i are complemented by transversely polarized distribution functions $\delta q_i(x, Q^2)$ (also called transversities). They are described as functions of the partonic momentum fraction x and a momentum transfer scale Q^2. Generally, transversity and helicity distributions are not the same since in the relativistic regime rotations do not commute with Lorentz boosts. In the formalism of the scattering matrix, the measurement of transverse asymmetries can relate to the transverse structure of the initial state of the investigated scattering process. A transverse single spin asymmetry (SSA) is defined as the ratio of the difference and the sum of cross sections dσ when the projectile's spin direction is flipped:

$$A_N = \frac{d\sigma^{\uparrow} - d\sigma^{\downarrow}}{d\sigma^{\uparrow} + d\sigma^{\downarrow}}. \tag{1}$$

Here, the spin quantization is in the direction normal to the scattering plane. For a spin-1/2 particle we distinguish spin up ($\uparrow$) and spin down ($\downarrow$).

Transversity is special in the way that it is chirally odd, i.e., a spin flip is required in the scattering process in order to make it measurable. This renders it completely unobservable in inclusive deep inelastic electron-proton scattering (DIS), and in the hard scattering part of high energy proton-proton collisions the helicity flip can only be achieved by the exchange of additional gluons in higher-twist effects. Therefore, transverse SSA have been expected to be very small at high energies where the hard scattering part can adequately be described by perturbative quantum-chromodynamics (pQCD). Surprisingly, asymmetries of up to $\approx 40\%$ have been measured in meson production of hadronic collisions at medium energies in the past [2, 3, 1]. These asymmetries are largest in the forward direction of the projectile and persist to the high center-of-mass energies of $\sqrt{s}$=62.4 GeV

and 200 GeV in p+p collisions at RHIC [4,5]. Furthermore, transverse asymmetries have been measured in semi-inclusive DIS experiments over a broad kinematic range [6–11].

This apparent contradiction has been relaxed by large theoretical progress in recent years that led to the inclusion of equally important initial and final state interactions in the process description. In the initial state the chiral-odd part needed for a transverse asymmetry can be provided by the quark's transverse momentum if it is correlated to the nucleon polarization (Sivers effect [12]). The quark does not have to be polarized in this case. Also, the Sivers function is non-universal and depends on the form of the gauge links in different processes when we compare hadronic collisions to electron-proton scattering. In this context, transverse single spin asymmetries are a powerful tool to test the validity of the fundamental concepts of pQCD when we compare the initial-state interaction of lepton-pair production via a virtual photon (Drell-Yan) to the final-state effects in semi-inclusive DIS [13]. For the Drell-Yan process it has been shown that this framework of transverse momentum dependent (TMD) parton distribution functions and the mechanism of spin-dependent higher-twist quark-gluon correlations [14, 15] describe the same type of physics in an intermediate transverse momentum range $\Lambda_{QCD} \ll q_\perp \ll Q$ where both methods can be applied [16]. From this comparison we expect the initially rising SSA to reach a maximum followed by a slow decline with increasing transverse momenta, qualitatively described by $1/q_\perp$. Observation of this behavior is still outstanding as it is experimentally challenging to reach the required kinematic range $q_\perp, Q \gg \Lambda_{QCD}$ in the forward direction of large asymmetries.

On the other hand, in the final state a spin dependent fragmentation of the out-going parton can similarly create a chiral-odd part within the scattering process (Collins effect [17]). The asymmetric fragmentation, however, will only reveal itself in an experiment if it is also correlated to the nucleon polarization through a non-vanishing transversity distribution. Due to helicity conservation, the gluons with spin-1 exhibit no transversity in leading order. Following the same argument the sea quark transverse polarization has to be small and the quark transversity distribution should be dominated by valence quark contributions at large partonic momenta. This behavior is exhibited by the longitudinal momentum fraction of the produced meson in the final state, $x_F = 2 \cdot p_l/\sqrt{s}$, where $\vec{p_l}$ points in the direction of the polarized projectile and x_F is approximately the difference between the momentum fractions of the projectile and target partons $x_1 - x_2$. Using this convention for x_F, the positive x_F is taken when the polarized beam is in the detector direction, with the other beam averaged to be unpolarized. For the negative x_F data, the opposite is done; the beam heading toward the detector is averaged to be unpolarized while the beam moving away from the detector is polarized.

In order to disentangle contributions from all possible sources of transverse asymmetries, measurements are needed over a wide kinematic range and with different probes. Additionally, transversity and spin-dependent fragmentation will have to be separated by either fragmentation free or transversity free experiments such as double spin asymmetries in Drell-Yan (A_{NN}) or interference fragmentation functions in two-hadron production from electron-positron annihilation.

2 Experimental setup

The PHENIX detector has been described in detail elsewhere [18–20]. In addition to the central arm calorimeters and tracking devices ($|\eta| < 0.35$), the results presented here rely on two sets of electromagnetic calorimeters in forward rapidities ($3.1 < |\eta| < 3.8$). Each of these calorimeters consists of 196 (220) $PbWO_4$ crystals with a cross section of 2.25×2.25 cm^2 and about 20 radiation lengths X_0 sitting 220 cm from the nominal vertex position in beam direction with full azimuthal coverage.

Situated in one of the collision points of the Relativistic Heavy Ion Collider, the PHENIX experiment makes use of the proton beams with polarizations up to $P \approx 55\%$ in up to 120 separate bunches in each ring. The stable polarization direction is transverse to the accelerator plane. Bunches are following a set of fill patterns with polarizations either up or down in order to reduce false asymmetries and other systematic effects resulting from correlations in detector and accelerator performances. As mentioned above, the forward and backward directions for single spin asymmetries can be obtained by summing over the different polarization directions in one beam, thereby effectively making this beam unpolarized. The forward direction is then defined by the direction of the polarized beam. Since we have two calorimeters at large rapidities and two polarized beams, we can use each two out of these four independent combinations for consistency checks.

3 Results

Transversely polarized data was taken in the year 2008 at $\sqrt{s}$=200 GeV with a recorded integrated luminosity of 5.2 pb^{-1} and beam polarizations of $P = 55\%$. Figure 1 shows the transverse single spin asymmetries for neutral pions and η-mesons as measured with the PHENIX central arm calorimeter.

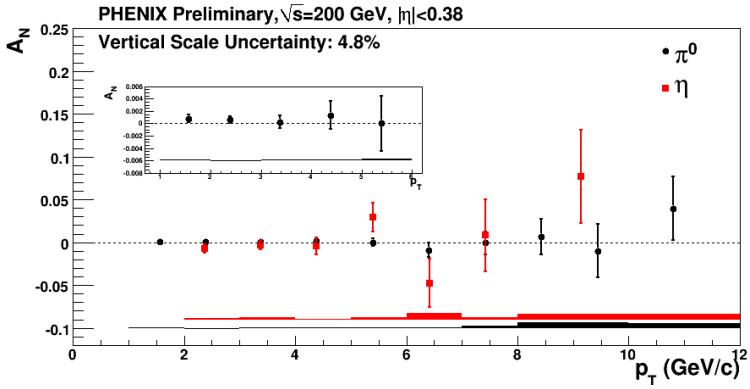

Figure 1: Transverse single spin asymmetries for π^0 and η-mesons at mid-rapidity.

Compared to previously published results, the reach in the pion transverse momentum has been extended from less than $p_T \approx 5$ GeV/c to over 10 GeV/c. At the same time, the statistical uncertainties are reduced by a factor of over 20 at low p_T; results for η-mesons have previously not been available. All mid-rapidity asymmetries are consistent with zero so far, leading to an upper limit for the gluon Sivers function within certain assumptions of the quark-induced part of the transverse asymmetries [21, 22].

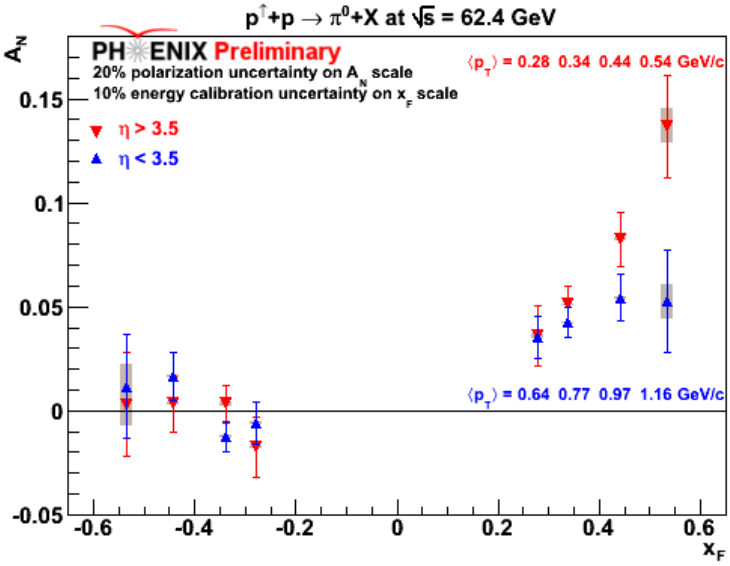

Figure 2: Transverse single spin asymmetries for neutral pions at $\sqrt{s}$=62.4 GeV at forward rapidities.

The forward calorimeters were installed in a staged approach beginning in 2006. One half was commissioned during a low energy run at $\sqrt{s}$= 62.4 GeV with an integrated luminosity of 40 nb^{-1}. Results are presented in Fig. 2 for neutral pions as function of x_F. The asymmetry scales directly with x_F, which is consistent with earlier observations from other experiments at lower center-of-mass energies [2,3,1,4,5]. The backward asymmetries so far all agree well with zero.

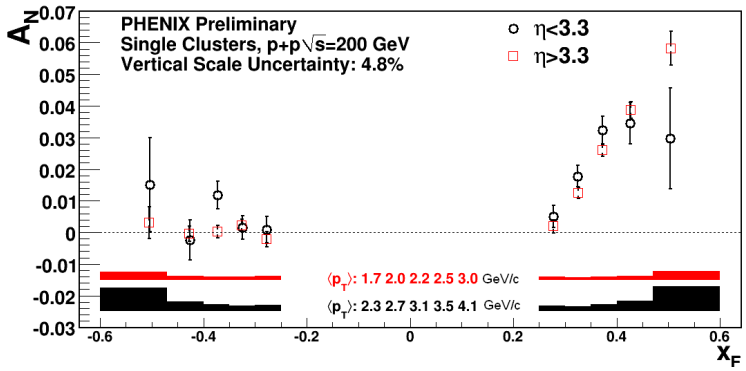

Figure 3: Transverse single spin asymmetries for inclusive electro-magnetic clusters at forward rapidities.

Whereas the applicability of perturbative QCD might still be doubtful at $\sqrt{s}$= 62.4 GeV, it certainly is well shown to work at high energies of $\sqrt{s}$= 200 GeV. The spatial constraints of the PHENIX forward calorimeters prevent the reconstruction of $\pi^0 \to \gamma\gamma$ at $E_\pi \gtrapprox 20$ GeV. Instead, in Fig. 3 we present results for inclusive electro-magnetic clusters. We can safely assume that these clusters are dominated by merged showers from the di-photon decay of neutral pions, as has been shown in Monte-Carlo studies based on PYTHIA generated events. Depending on the transverse momentum, about one in five clusters contains contributions from other mesonic decays or direct photons.

The transverse asymmetries show the same typical rise in forward direction. They

appear to be slightly smaller compared to STAR measurements of π^0 at the same collision energy, which may be due to differences in the kinematic coverage of the detectors.

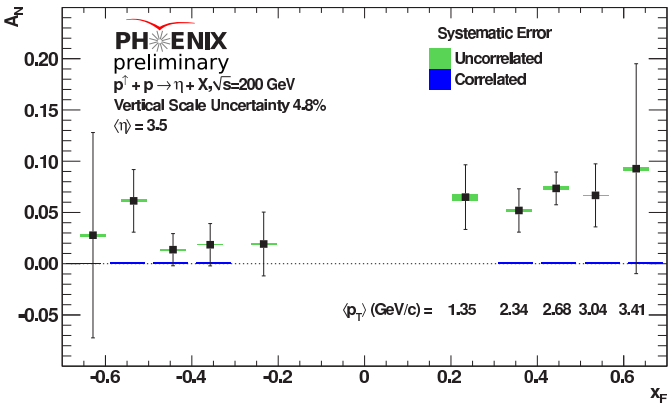

Figure 4: Transverse single spin asymmetry of η-mesons as function of rapidity.

PHENIX has also measured transverse asymmetries of η-mesons at large rapidities with sizable non-zero values for $x_F > 0$, see Fig. 4. They are comparable to the asymmetries of the π^0 in the same kinematic range, where we can expect variations from the iso-spin dependence, the fragmentation process, and the different masses. Backward asymmetries are close to being zero, although averaged over the whole $x_F < 0$ range they currently appear to be about $2 \cdot \sigma$ positive at this time.

4 Outlook

In addition to disentangle initial and final state effects, PHENIX has laid out a plan to measure asymmetries of different particles and particle correlations with greater precision in the near future. Correlations between particles at mid- and forward rapidities will access certain partonic momentum ranges. The measurements require large luminosities and improved trigger capabilities. Also, as laid out in a new decadal plan [23], transverse asymmetries in Drell-Yan production will help address questions of regarding the fundamental nature of QCD as well as universality breaking in the initial state in comparison with semi-inclusive DIS experiments.

References

[1] D.L. Adams et al., Phys.Lett. B264:462Ц466, 1991.
[2] R.D. Klem et al., Phys.Rev.Lett. 36, 929-931, 1976.
[3] R.D. Klem et al., Phys.Rev. D65, 092008, 2002.
[4] B.I. Abelev et al., Phys.Rev.Lett. 101:222001, 2008.
[5] I. Arsene et al., Phys.Rev.Lett. 101:042001, 2008.
[6] M.G. Alekseev et al., Phys. Lett. B692 240-246, 2010.
[7] M. Alekseev et al., Phys. Lett. B673, 127-135, 2009.

[8] E.S. Ageev et al., Nucl. Phys. B765, 31-70, 2007.
[9] V.Yu. Alexakhin et al., Phys. Rev. Lett. 94, 202002, 2005.
[10] A. Airapetian et al., Phys.Rev.Lett. 103, 152002, 2009.
[11] A. Airapetian et al., Phys.Lett. B693, 11-16, 2010.
[12] D.W. Sivers, Phys.Rev., D41:83, 1990.
[13] Z.-B. Kang, J.-W. Qiu, W. Vogelsang, and F. Yuan, Phys.Rev. D83:094001, 2011.
[14] A.V. Efremov and O.V. Teryaev, Phys.Lett. B150:383, 1985.
[15] J.-W. Qiu and G.F. Sterman, Phys.Rev.Lett. 589 67:2264Ц2267, 1991.
[16] X. Ji, J.-W. Qiu, W. Vogelsang, and F. Yuan. Phys.Rev.Lett. 591 97:082002, 2006.
[17] J.C. Collins, Nucl.Phys. B396:161Ц182, 1993.
[18] L. Aphecetche et al., Nucl.Instrum.Meth. A499:521Ц536, 2003.
[19] K. Adcox et al., Nucl.Instrum.Meth. A499:489Ц507, 2003.
[20] M. Allen et al., Nucl.Instrum.Meth. A499:549Ц559, 2003.
[21] S.S. Adler et al., Phys.Rev. Lett. 95:202001, 2005.
[22] M. Anselmino, U. DTAlesio, S. Melis, and F. Murgia, Phys.Rev. D74:094011, 2006
[23] Report available online at
www.phenix.bnl.gov/phenix/WWW/docs/decadal/2010/phenix_decadal10_full_refs.pdf

INFLUENCE OF PROTON DEFORMATION ON DOUBLE-PARTON SCATTERING AND SPIN PHYSICS

P. Filip

Institute of Physics, SAS, Dúbravská cesta 9, Bratislava, Slovakia
E-mail: Peter.Filip@savba.sk

Abstract

Based on the analogy with the ground-state deformation of nuclei we speculate on the existence, origin and consequences of the proton deformation in high-energy scattering experiments with unpolarized and polarized protons.

1 Introduction

Usually, the internal structure of particles is introduced when experimental indications suggest it to be present. For the proton, deviations from the point-like structure have been revealed by the pioneering measurements of Hofstadter [1]. In deep inelastic experiments the partonic structure of proton has been revealed, and naturally, spherical finite-size models of the proton (e.g. MIT bag model [2]) have been introduced. Since then, size of the proton has been carefully studied and even nowadays, precise spectroscopic measurements of muonic hydrogen [3] suggest (together with the spin crisis) that the internal structure of proton is still not well understood. In this contribution we insist that proton can be intrinsically deformed and the consequences of this internal property may be searched for in the present day experiments.

2 Deformation of proton

Proton is a spin 1/2 particle, with the internal partonic structure. From the formalism of QED we know that only for particles with spin $s \geq 1$ the quadrupole electromagnetic form-factor can be introduced. Also in NMR experiments, zero spectroscopic quadrupole moments are always observed for $s = 1/2$ nuclei (also protons). However, the nuclear physics strongly suggests that many nuclei with spin $s = 0$ and $s = 1/2$ are intrinsically deformed. Although having spin $s = 1/2$, the proton can also be deformed.

Theoretically, the appearance of quadrupole deformation in systems with Hamiltonians exhibiting the rotational symmetry is a non-trivial phenomenon. The effect involves the spontaneous symmetry breaking [4] and seems to be mathematically well understood. The intrinsic coordinate system, is introduced when "slow" and "fast" degrees of freedom are separated and adiabatic approximation is used. Self-deformation of the ground-state wave function in the intrinsic coordinate system is generated as a consequence of the quantum-mechanical interplay between the "slow" - vibrational degrees of system and a degeneracy of the energy levels of the fast constituents of the system. The energy decreases while the system gets deformed.

In mollecular physics fast degrees of freedom are the electrons and "slow" degrees of freedom are given by vibrations of nuclei in a given molecule. Similar situation is encountered also in the case of nuclei, where slow degrees of freedom are the vibrations of nuclear volume as a whole and fast degrees of freedom are the individual nucleons in the nucleus, with degenerated energy levels. Typical nuclei with spin $s = 0$ or $s = 1/2$ which are known to be deformed in their ground state are e.g. ^{154}Sm and ^{169}Tm.

The proton, a finite-size composite system containing virtual partons and three constituent quarks, can also be considered as a system with the fast and slow degrees of freedom. The fast degrees of freedom are the partons, bound together by strong gluonic forces. What kind of "slow" degrees of freedom can proton have ?

Within the framework of MIT bag model [2] one can consider surface vibrations of the spherical bag of partons (subjected to the external pressure of confining vacuum) as a prototype of slow vibrational degrees of freedom in the proton. One might suggest e.g. Roper resonance of the nucleon N(1440) to be a vibrational state. Considering the proton to be a bound state of di-quark and quark constituent clusters also allows one to introduce slow vibrational degrees of freedom.

For the applicability of Jahn-Teller theorem, degeneracy of the energy levels is a necessary condition, but we do not intend to proceed so far here. Our intention is merely to claim that proton can have an intrinsic quadrupole deformation, which is not observable via standard QED scattering and NMR measurements. (Let us remind here the formula for the spectroscopic quadrupole moment $Q_s = Q_o[3m_z^2 - s(s+1)]/[(s+1)(2s+3)]$, which hides the intrinsic deformation of nuclei with spin s=3 in quantum state m_z=$\pm$2, valid also in the case $s = 1/2$ and $m_z = \pm 1/2$; here Q_o is the intrinsic quadrupole moment).

3 Experimental signs of proton deformation

We have discussed whether proton can be deformed while having zero spectroscopic quadrupole moment and how this deformation can be generated. Let us mention now some indications that the proton is really deformed:
a) based on the similarity of Regge trajectories of mesons and baryons a deformation of proton has been anticipated many years ago by Migdal [5],
b) the existence of color hyperfine interaction among quarks suggests [6] a significant D-wave component in the wave function of proton,
c) very small gluonic contribution to the spin of the proton $\Delta g \approx 0$ seems to require a non-zero orbital momentum of quarks in the proton,
d) measured transition form factors of proton [7] also give the evidence for the intrinsic ground-state deformation of the proton,
e) significant difference between the proton radius measured from hyperfine muonic and electron hydrogen spectra has been found recently [3]. Surprising result obtained in PSI muonic measurements [3] might be related to the proton deformation, since the intrinsic quadrupole deformation increases the effective size of the charge distribution [8]:

$$\langle r^2 \rangle = \langle r^2 \rangle_{Sph} + \langle r^2 \rangle_{\beta_2} \tag{1}$$

A decrease of the deformation of prolate nuclei has been predicted and observed for the muonic atoms many years ago [9] and the charge radius of proton from the muonic PSI measurements [3] is smaller than the established CODATA value $r_p = 0.8768(69)$ fm.

Following the above arguments one can assume that proton is intrinsically deformed and search for the possible effects of deformation in high-energy proton-proton experiments and also in deep-inelastic $e-p$ scattering with unpolarized and polarized protons.

4 Double-parton scattering and DIS experiments

In heavy ion collision experiments with deformed nuclei, the effect of deformation generates the increased energy density in some configurations and modifies the initial excentricity (and its fluctuations) [10]. The effect is most pronounced in central collisions, where the effective self-orientation of (unpolarized) nuclei is anticipated. For prolate nuclei, longitudinal self-orientation is expected in collisions with the highest multiplicity due to the increased number of binary nucleon-nucleon interactions in this case. Selecting very high multiplicity events enhances the probability of collisions of longitudinally oriented nuclei in the sample.

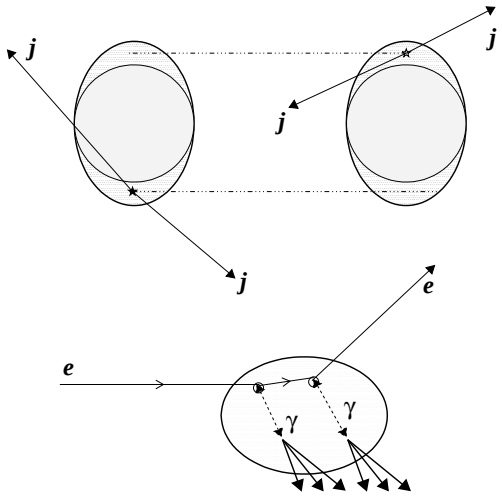

Figure 1: Double-parton $p-p$ interaction in non-spherical parts of colliding protons and double-parton deep inelastic $e-p$ event.

Based on the analogy with the number of binary nucleon-nucleon interactions in collisions of deformed nuclei [10] one can study a probability of double-parton interactions in ultra-relativistic $p-p$ and $p-\bar{p}$ experiments. In Fig.1 (upper panel) we show double-parton interaction in the non-spherical part of colliding deformed protons. Using the partonic version of the optical Glauber model simulation, it has been found [11] that a probability of multi-parton interaction depends on the mutual orientation of colliding deformed protons (see Fig.2). This might have an influence on the estimate of background processes while searching for the signature of new physics [12] in ultra-relativistic interactions of protons. In deep inelastic $e-p$ interactions (DIS), the lepton participating in the reaction can interact with more partons from the same proton. The possibility of two-photon exchange has been considered long time ago, however, the fact that a probability of such process can depend on the spatial orientation of deformed proton relative to the beam has not been considered.

In the case of spin physics, the enhanced probability of DIS interaction of protons oriented e.g. longitudinally relative to the lepton beam (see Fig.1) would introduce an effective increase/decrease of polarization which is not accounted for nowadays.

The result of the partonic version of the optical Glauber simulation of deformed proton-proton collisions is shown in Fig.2. A more detailed description of the simulation can be found in [11].

5 Summary and conclusions

The mechanism and indications of the anticipated proton deformation have been discussed. We suggest that the intrinsic proton deformation may influence the probability of double-parton interactions in p-p and e-p collisions. A double-parton interaction probability can depend on the geometrical orientation of the colliding (deformed) protons relative to the beam axis. This may increase/decrease the effective proton polarization in the sample of events obtained.

We have speculated that proton charge radius obtained in the PSI measurements [3] with muonic hydrogen may deviate from the previously established values as a consequence of the intrinsic proton deformation, as has been observed in the case of muonic nuclei [9].

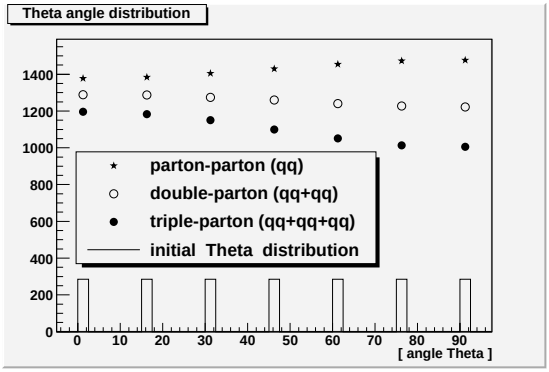

Figure 2: Distribution of polar angles of colliding deformed protons in parton-parton, double-parton and triple-parton $p-p$ events.

We also suggest, that models of the proton exhibiting spherical symmetry (e.g. [13] or [14]) could be modified in such a way, that in the intrinsic coordinate system a distribution of partons exhibits spatial quadrupole deformation. If the internal energy decreases when deviation from the spherical symmetry of the intrinsic proton charge distribution happens, the wave function of the precessing proton should contain an intrinsic spatial deformation, even though the spectroscopic quadrupole moment Q_s is nullified due to the precession at angle $\theta = 54.7$ degrees ($\cos^2\theta = 1/3$) relative to the magnetic field axis.

Acknowledgement: Work supported by the VEGA project 1/0171/11 in Slovakia.

References

[1] E.E. Chambers and R. Hofstadter, Phys. Rev. **103** (1956) 1454.
[2] C.E. DeTar and J.F. Donoghue, Ann. Rev. Nucl. Part. Sci. **33** (1983) 235.
[3] R. Pohl et al., Nature **466** (2010) 213.
[4] W. Nazarewicz, Int. Jour. of Mod. Phys. **E2** (1993) 51.
[5] A.B. Migdal, JETP Letters **46** (1987) 322.
[6] N. Isgur, G. Karl, R. Koniuk, Phys. Rev. **D25** (1982) 2394.
[7] C.E. Carlson and M. Venderhaegen, Phys. Rev. Lett. 100 (2008) 032004.
[8] A.J. Buchmann, Can. Jour. of Phys. **83** (2005) 455.
[9] J. Hüfner, Nucl. Phys. **60** (1964) 427; S. Bernow et al., Phys. Rev. Lett. **18** (1967) 787.
[10] P. Filip, H. Masui, R. Lednicky, N. Xu, Phys. Rev. **C80** (2009) 054903.
[11] P. Filip, Nucl. Phys. B (Proc. Suppl.) 219-220C (2011) 288.
[12] T. Aaltonen et al. (CDF Collaboration), Phys. Rev. Lett. **106** (2011) 171801.
[13] P. Závada, Eur. Phys. Jour. **C52** (2007) 121.
[14] S. Scopetta, Phys. Rev. **D72** (2005) 117502.

COMPASS RESULTS ON THE GLUON POLARISATION FROM THE OPEN-CHARM ANALYSIS

Celso Franco [1 †] on behalf of the COMPASS collaboration

(1) *LIP-Lisboa*
† *Celso@lip.pt*

Abstract

One of the main goals of the COMPASS experiment at CERN is the determination of the gluon contribution to the nucleon spin. To achieve this goal COMPASS uses a naturally polarised muon beam with an energy of 160 GeV and a fixed polarised target. Two types of materials were used for the latter: ^{6}LiD (polarised deuterons) during the years of 2002-2006 and NH_3 (polarised protons) in 2007. The gluons in the nucleon can be accessed directly via the **P**hoton **G**luon **F**usion (PGF) process. Among the channels studied by COMPASS, the production of charmed mesons is the one that tags a PGF interaction in the most clean and efficient way. This talk presents a result for the gluon polarisation, $\Delta g/g$, which is based on a measurement of the spin asymmetry for the production of D^0 mesons. These mesons are reconstructed through the invariant mass of their decay products. The purity of the D^0 spectra has been improved significantly using a new method based on Neural Networks. The $\Delta g/g$ result is also presented using a next-to-leading order (NLO-QCD) analysis of the PGF process. Such correction is relevant and was for the first time applied to an experimental measurement of the gluon polarisation.

1 Introduction

Over the last decade, the quark contribution to the nucleon spin was determined with a very good precision [1]:

$$\Delta\Sigma = 0.30 \pm 0.02 \pm 0.01 \quad (\text{at } \mathrm{Q}^2 = 3\ (\mathrm{GeV/c})^2). \tag{1}$$

This result is significantly smaller than the value of 60% expected from the Ellis-Jaffe sum rule [2]. Relativistic quark motion is responsible for the reduction from the value of 100%, expected in the naive quark-parton model. Taking into account the orbital momenta, L, of quarks and gluons, and the first moment of the gluon helicity contribution, $\Delta G = \int_0^1 \Delta g(x)dx$, the nucleon spin projection can be decomposed into the following sum:

$$S_z = \frac{1}{2} = \frac{1}{2}\Delta\Sigma + \Delta G + L_z. \tag{2}$$

Therefore, since all the spin contributions must sum to 1/2, the big question we need to answer is: where is the remaining part of the nucleon spin? Knowing that the gluons were the solution to the missing momentum in the nucleon, the obvious approach to solve this **spin puzzle** would be the determination of the gluon helicity ΔG.

2 Event selection

In order to be sensitive to the gluon polarisation one must tag a process involving a polarised lepton-gluon interaction. In COMPASS, one of the possibilities to do it is to reconstruct charmed mesons (see Fig. 1). This method provides a clean signature of PGF events, because in LO (leading order) QCD approximation the intrinsic charm mechanism was found to be non-important in the COMPASS kinematic domain (see, e.g. Ref. [3]). In this analysis the PGF process is tagged using D^0 meson production. This production is practically limited to a range of small x_{Bj} ($x_{Bj} < 0.1$), because at COMPASS kinematics the cross section for the PGF process decreases rapidly with x_{Bj}.

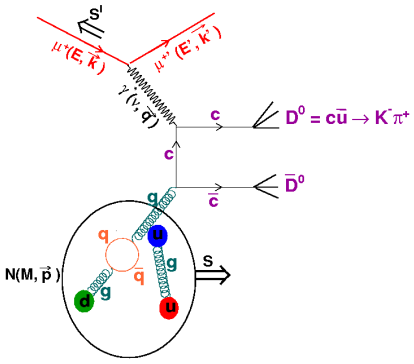

Figure 1: Open-Charm production via a polarised **P**hoton-**G**luon **F**usion process (PGF in LO).

The COMPASS spectrometer [4] was designed to reconstruct the D^0 mesons through the invariant mass of their decay products, $K\pi$ pairs, and for that purpose the RICH detector plays an extremely important role: the requirement of proper identification of kaon and pion candidates reduces significantly the combinatorial background underlying the resonance, which is centered on the D^0 mass (cf. Fig. 2). In addition, the following kinematic cuts are applied: on the fraction of the virtual photon energy carried by the D^0, $0.2 < z_{D^0} < 0.85$, and on the angle between the charmed meson direction and the resulting kaon in the D^0 center-of-mass, $|\cos\theta^*| < 0.65$. They are important to reduce the contamination of the PGF sample by events coming from processes that involve the fragmentation of a struck quark, because most of these events are collinear with the virtual photon direction or have a z_{D^0} values close to zero. The combinatorial background can be further reduced using the following channel: $D^* \to D^0\pi_{slow}$ with $D^0 \to K\pi$ (D^0 tagged with a D^*). By applying a cut on the difference of the reconstructed masses for the D^* and D^0, 3.2 MeV/c^2 $< M^{rec}_{D^*} - M^{rec}_{D^0} - M_\pi <$ 8.9 MeV/c^2, one can check that there is not much room left for the slow pion momentum. Due to this cut the purity of the D^0 signal is significantly improved, and as a consequence three new channels of lower purity can also be studied: $D^0 \to K\pi\pi^0$, $D^0 \to K_{sub}\pi$, and $D^0 \to K\pi\pi\pi$. The resonance observed in the first channel emerges from the combinatorial background as a 'bump', centered around -250 MeV/c^2 in the $D^0 \to K\pi$ spectra, due to the fact that the extra π^0 is not directly reconstructed for this analysis. The second channel represents the D^0 candidates without RICH identification for the kaon mass hypothesis (sub-threshold kaons with p(K) $<$ 9 GeV/c), and the last one involves another D^0 decay mode which helps to improve the statistical precision of the $\Delta g/g$ measurement. The final D^0 samples used in this analysis are shown in Fig. 2. Separate contributions from the COMPASS data on deuteron and proton targets can be seen in Ref. [4].

3 Method to extract the gluon polarisation

The number of D^0 candidates collected in a given target cell and time interval is:

$$\frac{d^k n}{dmdX} = a\phi\eta(s+b)[1 + P_t P_\mu f(\frac{s}{s+b}A^{\mu N\to\mu' D^0 X} + \frac{b}{s+b}A_B)]. \quad (3)$$

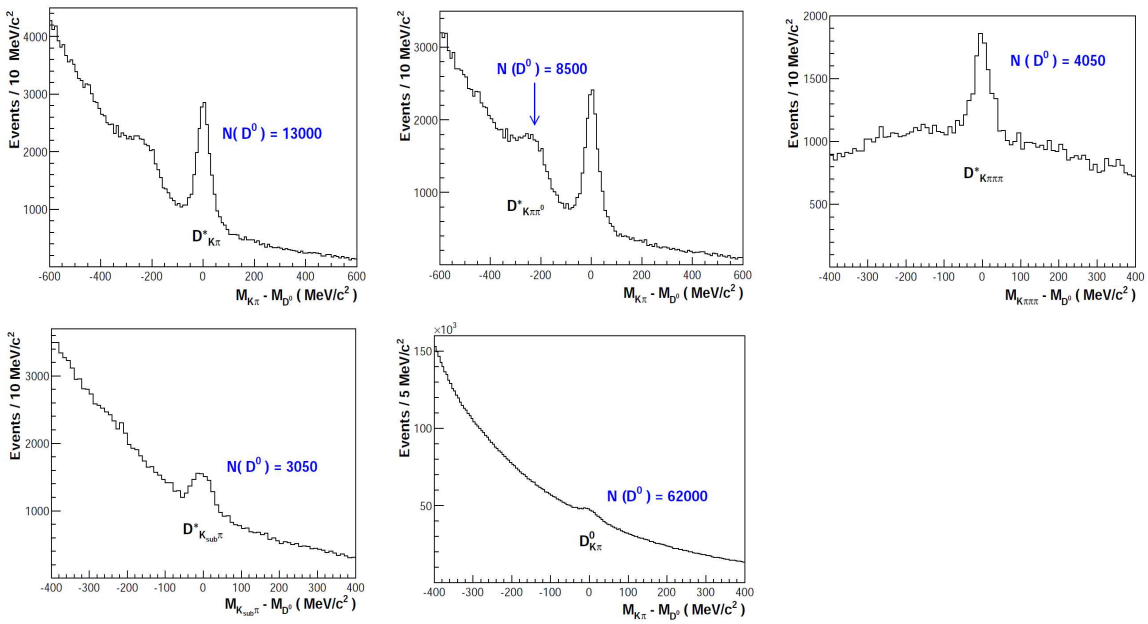

Figure 2: Invariant mass spectra for the $D^*_{K\pi}$, $D^*_{K\pi\pi^0}$, $D^*_{K\pi\pi\pi}$, $D^*_{K_{sub}\pi}$ and $D^0_{K\pi}$ samples. The symbol D^* denotes a D^0 meson tagged with a D^*. The subscript notation indicates the final state of a D^0 decay. Both deuteron and proton data are included in these samples.

$A^{\mu N\to\mu' D^0 X}$ is the longitudinal double spin asymmetry of the differential cross-section for events with a D^0 or $\bar{D}^0$ in the final state, and A_B is the corresponding asymmetry originating from combinatorial background events. Furthermore, $m = M_{K\pi}$ and the symbol X denotes a set of $k-1$ kinematic variables describing an event ($p_T^{D^0}$, E_{D^0}, Q^2, y, z, ...), whereas a, ϕ and η are the spectrometer acceptance, the incident muon flux integrated over the time interval, and the number of target nucleons respectively. The differential unpolarised cross-sections for signal and background events folded with the experimental resolution as a function of m and X are represented by $s = s(m, X)$ and $b = b(m, X)$ respectively. The ratio $s/(s+b)$ represents the signal purity of the reconstructed D^0 spectra. The information on the gluon polarisation is contained in the muon-nucleon asymmetry $A^{\mu N}$. The latter is defined in LO QCD as a convolution between the ratio of polarised/unpolarised partonic cross-sections, $(\Delta\hat{\sigma}/\hat{\sigma})^{\mu g\to\mu' c\bar{c}}$, and the ratio of polarised/unpolarised gluon structure functions $(\Delta g/g)$:

$$A^{\mu N} = \langle \hat{a}_{LL} \rangle \frac{\Delta g}{g} \qquad \text{with} \qquad \hat{a}_{LL} \equiv \frac{\Delta\hat{\sigma}_{\mu g}}{\hat{\sigma}_{\mu g}} = \left(\frac{\hat{\sigma}^{\rightleftarrows}_{\mu g} - \hat{\sigma}^{\rightleftarrows}_{\mu g}}{\hat{\sigma}^{\rightleftarrows}_{\mu g} + \hat{\sigma}^{\rightleftarrows}_{\mu g}} \right). \tag{4}$$

Four equations like eq. (3) are defined, i.e. one equation for each cell and spin configuration of the target. Since the factors $s/(s+b)$ and $a_{LL}(\equiv \langle \hat{a}_{LL} \rangle)$ have a large dispersion, a weighting method was used to minimize the statistical error. The signal weight, $\omega_S = P_\mu f a_{LL}[s/(s+b)]$, and the background weight, $\omega_B = P_\mu f D[b/(s+b)]$, were used, where D is the polarisation transfer from the muon to the virtual photon. By weighting events corresponding to each of four equations like eq. (3) with ω_S, and then similarly with ω_B, it becomes possible to solve the system of 8 equations in order to extract $\Delta g/g$ (see Ref. [5]). To solve the system, however, one needs a_{LL} and $s/(s+b)$ for every event.

In the next-to-leading order, the physical asymmetry is decomposed as follows:

$$A^{\mu N} = a_{LL}^{PGF} \frac{\Delta g}{g} + a_{LL}^{q} A_1, \tag{5}$$

where in a_{LL}^{PGF} all the soft, virtual and gluon bremstrahlung corrections to the LO-PGF process are included (cf. diagrams in Ref. [4]). The asymmetry a_{LL}^{q} accounts for the presence of physical background inside the D^0 resonance. It corresponds to an interaction between the virtual photon and a light quark, which subsequently emits a gluon that produces a $c\bar{c}$ pair. One of these charmed quarks may fragment into a non-PGF D^0. Finally, A_1 represents the inclusive asymmetry which is experimentally well known [6]. The contamination described by the second term of eq. (5) is negligible and it appears only in NLO or higher orders accuracy.

Using eqs. (3) and (4) or eqs. (3) and (5) one is able to determine $\Delta g/g$ at the LO or NLO accuracies. In order to make possible to use COMPASS results in global analyses, a set of virtual photon asymmetries, $A^{\gamma^* N \to \mu' D^0 X} = A^{\mu N}/D$, was determined in bins of $p_T^{D^0}$ and E_{D^0}. They are obtained from eq. (3) using as a signal weight the factor $\omega_S^{'} = P_\mu f D[s/(s+b)]$. Note that determined values of $A^{\gamma^* N}$ are independent of a_{LL} and therefore their determination does not depend on a theoretical interpretation. The criterium for the choice of the binning was to provide asymmetries which are independent of the COMPASS acceptance for the PGF process. A table containing values of $A^{\gamma^* N}(p_T^{D^0}, E_{D^0})$ can be found in Ref. [4, 5].

4 Analysing power

The analysing power for the Open-Charm production, a_{LL}, is dependent on the full knowledge of partonic kinematics. Consequently, this asymmetry is not experimentally accessible because only one D^0 meson is reconstructed per event; the information associated with the second charm quark is lost. Nevertheless, a_{LL} can be obtained from a dedicated Monte Carlo generator for production of heavy flavours (AROMA).

4.1 The analysing power in LO QCD

The AROMA generator is used without parton showers in order to generate D^0 events from LO-PGF processes. After a full Monte Carlo chain, where the generated events are constrained to the COMPASS acceptance, all D^0 mesons are reconstructed in the simulated spectrometer. The polarised and unpolarised partonic cross-sections are calculated using the information from the generator, and then the kinematic dependencies of a_{LL} are parameterised [4] with the help of a Neural Network [7]. Finally, the Monte Carlo parameterisation is used to obtain a_{LL} for each real data event.

4.2 The analysing power in NLO QCD

The phase space needed for NLO real gluon emission processes, $\gamma^* g \to c\bar{c}g$, is simulated through parton showers included in the AROMA generator. For every simulated event, the energy of parton showers (if present in the event) defines the upper limit of the integration over the energy of the unobserved gluon in the NLO emission process. This

integration reduces a differential cross-section for a three-body final state ($c\bar{c}g$) to a two-body one ($c\bar{c}$), which can be combined with the LO cross-section ($c\bar{c}$, PGF) and the two-body virtual and soft NLO corrections. The procedure guarantees a correct infra-red divergence cancellation. In this way, the total partonic cross-section at NLO accuracy is calculated on an event-by-event basis for the spin averaged as well as spin dependent case, and consequently a_{LL}^{PGF} at NLO accuracy is obtained. The same procedure is applied for the correction originating from a_{LL}^{q}. In NLO, $\Delta g/g$ is estimated from $A^{\gamma^* N}(p_T^{D^0}, E_{D^0})$ using $\langle a_{LL}^{PGF} \rangle$ and $\langle a_{LL}^{q} \rangle$ in bins of ($p_T^{D^0}$, E_{D^0}). For details see [5].

5 The signal purity

The Neural Network (NN) described in Ref. [7] is also used to parameterise $s/(s+b)$ on real data. Here, the goal is to obtain D^0 probabilities for every event. In Ref. [4] one can see the outcome of this parameterisation: the D^0 spectrum reveals a probability behavior in bins of $[s/(s+b)]_{\rm NN}$, i.e. its purity increases towards $[s/(s+b)]_{\rm NN} = 1$. Consequently, the statistical precision of $\Delta g/g$ is significantly improved due to a good separation of the physical events from the combinatorial background. To accomplish this, two data sets are used as inputs to the network. The first one contains the D^0 signal and the combinatorial background events. These events are called 'good charge combination' ones (*gcc*) reffering to the charges of particles from D^0 decays, and they are selected as described in Sec. 2. The second set, the 'wrong charge combination' events (*wcc*), is selected in a similar way except that the sum of charges of corresponding particles should not be zero. It contains only background events and is used as a background model. The NN performs a multi-dimensional comparison of *gcc* and *wcc* events in a ± 40 MeV/c^2 mass window around the D^0 mass. Within the *gcc* set, signal events are distinguished from combinatorial background by exploiting differences between the *gcc* and *wcc* sets in the shapes of distributions of kinematic variables as well as multi-dimensional correlations between them. An example of a properly chosen variable for the network is the kaon angular distribution in the D^0 center-of-mass, as shown in Fig. 3. The distributions in the side band bins, shown in the bottom plot of Fig. 3, illustrate the good quality of the background model.

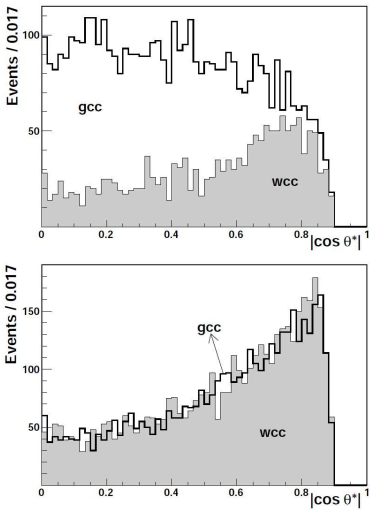

Figure 3: Example of the *gcc* and *wcc* distributions of |cos θ^*| in the D^0 center-of-mass. Top/bottom: region of the D^0 signal/sidebands.

The purity $[s/(s+b)]_{\rm NN}$ is obtained from a simple function applied to the NN output (see Ref. [5]). Thereafter, the mass dependence is added as a correction from a fit to the spectra in bins of $[s/(s+b)]_{\rm NN}$. By respecting the correct D^0 kinematic dependencies, this parameterisation allows us to use $s/(s+b)$ inside ω_S in an unbiased way.

6 Results and Conclusions

The LO and NLO results on the gluon polarisation are the following:

$$\left\langle \frac{\Delta g}{g} \right\rangle^{\text{LO}}_{\text{NLO}} = \begin{pmatrix} -0.08 \pm 0.21(\text{stat}) \pm 0.09(\text{syst}) & @\langle x_g \rangle = 0.11^{+0.11}_{-0.05} \\ -0.20 \pm 0.21(\text{stat}) \pm 0.09(\text{syst}) & @\langle x_g \rangle = 0.28^{+0.19}_{-0.10} \end{pmatrix}. \quad (6)$$

Both results are obtained at a scale of $\langle \mu^2 \rangle = 13$ (GeV/c)^2. The theoretical uncertainties associated with the NLO determination of a_{LL}^{PGF} and a_{LL}^{q} are still under study. Therefore, the systematic uncertainty is given as a preliminary value for the NLO result. Eq. (6) indicates that small values of $\Delta g/g$ are clearly favored in the x_g range of both measurements. These results are compatible with all the world measurements of the gluon polarisation, as shown in the left plot of Fig 4. In the right plot of Fig. 4 the two open charm results for $x\Delta g$ are compared to the global fits, which prefere small values of gluon helicity contribution, $\Delta G = \int_0^1 \Delta g(x) dx$, to the nucleon spin. In conclusion, the **spin puzzle** of the nucleon is still unresolved.

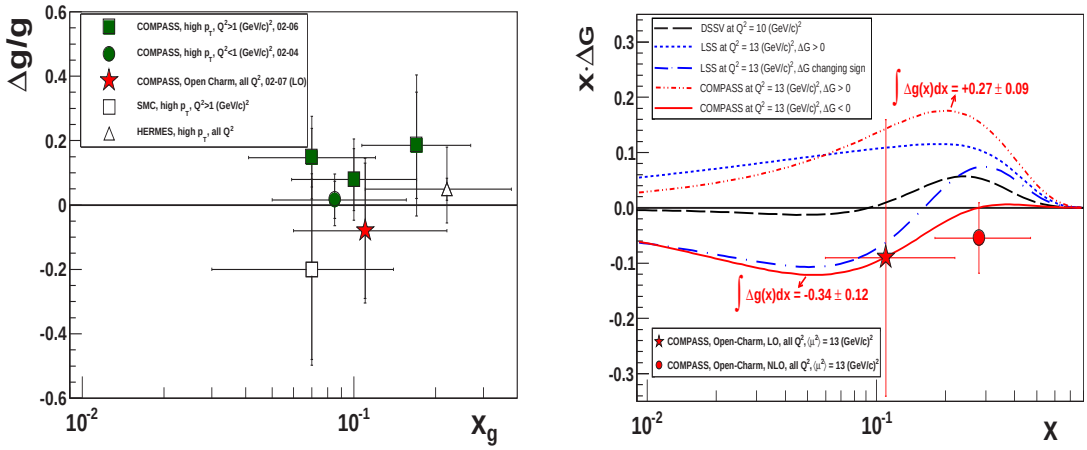

Figure 4: Left: world measurements on $\Delta g/g$. Right: parameterisations of $x\Delta g(x, Q^2)$ together with the LO and NLO results obtained from the Open-Charm analysis.

References

[1] COMPASS, V. Yu. Alexakhin et al., Phys. Lett. B **647** (2007) 8

[2] J. Ellis and R. Jaffe, Phys. Rev. D 9 (1974) 1444; ibid. 10 (1974) 1669.

[3] S.J. Brodsky, et al., Phys. Lett. B **93** (1980) 451

[4] `http://www.lip.pt/~celso/Franco_Dubna2011.pdf`

[5] COMPASS, M. G. Alekseev et al., *Leading and Next-to-Leading Order Gluon Polarisation in the Nucleon and Longitudinal Double Spin Asymmetries from Open Charm Muoproduction*, to be submitted to Phys. Rev. D.

[6] COMPASS, Ageev, E S et al., Phys. Lett. B **647** (2007) 330

[7] R. Sulej et al., Measur.Sci.Tech.18: 2486-2490, 2007

FORTHCOMING DRELL-YAN MEASUREMENTS AT COMPASS

A. Guskov [1] on behalf of the COMPASS collaboration

(1) *Joint Institute for Nuclear Research, Dubna, Russia*
University of Turin, INFN section of Turin, Turin, Italy
E-mail: avg@nusun.jinr.ru

Abstract

The COMPASS experiment at CERN is a universal facility which can operate with both muon and hadron beams as well as with unpolarized or longitudinally/transversely polarized liquid and solid targets. The availability of pion beam provides an access to the Drell-Yan physics, i.e. to the process where quark (target)-antiquark (beam) pair annihilates electromagnetically with a production of dilepton pair. The possibility to use in a future COMPASS Drell-Yan measurements a transversely polarized target together with negative pion beam will provide us unique opportunity to access a number of convolutions of transverse momentum dependent parton distribution functions (TMDs), which can not be measured with unpolarized targets.

1 Transverse momentum dependent PDFs

At leading twist, the quark structure of the hadron is completely described by three PDFs: the unpolarized distribution function $f_1(x)$, the helicity distribution $g_1(x)$ and transversity function $h_1(x)$. But there are several experimental observations of large azimuthal and spin asymmetries which perturbative QCD at leading twist in collinear approximation can not explain. In particular, large asymmetric azimuthal distributions of final-state leptons measured in high-energy collisions of pions and protons with nuclei [1] – [3] show a striking deviation from the so-called Lam-Tung sum rule [4], [5] that is based on collinear perturbative QCD, and seem to indicate the need to go beyond the collinear approximation. When considering non-zero quark transverse momentum k_T with respect to the hadron momentum, the nucleon structure is described at leading twist by eight PDFs. Two of five new functions: the Boer-Mulders function $h_1^{\perp}(x, k_T^2)$ describing the correlation between transverse spin and transverse momentum of the quark in an unpolarized nucleon and the Sivers function $f_{1T}^{\perp}(x, k_T^2)$ describing the influence of the transverse spin of the nucleon into the quark transverse momentum distribution, as well as transversity function h_1 are of great interest to further reveal the partonic (spin) structure of hadrons (see [6] for a review).

The Drell-Yan quark-antiquark annihilation process is an excellent tool to study transversity and k_T-dependent PDFs. In the DY process (Fig. 1) quark and antiquark annihilate into a lepton pair. Other kinds of hard processes can also access chirally odd PDFs, like semi-inclusive deep-inelastic scattering (SIDIS) where chirality is conserved through the convolution of PDFs with polarized quark fragmentation functions. There exist no fragmentation process in DY. In order to access spin structure information a

high-intensity hadron beam and a large-acceptance setup as well as a high-performance polarized target are required. These features are provided by the multipurpose large-acceptance COMPASS spectrometer.

2 Future Drell-Yan measurement at COMPASS

COMPASS is a fixed target experiment at the secondary beams of Super Proton Synchrotron at CERN [7]. The purpose of the experiment is the study of hadron structure and hadron spectroscopy with high intensity muon and hadron beams [8]. The COMPASS detector consists of two spectrometers built around two dipole magnets in order to detect particles scattered at large and small angles, respectively. It is equipped with a large number of precise tracking detectors, two electromagnetic calorimeters, two hadron calorimeters and particle identification system including RICH and two muon walls. Layout of a target region of the experiment can be optimized for a particular measurement. COMPASS operates with muon and hadron beams with momentum up to 200 GeV/c. During the first phase (2002-2011) of the experiment the longitudinal and transverse nucleon spin structures were studied via deep inelastic scattering with muon beam of high intensity. Production of hadron resonances via diffractive scattering, central production and photon exchange using pion and proton beams and hydrogen, tungsten, lead and nickel targets were also studied.

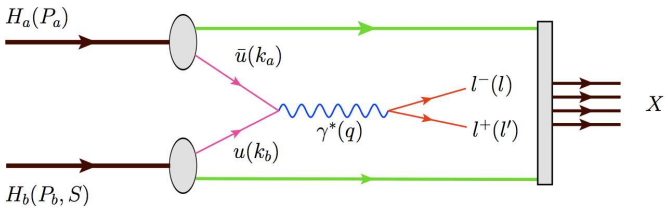

Figure 1: Feynman diagram of the Drell-Yan process.

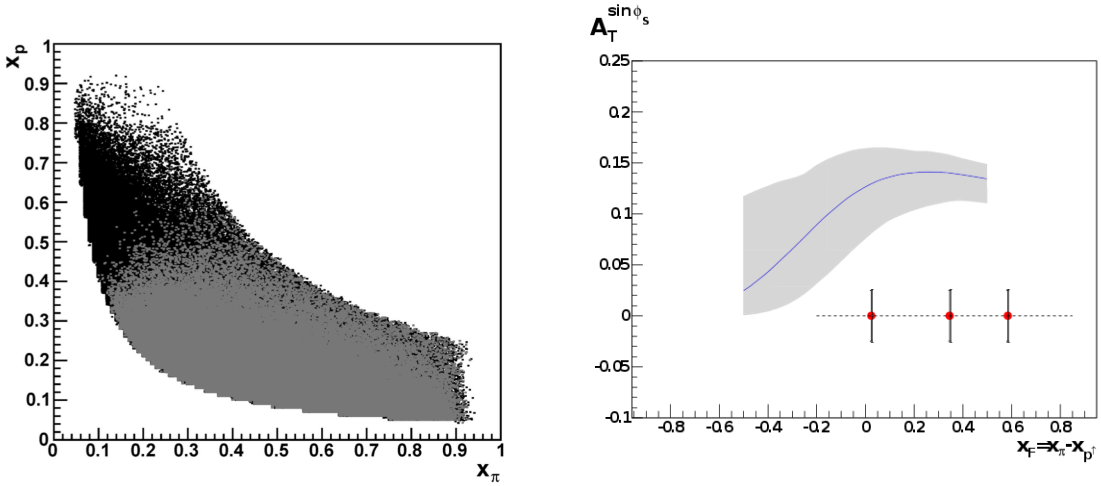

(a) (b)

Figure 2: **(a)** Kinematic range in x_π vs. x_p, covered by COMPASS (in grey) for 4 $GeV/c < M_{\mu\mu} <$ 9 GeV/c (Monte-Carlo simulation).**(b)** Expected error of the Sivers asymmetry for a measurement in three bins of $x_F = x_p - x_\pi$. Two years of data taking (280 days) is assumed.

Possible extension of COMPASS physic program is described in the COMPASS-II Proposal [10] which was approved by the CERN Research Board for the period of three

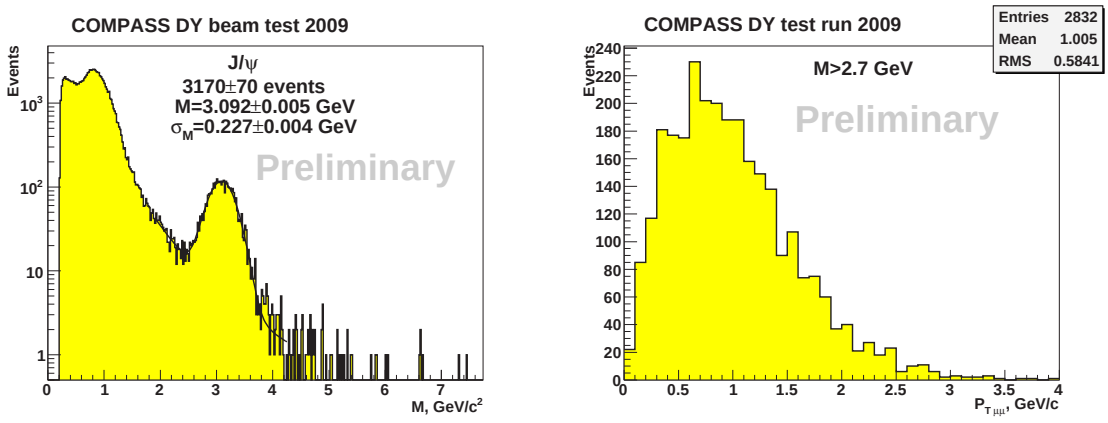

(a) (b)

Figure 3: **(a)** The measured $\mu^+\mu^-$ invariant mass distribution. The number of events is obtained from the fit in the J/ψ region. **(b)** P_T distribution for dileptons with $M_{\mu^+\mu^-} > 2.7\ GeV$

years starting since 2012. It consists of three general directions: tests of chiral perturbative theory, GPD program and Drell-Yan program.

Convolutions of PDFs of incoming pion and target proton can be accessed via the measurement of the lepton pair angular distributions in the final state. The Sivers and Boer-Mulders functions are T-odd objects. QCD predicts that the $f_{1T}^{\perp}$ and the $h_1^{\perp}$ functions extracted from DrellYan processes and those obtained from semi-inclusive DIS should have opposite sign [11], i.e.

$$f_{1T}^{\perp}\big|_{DY} = -\, f_{1T}^{\perp}\big|_{DIS}\,, \quad h_{1T}^{\perp}\big|_{DY} = -\, h_{1T}^{\perp}\big|_{DIS}\,. \tag{1}$$

COMPASS provides unique opportunity to test this QCD prediction because SIDIS and DY measurements can be done at the same setup and in overlapping kinematic ranges.

For Drell-Yan studies COMPASS will operate with 190 GeV/c π^- beam of high intensity (up to 10^8 s^{-1}) and transversely polarized NH_3 target. Hadron absorber will be installed just downstream the target to stop both secondary hadrons and unscattered beam pions to prevent their decay into muons and reduce the combinatorial background and occupancy of tracking detectors . Construction of the absorber will be optimized to minimize multiple scattering in material for muons. Dedicated trigger for the selection of a pair of oppositely charged muons will be provided. A safe range for dimuon masses, separated from J/ψ and Υ peaks, is 4-9 GeV/c^2. Kinematic range of x_π and x_p variables which are the fractions of the momentum carried by the interacting parton in the incoming pion and proton respectively, covered by COMPASS is shown on Fig. 2(a). Main part of potentially observed DY events correspond to annihilation of valence quarks ($x_\pi,\ x_p > 0.1$). According to the performed Monte Carlo study the average value of the dilepton transverse momentum PT will stay at about 1 GeV. In this range the TMD-induced effects are expected to be dominant. Two years of data taking with the beam intensity of $6 \times 10^7\ s^{-1}$ will allow to collect enough statistics (more than 200 000 DY events) to extract TMD PDFs. Expected error of the Sivers asymmetry for a measurement in three bins of $x_F = x_p - x_\pi$ is shown on Fig. 2(b).

Feasibility of Drell-Yan measurements at COMPASS was studied during three short beam tests. The most important three-day-long test was performed in 2009. The po-

larized target was simulated by two cylinders of polyethylene. A prototype hadron absorber was installed downstream of the target. The beam intensity of 8×10^7 pions/spill (spill length of 9.6 s) was used except for two runs when the beam intensity was increased up to 1.5×10^8/spill (integrated beam flux was equal to 3.7×10^{11} pions). J/ψ peak was used as a monitoring signal (see Fig. 3(a)). The number of expected J/ψ events based on the cross section, accumulated luminosity, apparatus acceptance and trigger/reconstruction performance is 3600 ± 600, the number of expected DY events in the mass range $4\ GeV/c^2 < M_{\mu\mu} < 9\ GeV/c^2$ is 110 ± 22. The number of registered J/ψ's (3170 ± 70) is in a good agreement with the expected from MC yield as well as the number of registered DY events (84 ± 10). Events with dimuon mass below J/ψ peak were also studied. Distribution of P_T of dimuon with $M_{\mu\mu} > 2.7\ GeV$ is shown of Fig. 3(b) and it corresponds to our expectations from the Monte Carlo.

3 Conclusion

Polarized Drell-Yan measurement is a part of COMPASS-II proposal. This proposal was approved by CERN SPSC for a first period of 3 years (1 year of Drell-Yan data taking). Three DY beam test were performed so far and the feasibility of the measurement with the COMPASS spectrometer was demonstrated. According to our estimations 2 years of data taking with the beam intensity of $2 \times 10^8\ s^{-1}$ will allow to collect enough statistics for test theory predictions and extract TMD PDFs. After one year of data taking with the beam intensity up to $10^8\ s^{-1}$ we aim to measure the Sivers asymmetry with a statistical accuracy of 1-2%. Comparison of Sivers and Boer-Mulders functions measured in DY and SIDIS also can be performed.

References

[1] NA10, S. Falciano et al., Z. Phys. C31 (1986) 513.

[2] E. Anassontzis et al., Phys. Rev. D38 (1988) 1377.

[3] J. S. Conway et al., Phys. Rev. D39 (1989) 92.

[4] C. S. Lam et al., Phys. Rev. D18 (1978) 2447.

[5] C. S. Lam et al., Phys. Rev. D21 (1980) 2712.

[6] V. Barone et al., Phys. Rept. 359 (2002) 1.

[7] P. Abbon , E. Albrecht et al., NIM, **A577**, 455-518 (2007).

[8] F. Bradamante, S. Paul et al., CERN Proposal COMPASS, CERN/SPSLC 96-14, SPSC/P297, CERN/SPSLC 96-30, SPSC/P297, Addendum 1.

[9] The COMPASS collab., COMPASS-II proposal, CERN/SPSC 2010-014, SPSC-P-340.

[10] The COMPASS collab., COMPASS-II Proposal: Questions & Answers, CERN/SPSC 2010-022, SPSC-M-772.

[11] J. C. Collins, Phys. Lett. B536 (2002) 43.

MEASUREMENT OF THE SPIN-STRUCTURE FUNCTION g_2 and VIRTUAL-PHOTON ASYMMETRY A_2 OF THE PROTON

A. Ivanilov (on behalf of the HERMES collaboration)

IHEP, Protvino
† *E-mail: ivanilov@mail.desy.de*

Abstract

The measurement of the spin-structure function $g_2(x, Q^2)$ and of the virtual-photon asymmetry $A_2(x, Q^2)$ of the proton is presented for the kinematic range $0.023 < x < 0.7$ and $1 < Q^2 < 15$ GeV^2. The data were collected by the HERMES experiment at the HERA storage ring at DESY while studying inclusive deep-inelastic scattering of 27.6 GeV longitudinally polarized leptons off a transversely polarized hydrogen gas target. The results are consistent with previous experimental data from CERN and SLAC.

The description of inclusive deep-inelastic scattering of longitudinally polarized charged leptons off polarized nucleons requires two nucleon spin-structure functions $g_1(x, Q^2)$ and $g_2(x, Q^2)$ in addition to the well-known structure functions $F_1(x, Q^2)$ and $F_2(x, Q^2)$. Here, $-Q^2$ is the squared four-momentum of the exchanged virtual photon with laboratory energy ν, $x = Q^2/2M\nu$ is the Bjorken scaling variable, and M is the nucleon mass. Ignoring quark mass effects, $g_2(x, Q^2)$ can be written as a sum of two terms

$$g_2(x, Q^2) = g_2^{\mathrm{WW}}(x, Q^2) + \bar{g}_2(x, Q^2)\,. \tag{1}$$

Here, $g_2^{\mathrm{WW}}(x, Q^2)$ is the twist-2 part derived by Wandzura and Wilczek [1]:

$$g_2^{\mathrm{WW}}(x, Q^2) = -g_1(x, Q^2) + \int_x^1 g_1(y, Q^2)\frac{d\,y}{y}\,. \tag{2}$$

The second term in Eq. (1), $\bar{g}_2(x, Q^2)$, is the twist-3 part of $g_2(x, Q^2)$. It arises from quark-gluon correlations in the nucleon and is the most interesting part of the function.

The spin-structure functions $g_1(x, Q^2)$ and $g_2(x, Q^2)$ can be related to the virtual photon-absorption asymmetries $A_1(x, Q^2)$ and $A_2(x, Q^2)$ (see *e.g.* Ref. [2]):

$$A_1 = \frac{g_1 - \gamma^2 g_2}{F1}, \qquad A_2 = \gamma\,\frac{g_1 + g_2}{F_1}\,, \tag{3}$$

where $\gamma = 2Mx/\sqrt{Q^2}$.

The measurement of the structure function g_2 requires a longitudinally polarized beam and a transversely polarized target. The inclusive differential cross section can be represented as a sum of two terms, the polarization-averaged part σ_{UU}, and the polarization-dependent part σ_{LT}. Here, the subscript UU indicates that both the beam and the target are unpolarized, while the subscript LT indicates a longitudinally polarized beam

and a transversely polarized target. The polarization-dependent part of the cross section at Born level, *i.e.* in the one-photon approximation, is given by [3]:

$$\frac{d^3\sigma_{LT}}{dxdyd\phi} = -h_l \cos\phi \frac{4\alpha^2}{Q^2}\gamma\sqrt{1-y-\frac{\gamma^2y^2}{4}} \cdot \left(\frac{y}{2}g_1(x,Q^2) + g_2(x,Q^2)\right). \quad (4)$$

Here, $h_l = +1$ (-1) for a lepton beam with positive (negative) helicity, α is the fine-structure constant, and $y = \nu/E$, where E is the incident lepton energy. The angle ϕ is the azimuthal angle about the beam direction between the lepton scattering plane and the "upwards" target spin direction.

A measurement of the inclusive cross sections (4) at angles ϕ and $\phi + \pi$ allows one to construct the asymmetry A_{LT}:

$$A_{LT}(x,Q^2,\phi) = h_l \frac{\sigma(x,Q^2,\phi) - \sigma(x,Q^2,\phi+\pi)}{\sigma(x,Q^2,\phi) + \sigma(x,Q^2,\phi+\pi)} = h_l \frac{\sigma_{LT}(x,Q^2,\phi)}{\sigma_{UU}(x,Q^2,\phi)} = -\cos\phi\, A_T(x,Q^2)\,, \quad (5)$$

which defines the asymmetry amplitude $A_T(x,Q^2)$. The amplitude provides an access to g_2 and A_2 using world data on the cross-section σ_{UU} and g_1. The cross-section σ_{UU} depends on the structure functions $F_{1,2}$, or, equivalently, on the function F_2 and the ratio of longitudinal to transverse virtual photon-absorption cross sections $R(x,Q^2)$. Finally, the function $g_2(x,Q^2)$ and the asymmetry $A_2(x,Q^2)$ can be evaluated from the amplitude A_T using functions g_1 and F_1 through the following relations:

$$g_2 = \frac{F_1}{\gamma(1+\gamma\xi)}\left(\frac{A_T}{d} - (\gamma - \xi)\frac{g_1}{F_1}\right), \quad (6)$$

$$A_2 = \frac{1}{1+\gamma\xi}\left(\frac{A_T}{d} + \xi(1+\gamma^2)\frac{g_1}{F_1}\right). \quad (7)$$

Here, $d = D\sqrt{1-y-\gamma^2y^2/4}/(1-y/2)$, $\xi = \gamma(1-y/2)/(1+\gamma^2y/2)$, $D = y(2-y)(1+\gamma^2y/2)/[y^2(1+\gamma^2) + 2(1-y-\gamma^2y^2/4)(1+R)]$.

We report a new measurement of the function g_2 and the asymmetry A_2. The data were collected during the years 2003 – 2005 with the HERMES spectrometer [4] using a longitudinally polarized positron or electron beam of energy 27.6 GeV scattered off a transversely polarized target of pure hydrogen gas internal to the HERA lepton storage ring at DESY. The nuclear polarization of the atoms was flipped at 1–3 minute time intervals. The average value of the proton-polarization magnitude was 0.78 ± 0.04. The lepton beam (positrons during 2003 – 2004 and electrons in 2005) was self-polarized in the transverse direction. Longitudinal orientation of the beam polarization was obtained by using a pair of spin rotators located before and after the HERMES spectrometer. The sign of the beam helicity was reversed every few months. The average value of the beam-polarization magnitude was found to be 0.34 ± 0.01. The scattered leptons were detected by the HERMES spectrometer within an angular acceptance of ± 170 mrad horizontally and $\pm(40 \div 140)$ mrad vertically. The leptons were identified using the information from an electromagnetic calorimeter, a transition-radiation detector, a preshower scintillating counter and a dual-radiator ring-imaging Čerenkov detector. The identification efficiency for leptons with momentum larger than 2.5 GeV exceeds 98%, while the hadron contamination is found to be less than 1%.

The kinematic constraints imposed on the events were: 1 GeV^2 $< Q^2 <$ 15 GeV^2, invariant mass of the virtual photon-nucleon system $W > 2.0$ GeV, $0.023 < x < 0.7$, and $0.10 < y < 0.85$. After applying data quality criteria, 6.9×10^6 events were available for the asymmetry analysis. The kinematic region covered by the experiment in (x, Q^2)-space was divided into six bins in x. Each of the six x-bins was subdivided into three logarithmically equidistant bins in Q^2. The range in ϕ-space (2π) was divided into 10 bins.

The measurement of the asymmetry $A_{LT}(x, Q^2, \phi)$ defined in Eq. (5) was performed by reversing the transverse target polarization and comparing the number of events in the same part of the detector:

$$A_{LT}(x, Q^2, \phi) = h_l \frac{N^{h_l\Uparrow}(x, Q^2, \phi)\mathcal{L}^{h_l\Downarrow} - N^{h_l\Downarrow}(x, Q^2, \phi)\mathcal{L}^{h_l\Uparrow}}{N^{h_l\Uparrow}(x, Q^2, \phi)\mathcal{L}_p^{h_l\Downarrow} + N^{h_l\Downarrow}(x, Q^2, \phi)\mathcal{L}_p^{h_l\Uparrow}}\,. \tag{8}$$

Here, $N^{h_l\Uparrow(\Downarrow)}$ is the number of scattered leptons in one bin of the 3-dimensional space (x, Q^2, ϕ) for the case of the lepton beam with positive or negative helicity h_l when the direction of the proton spin points up (down). $\mathcal{L}^{h_l\Uparrow(\Downarrow)}$ and $\mathcal{L}_p^{h_l\Uparrow(\Downarrow)}$ are the corresponding integrated luminosities and the integrated luminosities weighted with the absolute value of the beam and target polarization product, respectively. The asymmetry evaluated with Eq. (8) was unfolded for radiative QED and instrumental smearing effects to obtain the asymmetry corresponding to single-photon exchange in the scattering process. The unfolding procedure is described in [5]. It inflates the size of the statistical uncertainties especially in the lowest Q^2-bins at a given value of x. The magnitude of inflation reaches almost a factor of two at low values of x. The subdivision of x-bins into three bins in Q^2 decreases the error inflation by about a factor of 1.5 because at larger Q^2 the amount of smearing between x-bins is smaller and the pre-factors of A_T in Eq. (6) and (7) are larger in magnitude.

The asymmetry amplitude $A_T(x, Q^2)$ was obtained by fitting the unfolded asymmetries with the function $f(\phi) = -\cos\phi\, A_T(x, Q^2)$. The function $g_2(x, Q^2)$ and the asymmetry $A_2(x, Q^2)$ were evaluated (see Eq. 6) and (7)) from the amplitude $A_T(x, Q^2)$, using a world-data parameterization [6] for the $g_1(x, Q^2)$ and parametrizations of the structure function $F_2(x, Q^2)$ [7] and the ratio $R(x, Q^2)$ [8]. The structure function F_1 was calculated from the F_2 and R: $F_1(x, Q^2) = F_2(x, Q^2)(1 + \gamma^2)/[2x(1 + R(x, Q^2))]$.

The uncertainties on the measurements of the beam and target polarizations produce in total a 10% scale uncertainty on the value of A_T. Other sources of systematic uncertainties such as acceptance effects, beam and spectrometer misalignments, uncertainties in the target polarization direction and the unfolding procedure were evaluated by Monte-Carlo studies. Uncertainties stemming from parameterizations of $g_1(x, Q^2)$, $F_2(x, Q^2)$, and $R(x, Q^2)$ were estimated also. The total systematic uncertainty is several times less than the magnitude of the statistical uncertainty.

In order to study the x dependence, $g_2(x, Q^2)$ and $A_2(x, Q^2)$ in bins covering the same x range but with various Q^2 values were evolved to their mean value of Q^2 and then averaged. The results for the virtual-photon asymmetry A_2 and the function xg_2 as a function of x are presented in Fig. 1 together with data from the experiments E155 [9], E143 [10] and SMC [11]. The experiments have only slightly different values of average Q^2 for a particular value of x. The results are within their uncertainties in good agreement with each other. The solid curves represent values of A_2 and xg_2 evaluated with the

Wandzura-Wilczek relation (2) using the $g_1(x, Q^2)$ parameterization of Ref. [6]. The values were calculated at the average Q^2 of HERMES at each value of x.

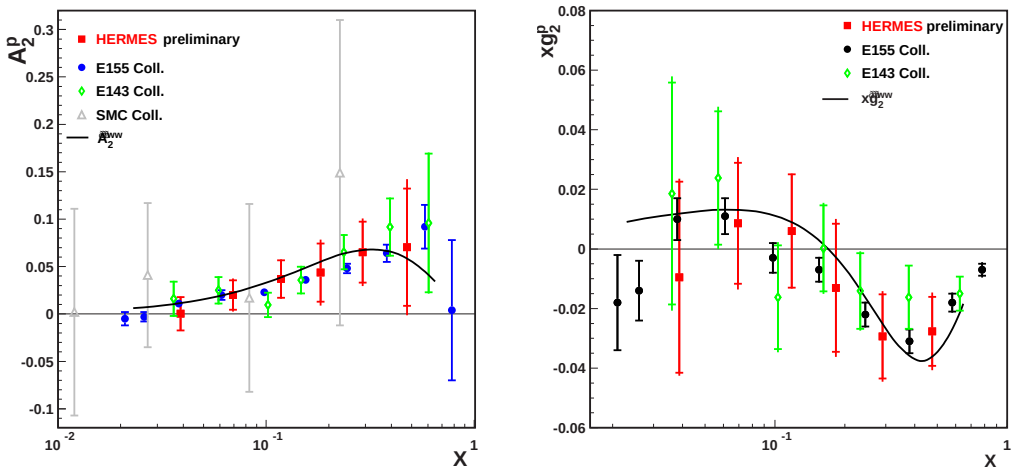

Figure 1: Left panel: The virtual-photon asymmetry A_2 of the proton as a function of x. Right panel: The spin-structure function $xg_2(x, Q^2)$ of the proton as a function of x. Data from the experiments E155 [9], E143 [10] and SMC [11] are presented also. The total error bars represent the quadratic sum of the statistical and systematic uncertainties. The statistical uncertainties are indicated by the inner error bars. The solid curve is the result of the Wandzura-Wilczek relation.

In conclusion, HERMES has measured the spin-structure function g_2 and the virtual-photon asymmetry A_2 of the proton in the kinematic range $0.023 < x < 0.7$ and $1 < Q^2 < 15$ GeV^2. The results on A_2 and g_2 are overall in good agreement with measurements of SMC at CERN, E143 and E155 at SLAC, but they are not statistically accurate enough to detect a deviation of g_2 from its Wandzura-Wilczek part.

References

[1] S. Wandzura and F. Wilczek, Phys. Lett. B **72** (1977), 195.
[2] M. Anselmino, A. Efremov, E. Leader, Phys. Rev. **261** (1995), 1.
[3] R. L. Jaffe, Comments Nucl. Part. Phys. **19** (1990), 239.
[4] K. Ackerstaff *et al.*, Nucl. Instr. and Meth. **417** (1998), 230.
[5] A. Airapetian *et al.*, Phys. Rev. D **75** (2007), 012007.
[6] P. L. Anthony *et al.*, Phys. Lett. B **493** (2000), 19.
[7] A. Airapetian *et al.*, JHEP **0511** (2011), 126.
[8] K. Abe *et al.*, Phys. Lett. B **452** (1999), 194.
[9] P. L. Anthony *et al.*, Phys. Lett B **553** (2003), 18.
[10] K. Abe *et al.*, Phys. Rev. D **58** (1998), 112003.
[11] D. Adams *et al.*, Phys. Rev. D **56** (1997), 5330.

OVERVIEW OF RECENT HERMES RESULTS

V.A. Korotkov
(on behalf of the HERMES Collaboration)

Institute for High Energy Physics, Protvino, Russia
E-mail: Vladislav.Korotkov@ihep.ru

Abstract

An overview of recent selected HERMES results is presented. The review topics include the study of the transverse momentum dependent distributions and the study of the deeply virtual Compton scattering.

1 Introduction

The HERMES experiment at DESY was designed to investigate the spin structure of the nucleon and, in particular, to measure the partonic composition of its spin projection: $S_z = \frac{1}{2} = \frac{1}{2}\Delta\Sigma + \Delta g + L_z^q + L_z^g$. Here $\frac{1}{2}\Delta\Sigma(\Delta g)$ describes the net integrated contribution of quark and antiquark (gluon) helicities to the nucleon helicity and $L_z^q(L_z^g)$ is the z component of the orbital angular momentum among all quarks (gluons). Measurements of longitudinal double-spin asymmetries (DSAs) in deep-inelastic scattering (DIS) of positrons off protons and deuterons [1] led to a value $\Delta\Sigma = 0.330 \pm 0.011(theo) \pm 0.025(exp) \pm 0.028(evol)$. The gluon polarization was obtained from longitudinal DSAs of charged hadrons with high transverse momentum [2]: $\frac{\Delta g}{g} = 0.049 \pm 0.034(stat) \pm 0.010(sys\text{-}exp)^{+0.126}_{-0.099}(sys\text{-}models)$ at $\langle x \rangle = 0.22$ at a scale $\langle \mu^2 \rangle = 1.35$ GeV^2. The both numbers are relatively small and, therefore, the essential contribution from the parton orbital angular momenta is required. In the last years the HERMES Collaboration intensively is studying the Generalized Parton Distributions (GPDs) and the Transverse Momentum Dependent distribution and fragmentation functions (TMDs), both of them can provide a useful information on the magnitude of parton orbital angular momentum. The GPDs can be measured by studying hard exclusive processes such as Deeply Virtual Compton scattering (DVCS). The study of TMDs requires a measurement of certain asymmetries in the semi-inclusive deep inelastic processes (SIDIS) of the hadron production

HERMES used the longitudinally polarized lepton beam (e^+ or e^-) of 27.6 GeV scattered off a transversely/longitudinally polarized or unpolarized gas target internal to the HERA storage ring. Scattered leptons and coincident hadrons were detected by the HERMES spectrometer [3]. Leptons were identified with an efficiency exceeding 98% and a hadron contamination of less than 1%. The HERMES dual-radiator ring-imaging Čerenkov detector allows full hadron identification in the momentum range $2 \div 15$ GeV. In the winter shutdown 2005/2006 the HERMES spectrometer was upgraded in the target region with a Recoil detector to improve the selection of exclusive processes. The Recoil detector comprises a set of silicon strip detectors located inside the HERA beam vacuum, surrounded by a scintillating-fiber tracker, a photon detector, and a 1 Tesla superconducting magnet.

2 TMDs

When the transverse momentum $\mathbf{p}_T$ of the quarks is not integrated out, a variety of new parton distribution functions (PDFs) arise, describing correlations between the quark or the nucleon spin with the quark transverse momentum. These poorly known PDFs, typically denoted as TMDs, encode information on the 3-dimensional structure of nucleons in momentum space and are increasingly gaining theoretical and experimental interest. At leading twist, eight TMDs, each with a specific probabilistic interpretation in terms of quark number densities, enter the SIDIS cross section in conjunction with either the chiral-odd Collins fragmentation function (FF) $H_1^\perp(z, \mathbf{k}_T^2)$, describing left-right asymmetries in the fragmentation of transversely polarized quarks, or well known spin-independent chiral-even $D_1(z, \mathbf{k}_T^2)$ FF. Here z and $\mathbf{k}_T$ denote the fraction of the energy of the exchanged virtual photon carried by the produced hadron and the transverse momentum of the fragmenting quark with respect to the outgoing hadron direction, respectively. Three of the eight TMDs survive the integration over $\mathbf{p}_T$ and correspond to usual collinear PDFs: $f_1(x)$, $g_1(x)$, and $h_1(x)$.

Generally, the differential SIDIS cross section can be represented as a superposition of spin-averaged and spin-dependent terms with various polarization states of the target and beam (see, e.g., [4] and referencies therein). Each of these terms is modulated by the sines and the cosines of the specific combination of the azimuthal angles of the target polarization, ϕ_S, and of the produced hadron, ϕ, both referred to the lepton scattering plane. The coefficients of this Fourier series are represented as convolutions of proper combinations of the TMDs and the FFs over the transverse momenta $\mathbf{p}_T$ and $\mathbf{k}_T$.

In the studies at HERMES, these Fourier amplitudes were extracted through a maximum-likelihood fit of the SIDIS events, alternately binned in x, z and $P_{h\perp}$, but unbinned in ϕ and ϕ_S. The events were selected subject to the kinematic requirements $W^2 > 10$ GeV, $0.1 < y < 0.95$ and $Q^2 > 1$ GeV. Coincident hadrons were accepted in the range $0.2 < z < 0.7$ only.

A case of an unpolarized beam and a transversely polarized target. Three leading-twist asymmetry amplitudes can be measured:

i) Sivers amplitude $2\langle \sin(\phi - \phi_S)\rangle_{UT}^h$ which is proportional to convolution of the Sivers TMD, $f_{1T}^\perp$, and usual FF;

ii) Collins amplitude, $2\langle \sin(\phi + \phi_S)\rangle_{UT}^h$, which is proportional to convolution of the transversity TMD, h_1, and the Collins FF;

iii) the $2\langle \sin(3\phi - \phi_S)\rangle_{UT}^h$ amplitude which is proprtional to convolution of the *pretzelocity* TMD, $h_{1T}^\perp$, and the Collins FF. The *pretzelocity* describes the correlation between the quark transverse momentum $\mathbf{p}_T$ and the transverse polarization of the quarks in a transversely polarized nucleon. In various models, such as the bag or spectator models, it appears [5] as the difference between the helicity and the transversity distributions, thus encoding pure relativistic effects in the quark motion within the nucleon. Final HERMES data on the Sivers [6] and the Collins [7] amplitudes have been published and will not considered in this review. The Collins and the Sivers amplitudes were extracted together with other four sine azimuthal asymmetry amplitudes (three of them are subleading-twist), related to other terms of the SIDIS cross section. These amplitudes are all consistent with zero for all hadron types, with the only exception of subleading-twist $2\langle \sin(\phi_S)\rangle_{UT}^h$ amplitude, which exhibits a large negative signal for π^-, similar to the corresponding Collins amplitude. Preliminary results for this amplitude and for the

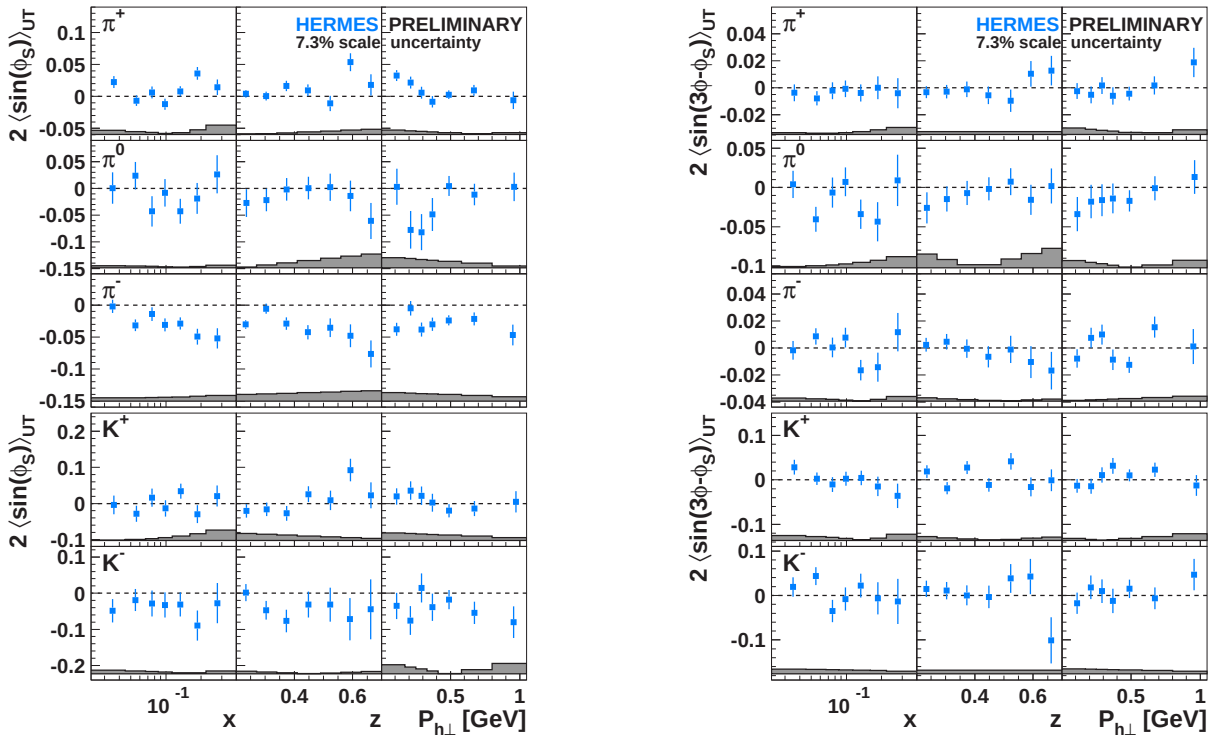

Figure 1: Asymmetry amplitudes $2\langle\sin(\phi_S)\rangle^h_{UT}$ (left panel) and $2\langle\sin(3\phi-\phi_S)\rangle^h_{UT}$ (right panel) for pions and charged kaons as a function of x, z, and $P_{h\perp}$. The shaded bands represent the systematic uncertainty. A common scale uncertainty 7.3% arises from the target polarization measurement.

leading twist $2\langle\sin(3\phi-\phi_S)\rangle^h_{UT}$ amplitude, are presented at Fig. 1 in left and right panel, respectively.

A case of a longitudinally polarized beam and a transversely polarized target. One leading-twist asymmetry amplitude can be measured: the $\cos(\phi-\phi_S)$ amplitude which is proportional to convolution of the *worm-gear*' TMD $g^{\perp}_{1T}$ and usual FF. This TMD describes the probability of finding a longitudinally polarized quark inside a transversely polarized nucleon. Fig. 2 presents the results for the $2\langle\cos(\phi-\phi_S)\rangle^h_{LT}$ asymmetry amplitudes for pions and charged kaons as a function of x, z, and $P_{h\perp}$. The results show a positive amplitude for π^- and possibly also for π^+ and K^+ whereas for π^0 and K^- they are found to be consistent with zero. The results for the sub-leading twist DSAs $2\langle\cos(\phi_S)\rangle^h_{LT}$ and $2\langle\cos(2\phi-\phi_S)\rangle^h_{LT}$, not shown here, are both consistent with zero for all measured mesons.

A case of an unpolarized target. The azimuthal asymmetry for hadron production in lepton DIS off unpolarized target was predicted to be non-zero many years ago due to the fact that the kinematics is noncollinear when the quark intrinsic transverse momentum is taken into account. Other possible sources of the asymmetry are perturbative gluon radiation and Boer-Mulders mechanism, which is due to the correlation of the quark intrinsic transverse momentum and intrinsic transverse spin. This correlation is described by the Boer-Mulders distribution function $h^{\perp}_1(x,k_T)$, which represents the transverse-polarization distribution of quarks inside an unpolarized nucleon. The corresponding amplitude proportional to convolution of $h^{\perp}_1(x,k_T)$ and the Collins FF.

At HERMES, the extraction of the unpolarized modulations was performed using a multi-dimensional unfolding procedure to correct for radiative and acceptance effects on

hydrogen and deuterium data, separately for positive and negative hadrons. The $2\langle\cos 2\phi\rangle_{UU}$ amplitudes as a function of x, y, z, and $P_{h\perp}$ for positive and negative hadrons produced off hydrogen target are presented in Fig. 3. The twist-3 $2\langle\cos\phi\rangle_{UU}$ amplitudes are extracted also but not shown here. An important feature shown by HERMES data is the different behavior of the amplitudes for positive and negative hadrons. Such difference can be considered as an evidence of a non-zero Boer-Mulders function. The extracted amplitudes for pions and kaons show different sizes and kinematic dependencies. This may be due to different features of Collins fragmentation into kaons and pions.

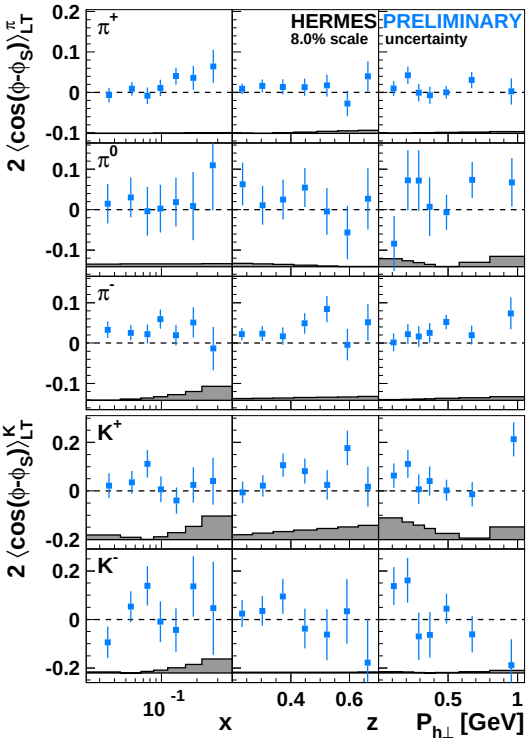

Figure 2: Double-spin asymmetry amplitudes $2\langle\cos(\phi-\phi_S)\rangle_{LT}^{h}$ for pions and charged kaons as a function of x, z, and $P_{h\perp}$. The shaded bands represent the systematic uncertainty. A common scale uncertainty 8.0% arises from the beam and target polarization measurement.

Inclusive production of hadrons. Substantial unexpected single-spin asymmetries have been observed in inclusive hadron production in hadron collisions (see, e.g., [8]). This stimulated interest in looking at inclusive electroproduction of hadrons, $ep \longrightarrow hX$, where only one hadron of the final state is tagged. HERMES has collected a rich data set on inclusive charged pion and kaon production, allowing precise measurements of single-spin asymmetries in the scattering from transversely polarized hydrogen target. The scattered lepton is not considered in the analysis and, therefore, the event sample is dominated by low-Q^2 quasi-real photoproduction. As the scattered lepton escapes detection, the usual DIS kinematics can not be available. Therefore, p_T, $x_F = 2p_L/\sqrt{s}$ with p_L being the longitudinal component of the hadron momentum, and the azimuthal angle ϕ of the hadron's transverse momentum with respect to the polarization direction of the target proton are measured using the incoming lepton beam as a reference.

In Fig. 4 preliminary results on the $\sin\phi$ amplitude of the transverse single-spin asymmetry in inclusive electroproduction of charged pions and kaons are shown as a function of p_T in three bins of x_F. All except the K^- exhibit significantly non-zero asymmetries, substantially larger for π^+ and K^+ than for π^-. The π^- amplitude changes sign going from low to large values of x_F. In general, the amplitudes rise with increasing of p_T and start to decrease at a value in p_T of about 1 GeV. As the origin of such asymmetries is unknown, one can try to compare these results with similar single-spin asymmetries. The SIDIS analogue presented in the previous section requires the presence of the lepton scattering plane, except for the Sivers effect. The later is also a $\sin\psi$ amplitude of the single-spin asymmetry with $\psi = \phi - \phi_S$. The ψ angle is approximately equal to the ϕ angle in the case of small angles between the incoming beam and the virtual-photon directions. The magnitude and behavior of the asymmetries in inclusive hadron production as a function of p_T resembles the one of the Sivers asymmetry versus $P_{h\perp}$. At the moment

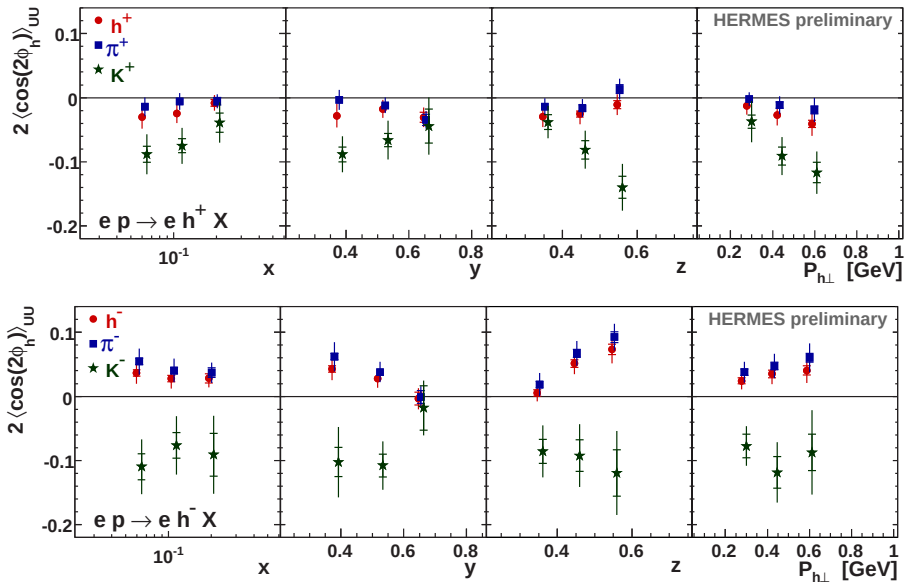

Figure 3: $2\langle\cos 2\phi\rangle_{UU}$ amplitudes for positive (top panel) and negative (bottom panel) hadrons, extracted from hydrogen data as a function of x, y, z, and $P_{h\perp}$.

it is difficult to judge if this coincidence is accidental or has a solid physical ground.

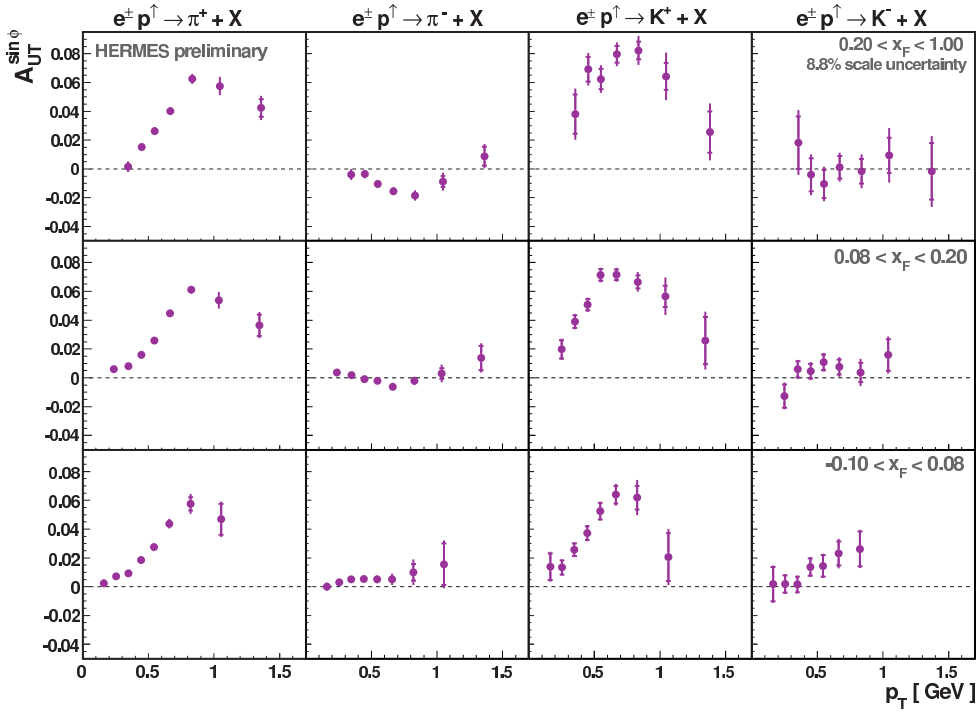

Figure 4: $A_{UT}^{\sin\phi}$ amplitudes for charged pions and kaons as a function of p_T for three bins of x_F.

3 DVCS

The DVCS process is one of the theoretically cleanest ways to study the GPDs. They encompass usual PDFs and elastic nucleon form factors as limiting cases and moments,

respectively, and provide correlated information on transverse spatial and longitudinal momentum distributions of partons. For the proton, a spin-$\frac{1}{2}$ target, there are four leading twist GPDs: E, $\widetilde{E}$, H, and $\widetilde{E}$. The GPDs are functions of the longitudinal parton momentum x, of the squared momentum transfer t and of the skewness parameter ξ. Moments of certain GPDS can be directly related to a value of the total angular momentum carried by partons in the nucleon.

DVCS process is experimentally indistinguishable from the electromagnetic Bethe-Heitler (BH) process as they have identical initial and final states. At HERMES energies, the exclusive $ep \longrightarrow ep\gamma$ cross-section is dominated by the BH contribution whereas the DVCS cross-section is very small. However, the interference term contributes significantly and produces specific azimuthal asymmetries which can be used to access the DVCS matrix elements at amplitude level.

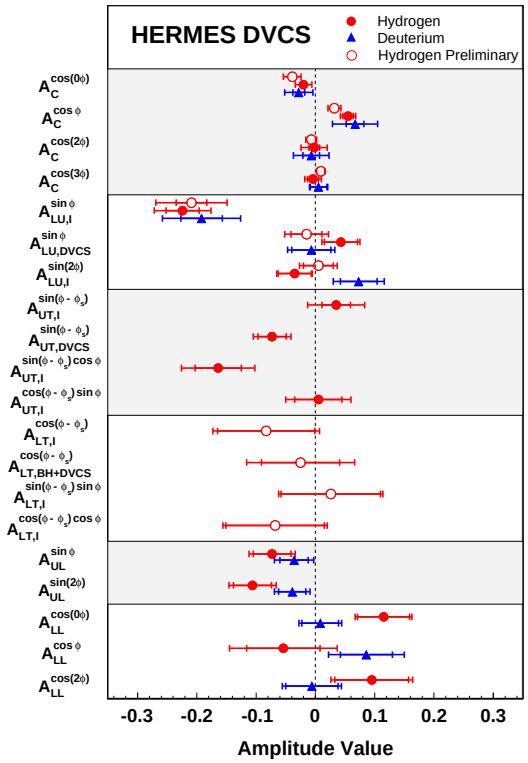

Figure 5: HERMES results for various DVCS amplitudes.

The variety of experimental setups used by HERMES (positive/negative lepton beam, positive/negative polarization of the beam, unpolarized or longitudinally/transversely polarized target) enabled the extraction of many asymmetry amplitudes. These are related to Compton Form Factors which are convolutions of the corresponding GPDs with the hard scattering coefficient functions (see, e.g., [9]). The asymmetries can be written as Fourier series in linear combinations of the angles ϕ and ϕ_S. The angle ϕ (ϕ_S) is the azimuthal angle between the lepton scattering plane and the plane defined by the real and the virtual photon (the azimuthal angle of the target polarization).

Figure 5 presents an overview of all azimuthal asymmetry amplitudes integrated over the entire HERMES kinematic range using the data taken in the years 1996–2007. This includes data on the unpolarized hydrogen [10] and deuterium [11] targets, the longitudinally polarized hydrogen [12] and deuterium [13] and the transversely polarized hydrogen [14, 15] target.

For data without Recoil detector information, the selection of DVCS/BH events was performed by requiring the missing mass, calculated using the lepton and the photon kinematics, to be equal to the proton mass within the resolution of the spectrometer. For such *unresolved* event sample, it is not possible to separate the *pure* DVCS/BH events from the associated process, where the nucleon in the final state is excited to a resonant state. Within the exclusive region, its contribution is estimated from a Monte Carlo simulation to be about 12% of the signal.

For data with Recoil detector information, kinematic event fitting was performed for every DVCS event candidate by using the measured kinematics of the electron, the photon and the proton candidate detected in the Recoil detector under the hypothesis that the process is *pure* DVCS/BH, i.e., $ep \rightarrow ep\gamma$. Detailed Monte Carlo studies showed that the

contamination of the background from the associated process is below 0.1%. It should be noted that the kinematic acceptance for this *pure* event sample is different from the acceptance for the *unresolved* event sample, especially for small values of $-t$.

In order to compare results under similar kinematic conditions, a *reference* event sample was created. For the *reference* sample, in addition to the selection criteria used for the *unresolved* sample, a hypothetical proton with 3-momenta calculated from the 3-momenta of electron and photon was required to be in the Recoil detector acceptance. For this subsample, background conditions are very similar to those for the *unresolved* sample. So that it can be used to understand and to compare to the background-free measurement. In Fig. 6, the $\sin(n\phi)$-amplitudes of the DVCS single-charge beam-helicity asymmetry extracted from 2006 and 2007 hydrogen data taken with a positron beam and fully operational Recoil detector are shown in projections versus $-t$, x_B, and Q^2 and also integrated over the entire acceptance. Results are shown for the *pure* elastic sample, the *reference* sample, and the *unresolved* sample.

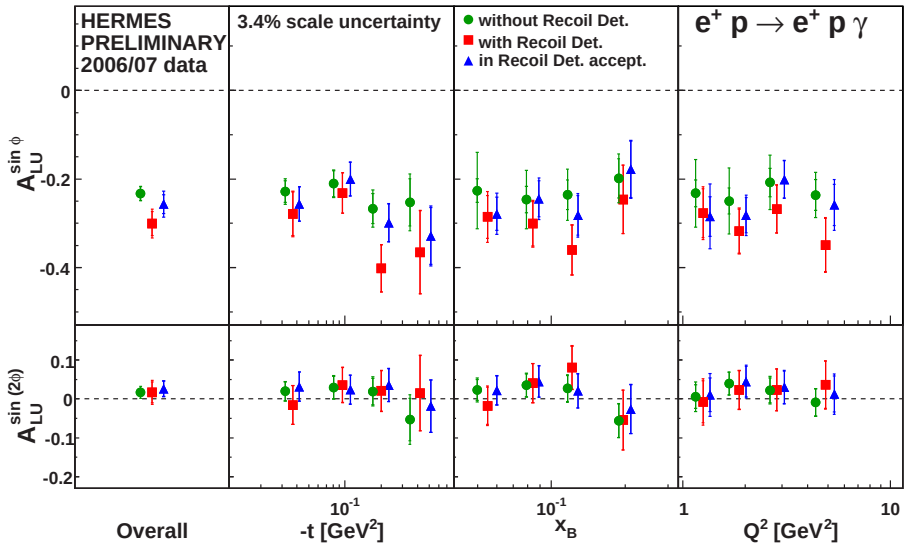

Figure 6: Amplitudes of the single-charge beam-helicity asymmetry of the *pure* (squares), *reference* (triangles) and *unresolved* (circles) samples extracted from 2006 and 2007 hydrogen data taken with fully operational Recoil detector. The inner error bars denote the statistical uncertainties and the total error bars the quadratic sum of the statistical and systematic uncertainties.

While the leading $\sin\phi$ amplitude shows no dependence on x_B and Q^2 in either sample, there is an indication for a non-flat tendency versus $-t$ for the *pure* elastic sample. For low values of $-t$, the *pure* elastic and the *reference* sample containing a mixture of processes deliver results that are compatible within uncertainties. For higher values of $-t$, the *pure* elastic amplitude shows a trend of a larger magnitude than that of the *reference* amplitude. The overall value of the sub-leading $\sin(2\phi)$-amplitude is compatible with zero within its statistical uncertainty for all samples.

There is no large difference of the results for the *pure* elastic sample with the results for the *reference* and *unresolved* samples as well with previously published results [10]. There is an indication that the *pure* elastic amplitude is larger in magnitude. Before drawing any conclusions, the asymmetry of the associated process needs to be studied. This is a subject of an ongoing dedicated analysis.

The systematic uncertainties are obtained from a Monte Carlo simulation estimating

the effects of limited acceptance, smearing and finite bin width. There is an additional scale uncertainty arising from the measurement of the beam polarization.

4 Summary

The HERMES Collaboration continued analysis of data which were collected in 1996-2007. Due to a lack of space, two subjects only are presented in this review, studies of the TMDs and the DVCS.

The studies of the various azimuthal asymmetries in SIDIS at HERMES allows to make a number of conclusions on the TMDs: i) the transverity h_1 and the Sivers $f_{1T}^{\perp}$ TMDs are different from zero (published); ii) the Collins FF $H_1^{\perp}$ is different from zero (published); iii) there is an indication that Boer-Mulders TMD $h_1^{\perp}$ may be non-zero; iv) the worm-gear TMD $g_{1T}^{\perp}$ is small but may be non-zero; v) the azimuthal asymmetries induced due to the pretzelocity TMD and due to the worm-gear TMD are consistent with zero within experimental uncertainties.

The variety of experimental setups used by HERMES (positive/negative lepton beam, positive/negative polarization of the beam, unpolarized or longitudinally/transversely polarized target) enabled the extraction of many asymmetry amplitudes.

First results with using of Recoil detector information were obtained. Basically, the results are compatible with those obtained without Recoil detector information. There is, however, an indication that the *pure* elastic amplitude is larger in magnitude with respect to what was obtained without Recoil detector. This could be related to an asymmetry from the associated DVCS process and is under study.

Acknowledgments. I wish to thank my colleagues in the HERMES collaboration. I thank the DSPIN-2011 Organising Committee for the financial support.

References

[1] A. Airapetian et al., Phys.Rev. **D75** (2007) 012007.
[2] A. Airapetian et al., JHEP **1008** (2010) 0130.
[3] K. Ackerstaff et al., NIM **A 417** (1998) 230.
[4] A. Bacchetta et al., JHEP **0702** (2007) 093.
[5] H. Avakian, A.V. Efremov, P. Schweitzer, and F. Yuan Phys.Rev. D **78** (2008) 114024.
[6] A. Airapetian et al., Phys.Rev.Lett. **103** (2009) 152002.
[7] A. Airapetian et al., Phys.Lett. **B693** (2010) 11.
[8] D.L. Adams et al., Phys.Lett. **B261** (1991) 201.
[9] A.V. Belitsky, D. Müller, A. Kirchner, Nucl.Phys. **B629** (2002) 323.
[10] A. Airapetian et al., JHEP **0911** (2009) 083.
[11] A. Airapetian et al., Nucl.Phys. **B829** (2010) 1.
[12] A. Airapetian et al., JHEP **1006** (2010) 019.
[13] A. Airapetian et al., Nucl.Phys. **B842** (2011) 265.
[14] A. Airapetian et al., JHEP **0806** (2008) 066.
[15] A. Airapetian et al., Phys.Lett. **B704** (2011) 15.

HARD EXCLUSIVE REACTIONS AT JLAB

Valery Kubarovsky
For the CLAS Collaboration

Jefferson Laboratory, Newport News, VA, USA

Abstract

Dedicated experiments to study Deeply Virtual Compton Scattering (DVCS) and Deeply Virtual Meson Production (DVMP) have been carried out at Jefferson Lab. DVCS helicity–dependent and helicity–independent cross sections and beam spin asymmetries have been measured, as well as cross sections and asymmetries for the π^0, η, ρ^0, ρ^+, ω and ϕ for exclusive electroproduction. The data were taken in a wide kinematic range in Q^2=1–4.5 GeV^2, x_B=0.1–0.5, and $|t|$ up to 2 GeV^2. The presented results offer a unique opportunity to study the structure of the nucleon at the parton level as one has access to Bjorken x_B and momentum transfer to the nucleon t at the same time.

1 Introduction

The mapping of the nucleon's structure in terms of the Generalized Parton Distributions (GPDs) is one of the major objectives of Jefferson Lab. The GPDs give access to the complex internal structure of the nucleon, such as correlations between parton transverse spatial and longitudinal momentum distributions. They provide a unified picture of the nucleon form factors, polarized and unpolarized parton distributions, and provide access to the contribution of the total parton angular momentum to the nucleon spin. There are four chiral-even GPDs, denoted H^q, $\tilde{H}^q$, E^q and $\tilde{E}^q$, and four chiral-odd GPDs, H_T^q, $\tilde{H}_T^q$, E_T^q and $\tilde{E}_T^q$, which depend on three kinematic variables: x, ξ and t. x is the average momentum fraction and ξ (skewness) is half the difference between the initial and final fractions of the momentum carried by the struck parton. The skewness can be expressed in terms of the Bjorken variable x_B as $\xi \simeq x_B/(2-x_B)$. t is the momentum transfer to the nucleon, $t = (p - p')^2$, where p and p' are the initial and final momentum of the nucleon. The H^q and E^q conserve nucleon helicity, while $\tilde{H}^q$ and $\tilde{E}^q$ are associated with a change in nucleon helicity. In the forward limit, $t \to 0$, H^q and $\tilde{H}^q$ are reduced to the parton density distributions $q(x)$ and parton helicity distributions $\Delta q(x)$. The forward limit of H_T^q is the transversity h_1^q. The first moments of the GPDs are related to the elastic form factors of the nucleon: Dirac form factor $F_1^q(t)$, Pauli form factor $F_2^q(t)$, axial-vector form factor $g_A^q(t)$ and pseudoscalar form factor $h_A^q(t)$.

Schematic diagrams for Deeply Virtual Compton Scattering (DVCS) and Deeply Virtual Meson Production (DVMP) in the GPD, or handbag, framework are illustrated in Fig. 1. The cross section depends actually on the Compton form factors (CFF) and they are the quantities that can be extracted from DVCS and DVMP experiments. In the leading twist, CFFs depend only on ξ (or x_B) and momentum transfer t. Although DVCS is the cleanest way of accessing GPDs there is no possibility to separate flavors using only this process. The variety of DVMP channels allows one to separate flavor and have access to the polarized quark/antiquark densities in the limit of momentum transfer $t \to 0$.

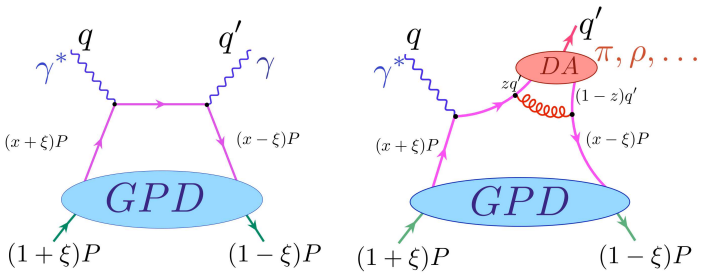

Figure 1: Schematic illustration of the GPD approach to DVCS (left) and DVMP (right).

2 Deeply virtual Compton scattering

CLAS has published DVCS beam-spin asymmetries (BSA) [1,2] and longitudinally polarized target asymmetries [3]. By fitting CLAS data in a largely model-independent way, the imaginary parts of the two Compton Form Factors $Im(\tilde{\mathcal{H}})$ and $Im(\mathcal{H})$ were extracted with uncertainties on the order of 30% [4]. In the framework of the dominance of the generalized parton distribution H and twist-2 accuracy, both real and imaginary parts of the Compton Form Factor $\mathcal{H}$ were extracted [5]. In addition to the CLAS data, helicity-independent and helicity-dependent DVCS cross sections were used in this analysis [6]. This is the first attempt to get access to the GPDs from experimental data. The CLAS group is now working on the determination of the absolute DVCS cross sections in a wide kinematic region. The preliminary data are shown in Fig. 2 for six kinematic points. Note the clear signature of the DVCS contribution above the Bethe-Heitler background.

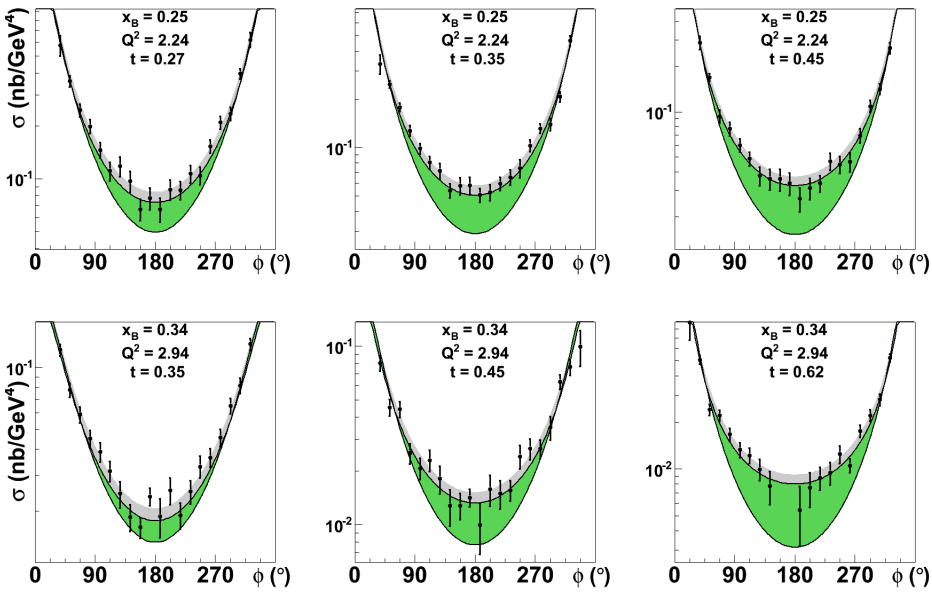

Figure 2: Preliminary DVCS cross section as a function of the angle ϕ for a few of the many kinematic bins in Q^2, x_B ant t. The lower black curves are due to a pure BH calculation, the upper curves are fits to the data – the differences are represented in green. Top: $Q^2 = 2.24$ GeV^2, $x_B = 0.25$, $-t$ =0.27, 0.35 and 0.45 GeV^2. Bottom: $Q^2 = 2.94$ GeV^2, $x_B = 0.34$, $-t$ =0.35, 0.45 and 0.62 GeV^2.

3 Pseudoscalar π^0 and η meson electroproduction

The reactions $ep \to e'p'\pi^0$ and $ep \to e'p'\eta$ were measured with the CLAS spectrometer at a beam energy of about 6 GeV [7, 8]. The pions and etas are identified through their 2γ decay channels. This has been made possible by constructing a high quality electromagnetic calorimeter consisting of 424 lead-tungsten crystals covering an angular range from 4.5° to 15°, which was positioned into the existing CLAS large acceptance detector.

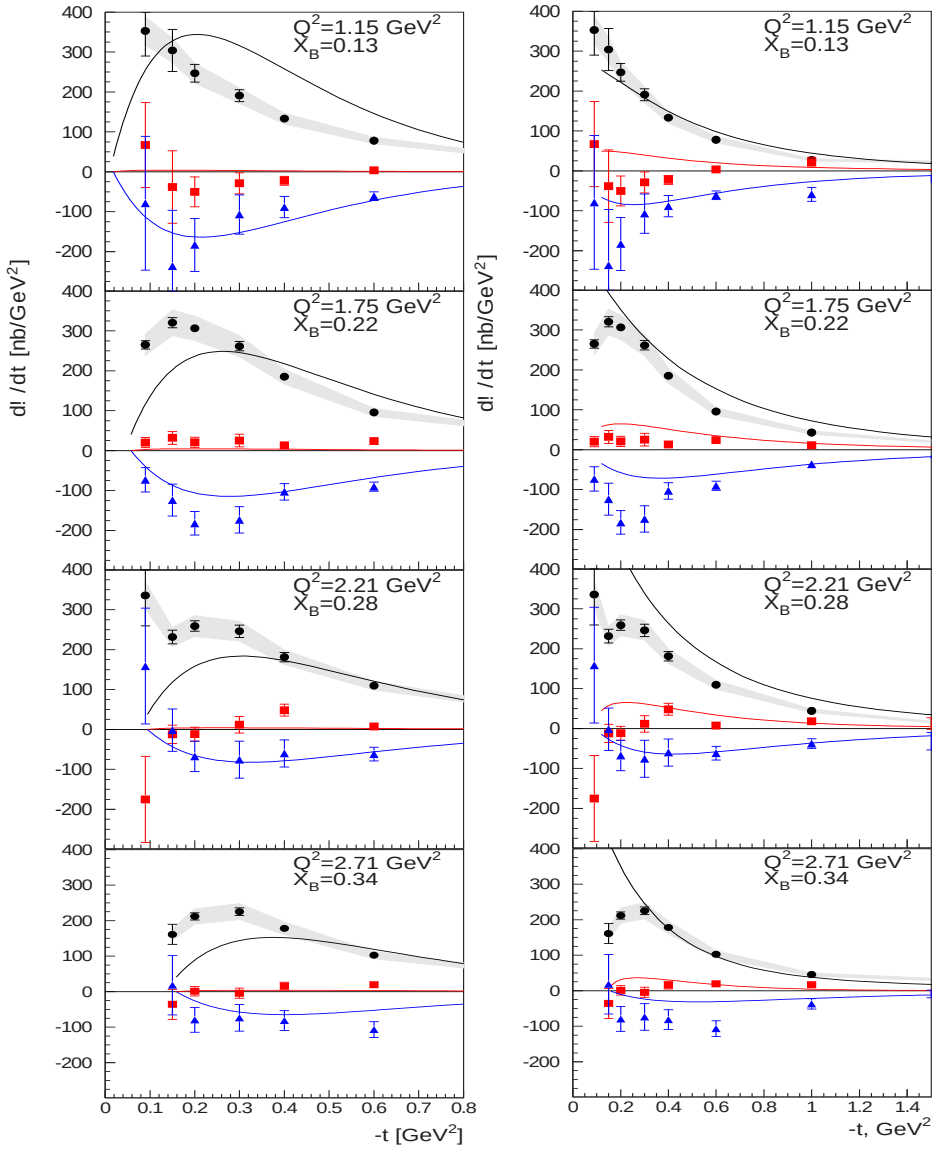

Figure 3: Extracted structure functions vs t for 4 of the 17 experimental kinematic bins (CLAS, preliminary). The data and curves are noted for $(d\sigma_T/dt + \epsilon d\sigma_L/dt)$-black, $d\sigma_{TT}/dt$ - blue, and $d\sigma_{TL}/dt$ - red, as defined in the text. The shaded bands reflects the experimental systematic uncertainties. On the left the data are compared with the model of Ref. [9] and on the right with that of [10].

The virtual photon cross section can be written as

$$2\pi\frac{d\sigma}{dtd\phi} = \sigma_T + \epsilon\sigma_L + \epsilon\sigma_{TT}\cos 2\phi + \sqrt{2\epsilon(1+\epsilon)}\sigma_{LT}\cos\phi_\pi + h\sqrt{\epsilon(1-\epsilon)}\sigma_{LT'}\sin\phi, \quad (1)$$

where ϕ denotes the azimuthal angle between the hadronic and leptonic scattering planes and h is the electron beam polarization.

The structure functions $\sigma_T + \epsilon\sigma_L$, σ_{TT}, and σ_{LT} as a function of $-t$ were obtained from fits to the differential cross section data for 17 intervals in Q^2 and x_B. Four out of 17 bins are presented in Fig. 3. The results of two GPD-based models [9, 10] are also superimposed in Fig. 3. For clarity, the data on the left in the figure is repeated on the right in the respective ranges of the calculations.

The longitudinal cross section $d\sigma_L/dt$, which is helicity conserving, is:

$$\frac{d\sigma_L}{dt} = \frac{4\pi\alpha_e}{\kappa Q^2}[(1-\xi^2)|\langle\tilde{H}\rangle|^2 - 2\xi^2 Re(\langle\tilde{H}\rangle\cdot\langle\tilde{E}\rangle) - \frac{t'}{4m^2}\xi^2|\langle\tilde{E}\rangle|^2], \quad (2)$$

where κ is a phase space factor and the brackets $\langle\tilde{H}\rangle$ and $\langle\tilde{E}\rangle$ denote the convolution of the hard kernel and GPDs $\tilde{H}$ and $\tilde{E}$

$$\langle\tilde{H}\rangle = \sum_\lambda \int_{-1}^{1} dx\mathcal{H}_{0\lambda,0\lambda}\tilde{H} \qquad \langle\tilde{E}\rangle = \sum_\lambda \int_{-1}^{1} dx\mathcal{H}_{0\lambda,0\lambda}\tilde{E} \quad (3)$$

without the Q^2 dependence which has been explicitly factored out for clarity.

The GPDs occur in the combination $F = (e_u F^u - e_d F^d)/\sqrt{2}$ for π^0 [9] . Since GPDs $\tilde{H}$, $\tilde{E}$ and H_T have opposite signs for u and d quarks there is a partial cancellation of the up and down quark GPDs entering the leading twist structure function (σ_L). This is not the case for $\bar{E}_T$ which contributes to σ_T and σ_{TT}. In addition the transverse cross sections are strongly enhanced by the chiral condensate through the parameter $\mu_\pi = m_\pi^2/(m_u + m_d)$, where m_u and m_d are current quark masses [9].

Thus, the contribution $d\sigma_L/dt$ in both calculations account for only a small fraction of the combined $d\sigma_T/dt + \epsilon d\sigma_L/dt$ in the kinematic regime under investigation. The inclusion of the quark helicity non-conserving GPDs, which involve the transverse contributions, primarily $d\sigma_T/dt$ and $d\sigma_{TT}/dt$, and to a smaller extent $d\sigma_{LT}/dt$ account rather well for the data. The contributions from transverse polarized photons were calculated as a twist-3 effect consisting of a twist-3 pion wave function and primarily the GPDs H_T and $\bar{E}_T(= 2\widetilde{H}_T + E_T)$, as follows:

$$\frac{d\sigma_T}{dt} = \frac{4\pi\alpha_e}{2\kappa}\frac{\mu_\pi^2}{Q^4}[(1-\xi^2)|\langle H_T\rangle|^2 - \frac{t'}{8m^2}|\langle\bar{E}_T\rangle|^2] \quad (4)$$

and

$$\frac{d\sigma_{TT}}{dt} = \frac{4\pi\alpha_e}{8\kappa}\frac{\mu_\pi^2}{Q^4}\frac{t'}{4m^2}|\langle\bar{E}_T\rangle|^2 \quad (5)$$

where

$$\langle H_T\rangle = \int dx\mathcal{H}_{0-,++}H_T,\ \langle\bar{E}_T\rangle = \int dx\mathcal{H}_{0-,++}\bar{E}_T \quad (6)$$

For π^0 electroproduction, $\mathcal{H}_{\mu'\lambda',\mu\lambda}$ is a convolution of a hard $\gamma q \to \pi q$ process amplitude $\mathcal{F}^P_{\mu'\lambda',\mu\lambda}$, with the pion wave function $\hat{\Psi}(\tau, \mathbf{b})$ taking into account transverse spatial and momentum fractions $\mathbf{b}$, and τ respectively

$$\mathcal{H}_{\mu'\lambda',\mu\lambda} = \int d\mathbf{b} d\tau \hat{\Psi}(\tau, \mathbf{b}) \mathcal{F}_{\mu'\lambda',\mu\lambda} \alpha_s e^{-S(\tau,\mathbf{b},Q^2)}. \quad (7)$$

A Sudakov form factor $exp[-S(\tau, \mathbf{b}, Q^2)]$ corrects for the soft gluon radiation from the transverse quark momenta and positions.

The result, shown in Fig. 3 gives a very large increase in $\sigma_T + \epsilon\sigma_L$, primarily due to $\bar{E}_T$ and H_T, which accounts rather well for the experimental data, the greatest difficulties ocurring as one approaches smaller $-t$. The calculated interference structure functions σ_{TT} and σ_{LT} also are in approximate accord with the data.

The presented results appear to provide compelling evidence for the the dominance of quark helicity-flip processes in π^0 electroproduction. Exclusive pseudoscalar meson electroproduction appear to be unique process which are directly related with the transversity GPDs $\bar{E}_T$ and H_T.

t-slopes and Transverse Spatial Structure

The electroproduction cross sections as a function of t can be expressed according to the following form: $d\sigma/dt \propto e^{B(x_B,Q^2)t}$. The t slope parameter $B(x_B, Q^2)$ is plotted as a function of x_B for various values of Q^2 in Fig. 4. The fact that the t-slope goes to zero for large x_B may be purely kinematical. However, even taking this into account, we note that $B_\perp$ falls with x_B in the region x_B from 0.1 to 0.5 where we have experimental data. This implies that the impact parameter spatial distribution is broadest at lowest x_B and becomes narrower at increasing x_B.

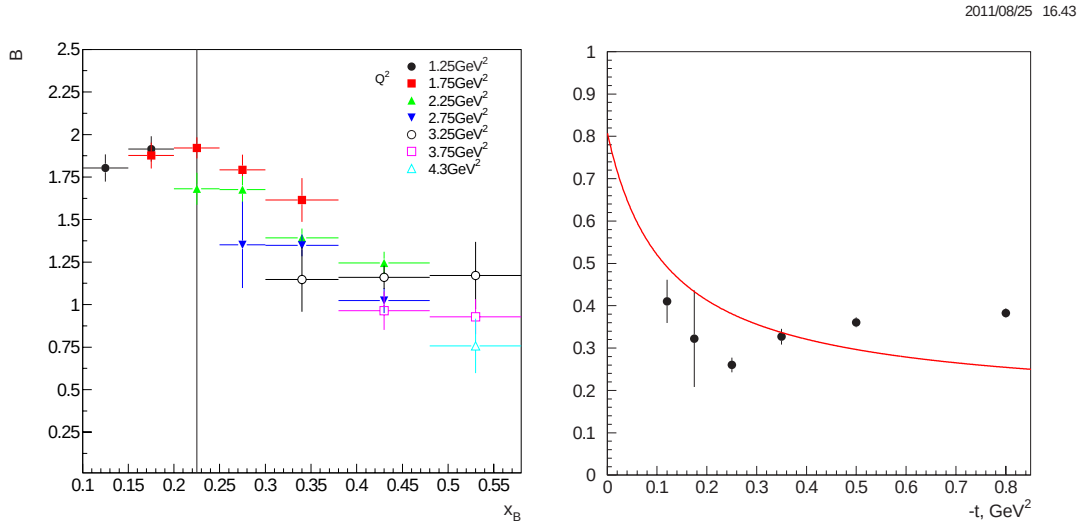

Figure 4: Left panel: the experimental t-slope parameters (CLAS, preliminary) obtained from fits to the data for various values of Q^2 and x_B. Right panel: the η/π^0 cross section ratio as a function of $-t$. Data points are from CLAS (preliminary) [7] and the curve is from the Ref. [9].

The ratio of cross sections for η and π^0

Even though current experiments are limited in Q^2 and t, it has been argued [11] that *precocious factorization* ratios of cross sections as a function of x_B could be valid at relatively lower Q^2 than for the cross sections themselves. The ratio of cross sections for π^0 and η electroproduction from a proton, averaged over x_B and Q^2, is presented in Fig. 4 as a function of t. This ratio is almost independent of x_B and Q^2 and varies from 0.3 to 0.4 with increasing t [7]. The GPD model [9] is in rather good agreement with CLAS data, which can be regarded as an indication of large contributions from the transverse GPDs. We note that the GPD prediction [9] for the η/π^0 ratio at very low t is in agreement with an estimate presented in [11].

Taking into account the good description of CLAS data by GPD models we can make a conclusion that pseudoscalar meson production provides a unique possibility to access the transversity GPDs.

4 Vector mesons electroproduction

The CLAS collaboration has already published the cross sections for the vpk : ρ^0 [12], ω [13] and ϕ [14]. For the ρ^+ channel, the first–ever measurement of its cross section was recently obtained [15]. The total longitudinal cross section $\sigma_L(\gamma^* p \to p\rho^0)$ as a function of W for fixed Q^2 is successfully described by the Regge-based model [16] for almost all of our (Q^2, W) range (see Ref. [17] for details).

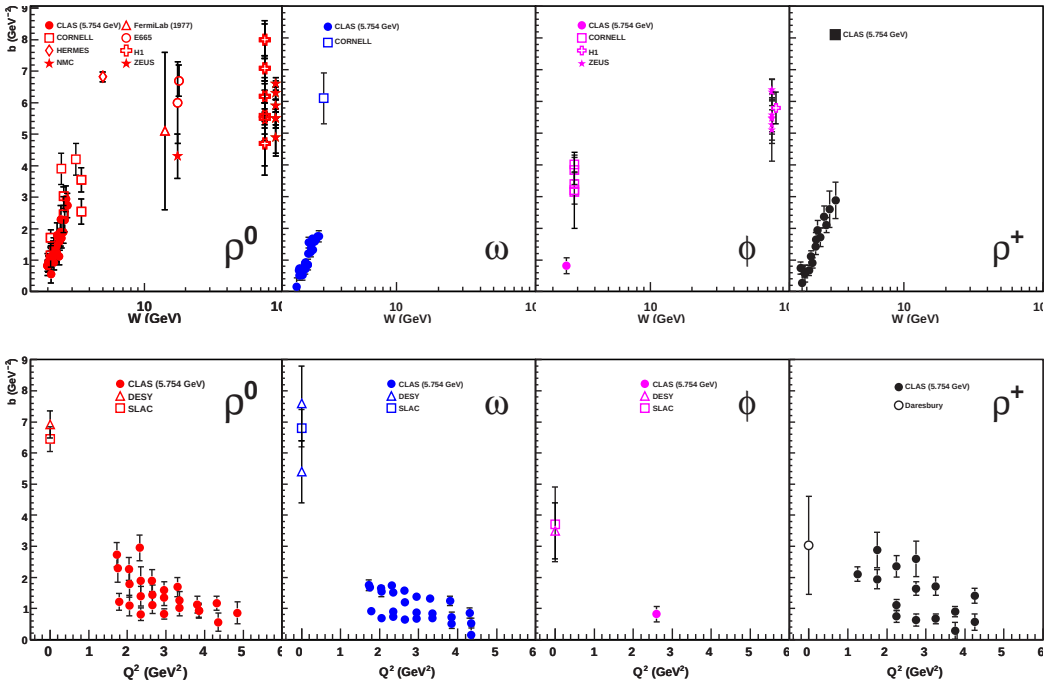

Figure 5: The t-slope parameter as a function of W (on the top) and as a function of Q^2 (on the bottom) for the ρ^0, ω, ϕ and ρ^+ channels.

The GPD models [18, 19] give a good description of the high and intermediate W

region, down to $W \sim 5$ GeV. At high W, the slow rise of the cross section is due to the gluon and sea contributions, while the valence quarks contribute only at small W. At lower W values, where the new CLAS data lie, both GPD models fail to reproduce the data. This discrepancy can reach an order of magnitude at the lowest W values. The trend of these particular GPD calculations is to decrease as W decreases, whereas the data increase. The same behavior was observed in the low W region for the exclusive electroproduction of the ρ^+. An attempt to reconcile the GPD calculation with the low W ρ^0 cross sections is presented in Ref. [17].

Comparison of the t slopes for the ρ^0, ω, ϕ and ρ^+ channels

Fig. 5 shows the slope of the differential cross section $d\sigma/dt$ for the ρ^0, ω, ϕ and ρ^+ channels as a function of W (on the top part) and as a function of Q^2 (in the bottom part). One can see the same trends of the slopes for all meson channels, which can be interpreted in simple and intuitive terms in the following way:

- The slope increases with W: the size of the reaction region increases as one probes the high W values (i.e. the sea quarks), which could mean that the sea quarks tend to extend to the periphery of the nucleon.
- The slope decreases with Q^2: as we go to large Q^2, the resolution of the probe increases and the reaction region becomes smaller and smaller.

5 Conclusion

Cross sections and asymmetries for γ, π^0, η, ρ^0, ρ^+, ω and ϕ exclusive electroproduction in a wide kinematic range of Q^2, t and x_B have been measured with CLAS and initial analyses already are showing remarkable results. The successful description of the CLAS pseudoscalar meson production data by GPD models opens a unique opportunity to access the transversity in the deeply exclusive reactions. We view the work presented here as leading into the program of the Jefferson Lab 12 GeV upgrade. The increased energy and luminosity will allow us to extend the analysis presented here at much higher Q^2 and x_B, as well as to perform Rosenbluth L/T separations.

We acknowledge the outstanding efforts of the staff of the Accelerator and Physics Divisions at Jefferson Lab that made this experiment possible. We also acknowledge useful discussions with G. Goldstein, S. Goloskokov, P. Kroll, J-M. Laget, S. Liuti, and A. Radyushkin. This work was supported by the U.S. Department of Energy and National Science Foundation. The Jefferson Science Associates (JSA) operates the Thomas Jefferson National Accelerator Facility for the United States Department of Energy under contract DE-AC05-06OR23177.

References

[1] S. Stepanyan et al., Phys. Rev. Lett. **87**:182002 (2001).
[2] F.-X. Girod et al., Phys. Rev. Lett. **100** :162002 (2008).
[3] S. Chen et al., Phys. Rev. Lett. **97**:072002 (2006).

[4] M. Guidal, Phys. Lett. B **689**,156 (2010).
[5] H. Moutarde, Phys. Rev. D **79**:094021 (2009).
[6] C. Munoz Camacho et al., Phys. Rev. Lett. **97**:262002 (2006).
[7] V. Kubarovsky et al. [arXiv:hep-exp/0802.1678].
[8] R. De Masi et al., Phys. Rev. C **77**:042201 (2008).
[9] S.V. Goloskokov and P. Kroll, Eur. Phys. J. **C65**, 137-151 (2010). S.V. Goloskokov and P. Kroll, Eur. Phys. J. **A47**, 112 (2011).
[10] G. R. Goldstein, J. O. Gonzalez Hernandez and S. Liuti, in preparation. G. R. Goldstein, J. O. Gonzalez Hernandez and S. Liuti, Phys. Rev. **D84**, 034007 (2011).
[11] M. I. Eides, L. L. Frankfurt and M. I. Strikman, Phys. Rev. D **59**, 114025 (1999).
[12] S. Morrow et al., Eur. Phys. J. A **39**, 5 (2009).
[13] L. Morand et al., Eur. Phys. J. A **24**, 445 (2005).
[14] J. P. Santoro et al., Phys. Rev. C **78**, 02510 (2008) .
[15] A. Fradi, thesis Univ. Paris-Sud at Orsay, 2009, [arXiv:hep-ph/1010.1198, hep-ph/1109.3775].
[16] J.-M. Laget, Phys. Lett. B **489**, 313 (2000);
F. Cano and J.-M. Laget, Phys. Rev. D **65**, 074022 (2002);
J. M. Laget, Phys. Rev. D **70**, 054023 (2004);
F. Cano and J. M. Laget, Phys. Lett. B **551**, 317 (2003).
[17] M. Guidal and S. Morrow, *Proceeding of the International Workshop "Exclusive reactions at high momentum transfer", Jefferson Laboratory, Newport-News, Virginia, USA, May 21-24 2007*, World Scientific, [arXiv:hep-ph/0711.3743].
[18] S.V. Goloskokov and P. Kroll, Eur. Phys. J.C **42**, (2005) 281; Eur.Phys. J.C **50**, 829 (2007).
[19] M. Vanderhaeghen, P.A.M. Guichon, and M. Guidal, Phys. Rev. D **60**, 094017 (1999).

GLUON POLARISATION IN THE NUCLEON FROM HIGH TRANSVERSE MOMENTUM HADRON PAIRS AT COMPASS

Krzysztof Kurek [1 †]

(1) *National Centre for Nuclear Research*
(2) *On behalf of the COMPASS Colaboration*
† *E-mail: kurek@fuw.edu.pl*

Abstract

The one of the main goals of the COMPASS spin physics programme is the measurement of the contribution of gluons to the nucleon spin. The gluon polarisation is determined from the longitudinal spin asymmetry in production of hadrons by 160 GeV/c polarised muons scaterred off a polarised nucleon target. The gluon polarisation is accessible by the selection of photon-gluon fusion events. The well-known method to identify PGF is selecting high-p_T hadron pairs in the final state. The new $\Delta G/G$ result for the complete $2002 - 2006$ COMPASS data set of high transverse momentum hadron pairs with $Q^2 > 1(\mathrm{GeV/c})^2$ is presented. A weighted method based on an Artificial Neural Network has been used. For the first time the gluon polarisation in three bins of x_G is shown.

1 Introduction

The COMPASS is a fixed target experiment at CERN laboratory. One of its goals is the direct measurement of the gluon polarization, important for understanding the spin structure of the nucleon. The experiment is using a 160 GeV polarised muon beam from SPS at CERN scattered off a polarized ^{6}LiD target [1].

In LO QCD approximation the only subprocess which probes gluons inside nucleon is a Photon-Gluon Fusion (PGF). There are two ways allowing direct access to gluon polarisation via the PGF subprocess available in the COMPASS experiment: the open-charm channel where the events with reconstructed D^0 mesons are used and the production of two hadrons with relatively high-p_T in the final state. The estimation of the gluon polarisation in the open-charm channel is much less Monte-Carlo (MC) dependent than in the high-p_T hadrons method, where the complicated background requires very good MC description of the data. On the other hand the statistical precision in high-p_T hadrons method is much higher than in the open charm channel. To increase statistical precision the statistically weighting method has been used. The Artificial Neural Network approach (ANN) was applied to built the statistical weights.

2 Gluon polarisation from events with high-p_T hadrons

The idea that the selection of events with high-p_T hadrons enhances the fraction of PGF events in the sample has been first time discussed in [2] and then revised in [3]. An

estimation of $\Delta G/G$ needs to know contributions from other processes and this makes the analysis model (Monte Carlo) dependent. This kind of analysis has been already performed before by the HERMES and the SMC experiments. Depending on the kinematic region covered by the data, two models based on Monte Carlo generators were used: PYTHIA at low Q^2 (HERMES [4] and COMPASS [5]), and LEPTO for $Q^2 > 1$ (GeV/c)^2 (SMC [6]). The new COMPASS result for large Q^2 is presented in this article.

The helicity asymmetry for two high-p_T hadrons can be expressed in the following way:

$$A_{LL}^{2h} = R_{PGF} a_{LL} \frac{\Delta G}{G} + A_{Bkg.}, \tag{1}$$

where a_{LL} and R_{PGF} are the analyzing power and the fraction of the PGF subprocess (estimated from MC) and A_{Bkg} denotes the asymmetry from different background processes which contribute to the observed two hadron final state. For large Q^2 these background processes are LO DIS and QCD-Compton. Taking into account that the inclusive asymmetry can also be decomposed in the same way the final formula for the gluon polarization can be schematically written as follows:

$$\Delta G/G \;=\; \frac{A_{LL}^{2h} + A^{corr}}{\beta}, \tag{2}$$

where A^{corr} is a combination of the inclusive asymmetry A_1 with some coefficients which together with β depend on the analyzing powers and the fractions of the background processes in the high-p_T as well as in the inclusive sample. The situation becomes more complicated in the case of low Q^2 region where additional background processes have to be taken into account [5]. To increase the statistical precision of the gluon polarisation measurement a weighting method of asymmetry extraction was used. The weight is $fDP_b\beta$, where f and D are the dilution and the depolarization factors, respectively, P_b is the beam polarisation. The weight has to be known on the event by event basis. Only f, D and P_b are calculated from data; β has to be obtained from MC. An ANN [7] trained on MC samples was used for the parametrization of the quantities which define β (fractions and a_{LL} for different subprocesses). As an input to the ANN training for the inclusive sample, x_{Bj} and Q^2 were selected, while for the high-p_T sample in addition transverse and longitudinal momenta of the two hadrons were used. This method depends largely on MC. Good data description with the MC as well as good ANN parameterizations are "key points" of this analysis.

3 Data selection, MC and ANN parameterizations

The data used in the analysis were collected in 2002-2006 years. An incoming, a scattered muon and an interaction vertex in the target were required for each event. The kinematic cuts $0.1 < y < 0.9$ and $Q^2 > 1$ (GeV/c)^2 were used. The latter cut ensures that the scale of the hard process is high enough and pQCD can be used. At least two charged hadrons in the interaction vertex with transverse momenta greater than 0.7 GeV/c and 0.4 GeV/c for leading and second hadrons respectively, are required. In addition the sum of the energy fraction of the two hadrons $z_1 + z_2 < 0.95$ is required. The total number of selected events is about 7.3 million. The LEPTO generator and the full simulation of the COMPASS spectrometer were used. To improve the data and MC agreement

some LEPTO parameters were tuned (k_T and parameters of fragmentation). Standard LEPTO tuning was used for systematic studies. In figure 1 examples of the data and MC comparison are shown for the momenta, transverse momenta of the hadrons and hadron multiplicity.

The comparison between standard and tuned LEPTO is also shown. We observe good agreement between data and MC, also the necessity for LEPTO tuning is clearly visible. An example of the quality of the ANN parametrization is given in figure. 2. It shows the probability of the DIS, QCD-Compton and PGF processes as a function of $\sum p_T^2$ for the MC and for the parametrization given by the ANN. Good agreement is observed. While the DIS probability reduces with p_T (p_{T_1}, p_{T_2} and $\sum p_T^2$), the QCD-Compton and PGF become the more significant contributions.

4 Systematic studies

The main contribution to the systematic error comes from the MC. In total, seven MC samples were generated with different combinations of fragmentation tuning. They consisted in default LEPTO or COMPASS tuning, parton shower (PS) on and off options, different choices of the PDFs and with different $R = \sigma_L/\sigma_T$ parametrization. The uncertainty of $\Delta G/G$ due to choice of A_1^d parameterization and stability of the ANN results were found to be small, $\delta(\Delta G/G)_{A_1^d} = 0.015$ and $\delta(\Delta G/G)_{NN} = 0.010$ respectively. The uncertainties of f, P_b, and P_t have an even smaller impact on the final result: $\delta(\Delta G/G)_{f,P_b,P_t} = 0.004$. The experimental false asymmetries appear if the acceptance ratio of the neighbouring cells is different for the data taken before and after the field reversal. They were searched for in a sample in which cuts on transverse momenta of the hadrons were lowered to $p_{T_{1,2}} > 0.35$ GeV and $Q^2 > 0.7$ GeV^2. This lead to a large increase in statistics and allowed more precise studies of the spectrometer stability. False asymmetries exceeding the statistical error were not found. Taking this error as a limit for the false asymmetries one obtains $\delta(\Delta G/G)_{false} = 0.019$. Finally the simplifications

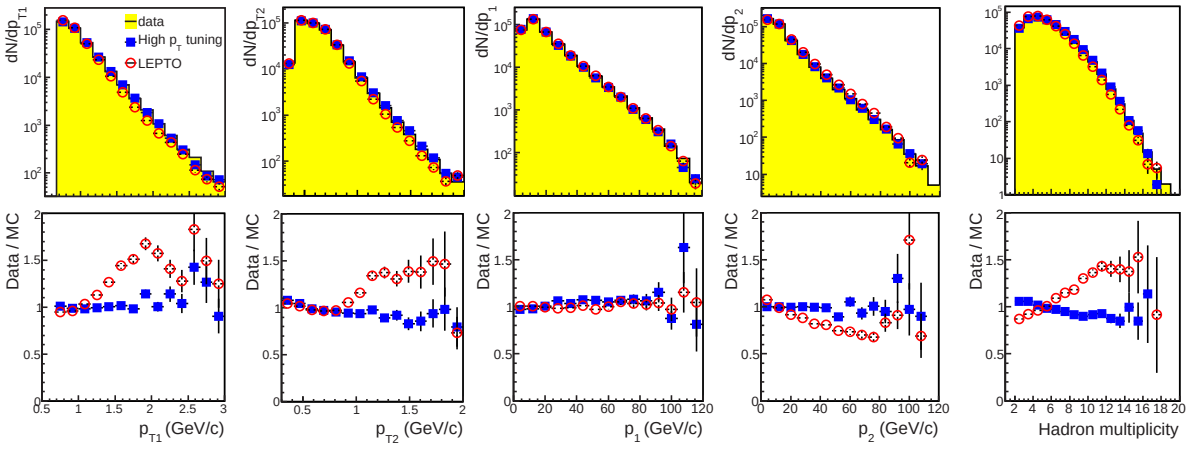

Figure 1: Comparison between data (histogram) and MC simulations using COMPASS tuning (full squares) and default LEPTO tuning (open circles), in terms of distributions and Data/MC ratios for the hadronic variables: p_{T_1}, p_{T_2}, p_1, p_2 and the hadron multiplicity, normalized to the number of events.

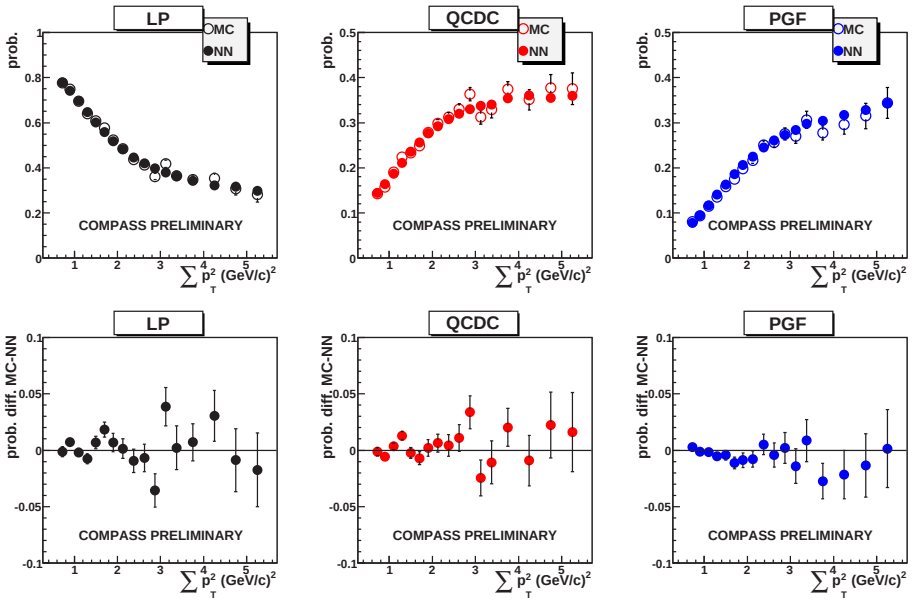

Figure 2: ANN parameterization and MC results comparison for fractions R_{PGF}, R_{QCDC}, R_{LP} in bins of $\sum p_T^2$.

and approximations used in the formula 2 leads to the error $\delta(\Delta G/G)_{form} = 0.035$ The

	total	bin 1	bin 2	bin 3
$\delta(\Delta G/G)_{MC}$	0.045	0.077	0.067	0.129
$\delta(\Delta G/G)_{A1^d}$	0.015	0.021	0.014	0.017
$\delta(\Delta G/G)_{NN}$	0.010	0.010	0.010	0.010
$\delta(\Delta G/G)_{f,P_b,P_t}$	0.004	0.007	0.007	0.010
$\delta(\Delta G/G)_{false}$	0.019	0.023	0.016	0.012
$\delta(\Delta G/G)_{form}$	0.035	0.026	0.039	0.057
TOTAL	0.063	0.088	0.081	0.143

Table 1: Summary of the systematic contributions.

contributions to the systematic uncertainty and their quadratic sum are presented in Table 1. They were also evaluated in three x_G bins defined below (see Table 2). The total systematic uncertainty of the $\Delta G/G$ results is estimated to be 0.063, which is slightly larger than the statistical error.

5 Results

The preliminary result for $\Delta G/G$ from high transverse momentum hadron pairs for large Q^2 ($Q^2 > 1$ (GeV/c)^2) is:

$$\Delta G/G = 0.125 \pm 0.060(stat.) \pm 0.063(syst.), \tag{3}$$

at $x_G = 0.09$ and hard scale $\mu^2 = 3$ GeV^2 .

The data cover the range $0.04 < x_G < 0.27$ and have been divided into three statistically independent subsamples by cuts on the x_G variable parameterised by the ANN. . The correlation between the generated and the parameterised x_G is about 62% As a consequence, the division leads to three x_G bins which have different mean values but a large overlap. The results, listed in Table 2, provide no evidence for any signicant dependence of $\Delta G/G$ on x_G.

	total	bin 1	bin 2	bin 3
x_G mean	$< x_G >= 0.09$	$< x_G >= 0.07$	$< x_G >= 0.10$	$< x_G >= 0.17$
x_G range	$0.04 < x_G < 0.27$	$0.04 < x_G < 0.12$	$0.06 < x_G < 0.17$	$0.11 < x_G < 0.27$
$\Delta G/G$	0.125 ± 0.060	0.147 ± 0.091	0.079 ± 0.096	0.185 ± 0.165

Table 2: Summary of the $\Delta G/G$ results.

The new result is also in very good agreement with $\Delta G/G$ obtained for the low Q^2 high-p_T analysis of 2002-2004 data: $\Delta G/G = 0.016 \pm 0.058(stat.) \pm 0.055(syst.)$ at $x_G \simeq 0.085^{+0.07}_{-0.035}$ and scale $\mu^2 \simeq 3$ (GeV/c)^2.

6 Summary

In conclusion, a direct measurement of the gluon polarisation extracted in the LO approximation has been performed on all COMPASS data taken with longitudinal polarised ^{6}LiD target. $\Delta G/G$ is extracted at from a large sample of DIS events with $Q^2 > 1$ GeV^2, including a high-p_T hadron pair, by a method based on the Neural Networks. This approach increased the statistical precision of the result by almost a factor two with respect to the standard method in which a set of cuts is applied to $p_{T_{1,2}}$ to optimize $\delta(\Delta G/G)$. For the first time the gluon polarisation was evaluated in three intervals of the fractional gluon momentum.

This work was supported by Polish Ministry of Science and Higher Education grant 41/N-CERN/2007/0.

References

[1] P.Abbon et al.,Nucl. Instr. Meth. **A** 577 (2007) 455.

[2] R.D.Carlitz, J.C.Collins, A.H.Mueller, Phys. Lett. **B** 214 (1988) 229.

[3] A.Bravar, D.von Harrach, A.Kotzinian, Phys. Lett. **B** 421 (1998) 349.

[4] HERMES Collab. A. Airapetian *et al.*, Phys. Rev. Lett. **84** (2000) 2584; A. Airapetian *et al.*, JHEP **08** (2010) 130.

[5] COMPASS Collab., E. Ageev *et. al.,*, Phys. Lett. **B** 633 (2006) 25.

[6] SMC, B.Adeva *et al.,* Phys. Rev.**D** 70 (2004) 012002.

[7] R. Sulej et al.,Meas. Sci. Tech.**18** (2007) 2486.

THE LIGHT NUCLEI SPIN STRUCTURE FROM THE HADRONIC INTERACTIONS AT INTERMEDIATE ENERGIES

P.K. Kurilkin[1†], V.P. Ladygin[1], T. Uesaka[2], V.V. Glagolev[1], Yu.V. Gurchin[1], A.Yu. Isupov[1], K. Itoh[3], M. Janek[1,4], J.-T. Karachuk[1,5], T. Kawabata[2], A.N. Khrenov[1], A.S. Kiselev[1], V.A. Kizka[1], A.B. Kurepin[6], A.K. Kurilkin[1], V.A. Krasnov[1,6], N.B. Ladygina[1], D. Lipchinski[5], A.N. Livanov[1,6], Y. Maeda[7], A.I. Malakhov[1], G. Martinska[8], S. Nedev[9], S.M. Piyadin[1], E.B. Plekhanov[1], J. Popovichi[5], S. Rangelov[9], S.G. Reznikov[1], P.A. Rukoyatkin[1], S. Sakaguchi[10], H. Sakai[3,11], K. Sekiguchi[10], M.A. Shikhalev[1], K. Suda[10], A.A. Terekhin[1,12], J. Urban[8], T.A. Vasiliev[1] and I.E. Vnukov[12]

(1) *Joint Institute for Nuclear Research, Dubna, Russia*
(2) *Center for Nuclear Study, University of Tokyo, Tokyo, Japan*
(3) *Department of Physics, Saitama University, Urawa, Japan*
(4) *Physics Department, University of Zilina, Zilina, Slovakia*
(5) *Advanced Research Institute for Electrical Engineering, Bucharest, Romania*
(6) *Institute for Nuclear Research, Moscow, Russia*
(7) *Kyushi University, Harozaki, Japan*
(8) *P.J.Safarik University, Kosice, Slovakia*
(9) *University of Chemical Technology and Metallurgy, Sofia, Bulgaria*
(10) *RIKEN (the Institute for Physical and Chemical Research), Saitama, Japan*
(11) *University of Tokyo, Tokyo, Japan*
(12) *Belgorod State University, Belgorod, Russia*
† *E-mail: pkurilkin@jinr.ru*

Abstract

The investigation of the light nuclei spin structure has been performed at the RIKEN (Japan) accelerator research facility and VBLHEP (JINR) using both polarized and unpolarized deuteron beams. The experimental results on the analyzing powers studies in $dp-$ elastic scattering, d(d,^{3}H)p and d(d,^{3}He)n reactions are presented. The result on the analyzing powers A_y, A_{yy} of the deuteron obtained at the Nuclotron (VBLHEP) at 880 and 2000 MeV are compared with relativistic multiple scattering model calculations. The data on the tensor analyzing powers for the d(d,^{3}H)p and d(d,^{3}He)n reactions obtained at $E_d = 200$ and 270 MeV demonstrate the sensitivity to the ^{3}H, ^{3}He and deuteron spin structure.

The wide experimental program on the study of the polarization effects in $dp-$ elastic scattering, $dp-$nonmesonic breakup, d(d,^{3}He)n, d(d,^{3}H)p and d(^{3}He,^{4}He)p reactions using internal and extracted beam at Nuclotron-M is discussed.

Studies of few-nucleon systems offer a good opportunity to investigate the nature of nuclear forces. Decades of intensive theoretical and experimental efforts led to a new generation of realistic nucleon-nucleon(NN) potentials: CD-Bonn, AV18, Nijmegen I,II and 93. They describe the rich set of experimental NN data up to 350 MeV. However, these realistic two-nucleon forces(2NF) fail to reproduce experimental binding energies for light nuclei, clearly showing underbinding. Natural candidates to fill the gaps are the

three-nucleon forces(3NFs). For 3N and 4N systems, one can achieve the correct binding energies with the 2π- exchange forces such as Tucson-Melbourne or Urbana IX 3NFs.

In addition to the first signal on 3NF effects resulting from discrete states, strong 3NF effects were observed in a study of the minimum of Nd elastic scattering cross-section at incoming nucleon energies higher than about 60 MeV. This was a reason of a number experiments all over the world at RIKEN, RCNP, KVI and IUCF. These studies shows that the inclusion of the 3NF does not always improve the description of precise data taken at intermediate deuteron energies. At higher energies both the cross-section and spin observables indicate the deficiencies of the present 3NF models. This might indicate that addition 3NF should be added to the 2π- exchange type forces. In addition, one can expect relativistic effects with increasing energy. So a new data at high energies are certainty required.

The program on the light nuclei structure investigation at the Nuclotron includes experiments with the use both internal and extracted polarized deuteron beams.

The study of the energy dependence of polarization observables for the $dp-$ elastic scattering and deuteron breakup reaction are conducted at the internal target station(ITS) setup. A detailed description of the experiment can be found in [1].

The analyzing powers measurements in dp-elastic scattering have been performed at ITS using polarized deuteron beam from polarized ion source (PIS) POLARIS at the energies 880 and 2000 MeV. The beam polarization measurement has been performed at 270 MeV where the precise data on the tensor and vector analyzing powers exist.

The results on the angular dependence of the vector A_y and tensor A_{yy} and A_{xx} analyzing powers in $dp-$ elastic scattering obtained at 880 MeV are shown by the solid symbols in Fig. 2. The solid, dash and dash-dotted lines are the results of the Faddeev calculations [2] using CD-Bonn NN potential, of the relativistic multiple scattering calculation [3] with the use CD-Bonn deuteron wave function(DWF), and the optical potential calculation [4] with the dibaryon DWF, respectively. One can see that Faddeev calculation without inclusion 3NF give a good description all the analyzing powers within achieved experimental accuracy. The multiple scattering model reproduces reasonably the angular dependencies of A_y over the whole range of measurements and A_{yy} at backward angles, while it fails to describe the behavior of A_{xx}. The optical potential calculation reproduce the behavior of A_{yy} only at the angles larger 100° in the c.m., while the analyzing powers A_y and A_{xx} are not described.

The results on the angular dependence of the vector A_y and tensor A_{yy} analyzing powers in $dp-$ elastic scattering at 2000 MeV are shown in Fig. 2. The data obtained

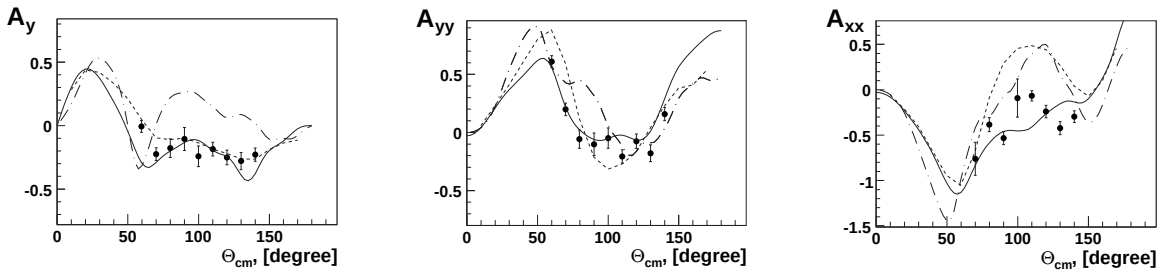

Figure 1: Vector A_y and tensor A_{yy} and A_{xx} analyzing powers in dp- elastic scattering at 880 MeV as a function of scattering angle in center of mass system. The lines are described in the text.

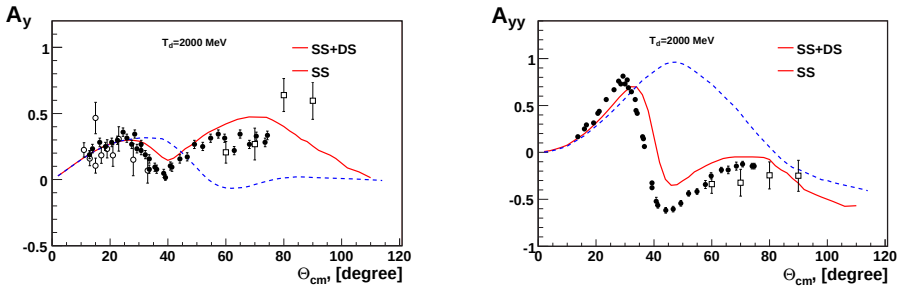

Figure 2: The angular dependencies of the vector A_y and tensor A_{yy} analyzing powers in dp- elastic scattering at 2000 MeV. Black points are the world data [5]. Open circle and square are the data obtained at LHE JINR at bubble chamber [7] and at Nuclotron, respectively. The lines are described in the text.

at Argonne National Laboratory (ANL) are presented by the solid symbols [5]. Open squares and circles are the data obtained at the ITS and at hydrogen bubble chamber [7] at JINR, respectively. The dashed and solid lines are the results of the relativistic multiple scattering model calculations [6] with and without of the double scattering term. One can see reasonable agreement with the data on the vector analyzing power and qualitative agreement for tensor analyzing power for the full calculation.

Future plans of DSS (Deuteron spin structure) - collaborations in spin studies are related with the construction of new polarized deuteron source. This source will provide the intensity up to 2×10^{10} particles per pulse and larger variety of the spin modes than POLARIS. Figure of merit of new source will be increased by a factor 10^3 compared with POLARIS.

The energy scan of the $dp-$elastic scattering observables and measurements of the analyzing powers in dp-nonmesonic breakup will be done using internal target and polarized deuteron beam from new PIS. As the first step the $dp-$elastic scattering and dp-nonmesonic breakup cross section measurements can be done with the current unpolarized ion source. The dp-nonmesonic breakup reaction will be investigated at ITS at the Nuclotron using $\Delta E - E$ techniques for the detection of two final protons. Fig. 3a presents the correlation of the $\Delta E - E$ information from 2 proton detectors. A kinematic relation are shown by the solid line. The preliminary results on the angular dependence

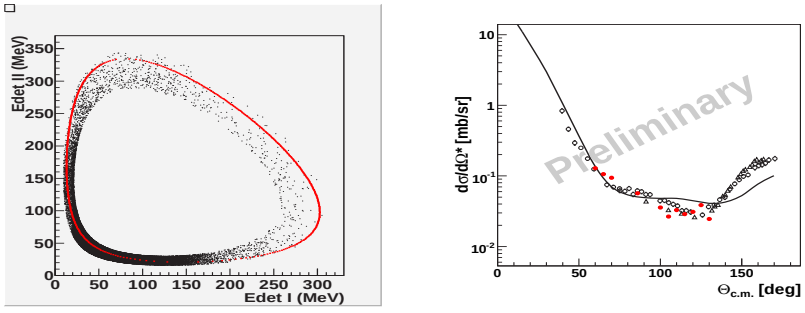

(a) (b)

Figure 3: **(a)** The correlation of the $\Delta E+E$ information from 2 proton detectors in case the dp-breakup reaction investigation at 500 MeV. $\Theta_1 = 34°$, $\Theta_2 = 29.8°$, $\phi_{12} = 180°$. **(b)** The results on the angular dependence of the dp-elastic cross section obtained at 880 MeV at Nuclotron in March 2011. World data [8] at 850 MeV and 940 MeV are marked by the open triangles and circles, respectively.

of the $dp-$elastic scattering cross section obtained at 880 MeV at the Nuclotron in March 2011 are presented in Fig. 3b by the solid symbols. They are compared with experimental data [8] obtained at 850 MeV and 940 MeV given by the open triangles and circles, respectively. Solid line are the result multiple scattering model calculations [3].

The measurements of polarization observables in $^3He(d,p)^4He$ are planning at Nuclotron-M using external deuteron beam and polarized ^3He target developed at Center for Nuclear Study of Tokyo University. The main goal of project is the measurements of the tensor analyzing power T_{20} and spin correlation $C_{y,y}$ in this reaction at the energies 1.0-1.75 GeV, where the contribution from the deuteron D-state is expected to reach the maximum.

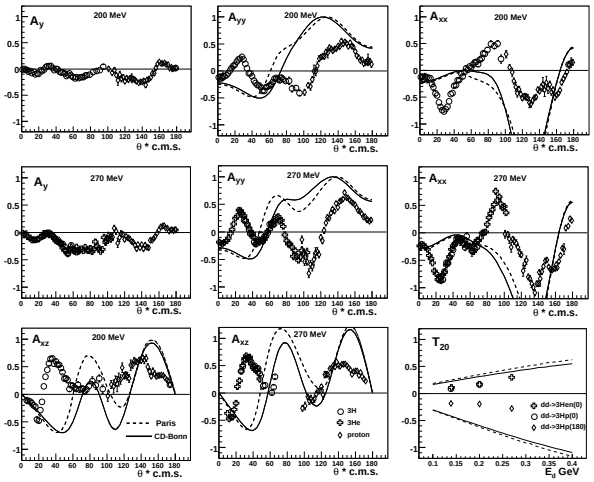

Figure 4: The analyzing powers data in d(d,^3He)n and d(d,^3H)p at 200 and 270 MeV. The curves are the calculation within one-nucleon-exchange approximation.

With the same magnetic spectrometer we are planning to study short range correlation from $\overrightarrow{d}\,d \to {}^3Hp(^3Hen)$ reactions. Fig. 4 shows the behavior of the analyzing powers obtained at 200 and 270 MeV at RIKEN by our collaboration [9]. These data are sensitive to the ^3He or ^3H spin structures at forward scattering angles and to the deuteron spin structure at backward angles. The tensor analyzing power T_{20} can be measured in a GeV region at Nuclotron-M.

New experimental data will ensure the important information about the light nuclei spin structure at short internucleonic distances, where the relativistic effects and 3N forces play an important role.

The work was supported in part by the RFBR under the Grant 10-02-00087a.

References

[1] T. Uesaka, V.P. Ladygin et al,, Phys. Part. Nucl. Lett., **3**, (2006) 35.

[2] H. Witala et al., private communication.

[3] N.B. Ladygina, Phys. Atom. Nucl, **71** (2008) 2039;
N.B. Ladygina, e-Print arXiv:0805.0321[nucl-th].

[4] M.A. Shikhalev, Phys. Atom. Nucl, **72** (2009) 588.

[5] M. Haji-Saied et al., Phys. Rev., **C36** (1987) 2010.

[6] N.B. Ladygina., e-Print arXiv:1108.5856[nucl-th].

[7] A.A. Terekhin et al., will be published in proceedings of XIV Workshop on High Energy Spin Physics, DSPIN-11, 2011.

[8] N.E. Booth et al., Phys. Rev. **D4** (1971) 1261;
J.C. Alder et al., Phys. Rev. **C6** (1972) 2010.

[9] A.K. Kurilkin et al., Eur. Phys. J. ST. **162** (2008) 133.

CONCEPT OF THE POLARIMETRY AT NUCLOTRON-NICA

V.P. Ladygin [1,†], and P.K. Kurilkin [1]

(1) *Joint Institute for Nuclear Research, Dubna, Russia*
† *E-mail: vladygin@jinr.ru*

Abstract

The concept of the deuteron beam polarimetry at Nuclotron-NICA is presented. The calibration of the existing deuteron beam polarimeter at Internal Target in the wide energy range will allow to obtain the accuracy of the vector and tensor beam polarization values of about 3-5%. The possible solutions for low energy, high energy and CNI polarimeters are discussed.

The problems of the proton beam polarimetry at NICA are briefly mentioned.

1 Introduction

New heavy ion and polarized particles collider NICA is planned for the energies $\sqrt{s_{NN}}$ ~4–13.8 GeV and up to $\sqrt{s}$ ~27 GeV for *dd*- and *pp*- collisions, respectively. The serious advantage of this facility is the availability of polarized deuterons (neutrons).The main topics of the spin studies at NICA is the spin content of nucleon, nuclear and color transparency in spin observables, polarization effects in hyperon production, single and double asymmetries in meson production, NN and light nuclei short-range spin structure [1].

Spin studies at Nuclotron-NICA with polarized deuterons and protons require the high precision polarimetry to obtain reliable values of beam polarization. This is especially important for 2-nucleon and 3-nucleon short range correlation spin structure studies [1–3] to reduce the systematic error due to beam polarization measurements for the comparison of the results obtained at different facilities.

Future plans of the spin studies with polarized deuterons at Nuclotron-NICA are related with the construction of new polarized deuteron source [4]. This source will provide the intensity up to $\sim 2 \cdot 10^{10}$ ppp and greater variety of the spin modes than POLARIS [5]. Figure of merit of new source will be increased by a factor of $\sim 10^3$ compared with POLARIS source [5]. Since deuteron is a spin-1 particle, the polarimeter should have a capability to determine simultaneously both vector and tensor components of the beam polarization. Moreover, the effective analyzing powers of the polarimeter should be known with high precision to provide small systematic errors while determining the beam polarization components.

The deuteron polarimetry at Nuclotron-NICA should satisfy to the following requirements [3].

- The effective analyzing powers for the reference polarimeter must be determined with polarized beam which polarization had been obtained by the absolute calibration method. This will significantly decrease the systematic error during the measurements of the beam polarization.

- The efficient polarimeters should be installed at different places of the accelerator, namely, after LINAC, inside the booster and the Nuclotron rings, at the extracted beam lines and inside the collider rings. Some of these polarimeters should be calibrated simultaneosly to establish the polarization standard for Nuclotron-NICA.
- The permanent monitoring of the beam polarization during data taking should be provided.
- The local polarimetry at each experimental setup is necessary for independent monitoring of the beam polarization.

It should be noted that the absolute determination of the deuteron beam polarization and, therefore, the obtaining of the analyzing powers with small systematic errors is very complicated goal. Due to this the deuteron polarimetry at Nuclotron-NICA should be based on the use of the precise data on the analyzing powers obtained at other facilities.

The requirements to the proton beam polarimetry is the same. However, the acceleration scheme for polarized protons and deuterons at NICA can be different [6]. The scheme of the proton polarimetry is under discussion.

2 Deuteron beam polarimetry at Nuclotron

The polarimeter based on the use of *dp*- elastic scattering at large angles ($\theta_{\rm cm} \geq 60^\circ$) at 270 MeV [7], where precise data on analyzing powers [8, 9] exist, has been developed at internal target station (ITS) at Nuclotron [10]. The accuracy of the determination of the deuteron beam polarization achieved with this method is better than 2% because of the values of the analyzing powers were obtained for the polarized deuteron beam, which absolute polarization had been calibrated via the $^{12}{\rm C}(d,\alpha)^{10}{\rm B}^*[2^+]$ reaction [11].

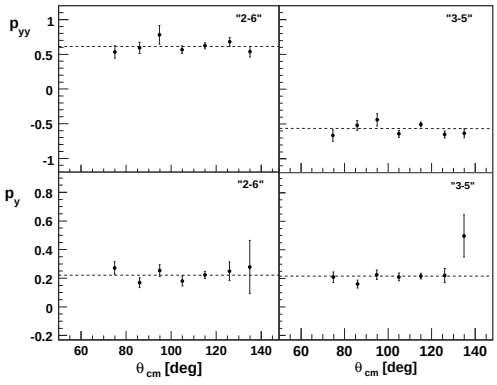

Figure 1: Tensor p_{yy} and vector p_y polarizations of the beam for "2-6" and "3-5" spin modes of POLARIS [5] as a function of the deuteron scattering angle in the cms.

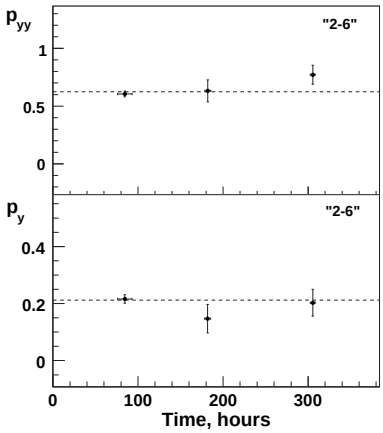

Figure 2: Tensor p_{yy} and vector p_y polarizations of the beam for the spin mode "2-6" of POLARIS [5] versus the elapsed time in hours.

The asymmetry measurements at several scattering angles were used to increase the polarimeter figure of merit. The values of the analyzing powers A_y, A_{yy}, A_{xx} and A_{xz}

at these angles were obtained by the cubic spline interpolation of the data taken from Refs. [8, 9]. Fig. 1 displays the values of the tensor p_{yy} and vector p_y polarizations of the beam for "2-6" and "3-5" spin modes of POLARIS [5] as a function of the deuteron scattering angle in the cms. One can see good agreement of the polarization values obtained at different scattering angles in the cms. The estimated figures of merit values for ITS polarimeter [7] are comparable with the figures of merit for the deuteron polarimeter used at the extracted beam at RIKEN [11]. Fig. 2 illustrates the polarization values for the spin modes "2-6" of POLARIS [5] as a function of the elapsed time in hours. One can see rather good time stability of the beam polarization values during ∼220 hours of the beam [7].

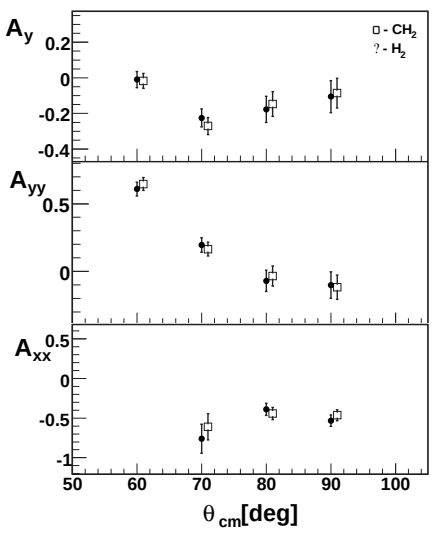

Figure 3: Analyzing powers A_y, A_{yy} and A_{xx} in $d-p$ elastic [12,13] and dCH_2 quasi-elastic scattering at 880 MeV [14].

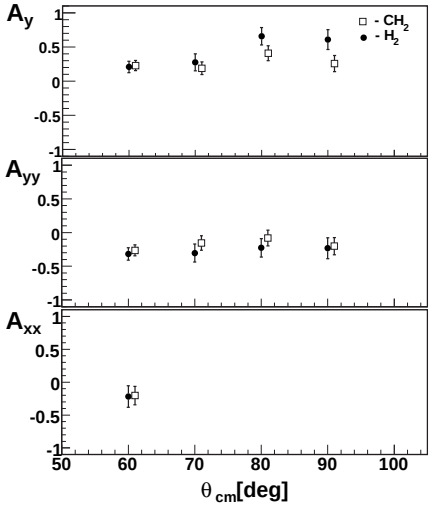

Figure 4: Analyzing powers A_y, A_{yy} and A_{xx} in $d-p$ elastic and dCH_2 quasi-elastic scattering at 2000 MeV [13].

The current polarimeter [7] is proposed as the reference deuteron polarimeter at Nuclotron-NICA. The Figs.3 and 4 demonstrate that the dp- elastic [12, 13] and dCH_2-quasi-elastic [14] scattering analyzing powers obtained at 880 and 2000 MeV [13] are large enough to provide the efficient beam polarization measurements. This polarimeter can work in the counting mode in the energy range of 300–2000 MeV and, therefore, can be used for permanent beam polarization monitoring [15].

One of the possible reactions for the tensor-vector deuteron polarimetry at high energies is dp- elastic scattering at small angles in the cms. Both tensor and vector analyzing powers have large values [16, 17]. The feasibility of the dp- elastic scattering events selection using information on the energy losses in the scintillator and timing information has been demonstrated at $\theta^d_{lab} \sim 8^\circ$ at the energies 1600 and 2000 MeV [18]. Such polarimeter can be installed at the Nuclotron extracted beam. It also can work in the counting mode to provide fast on-line polarimetry.

In the first run with polarized deuterons from new PIS [4] the following program of measurements will be realized.

- The measurements of the deuteron beam polarization will be performed at 270 MeV at ITS polarimeter [7].

- The ITS polarimeter will be calibrated in the energy domain of 300–2000 MeV [15].
- The external beam polarimeters based on *dp*- elastic [18] and *pp*- quasi-elastic [19] scattering at forward angles will be calibrated at 1600 MeV.
- Low energy polarimeter based on the use of the $dd \rightarrow tp$ reaction at 10 MeV will be calibrated also.

The goal of these calibrations is to establish the polarization standard for Nuclotron. This procedure will provide the error in the beam polarization measurements of ∼3% at the energies of 300–2000 MeV and better than ∼ 5% at higher energies. In this case the permanent monitoring of the extracted beam polarization stability can be provided either by the use of 2 flattops in the accelerator (one of them for ITS polarimeter) or by the external beam polarimeters [18, 19].

The deuteron beam polarimetry at high energy (larger than 1000 MeV/nucleon) can be provided either by the small angle *dp*- elastic scattering or by the measurements in the CNI region.

3 Project for low energy polarimeter

The energies of the accelerated deuterons and protons after LINAC LU-20 are 10 MeV and 20 MeV, respectively. Two different low energy deuteron polarimeters were used for a long period [20]. The first one based on the $d^3He \rightarrow p(0^\circ)^4He$ reaction was used for the measurements of the tensor component of the beam polarization. The second one utilized the d^4He- elastic scattering at backward angles was employed to measure the vector beam polarization. However, they cannot be used simultaneously to measure both polarization components. Also, the detection system is rather slow and, therefore, it is affected by the dead-time effects. We propose to design new low energy deuteron polarimeter based on the detection of the charged particles from the $dd \rightarrow {}^3Hp$ reaction at 10 MeV. Both deuteron vector and tensor analyzing powers at the scattering angle of ∼130° in the c.m. [21] are large enough to provide the efficient polarimetry. The cross section of this reaction at 10 MeV around a proton scattering angle of 130°-140° is about 2-3 mb/sr in the c.m. [21].

The dependencies of the proton and triton kinetic energies as the functions of the proton scattering angle in the c.m. for the initial deuteron energy 10 MeV are shown in Fig.5. The laboratory angles of the proton and triton versus the proton scattering angle in the c.m. are presented in Fig.6. The proton and triton detectors should be placed at ∼20° and ∼110° in the laboratory, respectively. The corresponding energies of the proton and triton are 3.5-4.0 MeV and 10.0-10.5 MeV, respectively.

The thin solid CD_2 and carbon targets will be used to obtain the effect on deuterium via CD_2-C subtraction procedure. This will avoid the use of the gaseous targets. However, the problem of the carbon background elimination appears.

The main option for the detection system is the double sided silicon strip detector developed at LHEP JINR for α-particles detection [22]. The proton and triton will be detected by two silicon microstrip detectors in coincidence. The strip size is 500 μm with the number of strips 32 in the both X and Y directions. For the size of the detector 1.6×1.6 cm^2 placed on the distance of 40 cm from the 50 mg/cm^2 CD_2 target, one can

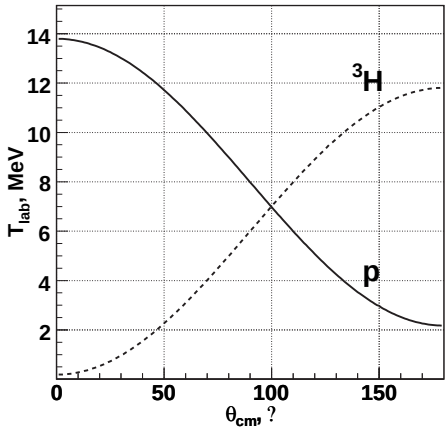

Figure 5: The proton and triton kinetic energies as the functions of the proton scattering angle in c.m. at the initial deuteron energy 10 MeV.

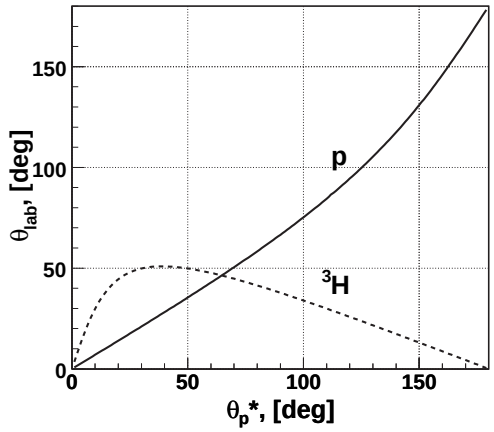

Figure 6: The laboratory angles of the proton and triton versus the proton scattering angle in the c.m.at the initial deuteron energy 10 MeV.

expect up to $3\times4\cdot10^4$ useful events/sec for the beam intensity $5\cdot10^{11}$ deuterons/sec. The precision of the scattering angle determination in this case will be around 1-2 mrad.

The binary reaction $dd \rightarrow p^3H$ will be selected by the proton and triton scattering angles correlation and complanarity condition. These selection criteria will significantly reduce the the contribution from the carbon content of the CD_2 target. The additional selection can be the energy depositions of the proton and triton in the silicon detector. The correlations of the X and Y coordinates for the proton and triton detectors are presented in Figs. 7 and 8, respectively. One can see the clean selection of the $dd \rightarrow ^3Hp$ events.

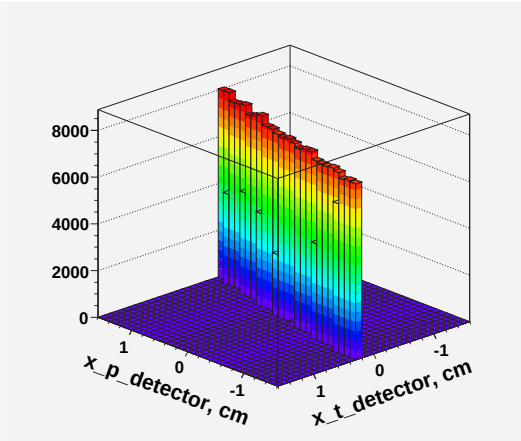

Figure 7: The correlation of the X-coordinates for protons and tritons registered by the silicon microstrip detector.

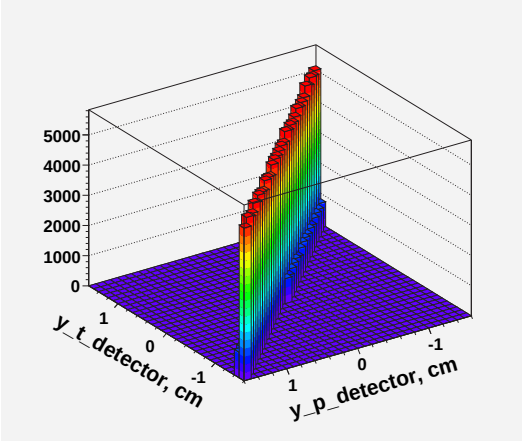

Figure 8: The correlation of the Y-coordinates for protons and tritons registered by the silicon microstrip detector.

The second option for the detector is the use of scintillation fiber hodoscope with 16-anodes photomultiplier Hamamatsu H6568. This option can provide the same angular determination.

The same polarimeter can be used also for the polarimetry of polarized 20 MeV protons. The measurements of the vector beam polarization will be based on the analysis of the left-right asymmetry of $p-d$ elastic scattering at 20 MeV and a proton scattering angle of 130°-140° in the c.m. If the additional detection of the $p-d$ elastic scattering events will be provided in the vertical plane, it will possible to measure the direction of the beam polarization vector. The $p-d$ elastic scattering events selection will be provided by the detection of the protons and deuterons by silicon microstrip detectors placed at the kinematically conjugated angles.

4 Developments for polarimetry at NICA

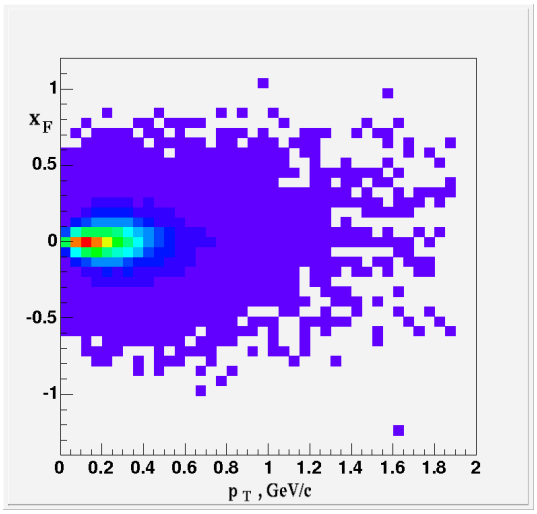

Figure 9: The $x_F - p_T$ acceptance for the π^0 production in the dd collisions at $\sqrt{s_{NN}}$=7.1 GeV.

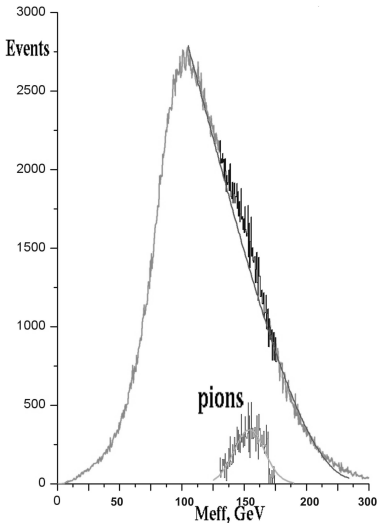

Figure 10: The distribution of 2γ effective mass M_{eff} obtained in dCu collisions at ∼2 GeV/nucleon at Nuclotron in March 2010.

One of the reactions to measure and to monitor the vector component of the polarized deuteron beam at NICA is quasi-elastic $NN \to \pi^{\pm,0}X$ reaction with the spectator nucleon tagging. The data on the single spin asymmetries (SSA) A_N obtained in pp-collision for π^+, π° and π^- inclusive production at 200 GeV [23] demonstrate the large values of SSA with their signs following to the polarization of the valence quarks in the pions. This regime occurs already at 22 GeV [1] corresponding to $\sqrt{s_{NN}}$ ∼7 GeV for the collider option. The SSA for pp- and np-collisions is expected to have the opposite signs at large x_F. Therefore, it is necessary to identify the spectator nucleon to separate pp- and np-interactions.

The results of the simulations for π^0 production in the dd- collisions at $\sqrt{s_{NN}}$= 7.1 GeV presented in Fig.9 show that quite large statistics can be obtained at large x_F to provide a local polarimetry at SPD or MPD. The spectator nucleons can be easily detected since their transverse momentum is below 200-300 MeV/c. The test run has been performed with 2 photon detectors at ITS at Nuclotron at ∼2 GeV/n in March 2010. The results on the 2γ effective mass presented in Fig.10 demonstrate the possibility to select π^0-s for

the polarimetry.

One of the possible reaction for the deuteron beam polarimetry at NICA is the dC-elastic scattering in the CNI region. However, serious theoretical and experimental efforts are required to use this method both at Nuclotron and at NICA.

The main option for high energy proton polarimetry is pp- elastic scattering [19] and pC- elastic scattering in the CNI region [25].

5 Conclusions

- The conception for the deuteron beam polarimetry at Nuclotron-NICA is formulated.
- In this conception the polarimeter at ITS [7] should play a key role being the reference deuteron polarimeter at Nuclotron-NICA.
- The proposed conception of the polarimetry will provide the precision in the deuteron beam polarization $\sim 5\%$ over the whole energy range of Nuclotron.
- Further serious work on the deuteron polarimetry scheme for Nuclotron-NICA with new PIS [4] is required.
- The NICA proton polarimetry concept also requires further investigations.

The authors thank their colleagues T. Uesaka, Yu.V. Gurchin, A.Yu. Isupov, K. Itoh, M. Janek, J.-T. Karachuk, T. Kawabata, A.N. Khrenov, A.S. Kiselev, V.A. Kizka, V.A. Krasnov, A.K. Kurilkin, N.B. Ladygina, A.N. Livanov, Y. Maeda, A.I. Malakhov, S.M. Piyadin, E.B. Plekhanov, S.G. Reznikov, S. Sakaguchi, H. Sakai, Y. Sasamoto, K. Sekiguchi, K. Suda, A.A. Terekhin, T.A. Vasiliev for their large contribution in the data taking at Nuclotron. They are grateful to Prof. A.D. Kovalenko for useful discussion.

The investigation has been supported in part by the Russian Foundation for Basic Research (grant No.10-02-00087a).

References

[1] V.P. Ladygin et al., AIP Conf.Proc.**1056** (2008) 420.
[2] V.P. Ladygin et al., EPJ Web Conferences **3** (2010) 04004.
[3] V.P. Ladygin et al.,J.Phys.Conf.Ser.**295** (2011) 012131.
[4] V.V. Fimushkin et al., Eur.Phys.J. ST **162** (2008) 275.
[5] N.G. Anishchenko et al., AIP Conf.Proc. **95** (1983) 445.
[6] A.D. Kovalenko et al., Proc. of the 2-nd Int. Part. Acc. Conf. (IPAC 2011), 4-9 Sep. 2011, San Sebastian, Spain; to be published.
[7] P.K. Kurilkin et al., Nucl.Instr.Meth. in Phys.Res. **A642** (2011) 45.
[8] K. Sekiguchi et al., Phys.Rev. **C65** (2002) 034003.
[9] K. Sekiguchi et al., Phys.Rev. **C70** (2004) 014001.

[10] A.I. Malakhov, et al., Nucl.Instr.Meth. in Phys.Res. **A440** (2000) 320; Yu.S. Anisimov, et al., Proc. of the 7-th Int. Workshop on Relativistic Nuclear Physics, 25-30 August 2003, Stara Lesna, Slovak Republic, p.117.

[11] K. Suda et al., Nucl.Instr.Meth. in Phys.Res. **A572**, 745 (2007).

[12] K. Suda et al., AIP Conf.Proc. **915** (2007) 920; AIP Conf.Proc. **1011** (2008) 241.

[13] P.K. Kurilkin et al., Eur.Phys.J. ST **162** (2008) 137; Int.J.Mod.Phys. **A24** (2009) 530.

[14] T. Uesaka et al., CNS Report **79**, Tokyo (2008).

[15] T. Uesaka et al., Phys.Part.Nucl.Lett. **3** (2006) 305.

[16] M. Bleszynski et al., Phys.Lett. **B87** (1979) 178; Phys.Lett. **B106** (1981) 42;
M. Haji-Saied et al., Phys.Rev. **C36** (1987) 2010.

[17] S.M. Piyadin et al., Int.J.Mod.Phys.**A26** (2011) 683.

[18] Yu.V. Gurchin et al., Phys.Part.Phys.Lett. **8** (2011) 943.

[19] L.S. Azhgirey et al., Nucl.Instr.Meth. in Phys.Res. **A497** (2003) 340.

[20] Yu.K. Pilipenko et al., AIP Conf. Proc. **570** (2001) 801.

[21] W. Grüebler et al., Nucl.Phys. **A193** (1972) 129;
V. König et al., Nucl.Phys. **A331** (1979) 1.

[22] A.V. Isaev et al., PTE **1** (2011) 43.

[23] D.L. Adams et al., Phys.Lett. **B261**, (1991) 201; Phys.Lett. **B264**, (1991) 462

[24] C.E. Allgower et al., Phys.Rev. **D65**, (2002) 092008

[25] A. Zelensky et al., AIP Conf.Proc.**1149** (2009) 731.

DEUTERON-PROTON AND DEUTERON-DEUTERON COLLISIONS AT INTERMEDIATE ENERGIES

N.B.Ladygina[1]

(1) *LHEP JINR*
E-mail: nladygina@jinr.ru

Abstract

The $dp \to dp$ and $dd \to {}^3He\ n$ reactions are considered in the energy range from a few hundred MeV up to 2 GeV. The approach is based on the multiple-scattering theory, where the few-body collisions are presented through two-body ones. The high-energy nucleon-nucleon interactions are described by t-matrix, which is parameterized in accordance with the modern phase-shift analysis data. The special attention is given to investigation of the rescattering effects in these reactions.

The theoretical predictions are obtained for the differential cross sections, vector and tensor analyzing powers. All results are presented in comparison with the existing experimental data.

During a few decades hadronic reactions with a participation of the light nuclei were extensively investigated at the energies of several hundred MeV. These processes are the simplest examples of the hadron nucleus collision that is why the interest to this reaction is justified. A number of experiments is aimed at getting some information about the deuteron or helium wave functions as well as nucleon-nucleon amplitudes from the scattering observables.

In this talk two reactions are considered. The first of them is the dp-elastic scattering in the deuteron energy range between 500 MeV and 2 GeV. The second reaction is the

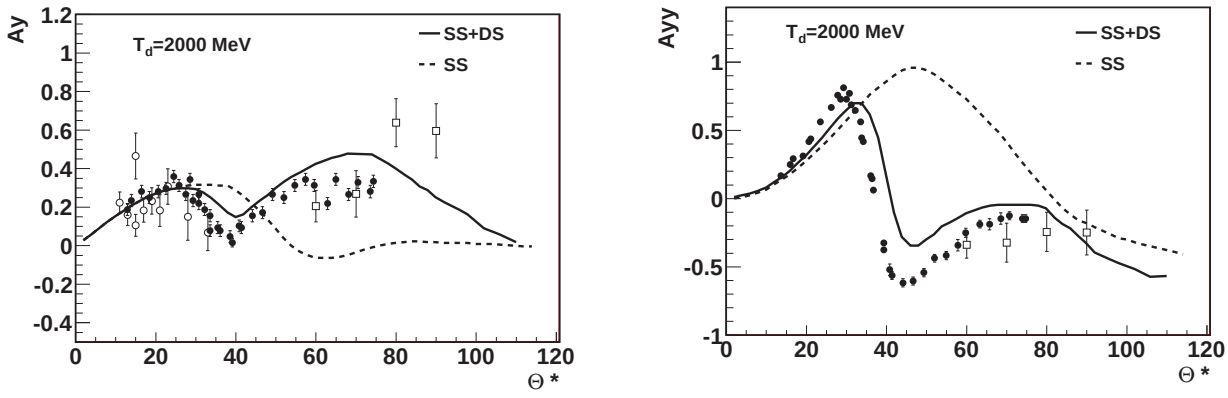

(a) **(b)**

Figure 1: **(a)** The vector,A_y, and **(b)** tensor, A_{yy}, analyzing powers of the deuteron in the $dp \to dp$ at $T_d = 2GeV$. The data taken from: • [8]; ◦ LHE JINR, hydrogen bubble chamber experiment, talk by A.Terekhin given at this conference; □ LHE JINR Nuclotron [9].

$dd \to {}^3He\ n$ at the energies from 200 MeV up to 520 MeV. The theoretical approach is based on the AGS-equations both for the three-nucleon interaction [1]

$$U_{\beta\alpha}(z) = (1 - \delta_{\beta\alpha})(z - H_\alpha) + \sum_{\gamma \neq \beta} T_\gamma(z) G_0(z) U_{\gamma\alpha}(z) \tag{1}$$

and for the four-nucleon case [2].

$$U_{\beta\alpha}(z) = (1 - \delta_{\beta\alpha})(z - H_\alpha) + \sum_{ik \not\subset \beta} T_{ik}(z) G_0(z) U_{ik,\alpha}(z) + \sum_{ik \not\subset \beta} V_\alpha \delta_{\alpha,ik}\ , \tag{2}$$

where α and β denote two-cluster partitions. As a consequence, the reaction amplitudes are expressed via two-nucleon T-matrix and free-propagator G_0. We iterate Eq.(1) over the nucleon-nucleon T-matrix up to second order term. In such a way, the plane-wave-impulse-approximations (PWIA), single scattering (SS) and double scattering (DS) contributions are taken into account for the $dp \to dp$ process. We do not solve here any equations in order to obtain nucleon-nucleon t-matrix. Instead the parameterized T-matrix are used in our calculations. This parameterization was offered by Love and Franey [3]. New model parameters were obtained [4] in accordance with the modern phase shift analysis data [5]. The applied approach was presented in details in refs. [6], [7].

The results of the calculations for the dp-elastic scattering are given in Fig.1. All calculation have been performed with the CD Bonn deuteron wave function. The angular dependencies of the vector, A_y, and tensor, A_{yy}, analyzing powers are presented at the deuteron energy of 2 GeV. Here, the solid curves correspond to the results of calculations including both the single scattering and double scattering terms. The results taking only

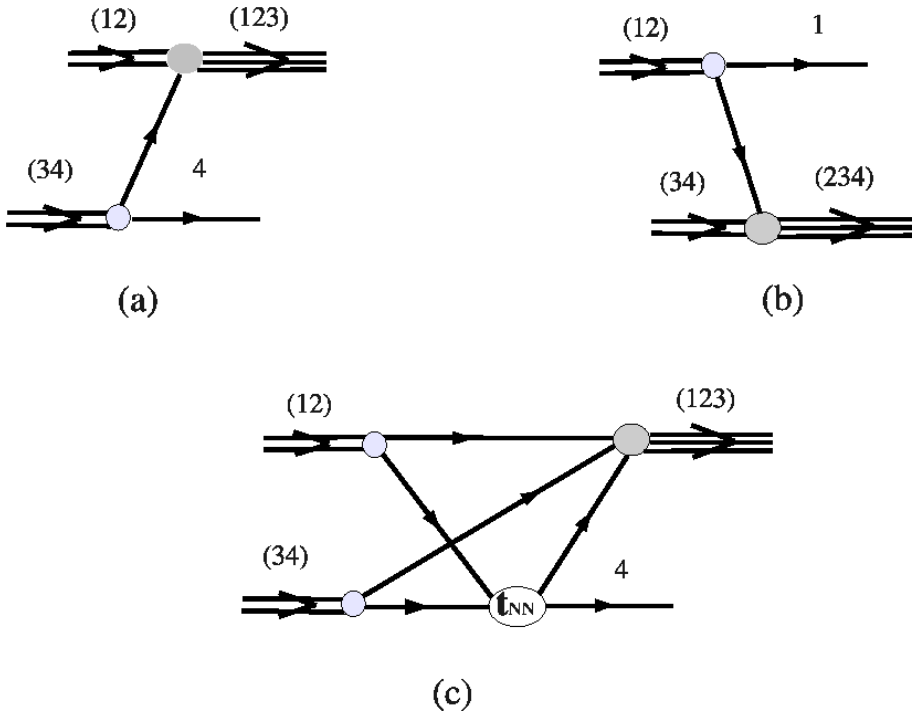

Figure 2: The diagrams taken into consideration for the $dd \to {}^3He\ n$ reaction: **(a),(b)** one-nucleon-exchange , **(c)** single scattering graphs.

SS-contribution into account are given with dashed curves. One can see the inclusion of the DS-term significantly improves the agreement between the theoretical predictions and experimental data, especially, for the tensor analyzing power.

For the $dd \to {}^3He\ n$ reaction the one-nucleon-exchange (ONE) and single scattering terms are included into consideration (Fig.2). Like it was done for the dp-elastic scattering, we use the parameterized helium and deuteron wave functions. Also the nucleon-nucleon T-matrix from refs. [3], [4] is applied in order to calculate rescattering diagram (Fig.2c).

The differential cross section of the $dd \to {}^3He\ n$ reaction is presented in Fig.3a at laboratory momentum of 1.109 GeV/c [11]. In order to demonstrate the contribution of the single scattering term, we have considered two cases. One of them corresponds to the calculations including only ONE terms. The results of these calculations are given with the dashed curves. The other case corresponds to the calculations taking into account both ONE and single scattering contributions. These results are presented with the solid curves. In our calculations we use the parameterized ${}^3He$ wave function [10] given in the separable form. As above, we use the CD Bonn deuteron wave function.

As expected, the contribution of the rescattering term is not large at small scattering angles ($\theta < 30^0$). It is in agreement with the results obtained in ref. [12]. However, the difference between these two curves increases with the angle and reaches the maximal value at 90^0. Taking the single scattering diagram into consideration significantly improves the agreement between the experimental data and theoretical predictions.

The formalism presented here gives us an opportunity to calculate not only the differential cross sections but also polarization observables. In this paper we have considered the energy dependence of tensor analyzing power T_{20} at the scattering angle equal to zero in the energy range between 200 MeV and 520 MeV (Fig.3b). The experimental data were obtained at RIKEN [13]. As it is mentioned above, the contribution of the single scattering term is not large at small angles. Nevertheless, one can observe some improvement of the agreement between the data and theory predictions. Unfortunately, we do not have enough experimental data to confirm this tendency.

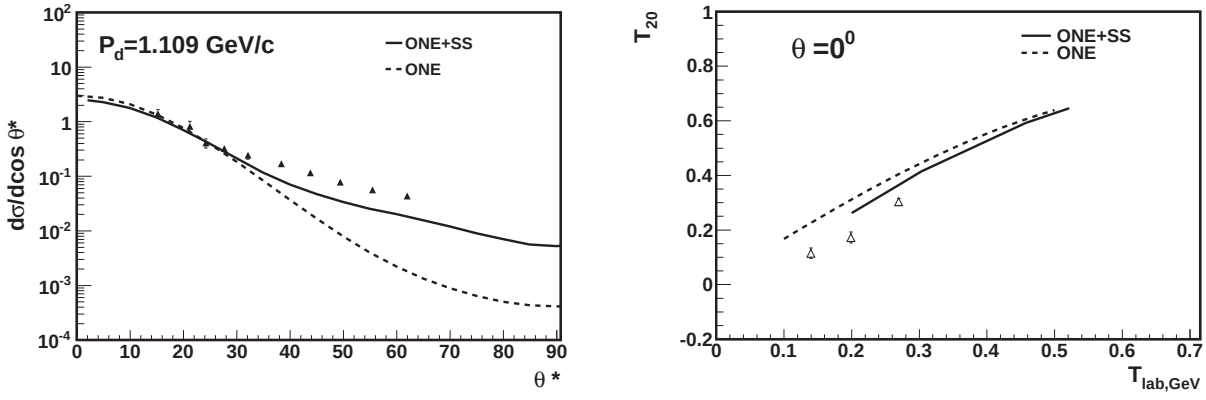

(a) **(b)**

Figure 3: **(a)**The differential cross section of the $dd \to {}^3He\ n$. The data taken from [11]. **(b)** The tensor analyzing power in the $dd \to {}^3He\ n$. The data taken from [13].

Acknowledgments. The author is grateful to Dr. V.P. Ladygin for fruitful discus-

sions. This work has been supported by the Russian Foundation for Basic Research under grant $N^{\underline{0}}$ 10-02-00087a.

References

[1] E.O.Alt, P.Grassberger, W.Sandhas, Nucl.Phys. **B2**, (1967) 167.
[2] P.Grassberger, W.Sandhas, Nucl.Phys.**B2**, (1967) 181.
[3] W.G.Love, M.A.Franey, Phys. Rev.C **24**, 1073 (1981)
[4] N.B.Ladygina, e-preprint nucl-th/0805.3021
[5] http://gwdac.phys.gwu.edu
[6] N.B.Ladygina, Phys.Atom.Nucl., **71**, (2008) 2039.
[7] N.B.Ladygina, Eur.J.Phys. **A42**, (2009) 91.
[8] M.Haji-Saied et al, Phys.Rev.**C36**, (1987) 2010.
[9] P.K.Kurilkin et al., Int.J.Mod.Phys.**A24**, (2009) 530
[10] V.Baru et al.,Eut.Phys.J.**A16**, (2003) 437
[11] G.Bizard et al.,Phys.Rev. **C22**, (1980) 1632.
[12] M. Janek et al., Eur.Phys.J. A 33 (2007) 39.
[13] V.P. Ladygin et al., Phys. Lett. **B598**, (2004) 47.

PRECURSOR EXPERIMENTS TO SEARCH FOR PERMANENT ELECTRIC DIPOLE MOMENTS (EDMs) OF PROTONS AND DEUTERONS AT COSY

Andreas Lehrach [1], Bernd Lorentz [1], William Morse [2], Nikolai Nikolaev [3 †] and Frank Rathmann [1]

(1) *Institut für Kernphysik and Jülich Center for Hadron Physics, Forschungszentrum Jülich, 52425 Jülich, Germany*
(2) *Physics Department, Brookhaven National Laboratory, Upton, NY 11973, USA*
(3) *Institut für Kernphysik and Jülich Center for Hadron Physics, Forschungszentrum Jülich, 52425 Jülich, Germany, and Landau Institute, 142432 Chernogolovka, Russia*
† *E-mail: n.nikolaev@fz-juelich.de*

Abstract

In this presentation we discuss a number of experiments on the search for proton or deuteron EDMs, which could be carried out at COSY-Jülich. Most promising is the use of an radio-frequency radial electric field flipper that would lead to the accumulation of a CP violating in-plane beam polarization by tiny spin rotations. Most crucial for storage ring searches for EDMs is the spin-coherence time, and we report on analytic evaluations which point at a much larger spin-coherence time for deuterons by about a factor of 200 compared to the one for protons, and at COSY, the spin coherence time for deuterons could amount to about 10^5 s.

1 Introduction

Electric dipole moments (EDM) are one of the keys to understand the origin of our Universe. The Universe as we know it has a microscopic net baryon number – about 0.2 baryons per cubic meter, or $\sim 10^{-10}$ of the density of relic photons. In 1967 Andrei Sakharov formulated three conditions for baryogenesis [1]:

1. Early in the evolution of the universe, the baryon number conservation must be violated sufficiently strongly,

2. the C and CP invariances, and T invariance thereof, must be violated, and

3. at the moment when the baryon number is generated, the evolution of the universe must be out of thermal equilibrium.

CP violation in kaon decays is known since 1964, it has been observed in B-decays and charmed meson decays. The Standard Model (SM) accommodates CP violation via the phase in the Cabibbo-Kobayashi-Maskawa matrix. CP and P violation entail non-vanishing P and T violating electric dipole moments (EDMs) of elementary particles $\vec{d} = d\vec{S}$. Although extremely successful in many aspects, the SM has at least two weaknesses:

neutrino oscillations do require extensions of the SM and, most importantly, the SM mechanisms fail miserably in the expected baryogenesis rate. Simultaneously, the SM predicts an exceedingly small electric dipole moment of nucleons $10^{-33} < d_n < 10^{-31}$ e·cm, way below the current upper bound for the neutron EDM, $d_n < 2.9 \times 10^{-26}$ e·cm, and also beyond the reach of future EDM searches [2]. In the quest for physics beyond the SM one could follow either the high energy trail or look into new methods which offer very high precision and sensitivity. Supersymmetry is one of the most attractive extensions of the SM and S. Weinberg emphasized in 1992 [3]: "Endemic in supersymmetric (SUSY) theories are CP violations that go beyond the SM. For this reason it may be that the next exciting thing to come along will be the discovery of a neutron electric dipole moment." The SUSY predictions span typically $10^{-29} < d_n < 10^{-24}$ e·cm and precisely this range is targeted in the new generation of EDM searches [2].

There is consensus among theorists that measuring the EDM of the proton, deuteron and helion is as important as that of the neutron. Furthermore, it has been argued some 25 years ago that T-violating nuclear forces could substantially enhance nuclear EDMs [4,5]. At the moment, there are no significant *direct* upper bounds available on d_p or d_d.

Non-vanishing EDMs give rise to the precession of the spin of a particle in an electric field. In the rest frame of a particle

$$\frac{d\vec{S}}{dt^*} = \mu\vec{S} \times \vec{B}^* + \vec{d} \times \vec{E}^*, \tag{1}$$

where in terms of the lab frame fields

$$\begin{aligned} \vec{E}^* &= \gamma(\vec{E} + \vec{\beta} \times \vec{B})\,, \\ \vec{B}^* &= \gamma(\vec{B} - \vec{\beta} \times \vec{E})\,. \end{aligned} \tag{2}$$

While ultra-cold electrically neutral atoms and neutrons can conveniently by stored in traps, the EDM of charged particle can only be approached with storage rings [6]. EDM searches of charged fundamental particles have hitherto been impossible, because of the absence of the required new class of electrostatic storage rings. An ambitious quest for a measurement of the EDM of the proton with envisioned sensitivity down to $d_p \sim 10^{-29}$ e·cm is under development at BNL [7]. The principal idea is to store protons with longitudinal polarization in a purely electrostatic ring: the EDM would cause a precession around the radial electric field and thus lead to a build-up of transverse polarization which could be measured by standard polarimetry. Related ideas on dedicated storage rings for the deuteron and helion EDM are being discussed at IKP of Forschungszentrum Jülich within the newly found JEDI collaboration[1].

Before jumping into construction of dedicated storage rings, it is imperative to test technical issues at existing facilities. Here we review several ideas for precursor experiments which could be performed at COSY subject to very modest additions to the existing machine. In a magnetic ring like COSY, the stable polarization axis in the absence of longitudinal magnetic fields is normal to the ring plane, and at the heart of the most promising proposal is a radio-frequency electric field (RFE) spin flipper which would rotate the spin into the ring plane. The resulting EDM-generated P and T non-invariant in-plane polarization which can be determined from the up-down asymmetry of the scattering of stored particles on the polarimeter. Unless show stoppers like false spin rotations

[1] Jülich Electric Dipole moment Investigations

via the magnetic moment pop up, one could theoretically aim for an upper bound for the deuteron of $d_d < 10^{-24}$ e·cm, which would be as valuable as the existing upper bounds on d_n [4, 5].

2 EDM searches: state of the art

The question of whether particles possess permanent electric dipole moments has a long-standing history, starting from the first search by Smith, Purcell, and Ramsey [8] for a neutron EDM, which, over the last 50 years or so, resulted in ever decreasing upper limits. In Table 1, we give current and anticipated EDM bounds and sensitivities for nucleons, atoms, and the deuteron and a rough measure of their probing power relative to the neutron (d_n). At this level, storage ring EDM measurements bear the potential of an order of magnitude higher sensitivity than the currently planned neutron EDM experiments at SNS (Oak Ridge), ILL (Grenoble-France), and PSI (Villigen, Switzerland) [9].

Particle	Current Limit	Goal	d_n equivalent	reference
Neutron	$< 2.9 \times 10^{-26}$	$\approx 10^{-28}$	10^{-28}	[10]
^{199}Hg	$< 3.1 \times 10^{-29}$	10^{-29}	10^{-26}	[11]
^{129}Xe	$< 6.0 \times 10^{-27}$	$\approx 10^{-30} - 10^{-33}$	$\approx 10^{-26} - 10^{-29}$	[12]
Proton	$< 7.9 \times 10^{-25}$	$\approx 10^{-29}$	10^{-29}	[11]
Deuteron		$\approx 10^{-29}$	$3 \times 10^{-29} - 5 \times 10^{-31}$	

Table 1: Current EDM limits in units of [e·cm], and long-term goals for the neutron, ^{199}Hg, ^{129}Xe, proton, and deuteron are given here. Neutron equivalent values indicate the EDM value for the neutron to provide the same physics reach as the indicated system.

3 Search for electric dipole moments of protons, deuterons, and ^{3}He at COSY

COSY has a history of highly successful operation of cooled polarized beams and targets – in fact, COSY is a unique facility for spin physics with hadronic probes on a world-wide scale. The IKP-COSY environment is ideally suited for a major (medium-sized) project involving spin and storage rings as it will be required for the search for permanent EDMs of charged fundamental particles (*e.g.*, protons, deuterons, and other light nuclei). JEDI is planning to search for EDMs of the proton and other charged particles in a storage ring with a statistical sensitivity of $\approx 2.5 \times 10^{-29}$ e·cm per year, pushing the limits even further and with the potential of an actual particle-EDM discovery.

The proposed new method employs radial electric fields (and magnetic fields) to steer the particle beam in the ring, electric quadrupole magnets to form a weak focusing lattice, and internal polarimeters to probe the particle spin state as a function of storage time. An RF-cavity and sextupole magnets will be used to prolong the spin coherence time (SCT) of the beam. For protons, it requires building a storage ring with a highly uniform radial E-field with strength of approx. 17 MV/m between stainless steel plates about 2 cm apart. The bending radius will be approx. 25 m, and including the straight sections such a machine would have a physical radius of approx. 30 m. The so-called magic momentum

of 0.7 GeV/c (232 MeV), is the one where the $(g-2)$ precession frequency is zero (see Table 2).

Particle	p (GeV/c)	E (MV/m)	B (T)
Proton	0.701	16.8	0
Deuteron	1.000	-4.03	0.16
^{3}He	1.285	17.0	-0.051

Table 2: Parameters for the transverse electric and magnetic fields required to freeze the spin in an EDM storage ring of radius $r = 30$ m.

4 Precursor experiments at COSY

The above cited tentative upper bound for the proton EDM as part of a nucleus in an electrically neutral atom, $|d_p| < 7.9 \times 10^{-25}$ e cm, derives from the *theoretical reinterpretation* of the upper bound for the EDM of ^{199}Hg [11]. We briefly review here possible first *direct* measurements of an upper limit for the proton and deuteron EDM using a normal magnetic storage ring like COSY. One needs to isolate a CP-violating precession of the spin caused by an electric field. Such experiments are widely considered must-do experiments, before embarking on the development and construction of storage rings with electrostatic deflectors.

4.1 RFE spin rotator with Siberian snake

Making use of a Siberian snake in COSY yields a stable longitudinal spin-closed orbit in a target section opposite the snake (see Fig. 1, top panel). Using two RF E-field systems in front and behind the snake (middle and bottom panels) allows one to provide a certain degree of depolarization in the beam due to the torque $\vec{d} \times \vec{E}$, where d denotes the proton electric dipole moment. When the RF E-field is reversed in polarity turn by turn, this torque produces a small mismatch between the two stable spin axes, hence the beam depolarizes. While the angle is exceedingly small ($\alpha \approx 10^{-7}$ rad, see Fig. 1, bottom panel), the number of turns n in the machine can be made very large ($n \approx 5 \cdot 10^{10}$). The sensitivity of this approach is rather limited to values of $d \approx 10^{-17} - 10^{-18}$ e cm, but a measurement would nevertheless constitute a first *direct* measurement of an upper limit for the proton EDM.

4.2 Dual beam method: protons and deuterons stored simultaneously

The dual beam method is equivalent to the $g-2$ measurement of the muon EDM d_μ, reported in [13]. It seems possible to store coasting proton and deuteron beams in COSY simultaneously. The way this would be achieved is by first injecting deuterons from the injector cyclotron into COSY and accelerating them to highest energy, where the beam lifetime reaches hundreds of hours. During the deuteron storage time, the injector cyclotron is tuned for protons, the stored deuterons in COSY are decelerated to

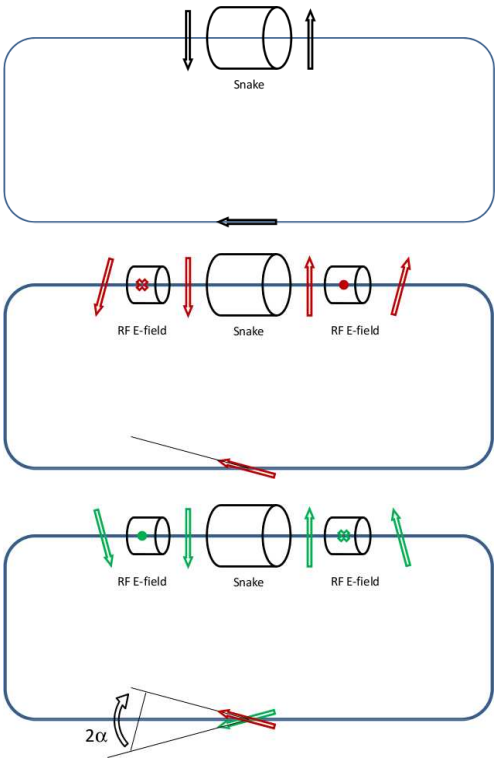

Figure 1: Concept of a proton EDM measurement using a Siberian snake in COSY. Top panel: Using the snake, the spin closed orbit is aligned along the direction of motion of the proton beam in the straight section opposite the snake. Middle panel: For odd turns in the machine, an electric RF E-field perpendicular to the ring plane in front and behind the snake rotates the stable spin axis by a small angle α away from the longitudinal direction. Bottom panel: For even turns in the machine where the RF E-field is reversed, the spin closed orbit is then rotated by an angle 2α, leading after n turns to a depolarization of the beam, $P(n) = P_0 \cdot \cos(2\alpha)^n$.

the injection momentum of approx. 300 MeV/c, electron cooled, and protons are injected. In order to cool both beams, the electron cooler voltage is switched to match the velocities of protons and deuterons for short time periods of about 10 s.

The search for the muon EDM made use of the fact that the magnetic fields in the $g-2$ experiment were well known, and one was able to relate the observed additional amount of spin rotation to the muon EDM. In our scenario, we would compare the spin precession due to the deuteron EDM using the protons as a means to determine the magnetic properties of the machine. Experimentally, the task boils down to the determination of the invariant spin axes of the simultaneously stored protons and deuterons using a polarimeter. Assuming a value for the proton EDM, derived from the measurement on ^{199}Hg (see Table 1), any mismatch of the invariant spin axes for deuterons and protons would be associated to an upper limit deuteron EDM. The sensitivity of this method to d_d would be similar to the one achieved in the $g-2$ determination of d_μ, *i.e.*, amount to about $d_d = 10^{-19}\ e \cdot cm$.

4.3 Morse-Orlov-Semertzidis resonance method for EDM measurements in storage rings

This idea for a measurement using an all magnetic ring is described in [14]. One would inject sideways polarization into a machine with a vertical invariant spin axis, the EDM produces a growing vertical polarization P_y, and using two sub-beams with different machine tunes that would be independently modulated, allows one to isolate the EDM of the orbiting particles. The sensitivity of this method for protons is estimated to reach $d_p = 10^{-29}$ e·cm/yr, but because of systematic errors, the idea is presently no longer

pursued at BNL. For COSY, in terms of precursor EDM measurements, this idea is being considered, although detailed evaluations have not been looked into yet.

4.4 The resonance EDM effect with RFE flipper

This is our favorite option and below we unfold its features in some more detail in the following sections.

5 The resonance RF electric flipper at COSY

The idea is to supplement a COSY magnetic ring with a radiofrequency electric flipper (RFE) which runs at a frequency tuned to the spin tune $G\gamma$. Much of the discussion is for deuterons at COSY but there emerges an interesting option also for protons.

5.1 Tipping the vertical polarization to the CP-violating in-plane polarization

Hereafter we focus on pure vertical ring magnetic field $\vec{B}$ and pure radial flipper field $\vec{E}$. An RFE flipper is added in a section where $\vec{B} = 0$. A non-vanishing EDM, $\vec{d} = ed\vec{S}$, gives rise to the precession of the spin $\vec{S}$ in an electric field $\vec{E}$ with $\omega_{\rm EDM} = edE$. A single pass through the flipper of length L with a radial electric field $\vec{E}$ would tilt the initial vertical spin $\vec{S} \parallel S_y$, and generate a longitudinal component $S_z = S_y \cdot \alpha$, where $\alpha = dEL/\beta c$. To appreciate the complexity of the task, for a beam of deuterons with $T = 100$ MeV, a RFE flipper of length $L = 1$ m, a realistic electric field of $E = 15$ kV/cm, and $d = 10^{-23}$ cm, one finds $\alpha = 2.4 \cdot 10^{-12}$.

5.2 The coherent buildup of the EDM effect: single spin problem

The so generated longitudinal spin would precess in the magnetic field of the ring with respect to the momentum vector with frequency $f_S = \gamma G f_R$, i.e., by an angle $\theta_S = 2\pi\gamma G$ per revolution, where G is the anomalous magnetic moment and f_R is the ring frequency. The tiny EDM spin rotations we are after do not disturb this precession. Compared to the ring circumference, such a flipper can be treated as a point-like element. In view of the minuscule α the change of the magnitude of the in plane polarization, $S_{||} = (S_x^2 + S_z^2)^{1/2}$, per pass is well approximated by $S_{||}(i+1) = S_{||}(i) + S_y \alpha \cos\theta(i)$. Upon summing over k passes, one obtains

$$S_{||} = S_y \sum_{l=1}^{k} \alpha \cos(l\theta_S)\,, \tag{3}$$

which for a static electric field, α =const, would simply oscillate around zero. Evidently, the electric field of the flipper must by modulated in sync with the precession of the spin: $E = E_0 \cos(l\theta_F) = E_0 \cos(\theta_F f_R t)$, *i.e.*, $\alpha = \alpha_E \cos(\theta_F f_R t)$, resulting in the Master

Equation

$$S_{||}(t) = S_y \sum_{l=1}^{k} \alpha_E \cos(l\theta_S)\cos(l\theta_F) = \frac{1}{2}\sum_{l=1}^{k}[\cos(l(\theta_S-\theta_F)) + \cos(l(\theta_S+\theta_F))]\text{Б}-,. \quad (4)$$

Only the resonance condition

$$\theta_F = \pm\theta_S \quad (5)$$

furnishes the coherent build-up of the EDM signal (hereafter without loss of generality $\theta_F = \theta_S$)

$$S_{||}(t) = \frac{1}{2} S_y \alpha_E \nu t. \quad (6)$$

Swapping the harmonic modulation for the rectangular one would enhance the EDM signal by a factor $4/\pi$:

$$S_{||}(t) = S_y \sum_{l=1}^{k} \alpha_E |\cos(l\theta_S)| = \frac{2}{\pi} S_y \alpha_E \nu t. \quad (7)$$

For the sake of analytic simplicity, we focus here on the harmonic RFE flipper, which must run at a frequency $f_F = G\gamma f_R = f_S$. By a judicious choice of the particle energy one could readily stay away of depolarizing resonances in the machine.

5.3 The RFE flipper disturbs the orbit and the spin tune

The presence in a ring of an RFE flipper with oscillating electric field would affect both the particle orbit and spin tune. First, the RFE flipper would generate an oscillating radial momentum $\Delta p_r = eE_0 L\cos(G\gamma f_R t_i)/\beta c$ per i-th pass, which is off-tune with the ring frequency and betatron frequency. For the above specified RFE filter and 100 MeV deuterons the bending angle is about $\pm 2\cdot 10^{-3}$, well within the machine acceptance of COSY. Second, the spin precession with respect to the momentum rotation also acquires an oscillating correction

$$\vec{\omega} = -\frac{e}{m}\left[G\vec{B} - \left(G - \frac{1}{\gamma^2-1}\right)\vec{\beta}\times\vec{E}\right] \quad (8)$$

to $G\gamma$ familiar for a pure magnetic ring, where the electric term combines the changes of the spin precession proper and of the cyclotron frequency. The net effect can be viewed as a frequency modulation of the spin tune, $G\gamma \to G\gamma[1 - y_F\cos(l\theta_S)]$ where for energies of the practical interest

$$y_F \approx \left(1 - \frac{1}{G(\gamma^2-1)}\right)\frac{\beta EL}{2\pi BR} \quad (9)$$

is numerically small (here R stands for the ring radius). Then our Master Equation entails only a time-independent weak reduction of the accumulation rate:

$$S_{||}(t) = S_y \sum_{l=1}^{k} \alpha_E \cos(l\theta_S)\cos(l\theta_S[1 - y_F\cos(l\theta_S)]) =$$

$$S_y \sum_{l=1}^{k} \alpha_E \cos^2(l\theta_S)\left[(1 - \frac{1}{2}y_F^2\cos^2(l\theta_S)\right] = \frac{1}{2}(1 - \frac{3}{8}y_F^2) S_y \alpha_E \nu t\,. \quad (10)$$

The Farley pitch correction [15] to the spin tune would be important in the practical experiment when the ring is run for a long time, but it does not effect a flow of our principal arguments.

5.4 Polarimetry and bunched vs. coasting beam

Each individual particle for the first time enters the RFE flipper with a certain $\vec{S}_y(0)$, which remains stable, and a certain in-plane component $\vec{S}_{xz}(0)$. Upon k revolutions, the overall polarization vector can be decomposed as $\vec{S}(t) = \vec{S}_y(0) + \hat{R}_y(k)\vec{S}_{xz}(0) + \vec{S}_{||}(t)$, where $\hat{R}_y(k)$ is a matrix of spin rotation around the y-axis upon k revolutions and $\vec{S}_{||}(t)$ is the in-plane polarization generated by the RFE flipper. Upon averaging over an ensemble $\langle \vec{S}_{xz}(0) \rangle = 0$, we keep $\vec{S}_y(0)$ for $\langle \vec{S}_y(0) \rangle$. For a finite-length bunch and/or coasting beam our earlier derivation holds for a particle which enters the flipper at $t = 0$. Particles which are behind by a fraction $0 < z < 1$ of the ring circumference enter the flipper at a different field advanced by time $\Delta t = z/f_R$ and the modified Master Equation reads

$$S_{||}(z,t) = S_y \alpha_E \sum_{l=1}^{k} \cos(l\theta_S) \cos(l\theta_S + z\theta_S) = \frac{1}{2} S_y \alpha_E f_R t \cos(z\theta_S)\,. \tag{11}$$

The bunch can be viewed as point-like and its polarization is uniform if the length of the bunch z_b satisfies the condition $z_b\theta_S \ll 1$.

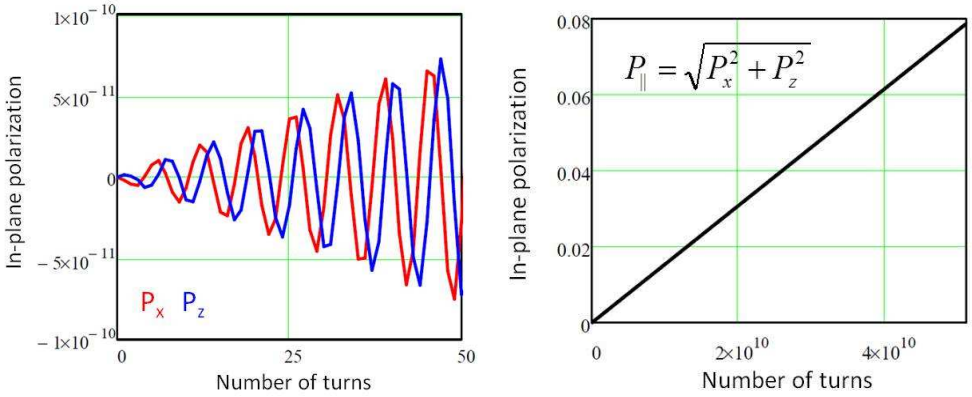

Figure 2: Left panel: Oscillating in-plane beam polarization components P_x and P_z (S_x and S_z) for the first 50 turns (revolutions) in the machine. Right panel: Evolution of the magnitude of the in-plane polarization $P_{||} = \sqrt{(P_x^2 + P_z^2)}$ during a spin coherence time of 10^5 s, which, under the specified conditions using 100 MeV deuterons in COSY corresponds to a total of 5×10^{10} turns in COSY.

The longitudinal component S_z, and the radial one S_x would oscillate, leading to $S_z = S_{||}(t)\cos(\theta_S f_R t)$ and $S_x = S_{||}(t)\sin(\theta_S f_R t)$, as shown in Fig. 2, where we show the results of modeling with spin rotation matrices. One would readily extract $S_{||}(t)$ from the relevant Fourier component of the up-down asymmetry

$$A_{u/d} = \frac{\int dt[N_{up}(t) - N_{down}(t)]\sin(\theta_S f_R t)}{\int dt[N_{up}(t) + N_{down}(t)]} \propto A_N S_{||}(t)\,, \tag{12}$$

where $N_{up/down}(t)$ are the corresponding count rates — this is a familiar technique. A simultaneous measurement of both S_x and S_z would have been an important cross check,

but a word of caution is in order: the in-plane magnetic fields are forbidden as the ordinary magnetic moment would cause a false precession of the vertical-to-in-plane spin. This seems to preclude the S_z polarimetry on a longitudinally polarized internal target with longitudinal holding magnetic field.

The use of a transversely polarized internal target, however, seems possible, although during the spin-flip process, it must run with empty cell but vertical guide field switched on, one would inject polarized particles into the cell only at the polarimetry stage, and, since one does not want to change the holding field polarity during the measurement, injection of different hyperfine states from the polarized source is necessary.

5.5 A null experiment

Complementing the radial electric field of the RFE flipper with the in-phase vertical magnetic field one can realize an exact cancellation of the flipper E field by the motional electric field, $\vec{E}^* = 0$, see Eq. (2). This would provide a null experiment for separation of the genuine EDM signal from false effects. On the other hand, an oscillating motional $\vec{B}^*$ only causes a weak frequency modulation of the spin tune and imposition of $\vec{B}^* = 0$ in the EDM run does not seem imperative.

5.6 Diffusion of the in-plane spin and spin coherence time

The extremely small single-pass rotation α_0 in the RFE flipper can only be overcome by an extremely large number of turns $f_R t$. While the vertical polarization is preserved by the holding field of the ring, the in-plane spins accumulated during the flipper process must all rotate coherently at one and the same rotation angle $\theta = \theta_S f_R t$ rather than evolving into a hedgehog. The spin coherency is one of the highest risk factors in all the EDM projects [7]. There is an important distinction between the lifetime of the polarization along the stable-spin axis, the spin coherence time (SCT) of the in-plane polarization when the beam idly rotates in the storage ring and the SCT during the build-up of the in-plane polarization.

5.6.1 Spin coherence time for an idle rotation

To a first approximation S_y is preserved irrespective of what happens to the rotating in-plane component of the spin. The spin tune $\theta_S = 2\pi\gamma G$ varies from revolution to revolution and from stored particle to particle because of the momentum fluctuations, $\theta = \theta_S + 2\pi G\delta\gamma = \theta_S + \delta\theta$. Hereafter $\theta_S = \gamma_0 G$ and γ_0 is defined for the average beam momentum ensured by cooling and RF bucket and by the very definition $\langle\delta\gamma\rangle = 0$. For the beginners, we swamp all imperfections, nonlinearities, betatron oscillations and whatever else into a Black Box which generates $\delta\gamma$ on the turn-by-turn basis, in the future all these effects need to be studied in detail. The average in-plane spin $\langle S_\parallel\rangle$ points at an angle $\theta = \theta_S f_R t$, while for an individual particle there is a cumulant spin precession slip $\Delta(k) = \sum_1^k \delta\theta_l$, so that

$$\langle S_\parallel\rangle = S_\parallel(0)\langle\cos\Delta\rangle = S_\parallel(0)\left\{1 - \frac{1}{2}\langle\Delta^2\rangle\right\} =$$
$$= S_\parallel(0)\left\{1 - 2\pi^2 G^2 f_R t\langle\delta\gamma^2\rangle\right\} = S_\parallel(0)(1 - t/\tau_{SC,NF})\,, \qquad (13)$$

where the subscript NF stands for No Flipper. It decreases with time because of the angular random walk (diffusion), which eventually shall evolve the spin arrow into a hedgehog, and

$$\tau_{SC,NF} \approx \frac{1}{2\pi^2 f_R G^2 \gamma^2 \beta^4} \cdot \left\langle \left(\frac{\delta p}{p}\right)^2 \right\rangle^{-1} \tag{14}$$

has a meaning of the SCT for an idle rotation in the absence of a spin flipper.

Admittedly, such a violent turn-by-turn randomization of the momentum fluctuations leads to an excessive spin diffusion and arguably Eq. (14) gives a lower bound on SCT. A discussion of more realstic scenarios with slow variations of the beam particle momenta will be reported elsewhere.

5.6.2 Spin coherence time with a running spin flipper

Still another source of spin decoherence is the fluctuation of the revolution (transit) time τ, described in terms of slip-factor, $\delta\tau/\tau = \eta\delta\gamma/\gamma\beta^2$, where

$$\eta = \frac{1}{\gamma_{tr}^2} - \frac{1}{\gamma^2}\,, \tag{15}$$

and γ_{tr} is the transition gamma-factor [16]. It produces a slip of the phase of the RFE flipper per pass $\delta\theta = 2\pi f_F \delta\tau$. Then the Master Equation will take the form

$$S_{||} = S_y \alpha_E \sum_{l=1}^{k} \cos(l\theta_S + \Delta(l))\ \cos(l\theta_S + \eta\Delta(l) i/\beta^2)\,, \tag{16}$$

where $\Delta_i = \sum_{n=1}^{i} \delta\theta_n$ is the cumulant precession slip before the i-th pass through the RFE flipper. Following the derivation of Eq. (13), we readily find

$$S_{||} = S_y \alpha_E \sum_{l=1}^{k} \cos^2(i\theta_S)(1 - l2\pi^2 G^2 C_{SD}^2 \langle\delta^2\gamma\rangle) = S_y \alpha_E \frac{1}{2} f_R t \left(1 - \pi^2 f_R t G^2 C_{SD}^2 \langle\delta\gamma^2\rangle\right)\,, \tag{17}$$

where

$$C_{SD} = 1 - \frac{\eta}{\beta^2}\,. \tag{18}$$

The corresponding SCT equals

$$\tau_{SC} = \frac{2}{C_{SD}^2}\tau_{SC,NF} \approx \frac{1}{C_{SD}^2 \pi^2 f_R G^2 \gamma^2 \beta^4} \cdot \left\langle \left(\frac{\delta p}{p}\right)^2 \right\rangle^{-1}\,. \tag{19}$$

Small $G_d = -0.143$ strongly enhances the deuteron SCT compared to the proton SCT (we ignore here a possible difference of C_{SD} for protons and deuterons),

$$\tau_{SC}^p \sim \tau_{SC}^d \cdot \left(\frac{G_d}{G_p}\right)^2 \sim \frac{1}{200}\tau_{SC}^d\,. \tag{20}$$

For non-relativistic particles $-\eta/\beta^2 \approx 1/\beta^2$ and the in-plane spin-diffusion is entirely dominated by the flipper phase slip and large C_{SD}^2 strongly suppresses τ_{SC}. There are

two strategies: either find a way to suppress C_{SD} or eliminate the flipper phase slip, *i.e.*, enforce $\eta = 0$. Strongly different G_p and G_d suggest the former strategy for protons and the latter for deuterons.

The SCT considerations do obviously favor running COSY at non-relativistic energies. For the reference case of 100 MeV deuterons, $\nu \approx 511$ kHz, and cooled beam with $\delta p/p = 10^{-4}$, our estimate yields $\tau_{SC}^{d}(\eta = 0) \sim 3 \cdot 10^5$ s.

A purely electrostatic rings would share the above spin decoherence mechanisms, although the analytic treatment would be substantially different from that for the point-like RFE flipper.

5.7 Running RFE flipper at higher frequencies?

5.7.1 Bad news for nonrelativistic deuterons?

Short bunches offer the possibility of operating the RFE flipper at higher frequency. One could run the flipper at any frequency $f_F = (\gamma G + K) f_R$, where $K = 0, \pm 1, \pm 2...$ is integer. Indeed, short bunches probe the E-field only at discrete times $t_i = i/f_R$ and $\cos(2\pi l f_F) = \cos(l\theta_S + 2\pi l K) = \cos(l\theta_S)$. Evidently, for an ideal particle, the build-up of the EDM signal wouldn't depend on K. The limitation on the bunch length becomes much more stringent, though:

$$z_b(\theta_S + 2\pi K) = x_b \theta_S \left(1 + \frac{K}{\gamma G}\right) \ll 1\,. \tag{21}$$

A similar bound is imposed on the length of the flipper, z_F, in units of the ring circumference: $z_F \theta_S (1 + K/\gamma G) \ll 1$.

Simultaneously, the troublesome flipper phase slip acquires the same factor $(1+K/\gamma G)$, so that C_{SD} in the diffusion rate will change to

$$C_{SD} = 1 - \left(1 + \frac{K}{\gamma G}\right) \cdot \frac{\eta}{\beta^2}\,. \tag{22}$$

For deuterons at COSY, $K/|G_d| \gg 1$ and running at higher frequencies invites an unwanted suppression of the SCT for nonrelativistic deuterons by still another small factor $\sim (G_d/K)^2$, *i.e.*, by almost two orders in magnitude.

5.7.2 Good news for protons: suppression of spin diffusion at magic energies

A closer look at Eq. (22) suggests an intriguing possibility of a set of magic energies at which the flipper phase slip would compensate the effect of the spin tune slip. We recall that η is large and negative valued for non-relativistic particles. Then by a judicious choice of $K = -N$ and γ such that

$$K + \gamma G < 0 \tag{23}$$

one could arrange for $C_{SD} = 0$, *i.e.,* for a vanishing spin diffusion rate. These magic energies are roots of an equation

$$\gamma^3 = -\frac{K}{G} + \frac{\gamma^3}{\gamma_{tr}^2}\left(\frac{K}{\gamma G_p} + 1\right)\,. \tag{24}$$

For protons $G_p = 1.793$ and solutions do exist for $-K = N = 2, 3, ...$ Because the transition energy is high, $\gamma_{tr}^2 >> 1$ (in one of regimes at COSY $\gamma_{tr}^2 \approx 3.3$), for a quick estimate of lowest roots one can resort to an iterative solution

$$\gamma_{N-1} = \left(\frac{N}{G_p}\right)^{1/3} \left(1 - \frac{1}{3\gamma_{tr}^2}\left[\left(\frac{N}{G_p}\right)^{2/3} - 1\right]\right) . \tag{25}$$

With the above specified γ_{tr}, the lowest magic energy at $N = 2$ equals $T_p \approx 29$ MeV, which is too low. The second root at $N = 3$ corresponds to $T_p \approx 133$ MeV, which is within the range of the existing COSY electron cooler. Besides a possibility of cooling, this magic energy is preferred because of longer beam lifetime. The third root gives $T_p \approx 210$ MeV. An asymptotic convergence of large-N magic energies to transition energy, *i.e.*, to an isochronous ring, is noteworthy:

$$\gamma_N^2 = \gamma_{tr}^2 - \beta_{tr}^2 \gamma_{tr}^5 G_p \cdot \frac{1}{N} . \tag{26}$$

This finding of spin-decoherence-free magic energies lifts the pessimism of Eq. (20) and paves the way to a high sensitivity searches for the proton EDM at COSY.

We strongly emphasize that the existence of magic energies only depends on the fact that the spin precession and flipper phase slips are locked to each other and does not depend on the exact model for the phase slip and for the momentum fluctuations.

5.7.3 Magic energies for deuterons at COSY

Deuterons also possess a sequence of magic energies albeit at higher energies. Since $G_d < 0$, here we look for $K = +1, 2, \ldots$. To a first approximation, deuterons and protons do share the same γ_{tr}. Assuming above γ_{tr}, the lowest magic energy at $K = 1$ equals $T_d \approx 0.9$ GeV, while at $K = 2$ our estimate is $T_d \approx 1.15$ GeV, which are accessible at COSY. Transition energy is tunable, for instance at $\gamma_{tr}^2 = 4$ we find the deuteron magic energies $T_d(K = 1) \approx 1.03$ GeV and $T_d(K = 1) \approx 1.33$ GeV.

Magic energies vindicate the harmonic modulated RFE flippers but leave open an issue of dynamic magnetic fields generated by dE/dt. For deuterons this menace, which deserves a separate treatment, can be circumvented by a flat-top RFE flipper.

5.8 Advantages of a rectangular (flat-top) modulated RFE flipper for deuterons

5.8.1 Even mode flat-top flipper

If running COSY with deuterons at magic energy would prove impractical, then the phase-slip of the flipper E-field emerges as a potential show-stopper for deuterons. Here we notice that this phase-slip can be entirely eliminated by employing a rectangular (flat-top) modulation of the RFE flipper,

$$E(t) = E_0(-1)^{N_F} , \qquad N_F = \mathrm{int}(\gamma G f_R t/\pi) . \tag{27}$$

which does not depend on the phase slip. The exact rectangular modulation is not imperative, what we are asking for is a flat top when the bunch passes through the flipper.

In order to avoid the effects of dynamical magnetic fields generated by dE/dt, the E-field must be inverted when the bunch is at 180 degree, the opposite side of the ring. The simplest solution is to lock the RFE flipper frequency to the ring frequency

$$f_F = \frac{1}{2N} f_R \,. \tag{28}$$

For deuterons $N = 3$, *i.e.*, $\gamma|G_d| = 1/2N = 1/6$ is a convenient option: here the flipper field is inverted once per $N = 3$ revolutions of the beam. However, that demands for somewhat higher kinetic energy: $\gamma_d = 1.169$, $T_d = 317$ MeV, $\beta = 0.52$, $f_R = 0.98$ MHz, and $\nu_F = 163$ kHz. The price tag for the higher energy of deuterons is a somewhat shorter spin coherence time: our Eq. (19) for $\eta = 0$ gives $\tau_{SC} \sim 6 \cdot 10^3$ s.

5.8.2 Odd-mode flat-top flipper: dedicated low-energy ring for the deuteron EDM?

Curiously enough, for the reason that $1/|G_d| = 7.0145$, the condition $\gamma|G_d| = 1/7$ is met at $\gamma = 1.00207$, *i.e.*, $T_d = 3.88$ MeV. Such deuterons will make 7 revolutions and pass the flipper 7 times per single spin turn. Then the flat-top cycle can be organized as follows:

Switch the flipper on when the bunch is on the opposite side of the ring. After 3 revolutions at $E > 0$ switch the field off so that the 4-th revolution is at $E = 0$, and then switch the flipper on again at inverted polarity, $E < 0$, when the bunch is opposite the flipper. The second inversion of the E-field is after the 7th revolution with a bunch opposite the flipper. This way we managed to exclude the 4th revolution which would have crossed a flipper at exactly the time when the E-field is inverted.

Low energy enhances both the single-pass tilt of the spin and spin coherence time but decreases the beam lifetime — the latter might prove a show stopper. Whether one can gain or not in sensitivity to EDM with such a curious option is worth of further scrutiny.

5.8.3 Half-integer-mode flat-top flipper

Still another interesting option is $1/\gamma|G_d| = 6.5$, when $\gamma = 1.07915$ and $T_d = 148.5$ MeV. The flipper period would comprise two spin turns and 13 revolutions of the beam and the sought for cycle must be organized as follows:

The flipper field $E > 0$ is switched on when the bunch is at 180 degree from the flipper, kept constant for revolutions 1, 2 and 3, inverted to $E < 0$ for revolutions 4, 5 and 6, switched off, $E = 0$, during the 7-th revolution, inverted to $E > 0$ for revolutions 8, 9 and 10, and $E < 0$ for revolutions 11, 12 and 13.

Running the flipper in such a mode is a challenging task, but an obvious benefit is the smaller T_d and the larger spin coherence time of $\tau_{SC} \sim 3 \cdot 10^4$s.

5.8.4 One-third-integer-mode flat-top flipper

A still more interesting option is $1/|G_d| = 20/3$, when the flipper period comprises 3 spin turns and 20 revolutions of the beam. The flipper field inversion pattern is as follows: $E > 0$ for revolutions 1, 2 and 3; $E < 0$ for revolutions 4, 5, 6 and 7; $E > 0$ for revolutions 8, 9 and 10; $E < 0$ for revolutions 11, 12 and 13 $E > 0$ for revolutions 14, 15, 16 and 17, and $E < 0$ for revolutions 18, 19 and 20. In this mode $\gamma = 1.0522$ and $T_d = 98$ MeV, and as we evaluated above, $\tau_{SC} \sim 10^5$s.

6 RF magnetic flipper

6.1 A proof of the principle at COSY

Remarkably, much of the spin dynamics in the suggested EDM experiment at COSY can be tested by swapping the RF electric flipper for an RF magnetic flipper (RFB) with a *radial* RF magnetic field. In such an RFB flipper the magnetic moment of the deuteron would do exactly the same job as the sought for EDM in the RFE flipper. The anomalous magnetic moment of the deuteron is $\sim 3 \cdot 10^{-15}$ e cm, while we speak of EDM of $\sim 10^{-24}$ e cm, consequently a single-pass magnetic tilt α_B can be made gigantic compared to the above estimated α_E for the expected EDM. This adds an entirely new dimension: while we dream of accumulation of a several per mill to several per cent in-plane polarization running RFE flipper for 10^5s, employing an RFB one could readily have single-pass tip angles $\alpha_B \sim 10^{-6}$. The net result will be that within seconds the accumulation of the in-plane polarization will end up in total consumption of the initial vertical polarization $S_y(0) = +1$, *i.e.*, ideally we get $S_\parallel = 1$ at $S_y = 0$, which then will be followed by the accumulation of the vertical polarization from the in-plane one down to $S_y = -1$ at $S_\parallel = 0$ and so forth. If the in-plane spin decoheres, the restoration of the vertical spin will be imperfect and the decay time of oscillations can be related to the spin coherence time.

However, an RFB flipper with a *longitudinal* magnetic field, tangential to the orbit, is doing exactly the same job! Indeed, the RFB flipper with *radial* field generates resonance forward and backward tips of the spin, which then precesses in the ring magnetic field.. The effects of the *longitudinal* vs. *radial* B-fields only differ by swapping S_z and S_y, *i.e.*, by a $\pi/2$ shift of the spin precession angle, otherwise the buildup of the in-plane polarization is exactly the same.

Remarkably, such a proof of principle with *longitudinal* RFB flipper has already been achieved at COSY in January 2011, the analysis is in progress and preliminary results have been reported at several meetings [17, 18]. The period of oscillations is obviously $\propto 1/\alpha_B$, *i.e.*, inversely proportional to RFB flipper magnetic field, which has indeed been seen in the COSY experiment [17, 18].

6.2 Systematics and ring imperfections with RFB flipper

The beauty of the COSY experiment with gigantic α_B is that one could have resorted to a conventional polarimetry of the oscillating vertical polarization S_y. In the EDM experiments with $S_\parallel$ in at most per mill range a variation of S_y can not be detected, which makes mandatory the polarimetry of the precessing in-plane polarizations S_x and S_z. Various sequels to the COSY experiment could distinguish the spin decoherence caused by RFE and RFB flippers and the one from the ring imperfections.

The former has been our major concern, the latter is for the most part an uncharted territory. We notice that running at magic energy one would eliminate the flipper effects and the remaining spin decoherence is a direct measure of the systematic effects driven by the ring imperfections. A second option has already been tried at COSY [17, 18]: rotate the vertical polarization to pure horizonal one, let $S_\parallel$ precess for a long time and rotate it back to the vertical one. This requires a perfect timing when the RFB flipper is turned on again: as we discussed in Section 5.4., a slip of the flipper phase by θ_{slip} with

respect to spin precession could suppress the recovered vertical polarization $\propto cos(\theta_{slip})$, which would imitate a spin decoherence. Much more advantageous is to look at a decay of oscillating S_x, which would measure spin decoherence in idle precession and give $\tau_{SC,NF}$ compounded by the possible decoherence from the ring imperfections.

The RFB flipper of the COSY experiment was run in a harmonic mode at a frequency $f_F = (1 + \gamma|G_d|)f_R$. For a better insight into spin decoherence mechanisms one needs to repeat the experiment at lower frequency $f_F = \gamma G_d f_R$ and test the predicted suppression of decoherence with flat-top modulated RFB. The experiments with protons are equally important to test the predicted change of τ_{SC} from deuterons to protons and to test the predicted existence of magic energies, as well as a search for a predicted magic energy of deuterons in the vicinity of $T_d \sim 1$ GeV. At last but not the least, decreasing the RFB field from micro- to nano- to pico-tesla range one could explore the systematics of the COSY ring down to the anticipated sensitivity of the EDM-experiments at COSY.

7 Summary and Conclusions

We reported on the first look into the potential of all-magnetic rings as EDM machines. The emerging strategy of the proton and deuteron EDM searches at COSY is as follows:

Running the COSY ring, supplemented with the above specified 20/3-mode flattop-modulated RFE flipper (for 98 MeV deuterons, $\nu_F = \gamma|G_d|\nu \sim 77$ kHz), for $\tau^d_{SC} = 10^5$ and assuming $d_d = 10^{-23}$ e·cm, the accumulated CP violating in-plane polarization of the deuteron could be as large as $S_{||} = 0.08$. To reach an upper bound of $d_d = 10^{-24}$ e·cm polarizations of $S_{||} = 0.008$ need to be determined, which is within the reach of state of the art polarimetry. Such an upper bound on the deuteron EDM of $d_d < 10^{-24}$ e·cm would be comparable to the results from the model-dependent reinterpretation of upper bounds on atomic EDMs [2], and size-wise is close to the ball-park neutron EDM bounds.

Magic energies at which the in-plane spin decoherence is strongly suppressed open entirely new perspectives for the proton (and perhaps the deuteron) EDM at COSY. The existence of magic energies is a model-independent feature of the rotation of the spin by a radiofrequency flipper.

True, regarding the systematics, we have presently touched only the tip of the iceberg in a very crude analytic approach and much more scrutiny of the ring lattice and imperfections which will affect polarization lifetime and also somewhat limit the sensitivity is in order. Specifically, one badly needs spin tracking tools capable of handling with controlled precision up to $\sim 10^{11}$ turns in a realistically modeled machine. A special care must be taken of false rotations via the magnetic moment in the RFE flipper - these might prove a main systematics and has to be thoroughly investigated. With all reservations, the RFE flipper experiment at COSY looks like a promising one. We especially emphasize again here the importance of extending further in-situ studies at COSY using very slow RF magnetic flippers to study systematic effects for both deuterons and protons. In the case of protons a confirmation of the existence of magic energies, and how well the spin decoherence is eliminated at these energies, need to be studied in dedicated RF magnetic flipper experiments — this chance of making COSY the proton EDM machine need not be overlooked.

8 Acknowledgments

We acknowledge fruitful discussions with Rudolf Maier, Yuri Senichev, Ed Stephenson, Hans Ströher and Richard Talman. We are grateful to the Workshop organizers for a chance to present our new ideas on the search for EDM at pure magnetic rings.

References

[1] A. Sakharov, *Pisma Zh.Eksp.Teor.Fiz.* **5**, 32 (1967), Reprinted in Sov. Phys. Usp. 34 (1991) 392-393 [Usp. Fiz. Nauk 161 (1991) No. 5 61-64].

[2] B. L. Roberts and W. J. Marciano (eds.), *Lepton Dipole Moments*, Advanced Series on Directions in High Energy Physics, Vol. 20 (World Scientific, 2010).

[3] S. Weinberg, *AIP Conf.Proc.* **272**, 346 (1993).

[4] V. Flambaum, I. Khriplovich and O. Sushkov, *Nucl.Phys.* **A449**, p. 750 (1986).

[5] V. Flambaum, I. Khriplovich and O. Sushkov, *Phys.Lett.* **B162**, 213 (1985).

[6] , I. Khriplovich, *Phys.Lett.* **B444**, 98 (1998).

[7] Y. K. Semertzidis, *AIP Conf.Proc.* **1182**, 730 (2009) and references therein.

[8] J. H. Smith, E. M. Purcell and N. F. Ramsey, *Phys. Rev.* **108**, 120(Oct 1957).

[9] S. K. Lamoreux and D. Golub, *Lepton Dipole Moments*, Advanced Series on Directions in High Energy Physics Vol. 20 (World Scientific, 2010), ch. 15, p. 583.

[10] C. Baker *et al.*, *Phys.Rev.Lett.* **98**, p. 149102 (2007).

[11] W. Griffith *et al.*, *Phys.Rev.Lett.* **102**, p. 101601 (2009).

[12] M. A. Rosenberry and T. E. Chupp, *Phys. Rev. Lett.* **86**, 22(Jan 2001).

[13] G. W. Bennett *et al.*, *Phys. Rev. D* **80**, p. 052008(Sep 2009).

[14] Y. F. Orlov, W. M. Morse and Y. K. Semertzidis, *Phys. Rev. Lett.* **96**, p. 214802.

[15] F. Farley, *Phys.Lett.* **B42**, 66 (1972).

[16] A. Chao and M. Tigner (eds.), *Handbook of accelerator physics and engineering* (World Scientific, 1999).

[17] E. Stephenson, Polarimeter and Spin Coherence Time Developments at COSY for a Storage Ring EDM Search *Proceedings of the 8th International Conference on Nuclear Physics at Storage Rings - STORI'11*, (2011), to be published.

[18] G. Guidoboni, Synchrotron Oscillations Effects on Observations of an RF-solenoid Spin Resonance for a Polarized Deuteron Beam at COSY *Proceedings of the 8th International Conference on Nuclear Physics at Storage Rings - STORI'11*, (2011), to be published.

A FEASIBILITY EXPERIMENT AT RHIC TO MEASURE THE ANALYZING POWER FOR DRELL-YAN PRODUCTION (A_NDY)

L. Nogach[4,†], E.C. Aschenauer[1], A. Bazilevsky[1], L.C. Bland[1], K. Drees[1], C. Folz[1], Y. Makdisi[1], A. Ogawa[1], P. Pile[1], T.G. Throwe[1], H.J. Crawford[2], J. Engelage[2], E.G. Judd[2], C.W. Perkins[2,3], A. Derevshchikov[4], N. Minaev[4], D. Morozov[4], G. Igo[5], M. Grosse Perdekamp[6], M.X. Liu[7], H. Avakian[8], E.J. Brash[8,9], C.F. Perdrisat[10], V. Punjabi[11], X. Li[12], M. Planinic[13], G. Simatovic[13], A. Vossen[14], G. Schnell[15], C. Van Hulse[15], A. Shahinyan[16], S. Abrahamyan[16], N. Liyanage[17], K. Gnanvo[17]

(1) *Brookhaven National Laboratory, USA*
(2) *University of California/Space Science Laboratory, Berkeley, USA*
(3) *Stony Brook University, USA*
(4) *Institute of High Energy Physics, Protvino, Russia*
(5) *University of California, Los Angeles, USA*
(6) *University of Illinois, USA*
(7) *Los Alamos National Laboratory, USA*
(8) *Thomas Jefferson National Accelerator Facility, USA*
(9) *Christopher Newport University, USA*
(10) *College of William and Mary, USA*
(11) *Norfolk State University, USA*
(12) *Shandong University, China*
(13) *University of Zagreb, Croatia*
(14) *Indiana University, USA*
(15) *University of the Basque Country and IKERBASQUE, Spain*
(16) *Yerevan Physics Institute, Armenia*
(17) *University of Virginia, USA*
† *E-mail: Larisa.Nogach@ihep.ru*

Abstract

Large transverse single spin asymmetries (SSA) were measured for pions produced in $p\uparrow p$-collisions up to RHIC energies. Sizeable SSA were also found in semi-inclusive deep inelastic scattering (SIDIS). Theory can explain such spin effects by going beyond collinear leading-twist perturbative QCD (pQCD) to include transverse momentum dependent (TMD) distribution and fragmentation functions. One of the most interesting TMDs is the Sivers function, which provides information on the correlation between the transverse spin of the nucleon and the transverse momentum distributions of the partons in the nucleon. It is particularly intriguing that theory predicts the Sivers function will change sign from SIDIS to Drell-Yan (DY) production. A_NDY is aiming to test that prediction and to establish requirements for future upgrades at RHIC to study DY production. The experiment configuration, achievements to date, status and plans are discussed.

1 A feasibility experiment to measure Drell-Yan

RHIC remains a unique machine that can accelerate and collide polarized proton beams at center-of-mass-energies $62 \leq \sqrt{s} \leq 500\ GeV$. The goal of the RHIC spin program is to

identify how the proton gets its spin from the quark and gluon constituents. Transverse SSA play an important role in understanding the spin structure of the proton because in the simple picture of collinear leading-twist perturbative QCD, they are expected to be small. Contrary to these expectations, significant spin effects in inclusive pion production in pp-collisions were first found at low energies ($\sqrt{s} \leq 20\ GeV$) [1, 2] and then measured at RHIC [3, 4]. Non-zero SSA were also observed in SIDIS from transversely polarized proton targets [5,6]. The experimental results have stimulated theory development which led to extensions of the collinear parton model by introducing spin-correlated transverse momentum (k_T) to parton distribution and fragmentation functions.

The Sivers mechanism attributes the transverse spin effects to a correlation between the parton k_T and spin of the proton [7]. To give a non-zero effect, it requires a final-state interaction in SIDIS. Theory predicts that the attractive final-state interaction in SIDIS becomes a repulsive initial-state interaction in DY process thereby resulting in a sign change for the Sivers function between the two processes [8]. New theoretical development and attempts of a global analysis of SIDIS and inclusive pion production at RHIC [9, 10] lead to the conclusion that it is essential to test the predicted sign change for DY in the x_F region that overlaps with SIDIS kinematics.

A feasibility experiment at RHIC, A_NDY, was proposed to test that prediction and to establish basic requirements for future upgrades at RHIC for DY measurements. Forward DY production is of interest not just for the analyzing power, it is also the most robust observable sensitive to low-x parton distributions for intercomparison to results in dAu pion production and to a future electron-ion collider. A_NDY is located at RHIC 2 o'clock Interaction Point (IP2), where beam polarization is always transverse. It thus can run in parallel with the RHIC W program at IP6 and IP8. A_NDY goals are: 1) to establish that large-x_F low-mass e^+e^--pairs from the DY process can be discriminated from background in pp-collisions at $\sqrt{s} = 500\ GeV$; 2) to provide sufficient statistical precision for the DY analyzing power measurement to test the theoretical prediction of a sign change compared to SSA for SIDIS. Yet another objective is to determine whether tracking for the charge sign discrimination is necessary for DY measurements or calorimetry alone would be sufficient.

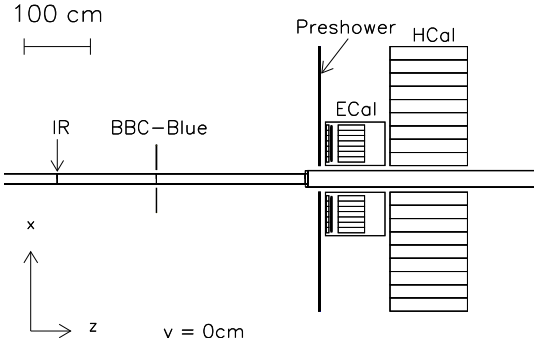

Figure 1: Top view of A_NDY configuration for RHIC 2011 run. The Blue beam travels in the positive z direction, and the Yellow beam in the opposite direction. IR indicates the center of the collision region.

2 2011 test run

A schematic view of the A_NDY setup for the 2011 run is shown in Fig. 1. The setup included: two beam-beam counters (BBC), located on both sides of the IR (BBC-Yellow is not shown), for minimum-bias triggering and luminosity measurement; two zero-degree calorimeters with shower maximum detectors (ZDC, not shown) for luminosity measurement and verifying that A_NDY can measure a known analyzing power; hadron calorimeter (HCal) — two modules of 9×12 lead-scintillating fiber cells placed symmetrically left and right of the beam pipe, to assess hadronic background and for jet reconstruction; small

electromagnetic calorimeter (ECal) — two 7×7 matrices of (4 cm)^2×40 cm lead glass cells, for photon/electron/π^0-reconstruction; preshower detector (two planes, 2.5 cm and 10 cm scintillating strips) to assist in photon/electron/hadron separation.

The primary goals for the 2011 run were: 1) to establish the impact of collisions at IP2 on IP6 (STAR) and IP8 (PHENIX) operation; 2) to demonstrate a means of HCal calibration; 3) to measure the hadronic background for comparison with simulations. Fig. 2 shows luminosities at three interaction points for a RHIC fill. Collisions at IP2 began when the bunch intensity had decreased to a preset value (in this case, 1.5×10^{11} ions per bunch). There is no noticeable effect from adding collisions at IP2 for this fill. The Collider-Accelerator Department (CAD) developed an automated procedure for bringing A$_N$DY into collisions, and repeatedly demonstrated that it can be done without significant impact on beam life time and luminosities at the other two interaction points. Along with these tests, A$_N$DY was taking data using a set of triggers: minimum bias (a condition on the time difference between the earliest hits in the BBC-Yellow and BBC-Blue to define a collision at IP2), energy sum in ECal, jets in HCal for physics, LED and cosmic-rays for monitoring. Integrated luminosity of 6.5 pb^{-1} was acquired. DY measurements set the goal of $\geq$ 100 pb^{-1}. CAD stated that $\sim$ 10 pb^{-1}/week could be delivered to IP2, but would require decreasing β^* from 3 m to 1.5 m. With 100 pb^{-1} of integrated luminosity and 50% beam polarization expected uncertainty for the DY analyzing power measurements is $\sim$ 0.03.

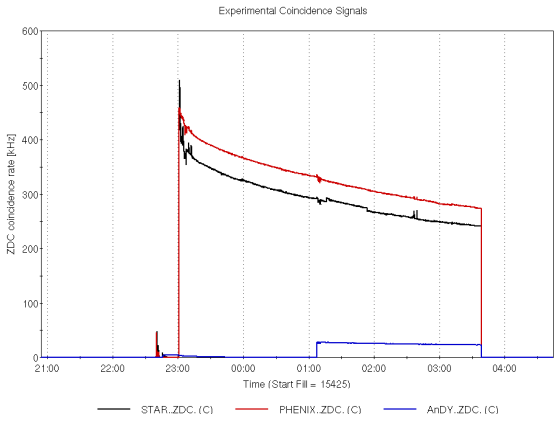

Figure 2: ZDC coincidence rate at three interaction points versus time for one RHIC store. Collisions at IP2 were initiated after bunch intensity had decreased to 1.5×10^{11} ions per bunch.

About 7.5×10^8 jet triggered events were collected during 2011 run. First step in the data analysis was to define the absolute energy scale of HCal. This was done using π^0-reconstruction [11]. An attempt at full jet reconstruction using this calibration is shown

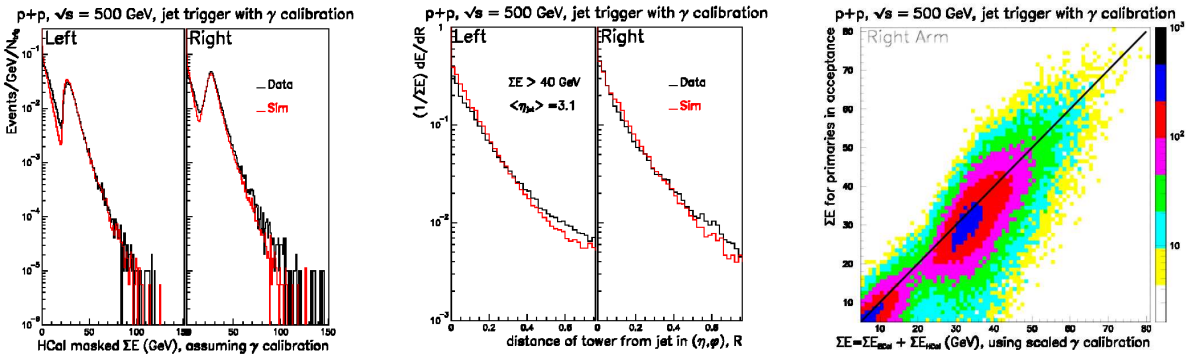

Figure 3: **(a)** Distribution of summed energy in HCal modules from the jet trigger. **(b)** Distribution of energy in the jet as a function of distance in η-ϕ space from the jet center (jet shape). **(c)** Jet energy from simulations versus reconstructed response in ECal+HCal.

in Fig. 3. There is a reasonable agreement between data and PYTHIA (version 6.222) + GEANT simulations for jet energy (Fig. 3a). The data show a somewhat broader jet shape than the simulations (Fig. 3b). Flattening of the jet shape at larger R is caused by an underlying event contribution, which appears to be smaller than a few percents. The jet energy scale was checked with the association analysis of the simulations: primaries from PYTHIA were projected to HCal, the energy of those in the acceptance was summed and correlated with the reconstructed energy in ECal+HCal. This correlation is shown in Fig. 3c, and it proves that the jet energy scale is quite well defined using the photon (neutral pion) calibration. The next step would be the more sophisticated algorithm for jet reconstruction and a look at the jet analyzing power.

3 Future plans

The A_NDY proposal that was endorsed by the Program Advisory Committee at BNL in May 2011, supposed two years of data taking for DY measurements: a 2012 run with the full calorimetry and a 2013 run with the magnet and tracking added. The initial approach was to build modular, left-right symmetric detectors for A_NDY. To reduce the luminosity requirements and taking into account that for the most robust measurement of the sign change the x_F region would overlap with SIDIS kinematics, the A_NDY acceptance was optimized. ECal, HCal and preshower detector will be stacked around the beam pipe to provide full azimuthal coverage. Electromagnetic calorimetry required for the complete A_NDY setup was loaned from JLab and delivered to BNL. The staging of the apparatus awaits a funding review. The first attempt at a transverse spin DY measurement will be in the RHIC 2013 run.

References

[1] D.L. Adams *et al.*, Phys. Lett. **B261** (1991) 201; **B264** (1991) 462.

[2] K. Krueger *et al.*, Phys. Lett. **B459** (1999) 412;
C.E. Allgower *et al.*, Phys. Rev. **D65** (2002) 092008.

[3] B. Abelev *et al.*, Phys. Rev. Lett. **101** (2008) 222001.

[4] I. Arsene *et al.*, Phys. Rev. Lett. **101** (2008) 042001.

[5] A. Airapetian *et al.*, Phys. Rev. Lett. **103** (2009) 152002; Phys. Lett. **B693** (2010) 11.

[6] M.G. Alekseev *et al.*, Phys. Lett. **B692** (2010) 240.

[7] D. Sivers, Phys. Rev. **D41** (1990) 83; **D43** (1991) 261.

[8] J.C. Collins, Phys. Lett. **B536** (2002) 43.

[9] Z. Kang, J. Qiu, W. Vogelsang, F. Yuan, Phys. Rev. **D83** (2011) 094001.

[10] A. Prokudin, Z. Kang, workshop "Opportunities for Drell-Yan Physics at RHIC", http://www.phenix.bnl.gov/WWW/publish/elke/TALKS/DY-May2011/Talks/AlexeiProkudin.pdf.

[11] C. Perkins, arXiv:1109.0650.

PRODUCTION OF THE POLARIZED PROTON/ANTIPROTON BEAM FROM THE INTERNAL TARGET OF U-70 ACCELERATOR

Yu.S. Fedotov [1], E.N. Lomakin [1], V.P. Kartashev [1], Yu.S. Khodyrev [1], S.B. Nurushev [1†], V.N. Zapolsky [1], V.A. Chetvertkova [2] and M.A. Chetvertkov [3]

(1) *Institute for High Energy Physics, Protvino*
(2) *Skobeltsyn Institute of Nuclear Physics, Moscow State University, Moscow*
(3) *Moscow State University, Moscow*
† *E-mail: Sandibek.Nurushev@ihep.ru*

Abstract

It is shown that the possibility exists for production and formation of the polarized proton beam from Λ^0 - decays using the internal target of the U-70 accelerator. Description of the beam channel and the calculated parameters of the beam for the SPASCHARM experiment are presented.

1. Introduction.

The main goal of the new polarization experiment SPASCHARM at U-70 accelerator consists of :

1) The accurate measurements of single spin asymmetries in the exclusive and inclusive productions of charged and neutral hadrons in reactions $p \uparrow p \to hX$, $p \uparrow A \to hX$.

2) The measurements of double-spin asymmetries in reactions $p \uparrow p \uparrow \to hX$.

Performing these experiments in the existing channel of a polarized proton beam (PPB) [1] is practically impossible due to difficulties in relocation of the set-up to another place (the area's limitation, the full disassembling and new assembling). For preservation of the set-up's position it was suggested in papers [2, 3] to create the new PPB using an internal production target (IPT) of the U-70 accelerator. This target is used as a source of neutral Λ - hyperons produced by the primary accelerated protons. In this case also as in the realized PPBs with an external target [1,4] polarized protons are produced from Λ^0 - decays. The results of detailed study of production and tracing of the polarized protons in the accelerator, optics of the new beam channel for formation and transportation of the PPB to the target of the experimental set-up are presented in this report. Also the preliminary analysis of optimal conditions for obtaining polarized antiprotons using the IPT is given.

2. Production and tracing the polarized protons in accelerator ring.

The choice of the IPT position was defined by the following requirements: necessity of the optimum use of the accelerator magnetic structure, presence of the free area for insertion of the new beam equipments and a zero Λ^0 – hyperon production angle. Layout of all systems is shown on Fig. 1. The IPT made of *Al* or *Be* is placed in the vacuum chamber at the middle of the magnetic block 23. The IPT has the cylindrical shape with length $l = 30\ mm$ (along the beam line) and the diameter of 3 mm. The IPT has

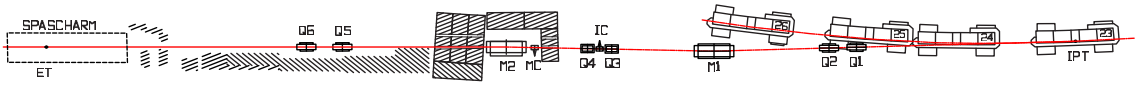

Figure 1: Joint layout of the accelerator's magnetic blocks 23 - 25, the internal production target (IPT), the beam channel equipment (Q1-Q6 – magnetic quadrupoles; M1, M2 - magnetic dipoles; IC, MC - intermediate and momentum collimators) and the set-up SPASCHARM with the experiment's target (ET).

the radial position of 40 *mm* outside of the equilibrium proton orbit in the accelerator. In this case the magnetic field of the second half ($\sim$ 5 m) of the block 23 separates neutral and unwonted charged particles immediately after the IPT. Then Λ^0 - hyperons decaying in the straight section of length 4.8 m (Λ^0 - life path is approximately 4 m at $\gamma_\Lambda \sim$ 50) between magnetic blocks 23 and 24 of the accelerator ring generate the polarized protons via weak decay. These protons travel in the block 24 through the area with screened magnetic field and leave the accelerator ring. The magnetic screen represents a ferromagnetic pipe with internal diameter of 35 mm at the input and 70 mm at the output of the block 24, respectively [5]. The tracking of the polarized protons was done using the code TRAEK [6]. The energy of the accelerated protons is 60 GeV and the duration of pulse is 1 s on the IPT. The polarized proton beam with momentum 40 GeV/c and momentum band $\pm$5% is accepted by the doublet of the quadrupole lens (Q1,Q2) of the PPB channel.

3. The beam optics and beam parameters

The optical scheme of the new beam channel (K-14/p) is given in Fig. 2. The calculations of beam parameters were done using code TRANSPORT [7] and the modified version of the code Decay Turtle [8]. The channel K-14/p consists of the 3 quadrupole doublets (Q1, Q2), (Q3,Q4), (Q5, Q6), two bending dipoles (M1, M2), intermediate collimator (IC) and the momentum collimator (MC). Unfortunately the chosen scheme of the channel K-14/p does not allow to satisfy completely to the well established requirements to the PPB channels [9–13]. In particular, in the horizontal plane the optics becomes neither unit nor achromatic after the dipole M2. The magnification coefficient is 1.7 in the vertical plane at the intermediate focus (IF). At this place may be installed the collimator IC for selection the fraction of the beam with average polarization $\pm\eta$ or the beam tagging detectors which permits to use the full flux of polarized protons [4, 11].

The momentum dispersion is created by the dipole M1 (bent angle α=45 mrad).This condition allows confidently to provide the momentum band $\leq \pm$5% (Δp/p) of the PPB. At the collimator MC the momentum dispersion is equal to 14 mm per 1 % (Δp/p). The PPB characteristics along the channel K-14/p and on the ET are calculated using the Monte-Carlo method (the processes of nuclear interaction of the accelerated protons with the IPT, the production of Λ^0-hyperons and their decays with production of the polarized protons are simulated). In particular, it has allowed making an estimation of the beam intensity on the ET: at the primary proton beam intensity of 10^{12} p/pulse and the energy 60 GeV on the Al target, the intensity of the PPB would approximately be $8{\cdot}10^5$ p/pulse. This number was confirmed by independent analytical calculation using the Hagedorn's table [13, 14].

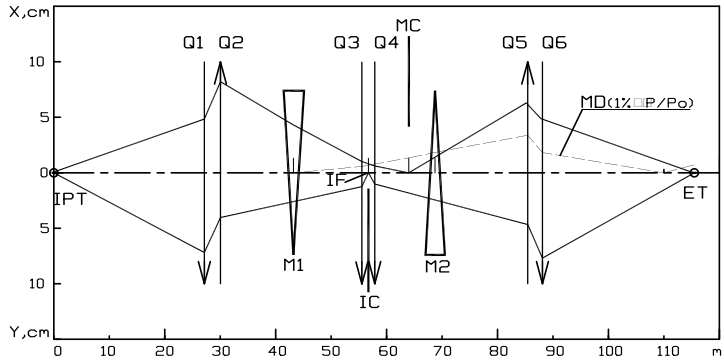

Figure 2: Beam optics of the channel K14/p. Upper half of the figure (OX): the side- ray (___) of the PPB and the momentum dispersion (_ _ _) of protons at 1%(ΔP/P) for the horizontal axis (x). Lower half of the figure (OY): the side- ray (___) of the PPB for vertical axis (y).

Fig. 3a presents the profile and the polarization distribution (η) of the protons in the vertical plane at the sectional view of the IF for the momentum band $\Delta p/p = \pm 5\%$. Both these curves are given for the polarized protons reaching the target ET. On this and other figures the values of all parameters are normalized to the 10^{12} accelerated protons interacting with the IPT. Fig. 3b shows the profiles for x (horizontal) and y (vertical) distributions for the total PPB with a polarization interval from -60% to +60% focused at the ET. On Fig. 3c momentum spectrum of the total PPB at the ET is presented.

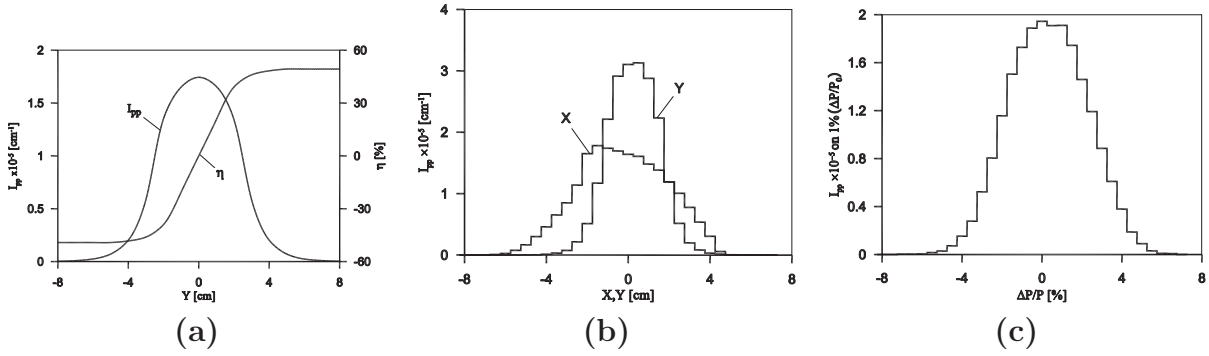

Figure 3: The calculated parameters of the total PPB (with polarizations from -60% to +60%). **(a)** The distributions of intensity (I_{pp}) and averege polarization (η) versus Y at the intermediate focus (IF); **(b)** the distributions of intensity for X and Y axes with the double focus at the experimental target (ET); **(c)** the momentum spectra at the ET.

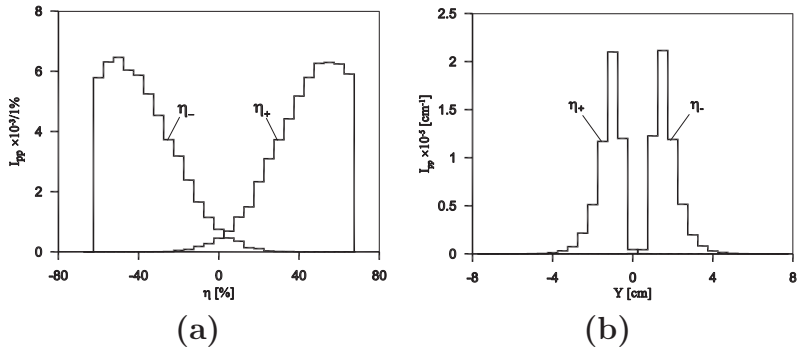

Figure 4: The calculated parameters for two fractions of the chosen PPBs (with average polarizations of η_-=-40% and η_+=+40%): **(a)** the distributions of intensity (I_{pp}) versus the polarization (η) of the beams with η_- and η_+ at the ET; **(b)** the distributions of intensity versus Y axis for the beams with η_- am η_+ at the ET.

Table 1: The PPB parameters produced on the EPT and calculated for the IPT at U-70 accelerator for the primary protons with intensity of 10^{13} p/ pulse and 10^{12} p/pulse respectively.

Parameters	**EPT (Al, l=300mm)**	**IPT (Al, l=30 mm)**
Momentum, GeV/c	40	∼40
Momentum dispersion at MC, mm/1%(Δp/p)	15.6	14.0
Momentum band, %	±4.5	±5.0
Magnification in the vertical plane at the IF	-2.68	-1.7
Sizes at the ET (σ_x/σ_y), mm	10.5/8.1	25/12.5
Divergences at the ET (σ'_x/σ'_y), mrad	6.5/6.0	3.5/4.0
Total intensity, p/pulse	$8.1{\cdot}10^7$	$8.0{\cdot}10^5$
Intensity with mean $\eta = \pm 40\%$ p/pulse	$2.6{\cdot}10^7$	$2.5{\cdot}10^5$
Background from $K^0_s \to \pi^+\pi^-$, %	∼1	∼1

Fig. 4a presents the intensities of polarized protons versus the polarization at the position of the ET: left line is for the average polarization $\eta_- = -40\%$; right line is for the average polarization $\eta_+ = +40\%$. The intensity of each of two polarized beams is equal to $3{\cdot}10^5$ polarized protons at the indicated above normalization. Fig. 4b presents the vertical profiles for two fractions of the polarized beams with average polarizations $\eta_- = -40\%$ and $\eta_+ = +40\%$ focused at the ET. The horizontal profiles of these two beams are similar to the shape of the total flux in the Fig. 3b but scaled by factor approximately 1/3. The momentum spectra for positive and negative polarizations are similar to that for the total PPB.

4. Discussions

The main parameters of the proposed PPB produced on the IPT are summarized in Table 1 and compared to the PPB obtained by the same method on the EPT [1]. Several features should be noted. First of all, the PPB intensity produced on the IPT is by two orders of magnitude smaller than that of the PPB produced on the EPT. The restriction comes out from the limit imposed on the primary intensity by the radiation conditions and small angular acceptance of the channel K-14/p. Another point is the size of the total beam at the ET. It is very large. This was caused by the chosen beam optics which is not optimal and limited by shortage of space. As result such beam may be used mostly in single spin asymmetry measurements by using the liquid hydrogen target. Such beam cannot be used with available polarized target having only 20 mm in diameter.

The two PPB with signs of polarization ± are separated by ∼40 mm and one needs to use two correcting magnets as it was done at the set-up FODS [1] in order to put both beams on the axis of the experimental set up SPASCHARM. In our case it is reasonable to place these magnets in the first part of channel K-14/p close to collimator IC.

5. Tagging detectors.

For effective use of accelerator time one needs the polarization and momentum tagging systems. As follows from Table 1 in order to get the momentum resolution of 0.5 % it is

enough to use the scintillation hodoscopes with 7 mm width of scintillating bars placed at the focal plane. Such hodoscope was successfully used earlier [4]. This should be done, since there is no space for putting the magnetic spectrometer. The hodoscope for tagging the polarization has 5 mm wide scintillating bars and should be placed at position PF.

Polarimeter. For an absolute calibration of the beam's polarization the elastic proton-proton scattering may be used. There are two options. First, one can use the existing polarized proton target and detect the pp-elastic scattering in the four-momentum transfer region $0.1 < |t|(GeV/c)^2 < 0.5$, where the analyzing power was already measured [15]. The scintillating hodoscopes in combination with GEM detectors may be used as tracking detectors. Second, one can detect the pp-scattering in the Coulomb-Nuclear Interference interval. In this case the liquid hydrogen target and a magnetic spectrometer should be used. The detailed description of such polarimeters one can find in paper [16].

6. Conclusions.

We studied the possibility of producing, accepting and transporting the polarized proton beam from the IPT. The Λ^0-s are produced on the internal production target of the U-70 accelerator. Our main goal was to bring such useful polarized beam to the experimental set-up installed on the beam channel K-14/p at the distance of 115 m from the IPT. The beam consists of three components with almost equal fluxes. Two parts have 40% polarization of opposite signs, while the third part has the zero average transverse polarization (but in principle the polarization has non zero longitudinal component. This fact may facilitate the use of the spin rotator). The total flux of the PPB is equal to $\sim 1 \cdot 10^6$ per pulse, the momentum is 40 GeV/c. The possibility of forming the beams with the transverse polarization - 40% or + 40% makes such beams very useful for the polarization experiments. Such beam may work in parallel with other ones under use by the internal and external target experiments. Nevertheless several problems are left unsolved: the large beam size, the reverse of the beam polarization, the polarized beam axes are not coinciding with the axis of the experimental set-up. We hope that these problems will be solved in time.

Described above scheme for PPB production is not suitable for getting the polarized antiprotons for several reasons. First of all the maximum yield of antilambdas occurs at its momentum ∼20 GeV/c. Second the negative charge of antiproton makes easier to extract it. In this case the magnetic block 24 extracts completely antiprotons without any field screening. The IPT for antiprotons may be inserted at the exit of the block 23. All antilambda decays in the straight section will be accepted. Assume also that the angular acceptance of the beam channel will be increased. In such conditions the preliminary estimation shows that intensity of antiprotons can be of order $5{\cdot}10^3$ – $5{\cdot}10^4$ polarized antiprotons per pulse at the energy of 14 GeV.

Acknowledgements. We would like to express our thanks for useful discussions to the collagues in IHEP: A. Afonin, V. Garkusha, E. Ludmirsky, V. Mochalov, E. Troyanov and A. Vasiliev. We are also grateful to M. Runtso for his help in presenting this report.

References

[1] Galyaev N.A. et al., IHEP Polarized Proton Beam, IHEP Preprint 92-159, Protvino (1992)

[2] V.A. Chetvertkova and S. B. Nurushev, Relativistic transformation of polarization vector and its practical applications, Proc. of XII Advanced Research Workshop on High Energy Spin Physics, DSPIN-07, Dubna (2007) 41

[3] V.A. Chetvertkova, and S. B. Nurushev, The possibility of producing the polarized proton (antiproton) beam on the internal production target of the accelerators/colliders, Proc. of XIX International Baldin Seminar on High Energy Physics Problems, Dubna, (2008) 89-94

[4] D. Grosnick et al., Nuc. Instr. Meth. A290 (1990) 269

[5] N.I. Golovnya et al., Atomnaya Energya, 32, 3, (1972) 244

[6] Fedotov Yu. S., Fronteau J., Keyser R., A Preliminary Note on a Program to Calculate Particle Trajectories in the Magnetic Field of the Serpukhov Accelerator., Pr. CERN – DD/CO/67/5, (1967)

[7] K.L. Brown et al., CERN Report (1980) 80-84

[8] D.C. Carey, The Optics of Charged Particle Beams, Harwood Academic, New York, (1987)

[9] P. Dalpiaz et al., CERN/ECFA/72/4, Vol.1 (1972) 284

[10] V.D.Apokin et al., Investigation of Polarization Effects in High Energy Hadron Interactions, T-03227, Serpukhov, (1976)

[11] V. Apokin, W. Bartle et al., Study of spin effects at SPS energies using a polarized proton beam, Proposal of Experiment, CERN/SPSC (1977) 77-61, 87

[12] S.B.Nurushev et al., Proc. of Intern. Symp. on High Energy Spin Physics with Polarized Beams and Polarized Targets, Lausanne, (1980) 501

[13] W. Atherton and N. Doble, CERN SPS/EA, June (1976) 76-16

[14] H. Grote et al., Atlas of particle production spectra, CERN (1970)

[15] A. Gaidot et al., Czech J. Phys. B26 (1976) 25-33

[16] S.B. Nurushev, The proton beam polarimetry at the IHEP U-70 facility, Proc. of XI Advanced Research Workshop on High Energy Spin Physics, DSPIN-05, Dubna, September 27 – October 1, (2005) 516-525

SURVEY OF NUCLEON ELECTROMAGNETIC FORM FACTORS

Charles F. Perdrisat[1†], and Vina Punjabi[2‡]

(1) *The College of William and Mary, Williamsburg, Virginia 23187, USA*
(2) *Norfolk State University, Norfolk, Virgina 23504, USA*
† *E-mail: perdrisa@jlab.org* ‡ *E-mail: punjabi@jlab.org*

Abstract

There has been much activity in the measurement of the elastic electromagnetic proton and neutron form factors in the last decade, and the quality of the data has been greatly improved by performing double polarization experiments, in comparison with previous unpolarized data. Here we review the experimental data base in view of the new results for the proton, and neutron, obtained at MIT-Bates, MAMI, and JLab. The rapid evolution of phenomenological models triggered by these high-precision experiments will be discussed.

1 Introduction

One of the fundamental goals of nuclear physics is to understand the structure and behavior of strongly interacting matter in terms of its basic constituents, quarks and gluons. An important step towards this goal is the characterization of the internal structure of the nucleon; the four Sachs elastic electric and magnetic form factors of the proton and neutron, G_{Ep}, G_{Mp}, G_{En} and G_{Mn}, are key ingredients of this characterization. The elastic electromagnetic form factors are directly related to the charge and current distributions inside the nucleon; these form factors are among the most basic observables of the nucleon.

The electromagnetic interaction provides a unique tool to investigate the internal structure of the nucleon. The measurements of electromagnetic form factors in elastic as well as inelastic scattering, and the measurements of structure functions in deep inelastic scattering of electrons, have been a rich source of information on the structure of the nucleon.

2 Recoil Polarization Method

The relationship between the Sachs electromagnetic form factors and the degree of polarization transfer in $^1H(\vec{e}, e'\vec{p})$ scattering was first developed by Akhiezer and Rekalo [1], and later discussed in more detail by Arnold, Carlson, and Gross [2].

For single photon exchange, the transferred polarization can be written in terms of the Sachs form factors:

$$P_n = 0 \quad (1)$$

$$\pm h P_l = \pm h \left(\frac{E_e + E'_e}{M} \right) \frac{\sqrt{\tau(1+\tau)}\, G_{Mp}^2(Q^2)\, \tan^2 \frac{\theta_e}{2}}{G_{Ep}^2(Q^2) + \frac{\tau}{\epsilon} G_{Mp}^2(Q^2)} \quad (2)$$

$$\pm h P_t = \mp h \frac{2\sqrt{\tau(1+\tau)}\, G_{Ep}\, G_{Mp}\, \tan \frac{\theta_e}{2}}{G_{Ep}^2(Q^2) + \frac{\tau}{\epsilon} G_{Mp}^2(Q^2)} \quad (3)$$

where $\tau = \frac{Q^2}{4m_p^2}$, ϵ is the longitudinal virtual photon polarization, and the $\pm$ stands for the two possible orientations of the electron beam helicity.

For each Q^2, a single measurement of the azimuthal angular distribution of the proton scattered in a secondary target (described later) gives both the longitudinal and transverse polarizations. Combining Eqs. 2 and 3 give:

$$\frac{G_{Ep}}{G_{Mp}} = -\frac{P_t}{P_l} \frac{(E_e + E'_e)}{2M} \tan \frac{\theta_e}{2}; \quad (4)$$

thus the ratio of electric to magnetic form factors of the proton is obtained directly from a simultaneous measurement of the two recoil polarization components. The kinematic factors in Eq. 4 are typically known to a precision far greater than the statistical precision of the recoil polarization components.

3 Results and Discussion

The unexpected results from JLab shown in Fig. 1, using the polarization transfer technique to measure the proton electric over magnetic form factor ratio, G_{Ep}/G_{Mp} [3–7], has been the revelation that the form factors obtained using the polarization and Rosenbluth cross section separation methods [8], were incompatible with each other, starting around $Q^2 = 3$ GeV^2 [9–11]. The form factors obtained from cross section data had suggested that $G_{Ep} \sim G_{Mp}/\mu_p$, where μ_p is the proton magnetic moment; the results obtained from recoil polarization data clearly show that the ratio G_{Ep}/G_{Mp} decreases linearly with increasing momentum transfer Q^2. It is well known by now that G_{Ep} is difficult to obtain from Rosenbluth separation, a technique which is also especially sensitive to systematics errors and subject to large, ϵ-dependent radiative corrections. The two-photon exchange contribution, neglected in the past, has been shown to be an important term to add to the standard radiative corrections for cross section data; it has a strong ϵ-dependence and brings the Rosenbluth form factor ratio closer to the recoil polarization results [12, 13]. Two-photon contributions are expected to affect the recoil polarization results only very weakly [13].

The neutron form factor ratios displayed in Fig. 2 show a very different behavior versus Q^2, explained in part by the neutron's neutrality: G_{En}=0 at Q^2=0. The most recent data from the GEn(I) JLab experiment extended the Q^2 range to 3.4 GeV^2 [14]. In Fig. 1 and Fig. 2 the vector dominance model (VMD) results of Refs. [15, 16] are shown, as well as a polynomial fit without asymptotic constrain, labeled as "my fit". More extensive information can be obtained from [17–19]

These striking results for the proton electromagnetic form factor ratio as well as high precision measurements of the neutron electric form factor shown in Fig. 2, all obtained through double polarization experiments, have put the field of nucleon elastic electromagnetic form factors into the limelight, giving it a new life.

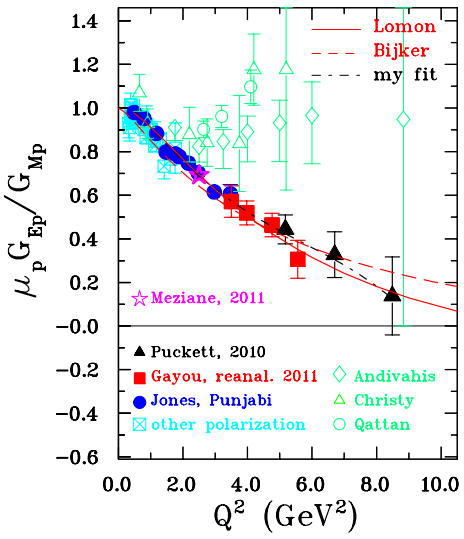

Figure 1: All recoil polarization results for $\mu_p G_{Ep}/G_{Mp}$; also included are selected Rosenbluth results (empty symbols). The solid and dashed lines are the results of the VMD calculations of Lomon and Bijker, Refs. [15, 16].

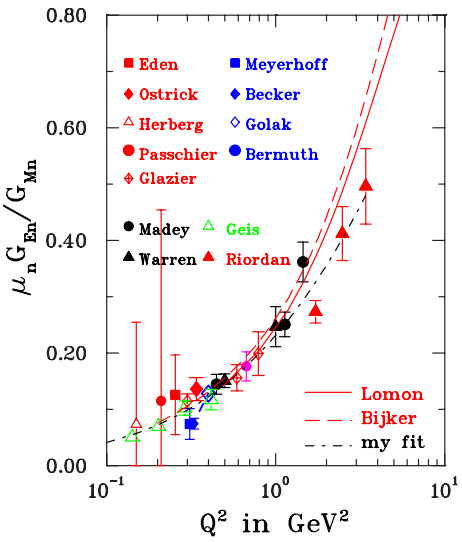

Figure 2: All polarization results for $\mu_n G_{En}/G_{Mn}$; also included are older Rosenbluth separation results. The solid and dashed lines are same as in Figure 1.

Figures 3 and 4 demonstrate a strikingly different behavior for the proton and neutron Dirac and Pauli form factor ratio multiplied by a Q^2 weighting factor; these form factors, $F_{1p,n}$ and $F_{2p,n}$ are obtained directly from the Sachs form factor ratios, as:

$$F_1(Q^2) = \frac{1}{1+\tau}(\tau + \frac{G_E}{G_M}) \text{ and } F_2(Q^2) = \frac{1}{1+\tau}(1 - \frac{G_E}{G_M})$$

The proton data are not yet close to the pQCD scaling prediction of Brodsky and Farrar [20], $Q^2F_2/F_1 \sim constant$, but the neutron data might display the expected pQCD behavior, albeit over a much smaller range of Q^2 than for the proton. The three curves shown in Fig. 3 and Fig. 4 are the same as in Figures 1 and 2.

The ratio data for proton and neutron can be used to obtain F_{1p} and F_{1n} and F_{2p} and F_{2n} (to be written here as $F_{1p,n}$ and $F_{2p,n}$) separately, with the help of fits to G_{Mp} and G_{Mn}, which are better defined experimentally than G_{Ep} and G_{En}. Using the fits of Kelly [21] for G_{Mp} and G_{Mn}, the separated values of $F_{1p,n}$ and $F_{2p,n}$, are shown in Fig. 5. Noticeable is the almost identical behavior of F_{2p}/κ_p and F_{2n}/κ_n. The difference between F_{1p} and F_{1n} at small Q^2 is dominated by the neutrality of the neutron; at the largest Q^2, their slope become very similar.

If one assumes that the matrix element of the hadronic current in elastic ep scattering is of the form $< N|e_u\bar{u}\gamma_\mu u + e_d\bar{d}\gamma_\mu d|N >$, where N stands for a nucleon, and e_u and e_d are the charge of the u and d "dressed" quarks, respectively; and with the further assumption of isospin symmetry for the corresponding u and d quark $F_{1p,n}^{u,d}$ and $F_{2p,n}^{u,d}$ form factors, implying:

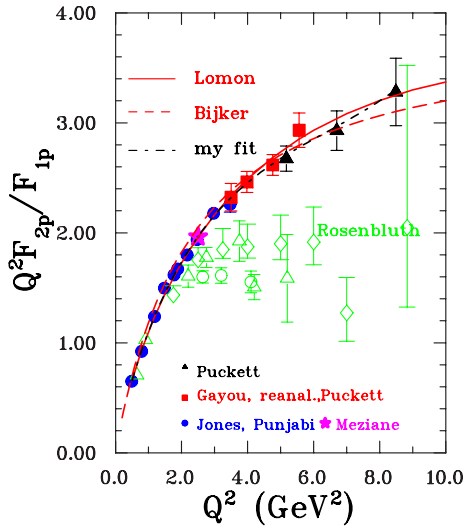

Figure 3: The perturbative QCD behavior of the Fermi and Dirac form factor ratio for proton, a slow down of the rise is visible.

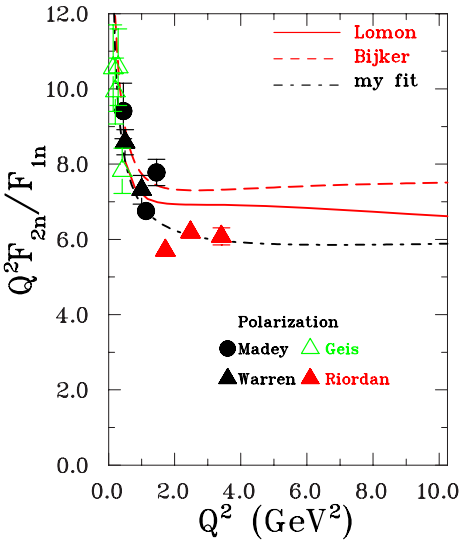

Figure 4: The perturbative QCD behavior of the Fermi and Dirac form factor ratio for neutron, the data is too limited to decide the behaviour.

$$F_{1n}^d = F_{1p}^u \text{ and } F_{1n}^u = F_{1p}^d,$$

and similar relations for F_2, the flavor separated u and d quark form factors in the nucleons are linear combinations of the measured form factors $F_{1p,n}$ and $F_{2p,n}$:

$$F_1^u = 2F_{1p} + F_{1n} \text{ and } F_1^d = F_{1p} + 2F_{1n},$$

and similar relations for $F_2^{u,d}$.

A similar flavor separation was recently published by Cates et al [22]. Here we use the VMD models cited and our own fit to get a more general view of these flavor separated form factors, as in Fig. 5. Remarkable is the similar Q^2-dependence of three of these form factors, The exception is F_1^u, which is twice as large as the others at Q^2=0, as expected, but may become 10 times larger than the three others at 10 GeV^2. The neutron data base stops at 3.4 GeV^2, so these curves are to be taken as a possibility, supported by the smooth behavior and excellent agreement of the Dirac and Pauli form factor demonstrated in Fig. 5 over the region of Q^2 where data exist.

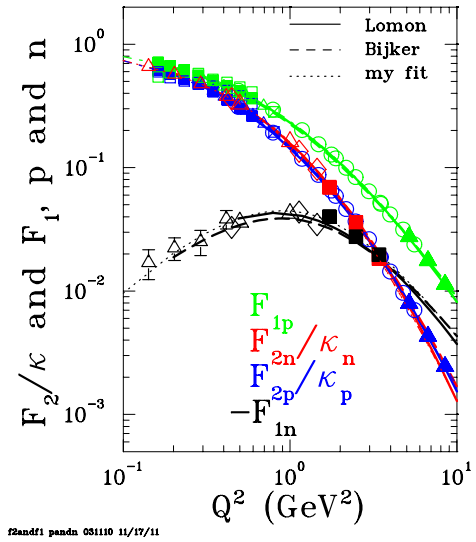

Figure 5: The Dirac and Pauli form factors of proton and neutron, as obtained from $\mu G_E/G_M$ with the help of the Kelly [21] parametrization of G_{Mp} and G_{Mn}.

Predicting nucleon form factors in the non-perturbative regime, where soft scattering processes are dominant, is very difficult. As a consequence there are many phenomenological models which attempt to explain the data in this domain; precise measurements of the nucleon form factors are necessary to constrain and test these models.

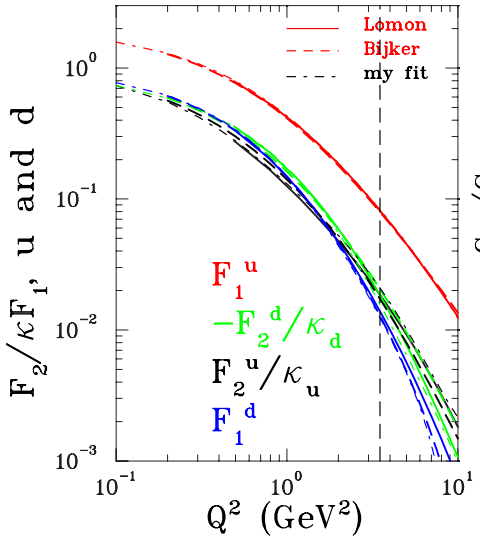

Figure 6: The separated u and d quark form factors corresponding to the three curves on the left, and assuming isospin symmetry.

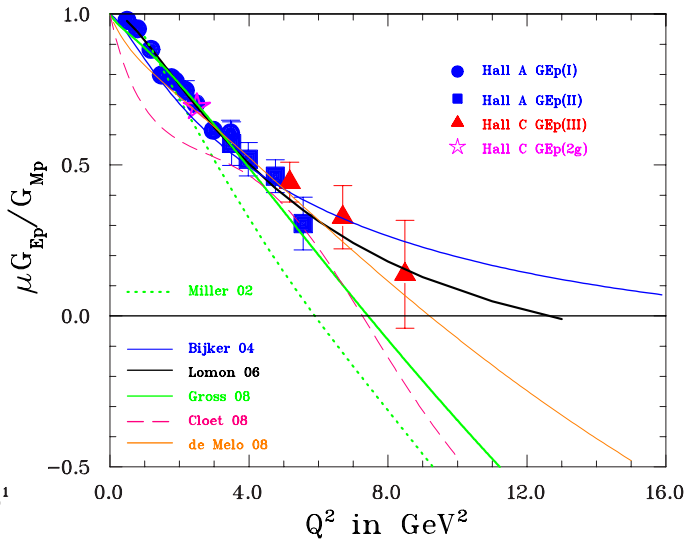

Figure 7: Predictions of form factor ratio with VMD models from Ref. [15, 16], with RCQM models of [23–25] and in Ref. [26] a parameter-free Faddeev equation for the nucleon is constructed to calculate the nucleon form factors. These predictions are compared to the data from GEp-I (filled circles), GEp-II (filled squares), and GEp-III (filled triangles) experiments.

There are several approaches to calculate nucleon form factors in the non-perturbative regime. The list includes vector meson dominance (VMD) models, relativistic constituent quark models (rCQM), the cloudy bag model, the di-quark model and the Dyson-Schwinger equation (DSE) model and more. In the VMD approach, the photon couples to the nucleon via vector mesons, whereas in QCD models the photon couples to the quarks directly. The generalized parton distributions (GPD) represent a framework within which hadrons are described in terms of quarks and gluons. Perturbative QCD predicts form factor values for large Q^2. We show results from some of these calculations here in Fig. 7.

Extended VMD fits, which provide a relatively good parametrization of all nucleon electromagnetic form factors, have been obtained. An example is the fit of Lomon [15], containing 11 parameters. Another VMD parametrization by Bijker and Iachello [16] achieves a good fit by adding a phenomenological contribution attributed to a quark-like intrinsic qqq structure (of rms radius ~ 0.34 fm) besides the vector-meson exchange terms.

Among the theoretical efforts to understand the structure of the nucleon in terms of quark and gluon degrees of freedom, constituent quark models have a long history too. In these models, the nucleon consists of three constituent quarks, which are thought to be valence quarks dressed with gluons and quark-antiquark pairs, and are much heavier than the QCD Lagrangian quarks. All other degrees of freedom are absorbed into the masses of these quarks. To describe the data presented here in terms of constituent quarks, it is necessary to include relativistic effects because the momentum transfers involved are up to 10 times larger than the constituent quark mass. Several RCQM calculations [23–25] are shown in Fig. 7.

A different approach is illustrated by deriving solutions to the Dyson-Schwinger equa-

tions to calculate form factors, a quantum field theoretical approach to hadron structure [26]. The mechanism for mass acquisition of the QCD quark to the dressed quark mass is related to the dynamical chiral symmetry breaking; it explains the mass growth with momentum as accumulation of a gluon cloud. By solving a Poincaré covariant Faddeev equation describing two dressed quarks, Cloët and Roberts [26] obtain nucleon form factors in a model in which two quarks are always correlated, and binding results from the exchange between the di-quark and the third quark. In Ref. [26] a parameter-free Faddeev equation for the nucleon is constructed, which describes the core of dressed quarks in the nucleon.

4 Form Factors with 11 GeV

Let us first state that G_{Ep}/G_{Mp} should be measured to as high a Q^2 as possible, and so should G_{En} and G_{Mn}; furthermore G_{Mp} should also be remeasured. The higher design energy of JLab 12 GeV will give access to higher momentum transfers in all form factor measurements, in the Q^2 range 10 to 20 GeV^2.

A large collaboration in Hall A will assemble a large solid angle detector, up to 70 msr for specific applications. The core of this project is a 120x120 cm^2 (48"x48") dipole magnet currently at BNL, which will be modified to allow positioning at angles as small as 12^0; the associated detector package will include GEM chambers for tracking, a large hadron calorimeter, and in a later phase a double polarimeter using GEMs also. This project is called the **Super Bigbite Spectrometer** [27], or SBS for short. Currently approved experiments requiring all or parts of the SBS include neutron and proton form factor measurements.

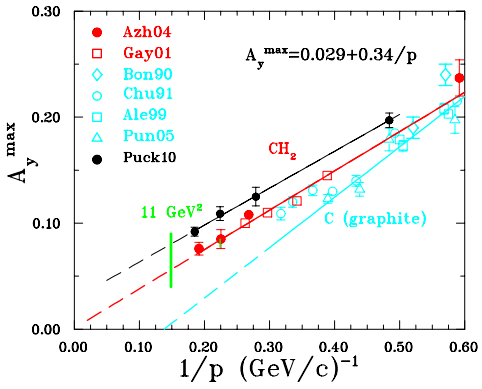

Figure 8: Maximum value of the analyzing power A_y^{max} versus the inverse of the proton momentum. The values from GEp(III) (black circles) are systematically larger than those in Azhgirey et al. [28]. The difference is thought to be due to the strict selection of single track events in the latter.

The motivation for a detector with uncommonly large solid angle is the rapid decrease of elastic form factors with Q^2, and therefore the precipitous decrease of all elastic cross sections, as follows:

$$\text{form factor: } FF \sim \frac{1}{Q^4} \tag{5}$$

$$\text{cross section: } d\sigma_{Mott} \times FF^2 \sim \frac{E^2}{Q^4}\frac{1}{Q^8} \tag{6}$$

Furthermore, double polarization e xperiments require either measurements of the polarization of the final state nucleon (p in $\vec{e}p \rightarrow e\vec{p}$, or $\vec{n}$), or a polarized target (^3He) in ($\vec{e}\vec{n} \rightarrow en$). Both methods have their limitations. For the series of proton form factor measurements reported in the first part of this paper, recoil polarization has been the method of choice. In this case another difficulty arises from the decrease of the analyzing power of the reaction used to determine the longitudinal and transverse polarization

components. In good approximation, the analyzing power decreases like the inverse of the proton momentum, as illustrated in Fig. 8, $A_y^{max} \sim \frac{1}{p} \sim \frac{1}{Q^2}$.

4.0.1 GEp(V) and GEn(II) Experiments

An illustration of the setup for the approved GEp(V) experiment is seen in Fig. 9; it shows the proton side, on the left from the beam, with the tracking GEM downstream from the dipole which are followed by a double polarimeter and a hadron calorimeter. On the electron side, right of the beam, a large leadglass calorimeter is preceded by GEM planes to further improve the position resolution. The dipole is followed by a set of 6 GEM planes, each made of 3 chambers side-by-side in the vertical direction; these will provide the tracking capability to reconstruct the location of the interaction vertex and the momentum vector of the proton. They will identify tracks originating from the target and in coincidence with an electron detected in the electromagnetic calorimeter BigCal. All individual GEMs are 40 times 50 cm in size. The trigger will in addition require signal from the hadron calorimeter HCal.

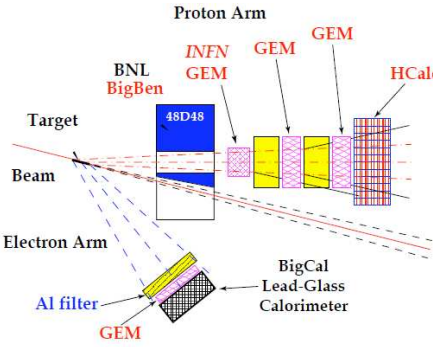

Figure 9: Schematic floor plan arrangement for the GEp(V) experiment using the SBS.

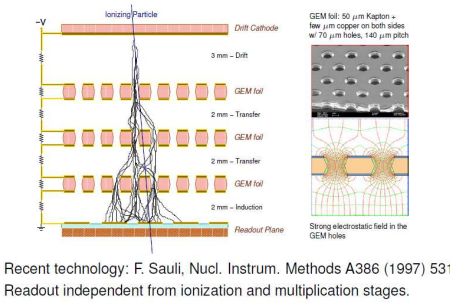

Figure 10: The GEM principle. Figure from the RD51 collaboration at CERN.

The choice of GEM detectors, rather than drift wire chambers for GEp(V), is dictated by the high fluxes of soft photons and charged particles expected because the detectors will be in direct view of the target.

The great strength of the GEM principle is that the amplification of the primary ionization electron produced in the drift region, occurs in between the copper foils on either side of a typically 50 μm thick kapton foils, with a potential difference of several hundred volts; this is illustrated in Fig. 10.

The device will be built around a BNL dipole, deflecting protons vertically by about 7^0 for favorable precession of the longitudinal polarization at Q^2 14.5 GeV^2. A cut on the side of the magnet will allow for placing the dipole at $\sim 12^0$ to the beam, 140 cm from the target center.

The expected error bars for GEp(V) [29] are shown in Fig.11. For the neutron electric form factor measurements (GEn(II)), the LH_2 target will be replaced by a gaseous, pressurized 50 cm long polarized ^3He target [30] with proven performance (see [14]). The neutron will be detected in the hadron calorimeter (HCal) required for the trigger in

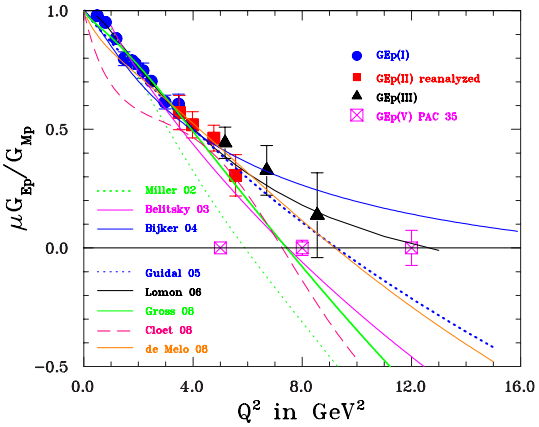

Figure 11: The anticipated results of GEp wide range of phenomenological model pred are shown, underlining the potential ability of these two experiments, to narrow the range of models able to reproduce the future data.

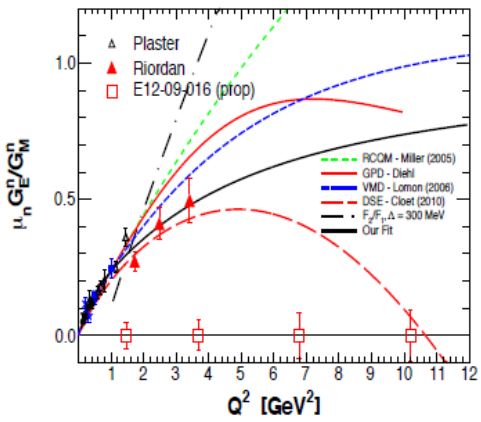

Figure 12: Current data for G_{En}/G_{Mn}; all data are from double polarization experiments; the empty squares on the zero line show the anticipated statistical uncertainty for the GEn(II) experiment.

GEp(V), preceded by planes of GEMs to veto charged particles and improve the position resolution; protons will be swept out by the SBS dipole. The scattered electrons will be detected in the permanent facility BigBite, a simple dipole with vertical bending, equipped with drift chambers, and a calorimeter. Fig.12 shows current data for G_{En}/G_{Mn}; all data are from double polarization experiments; the empty squares on the zero line show the anticipated statistical uncertainty for the GEn(II) experiment (E09-019). The Dyson-Schwinger calculation of Cloët et al predicts a zero crossing for G_{En}/G_{Mn}; the proposed data may definitively exclude many of the current model predictions. The possibility of detecting a zero crossing of the neutron electric form factor, as predicted by Cloët and Roberts, is within reach.

5 Conclusions

The increasingly common use of the double-polarization technique to measure the nucleon form factors, in the last 15 years, has resulted in a dramatic improvement of the quality of all four nucleon electromagnetic form factors, G_{Ep}, G_{Mp}, G_{En} and G_{Mn}. It has also completely changed our understanding of the proton structure, having resulted in a distinctly different Q^2- dependence for G_{Ep} and G_{Mp}, contradicting the prevailing wisdom of the 1990's based on cross section measurements and the Rosenbluth separation method, namely that G_{Ep} and G_{Mp} obey a "scaling" relation $\mu G_{Ep} \sim G_{Mp}$. A direct consequence of the faster decrease of G_{Ep} revealed by the JLab polarization experiments was the disappearance of the early scaling $F_2/F_1 \sim 1/Q^2$ predicted by perturbative QCD.

The main origin of this abrupt change in results is now understood in simple terms. The faster decrease of G_{Ep} reduces its contribution to the cross section significantly below the natural ratio prevailing at small Q^2, namely $G_{Ep}^2/G_{Mp}^2 \sim 1/\mu_p^2$. At the highest Q^2 for which we now have polarization data, 8.5 GeV^2, the contribution from the electric FF to the cross section is less than 1%. It has been realized in recent years, that to extract G_{Ep} from Rosenbluth separations at larger Q^2 requires a much better quantitative understanding of several of the radiative corrections contributions, including in particular

the one due two hard photon exchange. There are currently differences of order several %'s between the results of various radiative correction calculations. The two-hard-photon correction by itself might explain the whole discrepancy between Rosenbluth and recoil polarization results, but it does not affect recoil polarization results measurably, because these are measurements of ratios of form factors and both form factors are, in first order, modified similarly. Until the origin of the difference between cross section and polarization results is understood in full quantitative detail, it is safest to take the polarization results as the closest to the real, Born approximation, proton form factors.

The use of the polarization technique has also resulted in a constant progress in the measurement of G_{En}, which is intrinsically more difficult to obtain because of the smallness of this form factor, due to the overall zero charge of the neutron. Recent times have seen the maximum Q^2 for which we have polarization form factors grow to 1.5 GeV^2, with new data up to 3.4 GeV^2, and several experiments planned or proposed to significantly higher Q^2 values. Important progress has been made for G_{Mn} too, with new data with much improved error bars up to 4.8 GeV^2.

There is a well defined and ambitious program to continue form factor measurements for the nucleon, to the highest possible Q^2 once the ongoing 12 GeV upgrade of JLab is completed; as well as strong physics motivation to do so.

The future form factor program at JLab involves large collaborations of Universities and National Laboratories. It includes two Russian Laboratories: JINR in Dubna for a new hadron calorimeter (I. Savin), and ITEP in Protvino (A. Vasiliev) for parts of the electromagnetic calorimeter BigCal. LHP Dubna is committed to analyzing power measurements with the Nuclotron (N. Piskunov)

6 Acknowledgments

The authors wish to thank the organizers of the Dubna Dspin-11 workshop for their invitation to present this paper. The authors are supported by grants from the NSF(USA), PHY0753777 (CFP), and DOE(USA), DE-FG02-89ER40525 (VP).

References

[1] A. I. Akhiezer and M. P. Rekalo, Sov. J. Part. Nucl. **4**, 277 (1974); Fiz. Elem. Chast. Atom. Yadra **4**, 662 (1973).

[2] R.G. Arnold, C.E. Carlson, F. Gross, Phys. Rev. C **23**, 363 (1981).

[3] M.K. Jones *et al.*, Phys. Rev. Lett. **84**, 1398 (2000).

[4] O. Gayou *et al.*, Phys. Rev. Lett. **88**, 092301 (2002).

[5] V. Punjabi *et al.* Phys. Rev. C **71** (2005) 055202.

[6] A.J.R Puckett *et al*, Phys. Rev. Lett. **104**, 242301 (2010).

[7] M. Meziane *et al.* [GEp2gamma Collaboration], Phys. Rev. Lett. **106**, 132501 (2011).

[8] M.N. Rosenbluth, Phys. Rev. **79**, 615 (1950).

[9] L. Andivahis *et al.*, Phys. Rev. D **50** 5491 (1994).

[10] M.E.Christy *et al.*, Phys. Rev. **C70** 015206 (2004).

[11] I.A. Quatan *et al.*, Phys. Rev. Lett. **94** 142301 (2005).

[12] P.G. Blunden, W.Melnitchouk and J.A.Tjon, Phys. Rev. Lett. **91** (2003) 142304.

[13] Y.-C.Chen, A.Afanasev, S.J.Brodsky, C.E.Carlson, and M.Vanderhaeghen, Phys. Rev. Lett. **93**, 122301 (2004); A.V. Afanasev, S.J. Brodsky, C.E. Carlson, Y.C. Chen, M. Vanderhaeghen, Phys. Rev. D **72**, 013008 (2005).

[14] S. Riordan *et al*, Phys. Rev. Lett. **105**, 262302 (2010).

[15] E.L. Lomon, nucl-th/0609020; see also Phys. Rev. C **69**, 068201 (2002).

[16] R. Bijker and F. Iachello, Phys. Rev. C**69**, 068201 (2004).

[17] C.F. Perdrisat, V. Punjabi and M. Vanderhaeghen, Progress in Particle and Nuclear Physics, **59**, 694-764 (2007).

[18] C.F. Perdrisat and V. Punjabi, http://www.scholarpedia.org/article/Nucleon Form Factor.

[19] J. Arrington, K. de Jager, C. F. Perdrisat, J. Phys. Conf. Ser. **299**, 012002 (2011). [arXiv:1102.2463 [nucl-ex]].

[20] S Brodsky and G.R. Farrar, Phys. Rev. D **11**, 1309 (1975).

[21] J.J. Kelly, Phys. Rev. C **70**, 068202 (2004).

[22] G.D. Cates, C.W. de Jager, S. Riordan and B. Wojtsekhowski, P.R.L. **106**, 252003 (2011).

[23] M.R. Frank, B.K. Jennings, and G.A. Miller, Phys. Rev. C **54**, 920 (1996); G.A. Miller and M.R. Frank, Phys. Rev. C **65**, 065205 (2002).

[24] F. Gross and P. Agbakpe, Phys. Rev. C **73**, 015203 (2006).

[25] J.P.B. de Melo, T. Frederico, E. Pace, S. Pisano and G. Salme, Phys. Lett. B **671**, 153 (2009).

[26] I.C. Cloët and C.D. Roberts, Proc. of Sc. LC2008:047 (2008); arXiv:0811.2018 [nucl-th] (2008); I.C. Cloët, G. Eichmann, B. El-Bennich, T. Klähn and C.D. Roberts, Few Body Syst. **46**, 1 (2009)

[27] http://hallaweb.jlab.org/12GeV/SuperBigBite/

[28] L.S. Azhgirey *et al.*, Nucl. Inst. Meth. A **538**, 431 (2005).

[29] http://hallaweb.jlab.org/collab/PAC/PAC32/PR12-07-109-Ratio.pdf

[30] http://hallaweb.jlab.org/collab/PAC/PAC34/PR-09-016-gen.pdf

SPIN PHYSICS WITH CLAS

Y. Prok [1,2,†]

(1) *Christopher Newport University*
(2) *Thomas Jefferson National Accelerator Facility*
† *E-mail: yprok@jlab.org*

Abstract

Inelastic scattering using polarized nucleon targets and polarized charged lepton beams allows the extraction of double and single spin asymmetries that provide information about the helicity structure of the nucleon. A program designed to study such processes at low and intermediate Q^2 for the proton and deuteron has been pursued by the CLAS Collaboration at Jefferson Lab since 1998. Our inclusive data with high statistical precision and extensive kinematic coverage allow us to better constrain the polarized parton distributions and to accurately determine various moments of spin structure function g_1 as a function of Q^2. The latest results are shown, illustrating our contribution to the world data, with comparisons of the data with NLO global fits, phenomenological models, chiral perturbation theory and the GDH and Bjorken sum rules. The semi-inclusive measurements of single and double spin asymmetries for charged and neutral pions are also shown, indicating the importance of the orbital motion of quarks in understanding of the spin structure of the nucleon.

1 Introduction

One fundamental goal of Nuclear Physics is the description of the structure and properties of hadrons, and especially nucleons, in terms of the underlying degrees of freedom, namely quarks and the color forces between them. Much progress has been made over the last decades towards this goal, both experimentally (e.g., through structure function and form factor measurements) and theoretically (effective theories like the quark model, chiral perturbation theory as well as complete solutions of QCD on the lattice). At the same time, there are many important questions that require further investigation, such as: What is the quark structure of nucleons in the valence region, in particular in the limit of large momentum fraction carried by a single quark, $x \to 1$? How can we describe the transition from hadronic degrees of freedom to quark degrees of freedom for the nucleon? How can we describe the nucleon in three dimensions and what are the correlations between transverse momentum and spin? How does quark orbital angular momentum contribute to the spin of the nucleon? A program designed to study these questions, and utilizing the CLAS detector, 6 GeV polarized electron beam, and longitudinally polarized solid ammonia targets (NH_3 and ND_3) has been pursued by the CLAS Collaboration at Jefferson Lab since 1998. This program entails both inclusive measurements of inelastic electron scattering as well as coincident detection of leading hadrons (pions etc.) produced in such events. Due to the large acceptance of CLAS, a large kinematical region is accessed simultaneously. Both the scattered electrons and leading hadrons from the hadronization of the struck quark are detected, allowing us to gain information on its flavor.

1.1 Nucleon Helicity Structure at large x

The photon-nucleon asymmetry $A_1(x, Q^2)$ reflects the valence spin structure of the nucleon. Valence quarks are the irreducible kernel of each hadron, responsible for its charge, baryon number and other macroscopic properties. The region $x \to 1$ is a relatively clean region to study the valence structure of the nucleon since this region is dominated by valence quarks while the small x region is dominated by gluon and sea densities. Due to its relative Q^2-independence in the DIS region, the virtual photon asymmetry A_1, which is approximately given by the ratio of spin-dependent to spin averaged structure functions,

$$A_1(x) \approx \frac{g_1(x)}{F_1(x)}, \tag{1}$$

is one of the best physics observables to study the valence spin structure of the nucleon. At leading order,

$$A_1(x, Q^2) := \frac{\sum e_i^2 \Delta q_i(x, Q^2)}{\sum e_i^2 q_i(x, Q^2)}, \tag{2}$$

where $q = q \uparrow + q \downarrow$ and $\Delta q = q \uparrow - q \downarrow$ are the sum and difference between quark distributions with spin aligned and anti-aligned with the spin of the nucleon. The x dependence of the parton distributions provide a wealth of information about the quark-gluon dynamics of the nucleon. in particular spin degrees of freedom allow access to information about the structure of hadrons not available through unpolarized processes. Furthermore, the spin dependent distributions are more sensitive than the spin-averaged ones to the quark-gluon dynamics responsible for spin-flavor symmetry breaking. Several models make specific predictions for the large x behavior of quark distributions.

1.2 Moments and Sum Rules

The spin structure function g_1 is important in understanding the quark and gluon spin components of the nucleon spin, and their relative contributions in different kinematic regions. At high Q^2, g_1 provides information on how the nucleon spin is composed of the spin of its constituent quarks and gluons. At low Q^2, hadronic degrees of freedom become more important and dominate the measurements. There is particular interest in the first moment of g_1, $\Gamma_1(Q^2) = \int_0^{1-} g_1(x, Q^2)dx$, which is constrained at low Q^2 by the Gerasimov-Drell-Hearn sum rule [1] and at high Q^2 by the Bjorken sum rule [2] and previous DIS experiments. In our definition the upper limit of the integral does not include the elastic peak. Ji and Osborne [3] have shown that the GDH sum rule can be generalized to all Q^2 via

$$S_1(\nu = 0, Q^2) = \frac{8}{Q^2} \left[\Gamma_1(Q^2) + \Gamma_1^{el}(Q^2)\right], \tag{3}$$

where $S_1(\nu, Q^2)$ is the spin-dependent virtual photon Compton amplitude. S_1 can be calculated in Chiral Perturbation Theory (χPT) at low Q^2 and with perturbative QCD (pQCD) at high Q^2. Therefore, Γ_1 represents a calculable observable that spans the entire energy range from hadronic to partonic descriptions of the nucleon. Higher moments are also of interest: generalized spin polarizabilities, γ_0 and δ_{LT}, are linked to higher moments of spin structure functions by sum rules based on similar grounds as the GDH sum rule. Higher moments are less sensitive to the unmeasured low-x part since they are more weighted at high-x.

1.3 Flavor Decomposition of the Helicity Structure

If we want to understand the three-dimensional structure of the nucleon, we have to go beyond inclusive measurements that are only sensitive to the longitudinal momentum fraction x carried by the quarks. The large acceptance of CLAS allows us to collect data on semi-inclusive (SIDIS) reactions simultaneously. In these reactions, a second particle, typically a meson, is detected along with the scattered lepton. By making use of the additional information given by the identification of this meson, one can learn more about the polarized partons inside the nucleon than from DIS alone. The asymmetry measured by DIS experiments is sensitive to combinations of quark and anti-quark polarized parton distribution functions ($\Delta q + \Delta\bar{q}$), as well as (via NLO analyses) the gluon PDF ΔG. SIDIS experiments exploit the statistical correlation between the flavor of the struck quark and the type of hadron produced to extract information on quark and antiquark PDFs of all flavors separately. Combined NLO analyses of DIS and SIDIS data can therefore give a more detailed picture of the contribution of all quark flavors and both valence and sea quarks to the total nucleon helicity. Beyond the determination of the polarized PDFs, SIDIS data can also yield a plethora of new insights into the internal structure of the nucleon as well as the dynamics of quark fragmentation. For instance, looking at the z- and p_T-dependence of the various meson asymmetries (both double spin asymmetries and single spin target or beam asymmetries), one can learn about the intrinsic transverse momentum of quarks and their orbital angular momentum.

2 Measurements and Data Analysis

A_1 and g_1 were extracted from measurements of the double spin asymmetry $A_\parallel$ in inclusive ep scattering:

$$g_1 = \frac{F_1}{1+\gamma^2}[A_\parallel/D + (\gamma - \eta)A_2], \tag{4}$$

where F_1 is the unpolarized structure function, A_2 is the virtual photon asymmetry, and γ, D and η are kinematic factors. F_1 and A_2 are calculated using a parametrization of the world data, and $A_\parallel$ is measured. The spin asymmetry for ep scattering is given by:

$$A_\parallel = \frac{N_- - N_+}{N_- + N_+}\frac{C_N}{f P_b P_t f_{RC}} + A_{RC}, \tag{5}$$

where $N_-(N_+)$ is the number of scattered electrons normalized to the incident charge with negative (positive) beam helicity, f is the dilution factor needed to correct for the electrons scattering off the unpolarized background, f_{RC} and A_{RC} correct for radiative effects, and C_N is the correction factor associated with polarized ^{15}N nuclei in the target. $A_\parallel$ was measured by scattering polarized electrons off polarized nucleons using a cryogenic solid polarized target and CLAS in Hall B. The raw asymmetries were corrected for the beam charge asymmetry, the dilution factor and radiative effects. Since the elastic peak is within the acceptance range, the product of beam and target polarization was determined from the known ep elastic asymmetry.

The longitudinally polarized electrons were produced by a strained $GaAs$ electron source with a typical beam polarization of $\sim 70\%$. Two solid polarized targets were used:

$^{15}ND_3$ for polarized deuterons and $^{15}NH_3$ for polarized protons. The targets were polarized using the method of Dynamic Nuclear Polarization, with the typical polarization of 70-90% for protons, and 10-35% for deuterons. Besides the polarized targets, three unpolarized targets (^{12}C, ^{15}N, liquid ^{4}He) were used for background measurements. The scattered electrons were identified using the CLAS package [4], consisting of drift chambers, Cherenkov detector, time-of-flight counters and electromagnetic calorimeters. Data were taken with beam energies of 1.6, 2.4, 4.2 and 5.7 GeV, covering a kinematic range of of $0.05 < Q^2 < 4.5$ GeV^2 and $0.8 < W < 3.0$ GeV. The data include multi-particle final states,making it possible to investigate exclusive and semi-inclusive pion production, deeply virtual Compton scattering and other exclusive channels.

3 Results

3.1 Large x behavior of $A_1(x, Q^2)$

The photon-nucleon asymmetry A_1^p is shown in Figure 1. Along with the recent CLAS data, the plot shows results from previous experiments, and predictions from several models.

The models [5] include the suppression of transitions to states in the lowest even and odd parity multiplets with combined quark spin $S = \frac{3}{2}$, the suppression of transitions to states with helicity $h = \frac{3}{2}$, and the suppression of transitions to the states which couple only through symmetric components of the spin-flavor wavefunction. Also shown is the prediction of the hyperfine-perturbed quark model, which involves spin-spin interaction between quarks, mediated by one gluon or pion exchange [6]. Our data show a preference for the pQCD limit as $x \to 1$, and are also consistent with the hyperfine-perturbed quark model.

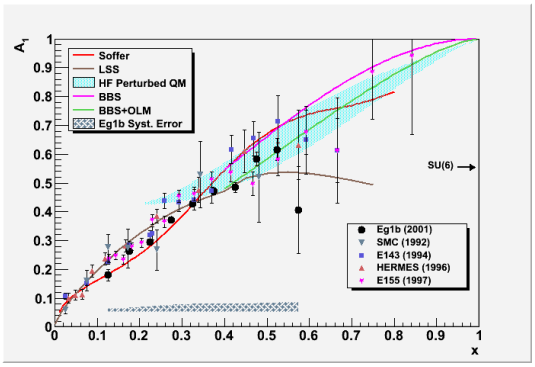

Figure 1: Asymmetry A_1^p plotted vs x could differentiate between the different models of valence spin structure of the nucleons.

3.2 Moments of $g_1(x, Q^2)$

The first moments of g_1^p and g_1^d are shown in Figure 2. The parametrization of world data is used to include the unmeasured contribution to the integral down to $x = 0.001$. Only the Q^2 bins is which the measured part constitutes at least 50% of the total integral are included. For the proton, the parametrization at high x ($1.09 < W < 1.14$ (1.15) GeV is used for the low (high) energy data). For the deuteron, the integration is carried out up to the nucleon pion production threshold at high x, excluding the quasi-elastic and electro- disintegration contributions. The integral is observed to turn over at low Q^2, consistent with the slope predicted by the GDH sum rule. In general the data are well described by the phenomenological models of Burkert and Ioffe [10] and Soffer and Teryaev [11]. The low Q^2 Γ_1 data are shown in more detail in the right-hand panels of Figs. 2. It is possible to make a quantitative comparison between our results for Γ_1^p and

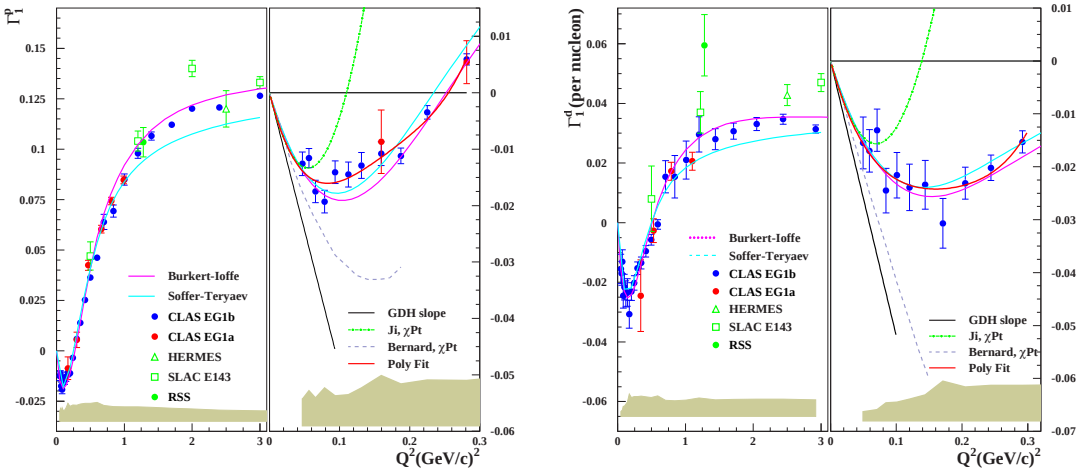

Figure 2: **(a)** Γ_1^p as a function of Q^2. **(b)** Γ_1^d as a function of Q^2. The EG1a [7], SLAC [8] and Hermes data [9] are shown for comparison. The filled circles represent the present data, including an extrapolation over the unmeasured part of the x spectrum using a model of world data.

Γ_1^d at low Q^2 and the next-to-leading order χPT calculation by Ji, Kao and Osborne [12], who find $\Gamma_1^p(Q^2) = -\frac{\kappa_p^2}{8M^2}Q^2 + 3.89Q^4 + ...$ and $\Gamma_1^n(Q^2) = -\frac{\kappa_n^2}{8M^2}Q^2 + 3.15Q^4 + ...$

Treating the deuteron as the incoherent sum of a proton and a neutron and correcting for the D-state,

$$\Gamma_1^d(Q^2) = \frac{1}{2}(1 - 1.5\omega_D)\left\{\Gamma_1^p(Q^2) + \Gamma_1^n(Q^2)\right\}, \tag{6}$$

one finds that $\Gamma_1^d(Q^2) = -0.451Q^2 + 3.26Q^4$. The low Q^2 results for Γ_1^p and Γ_1^d have been fit to a function of the form $aQ^2 + bQ^4 + cQ^6 + dQ^8$ where a is fixed at -0.455 (proton) and -0.451 (deuteron) by the GDH sum rule. For the proton, $b = 3.81 \pm 0.31$ (stat) $+0.44 - 0.57$ (syst) is extracted and for the deuteron, $b = 2.91 \pm 0.52$ (stat) ± 0.69 (syst) was obtained, both consistent with the Q^4 term predicted by Ji *et.al.* Our fit is shown in the right-hand panel of plots in Figs. 2 along with Ji's prediction. We find that the Q^6 term becomes important even below $Q^2 = 0.1$ GeV^2 and that this term needs to be included in the χPT calculations in order to extend the range of their validity.

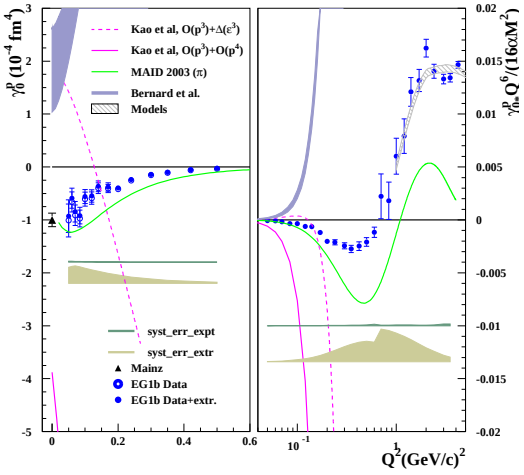

Figure 3: Generalized forward spin polarizability γ_0^p as a function of Q^2 for the full integral (closed circles) and the measured portion of the integral (open circles)

Higher moments of g_1 are interesting as well. In our kinematic domain these moments emphasize the resonance region over DIS kinematics because of extra factors of x in the integrand. The generalized forward spin polarizability

of the nucleon is given by [13]

$$\gamma_0(Q^2) = \frac{16\alpha M^2}{Q^6}\int_0^{x_0} x^2 \left\{ g_1(x,Q^2) - \frac{Q^2x^2}{4M^2} g_2(x,Q^2) \right\} dx, \tag{7}$$

where α is the fine structure constant. First results for the generalized forward spin polarizability of the proton for a range of Q^2 from 0.05 to 4 GeV^2 are shown in Fig. 3 Our data lie closest to the MAID 2003 [14] model, which is a phenomenological fit to single pion production data and includes only the resonance region. However, since γ_0 is weighted by an additional factor of x^2 compared to Γ_1, the contribution to the integral from the DIS part of the spectrum is rather small. The MAID model follows the trend of the data but significantly underpredicts them numerically.

The 4th order Heavy Baryon Chiral Perturbation calculation by Kao, Spitzenberg and Vanderhaeghen [15], shown by the dashed line in Fig. 3, also underpredicts the data. The authors note that the $O(p^4)$ correction term is of opposite sign to the $O(p^3)$ term and shows no sign of convergence. A leading order correction to account for $\Delta(1232)$ degrees of freedom, not shown, is also negative. By contrast, the χPT calculation of Bernard, Hemmert and Meissner [16], indicated by the grey band, including the resonance contribution, overpredicts the data. The $\Delta(1232)$ and vector meson contribution is negative (around -2×10^{-4} fm^4) but the discrepancy with the data suggests that this has been underestimated.

3.3 Quark-Hadron Duality

It is interesting to investigate a kinematic region in which both the hadronic and partonic descriptions of spin structure can be successfully used. Such 'dual' description has been successful in the case of unpolarized structure functions [18], but it is unclear whether it would hold in the polarized case, since at low Q^2 and W, g_1 is dominated by the $\Delta(1230)$ resonance, which has a negative spin asymmetry, but in the DIS region this asymmetry is positive. To test global 'duality', we average g_1 over x in the $1.08 < W < 2.00$ GeV region, and plot it as shown in Fig. 4. In this plot we also show the effect of including elastic contribution. An NLO DIS calculation [19] evolved to our kinematics is also shown as a band.
We see a rather good agreement between our data and the NLO DIS fit down to $Q^2 \sim 1.5$ GeV^2.

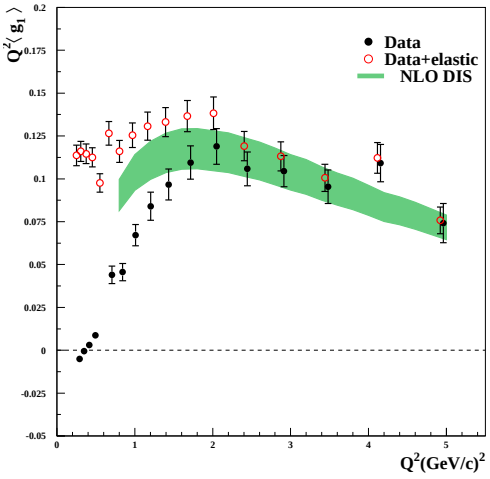

Figure 4: The Q^2 dependence of $Q^2 g_1(x,Q^2)$ averaged over a region in x corresponding to $1.08 < W < 2.00$ GeV for the proton.

3.4 Factorization tests

The semi-inclusive measurements of double spin asymmetries allow us to study factorization of $x, z = E_h/\nu$ and p_T dependency for charged and neutral pions. We study the

quantity g_1/F_1 as a function of kinematic variables for all three pion flavors [17]. The z-dependence of semi-inclusive g_1/F_1 is examined in Fig. 5. We compare the data with LO pQCD predictions obtained from the GRSV2000 [19] parametrization. The ratio should be approximately independent of z, broken by the different weights given to the polarized u and d quarks by the favored and unfavored fragmentation functions. This is indeed observed in the data, which are in good agreement with the model in both magnitude and z-dependence up to $z = 0.7$. The observed drop-off at high z for π^- is also expected due to increased importance of $d(x)$ with increasing z. The x-dependence of g_1/F_1 for π^+, π^-, π^0 are consistent with each other and follow the same trend as the inclusive result, which is expected if factorization works. The trend is for the ratio to increase with x, due to increasing dominance of polarized $u(x)$ at high x. The ratio g_1/F_1 has also been studied as a function of transverse component of the hadron momentum p_T. The data suggest that at small p_T, g_1/F_1 tends to decrease for π^+ and to decrease for π^-. This result indicates that quarks aligned and anti-aligned with the nucleon spin might have different transverse momentum distributions, but more data is needed to study this behavior.

4 Summary and Outlook

In conclusion, the spin asymmetries for the proton and the deuteron have been measured over a vast kinematic region, allowing systematic studies of various aspects of the nucleon spin structure at low and intermediate energies. Our data are consistent with an approach to $A_1 = 1$ as $x \to 1$ as required by pQCD. The first extraction of generalized forward spin polarizability γ_0^p was shown to be poorly described by the chiral perturbation theory even at our lowest $Q^2 = 0.05$ GeV^2/c^2. The semi-inclusive studies have shown interesting p_T dependence suggesting that the transverse momentum distributions may have non-trivial dependency on the flavor and helicity of quarks. These studies have led to several new proposals with 6 and 11 GeV beams. A recently completed run with 6 GeV beam will provide us with an order of magnitude more π^+, π^-, π^0 for g_1/F_1 on the proton.

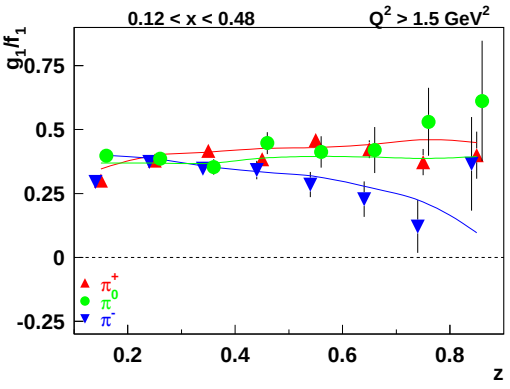

Figure 5: z-dependence of semi-inclusive g_1/F_1 for the proton target

The upcoming energy upgrade of Jefferson Lab will allow us to begin a next generation of spin structure studies and will provide a significant increase in kinematic coverage and statistical accuracy in inclusive and semi-inclusive measurements.

References

[1] S. Drell and A. Hearn, Phys. Rev. Lett. **16** (1966) 908; S. Gerasimov, Yad. Fiz. **2** (1965) 598.

[2] J.D. Bjorken *et al.*, Phys. Rev. **148** (1966) 1467.

[3] X. Ji and J. Osborne, J. Phys. G: Nucl. Part. Phys. **27** (2001) 127.

[4] B.A. Mecking *et al.*, Nucl.Instr.Meth **503/3** (2003) 513.

[5] F.E. Close and W. Melnitchouk, Phys. Rev. C **68** (2003) 035210.
[6] N. Isgur, Phys. Rev. D **59** (1999) 034013.
[7] R. Fatemi *et al.*, Phys. Rev. Lett **91** (2003) 222002.
[8] K. Abe *et al.*, Phys. Rev. Lett **78** (1997) 815.
[9] M. Amarian *et al.*, Phys. Rev. Lett **93** (2004) 152301.
[10] V.D. Burkert and B.L. Ioffe, Phys. Lett B **296** (1992) 223.
[11] J. Soffer and O.V. Teryaev, Phys. Lett B **545** (2002) 323.
[12] X. Ji *et al.*, Phys. Lett. B **472** (2000) 1.
[13] D. Drechsel *et al.* Phys. Rept. **378** (2003) 99.
[14] D. Drechsel, S. Kamalov, and L. Tiator, Nucl. Phys. A **645** (1999) 145.
[15] C. Kao *et al.*, Phys. Rev. D **67** (2003) 016001.
[16] V. Bernard *et al.*, Phys. Rev. D **67** (2003) 076008.
[17] H. Avakian *et al.*, JLAB-PHY-05-384, Sep 2005. 4pp., nucl-ex/0509032.
[18] E.D. Bloom and F.J. Gilman, Phys. Rev. Lett, **25** (1970) 1140;
[19] E.D. Gluck, E. Reya, M. Stratmann and W. Vogelsang, Phys. Rev. D, **63** (2001) 094005;

ABSOLUTE POLARIMETER FOR 200 MEV PROTON BEAM ENERGY

A. Zelenski[1†], M. Runtso[2], G. Atoian[1], A. Bogdanov[2], S. Nurushev[2], F. Pylaev[2]
D. Raparia[1] and E. Stephenson[3]

(1) *Brookhaven National Laboratory, Upton, NY, 11967*
(2) *National Resarch Nuclear University "MEPHI "), Moscow 115409*
(3) *IUCF, Bloomington, 47408*
† *E-mail: zelenski@bnl.gov*

Abstract

A new polarimeter for absolute proton beam polarization measurements at 200 MeV to accuracy better than ± 0.5% has been developed as a part of the RHIC polarized source upgrade. The polarimeter is based on the elastic proton-carbon scattering at 16.2^0 angle, where the analyzing power is close to 100% and was measured with high accuracy. The elastically and in-elastically scattered protons are clearly discriminated by the difference in the propagation length through copper absorber of precisely calculated thickness and energy deposition of the protons in the scintillator telescope detectors. The analyzing power of elastic scattering polarimeter was calibrated with the help of inclusive 12^0 polarimeter and have shown good agreement with simulation results. This technique can be used for accurate polarization measurements in the energy range of at least 160-250 MeV.

I. Polarization measurements technique. The polarized beam for RHIC spin physics experimental program is produced in the optically-pumped polarized H- ion source (OPPIS) and then accelerated in linear accelerator (Linac) to 200 MeV beam energy for strip-injection to Booster and further acceleration to 24.3 GeV in AGS for injection in RHIC [1].

The polarimetry is an essential component of the polarized collider facility. A complete set of polarimeters includes: Lamb-shift polarimeter at the source energy, a 200 MeV polarimeter after the Linac, and polarimeters in AGS and RHIC based on proton-Carbon scattering in Coulomb-Nuclear Interference region [2]. A polarized hydrogen jet polarimeter was used for the absolute polarization measurements in RHIC [3].

A 200 MeV polarimeter is based on proton-Carbon inclusive scattering at 12^0 angle and was calibrated to ± 5% absolute accuracy in calibration experiment by comparison with proton-Deutron elastic scattering. The ongoing program of the polarized source upgrade to 10 mA H-intensity and 85% polarization [4] requires more accurate absolute polarization measurements at very high peak intensity.

The precision absolute measurements at injection to Booster and AGS are also essential for depolarization studies in Booster and AGS.

The 200 MeV inclusive polarimeter was upgraded and calibrated to absolute accuracy better than ± 0.5% by using the proton-Carbon elastic scattering measurements in additional 16.2^0 arms. The analyzing power A_y for proton-Carbon elastic scattering at 200 MeV has been precisely measured in experiments at IUCF. The cross section and

analyzing power for the ground and 4.44-MeV states in ^{12}C has been reported in [7]. The results are presented in Fig. 1. Curve 1 (2) corresponds to protons in the ground state and exiting from the ground (4.44-MeV) state. The curve 3 represents the sum of the two data sets. The analyzing power for elastic scattering is: A_y= 99.35± 0.1% at 16.2^0 scattering angle. When A_y is close to 1, it improves the statistical precision at the fixed counting rate. Since the A_y is reaching maximum at this angle, the systematic error contribution to A_y will be minimal.

Without separation the A_y for inclusive scattering at 16.2^0 angle is diluted by inelastic processes to about 52% [5]. The well known first exited state in Carbon is at 4.44 MeV energy. The elastic scattering was selected by using the copper absorber with the variable thickness. The simulated number of elastically (198.5 MeV) and inelastically (194.1 MeV) scattered protons detected after absorber (vs the absorber thickness) have shown the significant difference.

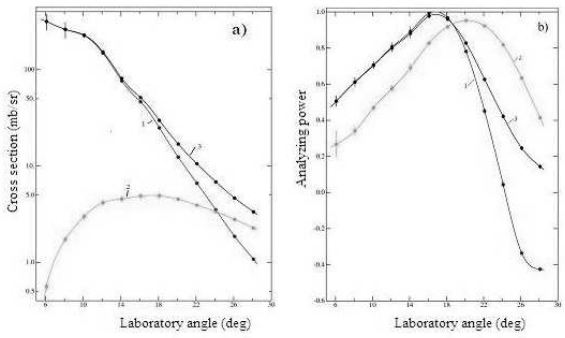

Figure 1: Measurements of the cross section (a) and analyzing power (b) for proton scattering from ^{12}C at 200 MeV.

2. Experimental setup. A new detector telescope arms were installed at 16.2^0 [4]. The telescope includes three scintillator detectors, with fast photomultipliers. A variable copper absorber is situated in between first and second detector. The absorber consists of three Cu blocks of a 12.7 mm thickness. For precise absorber thickness adjustment two variable step shaped copper ladders, arranged before the first detector were used. The first ladder is made with 1.0 mm step, the second with 0.1 mm step. This layout allowed the measurement in the absorber thickness range from zero to 49 mm (total absorption length for 198.4 MeV protons is about 43 mm).

With the thickness of the copper absorber chosen to be 41.5 mm thick, the elastic protons passed through the absorber and absorbed into the second scintillator, depositing 20.0 MeV of energy. The energy thresholds for the second and third detectors were set at 15 MeV, which further suppress the background. For the same configuration, inelastic protons from the formation of the 4.44-MeV state had a range in the copper absorber of 40.4 mm and came to a stop before entering the second detector.

3. Experimental results. a) Energy calibration. The energy of the proton beam out of the Linac can be varied by the RF-cavity phase tune. The energy measurements and calibration to at least ±0.5 MeV accuracy were done by using the magnetic spectrometer and cross-checked at injection to Booster. The experimental results of the counting rate measurements (S1S2 coincidence) at different beam energies are presented in Fig. 2.

At the absorber thickness 41.5 mm the suppression factor for 194.1 MeV scattered beam energy (which corresponds to a 4.4 MeV state excitation) is about 20 times in agreement with GEANT simulations. These measurements directly confirm the feasibility of elastic scattering separation by the absorber of properly fine tuned thickness.

The Linac beam energy can drift in time. The S2/S1 rate ratio is then used for the beam energy monitoring and tuning to improve polarization measurement accuracy.

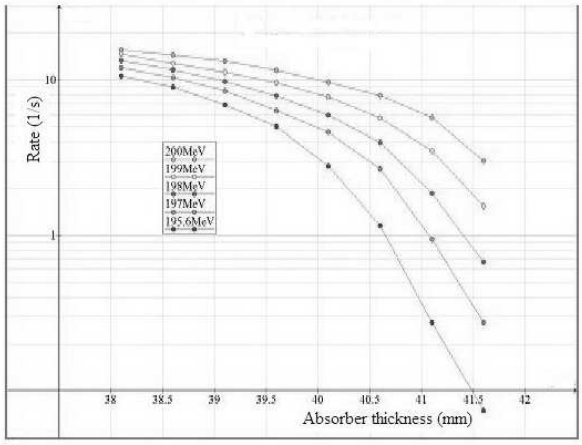

Figure 2: S2/S1 rate ratio after absorber vs. the absorber thickness at different primary beam energies . S1, S2 are the counting rates in the first and second telescope detectors.

b) A_y vs. copper absorber thickness. The measurements of A_y vs. absorber thickness are presented in Fig. 3. Since at 41.5 mm absorber thickness the analyzing power is completely determined by elastic scattering (as demonstrated above) the A_y should be saturated at 99.35% value, as precisely measured in experiments at IUCF [5]. Then the beam polarization of about 80-82% was calculated back from experimentally measured asymmetries. The analyzing power for inclusive 12^0 polarimeter was also calculated and then beam polarization measured by 12^0 polarimeter was used for 16.2^0 analyzing power measurements vs. absorber thickness (see Fig. 3. At zero thickness the A_y (16.2^0) = 52% in agreement with old calibrations [6].

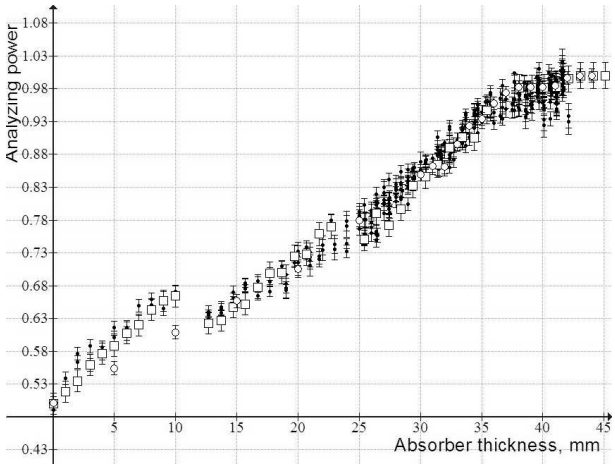

Figure 3: A_y (16.2^0) measurement vs. copper absorber thickness. The scale is normalized for A_y saturation at 0.9935 value extrapolated from precision measurements [5].

To understand the behavior of A_y vs absorber thickness dependence we must take into the consideration all excitation levels of carbon [8].

For Monte-Carlo simulation we took the spectrum of carbon excitation levels with elastic peak, 4.44 excitation level peak and the flat distribution of particle energy from zero to 194.1 MeV.

The combined analyzing power A_Σ for the mixture of three beams (elastic, 4.44 excitation level and average beam with distributed energy) with different analyzing power (A_1, A_2, A_3) can be expressed by the equation:

$$A_\Sigma = \frac{A_1 + A_2 k_2 + A_3 k_3}{1 + k_2 + k_3}$$

Here $k_2 = \frac{n_2}{n_1}$, $k_3 = \frac{n_3}{n_1}$, n_1, n_2, n_3 are beam intensities.

We took the cross section ratio k_2 and the values of A_1 and A_2 from Fig. 1 (a) and (b).

If we had only elastic events and 4.44 excitation level events (k_3=0), we should get 0.98 analyzing power for rising absorber thickness until excitation beam will be absorbed.

Taking into account low energy particles, using k_3 value from Carbon excitation spectrum [8] and getting the A_3 value from the normalization for to have at zero absorber thickness we have got Monte-Carlo simulation results, shown by squares in the Fig. 3

with good agreement with experimental points. The reason of steps on the borders of changing of solid blocks of absorber is the additional scattering of particles in the step shaped copper ladders, arranged before the first counter. The circles in the Fig. 3 show the simulated analyzing power, when all the absorbers are arranged only between S1 and S2 detectors.

c). Systematic errors. The small cross-section and additional strong suppression of inelastic (4.4 MeV state) by absorber reduce the elastic $A_y$dilution by inelastic component admixture to less than 0.1%. The beam energy and scattering angle errors are minimal for the analyzing power measurements near maximum value and do not exceed 0.1%. The estimate of the extrapolation error for 200 MeV beam energy and 16.2^0 angle was estimated at about 0.2%.

4. Summary. A new polarimeter for absolute proton beam polarization measurements at 200 MeV to accuracy better than $\pm 0.5\%$ has been developed as a part of the RHIC polarized source upgrade. The polarimeter is based on the elastic proton-carbon scattering at 16.2^0 angle, where the analyzing power is as large as 99.35% and was measured with high accuracy. The elastically and in-elastically scattered protons are clearly identified by the difference in the propagation through variable copper absorber and energy deposition of the stopped protons in the detectors. The rate difference in the subsequent detectors of telescope arms was used for the beam energy monitoring and tuning to improve polarization measurement accuracy. The 16.2^0 elastic scattering polarimeter was used for calibration of a high rate inclusive 12^0 polarimter, which was used for the on-line polarization tuning and monitoring and will be used as main polarimeter at higher luminosities.The rise of luminosity can be compensated simply by introducing the additional thickness of absorber.

References

[1] T. Roser, AIP Conf. Proc. **980** (2008) 15.

[2] Y. Makdisi, ibid, p. 58.

[3] A. Zelenski et al., NIM **A536** (2005) 248.

[4] A. Zelenski et al., SPIN2010 – 19th International Spin Physics Symposium, September 27 – October 2, 2010, Juelich, Germany.

[5] S.W. Wissink et al., Phys. Rev., **C45** (1992) R505.

[6] J.A. Rice, Master Thesis, Rice University, Houston, Texas, 1983.

[7] H.O. Meyer et al., Phys. Rev., **C27** (1983) 459.

[8] H. Karwowski et al., Indiana University Cyclotron Facility Report.

THE GPD PROGRAM AT COMPASS

A. Sandacz
On behalf of the COMPASS collaboration

National Centre for Nuclear Research, Warsaw, Poland
E-mail: sandacz@fuw.edu.pl

Abstract

The high energy polarised muon beam available at CERN, with positive or negative charge, make COMPASS a unique place for GPD studies. The COMPASS program of GPD studies is reviewed and various observables for this program and expected accuracies are discussed. The necessary developements of the experimental setup and the first results of the test runs are also presented.

1 Introduction

Generalised Parton Distributions (GPDs) [1–3] contain a wealth of information on the partonic structure of the nucleon. In particular, they allow a novel description of the nucleon as an extended object, sometimes referred to as 3-dimensional 'nucleon tomography' [4]. GPDs also allow access to such a fundamental property of the nucleon as the orbital angular momentum of quarks [2]. For reviews of the GPDs see Refs [5–7].

The mapping of the nucleon GPDs requires comprehensive experimental studies of hard processes, Deeply Virual Compton Scattering and Hard Exclusive Meson Production, in a broad kinematic range. In the future program [8] we propose to measure both DVCS and HEMP using an unpolarised proton target during a first period, in order to constrain mainly GPD H, and a transversely polarised ammonia target during another period in order to constrain the GPD E.

2 The proposed setup

The COMPASS apparatus is located at the high-energy (100-200 GeV) and highly-polarized $\mu^{\pm}$ beam line of the CERN SPS. At present it consists of a two-stage spectrometer comprising various tracking detectors, electromagnetic and hadron calorimeters, and particle identification detectors grouped around 2 dipole magnets SM1 and SM2 in conjunction with a longitudinally or transversely polarized target. By installing a recoil proton detector (RPD) around the target to ensure exclusivity of the DVCS and HEMP events, COMPASS could be converted into a facility measuring exclusive reactions within a kinematic domain from $x \sim 0.01$ to ~ 0.1, which cannot be explored at any other existing or planned facility in the near future. Thus COMPASS could explore the uncharted x domain between the HERA collider experiments and the fixed-target experiments as

HERMES and the planned 12 GeV extension of the JLAB accelerator. For values of x below 10^{-1}, the outgoing photon (or meson) is emitted at an angle below 10° which corresponds for the photon to the acceptance of the two existing COMPASS electromagnetic calorimeters ECAL1 and ECAL2. For charged particles such an angular range is within the acceptance of the tracking devices and the RICH detector. To access higher x values a large angular acceptance calorimeter ECAL0 is needed, which is presently under study.

The data will be collected with polarized μ^+ and μ^- beams. Assuming in total 280 days of data taking, μ^+ beam flux of $4.6 \cdot 10^8$ μ per SPS spill and three times smaller flux for μ^- beam, a reasonable statistics for the DVCS process can be accumulated for Q^2 values up to 8 GeV^2. It is worth noting that an increase of the number of muons per spill by a factor 4 could result in an increase in the range in Q^2 up to about 12 GeV^2.

3 Planned measurements

The complete GPD program at COMPASS will comprise the measurements of the DVCS cross section with polarized positive and negative muon beams and at the same time the measurements of a large set of mesons (ρ, ω, ϕ, π, η, ...).

3.1 Deeply Virtual Compton Scattering

DVCS is considered to be the theoretically cleanest of the experimentally accessible processes because effects of next-to-leading order and higher twist contributions are under theoretical control [9]. The competing Bethe-Heitler (BH) process,which is elastic lepton-nucleon scattering with a hard photon emitted by either the incoming or outgoing lepton, has a final state identical to that of DVCS so that both processes interfere at the level of amplitudes.

COMPASS offers the advantage to provide various kinematic domains where either BH or DVCS dominates. The collection of almost pure BH events at small x allows one to get an excellent reference yield and to control accurately the global efficiency of the apparatus. In contrast, the collection of an almost pure DVCS sample at larger x will allow the measurement of the x dependence of the t-slope of the cross section, which is related to the tomographic partonic image of the nucleon. In the intermediate domain, the DVCS contribution will be boosted by the BH process through the interference term. The dependence on ϕ, the azimuthal angle between lepton scattering plane and photon production plane, is a characteristic feature of the cross section [9].

COMPASS is presently the only facility to provide polarized leptons with either charge: polarized μ^+ and μ^- beams. Note that with muon beams one naturally reverses both charge and helicity at once. Practically μ^+ are selected with a polarisation of -0.8 and μ^- with a polarization of $+0.8$. The difference and sum of cross sections for μ^+ and μ^- combined with the analysis of ϕ dependence allow us to isolate the real and imaginary parts of the leading twist-2 DVCS amplitude, and of higher twist contributions.

In the following sections we show projections for DVCS measurements with an unpolarised proton target (3.1.1 and 3.1.2) and with a transversely polarised ammonia target

(3.1.3). For each target the integrated muon flux was taken the same as described in Sect. 2 and the value of the global efficiency was assumed to be equal to 0.1.

3.1.1 x-dependence of the t-slope of DVCS

The t-slope parameter $B(x)$ of the DVCS cross section $\frac{d\sigma}{dt}(x) \propto \exp(-B(x)\,|t|)$ can be obtained from the beam charge and spin sum of the cross sections after integration over ϕ and BH subtraction. The expected statistical accuracy of the measurements of $B(x)$ at COMPASS is shown in Fig. 1. The upper plot corresponds to the acceptance of the existing electromagnetic calorimeters, while the lower one is obtained assuming that in addition the new calorimeter ECAL0 will be also available. The systematic errors are mainly due to uncertainties involved in the subtraction of the BH contribution. At $x > 0.02$ they are small compared to the statistical errors. For the simulations the simple ansatz $B(x) = B_0 + 2\,\alpha' \log(\frac{x_0}{x})$ was used. As neither B_0 nor α' are known in the COMPASS kinematics, for the simulations shown in Fig. 1 we chose the values $B_0 = 5.83$ GeV^2, $\alpha' = 0.125$ and $x_0 = 0.0012$. The precise value of the t-slope parameter $B(x)$ in the COMPASS x-range will yield new and significant information in the context of 'nucleon tomography' as it is expected in Ref. [10].

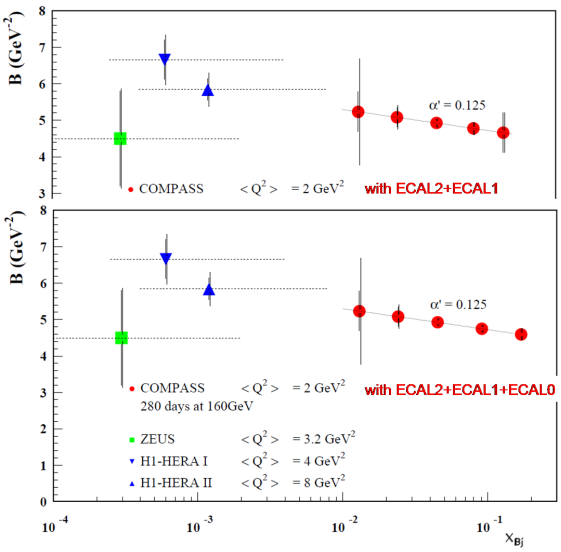

Figure 1: The x dependence of the fitted t-slope parameter B of the DVCS cross section. COMPASS projections are calculated for $1 < Q^2 < 8$ GeV^2 and compared to HERA results for which the mean value $< Q^2 >$ is in this range.

3.1.2 Beam charge and spin difference of cross sections

Fig. 2 shows the projected statistical accuracy for the beam charge and spin difference of cross section $\mathcal{D}_{\mathcal{CS},\mathcal{U}}$ measured as a function of ϕ in a selected (x, Q^2) bin. The difference is defined as

$$\mathcal{D}_{CS,U} = d\sigma^{\overleftarrow{+}} - d\sigma^{\overrightarrow{-}}\,, \tag{1}$$

with arrows indicating the orientations of the longitudinal polarisation of the beams. The difference $\mathcal{D}_{\mathcal{CS},\mathcal{U}}$ is sensitive to the real part of the DVCS amplitude which is a convolution of GPDs with the hard scattering kernel over the whole range of longitudinal momenta of exchanged quarks. Therefore measurements of this asymmetry provide strong constrains on the models of GPD. Two of the curves shown in the figure are calculated using the 'VGG' GPD model [11]. As this model is meant to be applied mostly in the valence region, typically the value $\alpha' = 0.8$ is used in the 'reggeized' parameterization of the correlated x, t dependence of GPDs. For comparison also the model result for the 'factorized' x, t dependence is shown, which corresponds to $\alpha' \approx 0.1$ in the reggeized ansatz. A recent theoretical development [12] exploiting dispersion relations for Compton form factors was

successfully applied to describe DVCS observables at very small values of x typical for the HERA and extended to include DVCS data from HERMES and JLAB. The prediction for COMPASS from this analysis are shown as additional curves.

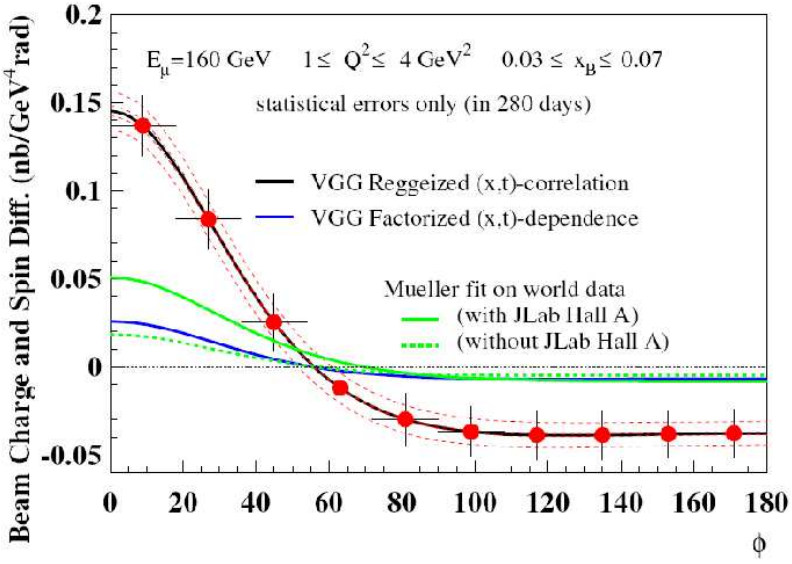

Figure 2: Projections for the beam charge and spin difference of cross sections measured at COMPASS for $0.03 \leq x \leq 0.07$ and $1 \leq Q^2 \leq 4$ GeV^2. The red and blue curves correspond to two variants of the VGG model [11] while the green curves show predictions based on the first fits to the world data [12].

As the overall expected data set from the GPD program for COMPASS will allow 9 bins in x vs. Q^2, each of them expected to contain statistics sufficient for stable fits of the ϕ dependence, a determination of the 2-dimensional x, Q^2 (or x, t) dependence will be possible for the various Fourier expansion coefficients c_n and s_n [9], thereby yielding information on the nucleon structure in terms of GPDs over a range in x. These data are expected to be very useful for future developments of reliable GPD models able to simultaneously describe the *full* x-range.

3.1.3 Predictions for the transverse target spin asymmetry

Transverse target spin asymmetries for exclusive photon production are important observables for studies of the GPD E, and for the determination of the role of the orbital momentum of quarks in the spin budget of the nucleon. The sensitivity of these asymmetries to the total angular momentum of u quarks, J_u, was estimated for the transversely polarised protons in a model dependent way in Ref. [13].

The transverse target spin asymmetries for the proton will be measured with the transversely polarised ammonia target, similar to the one used at present by COMPASS. Two options are considered for the configuration of the target magnet and the RPD, each with a different impact on the range of measurable energy of the recoil proton.

The transverse spin dependent part of the cross sections will be obtained by subtracting the data with opposite values of the azimuthal angle ϕ_s, which is the angle between the lepton scattering plane and the target spin vector. In order to disentangle the $|DVCS|^2$ and the interference terms with the same azimuthal dependence, it is necessary to take

data with both μ^+ and μ^- beams, because only in the difference and the sum of μ^+ and μ^- cross sections these terms become separated. Both asymmetries for the difference and the sum of μ^+ and μ^- of transverse spin dependent cross sections will be analysed. The difference (sum) asymmetry $A^D_{CS,T}$ ($A^S_{CS,T}$) is defined as the ratio of the μ^+ and μ^- cross section difference (sum) divided by the lepton charge-averaged, unpolarised cross section. Here CS indicates that both lepton charge and lepton spin are reversed between μ^+ and μ^-, and T is for the transverse target polarisation.

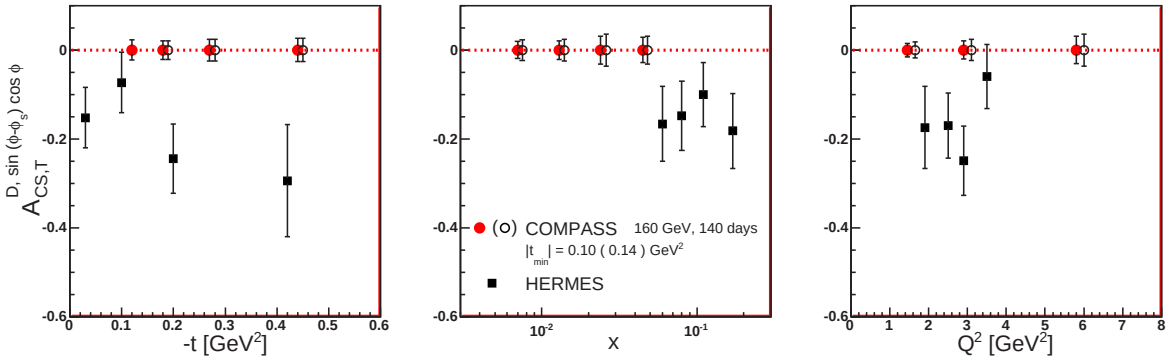

Figure 3: The expected statistical accuracy of $A^{D,\sin(\phi-\phi_s)\cos\phi}_{CS,T}$ as a function of $-t$, x and Q^2. Solid and open circles correspond to the simulations for the two considered configurations of the target region. Also shown is the asymmetry $A^{\sin(\phi-\phi_s)\cos\phi}_{U,T}$ measured by HERMES [13] with its statistical errors.

As an example, the results from the simulations of the expected statistical accuracy of the asymmetry $A^{D,\sin(\phi-\phi_s)\cos\phi}_{CS,T}$ are shown in Fig. 3 as a function of $-t$, x and Q^2 for the two considered configurations of the target region. Here $\sin(\phi-\phi_s)\cos\phi$ indicates the type of azimuthal modulations. This asymmetry is an analogue of the asymmetry $A^{\sin(\phi-\phi_s)\cos\phi}_{UT}$ measured by HERMES with unpolarised electrons, also shown in the figure. Typical values of the statistical errors of $A^{D,\sin(\phi-\phi_s)\cos\phi}_{CS,T}$, as well as of the seven remaining asymmetries related to the twist-2 terms in the cross section, are expected to be ≈ 0.03.

3.2 Hard Exclusive Meson Production

Hard exclusive vector meson production is complementary to DVCS as it provides access to various other combinations of GPDs. For vector meson production only GPDs H and E contribute, while for pseudoscalar mesons GPDs $\tilde{H}$ and $\tilde{E}$ play a role. We recall that DVCS depends on the four GPDs. Also in contrast to DVCS, where gluon contributions enter only beyond leading order in α_s, in HEMP both quark and gluon GPDs contribute at the same order. For example

$$H_{\rho^0} = \frac{1}{\sqrt{2}}(\frac{2}{3}H^u + \frac{1}{3}H^d + \frac{3}{8}H^g), \quad H_\omega = \frac{1}{\sqrt{2}}(\frac{2}{3}H^u - \frac{1}{3}H^d + \frac{1}{8}H^g), \quad H_\phi = -\frac{1}{3}H^s - \frac{1}{8}H^g.$$

Therefore by combining the results for various mesons the GPDs for various quark flavours and for gluons could be disentangled.

Data on exclusive production of vector mesons production, which will be recorded simultaneously to the DVCS measurements, will be used to determine corresponding

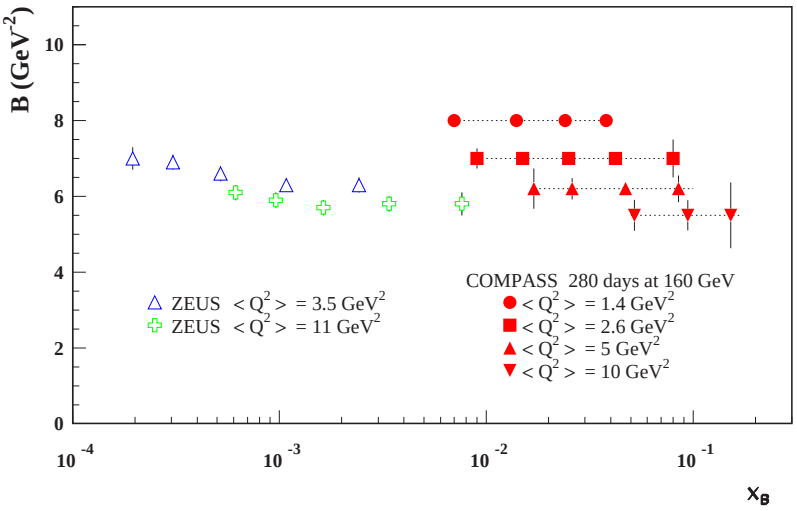

Figure 4: Projections for measuring the t-slope parameter B in exclusive ρ^0 production, calculated for $1 \geq Q^2 \geq 20$ GeV^2 compared to ZUES results with similar $< Q^2 >$. Only statistical erros are shown.

cross sections and t-slope parameters $B(x)$. As an example, in Fig. 4 we show projections for the ρ^0 meson. The simulations are based on a model developed for COMPASS, where the Q^2 and ν dependences are taken from the parameterisation of the NMC data and the absolute normalisation is obtained using predictions of Ref. [14]. The statistical precision expected for 280 days at 160 GeV muon beam energy is shown for different bins of x and Q^2. The data from ZEUS, which cover a lower x range are also shown for comparison. The projections for COMPASS include a dependence of the slope B on Q^2, as observed in both ZEUS and H1 experiments, but no correlation between the slope value and x was assumed here.

It was pointed out that vector meson production on a transversely polarised target is sensitive to the nucleon helicity-flip GPD E [5, 15]. This GPD offers unique views on the orbital angular momentum carried by partons in the proton [2] and on the correlation between polarisation and spatial distribution of partons [4]. The azimuthal asymmetry $A_{UT}^{\sin(\phi-\phi_s)}$ for exclusive production of a vector meson off a transversely polarised nucleon depends linearly on the GPD E and at COMPASS kinematic domain it can be expressed as

$$A_{UT}^{\sin(\phi-\phi_s)} \sim \sqrt{t_0 - t}\frac{\mathrm{Im}(\mathcal{E}^M \mathcal{H}_M^*)}{|\mathcal{H}_M|^2}\,, \tag{2}$$

where t_0 is the minimal momentum transfer. The quantities $\mathcal{H}_M$ and $\mathcal{E}_M$ are weighted sums of convolutions of the GPD $H^{q,g}$ and $E^{q,g}$, respectively, with the generalised distribution amplitude (GDA) of the produced meson and a hard scattering kernel [5]. The weights depend on the contributions of quarks of various flavours and of gluons to the production of meson M.

We note that the production of ρ, ω, ϕ vector mesons is already being investigated at COMPASS [16]. The preliminary results from COMPASS on the transverse target spin asymmetries for ρ^0 production off transversely polarised protons and deuterons were presented at this conference [17].

4 Validation tests and outlook

The setup used in 2008 and 2009 for the meson spectroscopy measurements with hadron beams happens to be an excellent *prototype* to perform validation measurements for DVCS. A first measurements of exclusive γ production on a 40 cm long LH target, with detection of the slow recoiling proton in the RPD have been performed during short test runs in 2008 and 2009 using 160 GeV μ^+ and μ^- beams. They were performed with the present hadron setup, all the standard COMPASS tracking detectors, the ECAL1 and ECAL2 electromagnetic calorimeters for photon detection and appropriate triggers. An efficient selection of single photon events, and suppression of the background is possible by using the combined information from the forward COMPASS detectors and the RPD.

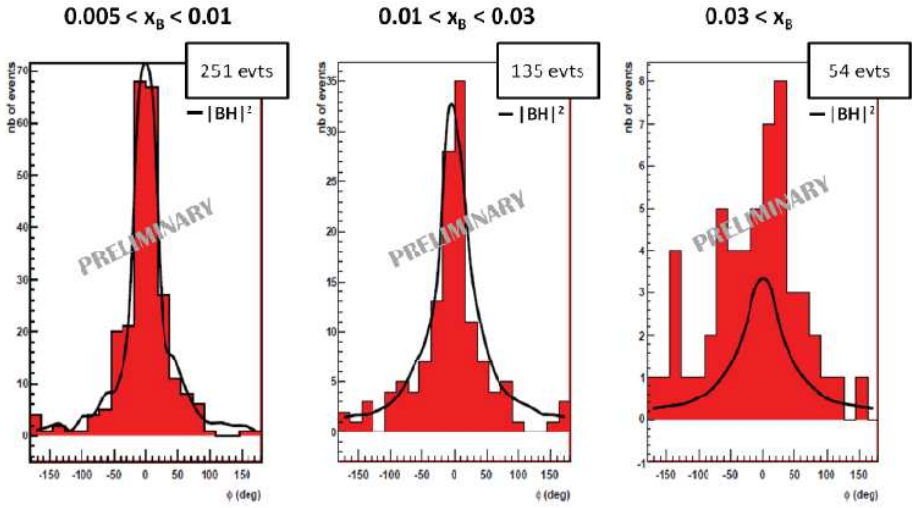

Figure 5: The distribution of the azimuthal angle ϕ for observed exclusive single photon production measured in the 2009 DVCS test run at COMPASS. The lines represent the expected BH event yield.

A way to identify the observed process, $\mu + p \rightarrow \mu' + \gamma + p'$, to which both the DVCS and Bethe-Heitler process contribute, is to look at the angle ϕ between the leptonic and hadronic planes. The observed distributions, after applying all cuts and selections and for $Q^2 > 1$ (GeV/c)^2, are displayed in Fig. 5 and compared to the predictions from the Monte Carlo simulations for the BH event yield. The Bethe-Heitler contribution shows a characteristic peak at $\phi \simeq 0$. The overall detection efficiency can be deduced from the relative normalization of the two distributions for the low x-region dominated by BH. The global efficiency is equal to 0.14 ± 0.05 in agreement with the value 0.1 assumed for the proposal [8].

The proposal to extend the physics program of COMPASS, including the GPD studies, was approved at CERN in 2010. A possible start of the GPD program, first with a 2.5 m long liquid hydrogen target, is planned for 2012. A few weeks run with the muon beam will be devoted to the comissioning of a 4 m long RPD being presently constructed, and of a central part (20%) of ECAL0, which will be available in 2012. It will be followed by a short physics run with an objective to measure t-slope for DVCS.

References

[1] D. Mueller *et al*, Fortsch. Phys. **42** (1994) 101.

[2] X. Ji, Phys. Rev. Lett. **78** (1997) 610; Phys. Rev. D **55** (1997) 7114.

[3] A.V. Radyushkin, Phys. Lett. B **385** (1996) 333; Phys. Rev. D **56** (1997) 5524.

[4] M. Burkardt, Phys. Rev. D **62** (2000) 071503; erratum-ibid. D **66** (2002) 119903; Int. J. Mod. Phys. A **18** (2003) 173; Phys. Lett. B **595** (2004) 245.

[5] K. Goeke, M.V. Polyakov and M. Vanderhaegen, Prog. Part. in Nucl. Phys. **47** (2001) 401.

[6] M. Diehl, *Generalized Parton Distributions*, DESY-thesis-2003-018, hep-ph/0307382.

[7] A.V. Belitsky and A.V.Radyushkin, Phys. Rep. **418** (2005) 1.

[8] The COMPASS Collaboration, *COMPASS-II Proposal*, CERN-SPSC-2010-014, SPSC-P-340, May 17, 2010.

[9] A.V. Belitsky, D. Müller and A. Kirchner, Nucl. Phys. **B 629** (2002) 323.

[10] M. Strikman and C. Weiss, Phys. Rev. **D69** (2004) 054012.

[11] M. Vanderhaeghen, P.A.M. Guichon and M. Guidal, Phys. Rev. Lett. **80** (1998) 5064; Phys. Rev. D **60** (1999) 094017;

[12] K. Kumericki and D. Mueller, hep-ph/0904.0458.

[13] A. Airapetian *et al*, JHEP **06** (2008) 066.

[14] S. Goloskokov and P. Kroll, Eur. Phys. J. C **53** (2008) 367.

[15] F. Ellinghaus, W.-D. Nowak, A.V. Vinnikov, and Z. Ye, Eur. Phys. J. **C46** 729 (2006), hep-ph/0506264.

[16] A. Sandacz, *Exclusive processes in leptoproduction at COMPASS*, in Proceedings of the International Conference on the Structure and the Interactions of the Photon, PHOTON09, Hamburg, 2009, ed. O. Behnke *et al*, Verlag Deutches Elektronen-Synchrotron, Hamburg, 2010, p. 294.

[17] P. Sznajder, this conference.

MEASUREMENT OF PROTON BEAM POLARIZATION AT RHIC IN RUN 11

D. Smirnov[1†] for the RHIC spin group

(1) *Brookhaven National Laboratory*
† *E-mail: dsmirnov@bnl.gov*

Abstract

At the Relativistic Heavy Ion Collider the measurement of the proton beam polarization is based on the observation of the azimuthal asymmetry of recoil products in elastic proton-proton and proton-carbon scattering processes. For the high energy beams (E = 24–250 GeV) scattered on a fixed target the asymmetry is maximal when induced by the coulomb-nuclear interference at a small momentum transfer squared $-t$. Fast measurements of the beam polarization are carried out few times during an accelerator store by the p-Carbon polarimeters utilizing a carbon filament as a target while the absolute polarization is provided by the H-jet polarimeter with a polarized hydrogen jet target. Recoil particles are detected by microstrip silicon detectors. For the 2011 run the readout system of the p-Carbon polarimeters was upgraded to cope with the increased beam intensity. We report the average beam polarization and discuss the systematic uncertainties associated with the measurement.

1 Introduction

At the Relativistic Heavy Ion Collider (RHIC) the polarization of the proton beams is measured by detecting recoil products from the elastic proton-proton ($pp \to pp$) and proton-Carbon ($pC \to pC$) scattering reactions on a fixed target. The beam polarization P is a statistical quantity defined as a fraction of the expected spin-dependent asymmetry $A_N = \frac{\sigma_\uparrow - \sigma_\downarrow}{\sigma_\uparrow + \sigma_\downarrow}$ measured in the experiment, i.e. $P = \varepsilon / A_N$ where ε and A_N are the observed and predicted asymmetries respectively. In general, the scattering cross section of particles with determined spin orientation $\sigma_{\uparrow/\downarrow}$ can be described by five independent helicity amplitudes corresponding to double-, single-, or no-spin flips between the initial and final states [1]. Each of the helicity amplitudes has an electromagnetic and hadronic part hence, making A_N dependent on contributions from both electromagnetic and strong interactions as well as their superposition. The asymmetry A_N, also known as the analyzing power, cannot be calculated exactly due to lack of precise theoretical framework for the strong force at smaller values of momentum transfer squared $-t$. However, with the assumption of negligible contribution from the hadronic spin-flip amplitude the analyzing power can be calculated exactly for a wide range of $-t$. It has been shown [2] that A_N has a maximum value of approximately 4–5% at $-t \approx 0.003$ GeV^2 and decreases with increasing $-t$. The kinematic region around the maximum is called the Coulomb Nuclear Interference (CNI) region, and corresponds to where the electromagnetic and strong forces become similar in strength and interfere with each other.

The measurements over the last decade demonstrated that the assumption of a small contribution of the hadronic spin-flip amplitude holds true within experimental uncertainties for the pp interactions at $\sqrt{s} \gtrsim 10$ GeV [3] whereas the same contribution at lower energies and in pC interactions may be non-zero [4, 5].

2 Experimental Setup

Precise knowledge of the beam polarization is essential for the spin physics program at BNL. To meet the program goals the RHIC utilizes two kinds of polarimeters. The first type includes the H-jet polarimeter that consists of a polarized atomic hydrogen jet target with a known polarization measured by a Breit-Rabi polarimeter [3]. It is located at one of the collision points and measures the kinematics of the protons recoiled from the vertical jet target. Both RHIC beams traverse the target simultaneously but do not interact with each other as they are vertically separated by ≈ 4 mm. The transverse size of the hydrogen jet is ≈ 6 mm which is wide enough to probe the entire cross section of the beam. The second type includes the p-Carbon polarimeters which operate by inserting an ultra-thin carbon ribbon target into the beam. A typical target size is $2.5\ \text{cm} \times 10\ \mu\text{m} \times 25$ nm. The high event rate and the small width of the targets allows one to measure polarization at different positions across the beam, i.e. a polarization profile. Since 2009 the RHIC has two independent p-Carbon polarimeters installed in each ring. Each polarimeter of this kind employs a set of six vertical and horizontal targets.

Figure 1 schematically illustrates the basic idea of the experimental setup for the RHIC polarimeters. A high energy polarized proton kicks a particle from the target which is then registered by a silicon strip detector. In the elastic CNI interaction the direction of the scattered proton does not change significantly while the recoil particle tends to stay in the plane perpendicular to the beam direction. In this optimal plane six detectors with 12 strips parallel to the beam line are installed as far as $\approx 18 - 19$ cm from the target at $\pm 45°$, $\pm 90°$, $\pm 135°$ w.r.t. the proton's spin direction in each of the p-Carbon polarimeters. Another set of six detectors is installed close to $\pm 90°$ at ≈ 80 cm from the jet target in the H-jet. All the detectors are mounted inside the vacuum chamber with readout preamplifier boards directly attached to the feed-through connector on the detector ports. The RHIC polarimeters employ a similar readout system based on the waveform digitizer modules. The data acquisition system provides timing and energy information for each event detected in the silicon detectors.

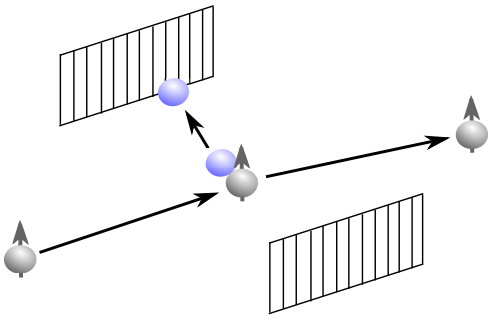

Figure 1: Schematic view of the RHIC polarimeters experimental setup. The shown direction of the silicon strips is typical for the H-jet polarimeter.

For the 2011 run the charge-sensitive preamplifiers in the p-Carbon polarimeters were replaced with current-sensitive ones. Due to this effort a significant reduction in the output signal length to ≈ 10 ns was achieved. The event pileup effects seen previously were minimized.

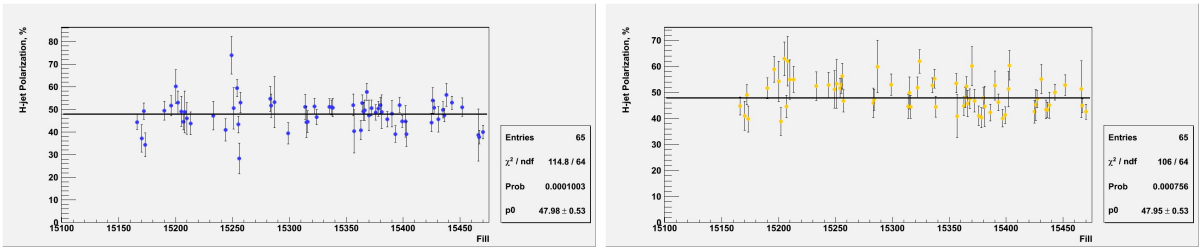

Figure 2: Average polarization in a accelerator store as measured by the H-jet polarimeter in the blue (a) and yellow (b) rings.

3 Analysis and Results

The energy response of the silicon detectors is calibrated with α-sources installed inside the vacuum polarimeter chambers. Emitted α particles have energy of ~ 5 MeV and completely stop in the detectors. While most of the recoil protons and carbon ions are also stopped in the detectors the latter travel much shorter distance in silicon. The region close to the surface of a silicon detector is known to be under-depleted when a bias voltage applied. The energy lost in this dead region cannot be measured. To account for these extra energy losses $E_{\rm loss}$ we calibrate each channel by fitting elastic events with a non-relativistic equation relating the measured time of flight $t_{\rm meas}$ and the measured energy $E_{\rm meas}$ as: $E_{\rm meas} + E_{\rm loss} = \frac{m}{2} \times L^2/(t_{\rm meas} + t_0)^2$, where m is the mass and L is the distance traveled by a recoil particle. An additional time of flight offset t_0 is also individually adjusted for each strip using the same data. Once the calibration parameters are identified the signal events are selected by applying a 3σ cut on the mass distribution. To further suppress the background we also constrain the kinematic energy range of recoil particles to be within a certain window. For thus defined elastic event dataset we define the yields according to the expected spin state of the incident beam particle and the left or right direction of the recoil particle with respect to the spin. These yields are plugged into the square root formula to calculate the asymmetry as: $\varepsilon = \left(\sqrt{N_L^{\uparrow}N_R^{\downarrow}} - \sqrt{N_L^{\downarrow}N_R^{\uparrow}}\right) \Big/ \left(\sqrt{N_L^{\uparrow}N_R^{\downarrow}} + \sqrt{N_L^{\downarrow}N_R^{\uparrow}}\right)$.

In order to take advantage of the higher statistics for the final polarization $P = \varepsilon/A_N$ we use the yields provided by the p-Carbon polarimeters. However, we choose not to rely on loose theoretical predictions for the pC analyzing power A_N but instead scale on average the final results to the polarization measured by the H-jet. The H-jet polarimeter provides an absolute measurement of the beam polarization. In fact, no knowledge about the pp A_N is required because the beam and the target are both protons, and the beam polarization is given by $P_{\rm beam} = -(\varepsilon_{\rm beam}/\varepsilon_{\rm target}) \times P_{\rm target}$. The beam polarization as measured by the H-jet is shown in Figure 2.

The strategy outlined above benefits from lower final statistical errors without introducing an additional systematic uncertainty due to poorly known A_N for pC interactions. However, the systematic uncertainties now include effects from both the p-Carbon and H-jet polarimeters. The global store-to-store correlated uncertainties include the normalization uncertainty (1.1–1.5%) and the uncertainty due to molecular background in the jet target ($\sim 2\%$). The store-to-store uncorrelated uncertainties decrease with the number of stores combined as $1/\sqrt{N}$ and are mainly defined by unstatistical fluctuations in

the p-Carbon measurements. These are believed to be induced by unaccounted energy losses of the recoil carbon ions in the target due to presumably unstable angle between the target ribbon and the beam. The results for run 2011 are available online at [6, 7].

4 Summary

The RHIC polarimeters performed well during the 2011 run. In this run we measured the average beam polarization of about 48% in both collider rings with the total uncertainty consistent with the requirements set by the RHIC spin physics program. The higher than in the preceding run average beam polarization is due to a better control of the beam orbit achieved by the accelerator group and other tune-up of the accelerator complex [8]. A careful offline analysis showed that the store-to-store correlated systematic uncertainties reduced with respect to the previous run. The improvement is attributed to a number of reasons including the reduction of the event pile-up effects, thanks to shortened signal pulses from the current-sensitive preamplifiers, and the use of thinner carbon targets in the p-Carbon polarimeters. The stable performance of the H-jet during 2011 has assured a higher acquired statistics which, in turn, decreased the global uncertainty due to the overall normalization. We confirmed the good performance of the absolute polarimeter by comparing the asymmetry A_N in the pp interactions with the same measured in the 2009 run (Figure 3) and found them to be in a good agreement. The details and results of the offline analysis can be found online at [6, 7].

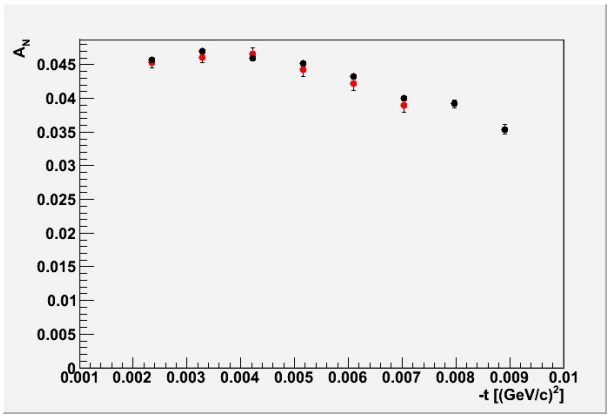

Figure 3: Analyzing power A_N for $pp \to pp$ scattering as a function of the momentum transfer $-t$. The 2011 and 2009 data is shown with black and red circles respectively.

References

[1] N. H. Buttimore *et al.*, Phys. Rev. D **59**, 114010 (1999) [hep-ph/9901339].

[2] A. T. Bates and N. H. Buttimore, Phys. Rev. D **65**, 014015 (2002) [hep-ph/0010014].

[3] H. Okada *et al.*, Phys. Lett. B **638**, 450 (2006) [nucl-ex/0502022].

[4] I. G. Alekseev *et al.*, Phys. Rev. D **79**, 094014 (2009).

[5] J. Tojo *et al.*, Phys. Rev. Lett. **89**, 052302 (2002) [hep-ex/0206057].

[6] Polarization results for p-Carbon measurements: http://www.phy.bnl.gov/cnipol/rundb/

[7] The store-by-store polarization results: http://www.phy.bnl.gov/cnipol/fills/

[8] H. Huang, Proceedings of the 2011 Particle Accelerator Conference, http://accelconf.web.cern.ch/AccelConf/PAC2011/papers/moocn3.pdf

TRANSVERSE SINGLE SPIN ASYMMETRIES AT LOW MOMENTUM TRANSFER AT STAR

D.N. Svirida[1†] for the STAR Collaboration

(1) *Institute for Theoretical and Experimental Physics, Moscow, Russia*
† *E-mail: Dmitry.Svirida@itep.ru*

Abstract

Elastic scattering of polarized protons at low momentum transfer is described by the interference of Coulomb and hadronic amplitudes. The presence of a spin flip part in the hadronic amplitude may indicate the contribution of exchanges other than the dominant Pomeron, or manifestation of hypothetic Pomeron spin flip component. The Coulomb term is well defined by QED.

This talk presents preliminary results on single spin asymmetries of transversely polarized proton-proton scattering at $\sqrt{s} = 200$ GeV. About 20 million elastic events were used to obtain the result in the $-t$ range of $0.005 - 0.035$ (GeV/c)^2. The fit of $-t$ dependence of the asymmetry does not indicate the presence of any spin flip hadronic amplitude.

Elastic pp-scattering at very small angles provides a unique tool to study dynamics of the strong interaction in the nonperturbative region. The total cross section was measured up to high energy and is in good agreement with a description using Regge pole exchange. At ultra-relativistic energies the main contribution comes from Pomeron or, in terms of perturbative QCD, multigluon exchange [1]. Most of the previous experiments were done with unpolarized beams and targets. The first measurement with polarized protons at high energies in the Coulomb nuclear interference (CNI) region at $\sqrt{s} = 19.4$ GeV was done by the E704 experiment [2] with moderate precision. RHIC with its polarized beams [3] published a number of more accurate measurements in the range $\sqrt{s} = 6.8-21.7$ GeV [4,5] over the last few years, however, only one measurement with limited statistics exists so far in the collider energy range [6].

Elastic scattering of two identical particles with spin 1/2 is described by 5 helicity amplitudes [7,8]. Two amplitudes $\phi_1(s,t)$=<++|M|++> and $\phi_3(s,t)$=<+−|M|+−> produce no spin flip and give the main contribution to the total and differential cross sections. Single spin flip amplitude $\phi_5(s,t)$=<++|M|+−> gives rise to the single spin asymmetry A_N through interference with dominant terms $\phi_1(s,t)$ and $\phi_3(s,t)$:

$$\sigma_{tot} = \frac{4\pi}{s} Im(\phi_1 + \phi_3)|_{t=0} \, , \tag{1}$$

$$\frac{d\sigma}{dt} = \frac{2\pi}{s^2}(|\phi_1|^2 + |\phi_2|^2 + |\phi_3|^2 + |\phi_4|^2 + 4|\phi_5|^2) \, , \tag{2}$$

$$A_N \frac{d\sigma}{dt} = -\frac{4\pi}{s^2} Im\{\phi_5^*(\phi_1 + \phi_2 + \phi_3 - \phi_4)\} \, . \tag{3}$$

The other two amplitudes $\phi_2(s,t)$ and $\phi_4(s,t)$ relate to double spin effects and are discussed in more details in another talk at this conference [9].

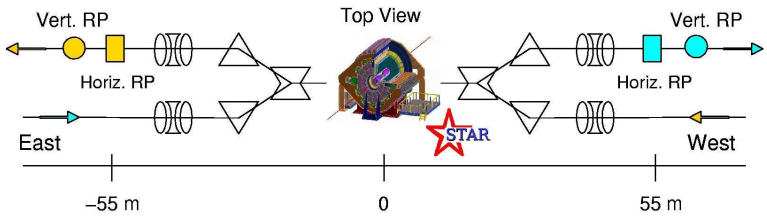

Figure 1: Layout of the setup for small-t measurements with the STAR detector.

Each of the amplitudes has hadron and Coulomb terms: $\phi_i = \phi_i^{em} + \phi_i^{had}$, and the electromagnetic part is calculable from QED. The main contribution to A_N is given by:

$$A_N \frac{d\sigma}{dt} = -\frac{8\pi}{s^2} Im(\phi_5^{em*}\phi_+^{had} + \phi_5^{had*}\phi_+^{em}) \ , \tag{4}$$

where $\phi_+ = (\phi_1 + \phi_3)/2$. Parametrisation of small ϕ_5^{had} is usually done in terms of ϕ_+: $\phi_5 = (\sqrt{-t}/m) \cdot r_5 \cdot Im\phi_+$.

The layout of the experiment at RHIC for the measurements of the observables in elastic proton-proton collisions at small momentum transfer is shown in Fig. 1. Protons scattered at very small angles at the interaction point (IP) travel close to the beams within the beam pipe until they reach Roman Pots (RP) located in the RHIC tunnel on both sides of the STAR detector. Each RP contains four silicon microstrip detectors, two for each of the orthogonal coordinates, and a trigger scintillation counter. The Roman Pot design allows to insert detectors very close to the beam without violation of the high accelerator vacuum. Two RP stations with detectors inserted horizontally (at 55.5 m from IP) and vertically (at 58.5 m) were used at each side of IP. More details of the detectors can be found in [10]. The trigger for elastic events requires hits in the matching counters on both sides of the IP and no simultaneous hits in the scintillators of the same RP station. The coordinates measured by the detectors relate to the scattering angles at the IP by the transport matrix T_{RP}:

$$\begin{pmatrix} x \\ y \end{pmatrix}_{RP} = T_{RP} \cdot \begin{pmatrix} \theta_x \\ \theta_y \end{pmatrix}_{IP} \tag{5}$$

where index $_{RP}$ denotes particular Roman Pot. The position of the RPs was selected so that the error introduced by unknown position of the interaction point was minimal.

Reconstruction of elastic events was performed in the following steps. Adjacent strips with charge values above 5σ from their pedestal averages were found and combined into clusters. Very noisy and dead strips were rejected (total 5 out of ~14000 in the active detector area). A threshold depending on the cluster width was applied to the total charge of the cluster. Clusters on each side of the IP were combined into track candidates; if there was more than one track candidate on a side, only those contributed by 4 or more planes were selected. Exactly one track candidate was required on each side with at least 6 silicon planes contributing to the whole event. Transport equation (5) was solved for each side. The corresponding distributions of angle differences between east and west sides are presented in Fig. 2. The strongest criterion for the elastic event selection is the strict kinematic correlation: the scattering angles are equal for both protons after interaction. The implementation of the selection was based on $\chi^2 = (\theta_x^{west} - \theta_x^{east})^2/\sigma_x^2 +$

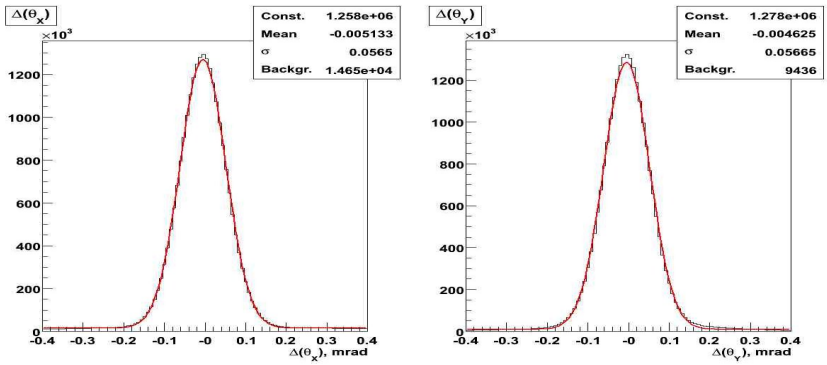

Figure 2: Elastic correlation — difference in scattering angles at IP for particles scattered to east and west in x (left) and y (right).

$(\theta_y^{west} - \theta_y^{east})^2/\sigma_y^2$, where $\sigma_x = \sigma_y = 0.057$ mrad, and a strong cut $\chi^2 < 5$ was used for this preliminary analysis (8.2% candidate elastic event loss). As a result of all cuts $19.3{\cdot}10^6$ events out of $32.9{\cdot}10^6$ elastic triggers recorded during the run were selected for asymmetry calculations.

Single spin asymmetry A_N was calculated in 5 t-bins using the square root formula [11, 6] individually for each fill and then averaged. The raw asymmetry as function of azimuthal angle ϕ for only $++$ and $--$ bunch polarizations can be written as:

$$\epsilon_N(\phi) = \frac{(P_B + P_Y)A_N \cos(\phi)}{1 + \delta(\phi)} = \frac{\sqrt{N^{++}(\phi)N^{--}(\pi+\phi)} - \sqrt{N^{--}(\phi)N^{++}(\pi+\phi)}}{\sqrt{N^{++}(\phi)N^{--}(\pi+\phi)} + \sqrt{N^{--}(\phi)N^{++}(\pi+\phi)}}, \quad (6)$$

where $N^{ij}(\phi)$ - number of events with bunch polarization pattern ij at the azimuthal angle ϕ. $P_{B/Y}$ are polarizations of blue and yellow beams, measured by RHIC polarimeters. The averaged polarization values were: $P_B + P_Y = 1.221 \pm 0.038$, $P_B - P_Y = -0.016 \pm 0.038$. From double spin asymmetries measured by [6] we know that $\delta(\phi) = P_B P_Y (A_{NN}\cos^2(\phi) + A_{SS}\sin^2(\phi))$ is less than 0.01. Using different bunch polarization combinations, more raw asymmetries can be introduced similar to (6): $\epsilon_B(\phi) \sim P_B \cdot A_N$, $\epsilon_Y(\phi) \sim P_Y \cdot A_N$ and $\epsilon'_N(\phi) \sim (P_B - P_Y) \cdot A_N$. $\epsilon_N(\phi)$ and $\epsilon'_N(\phi)$ are presented in Fig. 3 for $0.005 < |t| < 0.010$ (GeV/c)^2 and all 4 fills.

The preliminary results on the single spin asymmetry are shown in Fig. 4a in comparison with a theoretical curve without hadron spin-flip and with the best fit allowing

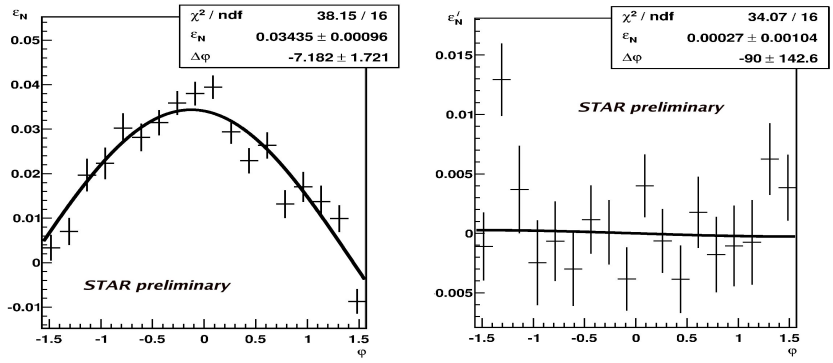

Figure 3: Raw single spin asymmetries ϵ_N (left) and ϵ'_N (right) for $0.005 < |t| < 0.010$ (GeV/c)^2.

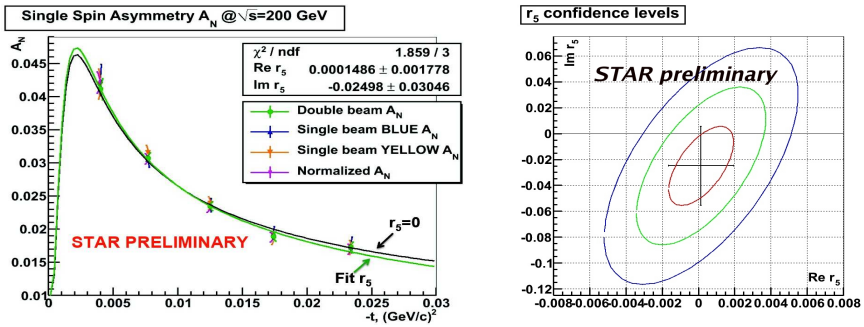

Figure 4: Single spin asymmetry A_N (left) and complex plane of parameter r_5 with contours of confidence level 1, 2 and 3-σ (right)

non-zero hadron spin-flip (see [12] for formula). Fig. 4b shows the fitted complex value of r_5. No evidence for a contribution from the hadron spin-flip amplitude ϕ_5 is observed.

Our preliminary results agree with the hypothesis that only Pomeron exchange, which contributes only to spin-nonflip amplitudes ϕ_1 and ϕ_3, survives at high energies. In agreement with other cited measurements of the proton-proton elastic scattering with $\sqrt{s} > 10$ GeV, we see no evidence of contributions from other amplitudes.

We thank the RHIC Operations Group and RCF at BNL, the NERSC Center at LBNL and the Open Science Grid consortium for providing resources and support. This work was supported in part by the Offices of NP and HEP within the U.S. DOE Office of Science, the U.S. NSF, the Sloan Foundation, the DFG cluster of excellence 'Origin and Structure of the Universe'of Germany, CNRS/IN2P3, FAPESP CNPq of Brazil, Ministry of Ed. and Sci. of the Russian Federation, NNSFC, CAS, MoST, and MoE of China, GA and MSMT of the Czech Republic, FOM and NWO of the Netherlands, DAE, DST, and CSIR of India, Polish Ministry of Sci. and Higher Ed., Korea Research Foundation, Ministry of Sci., Ed. and Sports of the Rep. Of Croatia, and RosAtom of Russia.

References

[1] S. Nussinov, Phys. Rev. Lett. **34**, (1975) 1286;
S. Nussinov, Phys. Rev. **D14**, (1976) 246.
[2] N. Akchurin et al., Phys. Rev. **D48**, (1993) 3026.
[3] M. Bai et al., Phys. Rev. Lett **96**, (2006) 174801.
[4] H. Okada et al., Phys. Lett. **B638**, (2005) 450;
I.G. Alekseev et al., Phys. Rev. **D79**, (2009) 094014.
[5] A. Bazilevsky, *private communication*, (2010).
[6] S. Bültmann et al., Phys. Lett. **B632**, (2006) 167;
S. Bültmann et al., Phys. Lett. **B647**, (2007) 98.
[7] N.H. Buttimore,E. Gotsman and E. Leader, Phys. Rev. **D18**, (1978) 694.
[8] T.L. Trueman, arXiv:**hep-ph/9610316**, (1996).
[9] I.G. Alekseev for the STAR Collaboration, these proceedings.
[10] S. Bültmann et al., Nucl. Instr. Meth. **A535**, (2004) 415.
[11] G.G. Ohlsen and Jr.P.W. Keaton, Nucl. Instr. Meth. **109**, (1973) 41.
[12] N.H. Buttimore et al., Phys. Rev. **D59**, (1999) 114010.

EXCLUSIVE ρ^0 PRODUCTION OFF TRANSVERSELY POLARIZED PROTONS AND DEUTERONS

P. Sznajder[1 †]
on behalf of the COMPASS experiment

(1) *National Centre for Nuclear Research, Warsaw*
† *E-mail: pawel.sznajder@cern.ch*

Abstract

The measurement of the transverse target spin asymmetry $A_{UT}^{\sin(\phi-\phi_s)}$ for exclusive production of ρ^0 mesons at the COMPASS experiment is discussed. The measurement of the asymmetry is done both for the protons and the deuterons. The asymmetry gives an access to the Generalized Parton Distribution function E, which is sensitive to the orbital angular momentum of quarks in the nucleon. The measured asymmetry is compatible with zero in the kinematic range: $1 < Q^2 < 12$ (GeV/c)^2, $0.003 < x_{Bj} < 0.35$ and $0.05 < p_t^2 < 0.5$ (GeV/c)^2 for protons or $0.01 < p_t^2 < 0.5$ (GeV/c)^2 for deuterons.

1. Introduction. In this analysis the transverse target spin asymmetry $A_{UT}^{\sin(\phi-\phi_s)}$ for exclusive production of ρ^0 mesons is measured. The asymmetry is measured at the COMPASS experiment [1] both for the polarized protons and deuterons. The asymmetry gives an access to the Generalized Parton Distribution function E, which is sensitive to the orbital angular momentum of quarks in the nucleon. The selected samples cover a broad kinematic region: $1 < Q^2 < 12$ (GeV/c)^2, $0.003 < x_{Bj} < 0.35$ and $0.05 < p_t^2 < 0.5$ (GeV/c)^2 for protons or $0.01 < p_t^2 < 0.5$ (GeV/c)^2 for deuterons.

The precise study of the spin structure of the nucleon is one of the main aims of the COMPASS experiment. It is now well established, that the spin of quarks accounts only for about 30% of the nucleon spin (*the nucleon spin crisis*). The direct measurements of the gluon polarization and pQCD fits to the spin dependent cross-sections and spin asymmetries indicate, that the gluon contribution is not large, consistent with zero. It is expected, that the missing part of the nucleon spin could be related to the orbital angular momentum of partons. The angular momentum of partons can be evaluated in the Generalized Parton Distribution formalism (GPD) [2].

2. The GPD formalism. The simplest reaction described by the GPD formalism is the Deeply Virtual Coulomb Scattering (DVCS). In this process a parton from the target nucleon interacts with the virtual photon and a real photon is produced. After interaction the parton is absorbed by the target nucleon. It was proven, that for longitudinal virtual photons with high virtuality Q^2 and the small momentum transfer to the nucleon t the amplitude for this process factories into two terms. The interaction between photons and partons is described by the perturbative theory, while the non-perturbative correlation between the emitted and the absorbed partons is described by the GPDs. For the Deeply Virtual Meson Production (DVMP), the description of the reaction is more complicated.

The formation of the meson is described by another non-perturbative part, the Generalized Distribution Amplitude (GDA) [2].

There are four parton helicity-conserving GPDs, $H^{q,g}$, $\widetilde{H}^{q,g}$, $E^{q,g}$, $\widetilde{E}^{q,g}$, defined for the specific quark flavour and for gluons. The GPDs $H^{q,g}$ and $\widetilde{H}^{q,g}$ are defined in the case where the target nucleon retains its helicity, while the GPDs $E^{q,g}$ and $\widetilde{E}^{q,g}$ are defined if the target nucleon changes its helicity. Each GPD depends on three kinematic variables, x, ξ and t, where x is the average longitudinal momentum fraction of the interacting parton, ξ is the half of the longitudinal momentum transferred to the target nucleon and t is the four-momentum transfer squared.

Depending on the type of the meson, its quark content and quantum numbers, there exists sensitivity to various types of GPDs and different quark flavours. The vector meson production is sensitive only to GPDs $H^{q,g}$ and $E^{q,g}$, while the scalar meson production is sensitive only to the GPDs $\widetilde{H}^{q,g}$ and $\widetilde{E}^{q,g}$. The GPD E is of a special interest, as it is related to the orbital angular momentum of quarks. Due to angular momentum conservation, orbital angular momentum must be involved if the proton helicity is changed, i.e. when $E \neq 0$.

One of the most interesting properties of the GPDs is the Ji's sum rule

$$\int_{-1}^{1} dx x \left[H^q\left(x,\xi,t=0\right) + E^q\left(x,\xi,t=0\right)\right] = 2J^q, \tag{1}$$

where the total angular momentum $J^q = L^q + S^q$ is the sum of the orbital angular momentum L^q and the spin S^q. These relation can be used to estimate a role of the quark orbital angular momentum in the nucleon spin puzzle.

3. Access to the GPDs through the exclusive ρ^0 production. The cross-section of exclusive meson production was obtained by M. Diehl and S. Sapeta in Ref. [3]. For a transversely polarized target the cross section in the COMPASS kinematics can be expressed in the following way

$$\left[\frac{\alpha_{em}}{8\pi^3}\frac{y^2}{1-\epsilon}\frac{1-x_{Bj}}{x_{Bj}}\frac{1}{Q^2}\right]^{-1}\frac{d\sigma}{dx_{Bj}dQ^2d\phi d\phi_s} \simeq \\ \frac{1}{2}\left(\sigma_{++}^{++}+\sigma_{++}^{--}\right)+\epsilon\sigma_{00}^{++}-S_T\sin\left(\phi-\phi_s\right)\mathrm{Im}\left(\sigma_{++}^{+-}+\epsilon\sigma_{00}^{+-}\right)+\dots\ , \tag{2}$$

where only terms relevant for this analysis are shown explicitly. Here S_T is the target polarization and ϵ is a kinematic-dependent virtual photon polarization parameter. The angle ϕ is the angle between the lepton plane, defined by the momenta of incoming and scattered leptons, and the hadron plane, defined by the momenta of virtual photon and produced meson. The angle ϕ_s is the angle between the lepton plane and the direction of the target spin. The spin-dependent photoabsorption cross sections and the interference terms σ_{mn}^{ij} are proportional to bilinear combinations of amplitudes for subprocess $\gamma^* p \to Vp$ with the photon helicity m and the target nucleon helicity i

$$\sigma_{mn}^{ij} \propto \sum_{\text{spins}} \left(A_m^i\right)^* A_n^j. \tag{3}$$

For vector mesons, the two terms in Eq. 2 give the access to the GPDs $H^{q,g}$ and $E^{q,g}$

$$\frac{1}{\Gamma'}\frac{\sigma_{00}^{++}}{dt} = \left(1-\xi^2\right)|\mathcal{H}_V|^2 - \left(\xi^2 + \frac{t}{4M_p^2}\right)|\mathcal{E}_V|^2 - 2\xi^2\,\mathrm{Re}\left(\mathcal{E}_V^*\mathcal{H}_V\right), \tag{4}$$

$$\frac{1}{\Gamma'}\,\mathrm{Im}\,\frac{\sigma_{00}^{+-}}{dt} = -\sqrt{1-\xi^2}\frac{\sqrt{t_0-t}}{M_p}\,\mathrm{Im}\left(\mathcal{E}_V^*\mathcal{H}_V\right), \tag{5}$$

where $\mathcal{H}_V$, $\mathcal{E}_V$ are weighted sums of the convolutions of the GPDs $H^{q,g}$ and $E^{q,g}$ with the GDA of the meson V and with the hard scattering kernel, t_0 is a minimal value of t depending on the event kinematics and $\Gamma' = (\alpha_{\mathrm{em}}x_{Bj})/(Q^6(1-x_{Bj}))$.

The cross section σ_{00}^{++} is equivalent to the cross section for longitudinal virtual photons σ_L, which can be calculated from the unpolarized cross section σ_0. The interference term σ_{00}^{+-} is related to the transverse target spin asymmetry

$$A_{UT}^{\sin(\phi-\phi_s)} = -\frac{\mathrm{Im}\left(\sigma_{++}^{+-} + \epsilon\sigma_{00}^{+-}\right)}{\sigma_0}. \tag{6}$$

Both leading twist terms σ_{00}^{++} and σ_{00}^{+-} can be extracted using measured decay angular distributions of the meson.

4. COMPASS experiment. In the COMPASS experiment the muon beam scatters off the lithium deuteride (^{6}LiD) or the ammonia target (NH_3), with polarized deuterons or protons, respectively. The target can be polarized transversely or longitudinally. The polarization is obtained by the Dynamic Nuclear Polarization method and is about 50% for ^{6}LiD and about 90% for NH_3. The dilution factor, i.e. the fraction of events originating from polarized deuterons or protons, for incoherent exclusive ρ^0 production is about 45% for ^{6}LiD and about 25% for NH_3. To minimise systematic effects due to a possible spectrometer instability and the acceptance variation, the target was divided into two cells in 2002-2004 and into three cells since 2006. The consecutive cells have opposite polarization. The polarization in each cell is reversed periodically.

The COMPASS setup is a 50 m long two stage spectrometer with excellent capability for tracking and particle identification. It is equipped with about 300 tracking detectors planes, which provide high redundancy for the reconstruction. The first stage, grouped around the first magnet, is dedicated to provide reconstruction of particles produced with small momenta. It is equipped with the electromagnetic and hadron calorimeters, the muon filter, providing reconstruction of scattered muons, and the large ring imaging Cerenkov detector. The second stage, grouped around the second magnet, is able to reconstruct particles produced with high momenta. This stage is equipped with the second set of calorimeters and the second muon filter.

5. Event selection. The data used in this analysis were taken in 2002-2004 and in 2007, for the transversely polarized deuteron and proton target, respectively. Each selected event contains a primary vertex with only one incoming and one outgoing muon track and with only two outgoing hadron tracks with opposite charges. It is assumed, that the outgoing hadron tracks come from the ρ^0 decay and they are pions. The ρ^0 resonance is selected by the cut on the reconstructed invariant mass $-0.3 < M_{\pi\pi} - M_{\rho^0} < 0.3$ GeV/c^2, where M_{ρ^0} is the nominal (PDG) mass of the ρ^0 resonance. Because recoiled target particle

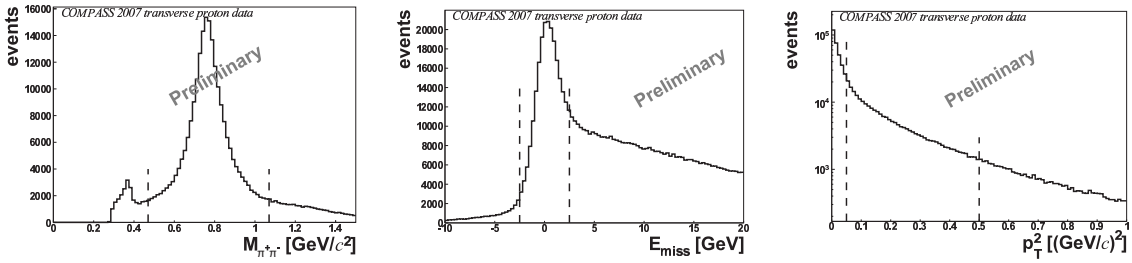

Figure 1: Distributions of $M_{\pi\pi}$, $E_{\rm miss}$ and p_t^2 for the NH_3 target with indicated cuts.

in unmeasured, the exclusivity is checked by the missing energy $E_{\rm miss} = (M_x^2 - M_p^2)/2M_p$, where M_p is the mass of the proton and M_x is the missing mass in the event. For exclusive events the reconstructed values of $E_{\rm miss}$ are close to zero. To select these events the cut $-2.5 < E_{\rm miss} < 2.5$ GeV is used. The cuts $0.05 < p_t^2 < 0.5$ (GeV/c)^2 for the proton target and $0.01 < p_t^2 < 0.5$ (GeV/c)^2 for the deuteron target are also used. The upper cuts on p_t^2 provide a further reduction of non-exclusive background. The lower cut on p_t^2 for the proton target suppresses a contribution from the coherent production on the target nuclei, while for the deuteron target it is applied to remove events with a large smearing of the azimuthal angle. Distributions of $M_{\pi\pi}$, $E_{\rm miss}$ and p_t^2 for the NH_3 target, with indicated cuts, are shown in Fig. 1.

For the selected sample the kinematic region $1 < Q^2 < 12$ (GeV/c)^2, $0.1 < y < 0.9$ (the fraction of incoming muon energy lost in the laboratory system), $0.003 < x_{Bj} < 0.35$, $W > 5$ GeV (the total energy in the virtual photon - nucleon center of mass system) and p_t^2 ranges indicated above is used.

6. Extraction of $A_{UT}^{\sin(\phi-\phi_s)}$ asymmetry. The number of observed events as a function of the $\phi - \phi_s$ angle can be expressed in the following way

$$N\left(\phi-\phi_s\right) \simeq Fna\left(\phi-\phi_s\right)\sigma_0\left(1 \pm fP_T A_{UT}^{\sin(\phi-\phi_s)}\sin\left(\phi-\phi_s\right)\right), \tag{7}$$

where F is the muon flux, n the number of target nucleons, a the acceptance, f the dilution factor, P_T the target polarization and the $A_{UT}^{\sin(\phi-\phi_s)}$ asymmetry is defined by Eq. 6.

Extraction of the $A_{UT}^{\sin(\phi-\phi_s)}$ asymmetry is based on the double ratio method. For instance, for the three-cell target used in 2007, the double ratio method is defined as

$$\mathrm{DR}\left(\phi-\phi_s\right) = \frac{N_{u/d}^{\uparrow}(\phi-\phi_s)}{N_c^{\downarrow}(\phi-\phi_s)}\frac{N_c^{\uparrow}(\phi-\phi_s)}{N_{u/d}^{\downarrow}(\phi-\phi_s)}, \tag{8}$$

where the number of observed events N_c corresponds to the central cell and $N_{u/d}$ corresponds to the sum of events from the upstream and downstream cells. The polarization of cells is indicated by the arrows. With Eq. 7, the formula for the double ratio can be expressed as

$$\mathrm{DR}\left(\phi-\phi_s\right) = \left(\frac{1+fP_T A_{UT}^{\sin(\phi-\phi_s)}\sin(\phi-\phi_s)}{1-fP_T A_{UT}^{\sin(\phi-\phi_s)}\sin(\phi-\phi_s)}\right)^2, \tag{9}$$

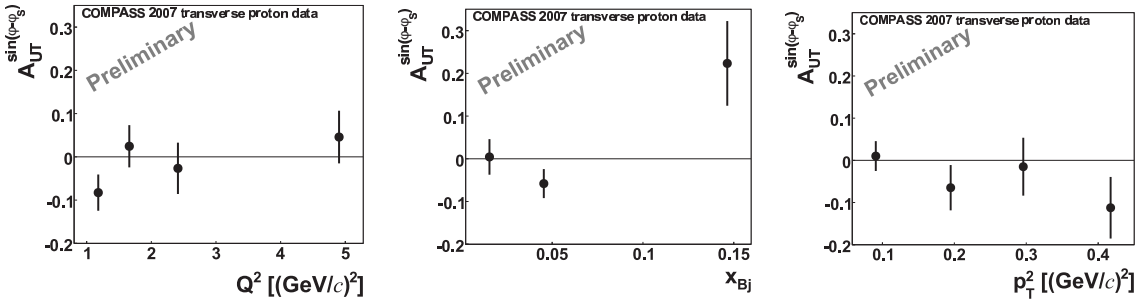

Figure 2: The $A_{UT}^{\sin(\phi-\phi_s)}$ asymmetry for protons as a function of Q^2, x_{Bj} and p_t^2.

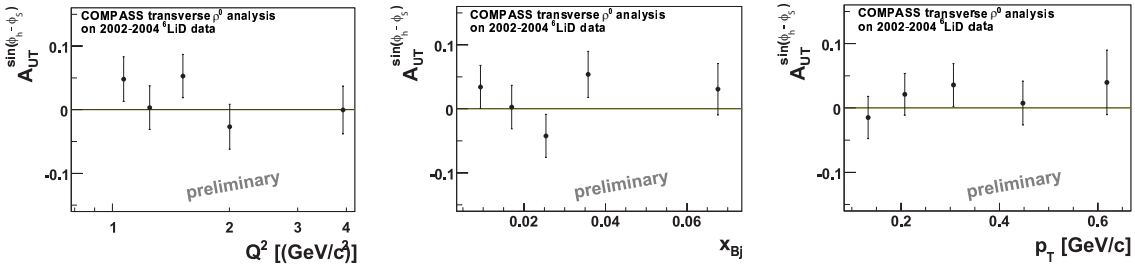

Figure 3: The $A_{UT}^{\sin(\phi-\phi_s)}$ asymmetry for deuterons as a function of Q^2, x_{Bj} and p_t.

where the flux, the number of target nucleons and the unpolarized cross section cancel. The acceptance also cancels provided the ratio of acceptances in different cells is constant before and after reversal of the target polarization, i.e. $a^{\uparrow}_{u/d}/a^{\downarrow}_{c} = a^{\downarrow}_{u/d}/a^{\uparrow}_{c}$. Values of the $A_{UT}^{\sin(\phi-\phi_s)}$ asymmetry are extracted from fits to the measured DR$(\phi-\phi_s)$ distributions.

7. Results. The extracted $A_{UT}^{\sin(\phi-\phi_s)}$ asymmetry for the protons as a function of Q^2, x_{Bj} and p_t^2 is shown in Fig. 2. In the covered kinematic range the asymmetry is small and compatible with zero. The results are in good agreement with the results obtained at the HERMES experiment [4] and with the GPD model of S. V. Goloskokov and P. Kroll [5], which predicts the asymmetry to be ≈ -0.02.

The results for the deuterons are shown in Fig. 3. In this case, however, the cut on p_t^2 does not eliminate the coherent production completely. In the covered kinematic range the asymmetry is also compatible with zero.

8. Recent developments of the analysis. The work on the estimation of an influence of the background on the $A_{UT}^{\sin(\phi-\phi_s)}$ asymmetry extraction as well as detailed systematic studies are in progress. Release of new results and dedicated paper are expected soon.

In the new analysis background asymmetry is calculated analysing fraction of background events as a function of $\phi-\phi_s$ angle. The fraction in a given $\phi-\phi_s$ bin is estimated analysing missing energy distribution, $E_{\rm miss}$, for this bin. Shape of $E_{\rm miss}$ distribution for semi-inclusive events is parametrized from MC studies and normalized to the data in large $E_{\rm miss}$ region (cf. Fig. 1).

The most important sources of possible systematic uncertainties checked in the new analysis are false asymmetries, data stability, method of background subtraction and

sensitivity to the MC. To suppress uncertainty of asymmetry extraction double ratio method is replaced by the binned likelihood method.

9. Summary and outlook. The transverse target spin asymmetry $A_{UT}^{\sin(\phi-\phi_s)}$ for exclusive production of ρ^0 mesons was measured for the protons and the deuterons. The results for both targets are compatible with zero in the broad kinematic range. The results are in good agreement with the results obtained at the HERMES experiment and with the predictions of the GPD model [5].

Data taken in 2010 at the COMPASS experiment will allow to increase about three times the present statistics of ρ^0 sample for transversely polarized protons. These data will be used to study exclusive channels with small cross-sections, e.g. the production of ϕ or ω mesons. The ω channel seems particularly interesting, as the $A_{UT}^{\sin(\phi-\phi_s)}$ asymmetry is expected to be large, about -0.1 [5]. Moreover separation of contributions of longitudinally and transversely polarized virtual photons and extraction of non-leading asymmetries are considered.

A new proposal for the COMPASS-II experiment has been approved [6]. Future GPD studies are a substantial part of this proposal. The use of a new detector, a large Recoil Proton Detector, will allow a clean selection of the sample of exclusive events for the studies of the DVCS and DVMP processes. The measurements with the unpolarized liquid hydrogen target are foreseen first, while the measurements with the transversely polarized NH_3 target are considered for the future.

References

[1] P. Abbon *et al.*, Nucl. Instrum. Meth. **A577**, (2007) 455-518

[2] M. Diehl, Phys. Rept. **388**, (2003) 41-277

[3] M. Diehl and S. Sapeta, Eur. Phys. J. **C41**, (2005) 515-533

[4] A. Airapetian *et al.*, Phys. Lett. **B679**, (2009) 100-105

[5] S.V. Goloskokov and P. Kroll, Eur. Phys. J. **C59**, (2009) 809-819

[6] F. Gautheron *et al.*, CERN Report No. CERN-SPSC-2010-014/SPSC-P-340, 2010

MEASUREMENT OF THE DIFFERENTIAL CROSS SECTION AND VECTOR ANALYZING POWER in $d-p$ ELASTIC SCATTERING AT 2.0 GeV

A.A Terekhin†, V.V. Glagolev,V.P. Ladygin and N.B. Ladygina

Joint Institute for Nuclear Researches, Joliot-Curie St., 6, Dubna, 141980, Russia
† *E-mail: aterekhin@jinr.ru*

Abstract

The results on the experimental data for the d-p elastic scattering at $T_d = 2$ GeV are reported. The measurements of the angular dependence of the vector analyzing powers A_y and differential cross section for the angles $12^o < \theta^* < 14^o$ in the c.m.s. were performed. The obtained data are in good agreement with the existing data and theoretical calculations made in the framework of the relativistic multiple scattering model.

The interest to the simple nuclear reactions has increased significantly in the latter days. It connected with the active research of nuclear forces and effects of non-nucleonic degrees of freedom. The study of polarizations effects is necessary to solve many modern problems of nuclear and the particle physics. Large number of experimental data for short-range spin structure of light nucleus has been accumulated.

Deuteron has relatively simple structure. It has spin equal 1. This feature allows to perform the various polarization experiments and to test the theory of scattering processes. The investigations of polarization observables for dp-elastic scattering have been performed at intermediate and high energies. For instance, the differential cross sections, the spin transfer coefficients K_{ij}, vector and tensor analyzing powers A_y, A_{yy}, A_{xx} and A_{xz}, as well as polarization P_y, has been obtained at $E_d^{lab} = 270$ MeV [1]. The differential cross section and the vector analyzing power are well reproduced by Faddeev calculations with modern nucleon-nucleon potentials and Tucson-Melbourne three-nucleon force [2]. On the other hand, A_{ij}, K_{ij} and P_y are not described by such calculations.

Relativistic effects and non-nucleonic degrees of freedom play an increasing role with the energy increasing. The main goal of the investigations at high energies is to search for such effects. Recently, the analyzing powers A_y and A_{ij} have been obtained at $T = 880$ MeV for the angular range of $60^o < \theta^* < 140^o$ in the c.m.s [3].

In connection with the modernization of Nuclotron and anticipation of the putting into operation of a new source of polarized deuterons, we turned to a database of deuteron-proton research on a hydrogen bubble chamber [4], exposed at Synchrophasotron. Some of these data were obtained with 3.35 GeV/c vector- polarized deuterons beam provided by the polarized ion source POLARIS.

The dp-elastic scattering reaction has the greatest losses in the region of small momentum transfers due to a number of methodical features. They are related both with the impossibility to observe the tracks with the momentum less than 80 MeV/c and the tracks orientation along the optical axis of photocamera.

These effects are demonstrated in Fig. 1, where the correlation of the scattering angle θ^* and azimutal angle φ is presented. Losses in another reactions were negligible. The millibarn-equivalent of the events was estimated as $C = 0.0003342 \pm 0.0000007$ mb/event.

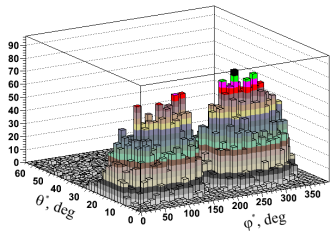

Figure 1: The correlation of the scattering angle θ^* and the azimutal angle φ for dp-elastic scattering events.

Evaluation of the vector polarization of an accelerated beam of deuterons beam was performed with the same data using the events from the reaction $dp \longrightarrow ppn$ [5]. The deuteron beam polarization was estimated as $p_y = 0.488 \pm 0.061$ [5], knowing the data for analyzing powers for elastic np- and pp-scattering [6, 7] at the corresponding energy, by measuring the azimuthally asymmetry of quasielastic scattering.

Values for the vector analyzing power A_y were obtained by processing the events that correspond to different spin states of the deuteron beam (such states correspond to the polarization mode 1 and 2).

The distribution of the scattering angle in the center of mass is shown in Fig. 2. The scattering angle spectrum was divided into consecutive intervals. The number of events in each interval was normalized to the width of the latter. The distribution on the azimuthal angle φ was constructed for each interval. For small scattering angles θ^* , intervals outside the region bounded by dotted lines in Fig. 3 corresponding to the lost events was excluded. The lost events was excluded symmetrically with respect to the values of 0^o and 180^o. The remaining events were used to calculate the differential cross section and analyzing power.

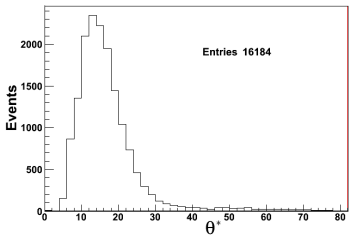

Figure 2: Distribution of events on scattering angle θ.

The R value for each choosen interval of θ^* was calculated as:

$$R = \frac{N_1 - N_2}{N_1 + N_2} \tag{1}$$

Here N_1 and N_2 - numbers of events for spin modes 1 and 2, respectively. In Fig. 4 an example of R distribution on an azimuthal angle for interval $12^o < \theta^* < 14^o$ is resulted.

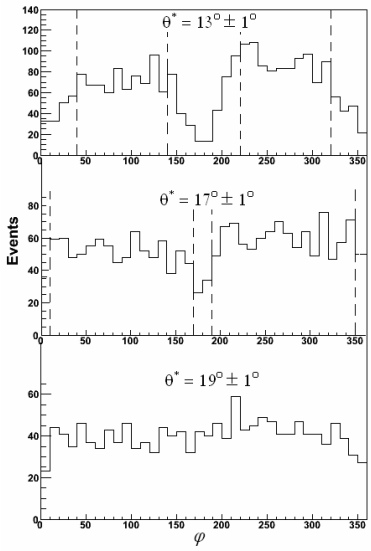

Figure 3: Distributions on azimutal angles φ for different θ.

For each angular interval parameters of the function $p_0 + p_1 sin(\varphi)$ were determined and analyzing power was calculated as:

$$A_y = \frac{2}{3}\frac{p_1}{p_y} \tag{2}$$

Here p_y is the vector polarization of the beam.

The events obtained both from polarized and unpolarized deuterons beams were used for calculation of the differential cross section. The analysis of the distribution of the scattering angle cosine in c.m.s was made. The corresponding interval $\Delta cos\theta^*$ was taken for each $\Delta\theta^*$. Then normalization to the intervals width $\Delta cos\theta^*$ was made.

The cross section calculate using the formula:

$$\frac{d\sigma}{d\Omega} = \frac{1}{2\pi} N(cos\theta^*) \frac{C}{\Delta cos\theta^*} \qquad (3)$$

where C - is the millibarn-equivalent of the events, $\Delta cos\theta^*$ - is the interval width of the distribution of the scattering angle cosine θ^* in the c.m.s.

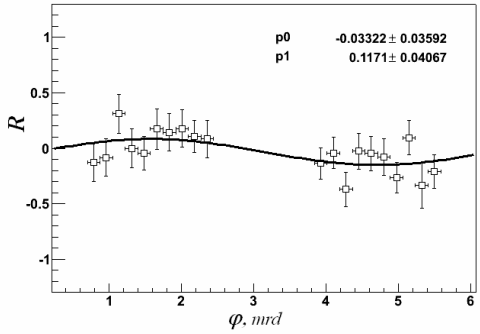

Figure 4: Example distribution of the value of R for the angular interval $12^o < \theta^* < 14^o$.

The theoretical predictions for differential cross section and analyzing power A_y have been obtained in the multiple-scattering-theory frame [8]. The single scattering and double scattering contributions into the reaction amplitude were taken into account. Since one-nucleon exchange (ONE) term gives considerable contribution only at backward angles, this term was not included into consideration.

Diagrams for single scattering (SS) and double scattering (DS) are presented in Fig. 5. All calculations were performed with the CD Bonn deuteron wave function [9]. The details of the theoretical description are given in the talk of N.B. Ladygina [10].

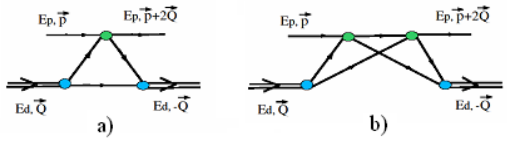

Figure 5: a) - single scattering. b) - double scattering.

The differential cross section as a function of the deuteron scattering angle in the c.m.s. in the domain of our measurements is presented in Fig. 6 The experimental data and calculations are presented in Fig. 7 in the wider angular range. One can see that the DS-term plays

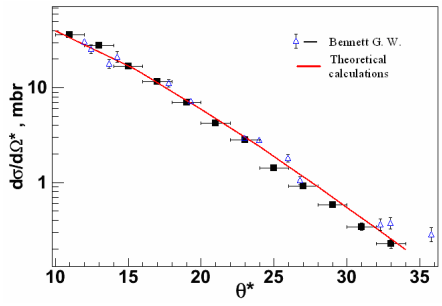

Figure 6: Solid squares – this work. Empty triangles – data from ref. [11].

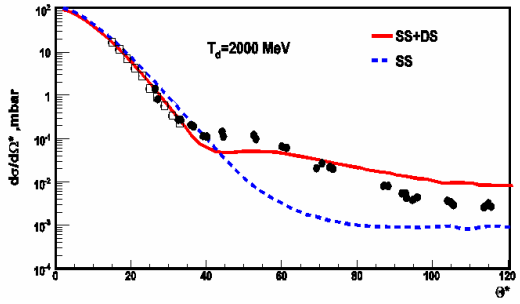

Figure 7: Empty boxes represent the results of this work. The solid circles are the data from ref. [11]. The dotted and solid lines are the calculations without and with DS term, respectively.

a significant role at $\theta^* < 35^o$, while SS dominates at small angels. Our experimental data on vector Analyzing Power A_y are compared with the predictions of the relativistic multiple scattering theory as well as with the ANL data (See Fig. 8). The data are in good agreement with each anther and with the calculation. The importance of the double scattering is demonstrated in Fig. 9 Also one can see that the single scattering dominates in the domain of our measurements.

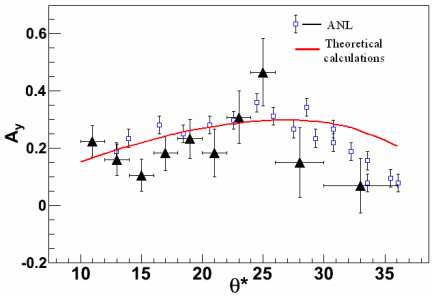

Figure 8: Solid triangles – this work. Empty squares – data obtained at ANL [12].

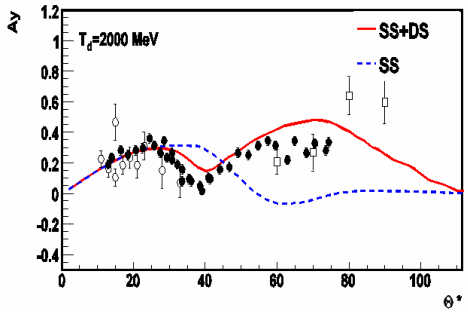

Figure 9: Empty circles represent the results of this work. The solid circles are the data from ref. [12]. Empty squares are the data taken from ref. [13].

The results on the differential cross-section and vector analyzing power A_y for dp-elastic scattering from the database of the deuteron-proton interactions in a hydrogen bubble chamber at $E_d = 2$ GeV have been obtained . The results agree well with the data obtained earlier at ANL (Argonne) [12]. The experimental data agree qualitatively with the calculations of relativistic multiple scattering theory [8] taking into account the double scattering.

The work has been supported in part by RFBF grant *No.* 10-02 -00087a.

References

[1] H. Sakai et al., Phys Rev Lett. **V.162** (2000) 143.
[2] S.A. Coon et. al., Nucl.Phys. **A317** (1979) 242.
[3] P.K. Kurilkin et al., EPJo. Special Topics, **V.162** (2008) 137-141.
[4] A.V. Belonogov et al., NIM **20** (1963) 114.
[5] V.V. Glagolev et al., Z. Phys. **A356** (1996) 183.
[6] V Marshak, et al., Phys.Rev. **C18** (1978) 1.
[7] G.A. Korolev et al., Phys.Lett. **B165** (1985) 4.
[8] N.B. Ladygina, Phys.Atom. Nucl. **71** (2008) 2039;
[9] R. Machleidt, Phys.Rev. **C63** (2001) 024001.
[10] N.B. Ladygina,talk at this conference.
[11] G. W. Bennett et al., Phys. Rev. Lett. **19** (1976) 387.
[12] M. Haji-Saied et al., Phys.Rev. **C 36** (1987) 2010.
[13] P.K. Kurilkin et. al., Int.J.Mod.Phys. **A24** (2009) 530.

SPIN DEPENDENT $\bar{p}\,^3$He CROSS SECTIONS AT LOW AND INTERMEDIATE ENERGIES

Yu.N. Uzikov [1†], J. Haidenbauer [2], B.A. Prmantayeva [3]

(1) *Joint Institute for Nuclear Research, LNP, Dubna, Russia*
(2) *Institute für Kernphysik Forschungszentrum Jülich, Germany*
(3) *L.N.Gumilyov Eurasian National University*
† *E-mail: uzikov@jinr.ru*

Abstract

Antiproton scattering off ^{3}He and ^{4}He targets is considered at beam energies below 300 MeV within the Glauber-Sitenko approach, utilizing the $\bar{N}N$ amplitudes of the Jülich model as input. Good agreement with available data on differential $\bar{p}\,^4$He cross sections and on $\bar{p}\,^3$He and $\bar{p}\,^4$He reaction cross sections is obtained. Predictions for polarized total $\bar{p}\,^3$He cross sections are presented, calculated within the single-scattering approximation and including Coulomb-nuclear interference.

The antinucleon-nucleon ($\bar{N}N$) interaction has been studied quite extensively over the last three decades or so mainly in view of the wealth of data collected at the LEAR facility at CERN, cf. the review [1]. Recently the PAX collaboration suggested [2] to use scattering of antiprotons off a polarized hydrogen target (^{1}H) as polarization buildup process based on the spin-filtering mechanism for producing a polarized antiproton beam. However, in contrast to the NN case, up to now the spin dependence of the $\bar{N}N$ interaction is still fairly poorly known. Therefore, it is an open question whether any sizeable polarization buildup can be achieved in $\bar{p}\,^1$H scattering. Several theoretical studies were performed with the aim to estimate the expected polarization buildup for antiprotons, employing different $\bar{p}p$ interactions [3–5]. Besides of using polarized protons as target one could also use light nuclei as possible source for the antiproton polarization buildup. Corresponding investigations for antiproton scattering on a polarized deuteron target were presented in Refs. [4, 6, 7]. As was shown in Refs. [4, 6] on the basis of the Glauber-Sitenko theory [9,10] with elementary $\bar{p}N$ amplitudes taken from the Jülich $\bar{N}N$ models [11,12,8,13], the $\bar{p}d$ interaction could provide a comparable or even more effective way than the $\bar{p}p$ interaction to obtain polarized antiprotons. This conjecture can be checked at a planned experiment [14] at the AD (Antiproton Decelerator) facility at CERN.

Yet another option could be the scattering of antiprotons off a polarized ^{3}He target. Since the polarization of the ^{3}He nucleus is carried mainly by the neutron, the $\bar{p}n$ amplitudes are expected to dominate the spin observables of this reaction. We present here the results [15] of calculatiuons of spin-dependent cross sections for the $\bar{p}\,^3$He interaction on the basis of an approach similar to that developed in Ref. [4]. Experimental information on $\bar{p}\,^3$He scattering is rather sparse. Thus, in order to examine the validity of the employed Glauber-Sitenko approach [10,17] at low and intermediate energies we consider also the $\bar{p}\,^4$He system where several measurements were performed at the LEAR facility at CERN (see Refs. [19, 20] and references therein). Though a few investigations of $\bar{p}\,^3$He and $\bar{p}\,^4$He scattering have been performed before [21, 22] based on the Glauber-Sitenko

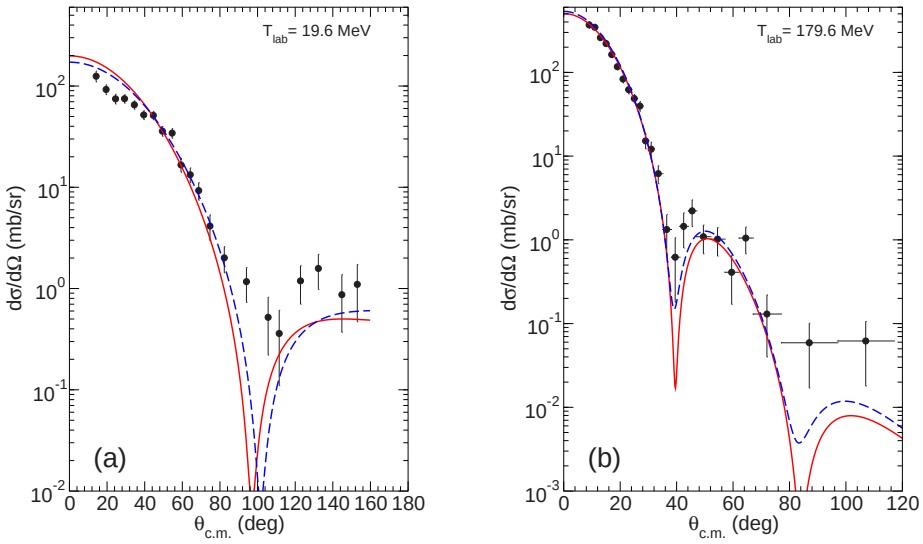

Figure 1: Differential cross section for $\bar{p}\,^4$He versus the c.m. scattering angle at $T_{lab} = 19.6$ MeV and 179.6 MeV, obtained within the approach of Ref. [17]. The solid and dashed lines are results based on the $\bar{N}N$ amplitudes of the Jülich models D and A, respectively. Data are taken from Refs. [20] (19.6 MeV) and [19] (179.6 MeV).

theory, none of them connects directly with amplitudes generated from potential models that are fitted to $\bar{N}N$ data. Using the approach of Ref. [17] and a parametrization of the elementary $\bar{p}N$ amplitudes of the Jülich models, given in Ref. [4], we calculated differential cross sections for elastic $\bar{p}\,^4$He scattering. The comparison with data available at beam momenta of 200 MeV/c [20] and 600 MeV/c [19] in Fig. 1 reveals that there is a rather good agreement [15] between experiment and theory. Furthermore, the calculated reaction cross sections for $\bar{p}\,^3$He and $\bar{p}\,^4$He, shown in Fig. 2, are also in good agreement with the data. Note that at $p \sim 600$ MeV/c the reaction cross sections for $\bar{p}\,^3$He and $\bar{p}\,^4$He are almost the same despite of the different number of nucleons in the ^{3}He and ^{4}He nuclei and this fact is well reproduced by theory, indicating for different shadowing effects for these nuclei. The total cross sections of $\bar{p}\,^3$He scattering can be written as

$$\sigma = \sigma_0 + \sigma_1 \mathbf{P}_{\bar{p}} \cdot \mathbf{P}_\tau + \sigma_2 (\mathbf{P}_{\bar{p}} \cdot \hat{\mathbf{k}})(\mathbf{P}_\tau \cdot \hat{\mathbf{k}}), \tag{1}$$

where $\mathbf{P}_{\bar{p}}$ ($\mathbf{P}_\tau$) is the polarization vector for antiproton (^{3}He) and $\hat{\mathbf{k}}$ is the unit vector in the beam direction. The purely hadronic total cross sections σ_0, σ_1, σ_2, were calculated here by the optical theorem. For the unpolarized cross section σ_0 the Glauber-Sitenko multistep scattering theory was used, whereas the polarized cross sections σ_1 and σ_2 were estimated within the single-scattering approximation [15]. The Coulomb-nuclear interference cross sections σ_i^{int} $(i = 0, 1, 2)$ and the Coulomb cross section are calculated along the lines of Ref. [4] and shown in Fig. 3. These results depend on the beam acceptance angle θ_{acc}.

Our results suggest that the magnitude of the spin-dependent cross sections σ_1 and σ_2 for $\bar{p}\,^3$He are comparable to those for $\bar{p}p$ and $\bar{p}d$, at least as far as the hadronic part is concerned. However, due to the larger charge of ^{3}He, Coulomb-nuclear interference effects

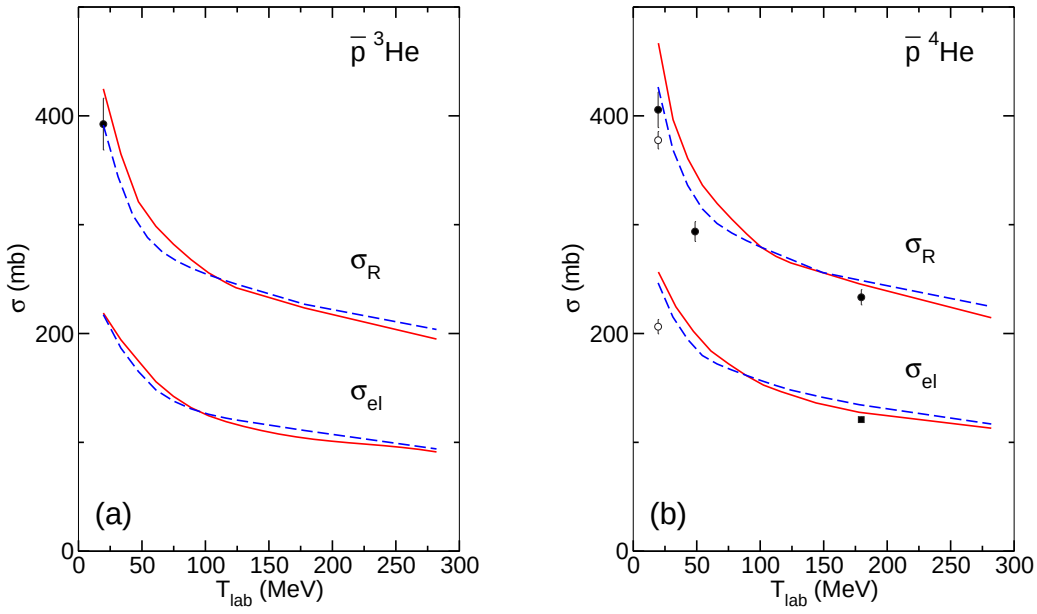

Figure 2: Integrated elastic (σ_{el}, lower curves) and total reaction (σ_R, upper curves) cross sections for $\bar{p}\,^3$He (a) and $\bar{p}\,^4$He (b) versus the beam kinetic energy T_{lab}. The solid and dashed lines are results for the $\bar{N}N$ models D and A, respectively, obtained on the basis of the Glauber-Sitenko approach [17]. Data for $\bar{p}\,^4$He are taken from Refs. [18] (filled circles), [19] (squares), and [20] (open circles). The data point for $\bar{p}\,^3$He is taken from Ref. [16].

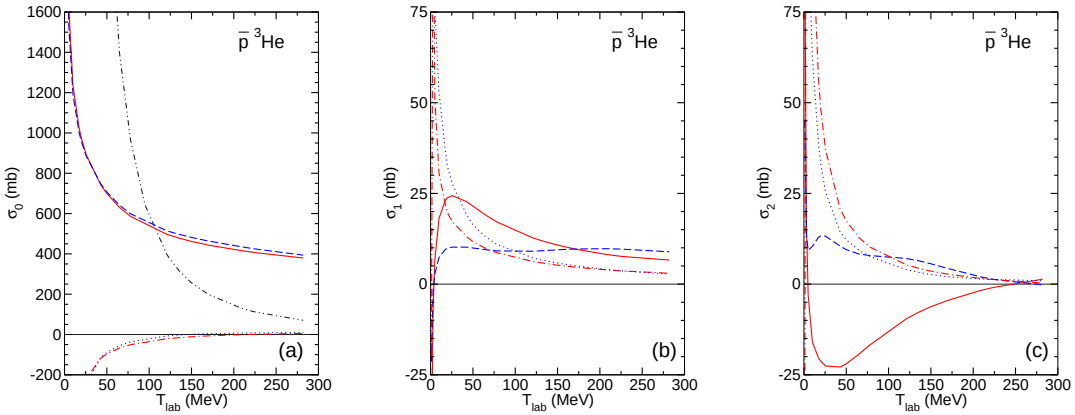

Figure 3: Total cross sections σ_0, σ_1 and σ_2 versus the antiproton laboratory energy T_{lab} for $\bar{p}\,^3$He scattering. Results based on the purely hadronic amplitude, σ_i^h, (model D: solid line, model A: dashed line) and for the Coulomb-nuclear interference term, σ_i^{int}, (D: dash-dotted line, A: dotted line), are presented. In case of σ_0 the Coulomb cross section is shown too (dash-double-dotted line). The employed acceptance angle is $\theta_{acc} = 10$ mrad.

turn out to be more important. Furthermore, since the total cross section is larger in case of ^{3}He the resulting efficiency of the polarization buildup tend to be somewhat smaller than those for $\bar{p}p$ and $\bar{p}d$.

This work was supported in part by the Heisenberg-Landau program.

References

[1] E. Klempt et al., Phys. Rept. **368** (2002) 119.
[2] V. Barone et al., arXiv:hep-ex/0505054.
[3] V.F. Dmitriev et al., Nucl. Instrum. Meth. B **266** (2008) 1122.
[4] Yu.N. Uzikov and J. Haidenbauer, Phys. Rev. C **79** (2009) 024617.
[5] V.F. Dmitriev, A.I. Milstein and S.G. Salnikov, Phys. Lett. B **690** (2010) 427.
[6] Yu. N. Uzikov and J. Haidenbauer, J. Phys. Conf. Ser. **295** (2011) 012087.
[7] S.G. Salnikov, arXiv:1106.4887 [hep-ph].
[8] V. Mull and K. Holinde, Phys. Rev. C **51** (1995) 2360.
[9] V. Franco and R.J. Glauber, Phys. Rev. **142** (1966) 1195.
[10] A.G. Sitenko, Fiz. Elem. Chastits. At. Yadra **4** (1973) 546.
[11] T. Hippchen, J. Haidenbauer, K. Holinde and V. Mull, Phys. Rev. C **44** (1991) 1323.
[12] V. Mull, J. Haidenbauer, T. Hippchen and K. Holinde, Phys. Rev. C **44** (1991) 1337.
[13] J. Haidenbauer, J. Phys. Conf. Ser. **295** (2011) 012094.
[14] C. Barschel et al., arXiv:0904.2325 [nucl-ex].
[15] Yu.N. Uzikov, J. Haidenbauer and B.A. Prmantayeva, Phys. Rev. C **84** (2011) 054011.
[16] F. Balestra et al., Phys. Lett. B **215** (1988) 247.
[17] W. Czyż and L. Leśniak, Phys. Lett. B **24** (1967) 227.
[18] F. Balestra et al., Phys. Lett. B **165** (1985) 265.
[19] Yu.A. Batusov et al., Sov. J. Nucl. Phys. **52** (1990) 776.
[20] F. Balestra et al., Phys. Lett. B **305** (1993) 18.
[21] L.A. Kondratyuk and M.Zh. Shmatikov, Yad. Fiz. **38** (1983) 361.
[22] G. Bendiscioli, A. Rotondi and A. Zenoni, Nuovo Cim. **105A** (1992) 1055.
[23] L.A. Kondratyuk, M.Zh. Shmatikov and R. Bizzarri, Yad. Fiz. **33** (1981) 795.

POLARIMETRY AT RHIC: RHIC POLARIZED BEAM IN RUN 2011

A. Zelenski†, L. Ahrens, I.G. Alekseev, E. Aschenauer, G. Atoian, M. Bai, A. Bazilevsky, M. Blaskiewicz, J.M. Brennan, K.A. Brown, D. Bruno, R. Connolly, A. Dion, T. D'Ottavio, K.A. Drees, W. Fischer, C.J. Gardner, J.W. Glenn, X. Gu, M. Harvey, T. Hayes, L. Hoff, H. Huang, R.L. Hulsart, J.S. Laster, C. Liu, Y. Luo, W.W. MacKay, Y. Makdisi, G.J. Marr, A. Marusic, F. Meot, K. Mernick, R.J. Michnoff, M.G. Minty, C. Montag, J. Morris, S. Nemesure, A. Poblaguev, V. Ptitsyn, V. Ranjbar, G. Robert-Demolaize, T. Roser, B. Schmidke, V. Schoefer, F. Severino, D. Smirnov, K. Smith, D. Steski, D. Svirida, S. Tepikian, D. Trbojevic, N. Tsoupas, J.E. Tuozzolo, G. Wang, M. Wilinski, K. Yip, A. Zaltsman

Brookhaven National Laboratory, Upton, NY
† *E-mail: zelenski@bnl.gov*

Abstract

In 2011 Run polarized proton beam collisions of a total energy $\sqrt{s} = 500$ GeV and peak luminosity up to 1.6×10^{32} cm^{-2}sec^{-1} was delivered to experiments for intermediate boson W production studies with the longitudinally polarized beams. The average beam polarization of a 48% was measured with the H-jet polarimeter. Apparently, there are no visible polarization losses during acceleration up to 100 GeV energy, where a 55-60% polarization was measured in Run 2009. Polarization losses at further acceleration to 250 GeV are caused by the presence of depolarizing resonances. As a result, significant polarization profiles of the beams are also generated. Polarization profiles were measured by the p-Carbon CNI polarimeters in the scanning mode of operation. Polarized beam luminosity is weighted by the polarization profiles and "effective" polarization, as seen in collisions was about 53% in Run 2011.

1 Introduction

The RHIC, heavy ion collider, is the first high-energy machine, where polarized proton acceleration was included in the primary design. RHIC is the first collider where the "Siberian snake" technique was successfully implemented to avoid the resonance depolarization during beam acceleration in AGS and RHIC [1] (see Fig. 1). It is also for the first time the intensity of the polarized beams produced in an Optically Pumped Polarized H^- Ion Source (OPPIS) was sufficient to charge RHIC to the maximum intensity limited by the beam-beam interaction. Every source pulse is eventually converted to the RHIC bunch. The source routinely produces about 10^{12} polarized H^- ions per pulse, about half of this intensity (5×10^{11} H^-/pulse) is accelerated in Linac to 200 MeV beam energy for the strip injection to the Booster. The maximum beam intensity in RHIC was limited to about 2×10^{11} protons/bunch, therefore excessive beam intensity was scraped at extraction from Booster. This allowed beam emittance reduction at injection to AGS, which reduces depolarization and increases RHIC luminosity.

There are two "Siberian snakes" in the each ring to meet the conditions that the "snake" rotation is much larger than the total rotation from all other resonances up to highest 250 GeV beam energy. The RHIC "full Siberian snake", which rotates spin direction for 180° is super-conducting helical magnet system of about 10 m long. Up to 120 beam bunches can be accelerated and were stored in each ring.

The polarization direction of every RHIC bunch is determined by the spin-flip control system in the polarized ion source. Every single source pulse is accelerated and becomes the RHIC bunch of the requested polarity. By loading selected patters of spin direction sequences in the rings the experiments have all possible spin directions combinations for colliding bunches which greatly enhance the systematic error control. Two 90° helical spin rotators in each ring produce the longitudinal polarization for experiments in STAR and PHENIX detectors. The rotators are tuned using "local polarimeters" based on asymmetry in neutron production for pp collisions. The STAR and PHENIX detectors provide complimentary coverage of the different polarization processes [2].

2 Polarimetry at RHIC

Precision, absolute polarization measurements in the wide energy range from a few keV (in the source) to 250 GeV (top RHIC energy) are required for accelerator tuning to minimize depolarization and finally for experimental data normalization. Therefore, the polarimetry is an essential component of the polarized collider facility. A complete set of polarimeters includes: Faraday rotation polarimeter for optical pumpng tuning and monitoring in the OPPIS, Lamb-shift polarimeter at the source energy of a 3–35 keV, a 200 MeV proton-Carbon polarimeter after the linac [3], and polarimeters in AGS and RHIC based on proton-Carbon scattering in Coulomb-Nuclear Interference (CNI) region [4]. A polarized hydrogen-jet polarimeter was used for the absolute polarization measurements in RHIC [5].

Recently a new polarimeter for absolute proton beam polarization measurements at 200 MeV to accuracy better than ±0.5% has been developed as a part of the RHIC

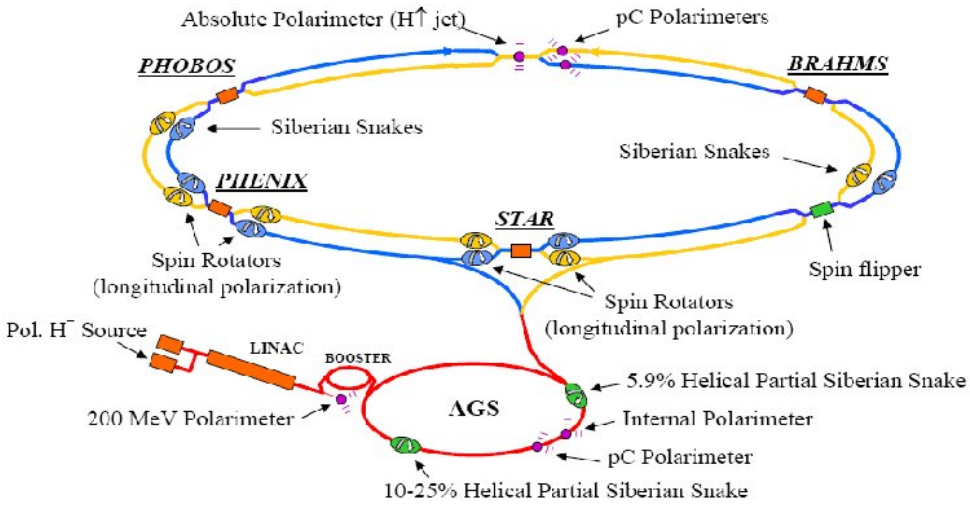

Figure 1: Accelerator-Collider complex RHIC polarization hardware layout.

polarized source upgrade. The polarimeter is based on the elastic proton-carbon scattering at 16.2 ° angle, where the analyzing power is close to 100% and was measured with high accuracy. The elastically and in-elastically scattered protons are clearly identified by the difference in the propagation through variable copper absorber and energy deposition of the protons in the detectors. This polarimeter Tawas used for calibration of a high rate inclusive 12T-polarimeter for the on-line polarization tuning and monitoring. This technique can be used for accurate polarization measurements in energy range of 160–250 MeV.

The proton-Carbon CNI polarimeters in AGS and RHIC are based on elastic proton scattering with low momentum transfer (Coulomb Nuclear Interference region) and measurement of asymmetry in recoil carbon nuclei production as described in detail elsewhere [6]. A very thin and narrow (30 nm thick 5 μm wide) carbon strip target placed in the high intensity circulating beam produces very high collision rate and an efficient DAQ system acquires up to 10^7 carbon events/sec. The polarization measurement during the beam energy ramp was implemented in AGS and RHIC, which provides an insight of polarization losses pattern. The carbon target width is much smaller than the beam size and polarization profile can be also measured.

The AGS proton-Carbon CNI polarimeter was upgraded for the 2011 Run with the new silicon detectors, amplifiers and new carbon-strip target drives. This upgrade improved the accuracy and reproducibility of polarization measurements and polarization profiles measurements in both vertical and horizontal planes. The polarization profile measurements with the "Jump-Quads" operation confirmed the expected reduction of horizontal polarization profile, which contributed to beam average polarization increase from AGS for about 5% [7]. The polarimeter can be also operated in a fast continuous sweep mode, while beam is stored in the AGS at 23.7 GeV. This measurement produces horizontal and vertical beam intensity profile measurements for the single AGS bunch. These measurements are used for cross-checking of the AGS IPMs measurements and machine set-up to minimize beam emittances.

The RHIC proton-Carbon CNI polarimeters is operated in scanning mode, giving polarization profiles and transverse beam intensity profile (beam emittance) measurements. The polarimeters function as wire scanners, providing a very good signal/noise ratio and high counting rate. This allows accurate bunch-by-bunch emittance measurements during fast target sweeps ($<$ 1 s) through the beam. Very thin carbon strip targets make these measurements practically non-destructive. Bunch by bunch emittance measurements are a powerful tool for machine set-up; in RHIC, individual proton beam transverse emittances can only be measured by CNI polarimeter scans.

The use of thin targets in a polarimeter is essential to reduce multiple scattering for recoil carbon ions and keep the event rate within detector and DAQ capabilities. Carbon strips used in polarimeter are 5–15 μm wide ($\sim$ 5 μg/cm^2 thickness), and contain about 10^{13} carbon atoms per mm of target length. The target length is 25 mm. High intensity circulating beam knocks out about $10^7 \div 10^8$ carbon nuclei/s, which cause the eventual target destruction. It was experimentally demonstrated that targets survive in the RHIC beam for at least 100–200 measurements at the full beam intensity, which corresponds to the one target lifetime of about one-to-two weeks. Multiple targets (six vertical and six horizontal) are attached to a target ladder to extend the time between maintenances. The precision procedure was developed to provide about $\pm$0.1 mm target alignment accu-

racy on the ladder, therefore the target positioning accuracy is limited only by the target straightness. A combination of linear and rotational motion in the target mechanism provides the target replacement and polarization scans operation. Using of precision linear stages and rotational vacuum feed-through gives target position accuracy of ± 0.2 mm. Time-of-flight and recoil carbon energy measurements are required for elastic scattering identification. Silicon-strip detectors are used in the polarimeters, which allow measurements of energy and arrival time of recoil Carbons in the RHIC ring vacuum environment. At full RHIC design intensity, the bunch width is about 8 ns and bunch spacing is 106 ns. To avoid prompt background, carbon nuclei should arrive at the detectors in the time window between two bunches.

Polarization and beam intensity profile measurements. The carbon target width of 5–15 μm is much smaller than the beam size. Therefore intensity and polarization profiles can be measured by the target scan. In scanning mode the counting rate dependence on the target position can be used for the beam intensity profile measurements in addition to polarization measurements. With high event rates, large statistics are accumulated in a very short time for fast target scans.

The absolute (average) beam polarization at 100–250 GeV beam energy was measured with a polarized H-jet polarimeter, which is also based on elastic proton-proton scattering in the CNI region. Due to particle identity, polarization of the accelerated proton beam can be directly expressed in terms of proton target polarization, which can be precisely measured by Breit-Rabi polarimeter. With the record beam intensity of a 12.4×10^{16} atoms/s obtained in this atomic beam source [4], and with increased bunch intensities in Run 2011 a statistical error of about 6–7% was obtained for polarization measurement in each RHIC store (see Fig. 2). There is a plan for the H-jet polarimeter silicon detectors upgrade for larger solid angle, energy range and better resolution. The goal of upgrade is 2–3 times event rate increase, which will reduce statistical error to about 5% in a single 8 hours store.

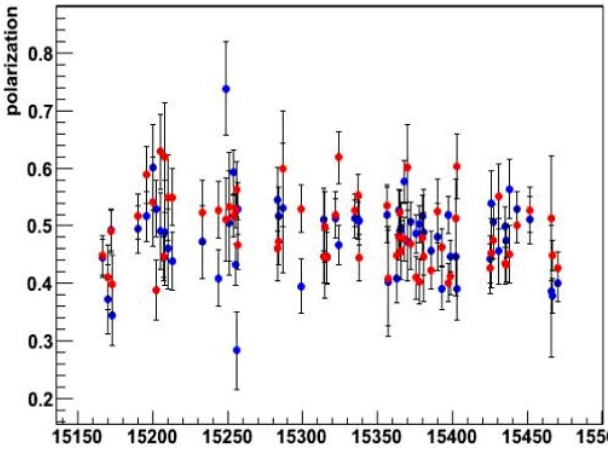

Figure 2: H-jet polarization measurements in RHIC in Run 2011.

The simultaneous measurements in p-Carbon and H-jet polarimeters provide the calibration for p-Carbon analyzing power. Fast pC polarimeter measures possible polarization losses during the store duration. Analyzing power of *pp* elastic scattering in CNI region has been accurately measured in experiments with H-jet polarimeter in energy range 24–250 GeV. This accuracy can be further improved after studies of molecular H_2 background and other systematic errors contributions. The statistical accuracy of the polarized H-jet polarimeter cannot be significantly improved because of strong intensity and density limitations for the polarized atomic beam target. But the accurately measured analyzing power can be used in the polarimeter with higher thickness un-polarized H_2-jet target and 100 times higher counting rate. It can be achieved with the un-polarized hydrogen jet target of a moderate about 10^{13} H_2/cm^2 thickness and increase of solid angle for recoil proton detection. This will result in less than 1% statistical accuracy for each fill.

3 Polarized beam in AGS and RHIC in Run 2011

In 2009 polarized Run the average polarization of about 55% was measured at 100 GeV beam energy. This polarization is equal to measured value at injection energy (within the systematic error of calibrations). It is expected, from spin dynamics simulations, that polarization losses from intrinsic resonances crossing at the energy ramp are higher at edge of beam, which should produce polarization distribution across the beam the polarization profile. These polarization profiles in RHIC were measured at injection energy, at 100 GeV and 250 GeV energies. The polarization profile values at 100 GeV were very close to the profile measurements at injection. This is another confirmation of small polarization losses at acceleration up to 100 GeV. In 2009 Run polarized protons was also for the first time successfully accelerated to 250 GeV beam energy and average polarization of a 36% was measured by the H-jet polarimeter. Significantly larger polarization profiles were also measured at 250 GeV beam energy.

A number of significant improvements in machine operation were implemented for 2011 Run. A "Jump-Quads" technique for polarization preservation during the passage of the week intrinsic resonances in AGS increased the beam polarization out of AGS for about 5–10% especially at the highest (2×10^{11} protons/bunch) beam intensity (see Fig. 3).

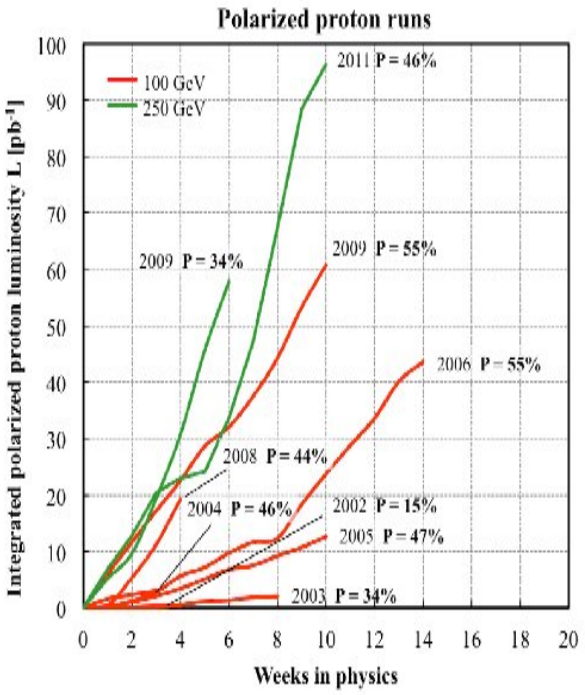

Figure 3: The polarized beam luminosity and polarization in Runs 2003-2011.

A new 9 MHz RF-cavity in RHIC improved the longitudinal matching in between AGS and RHIC and reduced the beam losses at the RHIC energy ramp. Spin tune stability was greatly improved with the implementation of the "tune feedback" system. This allowed the optimal choice of spin tune value to minimize depolarization and still keeping the stable machine operation. The beam position control system was also greatly improved, which reduced the vertical beam position motion to less than 0.1 mm, which is required for depolarization reduction [8]. As a result, the average polarization at 250 GeV was increased to 48% (see Fig. 2) and polarization profiles were reduced too accordingly. Another indicator of the improved machine control are the very close numbers for average polarization in Blue ($47.98 \pm 0.53\%$) and Yellow ($47.95 \pm 0.53\%$) rings, as measured by the H-jet polarimeter.

For colliding beams, the polarization profile is weighted with a product of two beam intensity profiles in transverse plane, therefore an "effective" polarization for colliding beams is somewhat higher than average polarization measured by the H-jet polarimeter [4]. In 2009 Run at 250 GeV beam energy these corrections were about 15% and "effective" polarization (as seen by colliding beams) was about 41%. In Run 2011 with the reduced polarization profiles the corrections were about 10% and "effective" polarization about

53%.

The RHIC upgrades allowed increase of the bunch intensity at injection to RHIC up to 2.0×10^{11} protons/bunch. The peak beam intensity accelerated to 250 GeV was increased to about 180×10^{11} protons in 109 bunches and peak beam luminosity 1.5×10^{32} cm^{-2}sec^{-1}. Average luminosity for the 8 hrs store was about 0.9×10^{32} cm^{-2}sec^{-1}. The RHIC performances in polarized Runs are shown in Fig. 3. In spite of 2 weeks downtime caused by technical problems (electrical power distribution system failure) the significant increase of integrated luminosity and polarization was achieved in Run 2011.

4 Summary and outlook

The RHIC spin program is a beneficiary of the latest development in the polarized ion source and polarized internal target technology. For the first time the polarized proton beam intensity in the high-energy accelerator is not limited by the polarized source intensity. In 2009-11 Runs polarized proton beam was successfully accelerated to 250 GeV energy. The beam polarization of a 55–60% at 100 GeV beam energy and 48% (53% as seen in collisions) at 250 GeV energy was measured with the polarized H-jet and p-Carbon CNI polarimeters. The plans for further polarization increase rely on polarized source upgrade to higher intensity and polarization [9]. Smaller beam emittance can be produced by strong beam scraping of the high-intensity beam after the Booster. This should reduce beam depolarization in AGS and RHIC and contribute to further luminosity increase. There is also a plan to eliminate a polarization decay (of about 10% during 8 hours store) which was observed in Run 11 by better choice of the operational tune value.

The depolarization studies and experimental data normalization are based on absolute polarization and polarization profiles measurement accuracy and ongoing program on polarimetry development and upgrades is an essential part of the RHIC spin program.

References

[1] T. Roser, AIP Conf. Proc **980** (2008) 15.

[2] I. Alekseev et al., NIM A **499** (2003) 392.

[3] A. Zelenski et al., "Precision absolute proton polarization measurements at 200 MeV beam energy", SPIN 2011, Julich, Journal of Physics, Conf. Series **295** (2011) 012132.

[4] A. Bazilevskiy, et al, "Precision measurements of the proton beam absolute polarization in RHIC", AIP Conf. Proc. **1149** (2009) 723.

[5] A. Zelenski et al., NIM A **536** (2005) 248.

[6] I. Nakagava et al., AIP Conf. Proc **980** (2008) 380.

[7] V. Schoefer et al., "Recent RHIC motivated polarized proton development in AGS", PAC 2011, THP079.

[8] H.Huang et al., "RHIC polarized proton operation", PAC 2011, MOOCN3.

[9] A.Zelenski et al., "The RHIC polarized source upgrade", SPIN2010, Julich, Journal of Physics: Conference Series **295** (2011) 012147.

TECHNICS
and
NEW DEVELOPMENTS

NUCLEAR MAGNETOMECHANICAL EFFECT AT NEGATIVE SPIN POLARIZATION

Y. F. Kiselev[1,†], F. Gautheron[2], J. Koivuniemi[2], W. Meyer[2], N. Doshita[3], H. Matsuda[3], A. Srnka[4].

(1) *Joint Institute for Nuclear Research, VBLHEP, 141980 Dubna Moscow Reg. Russia*,
(2) *Physics Department, University of Bochum, 44780, Germany*,
(3) *Department of physics, Faculty of Science, Yamagata Univ., 990-8560, Yamagata, Japan*,
(4) *Institute of Scientific Instruments of ASCR, 61264 Brno, Czech. Republic.*
† *E-mail: yury.kiselev@cern.ch*

Abstract

If the magnetic properties of electrons and nuclear spins are widely used in applications, to our knowledge, the mechanical resonance of nuclear spins has not been observed yet. Almost hundred years later the [E-de H] experiment with a freely suspended magnet [1] we are looking for a way to detect the nuclear magnetomechanical effect using Dynamic Nuclear Polarization method, the nuclear demagnetization at superlow temperature and the world largest polarized target at CERN.

1. Idea and Numeric estimations

"*The physical fact underlined all gyromagnetic effects is that the nuclear spin and the electron spin, as well as their orbital angular moments, generate a magnetic moment parallel to the angular momentum with a magnitude fixed through a characteristic constant ...*" [2]. The first magnetomechanical experiment by A. Einstein and W.J. de Haas [E-de H] was published in 1915 [1]. It was shown that a freely suspended magnet, placed in a solenoid field, has a mechanical resonant oscillations at a specific frequency of a weak magnetizing field. There was a proof that the law of conservation of electron orbital magnetic moment allows "*...the occurrence of compensating angular momentum of another kind; the latter will be a crude mechanical angular moment*" [1].

The concept of "Nuclear Spin" was elaborated much later in 1925÷1927. Assuming the equal numbers of protons and orbital electrons in the samples, one can see that, in an analogical to [E-de H] experiment, nuclear spins should be cooled down from room temperature ($\approx$ 300 K) to about 300 K$/(\mu_e/\mu_P)^2 \approx 7 \cdot 10^{-4}$ K, where μ_e/μ_P is the ratio of electron to proton magnetic moments. This spin temperature could be reached in solid dielectrics in two steps: by Dynamic Nuclear Polarization (DNP) method and then by demagnetization of spins in reduced field. The problem comes from the relaxation of the spin energy which goes mainly through the interaction of nuclear spins with electron impurities because an amount of lattice phonons with nuclear frequencies is extremely small at low temperatures. In irradiated ammonia (NH_3) [3], investigated below, these relaxation time reaches thousands hours at 2.5 T and of the order of a few minutes at zero field and at about of 60 mK in both cases. Obviously, to identify the nuclear magnetomechanical effect, the nuclear spin-lattice relaxation must be faster than relaxation caused by electron impurities to avoid ambiguous interpretation of the effect.

R. Pound showed [4] that, under certain conditions, the relaxation rate of quadrupole nuclei interacting with an electric field gradient can largely exceed the relaxation rate through paramagnetic impurities. If it is so in ammonia at super low temperatures, then the quadrupole nitrogen spins (I_N=1) could generate mechanical vibrations of a lattice. The effect may be enhanced during the cross-relaxation between proton and nitrogen spins because the proton moment (μ_P), and the energy, are an order of magnitude larger than for nitrogen (μ_N). The comparison of relaxation times of polarized proton through impurities and quadrupole spins can be estimated as follows [4]. The energy of dipolar interactions (E_{d-d}) between spins in NH_3 at a distance $\langle r_{PN}\rangle_{d-d}$ equals to

$$E_{d-d} = \frac{\mu_P \cdot \mu_N}{\langle r^3_{PN}\rangle_{d-d}} \approx \frac{1.4 \cdot 10^{-23} \cdot 2.0 \cdot 10^{-24}}{\langle r^3_{PN}\rangle_{d-d}} \approx \frac{3.0 \cdot 10^{-47}}{\langle r^3_{PN}\rangle_{d-d}}\,, \quad (c.g.s.) \tag{1}$$

which is considerably less than the interaction energy (W_q) between nitrogen quadrupole moment (eQ) and the averaged gradient of electric field in a lattice [5]

$$W_q = \frac{e^2Q}{4 \cdot \langle r^3_N\rangle_q}\langle(3\cos^2\theta - 1)^2)\rangle_\theta \approx \frac{(4.8 \cdot 10^{-10})^2 \cdot 2.0 \cdot 10^{-26}}{4 \cdot \langle r^3_N\rangle_q} \cdot \frac{4}{5} \approx \frac{9.0 \cdot 10^{-46}}{\langle r^3_N\rangle_q}\,, \tag{2}$$

where $\langle r_N\rangle_q$ is the average distance between nucleus and electron charges (e), θ is the angle between the principal axis of the field gradient tensor and the direction of the magnetic field. Assuming that in the same material $\langle r^3_{PN}\rangle_{d-d} \approx \langle r^3_N\rangle_q$ we obtain the ratio of quadrupole to dipolar relaxation times T_q/T_{d-d} as [4]

$$\frac{T_q}{T_{d-d}} \approx (E_{d-d}/W_q)^2 \approx (3.0 \cdot 10^{-47}/9.0 \cdot 10^{-46})^2 \approx 0.001\,, \tag{3}$$

If, for example, the relaxation time through the electron impurities is of about 1 hour, as it is in irradiated ammonia at about of 0.03 T and 60 mK, then the quadrupole relaxation from Eq. 3 yields the seconds. We use this feature of quadrupole relaxation to extract the nuclear magnetomechanical effect from relaxation through the electron impurities.

The conversion of nuclear moment into lattice vibrations must change both the energy $\langle H_q\rangle$ and the alignment $A(N)$ of nitrogen spin system. At a low magnetic field we have

$$\langle H_q\rangle = h\nu_q(3\cos^2\theta - 1)\langle 3{I_z}^2 - I(I+1)\rangle = h\nu_q(3\cos^2\theta - 1)A(N)\,, \tag{4}$$

where h is Plank's constant, $\nu_Q = 1/8(e^2qQ/h)$, (eq) is the value of the electric field gradient along the principal axis of the field gradient tensor, I is the spin and $\langle I_z\rangle$ is z-component of angular moment. It is clear from Eq. 4 that the lattice vibrations should come from varying angular moment $\langle I_z\rangle$ in alignment.

2. Experimental Results

The data were obtained with the Compass polarized target at CERN. It uses a powerful dilution refrigerator, a solenoid with a homogeneous longitudinal field of $2.5\pm4 \cdot 10^{-5}$ T and a dipole magnet producing a transverse field of 0.6 T. The dilution chamber consists of three cells (30+60+30) cm long and 4 cm in diameter (see Fig. 1), filled with irradiated and granulated ammonia [3]. Microwave (MW) cavity is also subdivided in three cells made of copper and electrically isolated from each other by MW-stoppers. It operates in

λ=4 mm wavelength range. Operating temperatures range is from 0.06 to 0.25 K. The nuclear polarization is measured by ten commercial "Liverpool" Q-meters connected to probing coils equally distributed along the target material [3]. The receiver circuits were permanently tuned to ν_0=106.42 MHz and fed by a RF-synthesizer. The frequency was scanned by 1000 steps within 600 kHz bandwidth.

Detailed investigation of the cross-relaxation in the ammonia at positive polarizations was done in [3], starting with high proton polarization of +89% and nitrogen polarization of +16%. The magnetic field was reduced to 0.045 T and raised back to 2.5 T several times. As a result the nitrogen polarization was increased up to +40%. It was also studied the line shape of both nuclear species but the relaxation processes were not considered.

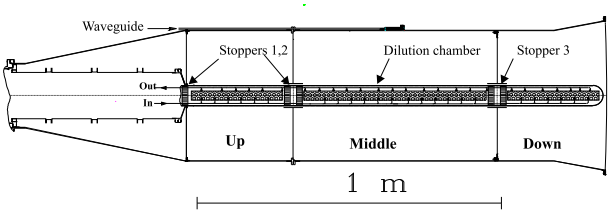

Figure 1: Up, Middle and Down microwave cells, powered through the waveguides. Electrical isolation between cells is performed with Stoppers 1,2,3; its design allows the free helium flow.

In this study, at field of 2.5 T, the proton spins in ammonia were polarized by the DNP method to ±80% then tests were performed in frozen mode without use of external alternative MW and RF-fields. With the positive polarization, sweeping up and down of the static magnetic field up to 0.03 T did not affect thermometers located near the ammonia. This means that at positive polarization the nuclear cross-relaxation is an adiabatic process which goes without any visible lattice effects. The cross-relaxation produces only a partial exchange between polarizations of spin species.

Nuclear magnetomechanical effect was only observed at negative polarizations. Fig. 2

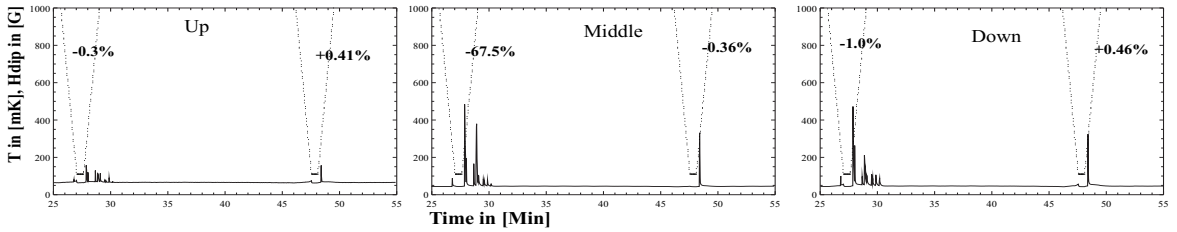

Figure 2: Magnetomechanical spectra obtained with RuO-thermometers. Dotted line shows the dipole field. Left and right percentages show the proton polarization before and after cross-relaxation. All spectral lines appear only during cross-relaxation and during the sweeping field.

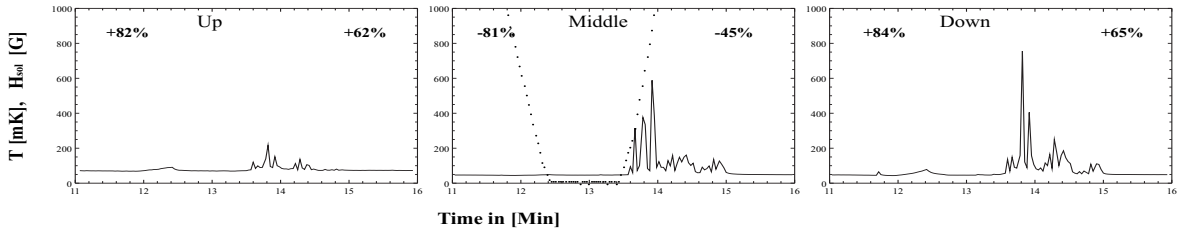

Figure 3: Magnetomechanical spectra of high resolution obtained in the uniform solenoid field (dotted line). Thermal pulses have characteristical durations of the order of 10 seconds in good agreement with estimation from Eq.3. This time the magnetic field went to zero for a minute to demonstrate an absence of relaxation through electron impurities during this short exposure.

shows thermal spectra recorded during double sweep through cross-relaxation field nearby 0.03 T. Since cells are electrically isolated from each other, we conclude that the obtained spectra comes from the mechanical vibrations of the lattice. Such the explanation also confirms and almost identical shapes of spectral lines in different cells, seen in Fig. 2; it is clear that vibrations are generated in the Middle-cell which had the highest and negative initial polarizations and then excitations are spread to the nearby cells due to the free helium flow through Stoppers (see Fig. 1). Fig. 3 shows the high resolution vibration spectra obtained in homogeneous solenoid field. Typical duration of relaxation processes is of the order of ten seconds which confirms the estimation from Eq. 3 and the proposition by Pound [4] about the important role of quadrupole nuclei in the spin lattice relaxation.

The fast relaxation observed here may clarify the shorter relaxation time of negatively polarized spin species when interacting with quadrupole nuclei through a weak dipolar interaction. Magnetomechanical effect may also influence the reachable polarization which is usually higher at negative than at positive polarization, if the material contains quadrupole nuclei. In this case DNP-method can "polarize" at lower temperatures.

3. Conclusion

1. Nuclear magnetomechanical effect was observed in the ammonia at super low temperatures and at negative nuclear polarizations. Effect consists in the transformation of nuclear magnetic moment into the mechanical vibration of the lattice.

2. Nitrogen spins in NH_3 produce the lattice vibrations when their alignment is varied during the proton-nitrogen cross-relaxatio at about of 0.03 T field.

3. Lattice vibrations were recorded with RuO-thermometers; they are spread along liquid helium and they cause the fast nuclear relaxation also in the nearby cells.

4. Evidence was produced, that, owing to a weak dipole-dipole coupling with quadruple spins, the magnetomechanical effect may produce a faster relaxation for negative compare to positive polarized spin species.

5. From the same reason, the negative reachable polarization should be higher than the positive one because, in this case, DNP-method can polarize at lower temperatures.

References

[1] A.Einstein and W.J.de Haas, Verhandl. d. Deut. Physic. Ges. **17**, (1915) 152.

[2] P.Heims and E.T. Jaines, Rev. Modern. Phys., **34**,(1962) 136.

[3] B. Adeva and SMC Collaboration at CERN, NIM in Phys. Res.**A419**, (1998),60-82.

[4] R.V. Pound, Phys. Rev. **D79**, (1950) 685.

[5] C.H. Townes and A.L.Schavlov, Microwave Spectroscopy, N.-Y., Toronto. London, (1955) 135-137.

SPIN-FLIPPING SYSTEMS FOR STORAGE RINGS

Ya.S. Derbenev [1], A.M. Kondratenko [2†], M.A. Kondratenko [2],
V.S. Morozov [1] and Yu.N. Filatov [3,4]

(1) *Thomas Jefferson National Accelerator Facility, Newport News, USA*
(2) *Science and Technique Laboratory Zaryad, Novosibirsk, Russia*
(3) *Moscow Institute of Physics and Technology, Dolgoprydny, Russia*
(4) *Join Institute for Nuclear Research, Dubna, Russia*
† *kondratenkom@mail.ru*

Abstract

This paper identifies the conditions providing stable multiple beam polarization reversals by small magnetic fields at the interaction points in a collider. We investigate the spin flipping schemes for the longitudinal and transverse polarization orientations. Such schemes are discussed for different types of storage rings, namely, for conventional storage rings, storage rings with Siberian snakes and figure-8 storage rings. The spin reversals are accomplished by rf magnetic fields oscillating at frequencies near a spin resonance. The proposed schemes are of interest for the beams of deuterons, protons and other particles.

Development of Spin-Flipping systems (SF systems) for storage rings, which allow for a controlled reversal of polarization direction at the interaction points, is an important problem of experimental physics. In principle, a spin reversal can be accomplished every particle turn without distorting the orbit at the interaction points. There are many papers on spin-flipping systems (see, for instance, [1–5]).

When choosing the devices producing the beam polarization reversal, the main problem is stability for multiple beam polarization reversals in the storage ring's experimental straight. This paper considers the problem of developing stable SF systems using small magnetic fields. We first state the general requirements towards the development of stable SF systems and then give examples of stable SF systems for a conventional storage ring, a storage ring with Siberian snakes and a figure-8 storage ring.

General requirements on SF systems

From the general point of view, development of SF systems using stationary fields is incompatible with stability of the spin motion. In a stationary case, the general spin motion is described by a periodic spin precession axis $\vec{n}$ and a generalized spin tune ν. The spin component along the $\vec{n}$ axis is repeated from turn to turn of a particle while the transverse spin component rotates every particle turn in the storage ring by an angle $2\pi\nu$ about this axis. With the exception of spin resonance points, the stable beam polarization direction points along the $\vec{n}$ axis. The particle spins transverse to the $\vec{n}$ axis are mixing due to the spin tune spread.

Let us illustrate the above using the example of spin motion in a conventional storage ring. In a conventional storage ring with vertical guiding field, the stable polarization

direction is vertical $\vec{n} = \vec{e}_y$. The spin precession frequency in such a storage ring in units of the circulation frequency $\nu = \gamma G$ is determined by the anomalous part of the gyromagnetic ratio G and is proportional to the particle energy. The polarization lying in the orbit plane is unstable and is lost within the time determined by the spread of particle parameters in the beam. It is convenient to depict the spin motion in the plane perpendicular to the $\vec{n}$ axis using a circular diagram shown in Fig. 1 where the grey arrows indicate the spin positions after every particle turn (the $\vec{n}$ axis direction is perpendicular to the plane of the figure).

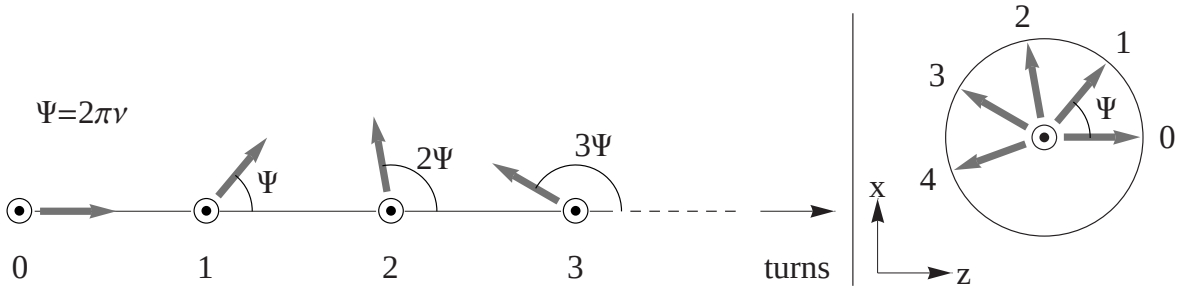

Figure 1: Circular diagrams of the spin motion in the stationary case

Figure 2 shows examples of circular diagrams of the spin motion in the place transverse to the $\vec{n}$ axis for different values of the spin tune. The case of $\nu = k$ corresponds to a spin resonance. In a spin resonance region, there is no preferred periodic axis $\vec{n}$, since all solutions become periodic. The stable polarization orientation is then determined by small spin perturbations, which set the new direction of the periodic axis $\vec{n}$ in the spin resonance region itself. In the case of $\nu = k+1/2$, there are sequential spin vector reversals occurring in the plane transverse to the $\vec{n}$ axis. When $\nu = k+1/4$, one can simultaneously organize subsequent spin reversals along both the radial and longitudinal directions with respect to the particle motion.

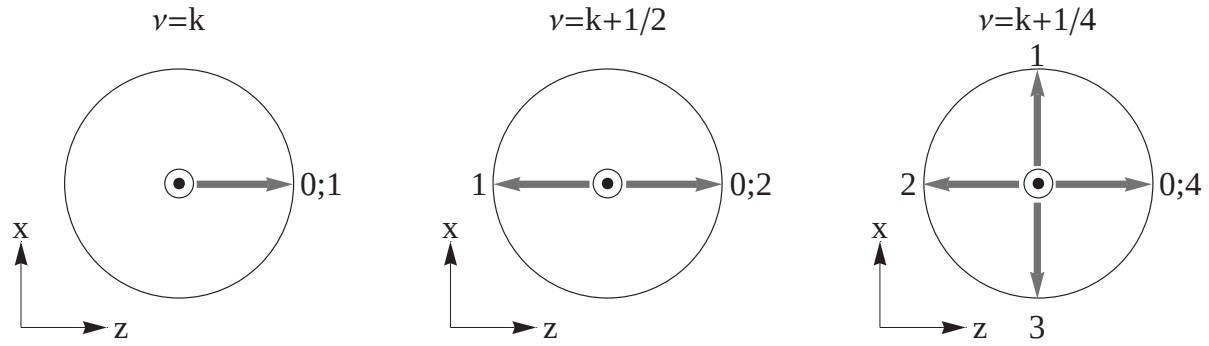

Figure 2: Examples of circular diagrams of the spin motion in the stationary case

In the stationary case, a spin direction reversal at a given azimuthal angle can only occur in the plane transverse to the $\vec{n}$ axis; therefore, the spin motion in SF systems with stationary fields cannot be stable. Typically, at the existing orbit spreads in storage rings, such a system depolarizes the beam during about $10^3 - 10^4$ particle turns.

Thus, for an SF system to provide stable polarization reversals during an extended period of time, it must employ non-stationary periodic fields. The spin field will then be periodic in the phases of these fields:

$$\vec{W}(\Psi_{\rm rf}) = \vec{W}(\Psi_{\rm rf} + 2\pi).$$

There then must exist a precession axis $\vec{n}$ with the property

$$\vec{n}(\Psi_{\rm rf}) = \vec{n}(\Psi_{\rm rf} + 2\pi).$$

Using small non-stationary fields is especially effective in the regions of spin resonances, when it becomes possible to stabilize a new polarization orientation with the frequency of the non-stationary field alternation.

The SF systems can be subdivided into two types: multi-turn and single-turn SF systems. In the former, the spin reversal is produced by a small time-varying field during a large number of particle turns in a storage ring. In the latter, the spin reversal is done by strong stationary fields of the storage ring while a time-varying field is used to stabilize the multiple spin reversals. It then becomes possible to do a reversal every particle turn.

When investigating stability of the spin motion in the SF systems of interest, it is also necessary to consider the accompanying effects arising due to the time-varying fields. Such effects include the effect of the synchrotron oscillations of particle energies, in particular, oscillations of particle phases inside a bunch, the effect of the accompanying electric fields induced by the time-varying magnetic fields. It is necessary to investigate excursions of the particle orbits and their stability in storage rings with SF systems. The introduced fields should not distort the orbit in the experimental straights. One has to account for the effect of the nearest natural spin resonances and, at least, of the $2^{\rm nd}$-order corrections to the spin motion, the effect of imperfections of the storage ring's magnetic lattice etc. For electron rings, radiation effects must be evaluated.

Multi-turn SF systems in conventional storage rings

Multi-turn SF systems can be realized in the beam energy regions near integer resonances. At an integer resonance point, any solution is repeated from turn to turn and is unstable. Introduction of an even small field (exceeding the strength of this resonance) singles out a new stable polarization direction. Let us illustrate how a multi-turn SF system can be organized using time-varying fields.

Three rotators placed in the experimental straight rotate the spin sequentially about the radial, vertical, and longitudinal directions on each particle turn by small angles φ_x, φ_y, φ_z, respectively. For simplicity, we assume that the particle orbits are not distorted outside of the rotator region. In a real situation, the particle orbit distortions organized in a special way can significantly reduce the required pulsed-field integrals in the rotators. Such rotators can be realized using dipoles and solenoids. Using these rotators, the polarization can be flipped along any of the indicated directions. For instance, to reverse the spin along the particle velocity (the SF system is working in the longitudinal direction), the radial and vertical rotators have to be turned on sequentially according to the time diagram shown in Fig. 3.

The pulse duration τ is chosen to be a multiple of the particle circulation period ($\tau = pT_0$) in the storage ring in such a way that the rotator turn angles during the time

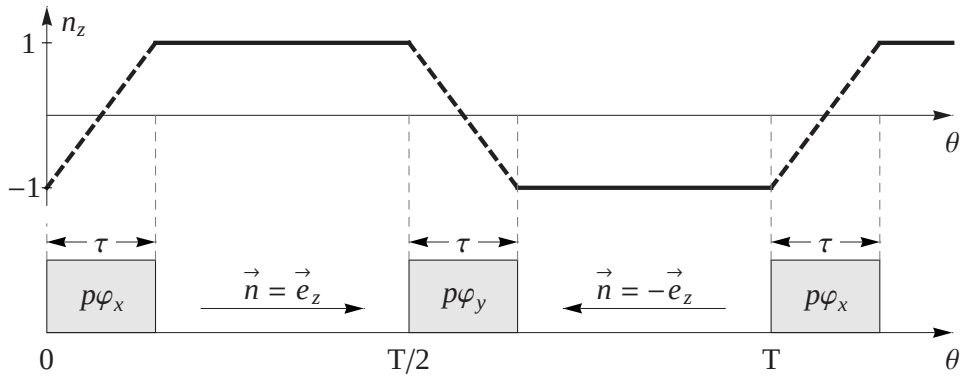

Figure 3: Time diagram of rotator operation in a multi-turn SF system

τ are equal to $p\varphi_x = \pi$ and $p\varphi_y = \pi$. The generalized spin tune in such a scheme is equal to a half $\nu = 1/2$ in the units of the induced field frequency $2\pi/T$. Thus, this scheme is optimal from the point of view of stability. The induced field period T is limited by the integer resonance strength w_k and by the spin tune spread $\Delta\nu = G\Delta\gamma$:

$$T \ll \min(\pi/w_k,\, \pi/\Delta\nu)\,.$$

To flip the polarization along the radial or vertical direction with this SF system, the rotator pair φ_y, φ_z or φ_z, φ_x, respectively, is used. One can easily see that this scheme is analogous to a storage ring with two Siberian snakes over a longer period $T \gg T_0$.

Many-turn SF systems based on spin resonance crossing

The development of SF systems based on adiabatic spin resonance crossing using rf fields was reported in many papers (see, for instance, [1–4]). Such schemes belong to the multi-turn SF systems' category and provide spin reversal along the direction of stable polarization. For cyclic adiabatic crossings, to support a stable spin motion, the phase difference between consecutive resonance crossings must not be an integer multiple of π: $\Delta\Psi \neq k\pi$. Since this phase difference for adiabatic crossings is large ($\Delta\Psi \gg 1$), to ensure stability of the polarization reversals in such schemes, stricter conditions must be satisfied than in other schemes described in this paper.

However, even high precision of parameters does not guarantee stability of multiple polarization reversals. In the case of adiabatic crossings, one should also account for the accompanying slow oscillations such as synchrotron oscillations and those caused by nearby resonances. The synchrotron oscillations in a storage ring can lead to a series of modulation resonances separated from the central resonance by the frequency of the synchrotron oscillations. These schemes require careful analysis of the stability of the spin motion.

In principle, a many-turn SF system can be organized using the transparent crossing technique [6, 7]. The requirements on the beam parameter spreads and on the crossing parameters in this case are somewhat reduced in comparison with the case of adiabatic

crossings but, even in this case, they are still more demanding than in other SF systems considered in this paper.

Single-turn SF systems in conventional storage rings

Single-turn SF systems were proposed and described in the paper [5]. For the energy values, when the fractional part of the spin tune is equal to a half $\gamma G = k + 1/2$, the polarization orientation lying in the orbit plane flips every turn in the storage ring's experimental straight. As pointed out above, such polarization dynamics is unstable. However, this dynamics can be made stable using a spin resonance $\gamma G = k + \nu_{\rm rf}$ induced by an rf field at a frequency $\nu_{\rm rf} = 1/2$.

Figure 4 shows schematic of a single-turn SF system with pulsed longitudinal field. The field is turned on at the time of bunch passing and changes sign on the next turn. The induced field period is equal to the time of two particle turns in the storage ring. Here φ_z denotes the small angle of spin rotation in the solenoid during each bunch passing, $\Psi_y = 2\pi\gamma G = 2\pi k + \pi$ is the angle of spin rotation about the guiding field during one particle turn in the storage ring.

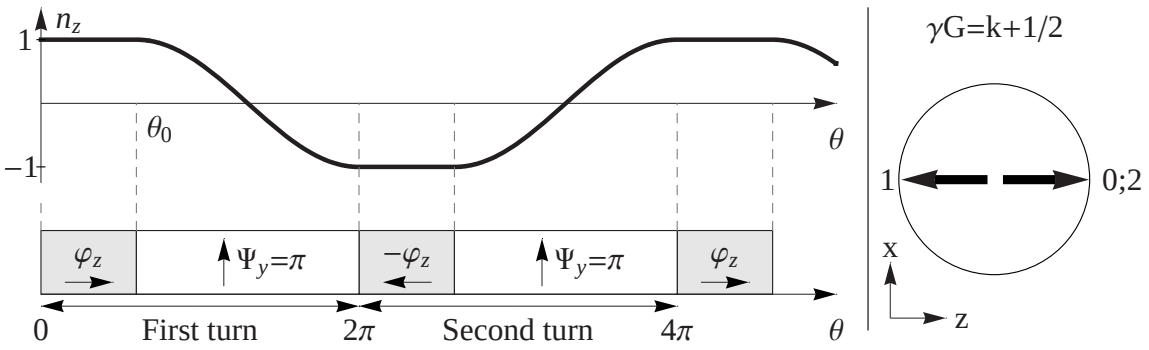

Figure 4: Schematic of a single-turn SF system with longitudinal field

The stable polarization orientation in the experimental straight is computed using

$$\vec{n}(0) = \frac{1}{\cos\dfrac{\pi\nu}{2}}\left(\cos\frac{\Psi_y}{2}\left(-\sin\frac{\varphi_z}{2}\,\vec{e}_x + \cos\frac{\varphi_z}{2}\,\vec{e}_y\right) - \sin\frac{\Psi_y}{2}\sin\frac{\varphi_z}{2}\,\vec{e}_z\right)$$

$$\vec{n}(2\pi) = \frac{1}{\cos\dfrac{\pi\nu}{2}}\left(\cos\frac{\Psi_y}{2}\left(-\sin\frac{\varphi_z}{2}\,\vec{e}_x + \cos\frac{\varphi_z}{2}\,\vec{e}_y\right) + \sin\frac{\Psi_y}{2}\sin\frac{\varphi_z}{2}\,\vec{e}_z\right)$$

The generalized spin tune is given by

$$\sin\frac{\pi\nu}{2} = \sin\frac{\Psi_y}{2}\cos\frac{\varphi_z}{2}$$

Approaching a half-integer resonance $\Psi_y \to 2\pi k + \pi$, one gets

$$\vec{n}(0) = -\vec{n}(2\pi) = \vec{e}_z\,, \qquad \nu = 2\gamma G + \frac{\varphi_z}{\pi} = 2k + 1 + \frac{\varphi_z}{\pi}\,.$$

Thus, for stable polarization reversal, the following condition has to be satisfied

$$\varphi_z \gg 2\pi|\Delta\gamma\, G|\,, \tag{1}$$

where $\Delta\gamma$ is determined by the particle energy spread in the beam.

In a similar way, an SF system can be constructed for the energy values determined by the relation $\gamma G = k + 1/4$. The induced field period becomes equal to four particle revolution periods. Longitudinal and radial field then have to be turned on alternately during bunch passing of the experimental straight as illustrated in Fig. 5.

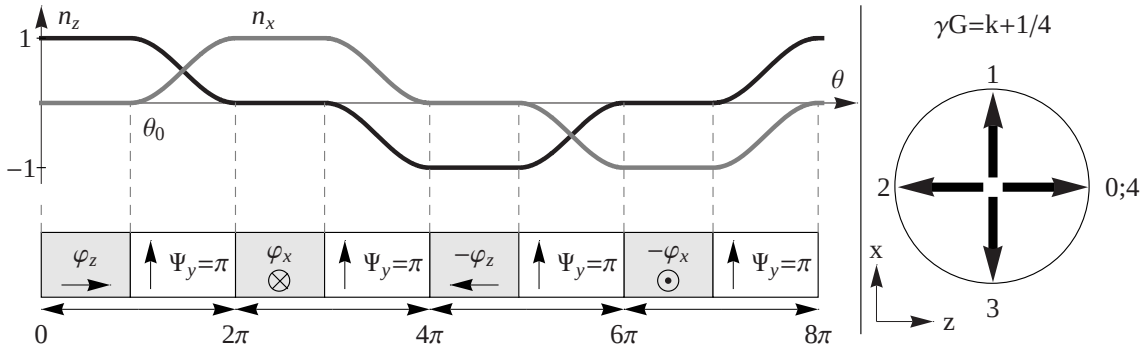

Figure 5: Schematic of a single-turn SF system with four-turn period

In such a scheme, in the induced resonance region $\gamma G = k \pm \nu_{\rm rf} = k \pm 1/4$, the stable polarization in the experimental straight changes from turn to turn during a complete period of the induced field in the following way:

$$\vec{n}(0) = -\vec{n}(4\pi) = \vec{e}_z\,, \qquad \vec{n}(2\pi) = -\vec{n}(8\pi) = \vec{e}_x\,.$$

The stability condition in this case is analogous to condition (1) for the SF system with a two-turn period:

$$\varphi_{x,\,z} \gg 2\pi|\Delta\gamma G|$$

In a similar way, one can construct any structure with the induced field period equal to q particle revolution periods in the storage ring.

SF systems in storage rings with Siberian snakes

As an example, let us consider a storage ring with one radial Siberian snake. One can show that in such a storage ring the stable polarization direction lies in the orbit plane and points along the radial direction in the straight (experimental straight) opposite to the snake. The generalized spin tune is independent of energy and is equal to a half. In such a storage ring, the relevant single-turn SF system is that based on the induced resonance $\nu_{\rm rf} = 1/2$. Since the stable polarization is radial directed along the axis $\vec{e}_x$, spin reversals can be organized along the directions lying in the (zy) plane.

To organize spin flipping along the velocity direction, the scheme shown in Fig. 2 can be used. The reversal stability condition can be obtained from (1) by replacing the spread $\Delta\gamma G$ with the spin tune spread in a storage ring with a snake $\Delta\nu$: $\varphi_z \gg 2\pi\Delta\nu$.

Note that the spin tune spread in a storage ring with a snake is significantly smaller than that in conventional storage rings and much lower magnetic field integrals are required to stabilize the reversals.

In a storage ring with two snakes, the stable polarization is vertical. Therefore, spin flipping can be organized along the directions lying in the (zx) plane. SF systems for a storage ring with two snakes are analogous to those for a storage ring with one snake.

SF systems for "figure-8" storage rings

Such a storage ring is being developed at Thomas Jefferson National Accelerator Facility, Newport News, VA, USA [8]. In this new type of storage ring under design, there is conceptually no need to introduce large field integrals, such as Siberian snakes, to control the beam polarization. A characteristic feature of such a storage ring is that the generalized spin tune does not depend on the energy and is equal to zero. The particles are at the $\nu = 0$ resonance. This means that any polarization orientation is repeated from turn to turn and there is no preferred polarization direction. Even small fields allow control of the beam polarization in the experimental straight by stabilizing the required polarization orientation. It becomes possible to efficiently control the polarization of a beam of particles with any anomalous magnetic moment including particles with small anomalous moments, such as deuterons.

For this kind of storage rings, a suitable SF system is a many-turn one considered above for conventional storage rings. For the spin reversals to be stable, the induced field period should not exceed the value $T \ll \pi/w_0$ determined by the strength of the $\nu = 0$ resonance.

Transformable storage ring types for SF systems

It was noted above that, for conventional storage rings, one can use both multi-turn and single-turn SF systems corresponding to integer and half-integer values of the spin tune:

$$\gamma G = k\,, \qquad \gamma G = k + 1/2\,.$$

To achieve stable spin reversals in a conventional storage ring at any energy, one can produce additional spin rotation to reach the nearest spin tune value. This can be done, for instance, using the scheme described in [9].

Single-turn SF systems are more suitable for storage rings with Siberian snakes ($\nu = 1/2$) while many-turn SF systems are more suitable for "figure-8" storage rings ($\nu = 0$). It should be pointed out that, by using large-integral stationary fields, one type of storage ring can be converted into the other. Thus, using two snakes with the same axes in opposite straights, the spin tune instead of being a half becomes a zero for any energy. This allows application of multi-turn SF systems in such storage rings. Inversely, introducing one Siberian snake in a "figure-8" storage ring changes the spin tune to one half, which allows usage of single-turn SF systems.

Acknowledgments

We would like to thank all participants of the seminars at JINR and JLAB for the useful discussions of the transparent spin resonance crossing technique, which inspired us to start studying the questions of SF system stability.

References

[1] D.D. Caussyn et al., Spin Flipping a stored polarized proton beam. Phys. Rev. Lett. 73, 2857 (1994);

[2] B.B. Blinov et al., Spin Flipping in the Presence of a Full Siberian Snake. Phys. Rev. Lett. 81, 2906 (1998).

[3] M.A. Leonova et al., SPIN@COSY: Spin-Manipulating Polarized Deuterons and Protons, AIP Conf. Proc. Vol. 1149, pp. 168-173, (2009)

[4] M. Bai et al., RHIC Spin Flipper Status and Simulation Studies, Proceedings of 2011 Particle Accelerator Conference, New York, NY, USA

[5] Ya.S. Derbenev and V. A. Anferov, RF driven stable spin-flipping motion of a stored polarized beam. , Phys. Rev. ST Accel. Beams 3, 094001 (2000)

[6] A.M. Kondratenko, M.A. Kondratenko, Yu. N. Filatov. "Multiple Spin Resonance Crossing In Accelerators", AIP Conference Proceedings, Malville, NY, Vol. 1149, p. 789, (2009)

[7] A.M. Kondratenko, M.A. Kondratenko, Yu. N. Filatov. "Transparent Spin Resonance Crossing In Accelerators", XIII Workshop on HESP DSPIN 2009 Proceedings, pp. 405-410, (2009).

[8] Y. Zhang et al., Design status of MEIC at JLab, in Proc. 2011 Particle Accelerator Conference (PAC'11), New York, NY, USA, March 2011, THP093.

[9] N.I. Golubeva, A.M. Kondratenko, Yu.N. Filatov "A jump in spin precession frequency as a method to pass spin resonance". Proceedings of the International Workshop "Deuteron-93". Dubna, 1994, p.374.

POLARIZED ION PRODUCTION VIA PASSAGE THROUGH A NICKEL FOIL

A.N. Fedorov, I.V. Gapienko and Yu.A. Plis†

Joint Institute for Nuclear Research, Dubna, Russia
† *E-mail: plis@nusun.jinr.ru*

Abstract

A proposal concerning ion polarization via pick-up of polarized ferromagnetic electrons was made by Zavoiskii in 1957, but the first experiment was carried out by Kaminsky in 1969. We reconsidered his results, corrected mistakes and propose to produce with use of this method a polarized neutron beam with an energy of 14 Mev through the reaction T(d,n)α. If we apply the zero field transition (Sona's method), the polarization of the deuterons reaches $\approx 2/3$. As a result, we can expect the beam of polarized neutrons ($P \leq 2/3$) with an intensity up to 1.5×10^7 neutrons per steradian, per μA of the deuteron beam. We show as the method may be used for producing polarized radioactive beams.

1 Introduction

A proposal concerning ion polarization via pick-up of polarized ferromagnetic electrons was made by Zavoiskii in 1957 [1]. The idea consists in passing a beam of protons (deuterons, tritons, helions, etc.) through a ferromagnetic foil magnetized to saturation. The transmitted neutralized component with captured polarized electrons is selected by electrostatically removing the remained charged beam. The foil should be in a strong magnetic field (higher than the "critical field" of hyperfine separation, which is proportional to Z^3). The method supposes an adiabatic transition of the atoms from a high magnetic field to a low field where the nuclei get polarized through hyperfine interaction. In this case ionization also should be in a low field.

But it seems possible to follow an another way suitable for heavy nuclei with use relatively low magnetic fields. If nuclei with spin 1/2 capture polarized electrons, the atoms (or hydrogenous ions) exit from the foil in two states $\psi_e^+\psi_N^+$ and $\psi_e^+\psi_N^-$. The atoms in the state $\psi_e^+\psi_N^-$ evolve as follows:

$1/\sqrt{2}(\Psi(1,0) + \Psi(0,0) \Rightarrow 1/2(\psi_e^+\psi_N^- + \psi_e^-\psi_N^+)\exp(-i\omega_1 t) +$
$1/2(\psi_e^+\psi_N^- - \psi_e^-\psi_N^+)\exp(-i\omega_2 t) = \exp(-i\omega_1 t)[1/2(1+\exp(i\Delta\omega t))\psi_e^+\psi_N^- +$
$1/2(1-\exp(i\Delta\omega t))\psi_e^-\psi_N^+]$.

In the course of time, the probabilities to detect these atoms in states $\psi_e^+\psi_N^-$ and $\psi_e^-\psi_N^+$ are respectively:

$$W^- = |[1+\cos(\Delta\omega t) + i\sin(\Delta\omega t)]/2|^2 = [1+\cos(\Delta\omega t)]/2, \quad (1)$$

$$W^+ = |[1-\cos(\Delta\omega t) - i\sin(\Delta\omega t)]/2|^2 = [1-\cos(\Delta\omega t)]/2. \quad (2)$$

Then, the nuclear polarization is $P = W^+ - W^- = -\cos(\Delta\omega t)$.

If a width of the atom velocity distribution $\delta(\Delta\omega L/v) > 2\pi$ (or $\delta v/v > 2\pi v/\Delta\omega L$), averaging with time gives zero polarization for the atoms in the initial state $\psi_e^+\psi_N^-$. As

the 2nd half of the beam has the polarization +1, the resulting nuclear polarization of all the beam is $P_{fin} = +1/2$.

We note that for nuclear spin 1, $P_3 = 8/27$ and $P_{33} = 0$, for nuclear spin 3/2, also only vector polarization is different from zero, $P_3 = 10/48$.

2 Polarized deuterons

The first successful experiment was carried out in 1969 by Kaminsky [2,3] and his results were partly confirmed by Feldman et al. [4]. The success was connected with use of channeling through a single crystal foil.

A beam of D^+ with a half angle of 0.01°was incident on a Ni(110) foil within 0.1° of the [110] direction (the critical acceptance angle $(1.6 - 1.8)°$). Two Ni(110) foils used were $\approx 2\mu$ thick. Two polycrystalline Ni foils with a thickness of $(1 - 2)\mu$m were also used but for them no polarization was detected. Rest gas pressure was $(1 - 2) \times 10^{-7}$ Torr. Inside the target holder the foils were kept in the magnetic field ≈ 160 G. Atoms emerging from the foil spent $(1 - 2) \times 10^{-7}$ sec in traversing a homogeneous magnetic field of ~ 10 G. After passing the weak field region the nuclear tensor polarization of the channeled deuterium atoms was determined [5] by measuring the angular distribution of α-particles emitted in the reaction $T(\vec{d}, n)\alpha$. Theoretically, the tensor polarization should be $P_{33} = -1/3$ (vector polarization $P_3 = 1/3$). The measured value is $P_{33} = -0.32 \pm 0.01$.

Kaminsky's results were strongly criticized (see the discussion in ref. [3]). In the used him configuration with a weak magnetic field of the transition region in the direction perpendicular to the field in the nickel film, electron spin can not follow the field. As our calculations show, this can be done only in a strong magnetic field.

The results of Feldman [4] are in a qualitative agreement ($P_{33} = -0.14 \pm 0.06$) with the polarization first observed by Kaminsky.

According to theoretical considerations, the spin polarization in the neutrals of the deuteron beam emerging from the foil is now attributed to the electrons captured in the tail of the surface electron distribution (Brandt and Sizmann [6]). One must accept that in the Kaminsky's experiments, the electrons are captured into the ground state of deuterium atoms.

3 Polarized neutrons

Our final goal is:

the measurement of the total cross-section differences $\Delta\sigma_L(nd)$ and $\Delta\sigma_T(nd)$ for n-d scattering (spins of neutrons and deuterons are parallel or antiparallel) with use a 14 MeV polarized neutron beam and polarized deuteron target. This experiment continues the preceding measurement of the $\Delta\sigma_L(np)$ and $\Delta\sigma_T(np)$ for n-p scattering at the Van de Graaff accelerator of Charles University in Prague.

Earlier, to produce polarized neutrons the reaction $T(d, \vec{n})\alpha$ was used [7], the polarization was transversal (perpendicular to the scattering plane).

We think that single-crystal nickel foils of thickness up to 2 μm will be grown epitaxially on NaCl crystals cleaved to expose the (110) plane. With use Sona's transitions we may get the vector polarization of deuterons and, respectively, neutrons up to $P_3 = 2/3$.

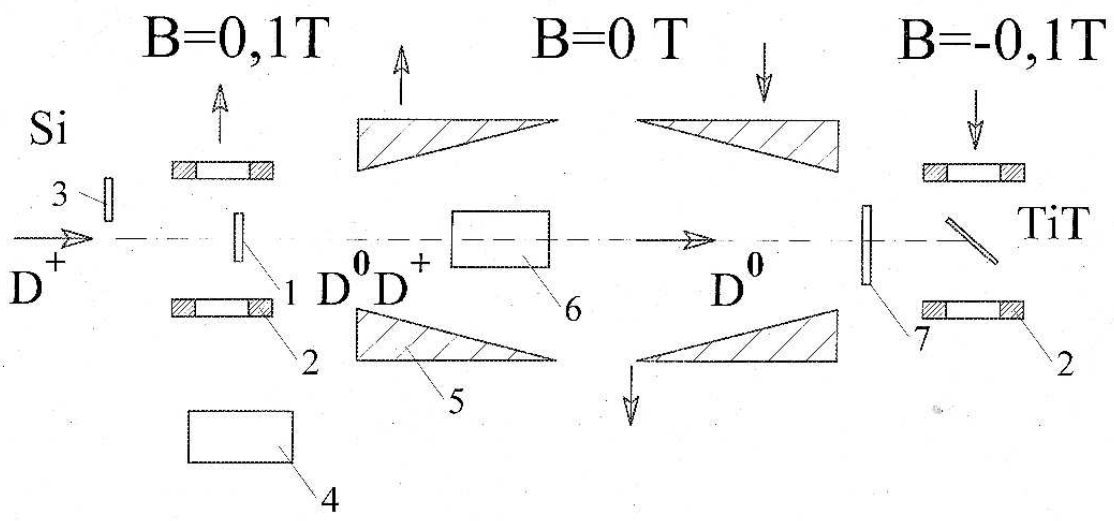

Figure 1: A scheme of the polarized deuteron source; 1 – a nickel foil, 2 – a permanent magnet (0.1 T), 3 – a solid state detector, 4 – a goniometer, 5 – polarizing permanent magnets (for Sona's transitions), 6 – electrostatic plates, 7 – a deuterated foil for the polarization measurement.

If target material TiT_N contains $N = 1.5$ tritium atoms/titanium atom, then the density ρ_{TiT_N} of the target material is $\rho_{TiT_N} = 0.85\rho_{Ti}(47.88 + 3.015N)/47.88 = 4.19\,\mathrm{g/cm^3}$, where $\rho_{Ti} = 4.505$ g/cm^3. The factor 0.85 arises from 15% expansion which the titanium lattice undergoes during tritiation.

If thickness of a target τ is measured in g/cm^2, the best approximation to use for the value of $dE_d/d\tau$ for deuterons incident in TiT_N is the value obtained by assuming Bragg's law: for N=1.5 [8]

$$dE_d/d\tau = 0.914(dE_d/d\tau)_{Ti} + 0.0863(dE_d/d\tau)_{T_2}. \tag{3}$$

The total yield of neutrons per an incident deuteron with an energy of $E_d(0)$ is given by

$$Y = \frac{n_T}{\rho_{TiT_N}} \int_0^{E_d(0)} \frac{\sigma(E_d)}{dE_d/d\tau}\, dE_d, \tag{4}$$

where n_T is the number of tritium atoms/cm^3, $dE_d/d\tau$ is the rate of the deuteron energy losses in a titanium tritide target, $\sigma(E_d)$ is the cross section of the T(d,n)^{4}He reaction.

The number n_T of tritium atoms/cm^3 equals $n_T = 1,5\rho_{TiT_N}6,022 \cdot 10^{23}/A_{TiT_N} = 7.22 \times 10^{22}$, where $A_{TiT_N} = 52.4$.

The deuteron range in cm is equals

$$R = \left(\frac{1}{\rho_{TiT_N}}\right) \int_0^{E_d(0)} \frac{dE_d}{dE_d/d\tau}\, dE_d. \tag{5}$$

As a result, the yield is $Y = 3 \times 10^{-5}$ neutrons per a deuteron, or 1.5×10^7 neutrons per steradian per μA of deuterons, the deuteron range is $R \approx 1.3\,\mu$m.

The activity of the TiT target is ≈ 0.45 Ci/cm^2.

If the TiT target is mounted in a strong magnetic field of an order 0.1 T, the 14-Mev neutrons produced at the angle 90° (CM) have the same value of vector polarization as deuterons, $P_n \leq 2/3$.The neutrons will be transversally polarized in the vertical plane, but with reversed direction compared to the deuteron beam polarization [9].

The deuteron polarization can be measured with the reaction D$(\vec{d}, p)$T. At the deuteron energy 200 keV $A_y = 0.224 \pm 0.017$ (Naqvi and Clausnitzer [10]).

4 Conclusion

It seems possible to get the nuclear polarized deuterium beam with an energy of about 150 keV with vector polarization up to 2/3 and zero tensor polarization via pick-up of electrons in a magnetized single crystal nickel foil.

The method now is being tested at the Laboratory of Nuclear Problems JINR and Czech Technical University in Prague.

The final aim is to produce the 14-MeV polarized neutron beam with polarization up to 2/3 for measuring the neutron-deuteron total cross section differences $\Delta\sigma_L$(nd) and $\Delta\sigma_T$(nd).

There is a possibility to apply this method for polarized heavy ion production.

The technology of fabrication of the single crystal Ni foils is known, but some additional work is necessary.

References

[1] E.K. Zavoiskii, *J. Exp. Theor. Phys.* **32** (1957) 408; English translation, *Sov. Phys. – JETP* **5** (1957) 338.

[2] M. Kaminsky, *Phys. Rev. Lett.* **23** (1969) 819.

[3] M. Kaminsky, in: Proc. of 3rd Int. Symp. on Polarization Phenomena in Nuclear Reactions, Madison, 1970, p.803.

[4] L.C. Feldman et al., *Radiation Effects* **13** (1972) 145.

[5] A. Galonsky, H.B. Willard, T.A. Welton, *Phys. Rev. Lett.* **2** (1959) 349.

[6] W. Brandt and R. Sizmann, *Phys. Lett.* **37A** (1971) 115.

[7] I. Wilhelm et al., *Nucl. Instr. & Meth.* **A317** (1992) 553.

[8] L. Granata, M. Lagonegro, *Nucl. Instr. & Meth* **70** (1969) 93.

[9] G.G. Ohlsen, *Rep. Progr. Phys.* **35** (1972) 717.

[10] A.A. Naqvi, G. Clausnitzer, *Nucl. Instr. & Meth.* **A324** (1993) 429].

RELATED PROBLEMS

KERR-NEWMAN GRAVITY BEYOND QUANTUM THEORY: ELECTRON AS A SYSTEM OF CLOSED HETEROTIC STRINGS

A. Burinskii [1 †]

(1) *Theor. Phys. Lab. NSI RAS*
† *E-mail: bur@ibrae.ac.ru*

Abstract

The observable gravitational and electromagnetic parameters of an electron: mass m, spin $J = \hbar/2$, charge e and magnetic moment $ea = e\hbar/(2m)$ indicate that electron should have the Kerr-Newman (KN) background geometry of the rotating black hole (BH) solutions. Due to the extremely high spin of the electron, the BH horizons disappear and the KN metric opens a topological defect in the form of a closed singular ring of the Compton radius $a = \hbar/(2m)$, [1]. This string is a closed heterotic string of the low energy string theory [2], and we identify it with a quark, q_0. On the other hand, the related with the KN string traveling waves form also a coupled pair of the opposite oriented heterotic strings (quark-antiquark pair $(q\bar{q})$), which perform a lightlike circular zitterbewegung and determine the wave properties of the electron in agreement with the Dirac equation. This stringy-quark structure of the electron indicates that electron is not pointlike, but forms a system of closed heterotic strings of the Compton radius. Experimental exhibition of the electron as a pointlike particle is related with the lightlike character of the Kerr heterotic strings, which results in the Lorentz contraction of the observable size of electron. We suggest that the stringlike structure of the electron and its Compton size should be experimentally observable by the novel methods of the "Deeply Virtual (nonforward) Compton scattering", [3].

One of the principal contradictions between Quantum theory and Gravity is the question on the shape and size of the electron. Quantum theory states that electron is pointlike and structureless, which is experimentally supported by the high energy scattering. In the same time, gravity based on the Kerr-Newman (KN) solution indicates unambiguously that electron should form a closed string of the Compton size. Reason of that is a specific structure of the KN gravitational field, which is concentrated near the Kerr singular ring, forming a type of a closed string. In 1968 Carter obtained that the KN solution for the charged and rotating black holes has $g = 2$ as that of the Dirac electron, which allowed one to consider KN solution as a consistent with gravity electron model. Mass of the electron in the units $G = \hbar = c = 1$ is $m \approx 10^{-22}$, while $a = J/m \approx 10^{22}$. Therefore, $a >> m$, and the black hole horizons disappear, opening a nontrivial topological defect and twosheeted spacetime generated by the naked Kerr singular ring. Gravitational field of the KN solution, concentrating near the Kerr singular ring, forms a closed gravitational waveguide – an analog of the closed gravitational strings [1], while the stringy traveling waves determine zitterbewegung and the wave properties of the electron.

The Kerr string takes the Compton radius, corresponding to the size of a "dressed" electron in QED and to the limit of localization of the electron in the Dirac theory. Structure of the KN string is very close to that of the fundamental heterotic string,

fundamental solution to the low-energy string theory. The heterotic strings carry the lightlike circular current and the lightlike traveling waves, which is similar to the lightlike structure of the Kerr singular ring. In [2] we started from the massless spinor equation and obtained the usual massive Dirac theory in which the mass is generated from an internal vortex dynamics by the Kaluza-Klein mechanism. However, contrary to the superstring constructions, we deal with four-dimensional space-time, in which the role of a compact manifold is played by the Kerr ring, performing a "compactification without compactification".

The Kerr-Newman solution in the Kerr-Schild form has the metric

$$g_{\mu\nu} = \eta_{\mu\nu} + 2Hk_\mu k_\nu,\ H = \frac{mr - e^2/2}{r^2 + a^2\cos^2\theta}, \qquad (1)$$

where $\eta_{\mu\nu}$ is metric of auxiliary Minkowski space in the Cartesian coordinates (t, x, y, z), and the Kerr coordinates r and θ are the spheroidal oblate coordinates. The function H is singular at $r = 0,\ \cos\theta = 0$, corresponding to the Kerr singular ring. The KN electromagnetic potential

$$A^\mu_{KN} = Re\frac{e}{r + ia\cos\theta}k^\mu, \qquad (2)$$

is aligned with null direction k^μ and is singular at the Kerr ring which forms a branch line of the Kerr spacetime in two sheets, corresponding to $r > 0$ and $r < 0$ in the Kerr oblate coordinate system. Vector field k^μ forms Principal Null Congruence (PNC) of KN space. The Kerr PNC is smoothly propagated via the Kerr disk $r = 0$ from the 'negative' sheet ($r < 0$) of spacetime to the 'positive' one ($r > 0$) (see Fig.1), and therefore, it covers the KN space twice: $k^{\mu(+)}$ for $r > 0$ and $k^{\mu(-)}$ for $r < 0$, leading to different metrics and different electromagnetic field on the 'positive' and 'negative' sheets [4]. Therefore, the Kerr ring creates a twosheeted background topology (see Fig. 1). This twosheetedness was principal puzzle of the Kerr geometry over a period of four decades and there appear two lines of investigation.

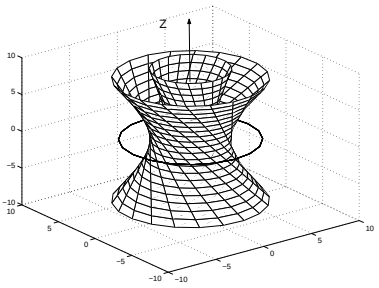

Figure 1: Vortex of the Kerr congruence. Twistor null lines are focused on the Kerr singular ring, forming a circular gravitational waveguide, or string with lightlike excitations.

(A) In 1968 Israel truncated negative KN sheet, $r < 0$, and replaced it by the *rotating disklike source* at $r = 0$, spanned by the Kerr singular ring at the disk boundary. López regularized this source, forming a vacuum bubble which covers the Kerr singular ring by a disklike ellipsoidal surface $r = r_e = e^2/(2m)$. The KN string is retained, taking a regularized form. This bubble source was realized as a regular soliton-like model (see refs. in [5]), formed by a domain wall interpolating between the external KN solution and a flat pseudovacuum state inside the bubble. Interior of the bubble is filled by Higgs field, forming a superconducting state, and the string represents the Nielsen-Olesen vortex on the rim of the bubble.

(B) In alternative approach, there were considered the stringlike models of the KN source, in which the KN twosheeted topology is retained and the KN singularity forms a closed twovalued 'Alice' string [1, 2].

Exact solutions for electromagnetic excitations on the Kerr-Schild background, [4], showed that there are no smooth harmonic solutions on the KN background. Excitations of the KN background have a 'paired' character: the lightlike 'circular' traveling waves appear coupled with the propagating outward 'axial' traveling waves (see Fig.2.1). Axial

waves are singular and tend asymptotically to the well known pp-wave (plane fronted) solutions, for which k_μ is asymptotically a covariantly constant Killing direction.

The pp-waves take very important role in superstring theory, forming singular classical solutions to a low-energy string theory. They form the massless field around the lightlike fundamental strings. The pp-waves may carry traveling electromagnetic and gravitational waves which represent propagating modes of the fundamental strings. It has been obtained that the field structure of the Kerr singular ring is very similar to that of the closed heterotic string [6]. The both are charged and contain the lightlike currents and traveling modes of one (say left) direction. The Kerr lightlike congruence k^μ is tangent to the KN closed string in the KN equatorial plane $\theta = \pi/2$, indicating that the cylindrical world-sheet $(t, \phi),\ 0 \leq \phi \leq 2\pi$ of the KN closed string is lightlike, and corresponds to a half of the period of the heterotic string $0 \leq \sigma \leq \pi$. Traveling waves of the heterotic string may be generated by dual rotations of the vector field (which corresponds to generalization of the low energy string theory to the F-theory), which is controlled by a complex axion-dilaton field. The lightlike heterotic strings form the principal elements of the quark electron structure, incorporating the both models of the KN source.

(A)*In the bubble model ,* the regular stationary KN electromagnetic field forms a closed heterotic string positioned on the disklike boundary of the vacuum bubble near the Kerr ring (quark-string q_0). The twisted KN potential (2) forms a non-trivial closed Wilson line which interacts with the Higgs field, resulting in the quantum contribution to the soliton spin $\hbar/2$, [5].

(B)*In the stringy models,* the traveling waves along the KN string may be identified with the circulating $q\bar{q}$ pairs, described by the Dirac equation. They are also obtained from the heterotic strings by an orientifold projection, as it is shown in the Figures 2.2-2.3.

Therefore, the schematic structure of KN electron model consists of three stringy quarks: q_0 - the closed heterotic string of the stationary KN field and the $q\bar{q}$ pair from traveling waves. The $q\bar{q}$ pair forms the Wilson loop with zero area and does not give a contribution to spin. However, the external electromagnetic field has to polarize the $q\bar{q}$ pair.

Summarizing, we conclude that the KN gravity predicts the existence of the closed

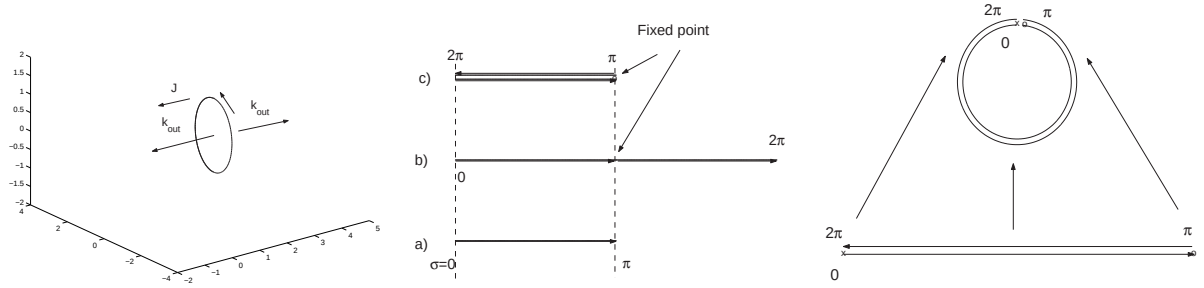

(2.1) **(2.2)** **(2.3)**

Figure 2: **(2.1)** Skeleton of Kerr geometry: the 'circular' and the lightlike 'axial' strings are coupled topologically. **(2.2a)** Half-period of an infinite lightlike (heterotic) string. **(2.2b)** Full period of the string, extended by mirror map. **(2.2c)** Orientifold projection of the heterotic string identified as a quark-antiquark pair. **(2.3)** Closed lightlike string formed as a circular projection of the heterotic quark-antiquark string.

Kerr string of the Compton size on the boundary of the disklike vacuum bubble of the Compton radius. Such a string should be experimentally observable, and there appears the question while it was not obtained earlier by the high energy scattering. Explanation of this fact is related with the lightlike character of the closed heterotic strings. The Lorentz effect for the relativistically rotating closed strings shall shrink their length, resulting in the observable pointlike image of the particle. Meanwhile, observation of the relativistic objects is a nontrivial process, which depends on the method of observation. For example, as it was shown by Penrose, the momentary photo-image of a relativistic sphere shouldn't display the Lorentz contraction.

We argue in [2] that the KN closed relativistic string, being probed by a real photon of high energy, shall display a pointlike structure. However, the situation should be different by the scattering of the deeply virtual photons with a low energy momentum transfer. Specifically, to visualize the KN relativistic string of the Compton size, there are necessary two special conditions:

a) the scattering should be *deeply virtual*, which means very large $Q^2 = q_{12}^2$, and $p \cdot q_{12}$,

b) the momentum transfer should be *relatively low* to provide a coherent diffractive scattering with the wavelengths comparable with the Compton extension of the string.

Both these conditions are satisfied in the novel approach, the Deeply Virtual Compton Scattering (DVCS), or a "non-forward Compton scattering", [3] which represents a new regime for probing the transverse shape and tomography of the particles [7].

Author is thankful to Organizing Committee for invitation and financial support, and also to many participants of the conference for useful discussions, and especially to A. Efremov, Yu. Obukhov, A. Radyushkin, O. Selyugin and O. Teryaev.

References

[1] A.Ya. Burinskii, Sov. Phys. JETP **39** (1974) 193;
D. D. Ivanenko and A. Ya. Burinskii, Izv. Vuz. Fiz. **5** (1975) 135.

[2] A. Burinskii, Proceedings of the QTS7 conference, Prague, August 2011 [arXiv:1112.0225], see also [arXiv:1104.0573, arXiv:1109.3872].

[3] A.V. Radyushkin, Phys. Rev, **D56** (1997) 5524;
X. Ji, Phys. Rev. **D55** (1997) 7114.

[4] A. Burinskii, First Award Essay of GRF 2009, Gen. Rel. Grav. **41** (2009) 2281, [arXiv:0903.3162 [gr-qc]].

[5] A. Burinskii, J. Phys. A: Math. Theor. **43** (2010) 392001 [arXiv: 1003.2928].

[6] A. Burinskii, Phys. Rev. **D 52** (1995) 5826 [arXiv:hep-th/9504139].

[7] P.Hoyer and Samu Kurki, Phys. Rev. **D 81** (2010) 013002 [arXiv:0911.3011].

ABOUT SPIN ELECTROMAGNETIC WAVE-PARTICLE WITH RING SINGULARITY

A.A. Chernitskii [1,2]

(1) *A. Friedmann Laboratory for Theoretical Physics, St.-Petersburg*
(2) *State University of Engineering and Economics,*
Marata str. 27, St.-Petersburg, Russia, 191002
E-mail: AAChernitskii@mail.ru, AAChernitskii@engec.ru

Abstract

An axisymmetric space-localized solution of nonlinear electrodynamics is considered as massive charged particle with spin and magnetic moment. The appropriate solution for nonlinear electrodynamics with ring singularity is investigated. In view of this problem the system of toroidal waves in linear electrodynamics is considered. The problem with boundary conditions on the singular ring of the toroidal coordinate system is investigated. The boundary conditions are taken taking into account the conformity between the toroidal and cylindrical waves on the ring. In this case the singular ring looks like convolute axis of cylindrical system. The appropriate system of wave modes are obtained in an integral form with the help of source function.

The present work is the part of the work on the construction of the field model for massive charged elementary particle with spin and magnetic moment as a soliton solution of nonlinear electrodynamics. This theme was discussed in my articles. See for example [1–5]

In this approach we have mass and spin of the particle as three dimensional space integral from the energy and angular momentum densities for electromagnetic field:

$$\mathrm{m} = \int\limits_V \mathcal{E}\, dv \ , \qquad \mathrm{s} = \left| \int\limits_V \mathbf{r} \times \boldsymbol{\mathcal{P}}\, dv \right| \ , \tag{1}$$

where $\mathcal{E} = \mathcal{E}(\mathbf{D}, \mathbf{B})$ is the energy density, $\mathbf{D}$ and $\mathbf{B}$ are electric and magnetic inductions, $\boldsymbol{\mathcal{P}} = \dfrac{1}{4\pi}\mathbf{D} \times \mathbf{B}$ is the Poynting vector. The function $\mathcal{E}(\mathbf{D}, \mathbf{B})$ defines the concrete model of nonlinear electrodynamics.

Here we consider the field configuration with ring singularity.

In general case the appropriate soliton solution in own coordinate system has a static part and quickly-oscillating part. The static part gives mass, spin, charge, and magnetic moment of the particle. The oscillating part gives the wave behavior of the particle.

The finding of the appropriate exact solution of nonlinear electrodynamics is the very difficult problem. But we can use approximate methods. The short report on the investigation of static solution with ring singularity for Born-Infeld nonlinear electrodynamics is contained in my article [6].

Now we investigate the oscillating part of the soliton solution with ring singularity. The present work is dedicated to construction the system of undistorted (standing) toroidal

waves in linear electrodynamics. The linear waves can be used in perturbation schemes for finding the soliton solution under consideration with the oscillating part.

It should be noted that the linear problem considered here is not trivial because the variables are not separated in Helmholtz equation for toroidal coordinates.

Here we will use the hypercomplex form for electrodynamics (see [7]). In this case the Clifford algebra with noncommutative product is used.

The hypercomplex form for representation of electromagnetic bivector is used: $\mathbf{F} = \mathbf{E} + \boldsymbol{\imath}\,\mathbf{B}$, where $\boldsymbol{\imath}$ is hyperimaginary unit.

According to my paper [8] we can write

$$\mathbf{F}(\mathrm{x}) = -\frac{1}{4\pi}\int\limits_{\Sigma'} \mathbf{S}(\mathrm{x}'-\mathrm{x})\,\mathbf{d\Sigma}'\,\mathbf{F}(\mathrm{x}') \quad , \tag{2}$$

where $\mathbf{S}(\mathrm{x})$ is the source function, Σ' is the three-dimensional hypersurface bounding the four-volume, and $\mathbf{d\Sigma}'$ is its inside oriented element.

Let us consider that the field $\mathbf{F}$ is harmonic wave. Thus we can write

$$\mathbf{F} = \mathbf{F}_\omega\,\mathrm{e}^{-\boldsymbol{\imath}\,\omega\,x^0} \quad . \tag{3}$$

where $\mathbf{F}_\omega = \mathbf{F}_\omega(\mathsf{x})$, $\mathsf{x} \equiv \{x^1, x^2, x^3\}$.

Let us consider the known toroidal coordinate system in three-dimensional space $\{u,\, v,\, \varphi\}$ with the following transformation formulas to cylindrical coordinates $\{\rho,\, \varphi,\, z\}$:

$$\rho = \frac{\rho_\circ\,\sinh v}{\cosh v - \cos u} \quad , \quad z = \frac{\rho_\circ\,\sin u}{\cosh v - \cos u} \quad , \tag{4}$$

where $\rho_\circ$ is the radius of the singular ring,

$$-\pi < u \leqslant \pi, \quad 0 \leqslant v < \infty, \quad 0 \leqslant \varphi < 2\pi.$$

We will use the modified toroidal coordinate system $\{\tau,\, \eta,\, \varphi\}$, where

$$\begin{aligned} &\tau = \operatorname{sech} v \quad , \qquad 0 \leqslant \tau \leqslant 1 \quad , \\ &\eta = -u \quad , \qquad\quad -\pi < \eta < \pi \quad . \end{aligned} \tag{5}$$

The coordinate τ ranges from 0 to 1 when the coordinate v ranges from ∞ to 0.

We have the following transformation formulas from the modified toroidal coordinates $\{\tau,\, \eta,\, \varphi\}$ to cylindrical ones

$$\rho = \frac{\rho_\circ\,\sqrt{1-\tau^2}}{1-\tau\,\cos\eta} \, , \quad z = -\frac{\rho_\circ\,\sin\eta}{1-\tau\,\cos\eta} \, , \tag{6}$$

As we can easy obtain the behavior of the modified toroidal coordinates near the singular ring ($\tau \to 0$) is the following:

$$\mathbb{b}^\tau \sim \frac{1}{\rho_\circ}\,(-\sin\eta\,\mathbb{b}_z + \cos\eta\,\mathbb{b}_\rho) \quad , \tag{7a}$$

$$\mathbb{b}^\eta \sim -\frac{1}{\rho_\circ\,\tau}\,(\cos\eta\,\mathbb{b}_z + \sin\eta\,\mathbb{b}_\rho) \quad , \tag{7b}$$

$$\mathbb{b}^\varphi \sim \frac{1}{\rho_\circ}\,(-\sin\varphi\,\mathbb{b}_1 + \cos\varphi\,\mathbb{b}_2) \quad , \tag{7c}$$

$$\mathfrak{m}_{\tau\tau} \sim \rho_\circ^2 \, , \quad \mathfrak{m}_{\eta\eta} \sim \rho_\circ^2\,\tau^2 \, , \quad \mathfrak{m}_{\varphi\varphi} \sim \rho_\circ^2 \quad , \tag{7d}$$

$$\mathrm{d}\mathbb{V} \sim \rho_\circ^3\,\tau\,\mathrm{d}\tau\,\mathrm{d}\eta\,\mathrm{d}\varphi \, , \tag{7e}$$

where $\mathbb{b}^i$ are the basis bivectors, $\mathfrak{m}_{ij}$ are the components of metric tensor, $\mathrm{d}\mathbb{V}$ is the three-dimensional volume element.

Let us introduce the following curvilinear coordinates:

$$\breve{\rho} \doteqdot \rho_\circ \tau \ , \quad \breve{\varphi} \doteqdot \eta \ , \quad \breve{z} \doteqdot \rho_\circ \varphi \ , \tag{8a}$$

$$\mathbb{b}^{\breve{\rho}} \doteqdot \rho_\circ \, \mathbb{b}^{\tau} \ , \quad \mathbb{b}^{\breve{\varphi}} \doteqdot \mathbb{b}^{\eta} \ , \quad \mathbb{b}^{\breve{z}} \doteqdot \rho_\circ \, \mathbb{b}^{\varphi} \ . \tag{8b}$$

As we can see in (8) with (7) the coordinates $\{\breve{\rho},\, \breve{\varphi},\, \breve{z}\}$ (8) near the ring looks locally like the cylindrical coordinates.

Thus we will consider that the toroidal wave solutions near ring is close to the radial-undistorted cylindrical waves propagating along the z axis. These cylindrical waves obtained in [8] have the following form:

$$\mathbb{C}^m_{\omega k_z} \mathrm{e}^{-\imath \omega x^0} \ , \tag{9}$$

where $\mathbb{C}^m_{\omega k_z} = \mathbb{C}^m_{\omega k_z}(\rho, \varphi, z)$ are cylindrical bivector eigenfunctions of operator $(-\imath \boldsymbol{\partial})$ corresponding undistorted waves ("Bessel beams", see my paper [8])

$$-\imath \boldsymbol{\partial} \, \mathbb{C}^m_{\omega k_z} = \omega \, \mathbb{C}^m_{\omega k_z} \ , \qquad \boldsymbol{\partial} \equiv \mathbb{b}^i \, \partial_i \ , \tag{10}$$

m is the index of the angle cylindrical function, k_z is the wavenumber corresponding to the propagation along the z axis.

The ring play a part of z axis for the toroidal system. In this case the appropriate wave number k_φ (instead of k_z for cylindrical waves) is quantized because of continuity condition for the field near the ring. Thus we have

$$\left.\begin{aligned} 2\pi \, \rho_\circ &= |m| \ \lambda_\varphi \\ |k_\varphi| &= \frac{2\pi}{\lambda_\varphi} \end{aligned}\right\} \qquad \Longrightarrow \qquad k_\varphi = \frac{m}{\rho_\circ} \ , \tag{11}$$

where m is integer (as positive as negative values is used), λ_φ is the wave-length at the ring.

Thus we consider that the toroidal wave near ring has the following form:

$$\mathbb{C}^{lm}_{\omega} \mathrm{e}^{-\imath \omega x^0} \sim \breve{\mathbb{C}}^{l}_{\omega k_\varphi} \mathrm{e}^{-\imath \omega x^0} \quad \text{for} \quad \tau \to 0 \ , \tag{12}$$

where $\mathbb{C}^{lm}_{\omega} = \mathbb{C}^{lm}_{\omega}(\tau, \eta, \varphi)$ are toroidal bivector eigenfunctions of operator $(-\imath \boldsymbol{\partial})$ corresponding undistorted waves, $\breve{\mathbb{C}}^{l}_{\omega k_\varphi} = \breve{\mathbb{C}}^{l}_{\omega k_\varphi}(\breve{\rho}, \breve{\varphi}, \breve{z}) = \breve{\mathbb{C}}^{l}_{\omega \frac{m}{\rho_\circ}}(\rho_\circ \tau, \eta, \rho_\circ \varphi)$ (see (11) and (8a)).

We consider the solutions in the form of some kind of standing toroidal waves but which can contain closed traveling waves. These closed traveling waves propagate along the ring and around the ring. The power flow through any closed surface containing the singular ring is absent. We will search these waves in the form

$$\mathbb{C}^{lm}_{\omega} \mathrm{e}^{-\imath \omega x^0} \ . \tag{13}$$

To obtain the functions $\mathbb{C}^{lm}_{\omega}$ we use formula (2) and boundary condition on the toroidal surface near the singular ring according to relation (12).

Let us consider the toroidal surface $\{\tau = \tau_\circ, -\pi < \eta \leqslant \pi, 0 \leqslant \varphi < 2\pi\}$. This surface will play the role of two-dimensional part of hypersurface Σ' in (2) such that the appropriate primed coordinates is $\{\tau' = \tau_\circ, -\pi < \eta' \leqslant \pi, 0 \leqslant \varphi' < 2\pi\}$.

After necessary substitutions we obtain

$$\begin{aligned}\mathop{\mathbb{\breve{C}}}\nolimits{}^{lm}_{\omega}(\tau,\eta,\varphi) = -\frac{1}{8\pi}\lim_{\tau_\circ\to 0}\int\limits_{\sigma'}\Bigg[\left(\mathrm{e}^{-\imath\omega\tilde{\mathfrak{r}}}+\mathrm{e}^{\imath\omega\tilde{\mathfrak{r}}}\right)\frac{\omega}{\tilde{\mathfrak{r}}}\,\mathop{\mathbb{\breve{C}}}\nolimits{}^{l}_{\omega\frac{m}{\rho_\circ}}\times\mathbf{d}\boldsymbol{\sigma}' \\ +\left(\frac{1}{\tilde{\mathfrak{r}}^3}\left(\mathrm{e}^{-\imath\omega\tilde{\mathfrak{r}}}+\mathrm{e}^{\imath\omega\tilde{\mathfrak{r}}}\right)+\frac{\omega}{\tilde{\mathfrak{r}}^2}\,\imath\left(\mathrm{e}^{-\imath\omega\tilde{\mathfrak{r}}}-\mathrm{e}^{\imath\omega\tilde{\mathfrak{r}}}\right)\right) \\ \cdot\left(\tilde{\mathfrak{r}}\left(\mathop{\mathbb{\breve{C}}}\nolimits{}^{l}_{\omega\frac{m}{\rho_\circ}}\cdot\mathbf{d}\boldsymbol{\sigma}'\right)+\tilde{\mathfrak{r}}\times\left(\mathop{\mathbb{\breve{C}}}\nolimits{}^{l}_{\omega\frac{m}{\rho_\circ}}\times\mathbf{d}\boldsymbol{\sigma}'\right)\right)\Bigg]\,, \qquad (14)\end{aligned}$$

where σ' is the toroidal surface bounding the singular ring such that $\rho_\circ$ is its big radius and $\tau_\circ$ is its small radius, $\mathbf{d}\boldsymbol{\sigma}'$ is its outside oriented element, $\mathop{\mathbb{\breve{C}}}\nolimits{}^{l}_{\omega\frac{m}{\rho_\circ}} = \mathop{\mathbb{\breve{C}}}\nolimits{}^{l}_{\omega\frac{m}{\rho_\circ}}(\rho_\circ\tau_\circ,\eta',\rho_\circ\varphi')$ is the appropriate cylindrical functions on the surface σ', $\tilde{\mathfrak{r}}$ is the distance from the point $\{\tau,\eta,\varphi\}$ to the point $\{\tau_\circ,\eta',\varphi'\}$, $\tilde{\mathbf{r}}$ is the appropriate radius bivector.

Thus here we have the integral representation for toroidal undistorted linear electromagnetic waves. This representation can be sufficient for the using of these functions.

References

[1] A. A. Chernitskii, J. High Energy Phys. **1999**, 12 (1999) Paper 10, arXiv:hep-th/9911093.

[2] A. A. Chernitskii, Encyclopedia of Nonlinear Science, ed. A. Scott, Routledge, New York and London, 2004, 67–69, arXiv:hep-th/0509087.

[3] A. A. Chernitskii, Adv. appl. Clifford algebras, **15** (2005) 27–53, arXiv:hep-th/0501161.

[4] A. A. Chernitskii, Proc. of the 17th. Int. Spin Physics Symposium, SPIN2006, AIP Conf. Proc. **V.915** (2007) 264–267, arXiv:hep-th/0611342.

[5] A. A. Chernitskii, Proc. of XII Adv. Res. Workshop on High Energy Spin Physics, DSPIN-07, JINR (2008) 433–436, arXiv:0711.2499.

[6] A. A. Chernitskii, Proc. of XIII Adv. Res. Workshop on High Energy Spin Physics, DSPIN-09, JINR (2010) 443–446, arXiv:0911.3230.

[7] A. A. Chernitskii, Int. J. Math. & Math. Sci. **31** (2002) 77–84, arXiv:hep-th/0009121.

[8] A. A. Chernitskii, Adv. appl. Clifford algebras, **13** (2003) 219–230, arXiv:hep-th/0401122.

[9] A. A. Chernitskii, Proc. of XI Adv. Res. Workshop on High Energy Spin Physics, DSPIN-05, JINR (2006) 234–239, arXiv:hep-th/0603040.

SPINNING PARTICLES IN DE SITTER SPACETIME

Yu.N. Obukhov [1†] and D. Puetzfeld [2‡]

(1) *Inst. Theoretical Physics, University of Cologne, Zülpicher Str. 77, 50937 Köln, Germany*
(2) *ZARM, University of Bremen, Am Fallturm, 28359 Bremen, Germany*
† *E-mail: yo@thp.uni-koeln.de* ‡ *E-mail: dirk.puetzfeld@zarm.uni-bremen.de*

Abstract

We report on the multipolar equations of motion for spinning test bodies in the de Sitter spacetime of constant positive curvature. The dynamics of spinning particles is discussed for the two supplementary conditions of Frenkel and Tulczyjew. Furthermore, the 4-momentum and the spin are explicitly expressed in terms of the spacetime coordinates with the help of the 10 Killing vectors available in de Sitter spacetime.

The multipolar equations of motion, commonly termed Mathisson-Papapetrou equations [1–11]

$$\dot{p}^{\alpha} = -\frac{1}{2}\, S^{\mu\nu} u^{\beta}\, R_{\mu\nu\beta}{}^{\alpha}, \qquad \dot{S}^{\alpha\beta} = 2p^{[\alpha}\, u^{\beta]}, \tag{1}$$

represent a self-consistent set of equations, which is widely used for description of spinning test bodies in General Relativity. Here " $\dot{}$ " $= D/ds = u^{\alpha}\nabla_{\alpha}$, and a test particle is described in terms of the 4-momentum p^{α}, the 4-velocity u^{α}, and the tensor of spin $S^{\alpha\beta}$. We report on the solution of the equations of motion (1) in a maximally symmetric 4-dimensional space represented by de Sitter spacetime. Our analysis extends well-known results from flat spacetime – in which the dynamics of spinning test bodies already becomes nontrivial [12–14] – to a manifold with non-vanishing curvature. In particular we make use of the two frequently used supplementary conditions [3, 12, 15]

$$S^{\alpha\beta}u_{\beta} = 0, \quad (*), \qquad S^{\alpha\beta}p_{\beta} = 0. \quad (**) \tag{2}$$

and are able to obtain analytic results. This is in contrast to the analysis in most other spacetimes in which the lack of symmetry – compared to de Sitter space – complicates the situation and usually necessitates to make additional simplifying assumptions. We should stress that our analysis is valid for both interpretations of the Mathisson-Papapetrou equations which can be found in the literature, i.e. it applies to point particles as well as to extended test bodies. One should keep in mind though, that there are preferences regarding the supplementary condition [16–19], depending on the system which is supposed to be described by the equations of motion. In the following our conventions and notation follows that of [20].

Spacetime with maximal symmetry. The curvature of de Sitter spacetime is given by $R_{\mu\nu\alpha}{}^{\beta} = \frac{1}{\ell^2}\left(g_{\alpha\mu}\delta^{\beta}_{\nu} - g_{\alpha\nu}\delta^{\beta}_{\mu}\right)$, where ℓ is a real constant. The first equation of motion from (1) then reduces to

$$\dot{p}^{\alpha} = \frac{1}{\ell^2}\, S^{\alpha\beta}u_{\beta}. \tag{3}$$

Tulczyjew condition. Assuming $(**)$ from (2), we introduce the 4-vector of spin via $\check{S}^\alpha := \eta^{\alpha\beta\mu\nu} p_\beta S_{\mu\nu}$. The inverse formula yields the spin tensor in terms of the spin vector: $S^{\alpha\beta} = \frac{1}{2M^2}\eta^{\alpha\beta\mu\nu} p_\mu \check{S}_\nu$, with $M^2 := p^\alpha p_\alpha$. As a result, the equations of motion of a spinning test body in the de Sitter spacetime under the Tulczyjew condition reduce to

$$\dot{p}^\alpha \overset{(**)}{=} 0, \qquad \dot{\check{S}}^\alpha \overset{(**)}{=} 0, \qquad p^\alpha \overset{(**)}{=} m\, u^\alpha, \tag{4}$$

where we introduced $m := p^\alpha u_\alpha$, or, equivalently

$$\dot{u}^\alpha \overset{(**)}{=} 0, \qquad \eta^{\alpha\beta\gamma\delta} u_\beta \dot{S}_{\gamma\delta} \overset{(**)}{=} 0. \tag{5}$$

The first equation actually means that the trajectories of the spinning bodies are the geodesics in the de Sitter space. The second equation describes the precession of the spin vector, or tensor, of a body during its motion along a geodesic curve.

Frenkel condition. The dynamics for $(*)$ from (2) have a certain similarity to the above case, however there are important differences. In particular, from (3) we immediately infer that, like in the previous case, the momentum is covariantly constant, $\dot{p}^\alpha = 0$. Following the same line of reasoning, we define the 4-vector of spin by $S^\alpha := \eta^{\alpha\beta\mu\nu} u_\beta S_{\mu\nu}$. The inverse formula yields the spin tensor in terms of the spin vector: $S^{\alpha\beta} = \frac{1}{2}\eta^{\alpha\beta\mu\nu} u_\mu S_\nu$ (we use the normalization $u^2 = 1$). Directly from the definition of the spin vector, we derive that the spin vector is Fermi-Walker transported. We thus have the system

$$\dot{p}^\alpha = 0, \qquad \rho^\alpha_\beta \dot{S}^\beta = 0. \tag{6}$$

Here $\rho^\alpha_\beta := \delta^\alpha_\beta - u^\alpha u_\beta$. Although this looks formally similar to (4), the actual dynamics is very different. In particular, the trajectories are no longer geodesics because the momentum does not coincide with the velocity. The above system can be simplified even further and we end up with the final system:

$$\dot{p}^\alpha \overset{(*)}{=} 0, \quad \dot{S}^\alpha \overset{(*)}{=} 0, \quad p^\alpha \overset{(*)}{=} m u^\alpha - S^{\alpha\beta}\dot{u}_\beta. \tag{7}$$

Hence, in de Sitter space the spin is also parallely transported under the Frenkel condition. Equivalently, one may look for solutions of the system

$$S^{\alpha\beta}\ddot{u}_\beta - m\dot{u}^\alpha \overset{(*)}{=} 0, \qquad \dot{S}^{\alpha\beta} + 2u^{[\alpha} S^{\beta]\gamma}\dot{u}_\gamma \overset{(*)}{=} 0. \tag{8}$$

Geodetic motion plus parallel transport of the spin ($\dot{u}^\alpha = 0$, $\dot{S}^\alpha = 0$) is a solution of (7). However, in general the motion of a spinning body described by (7) is more complicated. We introduce a new vector variable $Q^\alpha := \frac{1}{M^2} S^{\alpha\beta} p_\beta$, which has constant length and is orthogonal to the velocity – i.e. Q^α is spacelike. One can then show, that the second derivative of Q^a is actually the force which pushes the body away from the geodesic, i.e. in general one has $\dot{u}^\alpha = -\ddot{Q}^\alpha$. Furthermore the "$Q$-force" fulfills an oscillator equation

$$\ddot{Q}^\alpha + \omega^2 Q^\alpha = 0, \tag{9}$$

with the frequency $\omega := 2M/\sqrt{-S_\alpha S^\alpha} = M/\sqrt{\frac{1}{2}S_{\alpha\beta}S^{\alpha\beta}}$. Qualitatively, the dynamics of spinning bodies subject to the Frenkel condition in the de Sitter spacetime is similar to that in flat space [14]. Everything is determined by the initial conditions. If initially (at the proper time $s = 0$) spin is parallel to the momentum, i.e. $S^{\alpha\beta}p_\beta = 0$ (hence $Q^\alpha = 0$), then this is true on the whole trajectory that turns out to be geodesic. Otherwise, the trajectory is a geodesic curve, perturbed by the oscillatory motion of Q^α with the frequency ω.

Integrals of motion. The de Sitter spacetime has exactly the same number of Killing vectors as the total number of the "gravitational charges", that is, 10. Hence, we can try to find the momentum p^μ and the spin $S^{\mu\nu}$ without solving differential equations by just making use of the 10 conservation laws. This task is most straightforwardly treated in the conformally flat representation, i.e.

$$ds^2 = \varphi^2 \eta_{\alpha\beta} dx^\alpha dx^\beta, \qquad \eta_{\alpha\beta} = \mathrm{diag}(+1,-1,-1,-1). \tag{10}$$

The conformal factor depends only on the 4-dimensional "radius" $\sigma = \eta_{\alpha\beta} x^\alpha x^\beta$, namely,

$$\varphi = \frac{1}{1-\frac{\sigma}{4\ell^2}} = \frac{1}{1-\frac{\eta_{\alpha\beta}x^\alpha x^\beta}{4\ell^2}}. \tag{11}$$

In this representation, the Killing vectors [21] are as follows:

$$\underset{(\alpha)}{\xi} = \left(1+\frac{\sigma}{4\ell^2}\right)\partial_\alpha - \frac{x_\alpha x^\beta}{2\ell^2}\,\partial_\beta, \tag{12}$$

$$\underset{[\alpha\beta]}{\xi} = x_\alpha \partial_\beta - x_\beta \partial_\alpha. \tag{13}$$

Furthermore, we make use of the fact that the scalar

$$2\xi_\alpha p^\alpha + S^{\alpha\beta}\nabla_\alpha \xi_\beta = \mathrm{const} \tag{14}$$

is an integral of motion of the system (1) for any Killing vector ξ^α. By substituting (12) and (13) into (14), we have the algebraic system

$$2\,\underset{(\alpha)}{\xi}{}_\mu p^\mu + S^{\mu\nu}\nabla_\mu \underset{(\alpha)}{\xi}{}_\nu = 2\Pi_\alpha, \tag{15}$$

$$2\,\underset{[\alpha\beta]}{\xi}{}_\mu p^\mu + S^{\mu\nu}\nabla_\mu \underset{[\alpha\beta]}{\xi}{}_\nu = 2\Sigma_{\alpha\beta}. \tag{16}$$

Here Π_α and $\Sigma_{\alpha\beta} = -\Sigma_{\beta\alpha}$ are the $4+6=10$ constants of motion. This system is solved by

$$p^\mu = \frac{1}{\ell^2}\,\eta^{\mu\alpha}\Sigma_{\alpha\beta}x^\beta + \check{\eta}^{\mu\nu}\,\Pi_\nu, \tag{17}$$

$$S^{\mu\nu} = \hat{\eta}^{\mu\alpha}\hat{\eta}^{\nu\beta}\,\Sigma_{\alpha\beta} + \hat{\eta}^{\mu\alpha}\Pi_\alpha\,x^\nu - \hat{\eta}^{\nu\alpha}\Pi_\alpha\,x^\mu, \tag{18}$$

where we introduced $\hat{\eta}_{\mu\nu} := \left(1-\frac{\sigma}{4\ell^2}\right)\eta_{\mu\nu} + \frac{x_\mu x_\nu}{2\ell^2}$ and $\check{\eta}_{\mu\nu} := \left(1+\frac{\sigma}{4\ell^2}\right)\eta_{\mu\nu} - \frac{x_\mu x_\nu}{2\ell^2}$, i.e. we are able to express the momentum and the spin as functions of the constants of motion. Remarkably, the dependence on the spacetime coordinates is merely polynomial.

Summary. Qualitatively, the dynamics of spinning test bodies in de Sitter spacetime is similar to the one obtained in flat spacetime. For the Tulczyjew condition $(**)$, the body moves along a geodesic curve, whereas the spin vector is parallelly transported along the trajectory. In the Frenkel case $(*)$, the spin is still parallelly transported, but geodesic motion is just one special solution of the equations of motion. When the initial value of Q^α is nontrivial, then the body is affected by the spin-dependent force, the acceleration $\dot{u}^\alpha$ is nontrivial, and the trajectory oscillates around a geodesic with the frequency ω. Furthermore, the high symmetry of de Sitter spacetime allows for polynomial expressions – w.r.t. the spacetime coordinates – of the momentum and spin as functions of the constants of motion.

Acknowledgments. The authors are grateful to F.W. Hehl (Univ. Cologne) for stimulating discussions and constructive criticism. The work of Y.N.O. was partly supported by the German-Israeli Foundation. The work of D.P. has been supported by the DFG grant LA-905/8-1.

References

[1] M. Mathisson, *Acta Phys. Pol.*, **6** (1937) 163.

[2] A. Papapetrou, *Proc. Roy. Soc. London A*, **209** (1951) 248.

[3] W. Tulczyjew, *Acta Phys. Pol.*, **18** (1959) 393.

[4] B. Tulczyjew and W. Tulczyjew, *Recent Developments in General Relativity*, Polish Scientific Publishers, Warsaw (1962), page 465.

[5] W. G. Dixon, *Nuovo Cimento*, **34** (1964) 317.

[6] H. C. Corben, *Classical and quantum theories of spinning particles*, Holden-Day, San Francisco (1968).

[7] J. Madore, *Ann. Inst. Henri Poincaré*, **A11** (1969) 221.

[8] W. G. Dixon, *Phil. Trans. Roy. Soc. Lond. A*, **277** (1974) 59.

[9] W. G. Dixon, *Isolated gravitating systems in General Relativity*, Proceedings of the International School of Physics "Enrico Fermi," Course LXVII, edited by J. Ehlers, North Holland, Amsterdam (1979), page 156.

[10] D. Puetzfeld and Yu. N. Obukhov, *Phys. Rev. D.*, **76** (2007) 084025.

[11] W. G. Dixon, *Acta Phys. Pol. B Proc. Suppl.*, **1** (2008) 27.

[12] J. Frenkel, *Z. Phys.*, **37** (1926) 243.

[13] J. Weyssenhoff and A. Raabe, *Acta Phys. Pol.*, **9** (1947) 7.

[14] N. Kudryashova and Yu. N. Obukhov, *Phys. Lett. A*, **374** (2010) 3801.

[15] F. A. E. Pirani, *Acta Phys. Pol.*, **15** (1956) 389.

[16] W. Beiglböck, *PhD. thesis, University of Hamburg* (1965).

[17] W. Beiglböck, *Commun. Math. Phys.*, **5** (1967) 106.

[18] R. Schattner, *Gen. Rel. Grav.*, **10** (1979) 377.

[19] R. Schattner, *Gen. Rel. Grav.*, **10** (1979) 395.

[20] Yu. N. Obukhov and D. Puetzfeld, *Phys. Rev. D.*, **83** (2011) 044024.

[21] A. H. Bokhari and A. Quadir, *J. Math. Phys.*, **28** (1987) 1019.

DIRAC PARTICLE SPIN IN STRONG GRAVITATIONAL FIELDS

Yu.N. Obukhov [1], A.J. Silenko [2 †] and O.V. Teryaev [3]

(1) *Department of Mathematics, University College London, London, UK*
(2) *Research Institute of Nuclear Problems, Belarusian State University, Minsk, Belarus*
(3) *Bogoliubov Laboratory of Theoretical Physics, JINR, Dubna, Russia*
† *E-mail: silenko@inp.bsu.by*

Abstract

Dynamics of the Dirac particle spins in the general strong gravitational and electromagnetic fields is discussed. The general Hermitian Dirac Hamiltonian is derived. For the spatially isotropic metric, it is transformed to the Foldy-Wouthuysen representation. The quantum mechanical equations of motion are obtained and their semiclassical limit is analyzed. The agreement between the quantum mechanical and classical equations is shown. The helicity dynamics is calculated. Squaring the covariant Dirac equation explicitly shows a similarity of the interactions of electromagnetic and gravitational fields with a charged and spinning particle.

We analyze the dynamics of the Dirac particle spins in the general strong gravitational and electromagnetic fields. All denotations correspond to Ref. [1]. The spinor covariant derivatives are given by

$$D_\alpha = e^i_\alpha D_i, \qquad D_i = \partial_i + \frac{iq}{\hbar c}\,A_i + \frac{i}{4}\sigma^{\alpha\beta}\Gamma_{i\,\alpha\beta}. \tag{1}$$

The Dirac particle is characterized by the electric charge q, and A_i is the 4-potential of the electromagnetic field.

In our previous works, the Dirac particles in static and stationary spacetimes have been investigated in the weak field approximation [1–4]. Here we use the isotropic spatial coordinates, derive the general Hermitian Dirac Hamiltonian and then transform it to the Foldy-Wouthuysen (FW) representation.

The general form of the line element of an arbitrary gravitational field is given by

$$ds^2 = V^2c^2dt^2 - \delta_{\widehat{a}\widehat{b}}W^{\widehat{a}}{}_c W^{\widehat{b}}{}_d\,(dx^c - K^c cdt)\,(dx^d - K^d cdt). \tag{2}$$

The functions V and K^a, as well as the components of the 3×3 matrix $W^{\widehat{a}}{}_b$ may depend arbitrarily on t, x^a. The off-diagonal metric components g_{0a} are related to the effects of rotation. For the spatially isotropic coordinates,

$$V = V(x), \qquad W^{\widehat{a}}{}_b = \delta^a_b\,W(x), \qquad K^a = \frac{1}{c}\epsilon^{abc}\omega_b(x)x_c. \tag{3}$$

The Kerr metric in these coordinates is defined by

$$\begin{aligned} V &= \left(1-\frac{\mu}{2r}\right)\left(1+\frac{\mu}{2r}\right)^{-1} - \frac{\mu a^2 - 3\mu(\boldsymbol{a}\cdot\boldsymbol{n})^2}{2r^3} + \mathcal{O}(a^2r^{-4}),\\ W &= \left(1+\frac{\mu}{2r}\right)^2 + \frac{\mu a^2 - 3\mu(\boldsymbol{a}\cdot\boldsymbol{n})^2}{2r^3} + \mathcal{O}(a^2r^{-4}),\\ \boldsymbol{\omega} &= \frac{2\mu c}{r^3}\,\boldsymbol{a}\left(1-\frac{3\mu}{r}+\frac{21\mu^2}{4r^2}\right) + \mathcal{O}(a^3r^{-5}). \end{aligned} \tag{4}$$

Here $r := \sqrt{\boldsymbol{x}\cdot\boldsymbol{x}}$ and $\boldsymbol{n} = \boldsymbol{r}/r$. The expansion in powers of a/r is used. The constant vector $\boldsymbol{a} = (0, 0, a)$ is the rotation parameter of the Kerr solution and $\boldsymbol{a}\cdot\boldsymbol{n} = az/r$. Also, $\mu = GM/c^2$; the total mass M and the total angular momentum $\boldsymbol{J} = Mc\boldsymbol{a}$ define the Kerr black hole uniquely. These equations are obtained from the Arnowitt-Deser-Misner form [6] of the Kerr solution found earlier by Hergt and Schäfer [7] after dropping the terms violating the isotropy. In the weak field approximation, the Kerr metric reduces to the Lense-Thirring one. We have studied the dynamics of quantum and classical spin in this approximation in Ref. [1].

In order to discuss the Dirac spinors, we need the orthonormal frames. The preferable choice [1] is the Schwinger gauge:

$$e_i^{\widehat{0}} = V\,\delta_i^0, \qquad e_i^{\widehat{a}} = W^{\widehat{a}}{}_b\left(\delta_i^b - cK^b\,\delta_i^0\right), \qquad a = 1, 2, 3. \tag{5}$$

Tetrad (5) is characterized by the condition $e_a^{\widehat{0}} = 0, a = 1, 2, 3$.

The *Hermitian* Hamiltonian corresponding to the Dirac equation reads

$$\mathcal{H} = \beta mc^2 V + q\Phi + \frac{c}{2}\left(\pi_b\,\mathcal{F}^b{}_a\alpha^a + \alpha^a\mathcal{F}^b{}_a\pi_b\right) + \frac{c}{2}\left(\boldsymbol{K}\cdot\boldsymbol{\pi} + \boldsymbol{\pi}\cdot\boldsymbol{K}\right) + \frac{\hbar c}{4}\left(\Upsilon\gamma_5 + \boldsymbol{\Xi}\cdot\boldsymbol{\Sigma}\right), \tag{6}$$

where $V = e_0^{\widehat{0}}$, $\mathcal{F}^b{}_a = \sqrt{-g}e_{\widehat{a}}^b = VW^b{}_{\widehat{a}}$, $\pi_i = i\hbar\partial_i - \frac{q}{c}A_i$, and

$$\Upsilon = -V\epsilon^{\widehat{a}\widehat{b}\widehat{c}}\Gamma_{\widehat{a}\widehat{b}\widehat{c}} = -V\epsilon^{\widehat{a}\widehat{b}\widehat{c}}\mathcal{C}_{\widehat{a}\widehat{b}\widehat{c}}, \qquad \Xi_{\widehat{a}} = \frac{V}{c}\,\epsilon_{\widehat{a}\widehat{b}\widehat{c}}\Gamma_{\widehat{0}}{}^{\widehat{b}\widehat{c}} = \epsilon_{\widehat{a}\widehat{b}\widehat{c}}\,\mathcal{Q}^{\widehat{b}\widehat{c}}. \tag{7}$$

For the static and stationary rotating configurations, the pseudoscalar invariant vanishes ($\epsilon^{\widehat{a}\widehat{b}\widehat{c}}\mathcal{C}_{\widehat{a}\widehat{b}\widehat{c}} = 0$), and thus the corresponding term was absent in the special cases considered earlier [1]. But in general this term contributes to the Dirac Hamiltonian. Hamiltonian (6) is one of our central results and covers the general case of a spin-1/2 particle in an arbitrary curved spacetime.

We perform the FW transformation of the Dirac Hamiltonian with the help of the method developed in Ref. [8]. For the spatially isotropic metric (2),(3) with the Schwinger gauge, the FW Hamiltonian reads

$$\mathcal{H}_{FW} = \mathcal{H}_{FW}^{(1)} + \mathcal{H}_{FW}^{(2)}, \tag{8}$$

where

$$\begin{gathered}
\mathcal{H}_{FW}^{(1)} = \beta\epsilon' - \beta\tfrac{\hbar mc^4}{4}\left\{\tfrac{1}{2\epsilon'^2 + mc^2\{\epsilon', V\}}, \left[\boldsymbol{\Sigma}\cdot(\boldsymbol{\Phi}\times\boldsymbol{p}) - \boldsymbol{\Sigma}\cdot(\boldsymbol{p}\times\boldsymbol{\Phi}) + \hbar\boldsymbol{\nabla}\cdot\boldsymbol{\Phi}\right]\right\} \\
+\beta\tfrac{\hbar c^2}{16}\left\{\tfrac{1}{\epsilon'}, \left[\boldsymbol{\Sigma}\cdot(\boldsymbol{\mathcal{G}}\times\boldsymbol{p}) - \boldsymbol{\Sigma}\cdot(\boldsymbol{p}\times\boldsymbol{\mathcal{G}}) + \hbar\boldsymbol{\nabla}\cdot\boldsymbol{\mathcal{G}}\right]\right\}, \\
\mathcal{H}_{FW}^{(2)} = \tfrac{c}{2}\left(\boldsymbol{K}\cdot\boldsymbol{p} + \boldsymbol{p}\cdot\boldsymbol{K}\right) + \tfrac{\hbar c}{4}\boldsymbol{\Sigma}\cdot(\boldsymbol{\nabla}\times\boldsymbol{K}) - \tfrac{\hbar c^3}{16}\left\{\tfrac{1}{2\epsilon'^2 + mc^2\{\epsilon', V\}}, \{\mathcal{F}^2, \boldsymbol{\Sigma}\cdot\boldsymbol{Q}\}\right\}, \\
\epsilon' = \sqrt{m^2c^4V^2 + \tfrac{1}{2}c^2\{\mathcal{F}^2, \boldsymbol{p}^2\}}, \quad \boldsymbol{\mathcal{G}} = \boldsymbol{\nabla}(\mathcal{F}^2), \quad \boldsymbol{\Phi} = \mathcal{F}^2\boldsymbol{\nabla}V, \quad \boldsymbol{Q} = \boldsymbol{p}\times\boldsymbol{\nabla}\left(\boldsymbol{K}\cdot\boldsymbol{p}\right. \\
\left.+\boldsymbol{p}\cdot\boldsymbol{K}\right) - \boldsymbol{\nabla}\left(\boldsymbol{K}\cdot\boldsymbol{p} + \boldsymbol{p}\cdot\boldsymbol{K}\right)\times\boldsymbol{p} - \boldsymbol{p}\times(\boldsymbol{p}\times(\boldsymbol{\nabla}\times\boldsymbol{K})) - ((\boldsymbol{\nabla}\times\boldsymbol{K})\times\boldsymbol{p})\times\boldsymbol{p}.
\end{gathered} \tag{9}$$

The dynamical equation for the spin is obtained from the commutator of the FW Hamiltonian with the polarization operator $\boldsymbol{\Pi} = \beta\boldsymbol{\Sigma}$ and is given by

$$\frac{d\boldsymbol{\Pi}}{dt} = \frac{i}{\hbar}[\mathcal{H}_{FW}, \boldsymbol{\Pi}] = \boldsymbol{\Omega}^{(1)}\times\boldsymbol{\Sigma} + \boldsymbol{\Omega}^{(2)}\times\boldsymbol{\Pi}, \tag{10}$$

where $\boldsymbol{\Omega}^{(1)}$ is the operator of angular velocity of the spin rotation in the static gravitational field,

$$\boldsymbol{\Omega}^{(1)} = -\frac{mc^4}{2}\left\{\frac{1}{2\epsilon'^2 + mc^2\{\epsilon', V\}}, (\boldsymbol{\Phi}\times\boldsymbol{p} - \boldsymbol{p}\times\boldsymbol{\Phi})\right\} + \frac{c^2}{8}\left\{\frac{1}{\epsilon'}, (\boldsymbol{\mathcal{G}}\times\boldsymbol{p} - \boldsymbol{p}\times\boldsymbol{\mathcal{G}})\right\}, \quad (11)$$

and the contribution from the nondiagonal part of the metric is equal to

$$\boldsymbol{\Omega}^{(2)} = \frac{c}{2}\boldsymbol{\nabla}\times\boldsymbol{K} - \frac{c^3}{8}\left\{\frac{1}{2\epsilon'^2 + mc^2\{\epsilon', V\}}, \{\mathcal{F}^2, \boldsymbol{Q}\}\right\}. \quad (12)$$

It can be proved that quantum mechanical equations (10)–(12) agree with the corresponding classical ones derived from the general Pomeransky-Khriplovich formula [9] with the Schwinger gauge.

It is important to describe the semiclassical evolution of the helicity of a particle propagating in a strong gravitation field. The particle motion can be correctly characterized by the evolution of the *contravariant* world velocity or the unit vector in its direction. As a result, one can unambiguously define the helicity as a projection of the 3-component spin (pseudo)vector *in the particle rest frame* onto the direction of the unit vector along the contravariant velocity *in the world frame*. Thus, the helicity should be defined as

$$\zeta = (\boldsymbol{s}/s)\cdot(\boldsymbol{U}/U) = (\boldsymbol{s}/s)\cdot\boldsymbol{\mathcal{V}}/\mathcal{V},$$

where $\boldsymbol{U} = \{U^1, U^2, U^3\}$ and $\boldsymbol{\mathcal{V}} = \boldsymbol{U}/U^0$. The investigation of the helicity is simplified when the particle trajectory is infinite. In this case, one can apply the fact that the vector $\boldsymbol{N} = \boldsymbol{U}/U$ coincides with the vectors $\boldsymbol{v}/v$ and $\boldsymbol{p}/p$ at the initial and final parts of such a trajectory of the particle because of the very large distance to the field source. Here $\boldsymbol{v} = \{v^{\hat{1}}, v^{\hat{2}}, v^{\hat{3}}\}$ is the velocity in the anholonomic *coframe* and $\boldsymbol{p} = \{-p_1, -p_2, -p_3\}$ is the *covariant* momentum entering the classical and quantum Hamiltonians. For the spatially isotropic metric, the change of the helicity on the whole trajectory can be given by $\Delta\zeta' = \Delta\zeta$, where $\zeta' = (\boldsymbol{s}/s)\cdot\boldsymbol{n}$, $\boldsymbol{n} = \boldsymbol{v}/v = \boldsymbol{p}/p$. Evidently, $\zeta' = \cos\chi$, where χ is an angle between the $\boldsymbol{s}$ and $\boldsymbol{n}$ vectors.

In the semiclassical approximation, the angular velocity of the spin rotation *with respect to the momentum direction* is

$$\boldsymbol{o} = \frac{c^2}{\mathcal{F}V\gamma v}\,\boldsymbol{n}\times\boldsymbol{\Phi} + \frac{c}{2\gamma}\left[\boldsymbol{n}\times\boldsymbol{\nabla}(\boldsymbol{n}\cdot\boldsymbol{K}) + \boldsymbol{n}\times(\boldsymbol{n}\cdot\boldsymbol{\nabla})\boldsymbol{K}\right]. \quad (13)$$

This formula coincides with the corresponding classical one. However, Eq. (13) cannot be applied for the particle moving on a finite trajectory because the replacement of ζ by ζ' is incorrect in this case.

The electromagnetic and gravitational contributions to the covariant derivative (1) manifest an obvious similarity of the electromagnetic and gravitational effects. We further clarify this similarity by analyzing the squared Dirac equation.

Acting with the conjugate Dirac operator $(i\hbar\gamma^\alpha D_\alpha + mc)$ on the Dirac equation, we find the squared equation which can be reduced to the form

$$\left(-\hbar^2 g^{ij} D_i D_j - \frac{\hbar q}{2c}\,\sigma^{\alpha\beta}F_{\alpha\beta} + \frac{\hbar^2}{4}\,R - m^2c^2\right)\psi = 0, \quad (14)$$

where $F_{\alpha\beta} = e^i_\alpha e^j_\beta F_{ij}$ are the tensor-like electromagnetic field coefficients. The special form of Eq. (14) for the Dirac particle in a gravitational field has been obtained in Ref. [10].

Explicit computation yields

$$\begin{array}{c}\left[\pi^i\pi_i - \frac{\hbar}{2}\sigma^{\alpha\beta}\left(\frac{q}{c}F_{\alpha\beta} + m\Phi_{\alpha\beta}\right) + \frac{\hbar^2}{4}R + \frac{\hbar^2}{16}T - m^2c^2\right]\psi = 0, \\ T = 2\Gamma^i{}_{\alpha\beta}\Gamma_i{}^{\alpha\beta} + i\varepsilon^{\alpha\beta\mu\nu}\Gamma^i{}_{\alpha\beta}\Gamma_{i\,\mu\nu}\gamma_5, \quad \Phi_{\alpha\beta} = \frac{1}{2m}\left\{\pi^i, \Gamma_{i\,\alpha\beta}\right\}, \quad \gamma_5 = -i\hat{\gamma^0}\hat{\gamma^1}\hat{\gamma^2}\hat{\gamma^3}.\end{array} \tag{15}$$

In the semiclassical approximation, $\pi^i = mU^i$, and $\Phi_{\alpha\beta}$ coincides with the spin (and momentum) transport matrix in a gravitational field (see Ref. [1]) and with the tensor-like coefficients $\gamma_{\alpha\beta\lambda}u^\lambda$ [9]. $\Phi_{\alpha\beta}$ is analogous to the electromagnetic field tensor and leads to the Dirac gyro-gravitomagnetic ratio $g_{grav} = 2$ in perfect agreement with the equivalence principle which is also manifested in the interaction of spin with gravity [11]. This means [12] the absence of both the anomalous gravitomagnetic moment and the gravitoelectric dipole moment which are gravitational analogs of the anomalous magnetic moment and the electric dipole moment, respectively. Eq. (15) explicitly shows a similarity of the Dirac particle interactions with electromagnetic and gravitational fields caused by the similarity of the motion of spinning particles in any external classical fields (see Ref. [1]).

This work was supported in part by the BRFFR (Grant No. Ф10D-001), the program of collaboration BLTP/Belarus, the Deutsche Forschungsgemeinschaft (Grants No. HE 528/21-1 and No. 436 RUS 113/881/0), the RFBR (Grants No. 09-02-01149 and No. 09-01-12179), and the Russian Federation Ministry of Education and Science (grant No. MIREA 2.2.2.2.6546).

References

[1] Yu.N. Obukhov, A.J. Silenko, and O.V. Teryaev, Phys. Rev. **D80** (2009) 064044.

[2] A.J. Silenko and O.V. Teryaev, Phys. Rev. **D71** (2005) 064016.

[3] A.J. Silenko and O.V. Teryaev, Phys. Rev. **D76** (2007) 061101(R).

[4] A.J. Silenko, Acta Phys. Polon. B Proc. Suppl. **1** (2008) 87.

[5] F.W. Hehl and W.T. Ni, Phys. Rev. **D42** (1990) 2045.

[6] R. Arnowitt, S. Deser, and C. W. Misner, in *Gravitation: An Introduction to Current Research*, edited by L. Witten (Wiley, New York, 1962).

[7] S. Hergt and G. Schäfer, Phys. Rev. **D77** (2008) 104001; arXiv:0712.1515 [gr-qc].

[8] A.J. Silenko, Phys. Rev. **A77** (2008) 012116.

[9] A.A. Pomeransky and I.B. Khriplovich, Zh. Eksp. Teor. Fiz. **113** (1998) 1537 [J. Exp. Theor. Phys. **86** (1998) 839].

[10] S. M. Christensen and M. J. Duff, Nucl. Phys. **B154** (1979) 301.

[11] I.Yu. Kobzarev, L.B. Okun, Zh. Eksp. Teor. Fiz. **43** (1962) 1904 [Sov. Phys. JETP **16** (1963) 1343].

[12] O. V. Teryaev, Czech. J. Phys. **53** (2003) 47; arXiv:hep-ph/0306301.

AN ANALYTIC REVIEW OF DSPIN-11

A.V. Efremov[1] and J. Soffer[2]

[1]*Joint Institute for Nuclear Research, Dubna, Russia*
E-mail: efremov@theor.jinr.ru
[2]*Department of Physics, Temple University Philadelphia, Pennsylvania 19122-6082, USA*
E-mail: jacques.soffer@gmail.com

Abstract

A short analytical review of the main results of the DSPIN-11 Workshop is given

The XIV-Workshop on high energy spin physics (DSPIN-11) continued a series of similar conferences, the first of which took place 30 years ago in 1981 on the initiative of the outstanding theoretical physicist L.I.Lapidus. Since then each odd year (in even years large International Symposia in spin physics take place) similar conferences have been organized in Protvino or in Dubna. They give a possibility to present and discuss the news accumulated during the year. Another important specific feature was always an opportunity for a large number of physicists from the former USSR and other East European countries for whom distant trips were difficult for the financial (earlier also for bureaucratic) reasons to participate to the conference.

The special feature of this conference was a wider geography and a larger number of participants (113 persons and among them only 12 women) from the countries they represented: Algeria -1, Belarus-4, Belgium -1, Bulgaria -2, China -2, Czech Republic -5, Estonia -1, France -5, Germany -4, Holland -1, India -2, Iran -1, Italy -2, Poland -5, Portugal -1, Russia -25, Slovakia -1, Sweden -1, Switzerland -1, the UK -1, Ukraine -2, the USA -11, Uzbekistan -1, Vietnam -1. As always, many physicists from JINR (about 35) participated to the conference. The reason for the increasing popularity of the conference became, apparently, the fact that this year brought many new experimental results. Some of them were for the first time presented in Dubna.

X.Artru in his work, together with Z. Belghobsi, proposed a simple explanation of the Collins effect and the effect of jet handedness in the model of sequential fragmentation of quark and proposed the program of realization of the model in the Monte Carlo method. Also preliminary results of the new measurements of the structure function g_2 by the HERMES collaboration (A.Ivanilov) were reported for the first time.

Classical experiments on the study of the nucleon spin structure at high energies use both scattering leptons on polarized nucleons (HERMES, JLab, COMPASS) and collisions of the polarized protons (RHIC, IHEP, JINR). The joint description of such different high-energy processes becomes possible due to the application of the fundamental theory of strong interactions, quantum chromodynamics (QCD), and remarkable properties of factorization, local quark-hadron duality and asymptotic freedom, which allow one to calculate the characteristics of a process within the framework of perturbation theory (PT). At the same time, parton distribution functions, correlation and fragmentation functions, which are not calculable and therefore require modeling methods, are universal and do not depend on the process. A number of reports at the conference were dedicated to

the development and application of this type of models (P.Zavada - the original covariant model of nucleon, J.Soffer - quantum statistical model, N.Sharma - chiral model of constituent quarks and others).

The theoretical description of processes with the participation of spin and especially an internal transverse parton motion proves to be, as always, more complicated, so that the number of such functions increases and the picture connected with them loses to a considerable degree the simplicity of a parton model with its probabilistic interpretation. One of the difficulties here is the evolution of these functions with a change in the wavelength of a tester. An approach to its solution was presented in the talk of I.Cherednikov.

The quark helicity distributions in a nucleon are the most well studied so far. The results of their more accurate measurements by the COMPASS (Y. Bedfer) and CLAS (Y.Prok) collaborations were presented. Contemporary experimental data are sufficiently precise to include in their QCD-analysis not only the correction of perturbation theory but also contributions of higher twists (A.Sidorov, O.Shevchenko, V.Khandramay, E.Christova, G.Ramsey, H.Dahiya, D.Strózik-Kotlorz, F.Arbabifar). In this case, the positive polarization of strange quarks is excluded with high probability. However, the polarization of gluons agrees with the results of their direct measurement (although, with large uncertainty thus far) by the COMPASS (K. Kurek, C.Franco) and PHENIX+STAR (A.Bazilevsky, D.Svirida, I.Alekseev) collaborations, and its low value seems insufficient for resolving the so-called nucleon spin crisis.

Hope for its overcoming is now on the contributions of the orbital angular momenta of quarks and gluons which can be determined by measuring the so-called Generalized Parton Distributions (GPD). The 15-year history of their appearance and current situation was dwelled upon in the talk by A.Radyushkin - one of the founders of this direction in QCD. Different theoretical aspects of GPDs were considered in the talks by S.Goloskokov, S.Manaenkov, L.Szimanovski and K.Semenov-Tyan-Shanskiy. Different experimental aspects of their measurements and preparation for new ones were presented in the talks of A.Sandacz, A.Morreale and P.Sznajder (COMPASS), V.Korotkov (HERMES) and V.Kubarovsky (JLab).

Other important spin distribution functions manifest themselves in scattering of transversely polarized particles. The processes in which the polarization of only one particle (initial or final) is known are especially interesting and complicated from the theoretical point of view (and relatively simple from the point of view of experiment – such complementarities frequently occur). Such single spin asymmetries are related to the T-odd effects, i.e. they seemingly break invariance under time reversal. Here, however, we deal with an effective breaking connected not with the true noninvariance of fundamental (in our case, strong, described by QCD) interaction under time reversal, but with its simulations by thin effects of rescattering in the final or initial state.

The effects of single asymmetry have been studied by theorists (including Dubna theorists who have priority in a number of directions) for more than 20 years, but their study received a new impetus in recent years in connection with new experimental data on the single spin asymmetry in the semi-inclusive electro-production of hadrons off a longitudinally and transversely polarized targets (HERMES - V.Korotkov, CLAS - Y.Prok and COMPASS - C.Adolph, S.Elia). In particular, HERMES data on the so-called "Sivers distribution function" for secondary pions, related to the left-right asymmetry of parton distribution in transversely polarized hadron, are described by the existing theory. How-

ever, the data for positive kaons in the region of small x approximately 2,5 times larger than its predictions, which could testify to an essential role of a antiquark Sivers function. However, the new measurements of this asymmetry by the COMPASS collaboration do not confirm this deviation, which favors of another possibility – the influence of higher twist contributions.

New data on the single spin asymmetries of secondary pions and η-mesons in polarized proton-proton collisions with the energies RHIC (200x200 GeV) were presented by the PHENIX (O.Eyser) collaboration. They confirm amazingly large asymmetries in the region of the fragmentation of the polarized proton and their drop to zero in the central region of rapidities and the region of the nonpolarized proton beam obtained earlier at lower energies. This confirms their energy independence. However, PHENIX does not see a large difference in the asymmetries of η- and π^0-mesons obtained earlier by STAR. At the same time particular mechanisms of the origin of these asymmetries remain a riddle so far.

Thus, although single spin asymmetries on the whole are described by the existing theory, their development continues (I.Anikin). The T-odd distribution functions appearing here lose key properties of universality and become "effective", dependent on the process in which they are observed. In particular, the most fundamental QCD prediction is the change of the sign of the Sivers function in passing from the pion electro-production process to the Drell-Yan pair production on a transversely polarized target. This conclusion is planned to be checked in the COMPASS experiment (A.Guskov) and at colliders RHIC (L.Nogach), NICA and PANDA-PAX (M.Destefanis).

Significant interest and discussions were caused by new JLab data presented at the conference on measurements of the ratio of proton electric and magnetic form factors performed by the "technique of the recoil polarization" (Ch.Perdrisat). The previous JLab measurements showed that this relation was not constant, as it was considered for a long time, but linearly decreases with increase of momentum transfer Q^2 (the so-called "form factor crisis"). New data obtained in the past year (experiment GEp(III) with JINR participation) indicate flattening of this ratio in the Q^2=6-8 $[GeV]^2$ region. A question whether this behavior is due to incomplete calculation of radiative corrections, in particular, two-photon exchange, remains open yet.

As always, the sources of polarized particles (M.Chetvertkov, Yu.Plis, D.Karlovets), physics of the acceleration of polarized beams (Yu.Kondratenko), physics of polarimeters (V.Ladygin, A.Zelenskiy, M.Runtso, D.Smirnov), and the polarized target technique (Yu.Kiselev) were discussed at the conference.

Great interest was generated by the first results of experiments at the Large Hadron Collider (LHC) in CERN relating to spin physics (C. Buszello). In particular, the determination of spin and quantum numbers of Higgs- and Z-bosons, polarization of W, and also the spin phenomena in heavy quark physics. A number of talks were devoted to theoretical possibilities of Z' search and other exotics at LHC and future International Linear Collider (ILC) of electrons (V.Andreev, A.Tsitrinov, J.Körner).

Finally, considerable attention was given to the projects of further development of polarization studies. A large and detailed report about the project of eRHIC (collider of polarized protons of 250 GeV and nuclei with polarized electrons of 20 GeV) at BNL made by E.Aschenauer. Having a large luminosity (10^{34}), it will make it possible to increase the accuracy in measurement of gluon and quark spin distribution functions in a proton,

as well as GPDs by an order of magnitude. The plans of further studies at the modified accelerator at JLab (Y.Prok, V.Kubarovsky) were also discussed. The program of polarized proton beam formation from decay of Lambda-particles at the IHEP accelerator U-70 in Protvino for spin studies at the installation SPASCHARM under construction was presented by S.Nurushev. He emphasized the importance of the comparative study of the spin effects induced by particles and antiparticles. However special interest was caused by the plans of creation at IKP (Jüulich) of a unique European complex for determining the electric dipole moment (EDM) of a proton and nuclei (very detailed talk of N.Nikolaev). The matter is that the dipole moment of fundamental particles violates both space and time parity and its detection would indicate violation of the Standard Model and, in particular, a possibility of approach to the problem of understanding of baryon asymmetry of the Universe. The projected complex will make it possible to lower the limit of deuteron EDM measurement up to 10^{-24}.

The reports relate on the development at LHEP accelerating complex of JINR were also presented in the program of the conference (R.Kurilkin, N.Ladygina). The newest methods and the results of calculations of specific features of spin dynamics under acceleration at the Nuclotron of polarized protons and the lightest nuclei were also reflected (Yu.Kondratenko). Some new proposals for conducting polarization studies on the basis of the modernized complex Nuclotron-M and at the complex NICA projected at JINR were presented (O.Teryaev, O.Selyugin). Within the framework of DSPIN-11 two working discussions (leader A.Kovalenko) of vital problems of the infrastructure development for further studies in spin physics at the complex Nuclotron/NICA took place in which specialists of JINR, BNL, MEPI, ITEP and INR participated. Participants heard information about the project "SPRINT" (Spin Physics Research of Infrastructure at Nuclotron) being developed at LHEP, about polarimetry at the complex AGS/RHIC at BNL, in particular, problems of development and use of CNI-polarimeters and possibility of their use at the NICA collider, and other questions.

The spin community represented at the conference supported these plans to create new unique possibilities for conducting polarization studies at the accelerating complex of LHEP at JINR. The accelerating complex with such potentialities will not have competitions from other centers carrying out polarization studies, and the obtained data will help to solve the riddles of the spin effects which have not been solved since the 70s of the past century.

The summary of the meeting was made in the final report by J.Soffer.

The success of the conference was due to the support by the Russian Foundation for Basic Research, International Committee for Spin Physics, "Dynasty" Foundation, European Physical Society and the JINR programs of for international collaboration: Heisenberg-Landau, Bogoliyubov-Infeld and Blokhintsev-Votruba ones. This made it possible to provide noticeable financial support to participants from Russia and other JINR Member States. The materials of the conference, including all presented talks, are available on the site: `http://theor.jinr.ru/~spin/2011/`.

List of participants of DSPIN-11

Name (Institution, Town, Country)	E-mail address
1. **Abramov Victor (IHEP, Protvino, Russia)**	Victor.AbramovATihep.ru
2. **Adolph Christoph (Uni. Erlangen-Nurnberg, Germany)**	cadolphATcern.ch
3. **Alekseev Igor (ITEP, Moscow, Russia)**	igor.alekseevATitep.ru
4. **Andreyeu Vasili (Gomel Uni., Belarus)**	selfdeniedATtut.by
5. **Anikin Igor (JINR, Dubna, Russia)**	anikinATtheor,jinr,ru
6. **Arbabifar Fatemeh (Semnan Uni., Iran)**	farbabifarATgmail.com
7. **Artru Xavier (Uni. Lyon-1, France)**	x.artruATipnl.in2p3.fr
8. **Aschenauer Elke Caroline (BNL, Upton, USA)**	elkeATbnl.gov
9. **Bazilevsky Alexander (BNL, Upton, USA)**	shuraATbnl.gov
10. **Bedfer Yann (CEN, Saclay, France)**	Yann.BedferATcern.ch
11. **Belghobsi Zouina (LPT Uni. Jijel, Algeria)**	belghobATyahoo.fr
12. **Belov Aleksandr (INR, Moscow, Russia)**	belovATinr.ru
13. **Burinskii Alexander (NSI, Moscow, Russia)**	burATibrae.ac.ru
14. **Buszello Claus (Uppsala Uni., Sweden)**	claus.buszelloATcern.ch
15. **Chavleishvili Mikhail (JINR&Uni. "Dubna", Russia)**	chavleiATjinr.ru
16. **Cherednikov Igor (JINR, Dubna, Russia & Uni. Antw., Holland)**	igor.cherednikovATjinr.ru
17. **Chernitskii Alexander (Uni. Eng.&Econ., Petersburg, Russia)**	AAChernitskiiATengec.ru
18. **Chetvertkov Mikhail (MSU, Moscow, Russia)**	match88ATmail.ru
19. **Christova Ekaterina (INR&NE, Sofia, Bulgaria)**	echristoATinrne.bas.bg
20. **Cirilo-Lombardo Diego Julio (JINR, Dubna, Russia)**	diegoATtheor.jinr.ru
21. **Dahiya, Harleen (ANIT, Punjab, India)**	dahiyahATnitj.ac.in
22. **Deconinc Wouter (Coll. W&M, Williamsburg, USA)**	wdeconinckATwm.edu
23. **Destefanis Marco (Uni. Torino/INFN, Italy)**	destefanATto.infn.it
24. **Dorokhov Alexander (JINR, Dubna, Russia)**	dorokhovATtheor.jinr.ru
25. **Efremov Anatoly (JINR, Dubna, Russia)**	efremovATtheor.jinr.ru
26. **Elia, Carmine (Uni. Trieste, Italy)**	carmine.eliaATts.infn.it
27. **Ermolaev Boris (Ioffe PTI, Petersburg, Russia)**	boris.ermolaevATcern.ch
28. **Eyser, Kjeld Oleg (BNL, Upton, USA)**	keyserATbnl.gov
29. **Filip Peter (Inst. Phys. Slovak AS)**	Peter.FilipATsavba.sk
30. **Finger Miroslav (JINR, Dubna, Russia & Charles Uni, Prague CzR)**	miroslav.fingerATmff.cuni.cz
31. **Finger Michael (JINR, Dubna, Russia & Charles Uni, Prague CzR)**	michael.fingerATcern.ch
32. **Fiziev Plamen (JINR, Dubna, Russia)**	fizievATtheor.jinr.ru
33. **Franco Celso (LIP-Lisboa Portugal**	celsoATlip.pt
34. **Gerasimov Sergo (JINR, Dubna, Russia)**	gerasbATtheor.jinr.ru
35. **Glagolev Victor (JINR Dubna Russia)**	glagolevATsunhe.jinr.ru
36. **Goloskokov Sergey (JINR, Dubna, Russia)**	goloskkvAT jinr.ru
37. **Guskov Alexey (JINR, Dubna, Russia)**	avgATnusun.jinr.ru
38. **Ivanilov A. (IHEP, Protvino, Russia)**	ivanilovATihep.ru
39. **Ivanov Igor (Uni. Liege, Belgium)**	Igor.IvanovATulg.ac.be
40. **Janata Antonin (JINR, Dubna, Russia & Charles Uni, Prague CzR)**	janataATnusun.jinr.ru
41. **Kadykov Mikhail (JINR, Dubna, Russia)**	kadykovATjinr.ru
42. **Karlovets Dmitry (Tomsk Polytec., Uni, Russia)**	d.karlovetsATgmail.com
43. **Khandramai Viacheslav (Gomel Tech. Uni., Belarus)**	v.khandramaiATgmail.com
44. **Kiselev Yury, (JINR, Dubna, Russia & CERN)**	yury.kiselevATcern.ch
45. **Klopot Yaroslav (JINR, Dubna, Russia and CERN, CH)**	klopotATtheor.jinr.ru
46. **Kochelev Nikolai (JINR, Dubna, Russia)**	kochelevATtheor.jinr.ru
47. **Koerner Juergen (Uni. Mainz Germany)**	koernerATthep.physik.unimainz.de
48. **Kolganova Elena (JINR, Dubna, Russia)**	keaATtheor.jinr.ru
49. **Kondratenko Anatoli (NPO "Zaryad", Novosibirsk, Russia)**	kondratenkomATmail.ru
50. **Konstantinova Olga A. (Tomsk Uni, Russia)**	olgakonst87ATmail.ru
51. **Korotkov Vladislav (IHEP, Protvino, Russia)**	Vladislav.KorotkovATihep.ru
52. **Kovalenko Aleksandr (JINR, Dubna, Russia)**	kovalen@dubna.ru
53. **Kubarovsky Valery (JLab, NewportNews, USA)**	vpkATjlab.org
54. **Kurek, Krzysztof (SINS, Warsaw, Poland)**	KurekATfuw.edu.pl
55. **Kurilkin Pavel (JINR, Dubna, Russia)**	pkurilATsunhe.jinr.ru
56. **Ladygina Nadezhda (JINR, Dubna, Russia)**	nladyginaATjinr.ru
57. **Ladygin Vladimir (JINR, Dubna, Russia)**	vladyginATjinr.ru
58. **Lednicky Richard (JINR, Dubna, Russia & Ins.Phys., Prague, CzR)**	lednickyATfzu.cz
59. **Lyuboshitz Valery (JINR, Dubna, Russia)**	Valery.LyuboshitzATjinr.ru
60. **Lyuboshitz Vladimir (JINR, Dubna, Russia)**	LyuboshATsunhe.jinr.ru
61. **Machavariani Alexander (JINR, Dubna, Russia)**	machavarATjinr.ru

Name (Institution, Town, Country)	E-mail address
62. **Manayenkov Sergey (PNPI, Gatchina, Russia)**	smanATpnpi.spb.ru
63. **Morreale Astrid (CEA-Saclay, France)**	astrid.morrealeATcern.ch
64. **Musulmanbekov Genis (JINR, Dubna, Russia)**	genisATjinr.ru
65. **Neetika Sharma (Nat.Inst.Tech, Jalandhar, Punjab, India)**	neetikaphyATgmail.com
66. **Neznamov Vasily (FNC, Sarov, Russia)**	neznamovATvniief.ru
67. **Nguyen Suan Han (Vietnam Nat. Uni.)**	Lienbat76ATgmail.com
68. **Nikolaev Nikolai (Ins. f. Kernphysik, Juelich, Germany)**	N.NikolaevATfz-juelich.de
69. **Nogach Larisa (IHEP, Protvino, Russia)**	Larisa.NogachATihep.ru
70. **Nurushev Sandibek (IHEP, Protvino, Russia)**	Sandibek.NurushevATihep.ru
71. **Obukhov Yuri (Univ. College, London, UK)**	obukhovATmath.ucl.ac.uk
72. **Oganesian Armen (ITEP, Moscow, Russia)**	armenATitep.ru
73. **Pak Dmitriy (Uni Uzbek. & Inst. Mod. Phys. Lanzhou, China)**	dmipakATgmail.com
74. **Panebrattsev Yuri (JINR, Dubna, Russia)**	panebratATsunhe.jinr.ru
75. **Perdrisat, Charles (Coll. W&M USA)**	perdrisaATjlab.org
76. **Piskunov Nikolay (JINR, Dubna, Russia)**	piskunovATsunhe.jinr.ru
77. **Plis Yuri (JINR, Dubna, Russia)**	plisATnusun.jinr.ru
78. **Prok Yelena (Christopher Newport Uni, USA)**	yprokATjlab.org
79. **Radyushkin Anatoly (JINR, Dubna, Russia)**	radyushATtheor.jinr.ru
80. **Ramsey Gordon (Loyola Uni Chicago, USA)**	gprATgate.hep.anl.gov
81. **Reznikov Evgeniy (Dnipropetrovsk Uni., Ukrain)**	reznikovevgeniiATmail.ru
82. **Rossiyskaya Natalia (JINR, Dubna, Russia)**	Natalia.RossiyskayaATcern.ch
83. **Runtso Mikhail (MEPhI, Moscow, Russia)**	mfruntsoATmephi.ru
84. **Sandacz Andrzej (SINS, Warsaw, Poland)**	sandaczATfuw.edu.pl
85. **Savin Igor (JINR, Dubna, Russia)**	savinATsunse.jinr.ru
86. **Selyugin Oleg (JINR, Dubna, Russia)**	seluginATtheor.jinr.ru
87. **Semenov-Tyan-Shanskiy, Kiril (Ecole Polytech., France)**	Kirill.SemenovATcpht.polytechnique.fr
88. **Shevchenko Oleg (JINR, Dubna, Russia)**	shevATmail.cern.ch
89. **Shimanskiy Stepan (JINR, Dubna, Russia)**	Stepan.ShimanskiyATjinr.ru
90. **Shirkov Dmitriy (JINR, Dubna, Russia)**	shirkovdATtheor.jinr.ru
91. **Sidorov Alexander (JINR, Dubna, Russia)**	sidorovATtheor.jinr.ru
92. **Silenko Alexander (INP, Belarusian Univ., Minsk)**	silenkoATinp.bsu.by
93. **Sitnik Igor (JINR, Dubna, Russia)**	sitnikATdubna.ru
94. **Smirnov Dmitri (BNL, Upton, USA)**	dsmirnovATbnl.gov
95. **Soffer Jacques (Temple Univ., Philadelphia, USA)**	jacques.sofferATgmail.com
96. **Stepanov Sergey (Cent.JS Absolutist, Dnepropetrovsk, Ukr.)**	steps137ATgmail.com
97. **Strózik-Kotlorz Dorota (Opole Uni. Tech., Poland)**	d.strozik-kotlorzATpo.opole.pl
98. **Studenikin Alexander (MSU, Moscow, Russia)**	studenikATsrd.sinp.msu.ru
99. **Svirida Dmitry (ITEP, Moscow, Russia)**	Dmitry.SviridaATitep.ru
100. **Sznajder Pawel (SINS, Warsaw, Poland)**	pawel.sznajderATcern.ch
101. **Szymanowski Lech (SINS, Warsaw, Poland)**	lechszymATfuw.edu.pl
102. **Terekhin Arkady (JINR, Dubna, Russia)**	taaATuc.jinr.ru
103. **Teryaev Oleg (JINR, Dubna, Russia)**	teryaevATtheor.jinr.ru
104. **Tkachev Leonid (JINR, Dubna, Russia)**	tkatchevATjinr.ru
105. **Tokarev Mikhail (JINR, Dubna, Russia)**	tokarevATjinr.ru
106. **Tsytrinov Andrei (Gomel Tech. Uni., Belarus)**	tsytrinATrambler.ru
107. **Uzikov Yuri (JINR, Dubna, Russia)**	uzikovATnusun.jinr.ru
108. **Veermae Hardi (Tartu Uni., Estonia)**	hardi.veermaeATut.ee
109. **Yudin Ivan (JINR, Dubna, Russia)**	YudinATjinr.ru
110. **Zavada, Petr (Inst. Phys. Prague, CzR)**	zavadaATfzu.cz
111. **Zelenski, Anatoli (BNL, Upton, USA)**	zelenskiATbnl.gov
112. **Zemlyanichkina Elena (JINR, Dubna, Russia)**	Elena.ZemlyanichkinaATsunse.jinr.ru
113. **Zhang Pengming (IMP, Lanzhou, China)**	zhpmATimpcas.ac.cn